molecules

Special Issue Reprint

Heterocycles in Medicinal Chemistry

Edited by
Josef Jampilek

mdpi.com/journal/molecules

MDPI

Heterocycles in Medicinal Chemistry

Heterocycles in Medicinal Chemistry

Guest Editor

Josef Jampilek

MDPI

Basel • Beijing • Wuhan • Barcelona • Belgrade • Novi Sad • Cluj • Manchester

Guest Editor
Josef Jampilek
Department of Chemical
Biology
Palacky University
Olomouc
Czech Republic

Editorial Office
MDPI AG
Grosspeteranlage 5
4052 Basel, Switzerland

This is a reprint of the Special Issue, published open access by the journal *Molecules* (ISSN 1420-3049), freely accessible at: https://www.mdpi.com/journal/molecules/special_issues/Heterocycles_Medicinal_Chemistry.

For citation purposes, cite each article independently as indicated on the article page online and as indicated below:

Lastname, A.A.; Lastname, B.B. Article Title. *Journal Name* **Year**, *Volume Number*, Page Range.

ISBN 978-3-7258-8315-8 (Hbk)
ISBN 978-3-7258-8316-5 (PDF)
https://doi.org/10.3390/books978-3-7258-8316-5

© 2026 by the authors. Articles in this reprint are Open Access and distributed under the Creative Commons Attribution (CC BY) license. The reprint as a whole is distributed by MDPI under the terms and conditions of the Creative Commons Attribution-NonCommercial-NoDerivs (CC BY-NC-ND) license (https://creativecommons.org/licenses/by-nc-nd/4.0/).

Contents

About the Editor . . . . . **vii**

Josef Jampilek
Heterocycles in Medicinal Chemistry
Reprinted from: *Molecules* **2019**, *24*, 3839, https://doi.org/10.3390/molecules24213839 . . . . . **1**

Michelle H. Lee, Rena G. Lapidus, Dana Ferraris and Ashkan Emadi
Analysis of the Mechanisms of Action of Naphthoquinone-Based Anti-Acute Myeloid Leukemia Chemotherapeutics
Reprinted from: *Molecules* **2019**, *24*, 3121, https://doi.org/10.3390/molecules24173121 . . . . . **5**

Wojciech Pająk, Małgorzata Fabijańska, Jakub Wojciechowski, Wojciech M. Wolf, Anna Kilanowicz, Elżbieta Brzezińska and Justyn Ochocki
Fluorimetric Properties of 3-Aminoflavone Biomolecule (3-AF). X-ray Crystal Structure of New Polymorph of 3-AF
Reprinted from: *Molecules* **2019**, *24*, 2927, https://doi.org/10.3390/molecules24162927 . . . . . **25**

Jan Čejka, Ladislav Cvak, Simona Žižková, Bohumil Kratochvíl and Alexandr Jegorov
Dihydrogen Bond in the Aminoborane Complex of a Nicergoline Intermediate
Reprinted from: *Molecules* **2019**, *24*, 2548, https://doi.org/10.3390/molecules24142548 . . . . . **40**

Derya Osmaniye, Begüm Nurpelin Sağlık, Ulviye Acar Çevik, Serkan Levent, Betül Kaya Çavuşoğlu, Yusuf Özkay, Zafer Asım Kaplancıklı and Gülhan Turan
Synthesis and AChE Inhibitory Activity of Novel Thiazolylhydrazone Derivatives
Reprinted from: *Molecules* **2019**, *24*, 2392, https://doi.org/10.3390/molecules24132392 . . . . . **50**

Alfonso Soler-Bistué, Angeles Zorreguieta and Marcelo E. Tolmasky
Bridged Nucleic Acids Reloaded
Reprinted from: *Molecules* **2019**, *24*, 2297, https://doi.org/10.3390/molecules24122297 . . . . . **65**

Marta Szumilak and Andrzej Stanczak
Cinnoline Scaffold—A Molecular Heart of Medicinal Chemistry?
Reprinted from: *Molecules* **2019**, *24*, 2271, https://doi.org/10.3390/molecules24122271 . . . . . **82**

Jana Kubíčková, Katarína Elefantová, Lucia Pavlikova, Martin Cagala, Mário Šereš, Peter Šafář, et al.
Screening of Phenanthroquinolizidine Alkaloid Derivatives for Inducing Cell Death of L1210 Leukemia Cells with Negative and Positive P-glycoprotein Expression
Reprinted from: *Molecules* **2019**, *24*, 2127, https://doi.org/10.3390/molecules24112127 . . . . . **107**

Monika Šuleková, Lucia Váhovská, Alexander Hudák, Lukáš Žid and Vladimír Zeleňák
A Study of 5-Fluorouracil Desorption from Mesoporous Silica by RP-UHPLC
Reprinted from: *Molecules* **2019**, *24*, 1317, https://doi.org/10.3390/molecules24071317 . . . . . **124**

Wenzhi Wang, Lei Lei, Zhi Liu, Hongbo Wang and Qingguo Meng
Design, Synthesis, and Biological Evaluation of Novel Nitrogen Heterocycle-Containing Ursolic Acid Analogs as Antitumor Agents
Reprinted from: *Molecules* **2019**, *24*, 877, https://doi.org/10.3390/molecules24050877 . . . . . **139**

Viviana Pardo-Jiménez, Patricio Navarrete-Encina and Guillermo Díaz-Araya
Synthesis and Biological Evaluation of Novel Thiazolyl-Coumarin Derivatives as Potent Histone Deacetylase Inhibitors with Antifibrotic Activity
Reprinted from: *Molecules* **2019**, *24*, 739, https://doi.org/10.3390/molecules24040739 . . . . . **153**

Amra Ibric, Stefan Eckerstorfer, Martin Eder, Ivan Louko, Leopold Tunjic, Petra Heffeter, et al.
Position-Selective Synthesis and Biological Evaluation of Four Isomeric A-Ring Amino Derivatives of the Alkaloid Luotonin A
Reprinted from: *Molecules* **2019**, *24*, 716, https://doi.org/10.3390/molecules24040716 . . . . . **176**

Aneta Pokorna, Pavel Bobal, Michal Oravec, Lucie Rarova, Janette Bobalova and Josef Jampilek
Investigation of Permeation of Theophylline through Skin Using Selected Piperazine-2,5-Diones
Reprinted from: *Molecules* **2019**, *24*, 566, https://doi.org/10.3390/molecules24030566 . . . . . **194**

Mariana Paola Espinosa-Valdés, Sara Borbolla-Alvarez, Ana Elena Delgado-Espinosa, Juan Francisco Sánchez-Tejeda, Anabelle Cerón-Nava, Osvaldo Javier Quintana-Romero, et al.
Synthesis, In Silico, and In Vitro Evaluation of Long Chain Alkyl Amides from 2-Amino-4-Quinolone Derivatives as Biofilm Inhibitors
Reprinted from: *Molecules* **2019**, *24*, 327, https://doi.org/10.3390/molecules24020327 . . . . . **208**

Samir M. Awad, Yasser M. Zohny, Sahar A. Ali, Shahenda Mahgoub and Ahmed M. Said
Design, Synthesis, Molecular Modeling, and Biological Evaluation of Novel Thiouracil Derivatives as Potential Antithyroid Agents
Reprinted from: *Molecules* **2018**, *23*, 2913, https://doi.org/10.3390/molecules23112913 . . . . . **226**

Ameen Ali Abu-Hashem
Synthesis of New Furothiazolo Pyrimido Quinazolinones from Visnagenone or Khellinone and Antimicrobial Activity
Reprinted from: *Molecules* **2018**, *23*, 2793, https://doi.org/10.3390/molecules23112793 . . . . . **240**

Ana Bettencourt, Marián Castro, João Silva, Francisco Fernandes, Olga Coutinho, M. João Sousa, et al.
New Nitrogen Compounds Coupled to Phenolic Units with Antioxidant and Antifungal Activities: Synthesis and Structure–Activity Relationship
Reprinted from: *Molecules* **2018**, *23*, 2530, https://doi.org/10.3390/molecules23102530 . . . . . **260**

Ivan Malík, Jozef Csöllei, Ivan Solovič, Šárka Pospíšilová, Hana Michnová, Josef Jampílek, et al.
Dibasic Derivatives of Phenylcarbamic Acid against Mycobacterial Strains: Old Drugs and New Tricks?
Reprinted from: *Molecules* **2018**, *23*, 2493, https://doi.org/10.3390/molecules23102493 . . . . . **270**

Pavel Lasák, Kamil Motyka, Vladimír Kryštof and Jakub Stýskala
Synthesis, Bacteriostatic and Anticancer Activity of Novel Phenanthridines Structurally Similar to Benzo[*c*]phenanthridine Alkaloids
Reprinted from: *Molecules* **2018**, *23*, 2155, https://doi.org/10.3390/molecules23092155 . . . . . **307**

Bartolomeo Bosco, Andrea Defant, Andrea Messina, Tania Incitti, Denise Sighel, Angela Bozza, et al.
Synthesis of 2,6-Diamino-Substituted Purine Derivatives and Evaluation of Cell Cycle Arrest in Breast and Colorectal Cancer Cells
Reprinted from: *Molecules* **2018**, *23*, 1996, https://doi.org/10.3390/molecules23081996 . . . . . **331**

About the Editor

Josef Jampilek

Josef Jampilek completed his Ph.D. degree in Medicinal Chemistry at the Faculty of Pharmacy of the Charles University (Czechia) in 2004. In 2004–2011, he worked in expert and managerial posts in the R&D Division of the pharmaceutical company Zentiva (Czechia). Prof. Jampilek deepened his professional knowledge at the Medicinal Chemistry Institute of the Heidelberg University (Germany) and through multiple specialized courses. In 2017, he was designated as a Full Professor of Medicinal Chemistry. He works at the Faculty of Science of the Palacky University in Olomouc (Czechia) and the Faculty of Natural Sciences of the Comenius University in Bratislava (Slovakia). In addition, he is a visiting professor at the University of Silesia in Katowice (Poland) and an invited professor/expert at various higher educational institutions. He is an author/co-author of more than 30 patents/patent applications, more than 300 peer-reviewed scientific publications, 7 textbooks, more than 50 chapters in monographs, and many invited lectures at international conferences and workshops. He also received several awards for his scientific results, e.g., from Aventis, Elsevier, Willey, Sanofi and FDA. Since 2020, he has been listed in the "World's Top 2% Scientists - Leading minds in science" ranking announced by Stanford University and Elsevier. Prof. Jampilek is also an editor, guest editor and member of the editorial boards of several renowned international scientific journals. The research interests of Prof. Jampilek include drug design, medicinal chemistry, chemical biology, as well as transport nanosystems, especially of anti-infective, anti-proliferative and anti-inflammatory agents and agrochemicals.

molecules

MDPI

Editorial

Heterocycles in Medicinal Chemistry

Josef Jampilek [1,2,*]

[1] Department of Analytical Chemistry, Faculty of Natural Sciences, Comenius University, Ilkovicova 6, 842 15 Bratislava, Slovakia

[2] Regional Centre of Advanced Technologies and Materials, Faculty of Science, Palacky University, Slechtitelu 27, 783 71 Olomouc, Czech Republic

Received: 7 October 2019; Accepted: 23 October 2019; Published: 25 October 2019

Heteroatoms constitute a very common fragment of a number of active pharmaceutical ingredients as well as excipients; from the point of view of significance, it is all the same if these are isosterically/bioisosterically replaced carbons/carbon substructures in aliphatic structures or real heterocycles. Many heterocyclic scaffolds can be considered as privilege structures. Most frequently, nitrogen heterocycles or various positional combinations of nitrogen atoms, sulphur, and oxygen in five- or six-membered rings can be found. According to statistics, more than 85% of all biologically-active chemical entities contain a heterocycle. This fact reflects the central role of heterocycles in modern drug design. The application of heterocycles provides a useful tool for modification of solubility, lipophilicity, polarity, and hydrogen bonding capacity of biologically active agents, which results in the optimization of the ADME/Tox properties of drugs or drug candidates. The increasing presence of various heterocycles in drugs is related to advances in synthetic methodologies, such as metal-catalyzed cross-coupling and hetero-coupling reactions, that allow rapid access to a wide variety of functionalized heterocycles. On the other hand, many heterocyclic lead compounds were isolated from natural resources, and their structures were subsequently simplified and modified by medicinal chemists. Thus, heterocycles have critical importance for medicinal chemists, because using them, it is possible to expand the available drug-like chemical space and drive more effective drug discovery programs. As medicinal chemistry is "a chemistry-based discipline, also involving aspects of biological, medical, and pharmaceutical sciences" and "concerned with the invention, discovery, design, identification, and preparation of biologically active compounds, the study of their metabolism, the interpretation of their mode of action at the molecular level and the construction of structure-activity relationships", this Special Issue of *Molecules*, titled "Heterocycles in Medicinal Chemistry", is devoted to the following research topics focused on heterocycles: (i) synthesis and analysis; (ii) natural compounds; (iii) carbohydrates; (iv) drug design; (v) in silico investigations; (vi) biological screening; (vii) chemical biology and biological chemistry; (vii) biomaterials; and in general, other topics related to heterocycles.

The complexity and wideness of this issue are documented by two review articles. The first is a comprehensive up-to-date review focused on cinnoline derivatives exhibiting a broad spectrum of pharmacological activities such as antibacterial, antifungal, antimalarial, anti-inflammatory, analgesic, anxiolytic, and antitumor [1], and the second one deals with the research and applications of nucleotide analogues, especially the second-generation bridged nucleic acids [2].

Highly specific articles both present fluorimetric studies on the crystal structure of the new polymorphic form of 3-aminoflavone [3] and the investigations of the dihydrogen bond in the aminoborane complex of a nicergoline intermediate [4]. Sulekova et al. published a study evaluating the release of 5-fluorouracil from unmodified and modified mesoporous silica matrices [5]. A complex synthesis–analytical–galenical study described the synthesis of several piperazine-2,5-dione derivatives and their transdermal enhancement activity using theophylline as a model drug, and the prepared compounds can be potentially used as excipients in semi-solid drug formulations or transdermal therapeutic systems [6].

A unique screening of new potential drugs is represented by Awad et al. who focused on the design, synthesis, molecular modeling, and biological evaluation of novel 6-n-propyl-2-thiouracil analogues showing a promising anti-thyroid activity profile in reducing levels of thyroid hormones [7]. New histone deacetylases inhibitors derived from thiazolyl–coumarins have been designed by Pardo-Jiménez et al. Disulfide and hydroxamic acid derivatives were the most potent ones. The compounds exhibited antiproliferative effects and triggered a strong decrease in the expression levels of both α-smooth muscle actin and procollagen I; thus, these compounds decreased profibrotic effects on cardiac fibroblasts [8].

Psychiatric and neurodegenerative diseases are on the rise. Most neurodegenerative diseases cannot be cured; only their symptoms can be mitigated, or their progression hampered. Osmaniye et al. have reported the synthesis of novel thiazolylhydrazone derivatives as potential agents affecting Alzheimer's disease by significant selective inhibition of acetylcholinesterase activity [9].

A publication on pharmacological topics presents both the search for mechanisms of actions of naphthoquinone-based chemotherapeutics active against acute myeloid leukemia [10] and studies evaluating cryptopleurine (thienoquinolizidine derivatives and (epi-)benzo analogues) phenanthroquinolizidine alkaloids inducing cell death of leukemia cells [11].

Several piperazine derivatives of ursolic acid analogues synthesized by Wang et al. as anticancer agents showed the IC_{50} values approx. 2 μM on the Hela and MKN45 cell lines. In addition, the compounds induced apoptosis, decreased the apoptosis regulator (BCL2/BAX) ratio, disrupted mitochondrial potential, and suppressed the growth of Hela xenografts in nude mice [12]. A series of four possible A-ring amino derivatives of luotonin A, a topoisomerase I inhibitor, obtained by intramolecular cycloadditions and catalytic transfer hydrogenation, was evaluated for antiproliferative activity towards human tumor cell lines. It was found that the compound significantly arrested G2/M cell cycle, which means that inhibition of topoisomerase I is not the only biological target [13]. Synthesis of 2,6-diamino-substituted purine derivatives as analogues of reversine and their screening against breast and colorectal cancer cells and affecting the cell cycle was described by Bosco et al. The compounds caused a cycle arrest in the G2/M phase. It should be noted that the compounds were effective only in cells, where p53 was deleted or down-regulated [14].

In addition to cancers, the increasing resistance of microbial pathogens to existing drugs remains a global problem. Therefore, the design of new antimicrobial drugs is a major challenge. Based on the naturally occurring compounds khellinone and visnagenone, new furothiazolo pyrimido quinazolinones were synthesized and screened on their antimicrobial activities. Several compounds demonstrated promising antibacterial and antifungal activities [15]. Old drugs become a great inspiration for newly synthesized molecules. Based on the structures of old agents, Malik et al. published a series of dibasic derivatives of phenylcarbamic acid significantly effective against various mycobacterial strains [16]. A series of 1-amino-2-aryliden- amine-1,2-(dicyano)ethenes as antifungal agents effective against yeasts were reported by Bettencourt et al. [17]. Several synthesized long chain alkyl amides of 2-amino-4-quinolones demonstrated a high inhibition of biofilm formation of *Pseudomonas aeruginosa* [18].

Polypharmacology and multi-target drugs are a very popular approach in medicinal chemistry. True to this approach, Lasak et al. prepared a new series of phenanthridines derived from benzo[*c*]phenanthridine alkaloids. Several compounds expressed high antibacterial activity against *Bacillus subtilis*, *Micrococcus luteus*, and/or *Mycobacterium vaccae*, and some derivatives also showed cytotoxicity against K-562 and MCF-7 cancer cell lines. The anti-tumor effective compounds caused an arrest of cell-cycle, apoptosis-specific fragmentation of PARP-1 and increased the levels of p53 protein [19].

Acknowledgments: The guest editor wishes to thank all the authors for their contributions to this Special Issue, all the reviewers for their work in evaluating the submitted articles, and the editorial staff of *Molecules* for their kind assistance.

Conflicts of Interest: The author declares no conflict of interest.

References

1. Szumilak, M.; Stanczak, A. Cinnoline scaffold-A molecular heart of medicinal chemistry? *Molecules* **2019**, *24*, 2271. [CrossRef] [PubMed]
2. Soler-Bistue, A.; Zorreguieta, A.; Tolmasky, M.E. Bridged nucleic acids reloaded. *Molecules* **2019**, *24*, 2297. [CrossRef] [PubMed]
3. Pajak, W.; Fabijanska, M.; Wojciechowski, J.; Wolf, W.M.; Kilanowicz, A.; Brzezinska, E.; Ochocki, J. Fluorimetric properties of 3-aminoflavone biomolecule (3-AF). X-ray crystal structure of new polymorph of 3-AF. *Molecules* **2019**, *24*, 2927. [CrossRef]
4. Cejka, J.; Cvak, L.; Zizkova, S.; Kratochvil, B.; Jegorov, A. Dihydrogen bond in the aminoborane complex of a nicergoline intermediate. *Molecules* **2019**, *24*, 2548. [CrossRef]
5. Sulekova, M.; Vahovska, L.; Hudak, A.; Zid, L.; Zelenak, V. A Study of 5-fluorouracil desorption from mesoporous silica by RP-UHPLC. *Molecules* **2019**, *24*, 1317. [CrossRef] [PubMed]
6. Pokorna, A.; Bobal, P.; Oravec, M.; Rarova, L.; Bobalova, J.; Jampilek, J. Investigation of permeation of theophylline through skin using selected piperazine-2,5-diones. *Molecules* **2019**, *24*, 566. [CrossRef] [PubMed]
7. Awad, S.M.; Zohny, Y.M.; Ali, S.A.; Mahgoub, S.; Said, A.M. Design, synthesis, molecular modeling, and biological evaluation of novel thiouracil derivatives as potential antithyroid agents. *Molecules* **2018**, *23*, 2913. [CrossRef] [PubMed]
8. Pardo-Jiménez, V.; Navarrete-Encina, P.; Diaz-Araya, G. Synthesis and biological evaluation of novel thiazolyl-coumarin derivatives as potent histone deacetylase inhibitors with antifibrotic activity. *Molecules* **2019**, *24*, 739. [CrossRef] [PubMed]
9. Osmaniye, D.; Saglik, B.N.; Acar Cevik, U.; Levent, S.; Kaya Cavusoglu, B.; Ozkay, Y.; Kaplancikli, Z.A.; Turan, G. Synthesis and AChE inhibitory activity of novel thiazolylhydrazone derivatives. *Molecules* **2019**, *24*, 2392. [CrossRef] [PubMed]
10. Lee, M.H.; Lapidus, R.G.; Ferraris, D.; Emadi, A. Analysis of the mechanisms of action of naphthoquinone-based anti-acute myeloid leukemia chemotherapeutics. *Molecules* **2019**, *24*, 3121. [CrossRef] [PubMed]
11. Kubickova, J.; Elefantova, K.; Pavlikova, L.; Cagala, M.; Seres, M.; Safar, P.; Marchalin, S.; Durisova, K.; Bohacova, V.; Sulova, Z.; et al. Screening of phenanthroquinolizidine alkaloid derivatives for inducing cell death of L1210 leukemia cells with negative and positive P-glycoprotein expression. *Molecules* **2019**, *24*, 2127. [CrossRef] [PubMed]
12. Wang, W.; Lei, L.; Liu, Z.; Wang, H.; Meng, Q. Design, synthesis, and biological evaluation of novel nitrogen heterocycle-containing ursolic acid analogs as antitumor agents. *Molecules* **2019**, *24*, 877. [CrossRef] [PubMed]
13. Ibric, A.; Eckerstorfer, S.; Eder, M.; Louko, I.; Tunjic, L.; Heffeter, P.; Schueffl, H.H.; Marian, B.; Haider, N. Position-selective synthesis and biological evaluation of four isomeric A-ring amino derivatives of the alkaloid luotonin A. *Molecules* **2019**, *24*, 716. [CrossRef] [PubMed]
14. Bosco, B.; Defant, A.; Messina, A.; Incitti, T.; Sighel, D.; Bozza, A.; Ciribilli, Y.; Inga, A.; Casarosa, S.; Mancini, I. Synthesis of 2,6-diamino-substituted purine derivatives and evaluation of cell cycle arrest in breast and colorectal cancer cells. *Molecules* **2018**, *23*, 1996. [CrossRef] [PubMed]
15. Abu-Hashem, A.A. Synthesis of new furothiazolo pyrimido quinazolinones from visnagenone or khellinone and antimicrobial activity. *Molecules* **2018**, *23*, 2793. [CrossRef] [PubMed]
16. Malik, I.; Csollei, J.; Solovic, I.; Pospisilova, S.; Michnova, H.; Jampilek, J.; Cizek, A.; Kapustikova, I.; Curillova, J.; Pechacova, M.; et al. Dibasic derivatives of phenylcarbamic acid against mycobacterial strains: Old drugs and new tricks? *Molecules* **2018**, *23*, 2493. [CrossRef] [PubMed]
17. Bettencourt, A.; Castro, M.; Silva, J.; Fernandes, F.; Coutinho, O.; Sousa, M.J.; Proenca, M.F.; Areias, F. New nitrogen compounds coupled to phenolic units with antioxidant and antifungal activities: Synthesis and structure-activity relationship. *Molecules* **2018**, *23*, 2530. [CrossRef] [PubMed]

18. Espinosa-Valdes, M.P.; Borbolla-Alvarez, S.; Delgado-Espinosa, A.E.; Sanchez-Tejeda, J.F.; Ceron-Nava, A.; Quintana-Romero, O.J.; Ariza-Castolo, A.; Garcia-Del Rio, D.F.; Loza-Mejia, M.A. Synthesis, in silico, and in vitro evaluation of long chain alkyl amides from 2-amino-4-quinolone derivatives as biofilm inhibitors. *Molecules* **2019**, *24*, 327. [CrossRef] [PubMed]
19. Lasak, P.; Motyka, K.; Krystof, V.; Styskala, J. Synthesis, bacteriostatic and anticancer activity of novel phenanthridines structurally similar to benzo[c]phenanthridine alkaloids. *Molecules* **2018**, *23*, 2155. [CrossRef] [PubMed]

© 2019 by the author. Licensee MDPI, Basel, Switzerland. This article is an open access article distributed under the terms and conditions of the Creative Commons Attribution (CC BY) license (http://creativecommons.org/licenses/by/4.0/).

molecules

MDPI

Article

Analysis of the Mechanisms of Action of Naphthoquinone-Based Anti-Acute Myeloid Leukemia Chemotherapeutics

Michelle H. Lee [1,2], Rena G. Lapidus [1,2], Dana Ferraris [3] and Ashkan Emadi [1,2,*]

1 Department of Medicine Division of Hematology/Oncology University of Maryland School of Medicine, Baltimore, MD 21201, USA
2 Marlene and Stewart Greenebaum Comprehensive Cancer Center, University of Maryland School of Medicine, 22 South Greene Street, Baltimore, MD 21201, USA
3 Department of Chemistry, McDaniel College, 2 College Hill, Westminster, MD 21157, USA
* Correspondence: aemadi@umm.edu; Tel.: +1-410-328-6841; Fax: +1-410-328-6896

Academic Editor: Josef Jampilek
Received: 3 August 2019; Accepted: 25 August 2019; Published: 28 August 2019

Abstract: Acute myeloid leukemia (AML) is a neoplastic disorder resulting from clonal proliferation of poorly differentiated immature myeloid cells. Distinct genetic and epigenetic aberrations are key features of AML that account for its variable response to standard therapy. Irrespective of their oncogenic mutations, AML cells produce elevated levels of reactive oxygen species (ROS). They also alter expression and activity of antioxidant enzymes to promote cell proliferation and survival. Subsequently, selective targeting of redox homeostasis in a molecularly heterogeneous disease, such as AML, has been an appealing approach in the development of novel anti-leukemic chemotherapeutics. Naphthoquinones are able to undergo redox cycling and generate ROS in cancer cells, which have made them excellent candidates for testing against AML cells. In addition to inducing oxidative imbalance in AML cells, depending on their structure, naphthoquinones negatively affect other cellular apparatus causing neoplastic cell death. Here we provide an overview of the anti-AML activities of naphthoquinone derivatives, as well as analysis of their mechanism of action, including induction of reduction-oxidation imbalance, alteration in mitochondrial transmembrane potential, Bcl-2 modulation, initiation of DNA damage, and modulation of MAPK and STAT3 activity, alterations in the unfolded protein response and translocation of FOX-related transcription factors to the nucleus.

Keywords: acute myeloid leukemia (AML); naphthoquinone; reactive oxygen species (ROS); apoptosis; mechanism of action

1. Introduction

1.1. Chemistry of Naphthoquinones

Naphthoquinones ($C_{10}H_6O_2$) are oxidized naphthalenes ($C_{10}H_8$), and similar to other quinones, such as benzoquinone and anthraquinone, as they possess a conjugated electron system that can participate in chemical reactions transporting electrons to other molecules [1]. These reactions can result in the generation of free radicals, including highly active oxygen radicals called reactive oxygen species (ROS) [1]. Production of ROS occurs when quinones are reduced to semiquinones and subsequently to hydroquinones by one- or two-electron reductions via different enzymes [2–4]. While ROS, at low and highly regulated intracellular levels, contribute to normal cellular signaling function; excess ROS plays an important role in damaging cellular components, including proteins, lipids and nucleic acids [5]. Agents with similar structures to naphthoquinones have been approved for use by the FDA. For example, Mitomycin, a benzoquinone, is used in the clinic for intravesical therapy after transurethral resection of bladder

tumor for non-invasive (stage 0) or minimally invasive (stage I) bladder cancers, and in combination with 5-fluorouracil (5-FU) and radiation for treatment of stage I-III anal cancer [6,7]. Anthraquinones, such as daunorubicin, idarubicin, doxorubicin, epirubicin and mitoxantrone are commonly used for the treatment of many hematologic and solid neoplasms [8,9].

Natural and synthetic, oligomeric substituted and heterocyclic naphthoquinone derivatives have shown promising anti-neoplastic activities against epithelial, mesenchymal and hematopoietic malignancies [2,10–12]. Notwithstanding fifty years of basic, translational, and clinical studies, the mechanism by which naphthoquinone-containing agents induce cancer cell death remains somewhat unclear. The apparent redox-cycling and electrophilic properties of naphthoquinones culminating in ROS generation and induction of apoptosis have subjugated the field of mechanistic investigations of these compounds [13,14]. Nevertheless, several other mechanisms, including covalent alkylation of DNA, DNA intercalation, inhibition of topoisomerase II, epigenetic modulation, to name a few, might be significantly contributing to the cause of death in different cancer cells.

1.2. Acute Myeloid Leukemia

Acute myeloid leukemia (AML) is a neoplastic disorder characterized by rapidly proliferating myeloblasts in bone marrow, blood and occasionally other organs resulting in a very poor clinical outcome, particularly in elderly and medically unfit patients. The diverse cytogenetics and molecular mutations of myeloblasts among patients and even within one patient makes AML an extremely heterogeneous blood cancer [15,16]. Irrespective of their genetic characteristics, AML cells generate excess ROS [17]. In turn, these cells have prominent antioxidant machinery to mitigate the effects of additional ROS and maintain cellular oxidative states compatible with cell survival [17,18]. With this in mind, it was hypothesized that naphthoquinone-induced ROS augmentation in myeloblasts could cause an imbalance to the already stressed redox balance, overwhelming the ROS buffering capacity of the AML cells and cause cell death [13]. However, depending on the chemical structures of the naphthoquinone, certain derivatives might negatively affect other cellular machinery involved in the initiation and propagation of neoplastic phenomenon seen in AML. In this article, we aimed to analyze the entire publically available mechanism of actions of naphthoquinone-based anti-AML chemotherapeutics. We believe this will help chemists to synthesize new generations of anti-cancer naphthoquinones and also assist biologists and clinicians to design naphthoquinone-based combination chemotherapies rationally.

2. Results

2.1. Anti-Proliferative Activity

Table 1 shows the naphthoquinone derivatives that have been reported to have anti-AML activity. Mono- or di-substituted monomeric naphthoquinones, including menadione [19], juglone [20], lawson [21], glycinyl-1,4-naphthoquinone [22], plumbagin [23–27], lapachol (and nor-lapachol) [21,28,29], atovaquone [30,31], ramentaceone [32], cordiaquinone J [33], and TW-92 [34] showed anti-AML activity in different AML cell lines and primary cells from AML patients with wide IC_{50}s ranging from 0.6 to 100 micromolar (μM), Table 1. Atovaquone was found to have an additive effect when combined with standard induction chemotherapy (cytarabine and daunorubicin) in AML cell lines [31]. Multi-substituted naphthoquinones, including shikonin [35–39] and its derivative SH-7 [40], and other dihydroxy or dimethoxy 1,4-naphthoquinones [41,42], compared with mono- or di-substituted naphthoquinones, demonstrated superior in vitro activity against AML cells with IC_{50}s ranging 0.1–4 μM. Heterocyclic monomeric naphthoquinones included furanonaphthoquinones FNQ3 [43] and FN6-one [44], β-lapachone [45–49] and nor-β-lapachone [45,46,50,51], dunnione [47], and pterocarpanquinone LQB-118 [28,52]. FNQ3 was significantly more effective than low dose cytarabine in reducing cell viability ($p < 0.001$) and combining the two drugs led to an even greater reduction in cell viability in NB4 and U937 cells ($p < 0.01$) [43].

Table 1. Anti-acute myeloid leukemia (AML) naphthoquinones.

Structure	AML Cell Lines	IC_{50} (μM)	In Vivo	References
Mono- or di-substituted monomeric naphthoquinones				
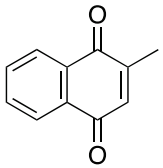 **Menadione** **2-methyl-1,4-naphthoquinone**	HL-60, U937	Not reported directly	Not tested	Yeo HS, et al. 2012
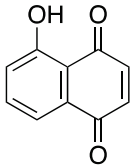 **Juglone** **5-hydroxyl-1,4-naphthoquinone**	HL-60	8	Not tested	Xu HL, et al., 2010
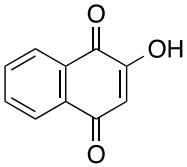 **Lawsone** **2-hydroxyl-1,4-naphthoquinone**	HL-60	>50	Not tested	Esteves-Souza A, et al., 2008
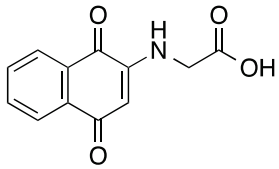 **2-glycinyl-1,4-naphthoquinone**	HL-60	3	Not tested	de Moraes TA, et al., 2014

Table 1. *Cont.*

Structure	AML Cell Lines	IC_{50} (μM)	In Vivo	References
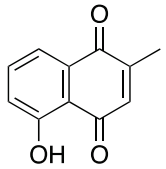 **Plumbagin** **5-hydroxy-2-methyl-1,4-naphthoquinone**	Kasumi-1, HL-60, U937	0.6–1.4	Activity: Tumor volume reduction Tolerability: No significant weight loss, tissue damage or behavior change (Xu KH, et al.)	Kawiak A, et al., 2007 Xu KH, et al., 2010 Gaascht F, et al., 2014 Kong X, et al., 2017 Zhang J, et al., 2017
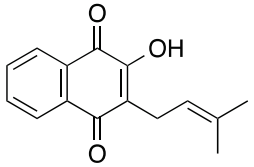 **Lapachol** **2-hydroxy-3-(3-methyl-2-butenyl)-1,4-naphthoquinone**	Kasumi-1 Primary cells from patients HL-60	Not reported directly >50	Not tested	de Souza Reis FR, et al., 2013 Esteves-Souza A, et al., 2008
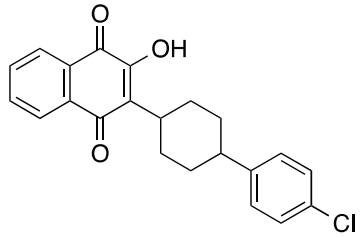 **Atovaquone** ***trans*-2-[4-(4-chlorophenyl)cyclohexyl]-3-hydroxy-1,4-naphthalenedione**	MOLM13, MV4-11, THP-1, NB4, Kasumi-1, HL-60, KG1, HEL	13.7–98.9	Decreased diseased burden and prolonged survival in the treatment group compared to the control group (Stevens AM, et al.)	Xiang M, et al., 2016 Stevens AM, et al., 2017

Table 1. *Cont.*

Structure	AML Cell Lines	IC_{50} (μM)	In Vivo	References
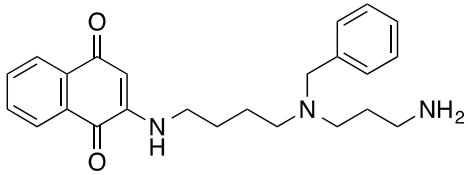 **2-((4-((3-aminopropyl)(benzyl)amino)butyl) amino)naphthalene-1,4-dione**	HL-60	10.5	Not tested	Esteves-Souza A, et al., 2008
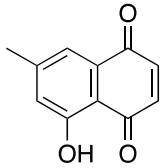 **Ramentaceone 7-Methyljuglone**	HL-60	8.8	Not tested	Kawiak A, et al., 2012
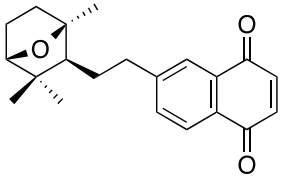 **Cordiaquinone J**	HL-60	2.7	Not tested	Marinho-Filho JD., et al., 2010
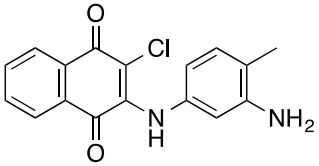 **TW-92 2-chloro-3-(3-amino-4-methyl-phenylamino)-1,4-naphthoquinone**	U937, peripheral blood mononuclear cells from AML patients	3.2	Not tested	Hallak M, et al., 2009

Table 1. *Cont.*

Structure	AML Cell Lines	IC_{50} (μM)	In Vivo	References
Multi-substituted monomeric naphthoquinones				
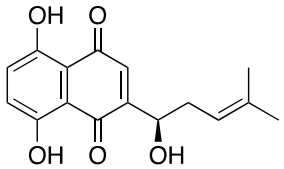 **Shikonin** **5,8-dihydroxy-2[(1*R*)-hydroxy-4-methylpent-3-en-1-yl]-3-methyl-1,4-naphthoquinone**	HL-60, U937, primary AML cells	3.8	Prolonged survival observed in the treatment group compared to the control group (Yang H, et al.)	Yang H, et al., 2009 Zhang B, et al. 2012 Zhao Q, et al., 2015 Trivedi, et al., 2016
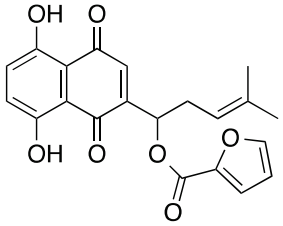 **SH-7** **1-(1,4-dihydro-5,8-dihydroxy-1,4-dioxonaphthalen-2-yl)-4-methylpent-3-enylfuran-2-caroxylate**	HL-60	2	Not tested	Yang F, et al., 2006
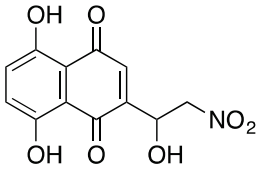 **5,8-dihydroxy-2-(1-hydroxy-2-nitroethyl)-1,4-naphthoquinone**	HL-60	0.14	Not tested	Beretta GL, et al., 2017

Table 1. *Cont.*

Structure	AML Cell Lines	IC_{50} (μM)	In Vivo	References
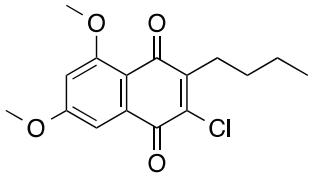 **3-butyl-2-chloro-5,7-dimethoxy-1,4- naphthoquinone**	HL-60	3.8	Not tested	Li K, et al., 2018
Heterocyclic monomeric naphthoquinones				
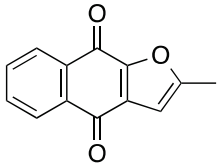 **FNQ3 (Furanonaphthquinone) 2-Methylnaphtho[2–*b*]furan-4,9-dione**	HL60, NB-4, U937, THP1, primary AML cells	5.9–8.2	Not tested	Desmond JC, et al., 2005
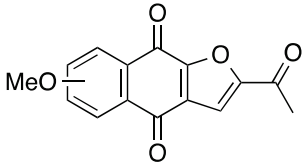 **FN6-one (Furonaphthoquinone)**	HL-60, U937	0.87–3.0	Not tested	Inagaki R, et al., 2013
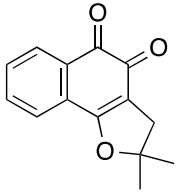 **Nor-β-lapachone**	HL-60, KG1, K562	0.4–17.2	Not tested	da Silva EN Jr, et al. 2007, 2010 Cavalcanti, et al., 2011 Araújo AJ, et al., 2012 Cardoso, et al., 2014

Table 1. *Cont.*

Structure	AML Cell Lines	IC_{50} (μM)	In Vivo	References
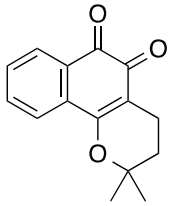 **β-lapachone 3,4-dihydro-2,2-dimethyl-2H-naphtho[1–b]pyran-5,6-dione**	HL-60	7.1	Not tested	Planchon SM, et al., 1995, 1999 da Silva EN Jr, et al. 2007, 2010 Inagaki, et al., 2015
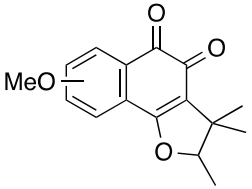 **Dunnione**	HL-60	0.9	Not tested	Inagaki, et al., 2015
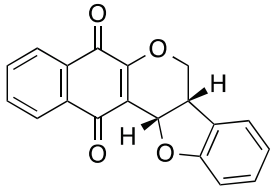 **LQB-118 (pterocarpanquinone)**	HL60, U937, Kasumi-1	6–9	Non-cytotoxic to normal BM cells in healthy control mice.	de Souza Reis, et al., 2013, Nestal De Moraes, et al., 2014

Table 1. *Cont.*

Structure	AML Cell Lines	IC_{50} (μM)	In Vivo	References
Dimeric naphthoquinones				
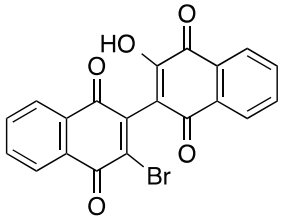 **3-bromo-3′-hydroxyl-dimeric 1,4-naphthoquinone**	MOLM-14, THP-1, primary AML cells	0.36–8.5	Tested for tolerability and side effects with IP and SC injections.	Lapidus, et al., 2016
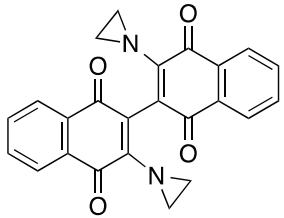 **3,3′-bis-aziridinyl-dimeric 1,4-naphthoquinone**	MOLM-14, THP-1, primary AML cells	0.18–2	Tested for tolerability with IP injections.	Carter-Cooper, et al., 2017

BM = bone marrow, IP = intraperitoneally, SC = subcutaneously.

By inhibiting HIV integrase, the hydroxylated dimeric naphthoquinones were originally synthesized as anti-HIV agents [53,54]. Redox modulating ability of these compounds resulted in studies to determine their potency against AML cells, as well as their therapeutic indices in relation to normal hematopoietic stem cells [4,55]. The IC_{50} values (μM) of 3-bromo-3′-hydroxyl-dimeric 1,4-naphthoquinone (BiQ1) against AML cell lines MOLM-14, THP1, and one primary AML cells from patients, as well as normal bone marrow cells were 5.5 ± 0.8, 4.2 ± 1.9, 0.4 and 14.5, respectively [55]. Bis-aziridinyl dimeric naphthoquinone containing two nitrogen mustard alkylating groups was synthesized to improve the potency and bioavailability of dimeric naphthoquinones [56]. This compound showed a potent anti-leukemic activity (IC_{50} range 0.18–2 μM) against three AML cell lines and four primary AML cells from patients [56]. Of note, the patient-derived AML cells had a heterogeneous cytogenetic and molecular mutation profile. In addition to inducing a decrease in cell survival and viability, exposure to the bis-aziridinyl dimeric naphthoquinone at concentrations relative to the respective IC_{50} values for 24 h resulted in a marked reduction in clonogenic activity—an in vitro assay to assess the capability of a single AML cell in the population to generate a colony—the quintessential anti-cancer in vitro assay [56]. Dimeric naphthoquinones had favorable therapeutic indices as demonstrated by their more potent IC_{50} values in AML cells compared to normal hematopoietic cells.

2.2. In Vivo Tolerability and Efficacy Studies

A few studies tested the tolerability and safety of naphthoquinone derivatives in vivo as wells as their anti-AML activity [4,24,35,40,56]. Plumbagin dosed 2 mg/kg via intraperitoneal injection, IP) daily for three weeks significantly reduced tumor volume in NB4 tumor xenograft in NOD/SCID mice; 153 mm^3 in plumbagin versus 194 mm^3 in control after one week of treatment and approximately 65% tumor volume reduction at the completion of the study [24]. In the same study using the same xenograft model, tumors of mice treated with doxorubicin (1 mg/kg thrice weekly) demonstrated greater regression in tumor volume than those treated with plumbagin ($p < 0.05$). However, doxorubicin at the doses tested was toxic to heart and liver (pathologic findings), whereas plumbagin treated mice did not show any obvious tissue changes.

Our group tested tolerability of a different naphthoquinone containing a compound called BiQ1 in mice dosed via IP and subcutaneous (SC) injections [4]. Mice tolerated eight days of IP injections dosed at 10 mg/kg with no overt weight loss or physical complications. However, mice were unable to ambulate, eat or drink with just two doses of 25 mg/kg IP injections. Interestingly, mice were able to tolerate SC doses of 25 mg/kg with the only overt side effect being irritation at the injection site. The poorer tolerability of IP versus SC at higher dose might be related to the acidity of BiQ1 injected in intra-abdominal cavity of mice causing peritonitis.

Carter-Cooper et al. reported that 3,3′-bis-aziridinyl dimeric naphthoquinone was well tolerated by NOD SCID gamma (NSG) mice after five consecutive days of 5, 10, and 15 mg/kg (IP) without significant weight loss [56]. Finally, Nestal de Moraes et al. reported that naphthoquinone derivatives may be safe against normal bone marrow-derived cells by testing compound LQB-118 IP in mice with normal bone marrow cells [52].

Atovaquone is an FDA-approved, anti-microbial drug that has been well tolerated, even in immunosuppressed patients with organ dysfunction. In a retrospective study of adult AML patients who underwent allogeneic hematopoietic stem cell transplant (HSCT), patients who received atovaquone for longer duration had lower rates of AML relapse over three years compared to those with lower atovaquone exposure (13% versus 23%, $p = 0.037$) [30]. *In vivo*, female mice treated with atovaquone 200 mg/kg daily demonstrated decreased disease burden compared to the control mice [31]. Furthermore, prolonged atovaquone survival of male xenografted mice compared to the control mice (median survival of 63 days in control mice versus only one mouse succumbing to disease by day 70 in the atovaquone group, $p = 0.0048$).

2.3. Mechanisms of Anti-AML Action

2.3.1. Induction of Apoptosis

The primary mechanism by which naphthoquinones reduce AML cell survival is via apoptosis. A dose- and time-dependent increase in apoptosis was observed with several naphthoquinone-based compounds. Induction of apoptosis rather than necrosis as the cause of cell death was evident by changes observed in cell morphology, cell cycle progression, and caspase activation. Interestingly, 5,8-dihydroxy-2-(1-hydroxy-2-nitroethyl)naphthalene-1,4-dione [41] and LQB-118 [52] induced apoptosis without significant changes observed in cell cycle. The anti-AML activity of these naphthoquinones appeared to be mediated through a combination of ROS enhancement and topoisomerase inhibition that ultimately led to DNA damage and cell death.

2.3.2. Alteration in Mitochondrial Membrane Potential

Naphthoquinone derivatives reduce mitochondrial membrane potential (MMP) by the opening of the mitochondrial permeability transition pore resulting in cytochrome C release into the cytosol and activating caspase-3; key features of the intrinsic pathway of apoptosis [57,58]. Hallak et al. reported that TW-74, a chloronaphthoquinone with a methyl group at the meta position, effectively killed U937 myeloid leukemia cells via early reduction of MMP, cytochrome C release and caspase activation [59]. We reported that hydroxylated dimeric naphthoquinone BiQ1 effectively inhibited induced depolarization of the mitochondrial transmembrane potential ($\Delta\Psi m$) as measured by flow cytometry with MitoPotential Red [4].

2.3.3. Reduction-Oxidation Imbalance

ROS are derived from the metabolism of oxygen, and they normally exist in balance with antioxidants in all cells. Oxidative stress occurs when this balance is disrupted, due to excess production of ROS and/or antioxidant diminution. Generation of ROS and the consequent increase in oxidative stress has proven to be fundamental in the cytotoxic activity of naphthoquinone derived compounds. Given the high proliferative index, most AML cells, compared with non-malignant cells, have a higher level of endogenous ROS, lower activities in respiratory chain complex and lower spare reserve capacity [60,61]. This phenomenon, as well as lower compensatory reserves that handle additional oxygen radicals [13,60], make AML cells particularly sensitive to oxidative stress [62]. Several studies have demonstrated that the presence of antioxidants significantly attenuates mitochondrial-dependent apoptosis and cell cycle arrest in naphthoquinone-treated tumor cells [24,34,63]. While antioxidants, such as N-acetyl cysteine (NAC) may serve to lessen naphthoquinone cytotoxicity by neutralizing ROS through increased glutathione production, they also could exert their actions by chemically interacting directly with naphthoquinones or their derivatives to reduce their cytotoxicity [1,64,65].

Much evidence exists in the literature linking redox imbalance and anti-AML activity. Treatment of leukemic cell lines with bis-aziridinyl dimeric naphthoquinone resulted in a dose-dependent increase in intracellular production of ROS within two hours of exposure [56]. Plumbagin similarly demonstrated increased intracellular ROS in NB4 cells that peaked after 1.5 h of exposure with a decline after two hours [66]. Xu and colleagues further demonstrated that ROS production was significantly increased in NB4 cells treated with plumbagin compared to healthy control cells, indicative of selective toxicity against neoplastic cells [24]. The chloro-amino-phenyl naphthoquinone TW-92 induced apoptosis in U937 cells, which was preceded by accumulation of intracellular hydrogen peroxide that was abolished by an inhibitor of NADPH oxidase [34]. U937 cells treated with TW-92 versus untreated cells showed a rapid decline in endogenous glutathione levels (65%) [34]. This depletion of glutathione may have contributed to the intracellular accumulation of hydrogen peroxide. Chau et al. compared intracellular H_2O_2 concentration in HL-60 cells treated with β-lapachone (a naphthoquinone) and camptothecin (a non-quinone topoisomerase inhibitor) [67]. The study found a seven-fold increase in H_2O_2 production in HL-60 cells treated with β-lapachone compared to a less than two-fold increase

in cells treated with camptothecin. This increase in H_2O_2 was markedly reduced in the presence of NAC, which corresponded with reduced β-lapachone-induced apoptosis as evidenced by reduced DNA fragmentation and sub-G1 hypodiploid cells. These results suggest that intracellular increase in H_2O_2 may be one mechanism by which naphthoquinones induce cell death.

2.3.4. DNA Damage

Quinones are able to induce DNA damage, as shown by the increase in histone H2Ax phosphorylation, a step which always follows double-stranded DNA breaks to activate apoptosis [68]. Quinones have also been shown to exert antitumor effects by inhibiting nuclear enzyme topoisomerases I and II [69]. Topoisomerase mediated DNA damage of leukemic cells was observed in the activity of a synthetic naphthoquinone derivative of alkannin and shikonin against HL-60 cells [41]. β-Lapachone (3,4-dihydro-2,2-dimethyl-2H-naphtho[1,2-b]pyran-5,6-dione) is also a topoisomerase I inhibitor [63], by the proposed mechanism of locking the enzyme onto the DNA and blocking replication fork movement [48].

Shikonin has been shown to inhibit both topoisomerases I and II in different cancer cells [70–72]. To overcome the poor solubility of Shikonin, its derivative SH-7 was synthesized [40]. SH-7 displayed significant cytotoxicity against HL-60 cells with IC_{50} of 2 μM and showed significant inhibition of topoisomerase II via stabilization of the topoisomerase II-DNA cleavable complex [40]. Bey et al. suggested that the anti-tumor activity of topoisomerases inhibitors may be attributed to the overexpression of the enzymes and associated deficiency of protective mechanism against DNA damage in cancer cells or to the increase in topoisomerase bioactivation by the NAD(P)H:quinone oxidoreductase (NQO1) [73].

2.3.5. Bcl-2 Modulation

Bcl-2 family of proteins are integral to the mitochondria-dependent pathway of apoptosis [74]. Cell death is regulated by a complex interaction between the pro-apoptotic and pro-survival members of the Bcl-2 family. Pro-apoptotic members of the Bcl-2 family, such as Bax or Bak translocate from the cytosol to the mitochondria, leading to the release of cytochrome C into the cytosol [75]. Anti-apoptotic proteins, Bcl-2 [76] and Mcl-1 [77] have been studied extensively, given their ability to induce chemo-resistance in different cancers, including AML. Venetoclax, a Bcl-2 inhibitor, in combination with azacitidine or decitabine or low-dose cytarabine is approved (conditionally) by the US Food and Drug Administration (FDA) for treatment of adult patients with newly-diagnosed AML who are age 75 years or older, or who have comorbidities that preclude use of intensive induction chemotherapy [78].

The antitumor activities of naphthoquinones may be mediated by their ability to up- or down-regulate the proteins in the Bcl-2 family [4,79,80]. Shikonin down-regulated antiapoptotic proteins, such as Bcl-2 and Bcl-XL in AML cells and induced apoptosis [79]. Plumbagin-treated NB4 cells had increased expression of Bax and Bak with a decrease in Bcl-XL within 8 h of treatment [24]. TW-92 decreased expression of Mcl-1, increased Bax expression without change in expression of Bcl-2 and induced apoptosis in U937 cells [34]. Chau and colleagues reported ectopic overexpression of Bcl-2 in HL-60 cells acquired resistant phenotype to β-lapachone with decreased intracellular H_2O_2 [67].

2.3.6. MAPK Pathway

Mitogen-activated protein kinase (MAPK) pathways are involved in the regulation of cellular stress response by transducing extracellular signals to the cell nucleus to impact transcription factors important for cell proliferation, differentiation, survival, and apoptosis [81]. Constitutive activation of the MAPK cascades drives the oncogenic transformation of normal fibroblasts and is commonly detected in cancers. Inappropriate activation of these pathways may play a role in leukemic transformation of myeloid cells and their ability to proliferate and escape programmed cell death [82]. Several naphthoquinones have shown the ability to impact the MAPK pathways to induce apoptosis in leukemic cells [34,37], which may be a promising therapeutic strategy for AML. In the shikonin and shikonin derivative study [37], these agent's influence on MAPK and AKT signaling cascades led to

apoptosis of AML cells in vitro by direct interaction, and down-regulation of c-MYC, a transcription factor integral to cell cycle regulation and proliferation [37]. More investigations are warranted on the role of MAPK cascades on naphthoquinone-induced apoptosis as it has been established that MAPK cascades converge to the mitochondria and promote mitochondrial-induced apoptosis by complex interplay with Bcl-2 family [83].

2.3.7. STAT3 Inhibition

Signal transducer and activator of transcription 3 (STAT3) is an oncogenic transcription factor that is often dysregulated in AML and can be used as a valid target for AML treatment [84]. Atovaquone is an anti-microbial drug that has recently been discovered to have antileukemic efficacy in vitro and in vivo [31]. Xiang and colleagues found that atovaquone diminishes the expression of gp130, a key protein involved in STAT3 activation which in turn potently inhibited STAT3 signaling from interleukin-6 (IL-6), a critical survival factor in AML [30]. The reduction of STAT3 activation consequently led to the reduction of STAT3 target genes mediating cell survival and proliferation culminating in apoptosis.

2.3.8. Unfolded Protein Response Modulation

Unfolded protein responses (UPR) is a mechanism by which cells are able to combat adverse effects of protein accumulation in the endoplasmic reticulum (ER) following ER stress by inducing activation of this pro-apoptotic pathway [85]. UPR plays an important role in chemo-resistance in cancer cells, including leukemia cells [86,87]. ERP57, a key protein situated on the ER, is involved in the proper folding of newly synthesized polypeptides, and is overexpressed in AML cells compared to healthy cells [36]. Overexpression of ERP57 significantly reduced Shikonin-induced apoptosis, though its expression is downregulated by Shikonin itself [36].

2.3.9. Forkhead Box (Fox) Proteins

Fox proteins are a family of transcription factors that regulate the expression of genes involved in cell proliferation, growth, and differentiation [88]. They recognize DNA breaks and initiate repair or excision by binding to the Forkhead response element region (FHRE). Members of Fox class M and O have been identified as essential components of oncogenic and tumor suppressive pathways and are often deregulated in leukemia.

FOXO3A is a tumor suppressor transcription factor that is a member of the FoxO subfamily [89]. High levels of phosphorylated FOXO3A was identified as an independent, poor prognostic factor in AML and was associated with increased leukemic cell proliferation, drug resistance, and shorter duration of remission [90]. Phosphorylation leads to cytoplasmic localization and inactivation of FOXO3A, which leads to the proliferation of leukemic cells in AML. Treatment of HL-60 cells with naphthoquinone LQB-118 resulted in FOXO3A nuclear translocation with upregulation of Bim, a pro-apoptotic member of the Bcl-2 family [52]. In contrast, U937 cells treated with LQB-118 had FOXO3A nuclear exclusion and Bim downregulation [52] suggesting that LQB-118 promotes differential modulation of FOXO3A localization in different AML subtypes.

Fox protein M1 (FOXM1) is a regulator of cell cycle progression and was found to be abnormally expressed in AML blasts [91]. LQB-118-treated U937 cells had progressively decreasing FOXM1 expression, with concurrent downregulation of Survivin [52]. Of note, Survivin is an anti-apoptotic protein that is correlated with poor prognosis in AML and is known to be regulated by FOXM1 [92].

3. Methods and Materials

3.1. Search Strategy and Inclusion Criteria

An electronic search was conducted on the MEDLINE database for articles published up to 7 August 2018, using the combined search terms *acute*, *leukemia*, and *naphthoquinone*. Seventy-eight articles were preliminarily identified. Studies that investigated the activity of naphthoquinone

derivatives against AML were selectively reviewed. Twenty-one publications reported that anti-AML efficacy, in addition to at least one proposed mechanism of action of the studied naphthoquinone(s) were included for this analysis. The reference lists of these selected articles were also examined to include any relevant publications not captured in the initial search. In this report, we will not compare or comment on the study designs of the included articles. Additionally, in studies that synthesized and analyzed multiple naphthoquinone derivatives with the same core structure, only the compound with the strongest activity against AML cells, as determined by their IC_{50} (i.e., concentration that decreases viable cell numbers by 50%) values, were included for discussion.

3.2. Cell Cultures

In the included studies, in vitro activities of the naphthoquinone derivatives were examined in AML cell lines, and myeloblasts isolated from peripheral blood (PB) and bone marrow (BM) of AML patients. Often, the cytotoxicity of the compounds was studied in normal human cell lines and primary cells from healthy donors as comparators. Just a few in vivo studies have been conducted to examine the safety and tolerability of naphthoquinone-based agents.

3.3. Cell Proliferation and Cell Survival Assays

Inhibition of cell growth was assessed by measuring cell metabolic activity by MTT-like assays, including 3-(4,5-dimethylthiazol-2-yl)-2,5-diphenyltetrazolium bromide (MTT), (3-(4,5-dimethylthiazol-2-yl)-5-(3-carboxymethoxyphenyl)-2-(4-sulfophenyl)-2H-tetrazolium) (XTT), and water-soluble tetrazolium salts (WST) assays. Cell viability was determined using trypan blue exclusion.

3.4. Analysis of Apoptosis

Apoptosis was measured using the Annexin V flow cytometric kits, or acridine orange/ethidium bromide stains. Means of cell death were further evaluated with cell cycle progression (propidium iodide), mitochondrial membrane potential, Western Blot analyses, nuclei staining, or caspase activation.

4. Conclusions

The ability of naphthoquinone analogs to affect multiple steps in the apoptotic pathway and cellular signaling pathways play a role in their anti-AML activity. The simple mono- and di-substituted naphthoquinones have the ability to inhibit cell growth of various AML cell lines at low micromolar concentrations with the most potent derivatives being the 5-hydroxy-substituted derivative plumbagin (0.6–1.4 μM). Consequently, plumbagin also increases intracellular ROS and decreases expression of Bcl-2, indicating that the increased potency may be due to multiple mechanisms of action. From the multi-substituted naphthoquinones, this same pattern is observed with the shikonin derivatives demonstrating low micromolar (shikonin and SH-7) and in one case, (5,8-dihydroxy-2-(1-hydroxy-2-nitroethyl)-1,4-naphthoquinone, 0.14 μM) sub-micromolar potency against AML cell lines. Most likely multiple mechanisms of action for these derivatives provides the robust activity, including inhibition of topoisomerase, down-regulation of Bcl-2/BclxL, and down regulation of c-Myc and maybe the unfolded protein response. Thus, depending on the oxidoreductases or other bases for altered electron donation, present in AML cells and a few other neoplastic cells, the electron-accepting potential of quinones could in principle be "tuned" to yield selective cytotoxicity for cells with a particular "redox" environment, allowing initiation of a cascade of electron transport only in malignant cells, with dysregulated redox state, and not in normal cells, with the consequent increase in ROS producing selective cell killing. The dimeric naphthoquinones represent some of the most potent compounds against AML cell lines, and they have the ability to increase intracellular ROS like plumbagin.

Author Contributions: Conceptualization, A.E.; methodology, M.H.L., R.G.L.; validation, D.F., A.E.; formal analysis, M.H.L., A.E.; writing—original draft preparation, M.H.L.; writing—review and editing, D.F., R.G.L., A.E.; visualization, D.F.; supervision, R.G.L., A.E.; funding acquisition, A.E.

Funding: The manuscript was partially funded by National Cancer Institute (NCI), grant number: P30CA134274.

Conflicts of Interest: The authors declare no conflict of interest. The funders had no role in the design of the study; in the collection, analyses, or interpretation of data; in the writing of the manuscript, or in the decision to publish the results.

References

1. Emadi, A.; Ross, A.E.; Cowan, K.M.; Fortenberry, Y.M.; Vuica-Ross, M. A chemical genetic screen for modulators of asymmetrical 2,2′-dimeric naphthoquinones cytotoxicity in yeast. *PLoS ONE* **2010**, *5*, e10846. [CrossRef] [PubMed]
2. Verma, R.P. Anti-cancer activities of 1, 4-naphthoquinones: A QSAR study. *Anti Cancer Agents Med. Chem.* **2006**, *6*, 489–499. [CrossRef]
3. Pidugu, L.S.; Mbimba, J.C.; Ahmad, M.; Pozharski, E.; Sausville, E.A.; Emadi, A.; Toth, E.A. A direct interaction between NQO1 and a chemotherapeutic dimeric naphthoquinone. *BMC Struct. Biol.* **2016**, *16*, 1. [CrossRef] [PubMed]
4. Lapidus, R.G.; Carter-Cooper, B.A.; Sadowska, M.; Choi, E.Y.; Wonodi, O.; Muvarak, N.; Natarajan, K.; Pidugu, L.S.; Jaiswal, A.; Toth, E.A.; et al. Hydroxylated Dimeric Naphthoquinones Increase the Generation of Reactive Oxygen Species, Induce Apoptosis of Acute Myeloid Leukemia Cells and Are Not Substrates of the Multidrug Resistance Proteins ABCB1 and ABCG2. *Pharmaceuticals* **2016**, *9*, 4. [CrossRef] [PubMed]
5. Bardaweel, S.K.; Gul, M.; Alzweiri, M.; Ishaqat, A.; HA, A.L.; Bashatwah, R.M. Reactive Oxygen Species: The Dual Role in Physiological and Pathological Conditions of the Human Body. *Eurasian J. Med.* **2018**, *50*, 193–201. [CrossRef] [PubMed]
6. Milla, P.; Fiorito, C.; Soria, F.; Arpicco, S.; Cattel, L.; Gontero, P. Intravesical thermo-chemotherapy based on conductive heat: A first pharmacokinetic study with mitomycin C in superficial transitional cell carcinoma patients. *Cancer Chemother. Pharmacol.* **2014**, *73*, 503–509. [CrossRef] [PubMed]
7. Vinayan, A.; Glynne-Jones, R. Anal cancer—What is the optimum chemoradiotherapy? *Best Pract. Res. Clin. Gastroenterol.* **2016**, *30*, 641–653. [CrossRef]
8. Hortobagyi, G.N. Anthracyclines in the treatment of cancer. An overview. *Drugs* **1997**, *54*, 1–7. [CrossRef]
9. Emadi, A.; Karp, J.E. The clinically relevant pharmacogenomic changes in acute myelogenous leukemia. *Pharmacogenomics* **2012**, *13*, 1257–1269. [CrossRef]
10. Driscoll, J.S. Quinone structure-antitumor activity relationships. *Cancer Chemother. Rep. Part 2* **1974**, *4*, 3–4.
11. Ross, A.E.; Emadi, A.; Marchionni, L.; Hurley, P.J.; Simons, B.W.; Schaeffer, E.M.; Vuica-Ross, M. Dimeric naphthoquinones, a novel class of compounds with prostate cancer cytotoxicity. *BJU Int.* **2011**, *108*, 447–454. [CrossRef] [PubMed]
12. Emadi, A.; Le, A.; Harwood, C.J.; Stagliano, K.W.; Kamangar, F.; Ross, A.E.; Cooper, C.R.; Dang, C.V.; Karp, J.E.; Vuica-Ross, M. Metabolic and electrochemical mechanisms of dimeric naphthoquinones cytotoxicity in breast cancer cells. *Bioorg. Med. Chem.* **2011**, *19*, 7057–7062. [CrossRef] [PubMed]
13. Irwin, M.E.; Rivera-Del Valle, N.; Chandra, J. Redox control of leukemia: From molecular mechanisms to therapeutic opportunities. *Antioxid. Redox Signal.* **2013**, *18*, 1349–1383. [CrossRef] [PubMed]
14. Zhang, H.; Fang, H.; Wang, K. Reactive oxygen species in eradicating acute myeloid leukemic stem cells. *Stem Cell Investig.* **2014**, *1*, 1–10.
15. Dohner, H.; Estey, E.; Grimwade, D.; Amadori, S.; Appelbaum, F.R.; Buchner, T.; Dombret, H.; Ebert, B.L.; Fenaux, P.; Larson, R.A.; et al. Diagnosis and management of AML in adults: 2017 ELN recommendations from an international expert panel. *Blood* **2017**, *129*, 424–447. [CrossRef] [PubMed]
16. Shih, A.H.; Jiang, Y.; Meydan, C.; Shank, K.; Pandey, S.; Barreyro, L.; Antony-Debre, I.; Viale, A.; Socci, N.; Sun, Y.; et al. Mutational cooperativity linked to combinatorial epigenetic gain of function in acute myeloid leukemia. *Cancer Cell* **2015**, *27*, 502–515. [CrossRef] [PubMed]
17. Guzman, M.L.; Rossi, R.M.; Karnischky, L.; Li, X.; Peterson, D.R.; Howard, D.S.; Jordan, C.T. The sesquiterpene lactone parthenolide induces apoptosis of human acute myelogenous leukemia stem and progenitor cells. *Blood* **2005**, *105*, 4163–4169. [CrossRef]

18. Emadi, A.; Sadowska, M.; Carter-Cooper, B.; Bhatnagar, V.; van der Merwe, I.; Levis, M.J.; Sausville, E.A.; Lapidus, R.G. Perturbation of cellular oxidative state induced by dichloroacetate and arsenic trioxide for treatment of acute myeloid leukemia. *Leuk. Res.* **2015**, *39*, 719–729. [CrossRef]
19. Yeo, H.S.; Shehzad, A.; Lee, Y.S. Prostaglandin E2 blocks menadione-induced apoptosis through the Ras/Raf/Erk signaling pathway in promonocytic leukemia cell lines. *Mol. Cells* **2012**, *33*, 371–378. [CrossRef]
20. Xu, H.L.; Yu, X.F.; Qu, S.C.; Zhang, R.; Qu, X.R.; Chen, Y.P.; Ma, X.Y.; Sui, D.Y. Anti-proliferative effect of Juglone from Juglans mandshurica Maxim on human leukemia cell HL-60 by inducing apoptosis through the mitochondria-dependent pathway. *Eur. J. Pharmacol.* **2010**, *645*, 14–22. [CrossRef]
21. Esteves-Souza, A.; Lucio, K.A.; Da Cunha, A.S.; Da Cunha Pinto, A.; Da Silva Lima, E.L.; Camara, C.A.; Vargas, M.D.; Gattass, C.R. Antitumoral activity of new polyamine-naphthoquinone conjugates. *Oncol. Rep.* **2008**, *20*, 225–231. [CrossRef] [PubMed]
22. de Moraes, T.A.; Filha, M.J.; Camara, C.A.; Silva, T.M.; Soares, B.M.; Bomfim, I.S.; Pessoa, C.; Ximenes, G.C.; Silva Junior, V.A. Synthesis and cytotoxic evaluation of a series of 2-amino-naphthoquinones against human cancer cells. *Molecules* **2014**, *19*, 13188–13199. [CrossRef] [PubMed]
23. Kawiak, A.; Piosik, J.; Stasilojc, G.; Gwizdek-Wisniewska, A.; Marczak, L.; Stobiecki, M.; Bigda, J.; Lojkowska, E. Induction of apoptosis by plumbagin through reactive oxygen species-mediated inhibition of topoisomerase II. *Toxicol. Appl. Pharmacol.* **2007**, *223*, 267–276. [CrossRef] [PubMed]
24. Xu, K.H.; Lu, D.P. Plumbagin induces ROS-mediated apoptosis in human promyelocytic leukemia cells in vivo. *Leuk. Res.* **2010**, *34*, 658–665. [CrossRef] [PubMed]
25. Gaascht, F.; Teiten, M.H.; Cerella, C.; Dicato, M.; Bagrel, D.; Diederich, M. Plumbagin modulates leukemia cell redox status. *Molecules* **2014**, *19*, 10011–10032. [CrossRef] [PubMed]
26. Kong, X.; Luo, J.; Xu, T.; Zhou, Y.; Pan, Z.; Xie, Y.; Zhao, L.; Lu, Y.; Han, X.; Li, Z.; et al. Plumbagin enhances TRAIL-induced apoptosis of human leukemic Kasumi1 cells through upregulation of TRAIL death receptor expression, activation of caspase-8 and inhibition of cFLIP. *Oncol. Rep.* **2017**, *37*, 3423–3432. [CrossRef]
27. Zhang, J.; Peng, S.; Li, X.; Liu, R.; Han, X.; Fang, J. Targeting thioredoxin reductase by plumbagin contributes to inducing apoptosis of HL-60 cells. *Arch. Biochem. Biophys.* **2017**, *619*, 16–26. [CrossRef]
28. de Souza Reis, F.R.; de Faria, F.C.; Castro, C.P.; de Souza, P.S.; da Cunha Vasconcelos, F.; Bello, R.D.; da Silva, A.J.; Costa, P.R.; Maia, R.C. The therapeutical potential of a novel pterocarpanquinone LQB-118 to target inhibitor of apoptosis proteins in acute myeloid leukemia cells. *Anti Cancer Agents Med. Chem.* **2013**, *13*, 341–351. [CrossRef]
29. Araujo, A.J.; de Souza, A.A.; da Silva Junior, E.N.; Marinho-Filho, J.D.; de Moura, M.A.; Rocha, D.D.; Vasconcellos, M.C.; Costa, C.O.; Pessoa, C.; de Moraes, M.O.; et al. Growth inhibitory effects of 3′-nitro-3-phenylamino nor-beta-lapachone against HL-60: A redox-dependent mechanism. *Toxicol. In Vitro* **2012**, *26*, 585–594. [CrossRef]
30. Xiang, M.; Kim, H.; Ho, V.T.; Walker, S.R.; Bar-Natan, M.; Anahtar, M.; Liu, S.; Toniolo, P.A.; Kroll, Y.; Jones, N.; et al. Gene expression-based discovery of atovaquone as a STAT3 inhibitor and anticancer agent. *Blood* **2016**, *128*, 1845–1853. [CrossRef]
31. Stevens, A.M.; Munoz, J.O.; Krueger, M.; Horton, T.M.; Redell, M. Atovaquone Demonstrates Single Agent Activity and an Additive Effect in Combination with Cytotoxic Chemotherapy (Cytarabine and Daunorubicin) in AML. *Blood* **2017**, *130*, 3899.
32. Kawiak, A.; Zawacka-Pankau, J.; Wasilewska, A.; Stasilojc, G.; Bigda, J.; Lojkowska, E. Induction of apoptosis in HL-60 cells through the ROS-mediated mitochondrial pathway by ramentaceone from Drosera aliciae. *J. Nat. Prod.* **2012**, *75*, 9–14. [CrossRef] [PubMed]
33. Marinho-Filho, J.D.; Bezerra, D.P.; Araujo, A.J.; Montenegro, R.C.; Pessoa, C.; Diniz, J.C.; Viana, F.A.; Pessoa, O.D.; Silveira, E.R.; de Moraes, M.O.; et al. Oxidative stress induction by (+)-cordiaquinone J triggers both mitochondria-dependent apoptosis and necrosis in leukemia cells. *Chem. Biol. Interact.* **2010**, *183*, 369–379. [CrossRef] [PubMed]
34. Hallak, M.; Win, T.; Shpilberg, O.; Bittner, S.; Granot, Y.; Levy, I.; Nathan, I. The anti-leukaemic activity of novel synthetic naphthoquinones against acute myeloid leukaemia: Induction of cell death via the triggering of multiple signalling pathways. *Br. J. Haematol.* **2009**, *147*, 459–470. [CrossRef] [PubMed]
35. Yang, H.; Zhou, P.; Huang, H.; Chen, D.; Ma, N.; Cui, Q.C.; Shen, S.; Dong, W.; Zhang, X.; Lian, W.; et al. Shikonin exerts antitumor activity via proteasome inhibition and cell death induction in vitro and in vivo. *Int. J. Cancer* **2009**, *124*, 2450–2459. [CrossRef] [PubMed]

36. Trivedi, R.; Muller, G.A.; Rathore, M.S.; Mishra, D.P.; Dihazi, H. Anti-Leukemic Activity of Shikonin: Role of ERP57 in Shikonin Induced Apoptosis in Acute Myeloid Leukemia. *Cell. Physiol. Biochem. Int. J. Exp. Cell. Physiol. Biochem. Pharmacol.* **2016**, *39*, 604–616. [CrossRef] [PubMed]
37. Zhao, Q.; Assimopoulou, A.N.; Klauck, S.M.; Damianakos, H.; Chinou, I.; Kretschmer, N.; Rios, J.L.; Papageorgiou, V.P.; Bauer, R.; Efferth, T. Inhibition of c-MYC with involvement of ERK/JNK/MAPK and AKT pathways as a novel mechanism for shikonin and its derivatives in killing leukemia cells. *Oncotarget* **2015**, *6*, 38934–38951. [CrossRef] [PubMed]
38. Zhao, B.; Yang, Y.; Wang, X.; Chong, Z.; Yin, R.; Song, S.H.; Zhao, C.; Li, C.; Huang, H.; Sun, B.F.; et al. Redox-active quinones induces genome-wide DNA methylation changes by an iron-mediated and Tet-dependent mechanism. *Nucleic Acids Res.* **2014**, *42*, 1593–1605. [CrossRef]
39. Zhang, B.; Chen, N.; Chen, H.; Wang, Z.; Zheng, Q. The critical role of redox homeostasis in shikonin-induced HL-60 cell differentiation via unique modulation of the Nrf2/ARE pathway. *Oxidative Med. Cell. Longev.* **2012**, *2012*, 781516. [CrossRef]
40. Yang, F.; Chen, Y.; Duan, W.; Zhang, C.; Zhu, H.; Ding, J. SH-7, a new synthesized shikonin derivative, exerting its potent antitumor activities as a topoisomerase inhibitor. *Int. J. Cancer* **2006**, *119*, 1184–1193. [CrossRef]
41. Beretta, G.L.; Ribaudo, G.; Menegazzo, I.; Supino, R.; Capranico, G.; Zunino, F.; Zagotto, G. Synthesis and Evaluation of New Naphthalene and Naphthoquinone Derivatives as Anticancer Agents. *Arch. Der Pharm.* **2017**, *350*, e1600286. [CrossRef] [PubMed]
42. Li, K.; Wang, B.; Zheng, L.; Yang, K.; Li, Y.; Hu, M.; He, D. Target ROS to induce apoptosis and cell cycle arrest by 5, 7-dimethoxy-1, 4-naphthoquinone derivative. *Bioorganic Med. Chem. Lett.* **2017**, *28*, 273–277. [CrossRef] [PubMed]
43. Desmond, J.C.; Kawabata, H.; Mueller-Tidow, C.; Simamura, E.; Heber, D.; Hirai, K.; Koeffler, H.P. The synthetic furanonaphthoquinone induces growth arrest, apoptosis and differentiation in a variety of leukaemias and multiple myeloma cells. *Br. J. Haematol.* **2005**, *131*, 520–529. [CrossRef] [PubMed]
44. Inagaki, R.; Ninomiya, M.; Tanaka, K.; Watanabe, K.; Koketsu, M. Synthesis and cytotoxicity on human leukemia cells of furonaphthoquinones isolated from tabebuia plants. *Chem. Pharm. Bull.* **2013**, *61*, 670–673. [CrossRef] [PubMed]
45. da Silva Junior, E.N.; de Souza, M.C.; Pinto, A.V.; Pinto Mdo, C.; Goulart, M.O.; Barros, F.W.; Pessoa, C.; Costa-Lotufo, L.V.; Montenegro, R.C.; de Moraes, M.O.; et al. Synthesis and potent antitumor activity of new arylamino derivatives of nor-beta-lapachone and nor-alpha-lapachone. *Bioorg. Med. Chem.* **2007**, *15*, 7035–7041. [CrossRef] [PubMed]
46. da Silva, E.N., Jr.; de Deus, C.F.; Cavalcanti, B.C.; Pessoa, C.; Costa-Lotufo, L.V.; Montenegro, R.C.; de Moraes, M.O.; Pinto Mdo, C.; de Simone, C.A.; Ferreira, V.F.; et al. 3-arylamino and 3-alkoxy-nor-beta-lapachone derivatives: Synthesis and cytotoxicity against cancer cell lines. *J. Med. Chem.* **2010**, *53*, 504–508. [CrossRef] [PubMed]
47. Inagaki, R.; Ninomiya, M.; Tanaka, K.; Koketsu, M. Synthesis, Characterization, and Antileukemic Properties of Naphthoquinone Derivatives of Lawsone. *ChemMedChem* **2015**, *10*, 1413–1423. [CrossRef] [PubMed]
48. Planchon, S.M.; Wuerzberger, S.; Frydman, B.; Witiak, D.T.; Hutson, P.; Church, D.R.; Wilding, G.; Boothman, D.A. Beta-lapachone-mediated apoptosis in human promyelocytic leukemia (HL-60) and human prostate cancer cells: A p53-independent response. *Cancer Res.* **1995**, *55*, 3706–3711. [PubMed]
49. Planchon, S.M.; Wuerzberger-Davis, S.M.; Pink, J.J.; Robertson, K.A.; Bornmann, W.G.; Boothman, D.A. Bcl-2 protects against beta-lapachone-mediated caspase 3 activation and apoptosis in human myeloid leukemia (HL-60) cells. *Oncol. Rep.* **1999**, *6*, 485–492. [CrossRef]
50. Cavalcanti, B.C.; Barros, F.W.; Cabral, I.O.; Ferreira, J.R.; Magalhaes, H.I.; Junior, H.V.; da Silva Junior, E.N.; de Abreu, F.C.; Costa, C.O.; Goulart, M.O.; et al. Preclinical genotoxicology of nor-beta-lapachone in human cultured lymphocytes and Chinese hamster lung fibroblasts. *Chem. Res. Toxicol.* **2011**, *24*, 1560–1574. [CrossRef] [PubMed]
51. Cardoso, M.F.; Rodrigues, P.C.; Oliveira, M.E.; Gama, I.L.; da Silva, I.M.; Santos, I.O.; Rocha, D.R.; Pinho, R.T.; Ferreira, V.F.; de Souza, M.C.; et al. Synthesis and evaluation of the cytotoxic activity of 1, 2-furanonaphthoquinones tethered to 1, 2, 3-1H-triazoles in myeloid and lymphoid leukemia cell lines. *Eur. J. Med. Chem.* **2014**, *84*, 708–717. [CrossRef] [PubMed]
52. Nestal de Moraes, G.; Castro, C.P.; Salustiano, E.J.; Dumas, M.L.; Costas, F.; Lam, E.W.; Costa, P.R.; Maia, R.C. The pterocarpanquinone LQB-118 induces apoptosis in acute myeloid leukemia cells of distinct molecular

subtypes and targets FoxO3a and FoxM1 transcription factors. *Int. J. Oncol.* **2014**, *45*, 1949–1958. [CrossRef] [PubMed]
53. Emadi, A.; Harwood, J.S.; Kohanim, S.; Stagliano, K.W. Regiocontrolled synthesis of the trimeric quinone framework of conocurvone. *Org. Lett.* **2002**, *4*, 521–524. [CrossRef] [PubMed]
54. Stagliano, K.W.; Emadi, A.; Lu, Z.; Malinakova, H.C.; Twenter, B.; Yu, M.; Holland, L.E.; Rom, A.M.; Harwood, J.S.; Amin, R.; et al. Regiocontrolled synthesis and HIV inhibitory activity of unsymmetrical binaphthoquinone and trimeric naphthoquinone derivatives of conocurvone. *Bioorg. Med. Chem.* **2006**, *14*, 5651–5665. [CrossRef] [PubMed]
55. Emadi, A.; Sadowska, M.; Carter-Cooper, B.; Wonodi, O.; Muvarak, N.; Rassool, F.; Jaiswal, A.; Baer, M.R.; Lapidus, R.G.; Sausville, E.A. Dimeric Naphthoquinones: Novel Anti-Leukemic Agents Modulating Cellular Redox Status. *Blood* **2013**, *122*, 1290.
56. Carter-Cooper, B.A.; Fletcher, S.; Ferraris, D.; Choi, E.Y.; Kronfli, D.; Dash, S.; Truong, P.; Sausville, E.A.; Lapidus, R.G.; Emadi, A. Synthesis, characterization and antineoplastic activity of bis-aziridinyl dimeric naphthoquinone—A novel class of compounds with potent activity against acute myeloid leukemia cells. *Bioorg. Med. Chem. Lett.* **2017**, *27*, 6–10. [CrossRef] [PubMed]
57. Green, D.R.; Reed, J.C. Mitochondria and apoptosis. *Science* **1998**, *281*, 1309–1312. [CrossRef] [PubMed]
58. Gerasimenko, J.V.; Gerasimenko, O.V.; Palejwala, A.; Tepikin, A.V.; Petersen, O.H.; Watson, A.J. Menadione-induced apoptosis: Roles of cytosolic Ca(2+) elevations and the mitochondrial permeability transition pore. *J. Cell Sci.* **2002**, *115*, 485–497. [PubMed]
59. Hallak, M.; Thakur, B.K.; Winn, T.; Shpilberg, O.; Bittner, S.; Granot, Y.; Levy, I.; Nathan, I. Induction of death of leukemia cells by TW-74, a novel derivative of chloro-naphthoquinone. *Anticancer Res.* **2013**, *33*, 183–190.
60. Sriskanthadevan, S.; Jeyaraju, D.V.; Chung, T.E.; Prabha, S.; Xu, W.; Skrtic, M.; Jhas, B.; Hurren, R.; Gronda, M.; Wang, X.; et al. AML cells have low spare reserve capacity in their respiratory chain that renders them susceptible to oxidative metabolic stress. *Blood* **2015**, *125*, 2120–2130. [CrossRef]
61. Gourdin, T.S.; Zou, Y.; Ning, Y.; Emadi, A.; Duong, V.H.; Tidwell, M.L.; Chen, C.; Rassool, F.V.; Baer, M.R. High frequency of rare structural chromosome abnormalities at relapse of cytogenetically normal acute myeloid leukemia with FLT3 internal tandem duplication. *Cancer Genet.* **2014**, *207*, 467–473. [CrossRef] [PubMed]
62. Mantymaa, P.; Guttorm, T.; Siitonen, T.; Saily, M.; Savolainen, E.R.; Levonen, A.L.; Kinnula, V.; Koistinen, P. Cellular redox state and its relationship to the inhibition of clonal cell growth and the induction of apoptosis during all-trans retinoic acid exposure in acute myeloblastic leukemia cells. *Haematologica* **2000**, *85*, 238–245. [PubMed]
63. Li, J.Z.; Ke, Y.; Misra, H.P.; Trush, M.A.; Li, Y.R.; Zhu, H.; Jia, Z. Mechanistic studies of cancer cell mitochondria- and NQO1-mediated redox activation of beta-lapachone, a potentially novel anticancer agent. *Toxicol. Appl. Pharmacol.* **2014**, *281*, 285–293. [CrossRef] [PubMed]
64. Bittner, S. When quinones meet amino acids: Chemical, physical and biological consequences. *Amino Acids* **2006**, *30*, 205–224. [CrossRef] [PubMed]
65. Wang, X.; Thomas, B.; Sachdeva, R.; Arterburn, L.; Frye, L.; Hatcher, P.G.; Cornwell, D.G.; Ma, J. Mechanism of arylating quinone toxicity involving Michael adduct formation and induction of endoplasmic reticulum stress. *Proc. Natl. Acad. Sci. USA* **2006**, *103*, 3604–3609. [CrossRef] [PubMed]
66. Zhao, Y.L.; Lu, D.P. Effects of plumbagin on the human acute promyelocytic leukemia cells in vitro. *Zhongguo Shi Yan Xue Ye Xue Za Zhi* **2006**, *14*, 208–211.
67. Chau, Y.P.; Shiah, S.G.; Don, M.J.; Kuo, M.L. Involvement of hydrogen peroxide in topoisomerase inhibitor beta-lapachone-induced apoptosis and differentiation in human leukemia cells. *Free Radic. Biol. Med.* **1998**, *24*, 660–670. [CrossRef]
68. Kuo, L.J.; Yang, L.X. Gamma-H2AX—A novel biomarker for DNA double-strand breaks. *In Vivo* **2008**, *22*, 305–309.
69. Boothman, D.A.; Trask, D.K.; Pardee, A.B. Inhibition of potentially lethal DNA damage repair in human tumor cells by beta-lapachone, an activator of topoisomerase I. *Cancer Res.* **1989**, *49*, 605–612.
70. Ahn, B.Z.; Baik, K.U.; Kweon, G.R.; Lim, K.; Hwang, B.D. Acylshikonin analogues: Synthesis and inhibition of DNA topoisomerase-I. *J. Med. Chem.* **1995**, *38*, 1044–1047. [CrossRef]

71. Fujii, N.; Yamashita, Y.; Arima, Y.; Nagashima, M.; Nakano, H. Induction of topoisomerase II-mediated DNA cleavage by the plant naphthoquinones plumbagin and shikonin. *Antimicrob. Agents Chemother.* **1992**, *36*, 2589–2594. [CrossRef] [PubMed]
72. Plyta, Z.F.; Li, T.; Papageorgiou, V.P.; Mellidis, A.S.; Assimopoulou, A.N.; Pitsinos, E.N.; Couladouros, E.A. Inhibition of topoisomerase I by naphthoquinone derivatives. *Bioorg. Med. Chem. Lett.* **1998**, *8*, 3385–3390. [CrossRef]
73. Bey, E.A.; Bentle, M.S.; Reinicke, K.E.; Dong, Y.; Yang, C.R.; Girard, L.; Minna, J.D.; Bornmann, W.G.; Gao, J.; Boothman, D.A. An NQO1- and PARP-1-mediated cell death pathway induced in non-small-cell lung cancer cells by beta-lapachone. *Proc. Natl. Acad. Sci. USA* **2007**, *104*, 11832–11837. [CrossRef] [PubMed]
74. Gross, A.; McDonnell, J.M.; Korsmeyer, S.J. BCL-2 family members and the mitochondria in apoptosis. *Genes Dev.* **1999**, *13*, 1899–1911. [CrossRef] [PubMed]
75. Liu, X.; Kim, C.N.; Yang, J.; Jemmerson, R.; Wang, X. Induction of apoptotic program in cell-free extracts: Requirement for dATP and cytochrome c. *Cell* **1996**, *86*, 147–157. [CrossRef]
76. O'Gorman, D.M.; Cotter, T.G. Molecular signals in anti-apoptotic survival pathways. *Leukemia* **2001**, *15*, 21–34. [CrossRef] [PubMed]
77. Kitada, S.; Zapata, J.M.; Andreeff, M.; Reed, J.C. Protein kinase inhibitors flavopiridol and 7-hydroxy-staurosporine down-regulate antiapoptosis proteins in B-cell chronic lymphocytic leukemia. *Blood* **2000**, *96*, 393–397.
78. Food and Drug Administration (FDA). *Venetoclax (VENCLEXTA)*; FDA: Baltimore, MD, USA, 2018.
79. Hsu, P.C.; Huang, Y.T.; Tsai, M.L.; Wang, Y.J.; Lin, J.K.; Pan, M.H. Induction of apoptosis by shikonin through coordinative modulation of the Bcl-2 family, p27, and p53, release of cytochrome c, and sequential activation of caspases in human colorectal carcinoma cells. *J. Agric. Food Chem.* **2004**, *52*, 6330–6337. [CrossRef]
80. Wang, X.; Wang, Y. Ginsenoside Rh2 Mitigates Pediatric Leukemia Through Suppression of Bcl-2 in Leukemia Cells. *Cell. Physiol. Biochem.* **2015**, *37*, 641–650. [CrossRef]
81. Zhang, W.; Liu, H.T. MAPK signal pathways in the regulation of cell proliferation in mammalian cells. *Cell Res.* **2002**, *12*, 9–18. [CrossRef]
82. Dash, A.; Gilliland, D.G. Molecular genetics of acute myeloid leukaemia. *Best Pract. Res. Clin. Haematol.* **2001**, *14*, 49–64. [CrossRef] [PubMed]
83. Miyoshi, N.; Uchida, K.; Osawa, T.; Nakamura, Y. A link between benzyl isothiocyanate-induced cell cycle arrest and apoptosis: Involvement of mitogen-activated protein kinases in the Bcl-2 phosphorylation. *Cancer Res.* **2004**, *64*, 2134–2142. [CrossRef] [PubMed]
84. Bruserud, O.; Nepstad, I.; Hauge, M.; Hatfield, K.J.; Reikvam, H. STAT3 as a possible therapeutic target in human malignancies: Lessons from acute myeloid leukemia. *Expert Rev. Hematol.* **2015**, *8*, 29–41. [CrossRef] [PubMed]
85. Sovolyova, N.; Healy, S.; Samali, A.; Logue, S.E. Stressed to death—Mechanisms of ER stress-induced cell death. *Biol. Chem.* **2014**, *395*, 1–13. [CrossRef]
86. Epple, L.M.; Dodd, R.D.; Merz, A.L.; Dechkovskaia, A.M.; Herring, M.; Winston, B.A.; Lencioni, A.M.; Russell, R.L.; Madsen, H.; Nega, M.; et al. Induction of the unfolded protein response drives enhanced metabolism and chemoresistance in glioma cells. *PLoS ONE* **2013**, *8*, e73267. [CrossRef]
87. Pyrko, P.; Schonthal, A.H.; Hofman, F.M.; Chen, T.C.; Lee, A.S. The unfolded protein response regulator GRP78/BiP as a novel target for increasing chemosensitivity in malignant gliomas. *Cancer Res.* **2007**, *67*, 9809–9816. [CrossRef]
88. Myatt, S.S.; Lam, E.W. The emerging roles of forkhead box (Fox) proteins in cancer. *Nat. Rev. Cancer* **2007**, *7*, 847–859. [CrossRef]
89. Liu, Y.; Ao, X.; Ding, W.; Ponnusamy, M.; Wu, W.; Hao, X.; Yu, W.; Wang, Y.; Li, P.; Wang, J. Critical role of FOXO3a in carcinogenesis. *Mol. Cancer* **2018**, *17*, 104. [CrossRef]
90. Kornblau, S.M.; Singh, N.; Qiu, Y.; Chen, W.; Zhang, N.; Coombes, K.R. Highly phosphorylated FOXO3A is an adverse prognostic factor in acute myeloid leukemia. *Clin. Cancer Res. Off. J. Am. Assoc. Cancer Res.* **2010**, *16*, 1865–1874. [CrossRef]

91. Nakamura, S.; Hirano, I.; Okinaka, K.; Takemura, T.; Yokota, D.; Ono, T.; Shigeno, K.; Shibata, K.; Fujisawa, S.; Ohnishi, K. The FOXM1 transcriptional factor promotes the proliferation of leukemia cells through modulation of cell cycle progression in acute myeloid leukemia. *Carcinogenesis* **2010**, *31*, 2012–2021. [CrossRef]
92. Adida, C.; Recher, C.; Raffoux, E.; Daniel, M.T.; Taksin, A.L.; Rousselot, P.; Sigaux, F.; Degos, L.; Altieri, D.C.; Dombret, H. Expression and prognostic significance of survivin in de novo acute myeloid leukaemia. *Br. J. Haematol.* **2000**, *111*, 196–203. [CrossRef] [PubMed]

Sample Availability: Samples of the compounds are not available from the authors.

© 2019 by the authors. Licensee MDPI, Basel, Switzerland. This article is an open access article distributed under the terms and conditions of the Creative Commons Attribution (CC BY) license (http://creativecommons.org/licenses/by/4.0/).

molecules

MDPI

Article

Fluorimetric Properties of 3-Aminoflavone Biomolecule (3-AF). X-ray Crystal Structure of New Polymorph of 3-AF

Wojciech Pająk [1], Małgorzata Fabijańska [2,*], Jakub Wojciechowski [3], Wojciech M. Wolf [3], Anna Kilanowicz [4], Elżbieta Brzezińska [1] and Justyn Ochocki [2,*]

1 Department of Analytical Chemistry, 1 Muszyńskiego Str., Medical University of Lodz, 90-151 Lodz, Poland
2 Department of Bioinorganic Chemistry, 1 Muszyńskiego Str., Medical University of Lodz, 90-151 Lodz, Poland
3 Institute of General and Ecological Chemistry, Łódź University of Technology, 116 Żeromskiego St., 90-924 Lodz, Poland
4 Department of Toxicology, 1 Muszyńskiego Str., Medical University of Lodz, 90-151 Lodz, Poland
* Correspondence: malgorzata.fabijanska@umed.lodz.pl (M.F.); justyn.ochocki@umed.lodz.pl (J.O.); Tel.: +48(42)-6779220 (J.O.)

Academic Editor: Josef Jampilek
Received: 2 July 2019; Accepted: 12 August 2019; Published: 13 August 2019

Abstract: The crystal structure of the new polymorphic form of 3-aminoflavone (3-AF) has been determined by single crystal X-ray diffraction. This report presents results of fluorimetric studies on 3-AF in methanol and aquatic solvents. Based on 3D fluorescence emission spectra, optimal values for excitation (λ_{ex}) and emission/analytical (λ_{em}) wavelength, the analytical concentration range as well as the range of concentration quenching for the studied compound were established. Moreover, the limit of detection (LOD) and the limit of quantification (LOQ) were determined. The results were compared with those obtained using the standard UV-Vis absorption spectrophotometric method. The effect of acidity (pH) and the concentration of halide anions (chlorides, bromides, iodides and fluorides) on fluorescence quenching were analysed.

Keywords: 3-aminoflavone; X-ray crystallography; fluorescence; LOD (limit of detection); LOQ (limit of quantification); concentration quenching

1. Introduction

Flavonoids belong to a group of plant secondary metabolites that display a wide spectrum of biological activity. Chemically, flavonoids have the general structure of a 15-carbon skeleton, which consists of two phenyl rings and a heterocyclic ring. The compounds are derivatives of benzo-γ-pyrone. The biological activity, metabolism, chemical and physical properties of flavonoids depend on the kind, number and position of the functional groups attached to the molecule. Natural flavonoids as well as their synthetic derivatives display various pharmacological activities, including anti-oxidative, anti-inflammatory, vasoprotective and anti-proliferative. This class of compounds has been a major object of scientific interest since the discovery of their anti-oxidative activity, i.e., the ability to scavenge free radicals and reactive oxygen species (ROS) [1–5].

Flavonoid derivatives, particularly complexes containing metals, also demonstrate biological and pharmacological properties. Their derivatives that could be applied in antineoplastic chemotherapy are particularly interesting [6]. For this purpose, among others, 3-aminoflavone complexes were synthesized [7–13]. The trans-Pt_2Cl_2 complex (referred to as TCAP) is an example of such synthesis. The compound appeared to be cytotoxic for many tested cancer cell lines. Besides that, it proved to be much less toxic for normal lymphocytes in comparison to cisplatinum, which decreases the number of

potential adverse effects. Therefore, it can be a potential drug in antineoplastic therapy if cisplatinum cannot be administered.

Ruthenium(III) is another metal which forms interesting complexes with 3-aminoflavone. In vitro and in vivo studies revealed good antineoplastic properties of this complex. Some ruthenium complexes, despite their low toxicity, demonstrate effective proapoptotic or antimetastatic properties. Thus, ruthenium complexes with flavonoid compounds could constitute an interesting group of compounds that have potential antineoplastic activity [14].

The ability of flavonoids to coordinate metal ions is also applied in the improvement of preparative and analytical techniques. Because of their structure and electron configuration, a great number of flavonoid compounds display fluorescence after excitation with visible or UV light. The structure of rings with a system of conjugated double bonds and delocalized π electrons makes the molecules highly sensitive colorimetric and fluorimetric reagents in analytical chemistry. Chelation of metal ions often affects or quenches the fluorescence in a specific way that can be measured and applied for the quantitative determination of flavonoid-metal complexes [6,15,16]. Furthermore, this method could be finally applied to the detection of potential drugs.

M. Rhia L. Stone et al. reported and discussed fluorescent antibiotics as new tools to fight bacteria resistance. Applications of fluorescent antibiotics include: Examining toxicity and mode of action of the drug, detecting the presence of antibiotics and diagnostic imaging of bacterial infection [17].

As a continuation of our study on metal complexes with flavone derivatives, a novel polymorph of 3-aminoflavone (Figure 1) was discovered, and its crystal structure as well as detailed fluorimetric study was described.

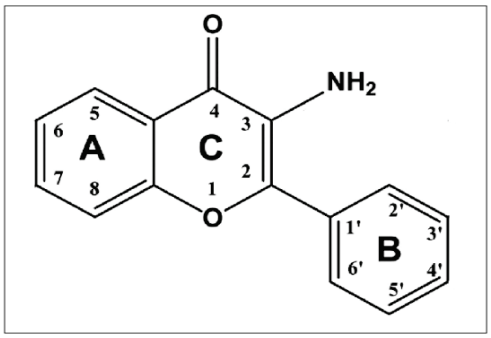

Figure 1. Structural formula of 3-aminoflavone.

2. Results and Discussion

2.1. Crystal Structure Studies

The molecular structure of a novel orthorhombic polymorph of 3-AF, i.e., **1o**, is presented in Figure 2a. Its superposition on the already reported monoclinic structure [13] **1m** is shown in Figure 2b. The former crystallizes in a chiral $P2_12_12_1$ space group while crystals of the latter adopt the centrosymmetric $P2_1/n$ symmetry. In both structures the benzopyran moieties are practically planar, root mean *square* (r.m.s.) deviations for **1o** and **1m** are 0.01 and 0.02 Å, respectively. Molecular conformation is restricted by the mutual positions of benzopyran and phenyl fragments and may be conveniently defined by the dihedral angle between both moieties, φ = 28.7(4) and 40.7(5)°, as in **1o** and **1m**, respectively. The exocyclic amine groups adopt diverse configurations in both polymorphs. In **1o** the nitrogen atom adopts the tetrahedral sp^3 configuration while in **1m** it is planar, indicating the sp^2 hybridization. Interestingly, none of the amine hydrogens are involved in the regular intermolecular hydrogen bonds. They form close contacts with the neighboring carbonyl oxygens, which may be regarded as intramolecular hydrogen bonds [O ··· N 2.673(4), 2.684(5) Å; O···H-N 114(2), 101(2)°; O ··· H 2.21(3), 2.36(2) Å for **1o** and **1m**, respectively. Bond lengths are close to those observed in related compounds. The major difference between both polymorphs is related to the exocyclic carbonyl bonds

conjugated with the endocyclic C=C bond. The former is slightly longer in **1m** as compared to that in **1o** (1.244(3) and 1.224(2) Å, respectively), while the latter behaves in the opposite way (1.358(3) and 1.381(2) Å, respectively). This indicates that the following electron delocalization is slightly higher in the reported orthorhombic polymorph **1o** than that in monoclinic **1m**.

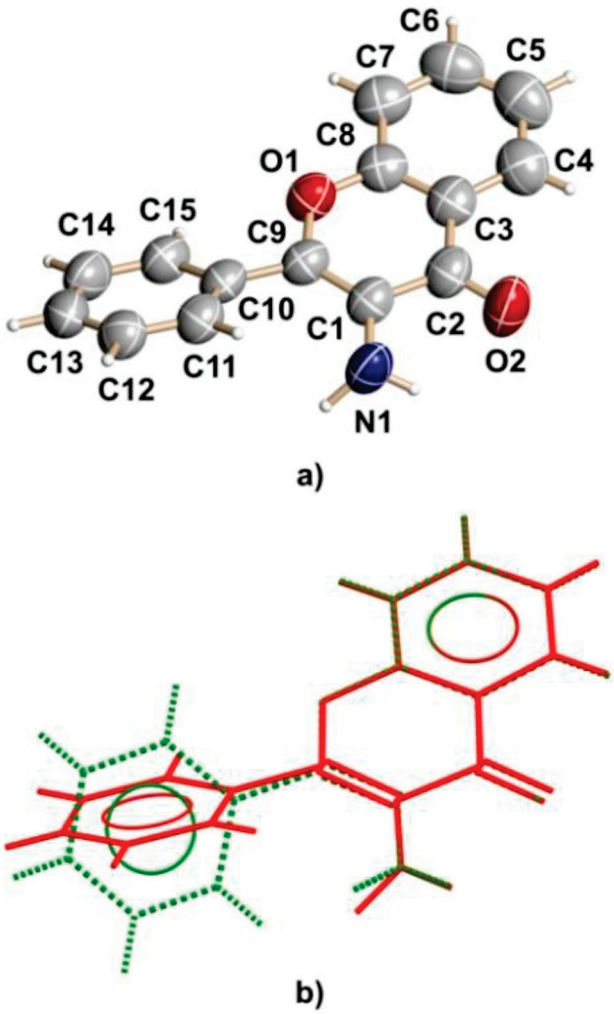

Figure 2. A view of **1o** with atom numbering scheme. Displacement ellipsoids for non-hydrogen atoms were draw with 50% probability level—(**a**); superposition of 3-AF molecules from crystal **1o** (red) and centrosymmetric **1m** (dashed green)—(**b**).

A CrystalExplorer program [18] was used to investigate differences in the packing and intermolecular interactions between both polymorphs. Hirshfeld surfaces mapped with electrostatic potential calculated at the B3LYP/6- 311++G(d,p) level and fingerprint plots (scattergrams of external (de) and internal (di) contact distance from atoms to Hirshfeld surface) for **1m** and **1o** are presented in Figure 3. The main difference is visualized as a negative charge above the amine group in **1o**. It can be assigned to a lone pair localized on the sp^3 hybridized nitrogen atom.

In both polymorphs, weak intermolecular interaction between amine groups can be observed. In **1m** it is a short (1.86(2) Å) H···H contact, while in **1o** it is a strong contact H···N (2.36(2) Å). The latter stabilizes infinite chains along the [100] twofold screw axis, which generates a helical arrangement of molecules. The search made with the CCDC Mercury program in CSD version 5.36 revealed 297 identical motifs created by the $–NH_2$ group with the average N···H contact distance 2.450 Å. Similar weak stacking interactions between benzopyrane moieties can be found in both polymorphs (distances between respective ring centroids are 3.586(2) Å and 3.661(2) Å in **1m** and **1o**, respectively).

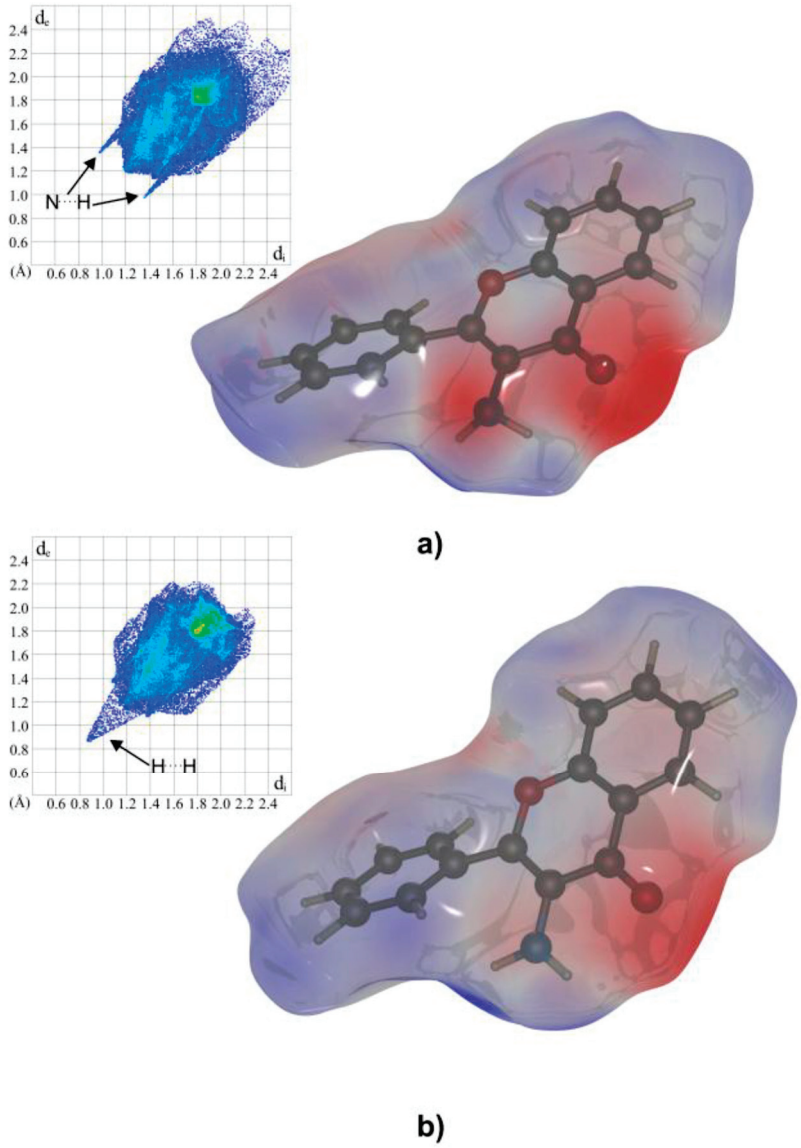

Figure 3. Hirshfeld surfaces mapped with electrostatic potential calculated with B3LYP/6-; 311++G(d,p) and the fingerprint plots for **1o**—(**a**) and **1m**—(**b**).

2.2. Electron Absorption Spectra (UV-Vis) of 3-Aminoflavone in Water and Methanol

In preliminary studies, spectra of 3-AF were recorded in water and methanol. The studies were aimed at estimating the solubility of the compound and checking its stability in solution.

(a) Absorption spectroscopy studies in methanol

It was established by us that the solubility of the studied compound is much better in methanol than in water. Figure 4 presents the UV-Vis spectrum of 3-aminoflavone, at a concentration of c = 100 μg/mL, which corresponds to a molar concentration c_m = 0.1 g/L(237.252 g/mol) = $4.215 \cdot 10^{-4}$ mol/L.

The observed spectrum has three distinctive bands with maxima at λ = 364, 305 and 243 nm with molar absorption coefficients 10,005, 5220 and 20,277, respectively. It was confirmed that the spectra are stable over time for at least a few days.

(b) Absorption Spectroscopy Studies in Water

The observed UV-Vis spectrum of 3-AF in water also has two distinct bands with maxima at λ = 352 nm and λ = 243 nm. A comparison of this spectrum with the 3-AF spectrum in methanol confirms general similarities between these two spectra. A change in the position of the long-wave band with the maximum at λ = 352 nm can be observed, i.e., a hypsochromic shift of 12 nm (in methanol,

the position was λ = 364 nm). Moreover, ex tempore studies revealed that 3-AF is poorly water soluble. It was estimated that at room temperature, solubility of 3-AF is not higher than 8 μg/mL. Thus, further fluorimetric studies were conducted in methanol, in which this compound dissolves relatively easily.

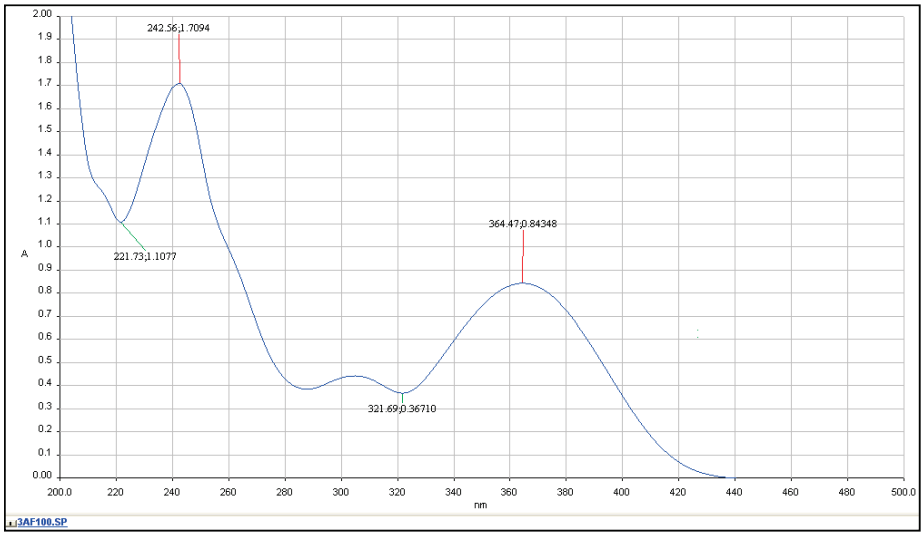

Figure 4. UV-Vis absorption spectrum of 3-aminoflavone in methanol at a concentration of 100 μg/mL, in quartz cuvette with l = 0.2 cm, at temperature t = 20 °C, with methanol as the reference.

2.3. Three-Dimensional Fluorescence Spectra of 3-Aminoflavone in Methanol

For the purpose of fluorimetric quantitative determination, it is necessary to calculate a pair of electromagnetic radiation wavelengths, for which fluorescence emission signal is maximal. The first is the wavelength of excitation fluorescence λ_{ex} and the other is the wavelength of emission fluorescence λ_{em}. These values are read at the maximum of the strongest emission band, performed using the 3D technique. Figure 5 presents a 3D spectrum of 3-aminoflavone in methanol, with marked λ_{ex} and λ_{em} of the strongest emission band, measured with the use of Hitachi F4500 spectrofluorimeter. These wavelengths allowed for proper selection of filters for quantitative fluorescence measurements on a Jenway 6285 fluorimeter.

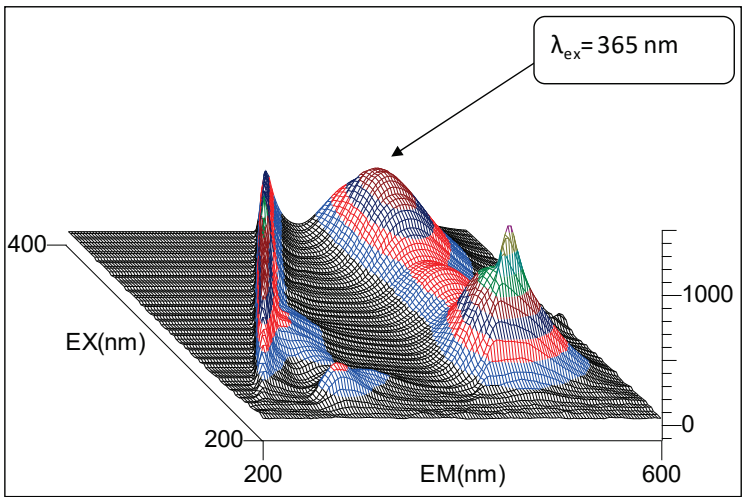

Figure 5. Three-dimensional spectrum of 3-aminoflavone in methanol. Intensity of fluorescence emission I_f in RFU (relative fluorescence unit). Instrument parameters. Measurement type: 3D scan; data mode: Fluorescence; EX (Excitation) sampling interval: 3.0 nm; EM (Emission) sampling interval: 3.0 nm; scan speed: 1200 nm/min; EX slit: 5.0 nm; EM slit: 5.0 nm; PMT (Photomultiplier Tube) voltage: 700 V; sensitivity: 1; threshold: 1.0.

It is easy to infer from the spectrum that the strongest fluorescence emission is observed for λ_{ex} = 365 nm (excitation filter) and for λ_{em} = 485 nm (analytical filter). These values are coordinates of the maximum of the strongest emission peak (Figure 5). The emission spectrum of 3-AF for the best excitation wavelength λ_{ex} = 365 nm is presented in Figure 6.

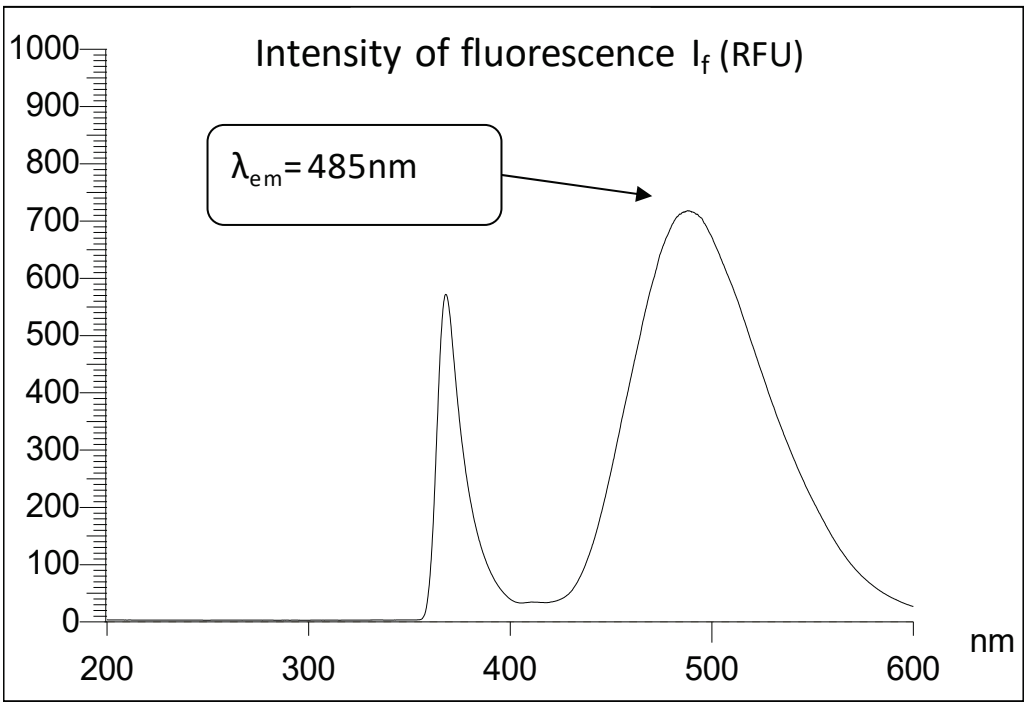

Figure 6. Emission spectrum of 3-aminoflavone in methanol at a concentration c = 0.1 μg/mL in quartz cuvette with a thickness l = 1 cm. Fluorescence excitation λ_{ex} = 365 nm; intensity of fluorescence emission I_f is presented in RFU (relative fluorescence unit).

2.4. Determination of Limit of Detection (LOD) and Quantification (LOQ) of 3-Aminoflavone by the Fluorimetric Method

The limit of detection and the limit of quantification are basic parameters in the process of validation of analytical methods [19]. In order to determine LOD and LOQ, adopting linear dependence y = (bx + a) (y and x are dependent and independent variable, respectively), we should calculate direction coefficient b, absolute term a, errors of these coefficients S_b, S_a and residual deviation $S_{y/x}$. These values are calculated according to the following formulas [19]:

$$b = \frac{n\Sigma x_i y_i - \Sigma x_i \Sigma y_i}{n\Sigma x_i^2 - (\Sigma x_i)^2} \quad a = \frac{1}{n}(\Sigma y_i - b\Sigma x_i)$$

$$S_b = \sqrt{\frac{n(\Sigma y_i^2 - b\Sigma x_i y_i - a\Sigma y_i)}{(n-2)\left[n\Sigma x_i^2 - (\Sigma x_i)^2\right]}} \quad S_a = \sqrt{\frac{1}{n} S_b^2 \Sigma x_i^2}$$

$$S_{y/x} = \sqrt{\frac{\Sigma(y_i - \hat{y}_i)^2}{(n-2)}} \text{ where } \hat{y}_i = a \cdot x_i + b$$

LOD can be calculated with two different methods, according to the formulas given below [20–22]:

a. method I: LOD = 3.3 · S_a /b

b. method II: LOD = 3.3 · $S_{y/x}$ /b

LOQ is a multiple of LOD, calculated according to the formula: LOQ = 3 · LOD.

In order to determine LOD and LOQ with the application of the fluorimetric method, a Jenway 6285 fluorimeter was used, which was equipped with a set of light filters for the excitation and emission beam. Filters were selected for transmission corresponding to the wavelengths previously determined using the 3D spectrum. Thus, the excitation filter λ_{ex} was selected with transmission at a wavelength of 350 nm, whereas the analytical filter λ_{em} = 470 nm.

In the preliminary experiment, the concentration range of 3-AF was determined, in which I_f was a linear function of the concentration, by measuring emission spectra of a series of six solutions in methanol with a concentration ranging from 10 µg/mL to 60 µg/mL, in steps of 10 µg/mL—see Figure 7.

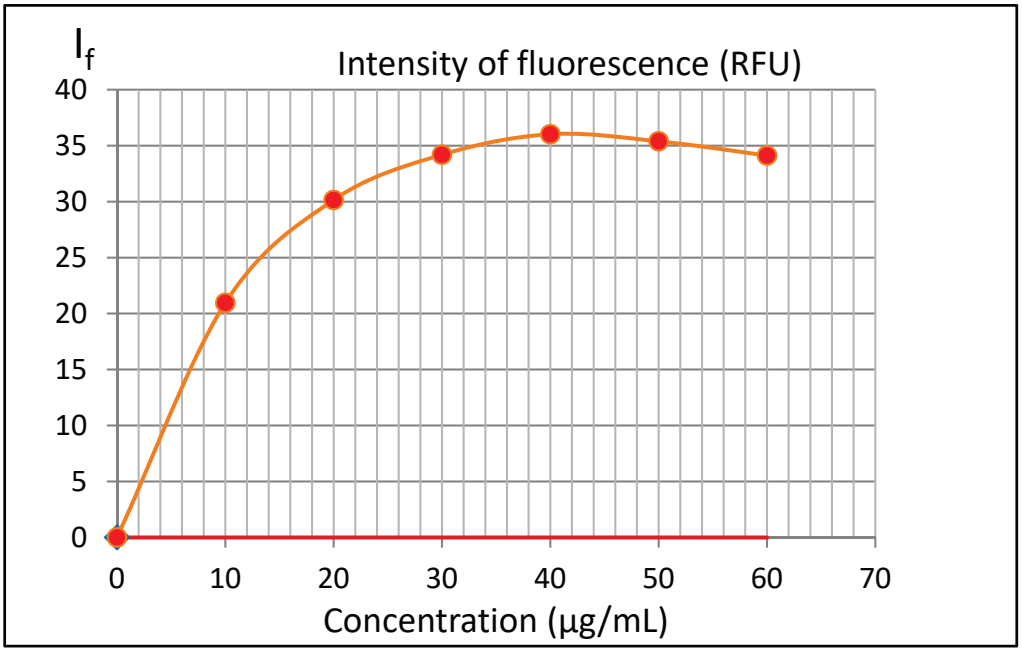

Figure 7. Intensity of fluorescence emission I_f as a function of 3-aminoflavone concentration in methanol. The fluorescence was measured in cuvette with a path length l of 1 cm. For excitation and emission, filters with wavelengths of 350 nm and 470 nm were used, respectively.

The above plot clearly shows the effect of concentration quenching. For concentrations above 10 µg/mL, the I_f value is no longer linear and for concentrations above 40 µg/mL, due to further concentration quenching, fluorescence emission I_f even decreases.

In order to determine the LOD and LOQ values, a series of ten solutions of 3-AF in methanol was analyzed, ranging from 1 µg/mL to 10 µg/mL, in steps of 1 µg/mL. Figure 8 presents fluorescence intensity I_f measurements as the function of 3-AF concentration.

In the presented study, linear regression was used (EXCEL 2010, REGLINP function). In order to determine LOD and LOQ, direction coefficient b, absolute term a, corresponding error S_a and the coefficient of determination R^2 were calculated. For the purpose of the alternative method of determining LOD and LOQ, $S_{y/x}$ was also calculated. The calculated coefficients b and a and corresponding errors S_a and $S_{y/x}$ are the following:

$$b = 1.9129 \pm 0.06258;\ a = 1.2783 \pm 0.3702;\ S_a = 0.3702;\ S_{y/x} = 0.6563$$

The value of the calculated coefficient of determination R^2 = 0.9905 means that the adopted linear model is well adjusted to experimental results. Considering the above results, one can determine LOD and LOQ values with two methods.

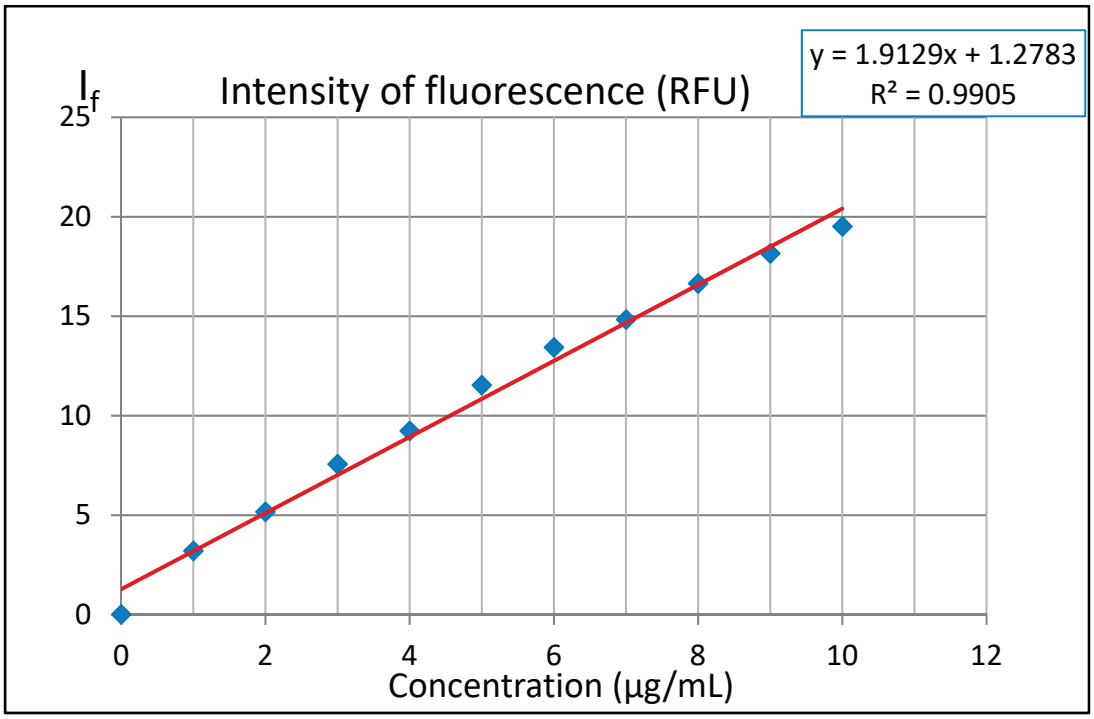

Figure 8. Fluorescence emission intensity dependence as a function of 3-aminoflavone concentration in methanol fitted with a linear function. The cuvette thickness l was 1 cm. For excitation and emission, filters with wavelengths of 350 nm and 470 nm were used, respectively.

Method I with the use of S_a: For b = 1.9129 and S_a = 0.3702 allows to obtain:

$$LOD = 3.3 \cdot S_a/b \approx 0.64 \mu g/mL;\ LOQ = 3 \cdot LOD \approx 1.92\ \mu g/mL$$

Method II with the use of $\mathbf{S_{y/x}}$: For b = 1.9129 and $S_{y/x}$ = 0.6563 allows to obtain:

$$LOD = 3.3 \cdot S_{y/x}/b \approx 1.13\ \mu g/mL;\ LOQ = 3 \cdot LOD \approx 3.40\ \mu g/mL$$

2.5. Determination of Limit of Detection (LOD) and Limit of Quantification (LOQ) of 3-Aminoflavone with UV-Vis Spectroscopy

In order to determine LOD and LOQ of the 3-AF compound with the UV-Vis spectroscopic method, a series of solutions of 3-AF in methanol, with concentrations ranging from 10 to 100 µg/mL, in steps every 10 µg/mL was prepared. The concentrations were selected in such a way that they allowed to determine the absorbance values to remain within the recommended range of 0.5–2 absorbance units A. Calculations were made for the strongest band, with a maximum at λ = 364 nm. Figure 9 shows the dependence of absorbance A (λ = 364 nm) as a function of 3-AF concentration.

Similar to the previous procedure, direction coefficient b, absolute term a and corresponding errors S_a and $S_{y/x}$ were calculated using REGLINP function in the EXCEL spreadsheet. The following values were obtained:

$$b = 0.00801 \pm 0.00005;\ a = 0.01253 \pm 0.00300;\ S_a = 0.00300;\ S_{y/x} = 0.00533$$

The calculated coefficient of determination R^2 = 0.9996 means that the adopted model is well adjusted to experimental results. Considering the above results, as in the fluorimetric calculations, LOD and LOQ values were obtained with two methods.

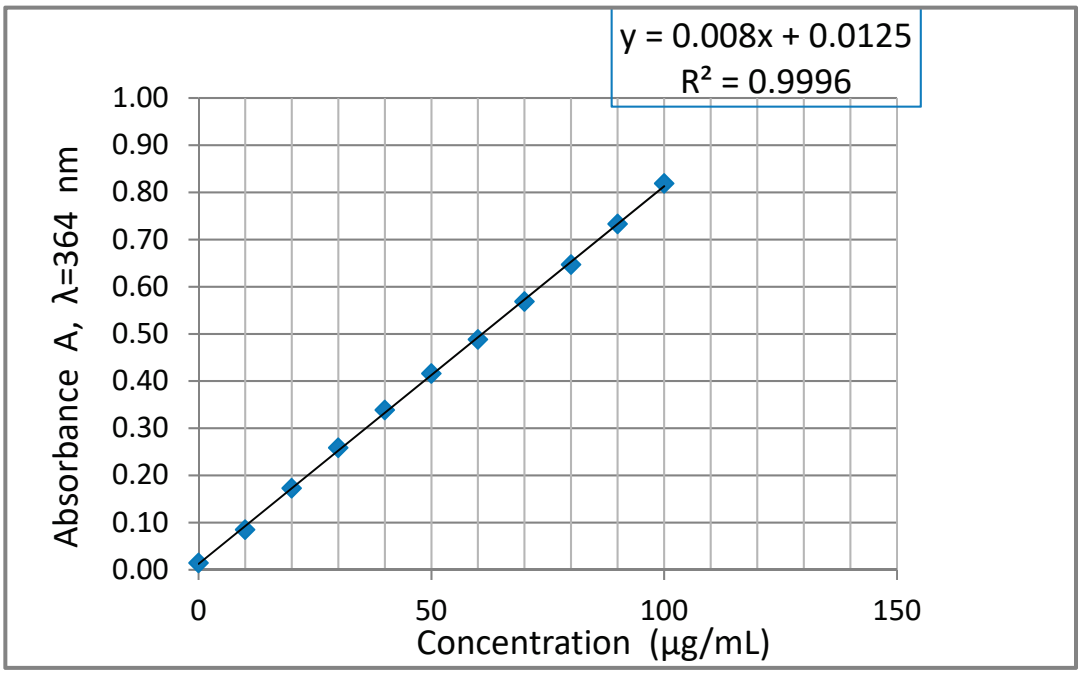

Figure 9. Dependence of absorbance A at λ = 364 nm as the function of 3-aminoflavone concentration in methanol. The quartz cuvette thickness l was 0.2 cm.

Method I with the use of S_a: For b = 0.00801 and S_a = 0.00300 allows to obtain:

$$LOD = 3.3 \cdot S_a / b \approx 1.24\ \mu g/mL,\ LOQ = 3 \cdot LOD \approx 3.71\ \mu g/mL$$

Method II with the use of $S_{y/x}$: For b = 0.00801 and $S_{y/x}$ = 0.00533 allows to obtain:

$$LOD = 3.3 \cdot S_{y/x} / b \approx 2.20\ \mu g/mL;\ LOQ = 3 \cdot LOD = 3 \cdot 2.20\ \mu g/mL = 6.60\ \mu g/mL$$

2.6. Studies on the Influence of pH on Fluorescence of 3-Aminoflavone Solutions

In order to evaluate the effect of pH on fluorescence of 3-AF, a solution of 3-AF in 5 mL of methanol at a concentration of 10 µg/mL and a water solution of HCl at a concentration 0.2 mol/L were prepared. After dilution, the HCl concentration decreased twofold, to the value of 0.1 mol/L, which results in pH ≈ 1 and 3-AF concentration of 5 µg/mL. For this solution, the 3D fluorescence spectrum was determined as well as optimal values for excitation, i.e., λ_{ex} = 356 nm and emission λ_{em} = 488 nm were calculated. These values are similar to those obtained for methanol solution, i.e., 365 and 485 nm, respectively.

Thus, to evaluate the effect of pH on fluorescence of 3-AF, a series of solution spectra of 3-AF in 5 mL of methanol at a concentration of 10 µg/mL and 5 mL of HCl with concentrations of 0.2, 0.02, 0.002, 0.0002 and 0.00002 mol/L were measured. After dilution, pH values of these solutions were around 1, 2, 3, 4 and 5, respectively. Figure 10 presents the relationship between fluorescence intensity I_f and pH.

The plot shows that an increase in the acidity of a solution is accompanied by a rapid decrease in 3-AF fluorescence. For pH = 1 it is about 8 times weaker than for pH = 5. Similar experiments were conducted for solutions in which hydrochloric acid was replaced by sulfuric acid. Moreover, here a strong decrease in 3-AF fluorescence was observed. Thus, it can be concluded that fluorescence quenching is caused not by a chloride anion, although the influence of some anions, particularly halide anions, is known, but hydronium ions H_3O^+. In order to analyze this phenomenon, UV-Vis spectra of 3-aminoflavone in these solutions were measured— see Figure 11.

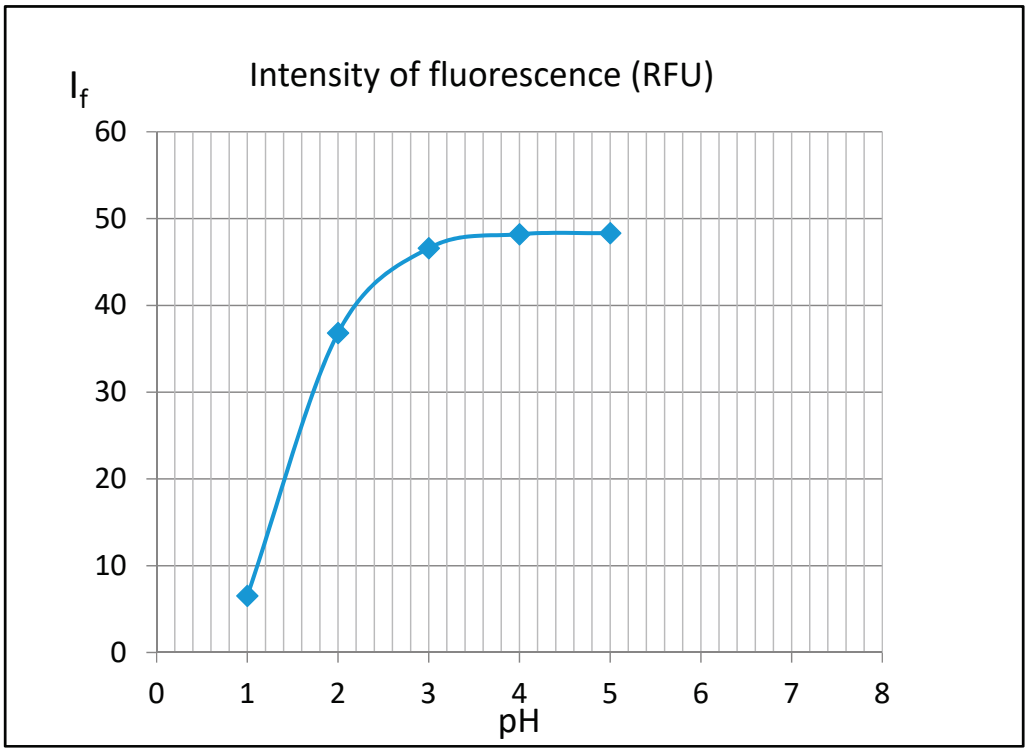

Figure 10. Relationship between fluorescence intensity I_f of 3-aminoflavone and pH. For excitation and emission, filters with wavelengths of 350 nm and 470 nm were used, respectively.

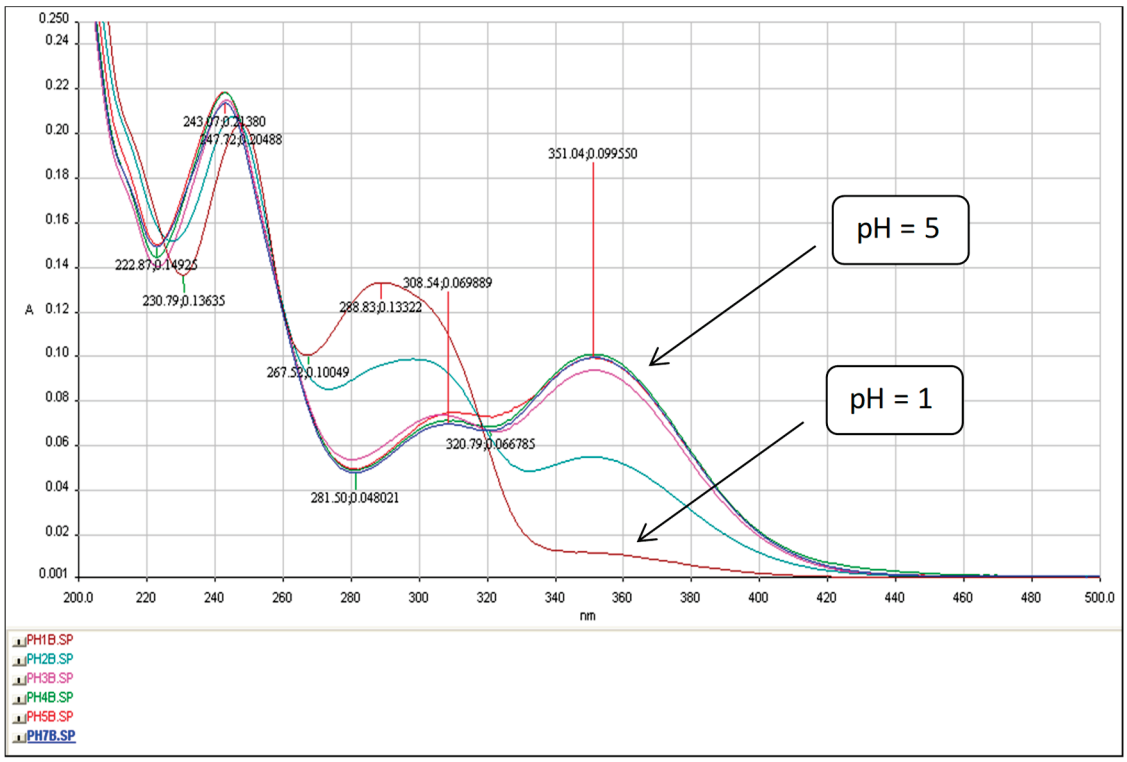

Figure 11. UV-Vis spectra of 3-aminoflavone (c = 5 μg/mL) in HCl solutions at pH = 1, 2, 3, 4, 5. l = 1 cm.

The plot clearly shows isosbestic points at λ ≈ 245, 260 and 320 nm. It confirms the presence of acid-base balance (mixture of neutral and protonated forms of 3-AF). Based on this plot, it can be

concluded that, for the band with a maximum at λ ≈ 350 nm, an increase in acidity (decreasing pH) is associated with a strong decrease in the absorbance value A. A strong decrease in fluorescence can be explained by the accompanied increase in the acidity of the solutions. The protonated form of 3-AF practically has no absorption band at λ ≈ 350 nm, which is used for fluorescence excitation of the 3-AF molecule.

2.7. Influence of Halide Anions on Fluorescence of 3-Aminoflavone

It is generally known that the environment can considerably affect emission spectra of a studied solution considering the position of emission bands and intensities. This influence is particularly strong for solutions containing halide anions. For example, chloride ions are a commonly known quenching agent for quinine [23].

In this study, an attempt to evaluate an influence of the concentration of these anions on the intensity of 3-AF fluorescence was also made. Mixtures of 3-AF solution in methanol with the corresponding halide anion solutions were prepared. A solution of 3-AF in methanol at a concentration of 10 μg/mL was used as a working solution. Next, to 5 mL of this solution a proper amount of aqueous solution of the particular anion was added. The mixture was filled with water to obtain 10 mL of a halide solution. For example, to prepare the solution with a chloride concentration of 0.1 mol/L, 1 mL of chloride solution with a concentration of 1 mol/L, 5 mL of 3-AF solution and 4 mL of distilled water were mixed to obtain the final 10 mL solution. The concentration of 3-AF in all experiments was always 5 μg/mL, i.e., a double dilution of the 3-AF solution. Results of halide concentration on fluorescence of 3-AF are presented in Figure 12.

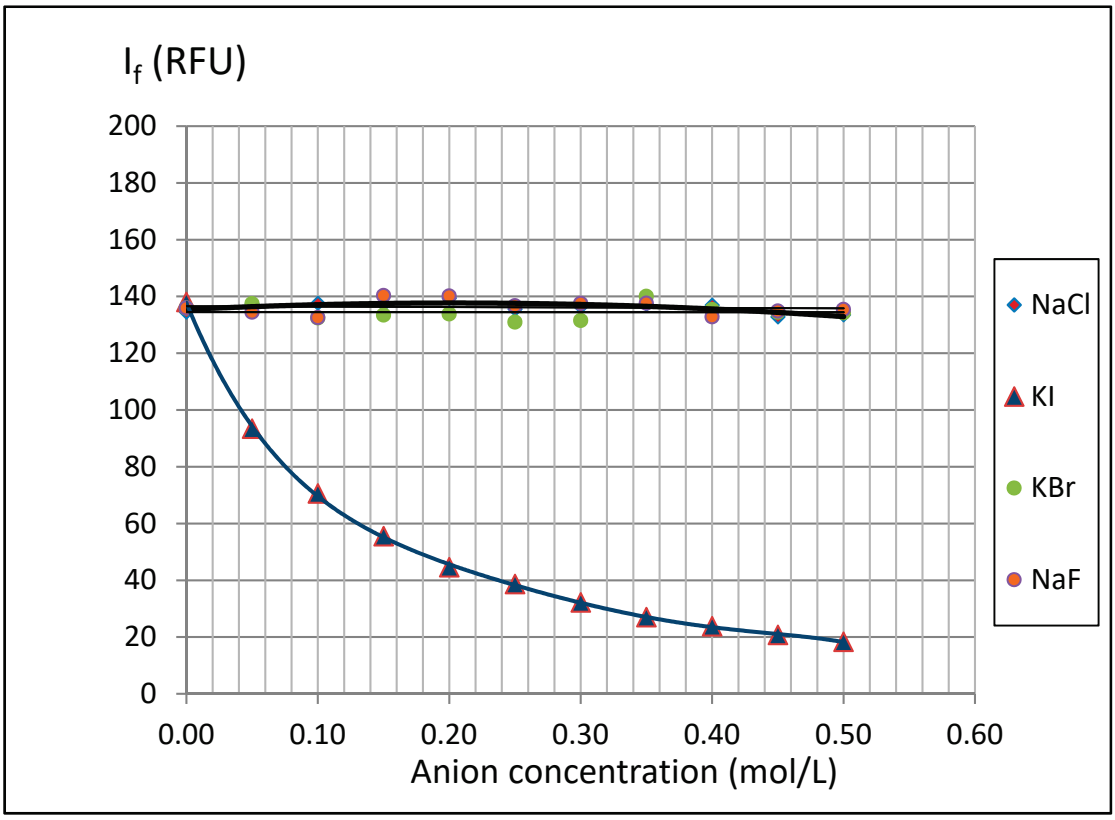

Figure 12. The relationship between fluorescence intensity I_f of 3-aminoflavone and **the** concentration of chloride, bromide, iodide and fluoride ions. The concentration of 3-aminoflavone was 5 μg/mL in cuvette with a path length of 1 cm. For excitation and emission, filters with wavelengths of 350 nm and 470 nm were used, respectively.

It can be observed that the presence of anions such as chloride, bromide and fluoride does not affect the fluorescence of 3-AF. However, strong fluorescence quenching by iodide ions was noted. In solution with iodide anions and concentration c = 0.5 mol/L, fluorescence intensity decreases from 138 RFU to 18 RFU, and this decay is almost eightfold. The mechanism of fluorescence quenching by iodide ions has been described by J. Najbar and M. Mac [24]. According to these authors, the phenomena are associated with the so-called external heavy-atom effect and with transferring the electron from the anion to the excited compound molecule. However, we would like to pay attention to another possible reason for the 3-AF quenching phenomenon. The 1 mol /L KI solution prepared for testing tends to change after a few hours from preparation to a slight yellow colour (oxidation of iodides to free iodine). The UV-Vis spectrum made for this solution has a wide absorption band with a maximum at $\lambda \approx 352$ nm. This is nearly the wavelength of the radiation used to excite 3-AF ($\lambda = 350$ nm) and very close to the location of the maximum of the long-term absorption band 3-AF ($\lambda = 364$ nm). It should be noted that the concentration of the KI solution (1 mol/L) is greater by several orders of magnitude than that of the examined compound—5 μg/mL ($2.11 \cdot 10^{-5}$ mol /L). The trace amounts of free iodine in the examined solution are therefore a "competitive" source of absorption of the radiation needed to excite the molecule of 3-AF and may be responsible for the fluorescence quenching.

Quantitative determinations of 3-aminoflavone cannot be performed in an aqueous environment because the compound is poorly soluble in water. Hence, in experiments we used methyl alcohol, in which this solubility is sufficient. The fluorimetric method cannot be applied for quantitative determinations if 3-AF concentration exceeds 40 μg/mL. At higher concentrations, the fluorescence intensity I_f decreases with increasing 3-AF concentration. We stated that the linear range of fluorescence intensity I_f vs concentration of 3-AF is limited to concentrations up to 10 μg/mL. The LOD calculated for this range was 0.64 μg/mL (the method with the use of S_a) or 1.92 μg/mL (the method with the use of $S_{y/x}$). The LOQ values were 1.13 and 3.40 μg/mL, respectively.

With regard to spectrophotometric measurements, the range of linear dependence of absorbance A on the concentration of 3-AF is much higher and reaches at least 100 μg/mL. Calculated LOD values were 1.24 μg/mL (the method with the use of S_a) and 3.71 μg/mL (the method with the use of $S_{y/x}$), respectively. The LOQ values are 2.20 and 6.59 μg/mL, respectively. It can be seen that these values are much higher ("worse") than those obtained with the application of the fluorimetric method.

The relationship between pH and 3-AF fluorescence was also analyzed. It is associated with protonation of 3-AF molecules, which manifests itself in clearly visible isosbestic points at $\lambda \approx 245$, 260 and 320 nm. Changes in absorption UV-Vis spectra, related to different pH values, confirm this phenomenon.

The effect of halide anions on luminescence quenching of 3-AF was analyzed. No significant effect of chloride, bromide or fluoride ions on fluorescence emission was observed. However, a strong fluorescence quenching by iodide ions was noted.

3. Materials and Methods

3.1. Materials

The 3-aminoflavone compound (IUPAC name: 3-amino-2-phenylchromen-4-one, $C_{15}H_{11}NO_2$, molar mass: 237.258 g/mol; PubChem CID: 248316), referred to as 3-AF, is a flavonoid compound whose structural formula is presented in Figure 1.

The 3-aminoflavone compound was synthesized and purified in our laboratory, and was used as a ligand in many metal complexes. Macroscopically, 3-aminoflavone is yellow and crystalline solid. The crystals are needle shaped, and their melting point ranges between 140 and 142 °C. It is significantly soluble in most organic solvents, but poorly soluble in water. The photophysical and electron properties of 3-AF have been recently reported [25]. The authors described results of theoretical as well as experimental studies. The theoretical calculations were made using the TD DFT model (time-dependent density functional theory). This low-cost calculation method, due to an effective

electron correlation, allowed to obtain a reliable description of ground and excited states of the molecule, the transition energies, electron densities and HOMO (highest occupied molecular orbital)/LUMO (lowest unoccupied molecular orbital) energy levels. In this study, an influence of the polarity of solvents on the absorption and emission spectra of 3-AF was also established. The solvent effect is less significant for absorption spectra and more pronounced for fluorescence spectra. For example, the maximum absorption of 3-AF in hexane is observed at the wavelength λ_{max} = 359 nm, while in the case of the aqueous solution, it is at λ_{max} = 353 nm. For fluorescence spectra the maximum emission of 3-AF in hexane is λ_{em} = 425 nm and for the aqueous solution it is λ_{em} = 490 nm.

It this work, we present the results of 3-AF fluorescence emission in methanol as a function of pH and halogen ion concentration as well as the method for the quantitative determination of 3-AF concentration.

3.2. Methods

The data of single crystal X-ray diffraction were collected on a Bruker AXS Smart Apex II CCD diffractometer (Karlsruhe, Germany) with Incoatec IμS Cu-Kα (λ = 1.54178 Å) as a source of radiation. The structure was solved by the direct method and subsequent Fourier syntheses and refined by full-matrix least squares on F2 using the SHELXS-2012 and SHELXL-2012 programs [26]. The scattering factors were those given in the SHELXL program (Goettingen, Germany). All non-hydrogen atoms were refined anisotropically. Hydrogen atoms were generated geometrically and refined as riding atoms with isotropic displacement factors equivalent to 1.2 times those of the atom to which they were attached, except for the two in the amine group, which were allowed to refine freely. Graphics were produced with XShell14 and CCDC Mercury (Cambridge, UK) [27,28].

Crystal data for 1o (3-AF polymorph): $C_{15}H_{11}NO_2$, M = 237.25, orthorhombic, a = 4.1492(4), b = 12.9988(12), c = 21.256(2) Å, V = 1146.46(19) Å^3, T = 296(5) K, space group $P2_12_12_1$ (no. 19), Z = 4, 12,758 reflections were measured, 2123 were unique (R_{int} = 0.0431) and 2049 were greater than $2\sigma(F^2)$. The final anisotropic full-matrix least-squares refinement on F^2 with 172 variables converged at R_1 = 0.0353 for the observed data and wR_2 = 0.1019 for all data. The CCDC deposition number was 1037205.

Fluorescence spectra were measured with the use a Jenway 6285 fluorimeter (spectral range from 190 to 850 nm, Gransmore Green Felsted Dunmow, UK) and Hitachi F4500 spectrofluorimeter (Tokio, Japan), which allows to record complex fluorescence spectra in the 2D and 3D techniques. UV-Vis spectra were registered on a UV-VIS Lambda 25 spectrophotometer (PerkinElmer, Waltham, Massachusetts, USA) in the range from 200 to 800 nm. UV-Vis absorption, as well as fluorescence spectra in the 3D technique, were measured in quartz cuvettes in the full transmission spectral range, λ > 200 nm. For quantitative fluorescence measurements, special plastic cuvettes with transmission λ > 300 nm were used.

4. Conclusions

In conclusion we elaborated a convenient method for quantitative determination of 3-aminoflavone (3-AF). We demonstrated that absorption and emission spectroscopy can be applied for determination of 3-AF. This is important in view of the ability of 3-AF to form coordination compounds with p-, d- and f-electron metal ions, which makes it an interesting component for analytical chemistry. Recently, we reported on the biological activity of the platinum(II) chloride complex of 3-AF as a potential anticancer drug. Our study on 3-aminoflavone could be a basis for further investigation of 3-AF as a powerful tool in a fluorimetric detection of metal complexes or new chemotherapeutics.

Author Contributions: Conceptualization, W.P. and J.O.; methodology, W.P. and J.W.; validation, W.P. and J.W.; formal analysis, W.P.; data curation W.P. and J.W.; writing—original draft preparation, W.P., M.F. and J.W.; writing—review and editing, J.O., W.P., M.F. and W.M.W.; supervision, A.K. and E.B.

Funding: This work was supported partly by Medical University of Lodz grants statute no.503/3-016-02/503-01, 503/3-045-01/503-31-001-17 and 503/3-016-03/503-31-001-18.

Acknowledgments: The authors thank Adam Darago (Department of Toxicology, Medical University, Łódź) and Karolina Brzezińska for his helpful assistance with fluorescent measurements.

Conflicts of Interest: The authors declare no conflict of interest.

References

1. Havsteen, B. Flavonoids, a class of natural products of high pharmacological potency. *Biochem. Pharmacol.* **1983**, *32*, 1141–1148. [CrossRef]
2. Nijveldt, P.; Nood, E.; Hoorn, D.E.C.; Boelens, P.G.; Norren, K.; Leeven, P.A.M. Flavonoids: A review of probable mechanisms of action and potential applications. *Am. J. Clin. Nutr.* **2001**, *74*, 418–425. [CrossRef] [PubMed]
3. Kośmider, B.; Osiecka, E. Flavonoid compounds: A review of anticancer properties and interactions with *cis*-diamminedichloroplatinum(II). *Drug Dev. Res.* **2004**, *63*, 200–211. [CrossRef]
4. Paszkiewicz, M.; Budzyńska, A.; Różalska, B.; Sadowska, B. Immunomodulacyjna ola polifenoli roślinnych. *Postępy Hig. Med. Dośw.* **2012**, *66*, 637–646. [CrossRef]
5. Nowak, A.; Zielonka, J.; Turek, M.; Klimowicz, A. Wpływ przeciwutleniaczy zawartych w owocach na proces fotostarzenia się skóry. *Postępy Fitoterapii* **2014**, *2*, 94–99.
6. Kasprzak, M.M.; Erxleben, A.; Ochocki, J. Properties and applications of flavonoid metal complexes. *R. Soc. Chem. Adv.* **2015**, *5*, 45853–45877. [CrossRef]
7. Fabijańska, M.; Studzian, K.; Szmigiero, L.; Rybarczyk-Pirek, A.J.; Pfitzner, A.; Cebula-Obrzut, B.; Smolewski, P.; Zyner, E.; Ochocki, J. Trans-Platinum(II) complex of 3-aminoflavone-synthesis, X-ray crystal structure and biological activities in vitro. *Dalton Trans.* **2015**, *44*, 938–947. [CrossRef] [PubMed]
8. Wong, E.; Giandomenico, C.M. Current status of platinum-based antitumor. *Drugs Chem. Rev.* **1999**, *99*, 2451–2466. [CrossRef] [PubMed]
9. Galański, M.; Keppler, B.K. Searching for the Magic Bullet: Anticancer Platinum Drugs Which Can Be Accumulated or Activated in the Tumor Tissue. *Med. Chem.* **2007**, *7*, 55–73. [CrossRef]
10. Kalinowska-Lis, U.; Ochocki, J.; Matławska-Wasowska, K. Trans geometry in Platinum antitumor complexes. *Coord. Chem. Rev.* **2008**, *252*, 1328–1345. [CrossRef]
11. Kośmider, B.; Osiecka, R.; Zyner, E.; Ochocki, J. Comparison between the genotoxicity of cis-Pt(ll) complex of 3-aminoflavone and cis-DDP in lymphocytes evaluated by the comet assay. *Chem. Toxicol.* **2005**, *28*, 231–244. [CrossRef] [PubMed]
12. Dauzonne, D.; Folléas, B.; Martinez, L.; Chabot, G.G. Synthesis and in vitro Cytotoxicity of a Series of 3-Aminoflavones. *Euro. J. Med. Chem.* **1997**, *32*, 71–82. [CrossRef]
13. Żurowska, B.; Erxleben, A.; Glinka, Ł.; Łeczycka, M.; Zyner, E.; Ochocki, J. Synthesis, spectroscopy and magnetism of novel metal complexes of 3-aminoflavone (3-af). X-ray crystal structure of 3-af and [Cu (3-af)$_2$ (NO_3) $_2$]. *Inorg. Chim. Acta* **2009**, *362*, 739–744. [CrossRef]
14. Ochocki, J.; Kasprzak, M.; Chęcińska, L.; Erxleben, A.; Zyner, E.; Szmigiero, L.; Garza-Ortiz, A.; Reedijk, J. Synthesis, single-crystal and solution structure analysis and in vitro cytotoxic activity of two novel complexes of ruthenium(II) with in situ formed flavanone-based ligands. *Dalton Tran.* **2010**, *39*, 9711–9718. [CrossRef] [PubMed]
15. Pyrzynska, K.; Pękal, A. Flavonoids as Analytical Reagents. *Crit. Rev. Anal. Chem.* **2011**, *41*, 335–345. [CrossRef]
16. Malesev, D.; Kunti, V. Investigation of metal–flavonoid chelates and the determination of flavonoids via metal–flavonoid complexing reactions. *J. Serb. Chem. Soc.* **2007**, *72*, 921–939. [CrossRef]
17. Stone, M.; Rhia, L.; Butler, M.S.; Phetsang, W.; Cooper, M.A.M.; Blaskovich, M.A.T. Fluorescent Antibiotics: New Research Tools to Fight Antibiotic Resistance. *Trends Biotechnol.* **2018**, *36*, 523–536. [CrossRef]
18. Spackman, M.A.; Jayatilaka, D. Hirshfeld surface analysis. *CrystEngCom.* **2009**, *11*, 19–32. [CrossRef]
19. Miller, J.; Miller, J.C. *Statistics and Chemometrics for Analytical Chemistry*, 6th ed.; Pearson Education Limited: London, UK, 2010.
20. Ermer, J.; Miller, J.H.M.B. *Method Validation in Pharmaceutical Analysis: A Guide to Best Practice*; Wiley-VCH Verlag GmbH&Co. KGaA: Weinheim, Germany, 2005.
21. Brereton, R.G. *Data Analysis for the Laboratory and Chemical Plant*; John Wiley & Sons Ltd.: Hoboken, NJ, USA, 2003.

22. *Validation of Analitical Procedures: Text and Methodology Q2 (R1)*; International Conference on Harmonisation of Technical Requirements for Registration of Pharmaceutical for Human Use: Geneva, Switzerland, 27 October 1994.
23. Gutow, H.J. Halide (Cl^-) Quenching of Quinine Sulfate Fluorescence: A Time-Resolved Fluorescence Experiment for Physical Chemistry. *J. Chem. Educ.* **2005**, *82*, 302. [CrossRef]
24. Najbar, J.; Mac, M. Mechanisms of fluorescence quenching of aromatic molecules by potassium iodide and potassium bromide in methanol-ethanol solutions. *J. Chem. Soc. Faraday Trans.* **1991**, *87*, 1523–1529. [CrossRef]
25. Wiśniewski, L.; Deperasińska, I.; Żurowska, B.; Szemijk-Hojniak, A. Effect of solvent polarity on photophysical parameters of 3-aminoflavone. *J. Photochem. Photobiol. A Chem.* **2011**, *224*, 62–67. [CrossRef]
26. Bruker. *APEX2, SAINT-Plus, XS, XL, XShell*; Bruker AXS Inc.: Madison, WI, USA, 2013.
27. Macrae, C.F.; Edgington, P.R.; McCabe, P.; Pidcock, E.; Shields, G.P.; Taylor, R.; Towler, M.; van de Streek, J. Mercury: Visualization and Analysis of Crystal Structures. *J. Appl. Cryst.* **2006**, *39*, 453–457. [CrossRef]
28. Groom, C.R.; Allen, F.H. The Cambridge Structural Database in Retrospect and Prospect. *Angew. Chem. Int. Ed.* **2014**, *53*, 662–671. [CrossRef]

Sample Availability: Samples of the compound 3-AF are available from the authors.

© 2019 by the authors. Licensee MDPI, Basel, Switzerland. This article is an open access article distributed under the terms and conditions of the Creative Commons Attribution (CC BY) license (http://creativecommons.org/licenses/by/4.0/).

molecules

MDPI

Article

Dihydrogen Bond in the Aminoborane Complex of a Nicergoline Intermediate

Jan Čejka [1,*], Ladislav Cvak [2], Simona Žižková [1], Bohumil Kratochvíl [1] and Alexandr Jegorov [2,3]

1 Department of Solid State Chemistry, University of Chemistry and Technology Prague, Technická 5, 166 28 Prague 6, Czech Republic
2 Teva Czech Industries s.r.o., Research and Development, Ostravská 29, 747 70 Opava-Komárov, Czech Republic
3 Teva Czech Industries s.r.o., Research and Development, Branišovská 31, 370 05 České Budějovice, Czech Republic
* Correspondence: Jan.Cejka@vscht.cz; Tel.: +420-702-909-061

Academic Editor: Josef Jampilek
Received: 28 May 2019; Accepted: 3 July 2019; Published: 12 July 2019

Abstract: An aminoborane side product from the nicergoline manufacture process was identified by single-crystal X-ray diffraction. As boranes of pharmaceutical molecules are quite rare, the binding potential of the BH_3 group was investigated and compared with similar compounds using Cambridge Structural Database (CSD). Surprisingly, the packing was stabilized by a dihydrogen bond, which triggered a false alert for too-short contact of hydrogen atoms in IUCR checkCIF. As the dihydrogen bond concept is not widely known, such an alert might mislead crystallographers to force $–CH_3$ optimal geometry to $–BH_3$ groups. The B–H distances equal to or less than 1.0 Å (17% of the CSD structures) are substantially biased when analyzing the structures of aminoborane complexes in CSD. To conduct proper searching, B–H bond length normalization should be applied in the CSD search.

Keywords: nicergoline; aminoborane; CSD; single crystal; X-ray structure; dihydrogen bond

1. Introduction

Sodium borohydride is widely used as a reducing agent in the synthesis of many active pharmaceutical substances. By contrast, the possibility that a reaction could be accompanied by the formation of a boron-containing side product is not usually considered. In the course of the reaction of daunomycin with sodium borohydride, various borate esters were observed. In this case, the coordination of boron to the drug proceeded via an oxygen atom [1]. For a number of other sodium borohydride-mediated reactions, the formation of borate esters was also observed [2].

Aminoboranes [3] are usually known as hydrogenation agents. They offer some advantages over sodium borohydride, such as good solubility in organic solvents. They are less sensitive to acids and can serve as chiral reducing agents [4–6]. On the other hand, they are generally weaker reducing agents. Despite their popularity, very few crystal structures of boranes of alkaloids or pharmaceutical molecules have been described. As a rare example, the crystal structures of several borane complexes of cinchona alkaloids have been reported [7].

During the years 1984 and 1985, we were developing a process for the manufacture of nicergoline (**1**). The process involved the reduction of ester **2** to alcohol **3** (Figure 1). For safety reasons, we avoided the utilization of $LiAlH_4$ and developed the reduction with $NaBH_4$ in methanol and/or ethanol. During the development of the process, we observed the formation of a lipophilic side product in the reaction mixture. However, the product disappeared during the standard workup: the addition of water, evaporation of methanol and/or ethanol, and isolation of crystalline alcohol **3** from aqueous solution.

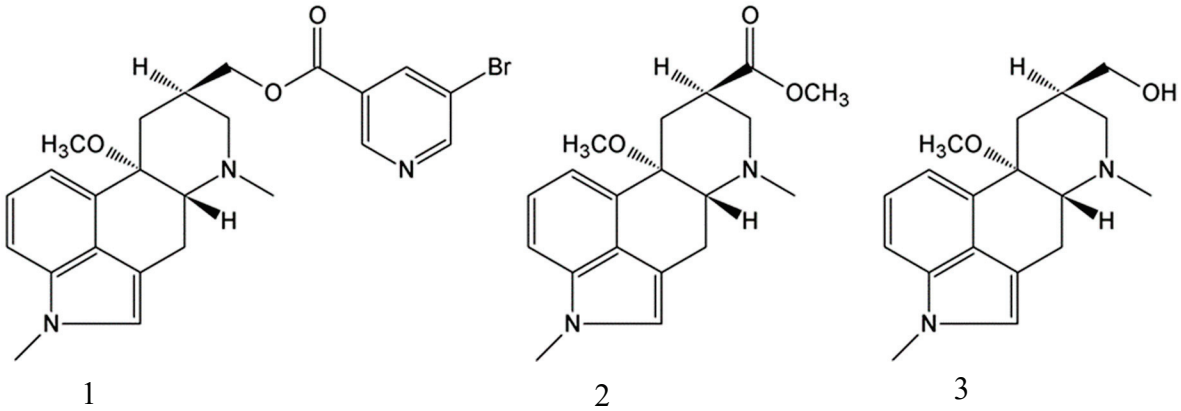

Figure 1. Scheme of nicergoline (**1**), ester (**2**), and alcohol (**3**-MeLuol) intermediates.

After the reduction, when the reaction mixture was worked up by partitioning between dichloromethane and water, the lipophilic side product remained in solution. It was isolated by chromatography of the dichloromethane phase and consequent crystallization from toluene. However, at that time, we were not able to reveal its structure when using NMR and MS. As the impurity was not present in the produced alcohol **3**, we abandoned our pursuit. At that time, the NMR identification failed because the potential presence of boron was not considered, and further attempts were unsuccessful.

We have thus reinvestigated this side product and decided to determine its structure using X-ray diffraction. X-ray structure determination was chosen because of "*its power to show totally unexpected and surprising structure with, at the same time, complete certainty*" [8]. And indeed, structure determination revealed the unexpected presence of boron, Figures 2 and 3.

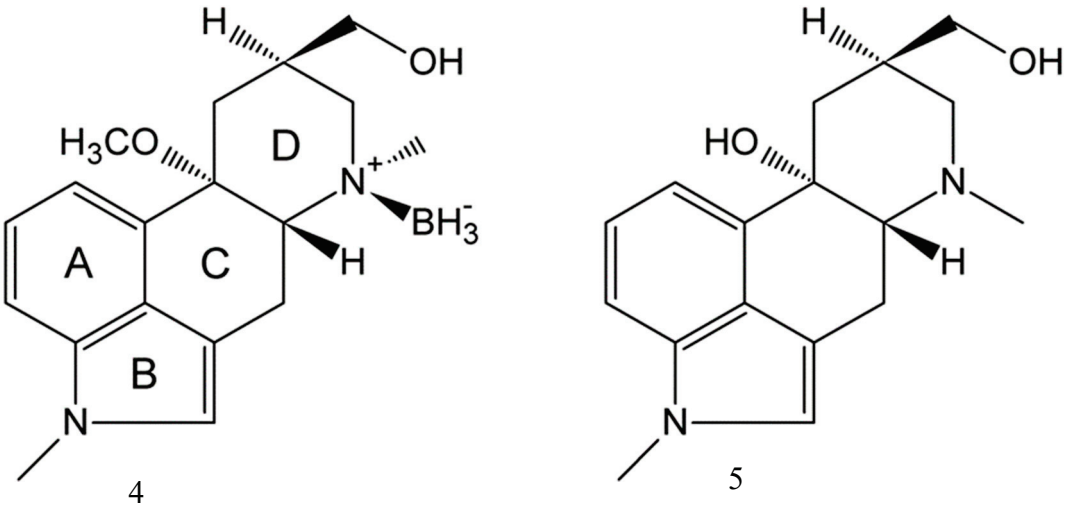

Figure 2. Scheme of BH_3-MeLuol complex (**4**) and Luol (**5**).

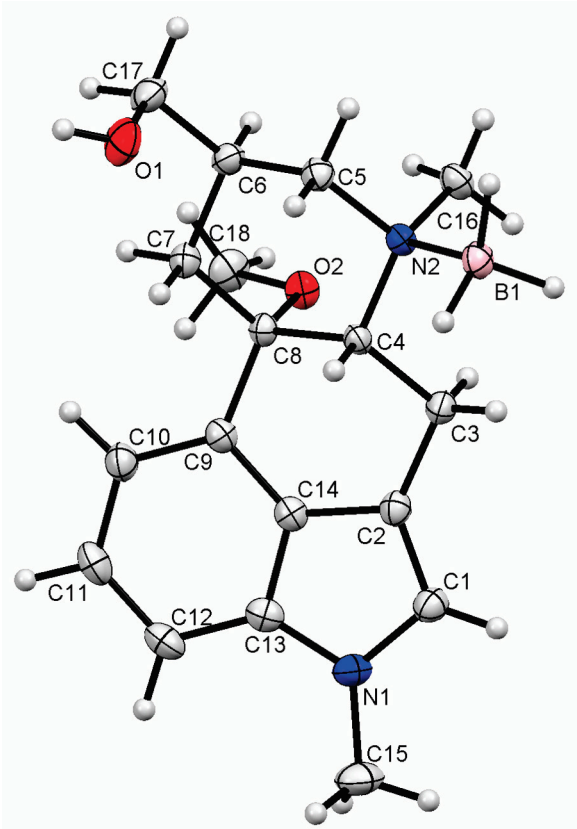

Figure 3. ORTEP drawing of BH_3-MeLuol (**4**) with atomic numbering, ADP drawn at 50% probability level.

Dihydrogen Bond

The dihydrogen bond is a relatively new phenomenon among weak intermolecular interactions. It is a non-conventional hydrogen bond, described by Crabtree et al. in 1996 as "*H–H or dihydrogen bond between a conventional hydrogen bond donor such as an NH or OH group as the weak acid component and an element-hydride bond as the weak base component, where the element in question can be a transition metal or boron*" [9]. It is rarely mentioned in crystallography textbooks [10]. For a complete review of the dihydrogen bonding concept, see [11].

2. Results and Discussion

2.1. Preparation of Single Crystals

Powder BH_3-MeLuol (**4)** (74 mg) was dissolved in ethyl formate (7 mL). The solution was allowed to slowly evaporate in open vial at 298 K. Single crystals were formed within two days after the volume of the solution was reduced to about two-thirds.

2.2. Single-Crystal X-ray Diffraction Structure

BH_3-MeLuol (**4;** borate(1-), trihydro-*N*6-(1methyl-10α-methoxy-9,10-dihydrolysergol(1+))) crystallizes in the orthorhombic system, space group $P\ 2_1\ 2_1\ 2_1$, one molecule in the asymmetric part of the unit cell. Full crystallographic details are given in Table 1. Please note that the systematic ergoline numbering *N*6 corresponds to *N*2 in the current crystal structure).

Table 1. Crystallographic data of the structures.

Empirical formula	$C_{18}H_{27}BN_2O_2$
Formula weight	314.24 g/mol
Temperature	180 K
Wavelength	1.54178 Å
Crystal system	Orthorhombic
Space group	$P\ 2_1\ 2_1\ 2_1$
Unit cell dimensions	a = 9.6759(14) Å
	b = 11.8394(16) Å
	c = 14.752(3) Å
V	1690.0(7) Å^3
Z	4
Density (calculated)	1.235 g/cm^3
Absorption coefficient	0.623 mm^{-1}
F_{000}	680.0
Crystal size	0.152 × 0.280 × 0.408 mm^3
Theta range for data collection	4.79° to 72.147°
Index ranges	$-11 \leq h \leq 11$, $-14 \leq k \leq 14$, $-17 \leq l \leq 18$
Reflections collected	20314
Independent reflections	3301 [R_{int} = 0.036]
Completeness to θ = 72.147°	99.999%
Max. and min. transmission	0.75 and 0.91
Refinement method	Full-matrix least-squares on F^2
Data/restraints/parameters	3301/5/226
Goodness-of-fit on F^2	1.001
Final R indices [$I > 2\sigma(I)$]	R_1 = 0.0311, wR_2 = 0.0731
R indices (all data)	R_1 = 0.0296, wR_2 = 0.0700
Extinction coefficient	189(4)
Largest diff. peak and hole	0.19 and −0.15 e·Å^{-3}
Flack x	0.06(18)

2.3. Impact of BH_3 on the MeLuol Conformation

The side product **4** is a derivative of MeLuol (**3**; 1-methyl-10α-methoxy-9,10-dihydrolysergol). The complexation of **3** with borane had a very low influence on the original molecular conformation of **3** [12,13]. An LSQ fit of the molecules was calculated in DSViewer [14] to provide an illustrative overview (Figure 4) of the particular conformations.

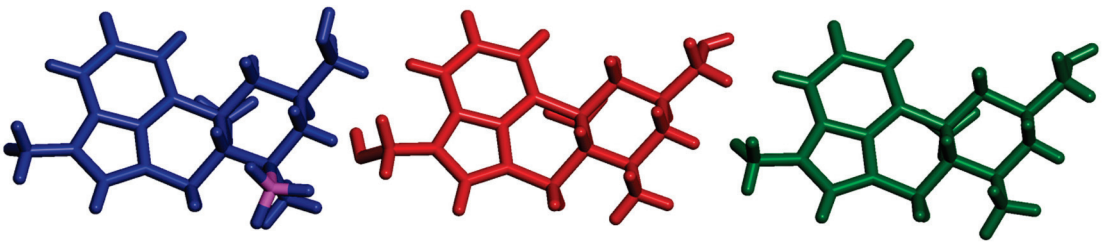

Figure 4. Parallel-oriented molecules of Luol derivatives. BH_3-MeLuol (**4**)—blue, Luol (**5**)—red, MeLuol (**3**)—green, boron—pink.

There are three subtle differences in the molecular conformations. The hydroxymethyl group of **4** is rotated to the torsion angle of C5–C6–C17–O1= −55.54(14)°. The corresponding dihedral angles are C7–C8–C20–O21 = 165.49(18)° in Luol (**5** = 1-methyl-10α-hydroxy-9,10-dihydrolysergol) and C7–C8–C19–O20 = 166.29(11)° for MeLuol (**3**). The conformational change is promoted by the change of molecular packing as the hydroxyl group binds to the same location occupied by borane in **4** and the lone pair of the tertiary amine in **3** and **5**. In **4**, the methyl adjacent to *N*2 amine adopts position switched to below plane, while its site is occupied by borane. Another difference can be found in the conformation of ring D (see Figure 2 for the ring system lettering), which is shallower in **4** compared

to **3** and **5** (Figure 5). The respective puckering amplitudes [15] of the chair conformations represent quantifications of the visual differences: 0.5359(14) Å for **4**, 0.578(2) Å for **5**, and 0.5792(11) Å for **3**.

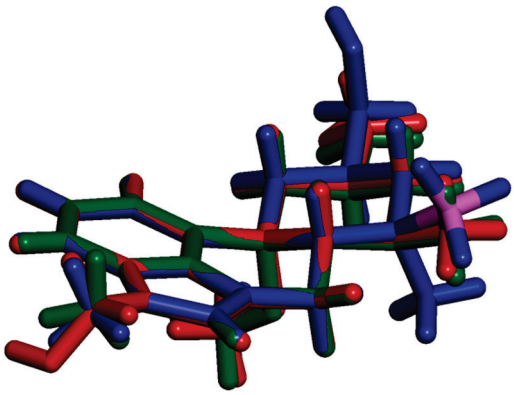

Figure 5. Side-oriented fitted molecules of Luol derivatives. BH_3-MeLuol (**4**)—blue, Luol (**5**)—red, MeLuol (**3**)—green, boron—pink.

2.4. Structural Features

2.4.1. Molecular Packing Compared to Related Derivatives

The positions and isotropic ADP's hydrogen atoms bonded to hetero atoms B and O were refined with soft restraints.

The molecular packing and conformation were compared with related structures of **3** and **5** (CCDC code: RAXPEM, JAZPAC) [12,13].

The molecules of **4** formed infinite zigzag chains via O–H ... H_2-(HB) bifurcated dihydrogen bonds along the *c*-axis. The fused rings of two adjacent molecules form an angle of 51°. The packing was stabilized by weak C–H ... π contacts.

In **5**, the molecules form similar infinite zigzag chains along *a*-axis using O–H ... N hydrogen bonds. Due to less space, the adjacent molecules are more tilted. They bind to each other in an almost perfect perpendicular arrangement. The angle between the fused rings of the neighboring molecules is 87°. The chains are crosslinked by an O–H ... O hydrogen bond to the first O–H group.

The molecules of **3** form virtually the same infinite zigzag chains along the *a*-axis by employing O–H ... N hydrogen bonds. As in **5**, due to less space, the adjacent molecules are more tilted. They bind to each other in an almost perfect perpendicular arrangement. The angle between the fused rings of the neighboring molecules is 88°. As there are no more hydrogen bond donors, the infinite rings are crosslinked, and crystal packing stabilized by weak C–H ... O improper hydrogen bonds.

2.4.2. Biased B–H Bonds in CSD

There are almost no structures of pharmaceutically used aminoboranes. As the dihydrogen bond is a relatively new phenomenon [9–11,16], more effort was invested in the investigation of binding features of the borane group intermolecular binding ability.

The coordination of borane in **4** was compared to X-ray structures of similar BH_3-*N*-methylcyclohexane-containing structures (CCDC code: XANFUN, QOPGOR) [17,18]. For the list of BH_3-*N* geometry, see Table 2. Under the brief inspection of the CIF data, it was clear that the B–H bond length distances of the published structures (XANFUN, QOPGOR) were set according to sp^3 geometry, but the B–H distances were erroneously fixed as equal to C–H bond distances. Interestingly, the CSD (May 2019) contains 488 structures with BH_3-*N* aminoboranes, when neglecting no-hydrogen and no-coordinate deposits. In 114 structures, all B–H bond lengths were smaller than 1.1 Å. The *d*(B–H) values are 1.0 Å or less for all B–H bonds in 86 structures (23 published during the last five years). The B–H bond length was experimentally determined as 1.190 Å by FTIR [19]. Deviations of the

B–H bond length of about 0.05 Å were reported, however, for terminal atoms, was about 0.1 Å [20]. Investigations based on CSD data mining, e.g., [21], are inevitably based on partially biased data, and the authors highlight the inaccuracy in hydrogen atom positions. By contrast, Crabtree et al., in 1996, used normalized B–H and N–H bond distances to avoid systematic underestimation of the bond lengths in the CSD structures [9].

Table 2. Aminoborane group comparison with published results.

Compound	*d*(B–N) (Å)	*d*(B–H) (Å)
4	1.6358(18)	1.144–1.160(13)
QOPGOR	1.608(4)	0.96 *
XANFUN	1.621(3)	0.96 *
ABUKAJ	1.600(3)	1.154(16)
DAZPIE	1.580(6), 1.574(5)	1.057–1.155(8), 0.97–1.21(8)
DORHAV	1.606(4)	1.02–1.13(3)
DUZNUI	1.627(3)	1.10–1.21(3)
WANTAI	1.610(4)	1.14–1.18(2)

* not refined, incorrect distance.

Structures containing *N*-BH_3 groups were extracted from CSD. The observations are summarized in histograms of B–H bond lengths in *N*-BH_3 groups giving a statistical overview of 2637 B–H bonds (879 BH_3 groups) in 488 CSD published structures (Figure 6). Using simple criteria, the data were split to two groups: structures in which position of the BH_3 hydrogen atoms were probably refined (1494 bonds in 318 structures), and structures with B–H bond distances set according to the optimal geometry or forced by strong restraints (1143 bonds in 170 structures). As the CSD does not contain standard uncertainties, the criterion—whether the BH_3 hydrogen atoms were refined—was based on the difference of min. and max. *d*(B–H) of each BH_3 group. In general, non-refined or firmly restrained BH_3 groups should have zero or very low variances of *d*(B–H). The criterion was set to 0.01 Å in the middle of the range of acceptable values, estimated from 0.000 to 0.020 Å. The histogram of all B–H bond lengths clearly showed two distinct statistical distributions with two strong maxima at 0.96–0.98 Å and 1.14–1.16 Å. On the other hand, the histogram of the B–H bond lengths for the group of structures with likely refined BH_3 groups had only one broad maximum at 1.14–1.16 Å, and fairly low remnants of 0.96–0.98 Å. The average value of B–H bond length of 1.118 Å for all structures was far from false values, those below 1.00 Å. When calculated from 318 likely refined structures, the average value was 1.144 Å. It should be noted that all non-refined BH3 groups were affected.

Unfortunately, the problem is likely connected to (415_ALERT_2_B Short Inter D-H..H-X) in the checkCIF/Platon IUCR validating tool [22]. "*Obviously, when atoms approach closer than the sum of their van der Waals radii there must be either a missed interaction, such as a hydrogen bond, or their positions are in some way in error*" [23]. On the other hand, the Platon software, which alerts for close contact, properly puts the dihydrogen bond on the list of the hydrogen bonds (CALC ALL procedure). Some authors, not aware of dihydrogen bond presence, may restrain or fix *d*(B–H) in the same way and with the same values as for C–H bonds (86 N-BH_3 groups containing CSD structures). "*Many single-crystal structure analyses are currently carried out by non-experts using the available black-box software*" [22]

The complete list of bond lengths, criterion setting, and statistical analysis is available in Supplementary Materials in the XLSX file.

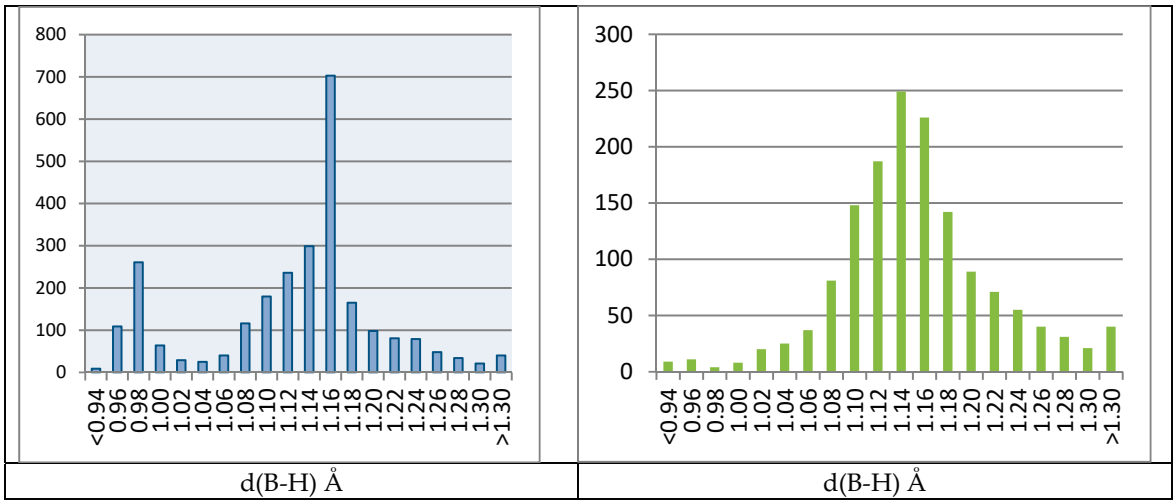

Figure 6. Histograms of bond lengths for all B–H bonds (**left**) and B–H bonds in probably refined BH_3 groups (**right**).

2.4.3. Impact of BH_3 on the Molecular Packing

Even when applying normalization of hydrogen atoms in CSD Conquest [24], the XANFUN and QOPGOR packing networks are built only by very weak improper dihydrogen bonds C–H … H. To find structures with hydrogen bond networks similar to **4**, a search was performed for the O–H … H–B–N motif, with *d*(H … H) limited to 2.5 Å. The following structures were found: ABUKAJ [25], DAZPIE [26], DORHAV [27], DUZNUI [28], and WANTAI [29]. In all five structures, the role of BH_3 in stabilizing the structure via dihydrogen bonds was obvious (Table 3).

Table 3. Dihydrogen bonds connected to BH_3 in similar compounds.

D–H … A*	D–H (Å)	D … A (Å)	H … A (Å)	D–H … A (°)	D … B (Å)	A … H … A′ (°)
4						
O1–H12 … H14	0.826(15)	2.983(17)	2.27(2)	145(2)	3.3911(18)	
O1–H12 … H15	"	2.809(17)	2.04(2)	156(2)	3.3911(18)	51.2(7)
C1–H11 … H13	0.938	3.184(17)	2.398(17)	141.3(3)	3.605(2)	
ABUKAJ						
O17–H17O … H18B	0.91(3)	2.881(15)	2.07(4)	148(3)	3.305	
O17–H17O … H18C	"	2.738(11)	1.93(3)	148(3)	"	56.1(10)
DAZPIE						
O22–H2 … H1A	0.97	3.00	2.14	147	3.394(9)	
O22–H2 … H1B	"	2.76	2.11	122	"	52
O12–H1 … H2A	1.12	2.890	2.28	112	3.408(8)	
O12–H1 … N21	"	3.460(4)	2.35	171	-	76
DORHAV						
O1–H1 … H91	0.78(3)	2.80(3)	2.05(4)	165(3)	3.249(5)	
DUZNUI						
O2–H1 … H1B1	0.89(3)	2.62(2)	1.76(4)	162(3)	3.498(3)	
WANTAI						
O–H10 … H2B	0.88(3)	2.68(2)	1.81(4)	173(3)	3.264(3)	

* D—hydrogen bond donor, A—hydrogen bond acceptor, H—hydrogen, B—boron. For complete list of proper and improper hydrogen bonds, including ARU codes, see Supplementary Materials.

Generally, there are only small variations of structure packing. The hydrogen bond to BH_3 is either single (DORHAV, DUZNUI, WANTAI) or bi-furcated (ABUKAJ, DAZPIE), similarly to the structure of **4**.

3. Materials and Methods

3.1. Single-Crystal X-ray Diffraction

Single-crystal X-ray crystallographic diffraction data were collected at 180 K using a Bruker D8 Venture diffractometer equipped with Cu Kα radiation (λ = 1.54178 Å), polycapillary monochromator, Photon 100 detector (Bruker ASX Inc., Madison, WI, USA). The habitus of the crystals could be described as parallel-oriented aggregates of pillars. The diffraction quality of the vast majority of the crystals was affected, producing diffused elongated diffraction spots that quickly lost diffraction power. Finally, a single crystal of outstanding quality was found, dipped in paraben oil, fixed to a 100 µm MicroMount mounted to the goniometer head, and immediately cooled to 180 K for data collection. The data collection, indexing of reflections, determination of the unit cell parameters, integration of the intensity of the reflections, and frame scaling were performed using the Bruker Saint software [30]. The structure was solved by direct methods with SIR92 [31] and refined with CRYSTALS [32]. Geometry calculations including puckering parameters were conducted in Platon [22]. Molecular visualization was provided by Mercury [33] and DS Viewer [14]. The positional and atomic displacement parameters of all non-hydrogen atoms were refined. All H atoms were located in a difference map, but repositioned geometrically, and were then initially refined with soft restraints on the bond lengths and angles to regularize their geometry (C–H in the range of 0.93–0.98 Å, B–H to 1.15 Å, and O–H to 0.82 Å) and U_{iso}(H) (in the range 1.2–1.5 times U_{eq} of the parent atom), after which the positions of carbon-bound hydrogen atoms were refined with riding constraints. The same set of soft restraints was used during the final stages of the refinement when the positional parameters of the hetero bound hydrogen atoms were refined. The absolute configuration was resolved by the refinement of Flack x = 0.06(18) and the calculation of Hooft y = 0.00(7) parameters [34]. The chiral centers were assigned as C4 *R*, N2 *S*, C6 *R*, and C8 *R*. The C8 configuration was calculated incorrectly by Platon software. The configuration of the chiral centers was in agreement with expected chirality. No additional solvent-accessible voids were found in the structure. The crystallographic data are summarized in Table 2.

CCDC 1919106 contains the supplementary crystallographic data for this paper. These data can be obtained free of charge via http://www.ccdc.cam.ac.uk/conts/retrieving.html (or from the CCDC, 12 Union Road, Cambridge CB2 1EZ, UK; Fax: +44 1223 336033; E-mail: deposit@ccdc.cam.ac.uk)

3.2. Materials Used

The historical source of **3**: Galena Co., Opava, Czech Republic (Teva Pharmaceutical Industries Ltd., Opava, Czech Republic) Solvents were obtained from commercial sources (Sigma Aldrich, Prague, Czech Republic).

MicroMount 100 µm, M1-L19-S2, MiTeGen, Ithaca, NY, USA.

Parabar 10312, HR2-643, Hampton Research, Irvine, CA, USA.

4. Conclusions

We have crystallized and solved the crystal structure of BH3-MeLuol with a remarkable hydrogen bond network featuring a dihydrogen bond. When comparing the molecular packing to the published CSD structures, we have encountered a problem with a significant occurrence of suspiciously short B-H bond lengths in the CSD. The values resemble methyl optimal geometry. We have demonstrated the statistical relation of the false values with the absence of hydrogen atoms refinement. Surprisingly, the B–H average distance, calculated from all B–H bonds, was only slightly biased. The B–H intermolecular contacts are up to 0.2 Å longer in almost 18% of the published structures, which affects statistical studies dealing with weak inter- and intramolecular interactions. A CSD user who is aware of the problem can handle it with an optional normalization of B–H lengths to at least 1.15 Å as available in the Conquest search. As the source of the bias is human error, we would like to emphasize this problem. The structures containing dihydrogen bonds trigger false alerts in IUCR checkCIF (based on Platon

software [22]) on short contacts between hydrogen atoms (*415_ALERT_2_B Short Inter D-H..H-X*). Some authors, not aware of the presence of the dihydrogen bond, may restrain or fix the B–H distances in the same way and using the same values as for C–H bonds.

We have found a group of N-BH3 containing structures in the CSD with a similar hydrogen bond network. Sometimes, likely due to its good accessibility the BH_3 group can compete with the available conventional hydrogen bond acceptors.

Supplementary Materials: The supplementary materials are available online.

Author Contributions: Writing—original draft, review and editing, structure refinement, CSD mining and comparison, J.Č.; synthesis, writing—synthetic part, bulk material preparation, L.C.; data collection, writing—review and editing, S.Ž.; manuscript writing coordination and review B.K.; conceptualization, writing—original draft, review and editing, single-crystal preparation, A.J.

Funding: This work was supported by the Czech Science Foundation (GAČR) project, Grant No. 17-02836S.

Conflicts of Interest: The authors declare no conflict of interest. The funders had no role in the design of the study; in the collection, analyses, or interpretation of data; in the writing of the manuscript, or in the decision to publish the results.

References

1. Schweitzer, B.A.; Egholm, M.; Koch, T.H. Mechanistic studies of the reduction of daunomycin with sodium borohydride. Formation and reaction of borate esters. *J. Am. Chem. Soc.* **1992**, *114*, 242–248. [CrossRef]
2. Liu, Q.; Xiong, F.-J.; He, Q.-Q.; Chen, F.-E. Development of an Efficient Process for the Decomposition of the Borate Complexes Formed during the Large-Scale Synthesis of (*S*)-1,2,4-Butanetriol. *Org. Process Res. Dev.* **2013**, *17*, 1540–1542. [CrossRef]
3. Niedenzu, K.; Dawson, J.W. Boron-Nitrogen Compounds. III.1,2 Aminoboranes, Part 2: The B-N Bond Character in Substituted Aminoboranes. *J. Am. Chem. Soc.* **1960**, *82*, 4223–4228. [CrossRef]
4. Narayana, C.; Periasamy, M. Hydroboration of prochiral olefins with chiral Lewis base–borane complexes: Relationship to the mechanism of hydroboration. *J. Chem. Soc. Chem. Commun.* **1987**, 1857–1859. [CrossRef]
5. Le Toumelin, J.-B.; Baboulène, M. Chiral intramolecular amine-borane complexes as reducing agents for prochiral ketones. *Tetrahedron Asymmetry* **1997**, *8*, 1259–1265. [CrossRef]
6. Burkhardt, E.R.; Matos, K. Boron Reagents in Process Chemistry: Excellent Tools for Selective Reductions. *Chem. Rev.* **2006**, *106*, 2617–2650. [CrossRef] [PubMed]
7. Hisaki, I.; Shizuki, N.; Sasaki, T.; Ito, Y.; Tohnai, N.; Miyata, M. Handedness Determination of 2_1 Helical Motifs and Hierarchical Analysis of Crystal Structures Based on the Motifs: The Case of Cinchona Alkaloid Derivatives. *Cryst. Growth Des.* **2010**, *10*, 5262–5269. [CrossRef]
8. Hodgkin, D.C. The X-ray Analysis of Complicated Molecules. *Science* **1965**, *150*, 979–988. [CrossRef] [PubMed]
9. Crabtree, R.H.; Siegbahn, P.E.M.; Eisenstein, O.; Rheingold, A.L.; Koetzle, T.F. A New Intermolecular Interaction: UnconventionalHydrogen Bonds with Element−Hydride Bonds as ProtonAcceptor. *Acc. Chem. Res.* **1996**, *29*, 348–354. [CrossRef] [PubMed]
10. Desiraju, G.R.; Steiner, T. *The Weak Hydrogen Bond: In Structural Chemistry and Biology*; International Union of Crystallography monographs on crystallography; first publ. in paperback; Oxford University Press: Oxford, UK, 2001; ISBN 978-0-19-850970-7.
11. Bakhmutov, V.I. *Dihydrogen Bonds: Principles, Experiments, and Applications*; Wiley-Interscience: Hoboken, NJ, USA, 2008; ISBN 978-0-470-18096-9.
12. Čejka, J.; Kratochvíl, B.; Cvak, L.; Jegorov, A. Crystal structure of 1-hydroxymethyl-10α-methoxy-9,10-dihydrolysergol, $C_{18}H_{24}N_2O_3$. *Z. Krist. New Cryst. Struct.* **2005**, *220*, 371–372. [CrossRef]
13. Čejka, J.; Kratochvíl, B.; Cvak, L.; Jegorov, A. Crystal structure of 1-methyl-10α-methoxy-9,10-dihydrolysergol, $C_{18}H_{24}N_2O_2$. *Z. Krist. New Cryst. Struct.* **2005**, *220*, 217–218. [CrossRef]
14. *Discovery Studio Modeling Environment*; Dassault Systèmes BIOVIA; Dassault Systèmes: San Diego, CA, USA, 2016.
15. Cremer, D.; Pople, J.A. General definition of ring puckering coordinates. *J. Am. Chem. Soc.* **1975**, *97*, 1354–1358. [CrossRef]

16. Flores-Parra, A.; Sánchez-Ruiz, S.A.; Guadarrama, C.; Nöth, H.; Contreras, R. BHδ—δ+HC Interactions in N-Borane and N-Chloroborane Adducts Derived from 1,3,5-Heterocyclohexanes. *Eur. J. Inorg. Chem.* **1999**, *1999*, 2069–2073. [CrossRef]
17. Peters, K.; Peters, E.-M.; Drinkuth, S.; Groetsch, S.; Christi, M. Crystal structure of (la,5β,8β,8aβ)-1-methyl-1,2,3,5,8,8a-hexahydro-5,8- epoxychinolin(N-B)boran, $C_9H_{10}NO(CH_3)(BH_3)$. *Z. Krist. New Cryst. Struct.* **2000**, *215*, 600–602. [CrossRef]
18. Peters, E.-M.; Peters, K.; Groetsch, S.; Christi, M. Crystal structure of (1α,2ß,8α)-2-methyl-8-phenyl-2-azabicyclo[4.2.0]oct- 5-ene(N-B)boran, $(C_6H_5)C_7H_9N(CH_3)(BH_3)$. *Z. Krist. New Cryst. Struct.* **2001**, *216*, 121–122. [CrossRef]
19. Kawaguchi, K. Fourier transform infrared spectroscopy of the BH_3 ν_3 band. *J. Chem. Phys.* **1992**, *96*, 3411–3415. [CrossRef]
20. Jones, D.S.; Lipscomb, W.N. Analysis of diborane X-ray diffraction data utilizing structure factors calculated from molecular wave functions. *Acta Crystallogr. Sect. A* **1970**, *26*, 196–207. [CrossRef]
21. Milovanović, M.M.; Andrić, J.M.; Medaković, V.B.; Djukic, J.-P.; Zarić, S.D. Investigation of interactions in Lewis pairs between phosphines and boranes by analyzing crystal structures from the Cambridge Structural Database. *Acta Crystallogr. Sect. B Struct. Sci. Cryst. Eng. Mater.* **2018**, *74*, 255–263. [CrossRef] [PubMed]
22. Spek, A.L. Structure validation in chemical crystallography. *Acta Crystallogr. Sect. D Biol. Crystallogr.* **2009**, *65*, 148–155. [CrossRef] [PubMed]
23. Spek, A.L. Single-crystal structure validation with the program *PLATON*. *J. Appl. Crystallogr.* **2003**, *36*, 7–13. [CrossRef]
24. Bruno, I.J.; Cole, J.C.; Edgington, P.R.; Kessler, M.; Macrae, C.F.; McCabe, P.; Pearson, J.; Taylor, R. New software for searching the Cambridge Structural Database and visualizing crystal structures. *Acta Crystallogr. Sect. B Struct. Sci.* **2002**, *58*, 389–397. [CrossRef] [PubMed]
25. Blakemore, P.R.; Kim, S.-K.; Schulze, V.K.; White, J.D.; Yokochi, A.F.T. Asymmetric synthesis of (+)-loline, a pyrrolizidine alkaloid from rye grass and tall fescue. *J. Chem. Soc. Perkin Trans. 1* **2001**, 1831–1847. [CrossRef]
26. Groselj, U.; Bevk, D.; Jakse, R.; Meden, A.; Stanovnik, B.; Svete, J. *CCDC 286431: Experimental Crystal Structure Determination*; The Cambridge Crystallographic Data Centre: Cambridge, UK, 2006.
27. White, J.M.; McClure, M.S. *CCDC 1026489: Experimental Crystal Structure Determination*; The Cambridge Crystallographic Data Centre: Cambridge, UK, 2014.
28. Gainsford, G.J.; Luxenburger, A.; Woolhouse, A.D. *CCDC 790649: Experimental Crystal Structure Determination*; The Cambridge Crystallographic Data Centre: Cambridge, UK, 2010.
29. Pinaka, A.; Vougioukalakis, G.; Dimotikali, D.; Psyharis, V.; Papadopoulos, K. A Convenient One-Step Synthesis of Stable β-Amino Alcohol N-Boranes from α-Amino Acids. *Synthesis* **2012**, *44*, 1057–1062. [CrossRef]
30. *Apex 3, Saint*; Bruker AXS Inc.: Madison, WI, USA, 2016.
31. Altomare, A.; Cascarano, G.; Giacovazzo, C.; Guagliardi, A.; Burla, M.C.; Polidori, G.; Camalli, M. SIR92—A program for automatic solution of crystal structures by direct methods. *J. Appl. Cryst.* **1994**, *27*, 435. [CrossRef]
32. Betteridge, P.W.; Carruthers, J.R.; Cooper, R.I.; Prout, K.; Watkin, D.J. CRYSTALS version 12: Software for guided crystal structure analysis. *J. Appl. Cryst.* **2003**, *36*, 1487. [CrossRef]
33. Macrae, C.F.; Bruno, I.J.; Chisholm, J.A.; Edgington, P.R.; McCabe, P.; Pidcock, E.; Rodriguez-Monge, L.; Taylor, R.; Streek, J.V.D.; Wood, P.A. Mercury CSD 2.0—New features for the visualization and investigation of crystal structures. *J. Appl. Crystallogr.* **2008**, *41*, 466–470. [CrossRef]
34. Hooft, R.W.W.; Straver, L.H.; Spek, A.L. Determination of absolute structure using Bayesian statistics on Bijvoet differences. *J. Appl. Cryst.* **2008**, *41*, 96–103. [CrossRef]

Sample Availability: Not available.

© 2019 by the authors. Licensee MDPI, Basel, Switzerland. This article is an open access article distributed under the terms and conditions of the Creative Commons Attribution (CC BY) license (http://creativecommons.org/licenses/by/4.0/).

molecules

MDPI

Article

Synthesis and AChE Inhibitory Activity of Novel Thiazolylhydrazone Derivatives

Derya Osmaniye [1,2], Begüm Nurpelin Sağlık [1,2], Ulviye Acar Çevik [1,2], Serkan Levent [1,2], Betül Kaya Çavuşoğlu [1], Yusuf Özkay [1,2,*], Zafer Asım Kaplancıklı [1] and Gülhan Turan [1]

1 Department of Pharmaceutical Chemistry, Faculty of Pharmacy, Anadolu Universty, 26470 Eskişehir, Turkey
2 Doping and Narcotic Compounds Analysis Laboratory, Faculty of Pharmacy, Anadolu Universty, 26470 Eskişehir, Turkey
* Correspondence: yozkay@anadolu.edu.tr; Tel.: +90-222-335-0580/3603

Academic Editor: Josef Jampilek
Received: 30 May 2019; Accepted: 25 June 2019; Published: 28 June 2019

Abstract: Alzheimer's disease (AD) is the most common of the degenerative brain diseases and is described together with the impairment of cognitive function. Patients with AD lose the capability to code new memories, and life conditions are extremely difficult. The development of new drugs in this area continues at a great pace. A novel series of thiazole-piperazine hybrids, aimed against Alzheimer's disease (AD), have been synthesized. The structure identification of synthesized compounds was elucidated by ^{1}HNMR, ^{13}C-NMR, and LCMSMS spectroscopic methods. The inhibitory potential of the synthesized compounds on cholinesterase enzymes was investigated. The compounds **3a**, **3c** and **3i** showed significant inhibitory activity on the acetylcholinesterase (AChE) enzyme. On the other hand, none of the compounds showed significant inhibitory activity on the butyrylcholinesterase (BChE) enzyme. In addition to enzyme inhibition studies, enzyme kinetic studies were performed to observe the effects of the most active inhibitor compounds on the substrate–enzyme relationship. In addition to in vitro tests, docking studies also indicated that compound **3c** potentially acts as a dual binding site AChE inhibitor.

Keywords: thiazolylhydrazone; acetylcholinesterase; butyrylcholinesterase; enzyme inhibition; docking

1. Introduction

Alzheimer's disease (AD) is a condition that rapidly threatens public health, with an increasing number of affected individuals as the world population increases. Currently, there are 35 million people with AD dementia in the world, and this number will increase to approximately 100 million globally by 2050 if treatments are not found [1]. There are two main hypotheses about the main factors and causes contributing to AD: the cholinergic and β-amyloid hypotheses. For each hypothesis, the key to slowing the progression of the disease is either to reduce cholinergic activity or to reduce the accumulation of β-amyloid plaques as a major pathological sign, respectively [2–5]. There are also other major factors of AD that must be considered. One of them is the hyperphosphorylation of tau protein, which results in insoluble tau deposits that affect microtubule stability and possibly increase the toxicity of β-amyloid. There is also concern over reactive oxygen species (ROS) and their promotion of the disease pathology by affecting oxidative stress, which has been found to thoroughly relate to amyloid plaques [6].

Interestingly, the new data suggest that the decrease in cholinergic activity and the accumulation of β-amyloid plaques are related. One relationship presented is the evidence that acetylcholinesterase (AChE) increases the deposition of β- amyloid plaques, which in turn increases the expression of AChE. Significantly, brain levels of another enzyme that hydrolyses ACh, butyrylcholinesterase (BuChE), show progressive and significant increases in AD [7,8].

The pharmacological effects of AChE inhibitors are the inactivation of enzyme activity, resulting in the increased stimulation of postsynaptic cholinergic receptors in peripheral and/or central nervous systems and the depletion of synaptic acetylcholine (ACh). AChE inhibitors can be divided into two groups according to their mode of action: irreversible and reversible. Reversible, noncompetitive or competitive, inhibitors play a leading role in the pharmacotherapy of AD symptoms. They show their therapeutic effects via maintaining the ACh level through retarding the rate of its hydrolysis. Consequently, commonly well-tolerated drugs compensate for the loss of working brain cells and improve cholinergic neurotransmission in the anterior brain regions. Above and over AD, reversible AChE inhibitors of different chemical structures have significant pharmacological application in the treatment of neurological disorders appearances such as Parkinson's disease dementia, Lewy bodies, and myasthenia gravis, and also as prophylactics against nerve agent intoxication [9].

Among all well-known AChE inhibitors used medically, four different sub-classes can be used to simplify comparison relative to their structural origins and functional groups.

Donepezil and Tacrine best signify examples of synthetic AChE inhibitors with unique structural nuclei, such as *N*-benzyl piperidine and acridine, respectively. However, Tacrine (1,2,3,4-tetrahydroacridin-9-amine) has since been removed from the market due to adverse effects, including hepatotoxicity in a significant percentage of patients. On the other hand, Huperzin A and Galantamine are examples of natural products that display strong, selective and reversible inhibitory activity against AChE. Physostigmine and its derivative Rivastigmin are examples of carbamate-type AChE inhibitors [8,10].

A thiazole derivative, Acotiamide, has been reported to be a new selective AChE inhibitor for the treatment of functional dyspepsia [11]. This development caused the enhancement of studies on the structure of thiazole as an AChE inhibitor [12–16]. Some 2-Aminothiazole derivatives were also patented in 2014 and 2015 that showed inhibitory activity against AChE [17,18].

Although the new thiazole derivatives have different substituents, the 2-amino-4-substituted thiazole as a common structure has supported us in this study (Figure 1).

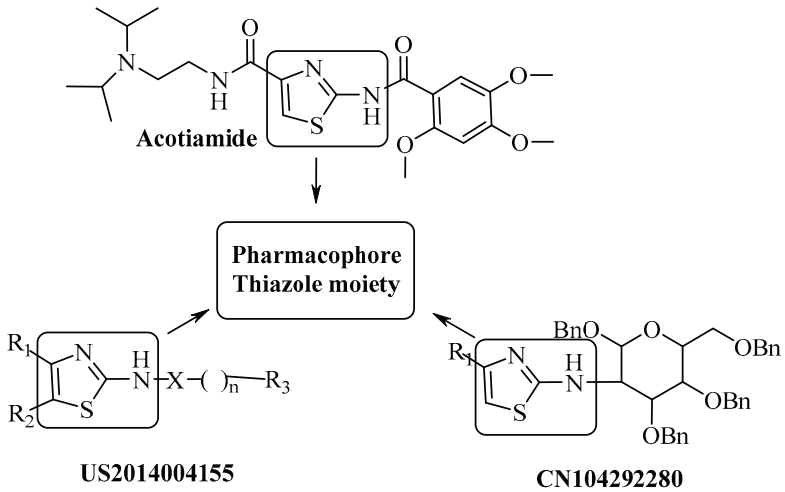

Figure 1. 2-amino-4-substituted thiazole as a pharmacophore for acetylcholinesterase (AChE).

On the other hand, there are many studies on novel AChE inhibitor compounds for use as donepezil analogues, having a pharmacophore benzylamine moiety as a basic center [19–24] (Figure 2). The compounds we synthesized in this study included a benzylamine moiety and thiazole bridges with aromatic groups at both ends [7,25,26].

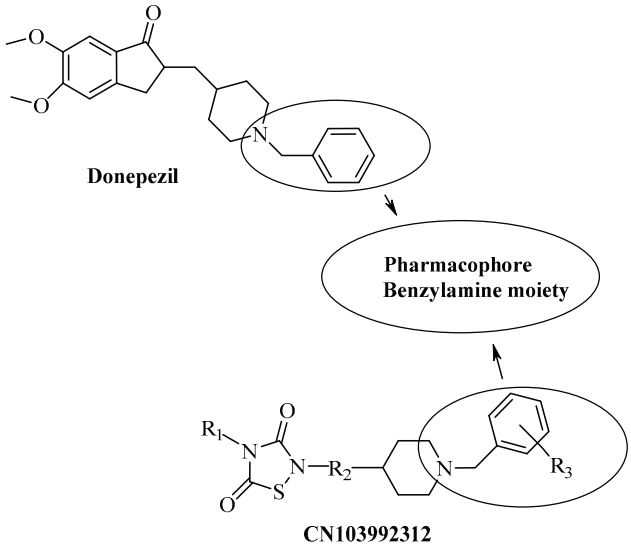

Figure 2. Some AchE inhibitors, including a benzylamine moiety.

Monoamine oxidase (MAO) enzymes play an important role in the regulation of different biological processes, and thus they are a significant target in drug design for the treatment of psychiatric and neurological diseases. Especially for symptoms of Parkinson's and Alzheimer's diseases, MAO-B (Monoamine oxidase B) inhibitors are generally used. On the other hand, MAO-A (Monoamine oxidase A) inhibitors are clinically used as antidepressants and anxiolytics. Therefore, in the treatment of Alzheimer's disease, the evaluation of monoamine oxidase enzyme inhibitory activity is generally preferred along with cholinesterase inhibition assays [27–29].

Based on these findings, we became interested in the biological evaluation of 2-aminothiazoles as anticholinesterase agents. Herein, we describe the synthesis of novel thiazole derivatives bearing a benzylamine moiety and focus on their anticholinesterase effects on AChE (Figure 3).

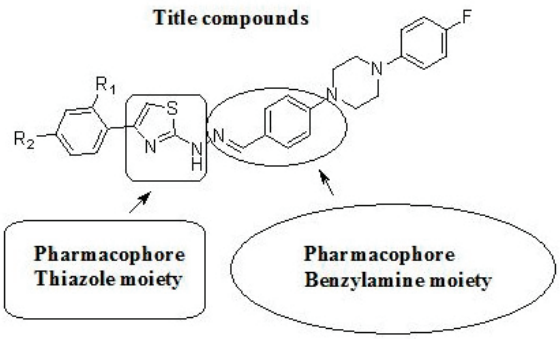

Figure 3. General structure of target compounds.

2. Results and Discussion

2.1. Chemistry

The compounds **3a**–**k** were synthesized as outlined in Scheme 1. Firstly, 4-(4-(4-fluorophenyl) piperazin-1-yl)benzaldehyde was synthesized by a reaction of 1-(4-fluorophenyl)piperazine and 4-Fluorobenzaldehyde. Then, aldehyde (**1**) reacted with thiosemicarbazide, which was performed in ethanol with a catalytic amount of CH_3COOH to provide 2-(4-(4-(4-fluorophenyl)piperazin-1-yl)benzylidene)hydrazine-1-carbothioamide (2) in good yields. Finally, target compounds (**3a**–**l**) were prepared through ring closure reaction using obtained thiosemicarbazide (**2**) and an appropriate 2-bromoacetophenone. The final compounds were purified, and their structures were characterized by

spectroscopic methods (^{1}H-NMR, ^{13}C-NMR, and LCMSMS). In the ^{1}H NMR spectrum, 1,4-disubstituted benzene protons had doublet peaks between 7.52 ppm and 7.55 ppm. Fluorophenyl hydrogens and disubstitue phenyl hydrogens gave multiplet peaks between 6.97 ppm and 7.12 ppm. Thiazole hydrogens had singlet peaks between 7.09 ppm and 7.68 ppm. Hydrazone protons gave singlet peaks between 7.94 ppm and 7.97 ppm. In the ^{13}C NMR spectrum, aliphatic peaks belonging to substituents were observed between 21 ppm and 55 ppm. Aromatic carbons were gained between 102 ppm and 169 ppm. Carbonyl carbon gave a peak over 168 ppm. All masses were in accordance with the estimated M+H values. Structure elucidations of the final compounds were performed by IR, ^{1}H-NMR, ^{13}C-NMR, and MS spectroscopic methods (see Supplementary Materials)

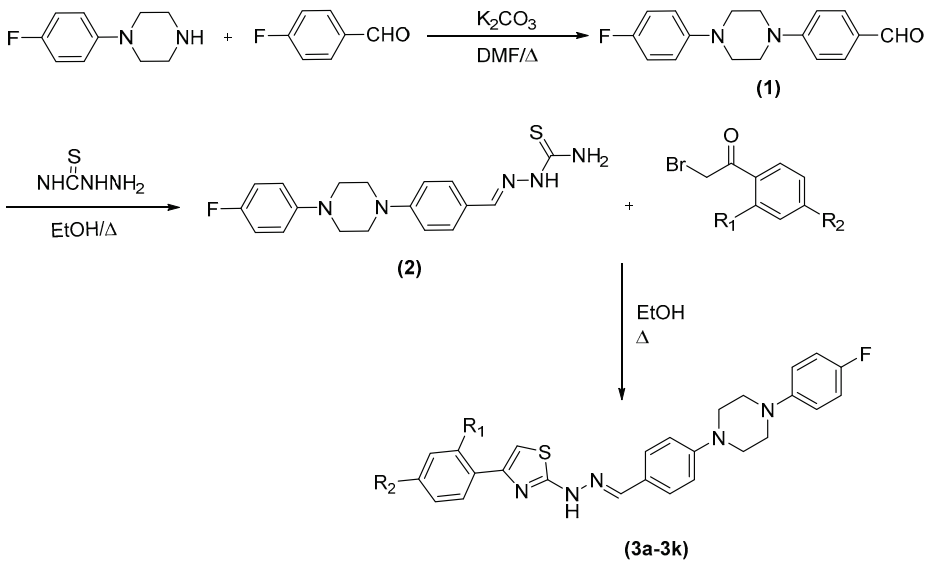

Compounds	R_1	R_2
3a	-H	-H
3b	-H	-CH_3
3c	-H	-OCH_3
3d	-H	-NO_2
3e	-H	-CN
3f	-H	-F
3g	-H	-Cl
3h	-H	-Br
3i	-H	-CF_3
3j	-CH_3	-CH_3
3k	-Cl	-Cl

Scheme 1. Synthesis of the target compounds **(3a–k)**.

2.2. Anticholinesterase Activity Assay

To determine the potential interest of the thiazole-piperazine synthesized, AChE and butyrylcholinesterase (BChE) inhibitory potency was evaluated according to a modified Ellman method with commercially obtainable donepezil as the reference standard. Initially, all the obtained compounds were tested at 10^{-3} M and 10^{-4} M concentrations and the ChE inhibitory results are outlined in Table 1. With respect to the activity results, it was determined that most of the tested compounds showed better inhibitory activity against AChE than BChE activity. Compounds **3a**, **3c** and **3i** indicated more than 50% activity at the 10^{-4} M concentration. Then, the IC_{50} values of the active compounds were determined using 10^{-3}–10^{-9} M concentrations against AChE, along with the reference drug donepezil (Table 1). The IC_{50} values of the compounds **3a**, **3c** and **3i** were calculated as

0.0496 ± 0.002 μM, 0.0317 ± 0.001 μM and 0.2158 ± 0.010 μM, respectively, for AChE. According to the results of activity tests, some general results can be listed as follows. The compounds **3a**, **3c** and **3i** contain the non-substituted, methoxy and trifluoromethyl substituents on the phenyl ring, respectively. The most potent AchE inhibitory activity was observed for the compounds with methoxy at the para position of the benzene ring (**3c**), with IC_{50} values of 0.0317 μM.

2.3. Monoamine Oxidase Activity Assay

In order to investigate the monoamine oxidase enzyme inhibitory effects of synthesized compounds, MAO-A and MAO-B enzyme activities were performed by using a fluorometric inhibition method. Moclobemide and selegiline were used as standard drugs for MAO-A and MAO-B enzymes, respectively. Test compounds and standard drugs were used in the same concentrations as in AChE and BChE enzyme activity assays. In Table 2, MAO enzyme inhibitory results are given. According to these findings, none of the tested compounds displayed remarkable inhibition potency against the MAO-A enzyme. It was seen that synthesized compounds showed better inhibition profile against MAO-B that MAO-A. The obtained compounds showed generally moderate activity against the MAO-B enzyme. Compounds **3a**, **3c** and **3d** showed inhibition profiles with 2.107 ± 0.086 μM, 1.015 ± 0.042 μM and 5.204 ± 0.153 μM IC_{50} values, respectively.

2.4. Enzyme Kinetic Studies

To decide the mechanism of enzyme inhibition, the kinetic study was performed with the most active compounds, **3a**, **3c** and **3i**. The type of inhibition was estimated by means of linear Lineweaver-Burk lands, and the substrate speed curves in the presence and absence of **3a**, **3c** and **3i** of the strongest compounds were verified in the enzyme kinetics analysis. Compounds used for kinetic study were ready at concentrations of $2 \times IC_{50}$, IC_{50} and $IC_{50}/2$. In the initial velocity measurements, different substrate concentrations, ranging from 600 μM to 18.75 μM, were used for the AChE enzyme. The secondary plots of the Km/Vmax (slope) versus changing concentrations were used to determine Ki (intercept on the x-axis) values of compounds [30]. The graphical analyses of steady-state inhibition data for representative compound **3c** are exhibited in Figure 4. Reversible inhibition comprises of the ensuing subtypes: competitive, uncompetitive, noncompetitive or mixed-type. Such inhibitions can be determined using Lineweaver–Burk plots. According to the Lineweaver–Burk graphics, mixed type inhibition can be allowed if the lines do not cross the x or y axis at the same point. Based on the gained plot, a mixed type of inhibition by compound **3c** was established. That is, the compound can bind to the enzyme–substrate complex or to the free enzyme. It also means that the compound is a reversible inhibitor; reversible compounds can be bound to the enzyme by non-covalent interactions such as ionic bonds, hydrophobic interactions and hydrogen bonds deprived of any chemical bonding or reaction with the enzyme. These interactions take place quickly and can be easily reversed. For that reason, the enzyme–inhibitor complex is rapidly degraded immediately before irreversible inhibition. With this feature, these reversible inhibitors exhibit a lower risk of side effects than irreversible inhibitors. As a result, enzyme kinetics studies have shown the biological importance of compound **3c** owing to its mixed type forces, as opposed to reversible enzyme inhibitors.

Table 1. Inhibition (%) of compounds **3a–k** against AChE and butyrylcholinesterase (BChE) enzymes.

Comp.	AChE % Inhibition		BChE % Inhibition		AChE IC_{50} (μM)	Comp.	AChE % Inhibition		BChE % Inhibition		AChE IC_{50} (μM)
	10^{-3} M	10^{-4} M	10^{-3} M	10^{-4} M			10^{-3} M	10^{-4} M	10^{-3} M	10^{-4} M	
3a	84.20 ± 0.89	70.58 ± 0.75	21.53 ± 0.38	19.32 ± 0.28	0.0496 ± 0.002	**3g**	64.55 ± 0.67	37.80 ± 0.60	38.54 ± 0.35	20.25 ± 0.35	-
3b	75.28 ± 1.05	45.90 ± 0.88	37.40 ± 0.67	25.34 ± 0.58	-	**3h**	75.33 ± 1.06	47.12 ± 0.74	40.65 ± 0.68	35.52 ± 0.41	-
3c	88.45 ± 1.10	72.20 ± 0.97	27.96 ± 0.43	21.64 ± 0.65	0.0317 ± 0.001	**3i**	80.70 ± 1.02	62.79 ± 0.82	45.35 ± 0.52	35.36 ± 0.39	0.2158 ± 0.010
3d	76.70 ± 1.12	38.55 ± 0.76	35.38 ± 0.49	31.85 ± 0.56	-	**3j**	53.75 ± 0.62	26.90 ± 0.55	31.88 ± 0.47	25.66 ± 0.49	-
3e	71.20 ± 0.90	42.32 ± 0.63	31.79 ± 0.61	24.86 ± 0.38	-	**3k**	35.66 ± 0.57	20.40 ± 0.30	28.59 ± 0.25	20.96 ± 0.61	-
3f	78.40 ± 1.04	48.15 ± 0.87	28.19 ± 0.42	20.45 ± 0.35	-	**Donepezil**	99.37 ± 1.16	98.64 ± 1.09	-	-	0.0287 ± 0.005

Table 2. Inhibition (%) of compounds **3a–3k** against MAO-A and MAO-B enzymes.

Comp.	MAO-A % Inhibition		MAO-B % Inhibition		MAO-B IC_{50} (μM)	Comp.	MAO-A % Inhibition		MAO-B% Inhibition		MAO-B IC_{50} (μM)
	10^{-3} M	10^{-4} M	10^{-3} M	10^{-4} M			10^{-3} M	10^{-4} M	10^{-3} M	10^{-4} M	
3a	38.20 ± 0.95	20.15 ± 0.63	78.25 ± 1.05	70.23 ± 0.99	2.107 ± 0.086	**3g**	48.23 ± 0.97	30.21 ± 0.50	68.12 ± 1.12	41.75 ± 0.86	-
3b	44.21 ± 1.08	25.75 ± 0.80	60.82 ± 1.11	46.7 ± 0.98	-	**3h**	34.17 ± 0.58	22.19 ± 0.47	68.92 ± 1.25	39.11 ± 0.63	-
3c	38.65 ± 0.58	21.79 ± 0.55	85.12 ± 1.00	70.26 ± 0.85	1.015 ± 0.042	**3i**	38.19 ± 0.78	22.75 ± 0.54	59.08 ± 0.77	40.25 ± 0.58	-
3d	50.98 ± 0.97	39.12 ± 0.71	75.66 ± 1.06	65.17 ± 0.97	5.204 ± 0.153	**3j**	48.21 ± 0.88	40.23 ± 0.52	69.20 ± 1.20	40.75 ± 0.92	-
3e	47.22 ± 0.88	23.50 ± 0.60	58.11 ± 0.90	43.08 ± 0.71	-	**3k**	35.20 ± 0.48	19.14 ± 0.40	55.09 ± 0.92	34.17 ± 0.81	-
3f	30.11 ± 0.47	19.28 ± 0.41	57.33 ± 1.03	39.20 ± 0.79	-	**Moclobemide**	91.25 ± 2.8	78.20 ± 2.55	-	-	-
						Selegiline	-	-	98.21 ± 2.05	94.12 ± 1.96	0.040 ± 0.002

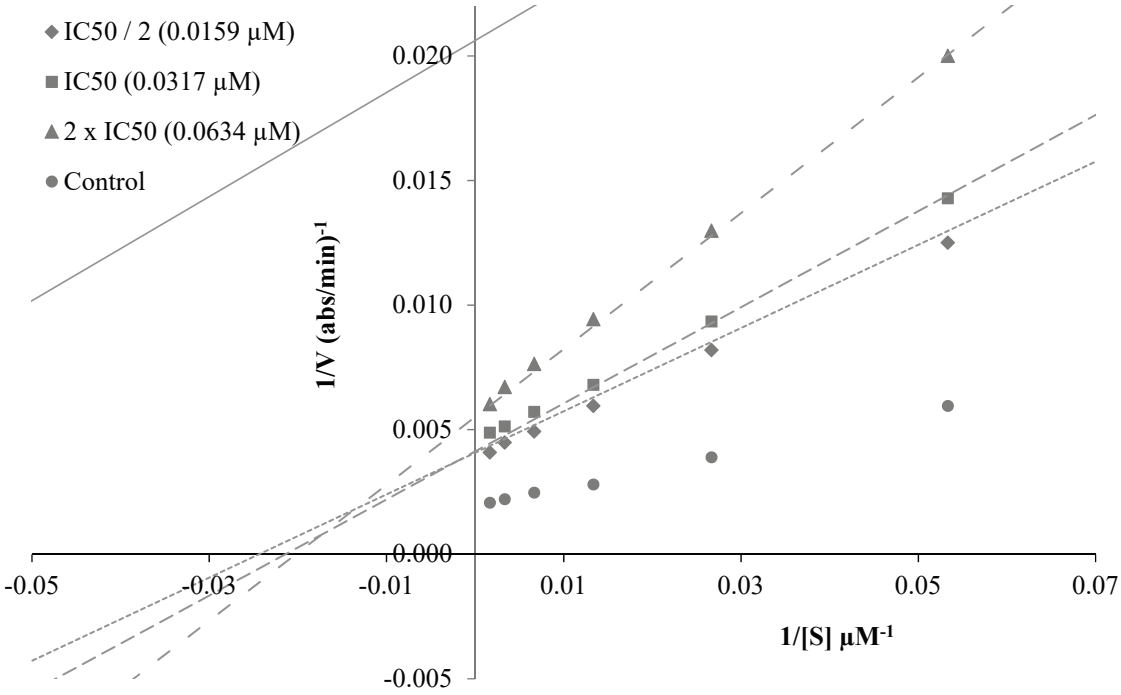

Figure 4. *Cont.*

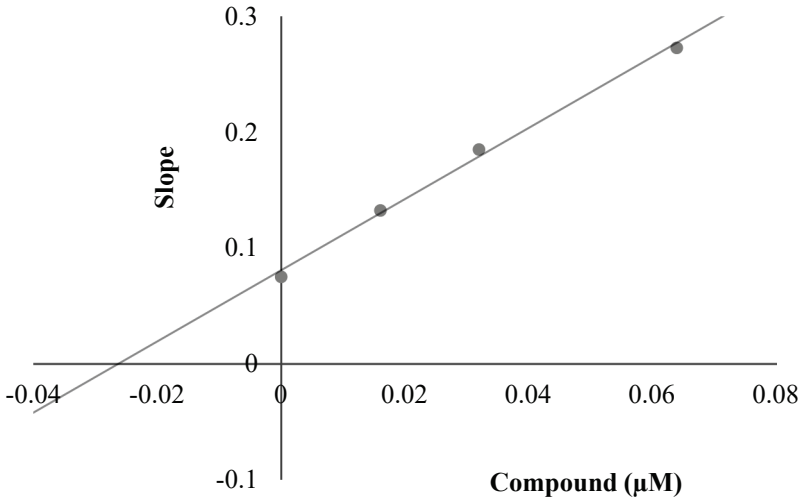

Figure 4. (**A**) Lineweaver–Burk plots for the inhibition of AChE by compound **3c**. [S], substrate concentration (μM); V, reaction velocity (abs/min)$^{-1}$. (**B**) Secondary plot for the calculation of steady-state inhibition constant (K_i) of compound **3c**. Ki was calculated as 0.0197 μM.

2.5. Molecular Docking Studies

Docking studies were performed in order to gain more insight into the binding mode of compound **3c** to the AChE enzyme. Studies were carried out by using the X-ray crystal structure of Homo sapiens AChE (hAChE PDB ID:4EY7) [31], obtained from the Protein Data Bank server (www.pdb.org).

The 5,6-dimethoxy indanone moiety binds to the peripheral anionic site (PAS) of the enzyme active region by interacting with Trp286 and Phe295 amino acid residues. The rest of the structure, a benzylpiperidine group, binds to the catalytic anionic site (CAS) by interacting with Trp86 [31]. The docking pose of compound **3c** is presented in Figure 5. It can be seen from this figure that compound **3c** settles in the CAS and PAS regions of the enzyme active site, in a similar position to

donepezil. This compound could bind to both PAS and CAS by interacting with Trp286 and Trp86 amino acids, respectively.

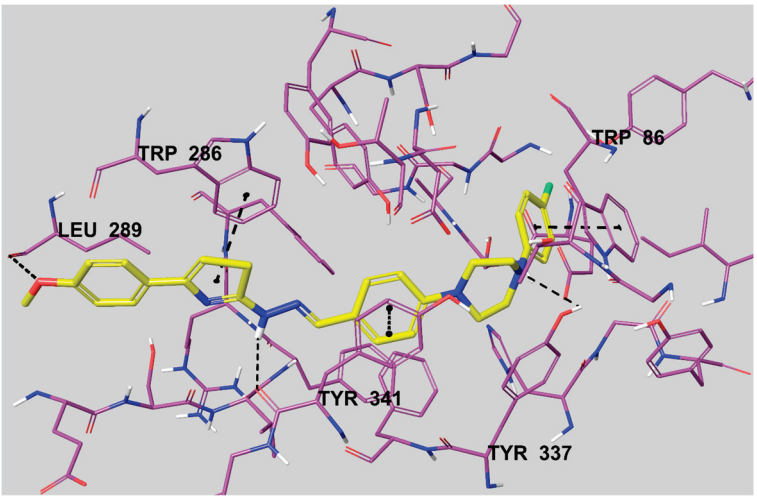

Figure 5. The interacting mode of compound **3c** in the active region of AChE. The inhibitor, colored with yellow, and the important residues, colored with purple, in the active site of the enzyme are presented by a tube model.

According to Figure 5, the thiazole ring creates a π-π interaction with the indole of Trp286. The other π-π interaction is seen between the 4-fluorophenyl ring and the indole of Trp86. The last similar interaction is observed between the phenyl ring, near to the piperidine ring, and the phenyl of Tyr341. There are three hydrogen bonds besides these mentioned interactions. The first of the hydrogen bonds is seen between the oxygen atom of the 4-methoxyphenyl moiety and the carbonyl of Leu289. Also, it is understood that the nitrogen atoms of the imine group and the piperidine ring form a basic center. The amino of the imine group establishes a hydrogen bond with the carbonyl of Tyr341. The last hydrogen bond is observed between the nitrogen atom of the piperidine ring and the hydroxyl of Tyr337.

2.6. Prediction of Blood–Brain Barrier (BBB) Permeability

It is known that drugs that specifically target the central nervous system (CNS) have to pass the blood–brain barrier (BBB). Thus, penetration to the BBB is very important for CNS drug candidates, and should be clarified as early as possible in the drug discovery studies [32]. Therefore, the BBB permeability of the synthesized compounds (**3a**–**k**) was calculated by a CBLigand-BBB prediction server [33]. This online predictor practices two different algorithms, AdaBoost and Support Vector Machine (SVM), combining with four different fingerprints, employed to predict if a compound can pass (+) or cannot pass (−) the BBB. Predictor scores are higher than 0 if a compound can pass the BBB. Calculations for all compounds resulted in BBB (+), which is essential for AchE inhibitors to display their biological activity.

3. Materials and Methods

3.1. Chemistry

All chemicals used in the syntheses were purchased either from Merck Chemicals (Merck KGaA, Darmstadt, Germany) or Sigma-Aldrich Chemicals (Sigma-Aldrich Corp., St. Louis, MO, USA). The reactions and the purities of the compounds were observed by thin layer chromatography (TLC) on silica gel 60 F254aluminum sheets obtained from Merck (Darmstadt, Germany). Melting points of the synthesized compounds were recorded by MP90 digital melting point apparatus (Mettler Toledo,

Ohio, USA) and were presented as uncorrected. ^{1}H NMR and ^{13}C NMR spectra were recorded by a Bruker 300 MHz and 75 MHz digital FT-NMR spectrometer (Bruker Bioscience, Billerica, MA, USA) in DMSO-d_6, respectively. In the NMR spectra, splitting patterns were designated as follows: s: singlet; d: doublet; t: triplet; m: multiplet. Coupling constants (*J*) were reported as Hertz. LC-MS-MS studies were performed on a Schimadzu, 8040 LCMSMS spectrophotometer (Shimadzu, Tokyo, Japan).

3.1.1. Synthesis of 4-(4-(4-fluorophenyl)piperazin-1-yl)benzaldehyde (1)

To a stirred solution of 1-(4-fluorophenyl)piperazine (2.23 g, 0.0124 mol) in DMF (20 mL), 4-fluorobenzaldehyde (1.34 mL, 0.0124 mol) was added, followed by potassium carbonate (1.71 g, 0.0124 mol). The resulting mixture was heated to reflux at 160 °C. After the completion of the reaction, the mixture was poured into iced water after cooling, and the precipitated product was washed with water, dried, and recrystallized from ethanol.

3.1.2. Synthesis of 2-(4-(4-(4-fluorophenyl)piperazin-1-yl)benzylidene)hydrazine-1-carbothioamide (2)

A mixture of 4-(4-(4-fluorophenyl)piperazin-1-yl)benzaldehyde (**2**) (3.18 gr, 0.0112 mol), thiosemicarbazide (1.01 gr, 0.0112 mol), and a catalytic quantity of acetic acide (CH_3COOH) was refluxed in ethanol (50 mL) for 24 h. After the completion of the reaction, the mixture was cooled, the precipitated product was filtered, washed with cold ethanol, dried, and recrystallized from methanol.

3.1.3. General procedure for the synthesis of target compounds (**3a–j**)

To a stirred solution of 2-(4-(4-(4-fluorophenyl)piperazin-1-yl)benzylidene)hydrazine-1-carbothioamide (**2**) (0.84 mmol) in EtOH (20 mL), appropriate 2-bromo-1-(2,4-substituephenyl)ethan-1-one derivatives (0.84 mmol) were added, and then refluxed for 10 h. The precipitated product was filtered, washed with cold ethanol, dried, and recrystallized from ethanol.

2-(2-(4-(4-(4-fluorophenyl)piperazin-1-yl)benzylidene)hydrazineyl)-4-phenylthiazole (**3a**)

Yield: 85 %, M.P. = 247.6–249.9 °C, ^{1}H-NMR (300 MHz, DMSO-d_6): 3.20–3.22 (m, 4H, piperazine), 3.35–3.38 (m, 4H, piperazine), 6.97–7.09 (m, 6H, fluorophenyl, disubstituephenyl), 7.27 (s, 1H, thiazole), 7.32 (t, 1H, *J* = 5.8 Hz, monosubstituephenyl), 7.41 (t, 2H, *J* = 7.3 Hz, monosubstituephenyl), 7.53 (d, 2H, *J* = 8.8 Hz, disubstituepheyl), 7.86 (d, 2H, *J* = 8.4 Hz, monosubstituephenyl), 7.95 (s, 1H, −N=CH−), 11.93 (s, 1H, −NH). ^{13}C-NMR (75 MHz, DMSO-d_6): δ = 48.1 (CH2), 49.5 (CH2), 103.6 (CH), 109.3 (CH), 115.5 (CH), 115.8 (J_2 = 21.6 Hz, CH), 118.0 (J_3 = 7.4 Hz, CH), 125.3 (C), 126.0 (CH), 128.0 (CH), 129.1 (CH), 135.3 (C), 138.0 (C), 142.2 (CH), 148.2 (C), 151.9 (C), 156.7 (J_1=234.4 Hz, C), 168.9 (C). ESI-MS $[M + H]^+$: 458.

2-(2-(4-(4-(4-fluorophenyl)piperazin-1-yl)benzylidene)hydrazineyl)-4-(p-tolyl)thiazole (**3b**)

Yield: 80%, M.P. = 187.5–189.2 °C, ^{1}H-NMR (300 MHz, DMSO-d_6): 2.32 (s, 3H, $-CH_3$), 3.22–3.23 (m, 4H, piperazine), 3.35–3.37 (m, 4H, piperazine), 7.02–7.07 (m, 6H, fluorophenyl, disubstituephenyl), 7.19–7.22 (m, 3H, thiazole, disubstituephenyl), 7.52 (d, 2H, *J* = 8.8 Hz, disubstituepheyl), 7.74 (d, 2H, *J* = 8.1 Hz, disubstituephenyl), 7.94 (s, 1H, −N=CH−), 11.89 (s, 1H, −NH). ^{13}C-NMR (75 MHz, DMSO-d_6): δ = 21.2 (CH_3), 48.0 (CH_2), 49.5 (CH_2), 102.7 (CH), 114.52 (C), 115.5 (CH), 115.8 (J_2 = 21.8 Hz, CH), 118.0 (J_3 = 7.5 Hz, CH), 125.3 (C), 126.0 (CH), 127.9 (CH), 129.6 (CH), 131.8 (C), 132.6 (C), 137.2 (C), 142.2 (CH), 148.2 (C), 151.9 (C), 157.1 (J_1 = 234.7 Hz, C), 168.7 (C). ESI-MS $[M + H]^+$: 472.

2-(2-(4-(4-(4-fluorophenyl)piperazin-1-yl)benzylidene)hydrazineyl)-4-(4-methoxyphenyl)thiazole (**3c**)

Yield: 79%, M.P. = 241.7–244.4 °C, ^{1}H-NMR (300 MHz, DMSO-d_6): 3.22–3.23 (m, 4H, piperazine), 3.35-3.37 (m, 4H, piperazine), 3.78 (s, 3H, $-OCH_3$), 6.96 (d, 2H, *J* = 8.8 Hz disubstituephenyl), 7.02–7.07 (m, 6H, fluorophenyl, disubstituephenyl), 7.09 (s, 1H, thiazole), 7.52 (d, 2H, *J* = 8.7 Hz, disubstituephenyl), 7.55 (d, 2H, *J* = 8.8 Hz, disubstituephenyl), 7.78 (d, 2H, *J* = 8.8 Hz, disubstituephenyl),

7.94 (s, 1H, −N=CH−), 11.88 (s, 1H, −NH). ^{13}C-NMR (75 MHz, DMSO-d_6): δ = 48.0 (CH_2), 49.5 (CH_2), 55.6 (CH_3), 101.5 (CH), 114.4 (CH), 115.5 (CH), 115.8 (J_2 = 21.8 Hz, CH), 118.0 (J_3 = 7.6 Hz, CH), 125.3 (C), 127.3 (CH), 127.9 (CH), 138.9 (C), 142.1 (CH), 148.2 (C), 151.9 (C), 156.8 (J_1 = 228.4 Hz, C), 159.2 (C), 168.7 (C). ESI-MS [M + H]$^+$: 488.

2-(2-(4-(4-(4-fluorophenyl)piperazin-1-yl)benzylidene)hydrazineyl)-4-(4-nitrophenyl)thiazole (**3d**)

Yield: 84%, M.P. = 236.6–238.9 °C. ^{1}H-NMR (300 MHz, DMSO-d_6): 3.28–3.30 (m, 4H, piperazine), 3.40–3.42 (m, 4H, piperazine), 7.05–7.12 (m, 6H, fluorophenyl, disubstituephenyl), 7.55 (d, 2H, J = 8.8 Hz, disubstituephenyl), 7.68 (s, 1H, thiazole), 7.97 (s, 1H, −N=CH−), 8.10 (d, 2H, J = 9.0 Hz, disubstituepheyl), 8.27 (d, 2H, J = 9.0 Hz, disubstituephenyl), 12.06 (s, 1H, −NH). ^{13}C-NMR (75 MHz, DMSO-d_6): δ = 47.9 (CH_2), 49.9 (CH_2), 108.6 (CH), 115.7 (CH), 116.0 (J_2 = 21.9 Hz, CH), 118.6 (J_3 = 7.5 Hz, CH), 124.6 (CH), 125.3 (C), 126.8 (CH), 128.0 (CH), 141.2 (C), 142.8 (CH), 146.6 (C), 147.3 (C), 148.9 (C), 151.7 (C), 157.3 (J_1 = 235.7 Hz, C), 169.2 (C). ESI-MS [M + H]$^+$: 503.

4-(2-(2-(4-(4-(4-fluorophenyl)piperazin-1-yl)benzylidene)hydrazineyl)thiazol-4-yl)benzonitrile (**3e**)

Yield: 77%, M.P. = 251.2–254.8 °C,^{1}H-NMR (300 MHz, DMSO-d_6): 3.20–3.22 (m, 4H, piperazine), 3.35-3.36 (m, 4H, piperazine), 7.00–7.06 (m, 6H, fluorophenyl, disubstituephenyl), 7.53 (d, 2H, J = 8.8 Hz, disubstituephenyl), 7.58 (s, 1H, thiazole), 7.85 (d, 2H, J = 8.5 Hz, disubstituepheyl), 7.97 (s, 1H, −N=CH−), 8.03 (d, 2H, J = 8.5 Hz, disubstituephenyl), 12.01 (s, 1H, −NH). ^{13}C-NMR (75 MHz, DMSO-d_6): δ = 47.9 (CH_2), 49.5 (CH_2), 107.5 (C), 109.9 (CH), 115.5 (CH), 115.8 (J_2 = 21.9 Hz, CH), 118.1 (J_3 = 7.4 Hz, CH), 119.5 (C), 125.1 (C), 126.6 (CH), 128.0 (CH), 133.1 (CH), 139.3 (C), 142.7 (CH), 148.1 (C), 149.3 (C), 151.9 (C), 156.8 (J_1 = 242.1 Hz, C). 169.2 (C). ESI-MS [M + H]$^+$: 483.

4-(4-fluorophenyl)-2-(2-(4-(4-(4-fluorophenyl)piperazin-1-yl)benzylidene)hydrazineyl)thiazole (**3f**)

Yield: 75%, M.P. = 250.1–251.9 °C, ^{1}H-NMR (300 MHz, DMSO-d_6): δ 3.19-3.22 (m, 4H, piperazine), 3.35–3.38 (m, 4H, piperazine), 7.01–7.06 (m, 6H, fluorophenyl, disubstituephenyl), 7.19–7.26 (m, 3H, thiazole, disubstituephenyl), 7.52 (d, 2H, J = 8.8 Hz, disubstituepheyl), 7.90 (dd, 2H, J_1 = 5.6 Hz, J_2 = 8.1 Hz, disubstituephenyl), 7.95 (s, 1H, −N=CH−), 11.92 (s, 1H, −NH). ^{13}C-NMR (75 MHz, DMSO-d_6): δ = 48.0 (CH_2), 49.5 (CH_2), 103.4 (CH), 115.5 (CH), 115.8 (J_2 = 21.7 Hz, CH), 115.9 ($J_{2'}$ = 21.3 Hz, CH), 118.0 (J_3 = 7.4 Hz, CH), 125.2 (C), 127.9 (CH), 127.9 ($J_{3'}$ = 7.6 Hz, CH), 131.9 (C), 142.3 (CH), 148.2 (C), 149.9 (C), 151.9 (C), 156.7 (J_1 = 233.2 Hz, C), 162.1 ($J_{1'}$ = 245.1 Hz, C), 168.9 (C). ESI-MS [M + H]$^+$: 476.

4-(4-chlorophenyl)-2-(2-(4-(4-(4-fluorophenyl)piperazin-1-yl)benzylidene)hydrazineyl)thiazole (**3g**)

Yield: 73%, M.P. = 236.2–238.8 °C, ^{1}H-NMR (300 MHz, DMSO-d_6): 3.20–3.23 (m, 4H, piperazine), 3.35–3.39 (m, 4H, piperazine), 7.02–7.07 (m, 6H, fluorophenyl, disubstituephenyl), 7.34 (s, 1H, thiazole), 7.46 (d, 2H, J = 8.6 Hz, disubstituepheyl), 7.53 (d, 2H, J = 8.8 Hz, disubstituephenyl), 7.87 (d, 2H, J = 8.6 Hz, disubstituephenyl), 7.95 (s, 1H, −N=CH−), 11.94 (s, 1H, −NH). ^{13}C-NMR (75 MHz, DMSO-d_6): δ = 47.9 (CH_2), 49.6 (CH_2), 104.4 (CH), 115.5 (CH), 115.8 (J_2 = 21.9 Hz, CH), 118.1 (J_3 = 7.6 Hz, CH), 125.3 (C), 127.7 (CH), 127.9 (CH), 129.1 (CH), 132.3 (C), 134.1 (C), 142.4 (CH), 148.0 (C), 149.1 (C), 151.9 (C), 156.8 (J_1 = 234.7 Hz, C), 169.0 (C). ESI-MS [M + H]$^+$: 492.

4-(4-bromophenyl)-2-(2-(4-(4-(4-fluorophenyl)piperazin-1-yl)benzylidene)hydrazineyl)thiazole (**3h**)

Yield: 80%, M.P. = 243.2–246.7 °C, ^{1}H-NMR (300 MHz, DMSO-d_6): 3.20–3.23 (m, 4H, piperazine), 3.35–3.38 (m, 4H, piperazine), 7.02–7.07 (m, 6H, fluorophenyl, disubstituephenyl), 7.35 (s, 1H, thiazole), 7.53 (d, 2H, J = 8.8 Hz, disubstituepheyl), 7.59 (d, 2H, J = 8.6 Hz, disubstituephenyl), 7.80 (d, 2H, J = 8.6 Hz, disubstituephenyl), 7.95 (s, 1H, −N=CH−), 11.93 (s, 1H, −NH). ^{13}C-NMR (75 MHz, DMSO-d_6): δ = 48.0 (CH_2), 49.5 (CH_2), 104.5 (CH), 115.5 (CH), 115.8 (J_2 = 21.9 Hz, CH), 118.1 (J_3 = 7.7 Hz,

CH), 120.9 (C), 125.2 (C), 127.9 (CH), 128.0 (CH), 132.0 (CH), 134.5 (C), 142.4 (CH), 148.1 (C), 149.7 (C), 151.9 (C), 156.8 (J_1 = 234.4 Hz, C), 169.0 (C). ESI-MS [M + H]$^+$: 536.

2-(2-(4-(4-(4-fluorophenyl)piperazin-1-yl)benzylidene)hydrazineyl)-4-(4-(trifluoromethyl)phenyl) thiazole (**3i**)

Yield: 79%, M.P. = 237.8–240.1 °C, ^{1}H-NMR (300 MHz, DMSO-d_6): δ 3.21–3.23 (m, 4H, piperazine), 3.35–3.38 (m, 4H, piperazine), 7.01–7.07 (m, 6H, fluorophenyl, disubstituephenyl), 7.51–7.55 (m, 3H, thiazole, disubstiuephenyl), 7.76 (d, 2H, *J* = 8.4 Hz, disubstituephenyl), 7.96 (s, 1H, −N=CH−), 8.06 (d, 2H, *J* = 8.1 Hz, disubstituephenyl), 12.00 (s, 1H, −NH). ^{13}C-NMR (75 MHz, DMSO-d_6): δ = 48.0 (CH_2), 49.5 (CH_2), 106.5 (CH), 115.5 (CH), 115.8 (J_2 = 21.7 Hz, CH), 118.0 (J_3 = 7.6 Hz, CH), 124.8 (q, J_1 = 269.9 Hz, C), 125.1 (C), 126.0 (q, J_3 = 3.5 Hz, CH), 126.5 (CH), 127.5 (q, J_2 = 31.5 Hz, CH), 128.0, (C) 138.9 (C), 142.6 (CH), 148.2 (q, J_4 = 1.7 Hz, C), 149.5 (C), 152.0 (C), 156.7 (d, J_1 = 234.5 Hz, C), 169.1 (C). ESI-MS [M + H]$^+$: 526.

4-(2,4-dimethylphenyl)-2-(2-(4-(4-(4-fluorophenyl)piperazin-1-yl)benzylidene)hydrazineyl)thiazole (**3j**)

Yield: 81%, M.P. = 240.6–243.1 °C. ^{1}H-NMR (300 MHz, DMSO-d_6): δ 2.27 (s, 3H, −CH_3), 2.41 (s, 3H, −CH_3), 3.19–3.22 (m, 4H, piperazine), 3.34–3.37 (m, 4H, piperazine), 6.81 (s, 1H, thiazole), 7.01–7.06 (m, 7H, fluorophenyl, trisubstituephenyl), 7.50 (d, 2H, *J* = 8.0 Hz, disubstituephenyl), 7.52 (d, 2H, *J* = 8.9 Hz, disubstituephenyl), 7.94 (s, 1H, −N=CH−), 11.83 (s, 1H, −NH). ^{13}C-NMR (75 MHz, DMSO-d_6): δ = 21.1 (CH_3), 21.6 (CH_3), 48.0 (CH_2), 49.5 (CH_2), 105.7 (CH), 115.5 (CH), 115.8 (d, J_2 = 21.8 Hz, CH), 118.0 (d, J_3 = 7.5 Hz, CH), 125.4 (C), 126.8 (CH), 127.9 (CH), 129.6 (CH), 131.9 (CH), 132.6 (C), 135.5 (C), 137.0 (C), 142.1 (CH), 148.2 (C), 151.1 (C), 151.9 (C), 156.7 (d, J_1 = 234.4 Hz, C), 167.8 (C). ESI-MS [M + H]$^+$: 486.

4-(2,4-dichlorophenyl)-2-(2-(4-(4-(4-fluorophenyl)piperazin-1-yl)benzylidene)hydrazineyl) thiazole (**3k**)

Yield: 78%, M.P. = 216.2–219.3 °C, ^{1}H-NMR (300 MHz, DMSO-d_6): δ 3.22–3.24 (m, 4H, piperazine), 3.36–3.38 (m, 4H, piperazine), 7.02–7.07 (m, 6H, fluorophenyl, disubstituephenyl), 7.36 (s, 1H, thiazole), 7.49 (dd, 1H, J_1 = 2.2 Hz, J_2 = 8.6 Hz, trisubstituepheyl), 7.53 (d, 2H, *J* = 8.9 Hz, disubstituephenyl), 7.67 (d, 1H, *J* = 2.2 Hz, trisubstituephenyl), 7.91 (d, 1H, *J* = 8.5 Hz, trisubstituephenyl), 7.96 (s, 1H, −N=CH−), 11.96 (s, 1H, −NH). ^{13}C-NMR (75 MHz, DMSO-d_6): δ = 47.9 (CH2), 49.6 (CH2), 109.2 (CH), 115.6 (CH), 115.8 (J_2 = 21.8 Hz, CH), 118.1 (J_3 = 7.5 Hz, CH), 125.3 (C), 127.9 (CH), 128.0 (CH), 130.2 (CH), 132.0 (C), 132.7 (CH), 132.9 (C), 142.5 (CH), 146.3 (C), 147.9 (C), 151.9 (C), 156.9 (J_1 = 234.9 Hz, C), 168.0 (C). ESI-MS [M + H]$^+$: 526.

3.2. Activity Studies

3.2.1. Anticholinesterase Activity Assay

The inhibitory capacity of the obtained compounds on AChE and BChE biological activities was assessed using a modified Ellman's spectrometric method, as described in our previous studies [34–38]. Donepezil were used as a reference drug. All pipetting procedures in the enzyme inhibition assay were carried out via a robotics system, Biotek Precision XS (Winooski, VT, USA). A BioTek-Synergy H1 microplate reader (Winooski, VT, USA) was used to carry out measurements of percent inhibition at 412 nm, and the IC_{50} values of the selected compounds were performed as previously described.

3.2.2. Monoamine Oxidase Activity Assay

To investigate the MAO-A and MAO-B enzyme inhibition profiles of the synthesized compounds, the fluorometric enzyme inhibition assay was carried out, as previously defined by us [30,38–40]. Ampliflu™ Red (10-Acetyl-3,7-dihydroxyphenoxazine) was used as a fluorescence reagent in this assay. All reagents and enzymes (Ampliflu™ Red, peroxidase from horseradish, hMAO-A, hMAO-B,

H2O2, tyramine hydrochloride, moclobemide and selegiline) were supplied by Sigma-Aldrich (Steinheim, Germany).

3.2.3. Kinetic Studies of Enzyme Inhibition

In order to determine the type of inhibition on AChE, enzyme kinetic studies were carried out for compound **3c**. The enzyme kinetic assay was performed by means of Ellman's method, in keeping with the previous studies reported by our research group [34–38].

3.3. Molecular Docking Studies

Docking studies using the in silico procedure were carried out for compound **3c** in order to determine the binding modes on the AChE enzyme active site. The X-ray crystal structure (PDB ID: 4EY7) [28] of AChE from the Protein Data Bank server (www.pdb.org) was provided, and the docking procedure was performed as described in our previous work [34–38].

3.4. Prediction of BBB Permeability

The BBB permeability of the compounds was evaluated by an online BBB Predictor [33].

4. Conclusions

AD is a progressive neurodegenerative disease related to the presence of extracellular neuritic plaques, or senile confusion in the intracellular neurofibrillary areas of the brain. Currently, there are 35 million people with AD dementia in the world, and this number will increase to approximately 100 million globally by 2050 if treatments are not found. In the present work, a series of novel thiazole-piperazine analogs (**3a**–**k**) were designed, synthesized and evaluated as inhibitors against AChE and BChE. Compounds **3a**, **3c** and **3i** (IC_{50} 0.0496, 0.0317 and 0.0287 μM against AChE, respectively) are the most potent ones in the series. None of them show strong affinity for BChE. So as to elucidate their in silico properties and the type of inhibition, binding studies and enzyme kinetics were performed for these compounds. The kinetic studies suggested that these compounds were reversible and mixed type enzyme inhibitors.

Donepezil can bind strongly to the enzyme active region owing to its dual binding sites. The 5,6-dimethoxyindanone moiety binds to the peripheral anionic site (PAS) of the enzyme active region by interacting with the Trp286 and Phe295 amino acid residues. The rest of the structure, the benzylpiperidine group, binds to the catalytic anionic site (CAS) by interacting with Trp86 [34]. In keeping with the molecular docking studies, compound 3c displayed effective AChE inhibition capability based on multiple binding patterns in the PAS and CAS of AChE. As already known, donepezil was able to bind strongly to the enzyme active region owing to its dual binding sites.

Supplementary Materials: The following are available online, Figure S1: 2-amino-4-substituted thiazole as a pharmacophore for acetylcholinesterase (AChE), Figure S2: Some AchE inhibitors, including a benzylamine moiety, Figure S3: General structure of target compounds, Figure S4: (**A**) Lineweaver–Burk plots for the inhibition of AChE by compound **3c**. [S], substrate concentration (μM); V, reaction velocity $(abs/min)^{-1}$. (**B**) Secondary plot for the calculation of steady-state inhibition constant (K_i) of compound **3c**. Ki was calculated as 0.0197 μM, Figure S5: The interacting mode of compound **3c** in the active region of AChE. The inhibitor, colored with yellow, and the important residues, colored with purple, in the active site of the enzyme are presented by a tube model, Table S1: Inhibition (%) of compounds **3a**–**k** against AChE and butyrylcholinesterase (BChE) enzymes, Table S2: Inhibition (%) of compounds **3a**–**3k** against MAO-A and MAO-B enzymes.

Author Contributions: Y.Ö. and Z.A.K. conceived and designed the experiments; D.O. performed the synthesis; S.L. performed analysis studies; B.N.S., performed activity tests; B.N.S. performed docking studies; D.O., U.A.Ç., B.N.S., S.L., B.K.Ç., Y.Ö. and Z.A.K. wrote the paper.

Funding: This study was financially supported by Anadolu University Scientific Projects Fund, Project No: 1905S033.

Conflicts of Interest: The authors declare no conflict of interest.

References

1. Alzheimer's Association. Alzheimer's disease facts and figures. *Alzheimers Dement.* **2015**, *11*, 332–384.
2. Eghtedari, M.; Sarrafi, Y.; Nadri, H.; Mahdavi, M.; Moradi, A.; Moghadam, F.H.; Emami, S.; Firoozpour, L.; Asadipour, A.; Sabzevari, O.; et al. New tacrine-derived AChE/BuChE inhibitors: Synthesis and biologicalevaluation of 5-amino-2-phenyl-4H-pyrano[2,3-b]quinoline-3-carboxylates. *Eur. J. Med. Chem.* **2017**, *128*, 237–246. [CrossRef] [PubMed]
3. Castro, A.; Martinez, A. Targeting Beta-Amyloid Pathogenesis Through Acetylcholinesterase Inhibitors. *Curr. Pharm. Design* **2006**, *12*, 4377–4387. [CrossRef]
4. Pisoni, D.S.; da Costa, J.S.; Gamba, D.; Petzhold, C.L.; Borges, A.C.A.; Ceschi, M.A.; Lunardi, P.; Gonçalves, C.A.S. Synthesis and AChE inhibitory activity of new chiral tetrahydroacridine analogues from terpenic cyclanones. *Eur. J. Med. Chem.* **2010**, *45*, 526–535. [CrossRef] [PubMed]
5. Sheng, R.; Xu, Y.; Hu, C.; Zhang, J.; Lin, X.; Li, J.; Yang, B.; He, Q.; Hu, Y. Design, synthesis and AChE inhibitory activity of indanone and aurone derivatives. *Eur. J. Med. Chem.* **2009**, *44*, 7–17. [CrossRef] [PubMed]
6. Padurariu, M.; Ciobica, A.; Lefter, R.; Serban, I.L.; Stefanescu, C.; Chirita, R. The oxidative stress hypothesis in Alzheimer's disease. *Psychiat. Danub.* **2013**, *25*, 401–409.
7. Stanton, F.; McHardy, H.Y.; Wang, L.; McCowen, S.V.; Valdez, M.C. Recent advances in acetylcholinesterase Inhibitors and Reactivators: An update on the patent literature (2012-2015). *Expert. Opin. Ther. Pat.* **2017**, *27*, 455–476.
8. Lane, R.M.; Potkin, S.G.; Enz, A. Targeting acetylcholinesterase and butyrylcholinesterase in dementia. *Int. J. Neuropsychopharmacol.* **2006**, *9*, 101–124. [CrossRef] [PubMed]
9. Colovic, M.B.; Krstic, D.Z.; Lazarevic-Pasti, T.D.; Bondzic, A.M.; Vasic, V.M. Acetylcholinesterase Inhibitors: Pharmacology and Toxicology. *Curr. Neuropharmacol.* **2013**, *11*, 315–335. [CrossRef] [PubMed]
10. McEneny-King, A.; Osman, W.; Edginton, A.N.; Rao, P.P.N. Cytochrome P450 binding studies of novel tacrine derivatives: Predicting the risk of hepatotoxicity. *Bioorg. Med. Chem. Lett.* **2017**, *27*, 2443–2449. [CrossRef] [PubMed]
11. Matsunaga, Y.; Tanaka, T.; Yoshinaga, K.; Ueki, S.; Hori, Y.; Eta, R.; Kawabata, Y.; Yoshii, K.; Matsumura, T.; Furuta, S.; et al. Acotiamide hydrochloride (Z-338), a new selective acetylcholinesterase inhibitor, enhances gastric motility without prolonging QT interval in dogs: Comparison with cisapride, itopride, and mosapride. *J. Pharmacol. Exp. Ther.* **2011**, *336*, 791–800. [CrossRef] [PubMed]
12. Sahin, Z.; Ertas, M.; Bender, C.; Bülbül, E.F.; Berk, B.; Biltekin, S.N.; Yurttaş, L.; Demirayak, Ş. Thiazole-substituted benzoylpiperazine derivatives as acetylcholinesterase inhibitors. *Drug Dev. Res.* **2018**, *79*, 406–425. [CrossRef] [PubMed]
13. Madni, M.; Ahmed, M.N.; Hameed, S.; Ali Shah, S.W.; Rashid, U.; Ayub, K.; Tahir, M.N.; Mahmood, T. Synthesis, quantum chemical, in vitro acetyl cholinesterase inhibition and molecular docking studies of four new coumarin based pyrazolylthiazole nuclei. *J. Mol. Struct.* **2018**, *1168*, 175–178. [CrossRef]
14. Ibrar, A.; Khan, A.; Ali, M.; Sarwar, R.; Mehsud, S.; Farooq, U.; Halimi, S.M.A.; Khan, I.; Al-Harrasi, A. Combined in vitro and in Silico Studies for the anticholinesterase activity and pharmacokinetics of coumarinyl thiazoles and oxadiazoles. *Front. Chem.* **2018**, *6*, 1–11. [CrossRef] [PubMed]
15. Tripathi, R.K.P.; Sasi, V.M.; Gupta, S.K.; Krishnamurthy, S.; Ayyannan, S.R. Design, synthesis, and pharmacological evaluation of 2-amino-5-nitrothiazole derived semicarbazones as dual inhibitors of monoamine oxidase and cholinesterase: Effect of the size of aryl binding site. *J. Enzym. Inhibit. Med. Chem.* **2018**, *33*, 37–57.
16. Channar, P.A.; Shah, M.S.; Saeed, A.; Khan, S.U.; Larik, F.A.; Shabir, G.; Iqbal, J. Synthesis, characterization and cholinesterase inhibition studies of new arylidene aminothiazolylethanone derivatives. *Med. Chem.* **2017**, *13*, 648–653. [CrossRef] [PubMed]
17. Huadong, Z.H.; Pharmaceutical Co LTD. 2-aminothiazole Derivatives and Methods of Preparing and Using the Same. US2014004155, 2 January 2014.
18. Huaihai Inst Technology. Amino Sugar Thiazole Derivative as well as Synthetic Method and Application Thereof. CN104292280, 21 January 2015.
19. Zhang, P.; Shengtao, X.; Zhu, Z.; Xu, J. Multi-target design strategies for the improved treatment ofAlzheimer's disease. *Eur. J. Med. Chem.* **2019**, *176*, 228–247. [CrossRef] [PubMed]

20. Salehi, N.; Mirjalili, B.B.F.; Nadri, H.; Abdolahi, Z.; Forootanfar, H.; Samzadeh-Kermani, A.; Küçükkılınç, T.T.; Ayazgok, B.; Emami, S.; Haririan, I.; et al. Synthesis and biological evaluation of new N-benzylpyridinium-based benzoheterocycles as potential anti-Alzheimer's agents. *Bioorg. Chem.* **2019**, *83*, 559–568. [CrossRef]
21. Sharma, P.; Tripathi, A.; Tripathi, P.N.; Prajapati, S.K.; Seth, A.; Tripathi, M.K.; Srivastava, P.; Tiwari, V.; Krishnamurthy, S.; Shrivastava, S.K. Design and development of multitarget-directed N-Benzylpiperidine analogs as potential candidates for the treatment of Alzheimer's disease. *Eur. J. Med. Chem.* **2019**, 510–524. [CrossRef]
22. Sang, Z.; Qiang, X.; Li, Y.; Xu, R.; Cao, Z.; Song, Q.; Wang, T.; Zhang, X.; Liu, H.; Tan, Z.; et al. Design, synthesis and evaluation of scutellarein-O-acetamidoalkylbenzylamines as potential multifunctionalagents for the treatment of Alzheimer's disease. *Eur. J. Med. Chem.* **2017**, *135*, 307–323. [CrossRef] [PubMed]
23. Sang, Z.; Qiang, X.; Li, Y.; Yuan, W.; Liu, Q.; Shi, Y.; Ang, W.; Luo, Y.; Tan, Z.; Deng, Y. Design, synthesis and evaluation of scutellarein-*O*-alkylamines as multifunctional agents for the treatment of Alzheimer's disease. *Eur. J. Med. Chem.* **2015**, *94*, 348–366. [CrossRef] [PubMed]
24. Qiang, X.; Sang, Z.; Yuan, W.; Li, Y.; Liu, Q.; Bai, P.; Shi, Y.; Ang, W.; Tan, Z.; Deng, Y. Design, synthesis and evaluation of genistein-*O*-alkylbenzylamines as potential multifunctional agents for the treatment of Alzheimer's disease. *Eur. J. Med. Chem.* **2014**, *76*, 314–331. [CrossRef] [PubMed]
25. Simovay, J.; Pharmaceutical Co. 1,2,4-Thiadiazole-3,5-Dione Derivatives, and Pharmaceutical Composition and Application Thereof. CN103992312, 20 August 2014.
26. Qiang, X.; Sang, Z.; Yuan, W.; Li, Y.; Liu, Q.; Bai, P.; Shi, Y.; Ang, W.; Tan, Z.; Deng, Y. Design, synthesis and evaluation of scutellarein-O-alkylamines as multifunctional agents for the treatment of Alzheimer's disease. *Eur. J. Med. Chem.* **2014**, *13*, 348–366.
27. Ramsay, R.R. Monoamine oxidases: The biochemistry of the proteins as targets in medicinal chemistry and drug discovery. *Curr. Top. Med. Chem.* **2012**, *12*, 2189–2209. [CrossRef] [PubMed]
28. Legoabe, L.; Petzer, A.; Petzer, J.P. 2-acetylphenol analogs as potent reversible monoamine oxidase inhibitors. *Drug Des. Devel. Ther.* **2015**, *9*, 3635–3644. [CrossRef]
29. Garcia-Miralles, M.; Ooi, J.; Bardile, C.F.; Tan, L.J.; George, M.; Drum, C.L.; Lin, Y.; Hayden, M.R.; Pouladi, M.A. Treatment with the MAO-A inhibitor clorgyline elevates monoamine neurotransmitter levels and improves affective phenotypes in a mouse model of Huntington disease. *Exp. Neurol.* **2016**, *278*, 4–10. [CrossRef]
30. Can, Ö.D.; Osmaniye, D.; Demir Özkay, Ü.; Sağlık, B.N.; Levent, S.; Ilgın, S.; Baysal, M.; Özkay, Y.; Kaplancıklı, Z.A. MAO enzymes inhibitory activity of new benzimidazole derivatives including hydrazone and propargyl side chains. *Eur. J. Med. Chem.* **2017**, *131*, 92–106. [CrossRef]
31. Cheung, J.; Rudolph, M.J.; Burshteyn, F.; Cassidy, M.S.; Gary, E.N.; Love, J.; Height, J.J. Structures of human acetylcholinesterase in complex with pharmacologically important ligands. *J. Med. Chem.* **2012**, *55*, 10282–10286. [CrossRef]
32. Carpenter, T.S.; Kirshner, D.A.; Lau, E.Y.; Wong, S.E.; Nilmeier, J.P.; Lightstone, F.C. A Method to Predict Blood-Brain Barrier Permeability of Drug-Like Compounds Using Molecular Dynamics Simulations. *Biophys. J.* **2014**, *107*, 630–641. [CrossRef] [PubMed]
33. Online BBB Predictor. Available online: http://www.cbligand.org/BBB/index.php (accessed on 1 June 2019).
34. Acar Çevik, U.; Sağlık, B.N.; Levent, S.; Osmaniye, D.; Kaya Çavuşoğlu, B.; Özkay, Y.; Kaplancıklı, Z.A. Synthesis and AChE-inhibitory activity of new benzimidazole derivatives. *Molecules* **2019**, *24*, 861. [CrossRef] [PubMed]
35. Özkay, Ü.D.; Can, Ö.D.; Sa ˘glık, B.N.; Cevik, U.A.; Levent, S.; Özkay, Y.; Ilgın, S.; Atlı, Ö. Design, synthesis, and AChE inhibitory activity of new benzothiazole–piperazines. *Bioorg. Med. Chem. Lett.* **2016**, *26*, 5387–5394. [CrossRef] [PubMed]
36. Saglık, B.N.; Ilgın, S.; Özkay, Y. Synthesis of new donepezil analogues and investigation of their effects on cholinesterase enzymes. *Eur. J. Med. Chem.* **2016**, *124*, 1026–1040. [CrossRef] [PubMed]
37. Hussein, W.; Saglık, B.N.; Levent, S.; Korkut, B.; Ilgın, S.; Özkay, Y.; Kaplancıklı, Z.A. Synthesis and biological evaluation of new cholinesterase inhibitors for Alzheimer's disease. *Molecules* **2018**, *23*, 2033. [CrossRef] [PubMed]
38. Tok, F.; Koçyigit Kaymakçıoglu, B.; Saglık, B.N.; Levent, S.; Özkay, Y.; Kaplancıklı, Z.A. Synthesis and biological evaluation of new pyrazolone Schiff bases as monoamine oxidase and cholinesterase inhibitors. *Bioorg. Chem.* **2019**, *84*, 41–50. [CrossRef] [PubMed]

39. Can, N.Ö.; Osmaniye, D.; Levent, S.; Sağlık, B.N.; Korkut, B.; Atlı, Ö.; Özkay, Y.; Kaplancıklı, Z.A. Design, synthesis and biological assessment of new thiazolylhydrazine derivatives as selective and reversible hMAO-A inhibitors. *Eur. J. Med. Chem.* **2018**, *144*, 68–81. [CrossRef] [PubMed]
40. Can, N.Ö.; Osmaniye, D.; Levent, S.; Sağlık, B.N.; İnci, B.; Ilgın, S.; Özkay, Y.; Kaplancıklı, Z.A. Synthesis of New Hydrazone Derivatives for MAO Enzymes Inhibitory Activity. *Molecules* **2017**, *22*, 1381. [CrossRef]

Sample Availability: Samples of the compounds **3a**–**k** are available from the authors.

© 2019 by the authors. Licensee MDPI, Basel, Switzerland. This article is an open access article distributed under the terms and conditions of the Creative Commons Attribution (CC BY) license (http://creativecommons.org/licenses/by/4.0/).

molecules

MDPI

Review

Bridged Nucleic Acids Reloaded

Alfonso Soler-Bistué [1], Angeles Zorreguieta [2] and Marcelo E. Tolmasky [3,*]

1 Instituto de Investigaciones Biotecnológicas Dr. Rodolfo A. Ugalde, Instituto Tecnológico de Chascomús, CONICET, Universidad Nacional de San Martín, San Martín 1650, Argentina; asoler@iib.unsam.edu.ar
2 Fundación Instituto Leloir, IIBBA-CONICET, Buenos Aires C1405BWE, Argentina; azorreguieta@leloir.org.ar
3 Center for Applied Biotechnology Studies, Department of Biological Science, California State University Fullerton, Fullerton, CA 92834-6850, USA
* Correspondence: mtolmasky@fullerton.edu; Tel.: +1-657-278-5263

Academic Editor: Josef Jampilek
Received: 31 May 2019; Accepted: 18 June 2019; Published: 21 June 2019

Abstract: Oligonucleotides are key compounds widely used for research, diagnostics, and therapeutics. The rapid increase in oligonucleotide-based applications, together with the progress in nucleic acids research, has led to the design of nucleotide analogs that, when part of these oligomers, enhance their efficiency, bioavailability, or stability. One of the most useful nucleotide analogs is the first-generation bridged nucleic acids (BNA), also known as locked nucleic acids (LNA), which were used in combination with ribonucleotides, deoxyribonucleotides, or other analogs to construct oligomers with diverse applications. However, there is still room to improve their efficiency, bioavailability, stability, and, importantly, toxicity. A second-generation BNA, BNA^{NC} (2′-*O*,4′-aminoethylene bridged nucleic acid), has been recently made available. Oligomers containing these analogs not only showed less toxicity when compared to LNA-containing compounds but, in some cases, also exhibited higher specificity. Although there are still few applications where BNA^{NC}-containing compounds have been researched, the promising results warrant more effort in incorporating these analogs for other applications. Furthermore, newer BNA compounds will be introduced in the near future, offering great hope to oligonucleotide-based fields of research and applications.

Keywords: oligonucleotides; bridged nucleic acids; locked nucleic acids; antisense; antibiotic resistance; hypercholesterolemia; myotonic dystrophy; CRISPR; Cas9; hematologic malignancies

1. Oligonucleotides and Analogs

Oligonucleotides are short oligomers composed of ribonucleotides or deoxyribonucleotides. They have multiple uses in basic research, diagnostics, and therapeutics. Their most basic and widespread use is in primer-based techniques, which are used in the most diverse kinds of biological research or development projects, such as polymerase chain reaction (PCR), library construction, single nucleotide polymorphisms detection, gene silencing, tiling arrays, and many others. Besides these applications, oligonucleotides were also found to be immensely useful in the development of gene-silencing techniques. Several approaches were attempted to reduce the undesirable expression of genes, utilizing a variety of strategies, the vast majority of which have in common the utilization of antisense oligonucleotides [1–3]. Many of these compounds are known with different names descriptive of their mechanism of action, like external guide sequences [4,5], ribozymes [6,7], aptamers [8,9], short interfering RNA [10–12], and microRNA [13,14]. These compounds interfere with gene expression by steric hindrance of transcription or translation, or by inducing enzymatic cleavage of the target mRNA [3,4,11,13]. The rapid increase in the techniques and applications for which these compounds are integral components, together with the progress in nucleic acid research, led to the design of analogs that are more appropriate to enhance efficiency and achieve specific objectives in each case.

In general, nucleic acid analogs should a) have higher affinity per nucleotide unit than the cognate sequence, without changing the structure of duplexes, b) be resistant to nucleases, and c) have low toxicity. The first oligonucleotide analogs consisted of relatively minor modifications to the natural counterparts, such as the replacement of an oxygen atom by sulfur (phosphorothioate) [15,16], methyl (methylphosphonate) [17], or amino groups (phosphoramidate) (Figure 1). The value of using nucleotide analogs was illustrated by the first FDA approved antisense drug, fomivirsen, a 21-nucleotide oligomer composed of phosphorothioate units designed for the treatment of cytomegalovirus retinitis [10,18]. Subsequently, more modifications were introduced to the nucleotide molecule, such as adding chemical groups to the 2′ position of the ribose as in 2′-*O*-methyl compounds (Figure 1) or making more drastic structural changes replacing or modifying the ribose, substituting the nature of the bonds, or modifying the charge of the oligonucleotide, obtaining neutral or cationic derivatives. Examples of these compounds are morpholino phosphoroamidates [19], peptide nucleic acids [20,21], nucleotides with modified nucleobases [22], guanidinium-linked oligomers [23], and locked nucleic acids (LNA) [24] (Figure 1). Exhaustive listings and a description of oligonucleotide analogs and their applications can be found in recent reviews [3,6,16,23,25–27]. A derivative of LNA, 2′-*O*,4′-aminoethylene bridged nucleic acid (BNA), also known as 2′,4′-BNA^{NC} (BNA^{NC}) [28–31] (Figure 1) has been recently introduced and other derivatives have followed or are in development. As a consequence, LNA is considered the earliest generation of bridged nucleic acids (BNA). This review will focus on the properties and applications of BNA^{NC}-containing compounds.

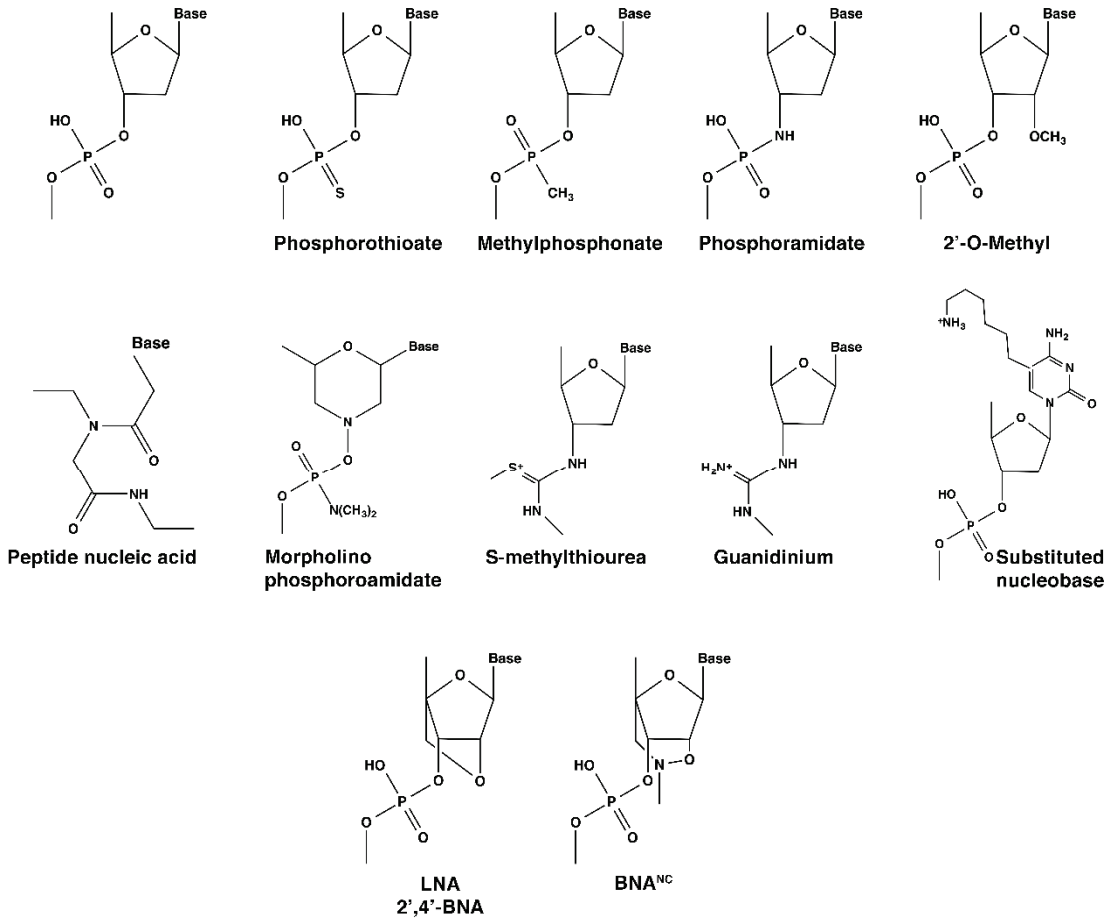

Figure 1. Chemical structures of nucleotide analogs.

2. LNA—A Brief Overview

LNA compounds, first introduced in the late 1990s, are bicyclic nucleotide analogs in which the furanose ring is modified by the introduction of a methylene group linking the 2′-oxygen and

the 4′-carbon (2′-*O*,4′-methylene-β-D-ribofuranosyl nucleotides) [32–37]. They are characterized by reduced flexibility of the ribose residue and exist in a locked *N*-type conformation, which favors the formation of stable duplexes with DNA or RNA [34]. Numerous structural and thermal stability studies on complexes formed by LNA oligomers and complementary DNA or RNA oligonucleotides showed higher melting temperatures and specificity when compared to the unmodified isosequential compounds [32,34,37–39]. LNA-containing oligomers are usually synthesized as chimeras containing a combination of ribonucleotide/deoxyribonucleotide or other nucleotide analogs and LNA residues [40–44]. The incorporation of LNA in oligonucleotides leads to melting temperature increases of 3–9 °C per residue [45]. Most LNA-containing chimeras can be classified into two kinds, gapmers and mixmers. Gapmers consist of oligomers where the LNA residues are located at the ends of the compound. Mixmers include the LNA and the other residues interspersed in different configurations throughout the sequence. LNA-containing oligomers have been used for diagnostics and other applications, as probes or primers for hybridization, amplification, mutagenesis, sequencing, and SNP genotyping [46–53], in addition to gene repair [54] and antisense drugs [13,41,42,55]. While the increased binding capacity is advantageous in many antisense applications, it can also be detrimental due to the formation of duplex structures that cannot be recognized as substrates by the enzymes recruited to degrade the target molecule. The high affinity of LNA-containing oligonucleotides can also result in toxic effects due to unspecific off-target binding. Fortunately, recent studies showed that LNA-containing oligomers were innocuous in primates [56] and relatively safe in humans [57–59]. Furthermore, these compounds failed to show genotoxicity [60]. However, these results are far from definitive; other studies showed hepatoxicity [61–64]. Although the toxicity determinations of LNA-containing oligomers are encouraging, case-by-case studies will decide the possibility of development as therapies for human disease. At the moment, numerous potential drugs based on this nucleic acid analog are already in clinical trials (e.g., Miravirsen, MRG-106, and ISTH0036) [10,11]. An obstacle in the development of LNA-containing oligomers as drugs, particularly in silencing prokaryotic genes, is the low or null uptake by bacterial cells. Gymnotic uptake of LNA-containing oligomers was shown in eukaryotic and prokaryotic cells [65–67]. However, although internalization by diverse pathways and reasonable levels of activity were reported in the case of eukaryotic cells [68–72], the levels of internalization into bacterial cells seems not to be enough for productive inhibition of gene expression [66]. LNA-containing oligomers could be delivered to cultured eukaryotic cells by transfection reagents [73–76]. Other strategies to facilitate uptake, such as conjugation to cell penetrating peptides (CPP), which are usually cationic, has been challenging and reports of their utilization to silence gene expression are scarce. Turner et al. [77] reported the attachment of a CPP to an LNA/2′-*O*-methyl oligonucleotide; cell uptake of this compound was significantly increased with respect to the naked antisense, but levels of inhibition of gene expression were disappointing. An LNA/DNA gapmer designed to target the amikacin resistance *aac(6′)-Ib* gene mRNA and elicit cleavage by the endogenous RNase P [4] was covalently bound to a CPP. The compound produced a modest reduction in the levels of resistance to amikacin in a clinical *Acinetobacter baumannii* isolate [78]. LNA-containing compounds were also delivered inside target cells using nanoparticles [79]. An 8-nucleotide LNA oligomer complementary to the oncogenic miR21 included in micelles could be delivered inside cancer cells and induced apoptosis [79]. Furthermore, these assays showed tumor growth inhibition in an animal model [79].

In summary, LNA-containing compounds show great promise as therapeutic agents [42,80,81]. However, more research is needed to improve cell penetration while keeping their biological activity and reduced toxicity. Comprehensive descriptions of properties and applications of LNA containing oligomers have been recently published [82–86].

3. BNA^{NC}

The success and advantages of LNA-containing oligomers for diverse applications stimulated the search for similar compounds, improving their properties. Many derivatives were recently

introduced, like BNA^{NC} with different substitutions at the N atom (of which a methyl group is the most commonly used to date) (Figure 1) [87], 2′-*O*,4′-*C*-ethylene-bridged nucleic acid (ENA) [88], 2′-*O*,4′-*C*-methylenoxymethylene-bridged nucleic acid [89], or unlocked nucleic acids (UNA) [90,91]. The bridge in the different BNA compounds can have a different number of members in the ring, the most widely used to date being BNA^{NC}, a six-member ring [30,31]. Oligonucleotides containing BNA^{NC} are more resistant to nucleases and less toxic than isosequential compounds containing LNA residues, they show high thermal stability and water solubility, and elicit RNase H degradation of a target RNA [29,62,87,92].

Twelve-mer oligodeoxynucleotides containing a variable number of BNA^{NC} or LNA residues showed a similar increase in melting temperature (Tm) per modified residue (4.7 to 7.0 °C) in comparisons of duplex stabilities with complementary single-stranded RNA (ssRNA). However, this was not the case for duplexes with complementary single-stranded DNA (ssDNA) [29]. Increasing the number of BNA^{NC} residues in the oligonucleotides did not result in a significant Tm increase (−1.0 to 1.8 °C) as was the case when the analog used was LNA (1.3 to 3.0 °C) [29]. While the Tm values of the unsubstituted oligodeoxynucleotide in duplex with complementary ssRNA was about 5 °C higher than with complementary ssRNA, the Tm values for substituted oligonucleotides were higher for duplexes with complementary ssRNA. Furthermore, the values were higher for oligonucleotides substituted with BNA^{NC} than those that included LNA residues [29]. These results indicate that BNA^{NC} residues conferred a higher RNA selective binding affinity to the antisense oligomers. BNA^{NC}-containing oligonucleotides also showed higher mismatch discrimination properties as well as more stable triplexes than LNA-containing oligomers [29,93]. BNA^{NC}-containing oligonucleotides have the potential to be utilized in diverse applications. In this review, we will focus on their utilization for diverse uses. The different applications of the compounds reviewed in this article are summarized in Table 1.

Table 1. BNA^{NC} applications.

Organism	Function or Disease	Target	Chemical Nature of Oligonucleotide	Sequence of Active Oligomer	Reference
A. baumannii	Resistance to aminoglycosides	*aac(6′)-Ib*	BNA^{NC}/DNA conjugated to (RXR)$_4$XB [1]	(RXR)$_4$XB-Cys-SMCC-C6 amino-cTgctGcgtAacaTc	[94]
Cell lines	Myotonic dystrophy type 1	*DMPK* [2]	BNA^{NC}/DNA gapmer	CGGAGcggttgtgaaCTGGC	[95]
Murine, human cell lines, and mice	Hypercholesterolemia	*PCSK9* [3]	BNA^{NC}/DNA mixmer	CCaggCCTaTgagggTgCCg	[92]
Human gene	Hematologic malignancies	*DNTM3A* [4]	BNA^{NC}/DNA mixmers	cgccaAgcgGctcatgtt cgccAAgcagctcAtgtt cgccAAgtgGctcAtgtt cgccaAggggCtcatgtt cgccAAgctgCtcAtgtt	[96]
Human gene	CRISPR-Cas9 specificity	*WAS* [5]	crRNA with BNA^{NC} substitutions	uggauggagGAAugaggagu	[97]
Human gene	CRISPR-Cas9 specificity	*EXM1* [6]	crRNA with BNA^{NC} substitutions	gaguccgagcaGAAgaagaa	[97]

[1] R, arginine; X, 6-aminohexanoic acid; B, β-alanine; [2] Dystrophia myotonica protein kinase; [3] Proprotein convertase subtilisin/kexin type 9; [4] Human DNA methyltransferase 3A; [5] Gene responsible for Wiskott-Aldrich Syndrome; [6] Homeobox protein EMX1.

3.1. Antisense Inhibition of Resistance to Amikacin by a BNA^{NC}-Containing Oligomer

The inhibition of the expression of genes coding for antimicrobial resistance enzymes by diverse antisense mechanisms is the object of intense investigation, as a way to deal with the growing multiresistance problem [4,98–101]. An active antisense molecule could be combined as an adjuvant to the cognate antibiotic to treat resistant infections. The concept of treating resistant infections with combinations of antibiotic/inhibitor of resistance has reached the stage of human use in the case of β-lactam antibiotics that are administered in combination with β-lactamase inhibitors [99,102,103]. However, combinations of other kinds of antibiotics with inhibitors of resistance are still in experimental

stages [99,104]. In particular, antisense inhibition of antibiotic resistance genes was explored using oligomers of different natures that interfere with the expression of resistance by different mechanisms [41, 42,78,98,101,105–108]. The *aac(6′)-Ib* gene codes for an acetyltransferase responsible for the resistance to amikacin and other aminoglycosides found in the vast majority of AAC(6′)-I-producing Gram-negative clinical isolates [104,109]. An antisense oligodeoxynucleotide complementary to a duplicated sequence located at the translation initiation location of the *aac(6′)-Ib* allele found in a clinical *Acinetobacter baumannii* isolate [110] inhibited translation in vitro [94]. An isosequential 15-residue antisense mixmer, including four BNA^{NC} and 11 deoxynucleotide residues, was covalently bound to the permeabilizing peptide $(RXR)_4XB$ (R, arginine; X, 6-aminohexanoic acid; B, β-alanine) to generate a compound resistant to nucleases and capable of penetrating the Gram-negative envelope to reach the cytosol. This BNA^{NC}-containing mixmer, designated CPPBD4, successfully inhibited growth in a liquid culture containing amikacin. Furthermore, a combination of CPPBD4/amikacin reduced the mortality of *Galleria mellonella* infected with amikacin-resistant *A. baumannii* to levels comparable to those of the uninfected controls [94].

BNA^{NC}-containing oligomers were also researched as elicitors of RNase P-mediated specific mRNA degradation, an antisense methodology known as external guide sequence (EGS) technology [4,111]. In this approach, antisense oligomers, known as EGSs, interact with the target mRNA, forming a structure that is recognized as a substrate by the endogenous RNase P. Then, the enzyme cleaves the mRNA, preventing its translation [5]. Early experiments showed that EGS molecules efficiently reduced the expression of *aac(6′)-Ib* and levels of resistance to amikacin [108]. Analysis of various nuclease-resistant oligonucleotide analogs indicated that DNA/LNA hybrid oligomers were efficient EGSs that reversed *aac(6′)-Ib*-mediated resistance to amikacin in a hyperpermeable *Escherichia coli* strain [42]. Furthermore, conjugation of a selected DNA/LNA hybrid oligomer to the cell permeabilizing peptide $(RXR)_4XB$ reduced the levels of resistance to amikacin of an *aac(6′)-Ib*-containing *Acinetobacter baumannii* clinical isolate [41,78]. Assessment of isosequential hybrid oligomers containing BNA^{NC} in the place of the LNA residues showed that they failed to elicit cleavage of the mRNA at levels comparable to those found when testing LNA/DNAs [41].

3.2. Reversion of Splicing and Reduction of RNA Foci in Myotonic Dystrophy Cells by BNA^{NC} Gapmers

Myotonic dystrophy type 1 patients may suffer from skeletal muscle weakening and wasting, abnormalities in heart function, cataracts, breathing problems, speech and swallowing disorders, and other impairing symptoms [112]. The molecular basis of this condition is the presence of a CUG repeat expansion within the *DMPK* gene 3′-untranslated region [113,114]. This kind of genetic modification, in which a group of nucleotides that in healthy genes is repeated a variable number of times, exists in an abnormally high number of repeat-characterized diseases, known as microsatellite expansion disorders [115,116]. The *DMPK* gene anomaly causes the mRNA to remain in the nucleus and to form foci structures, resulting in defects in developmentally regulated alternative splicing [117]. Removal of the toxic RNA species using antisense oligomers that induce RNase H cleavage is being intensely researched as a therapeutic strategy. Early work by researchers at IONIS Pharmaceuticals utilizing a gapmer consisting of a short DNA stretch flanked by 2′-*O*-methoxyethyl residues designed to induce cleavage of the toxic RNA in muscle cells showed encouraging splicing changes, but stopped short of the goals of the trial [95]. The potency of these compounds can be substantially increased by replacing the 2′-*O*-methoxyethyl analogs with LNA residues [62]. However, antisense LNA-containing gapmers showed high hepatotoxicity [62–64]. The potency and toxicity of BNA^{NC}-containing gapmers as compared to isosequential LNA-containing gapmers was recently determined [95]. Both compounds were nearly equally efficient in inducing the cleavage of the CUG repeat expansion-containing mRNA in cells transformed with a plasmid designed to express this RNA species. However, comparison of the toxicity of both antisense compounds showed that the LNA-containing gapmer induced an increase in caspases, the apoptosis effector proteins, that was not observed with BNA^{NC}-containing gapmers [95]. Interestingly, a comparison of the region targeted showed that a gapmer complementary

to a non-repetitive region of the RNA was more specific in eliciting degradation of the toxic RNA than a gapmer complementary to a segment containing the CUG repeats (Table 1) [95]. These studies indicate that the use of BNA^{NC}-containing gapmers could open new venues for developing therapies against myotonic dystrophy type 1.

3.3. Reduction of Cholesterol Levels by BNA^{NC} Mixmers in Hypercholesterolemic Mice

Proprotein convertase subtilisin/kexin type 9 (PCSK9) plays a role in the maintenance of cholesterol balance [118]. Gain-of-function mutations in this gene are associated with an increase in low-density lipoprotein cholesterol levels (i.e., autosomal dominant hypercholesterolemia), a known risk factor for coronary heart disease [119]. Conversely, loss-of-function mutations are responsible for low plasma low-density lipoprotein cholesterol (LDL-C) levels and reduced incidence of cardiovascular disease [120]. These phenotypes are the consequence of the ability of PCSK9 to interact with the LDL receptor (LDLR). The complex PCSK9–LDLR is transported from the cell's surface to the endosome, where LDLR is degraded [121]. The involvement of PCSK9 in the modulation of LDL-C levels led to attempts to suppress its synthesis or activity that resulted in the development of drugs that have been approved by the FDA [122–126]. In particular, the inhibition of the expression of PCSK9 by antisense oligonucleotide analogs was attempted by several research groups. A 2′-*O*-methoxyethyl-modified phosphorothioate oligonucleotide analog modestly reduced hepatic PCSK9 mRNA and LDL-C in treated mice [127]. In another study, an LNA-containing gapmer was found to be more efficient at lowering PCSK9 mRNA and LDL-C while increasing LDLR levels [74]. However, LNA-containing gapmers usually show high hepatotoxicity. BNA^{NC}-containing oligomers could be a better option to design compounds that show high efficiency without the high levels of toxicity observed when the analog used is LNA. Yamamoto et al. [92] tested LNA- and BNA^{NC}-containing antisense mixmers in cultured cells as well as in mice. Cells transfected with mixmers containing one or the other analog showed a dose-dependent reduction of PCSK9 mRNA and increase of LDLR protein levels. Also, the administration of these compounds to atherogenic diet-fed mice biweekly for six weeks resulted in a reduction of PCSK9 mRNA and LDL-C as well as an increase in high-density lipoprotein cholesterol. However, the comparison also showed that the animals treated with the BNA^{NC}-containing antisense mixmer experienced a reduction of LDL-C after a shorter time and tolerance was higher. These comparative studies identified BNA^{NC}-containing antisense compounds as better candidates than LNA-containing compounds.

3.4. Diagnostics of Hematologic Malignancies by the Detection of Somatic Mutations Using BNA^{NC} Mixmers

DNA methylation, an epigenetic modification, is involved in critical cellular processes, such as replication and transcription. Hypomethylation is correlated to some human cancers [128]. The human DNA methyltransferase 3A (DNMT3A) is a 130 kDa protein that includes three domains, one of which is the *S*-adenosyl methionine-dependent methyltransferase that recognizes and binds DNA to catalyze the transfer of a methyl group to the C5 position of cytosine from *S*-adenosyl methionine [129]. The nuclear DNMT3A molecules can exist in oligomeric form as dimers, tetramers, and larger structures held by interactions of binding interfaces in the methyltransferase domain [130].

Numerous hematologic malignancies are characterized by the presence of somatic mutations in the DNA methyltransferase 3A (DNMT3A) gene [128]. Mutations on this gene are found in up to 35% of cases of different myeloid malignancies [131–137]. The detection of mutations in this gene could, therefore, be a component of a group of tests to predict a higher risk of myeloid malignancies [138,139]. Techniques used to detect DNMT3A mutations include DNA sequencing, high-resolution DNA melting, restriction fragment length polymorphism, and denaturing high-performance liquid chromatography [140–144]. A microsphere-based suspension assay that utilizes oligonucleotide analogs, LNA- or BNA^{NC}-containing, as probes specific for wild type or mutant alleles was more efficient than direct sequencing [96]. In this study, LNA- or BNA^{NC}-containing oligonucleotides specific for the wild type or four mutations within the codon R882 were coupled

to fluorescently labeled microspheres, which were used in hybridization assays against DNMT3A amplicons. The utilization of LNA- or BNA^{NC}-containing analogs facilitated the design of sequences that can discriminate between sequences that differed in a single nucleotide. A comparison of isosequential oligonucleotides that differ in the nature of the analog residues showed that BNA^{NC}-containing compounds showed the highest sensitivity, as well as specificity. These researchers concluded that BNA^{NC}-containing probes, coupled with fluorescently labeled microspheres, are suitable reagents to detect DNMT3A R888 mutations [96].

3.5. Incorporation of BNA^{NC} Residues to crRNA as an Enhancer of Cas9 Endonuclease Specificity

Bacteria have evolved numerous strategies to defend against the presence of foreign genetic material, such as bacteriophage genomes, transposons, and plasmids. They include restriction-modification systems, abortive infections and adsorption blockage, and surface exclusion [145–147]. While these systems are relatively unspecific, the latest discovered defense system, known as "clustered regularly interspaced short palindromic repeats" (CRISPR) is specific and, in a surprisingly analogous mode to vertebrate immune systems, it requires previous exposure to the foreign genetic material to create a memory record that can elicit a quick response in future exposure events [148]. In this system, small guide RNA molecules (crRNAs) guide the sequence-specific cleavage of foreign nucleic acids [149]. However, differences in molecular mechanisms permitted the classification in two classes, class 1 and 2, which depend on a multiprotein complex or a single protein, respectively [149]. Each class is further divided into three types. In particular, the class 2, type II system, which depends on the endonuclease Cas9 (Figure 2), has been developed as a tool for numerous applications, such as the generation of mutants, gene editing, bacterial species identification and typing, antibacterial agents, genome-wide screening in mammalian cells, regulation of gene expression (through the use of dCas9, a derivative that lost the cleavage activity), and others [148–152].

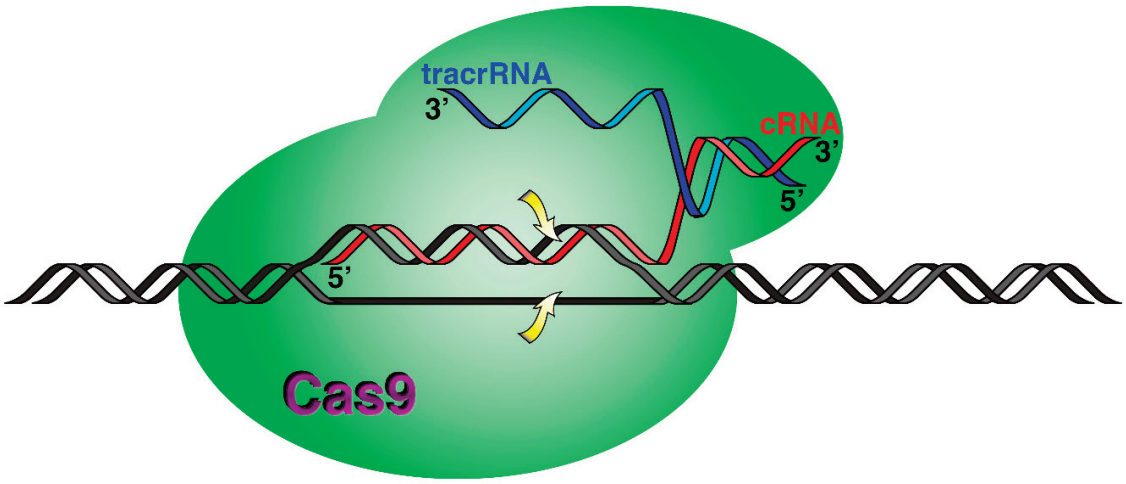

Figure 2. Molecular mechanism of Cas9-mediated digestion of a target DNA. The crRNA and tracrRNA are shown in red and blue, respectively. The arrows indicate the point of cleavage on each target DNA strand.

The Cas9 system relies on two RNA molecules, a crRNA that includes a 20-nucleotide sequence complementary to the target DNA and a trans-acting molecule (tracrRNA) that acts as bridge between the crRNA and the Cas9 endonuclease (Figure 2) [153–155]. Experiments in which the tracrRNA and crRNA are covalently bound, forming a single guide RNA (sgRNA) showed that sgRNAs form viable complexes that result in target cleavage [155]. The Cas9 protein first recognizes protospacer-adjacent motif (PAM) sequences on the target DNA. The role of the PAM sequences is to help in distinguishing self from foreign DNA. Then, a crRNA 20-nucleotides region pairs with the target DNA, forming the multicomponent complex that causes Cas9 double-stranded blunt-ended cleavage [153,156,157].

The Cas9 system has been widely adapted for gene editing and other applications [152,158–161]. An important consideration in the use of CRISPR-Cas9 as a tool is its specificity. While mutations in the PAM sequences usually interfere with cleavage of the target, mutations within the target sequence that interacts with crRNA (or sgRNA) can be tolerated, permitting digestion at off-target locations [162,163]. Since enhancing the specificity of cleavage is such an important aspect for numerous applications of CRISPR-Cas9, it is not surprising that several approaches have been tested to reduce off-target action [97,164–166]. The vast majority of these studies focused on the Cas9 protein [165,167–170]. Few others concentrated on modifications to the crRNA [97,170–172]. Cromwell et al. recently took advantage of the enhanced mismatch discrimination of BNA^{NC}-containing oligomers to design crRNA molecules that elicit cleavage specificity by the cas9 endonuclease [97]. Two crRNA molecules directed to the Wiskott–Aldrich syndrome (WAS) [173] and the homeobox EMX1 [174] genes that are known to also affect off-target sites were used to test the effect of replacing from one to four nucleotides with BNA^{NC} residues. In vitro cleavage assays were carried, out using as the target the wild type WAS or EMX1 sequences and five sequences including one, two, or three nucleotide substitutions for each of the genes. These wild type and modified target sequences were incubated in the presence of the endonuclease and crRNA or the isosequential variants, including one to eight BNA^{NC} residue replacements. While the crRNA molecules directed cleavage of the wild type and all of the modified targets, a crRNA containing BNA^{NC} residues at positions 12–14 isosequential to the EXM1 crRNA (Table 1) specifically guided cleavage of the wild type target. Similarly, a crRNA containing BNA^{NC} residues at positions 10–12 (Table 1) guided cleavage of the wild type and only one of the modified targets. These results showed a significant enhancement of specificity in vitro when three nucleotides were replaced by BNA^{NC} residues. Interestingly, BNA^{NC}-containing crRNA molecules are compatible with Cas9 variants with improved specificity. Following these encouraging results, experiments to find out if the enhanced specificity observed in the in vitro experiments described above also occurs in vivo were carried out. Cas9-producing U2OS and HeLa cells were transfected with the unmodified and modified crRNA molecules, targeting the WAS and EXM1 genes. The levels of cleavage at the target and off-target sites were consistent with those observed in vitro. This work established that BNA^{NC}-containing crRNAs could be a venue for improving Cas9 cleavage specificity [97].

4. Final Remarks

In the past few years, oligonucleotides have been used for an increasing number of applications in basic science, as well as in clinics and other settings. In particular, applications related to human health include detection and diagnostics of pathologies caused by mutations, silencing of undesirable genes responsible for numerous genetic conditions, or interference with the expression of bacterial or viral genes to fight infection. The increased utilization of these compounds requires the constant search for improvement of their properties. The key aspects that enhance the usability and efficiency of oligonucleotides are their stability, specificity, and bioavailability. While the latter has been dealt with by conjugating the compounds to permeabilizing peptides, using transfecting agents, packaging them into liposomes, and combining them with nanoparticles, stability and specificity were dramatically improved by the substitution of ribonucleotide or deoxyribonucleotide residues with analogs. The success observed by these chemical modifications incentivized the search for new and varying nucleotide analogs that enhanced the resistance to nucleases, specificity, affinity, and activity of the oligomers. The first-generation BNA, known as LNA, has been used for several applications with great success. However, despite the promising results achieved with LNA-containing oligomers, toxicity has been an impediment for their development as therapeutic agents. Conversely, oligonucleotide analogs, including the second generation of BNA compounds, BNA^{NC}, show lower toxicity while preserving and, in some cases, improving on the LNA-containing oligomers. Furthermore, next-generation BNA compounds are in the pipeline, and some are or will soon be available for experimentation [87,175]. The success experienced using these nucleotide analogs, and the vigorous efforts to continue developing

next-generation variants offer promising alternatives to continue the development of new and improved applications of oligonucleotides for research as well as diagnostics and therapeutics.

Author Contributions: All authors contributed equally to writing this article.

Funding: Authors' work cited in this review article was funded by Public Health Service Grant 2R15AI047115 from the National Institutes of Health.

Acknowledgments: Authors' work cited in this review article was funded by Public Health Service Grant 2R15AI047115 from the National Institutes of Health. AZ and ASB are Career members of the Consejo Nacional del Investigaciones Científicas y Tecnológicas (CONICET).

Conflicts of Interest: The authors declare no conflict of interest. The funders had no role in the writing of the manuscript, or in the decision to publish the results.

References

1. Bennett, C.F.; Swayze, E.E. RNA targeting therapeutics: Molecular mechanisms of antisense oligonucleotides as a therapeutic platform. *Annu. Rev. Pharmacol. Toxicol.* **2010**, *50*, 259–293. [CrossRef] [PubMed]
2. Thomason, M.K.; Storz, G. Bacterial antisense RNAs: How many are there, and what are they doing? *Annu. Rev. Genet.* **2010**, *44*, 167–188. [CrossRef] [PubMed]
3. Rasmussen, L.C.; Sperling-Petersen, H.U.; Mortensen, K.K. Hitting bacteria at the heart of the central dogma: Sequence-specific inhibition. *Microb. Cell Fact.* **2007**, *6*, 24. [CrossRef]
4. Davies-Sala, C.; Soler-Bistue, A.; Bonomo, R.A.; Zorreguieta, A.; Tolmasky, M.E. External guide sequence technology: A path to development of novel antimicrobial therapeutics. *Ann. N.Y. Acad. Sci.* **2015**, *1354*, 98–110. [CrossRef] [PubMed]
5. Forster, A.C.; Altman, S. External guide sequences for an RNA enzyme. *Science* **1990**, *249*, 783–786. [CrossRef] [PubMed]
6. Burnett, J.C.; Rossi, J.J. RNA-based therapeutics: Current progress and future prospects. *Chem. Biol.* **2012**, *19*, 60–71. [CrossRef] [PubMed]
7. Li, M.J.; Kim, J.; Li, S.; Zaia, J.; Yee, J.K.; Anderson, J.; Akkina, R.; Rossi, J.J. Long-term inhibition of HIV-1 infection in primary hematopoietic cells by lentiviral vector delivery of a triple combination of anti-HIV shRNA, anti-CCR5 ribozyme, and a nucleolar-localizing TAR decoy. *Mol. Ther.* **2005**, *12*, 900–909. [CrossRef]
8. Ni, X.; Castanares, M.; Mukherjee, A.; Lupold, S.E. Nucleic acid aptamers: Clinical applications and promising new horizons. *Curr. Med. Chem.* **2011**, *18*, 4206–4214. [CrossRef]
9. Ellington, A.D.; Szostak, J.W. In vitro selection of RNA molecules that bind specific ligands. *Nature* **1990**, *346*, 818–822. [CrossRef]
10. Crooke, S.T.; Witztum, J.L.; Bennett, C.F.; Baker, B.F. RNA-Targeted Therapeutics. *Cell Metab.* **2018**, *27*, 714–739. [CrossRef]
11. Setten, R.L.; Rossi, J.J.; Han, S.P. The current state and future directions of RNAi-based therapeutics. *Nat. Rev. Drug Discov.* **2019**, *18*, 421–446. [CrossRef] [PubMed]
12. Caplen, N.J.; Parrish, S.; Imani, F.; Fire, A.; Morgan, R.A. Specific inhibition of gene expression by small double-stranded RNAs in invertebrate and vertebrate systems. *Proc. Natl. Acad. Sci. USA* **2001**, *98*, 9742–9747. [CrossRef] [PubMed]
13. van Rooij, E.; Kauppinen, S. Development of microRNA therapeutics is coming of age. *EMBO Mol. Med.* **2014**, *6*, 851–864. [CrossRef] [PubMed]
14. van Rooij, E.; Sutherland, L.B.; Qi, X.; Richardson, J.A.; Hill, J.; Olson, E.N. Control of stress-dependent cardiac growth and gene expression by a microRNA. *Science* **2007**, *316*, 575–579. [CrossRef]
15. Eckstein, F. Nucleoside phosphorothioates. *J. Am. Chem. Soc.* **1966**, *88*, 4292–4294. [CrossRef]
16. Eckstein, F. Phosphorothioates, essential components of therapeutic oligonucleotides. *Nucleic Acid Ther.* **2014**, *24*, 374–387. [CrossRef] [PubMed]
17. Ts'o, P.O.; Miller, P.S.; Aurelian, L.; Murakami, A.; Agris, C.; Blake, K.R.; Lin, S.B.; Lee, B.L.; Smith, C.C. An approach to chemotherapy based on base sequence information and nucleic acid chemistry. *Ann. N.Y. Acad. Sci.* **1987**, *507*, 220–241. [CrossRef]
18. Geary, R.S.; Henry, S.P.; Grillone, L.R. Fomivirsen: Clinical pharmacology and potential drug interactions. *Clin. Pharmacokinet.* **2002**, *41*, 255–260. [CrossRef]

19. Mellbye, B.L.; Weller, D.D.; Hassinger, J.N.; Reeves, M.D.; Lovejoy, C.E.; Iversen, P.L.; Geller, B.L. Cationic phosphorodiamidate morpholino oligomers efficiently prevent growth of *Escherichia coli* in vitro and in vivo. *J. Antimicrob. Chemother.* **2010**, *65*, 98–106. [CrossRef]
20. Gupta, A.; Mishra, A.; Puri, N. Peptide nucleic acids: Advanced tools for biomedical applications. *J. Biotechnol.* **2017**, *259*, 148–159. [CrossRef]
21. Nielsen, P.E. Peptide nucleic acids (PNA) in chemical biology and drug discovery. *Chem. Biodivers.* **2010**, *7*, 786–804. [CrossRef]
22. Le, B.T.; Hornum, M.; Sharma, P.K.; Nielsen, P.; Veedu, R.N. Nucleobase-modified antisense oligonucleotides containing 5-(phenyltriazol)-2 ′-deoxyuridine nucleotides induce exon-skipping in vitro. *RSC Adv.* **2017**, *7*, 54542–54545. [CrossRef]
23. Meng, M.; Ducho, C. Oligonucleotide analogues with cationic backbone linkages. *Beilstein J. Org. Chem.* **2018**, *14*, 1293–1308. [CrossRef]
24. Petersen, M.; Wengel, J. LNA: A versatile tool for therapeutics and genomics. *Trends Biotechnol.* **2003**, *21*, 74–81. [CrossRef]
25. Sharma, V.K.; Rungta, P.; Prasad, A.K. Nucleic acid therapeutics: Basic concepts and recent developments. *RSC Adv.* **2014**, *4*, 16618–16631. [CrossRef]
26. Sully, E.K.; Geller, B.L. Antisense antimicrobial therapeutics. *Curr. Opin. Microbiol.* **2016**, *33*, 47–55. [CrossRef]
27. Iversen, P.L. Phosphorodiamidate morpholino oligomers: Favorable properties for sequence-specific gene inactivation. *Curr. Opin. Mol. Ther.* **2001**, *3*, 235–238.
28. Miyashita, K.; Rahman, S.M.; Seki, S.; Obika, S.; Imanishi, T. N-Methyl substituted 2′,4′- BNANC: A highly nuclease-resistant nucleic acid analogue with high-affinity RNA selective hybridization. *Chem. Commun.* **2007**, 3765–3767. [CrossRef]
29. Rahman, S.M.; Seki, S.; Obika, S.; Yoshikawa, H.; Miyashita, K.; Imanishi, T. Design, synthesis, and properties of 2′,4′-BNA(NC): A bridged nucleic acid analogue. *J. Am. Chem. Soc.* **2008**, *130*, 4886–4896. [CrossRef]
30. Rahman, S.M.; Seki, S.; Utsuki, K.; Obika, S.; Miyashita, K.; Imanishi, T. 2′,4′-BNA(NC): A novel bridged nucleic acid analogue with excellent hybridizing and nuclease resistance profiles. *Nucleosides Nucleotides Nucleic Acids* **2007**, *26*, 1625–1628. [CrossRef]
31. Fujisaka, A.; Hari, Y.; Takuma, H.; Rahman, S.M.A.; Yoshikawa, H.; Pang, J.; Imanishi, T.; Obika, S. Effective syntheses of 2′,4′-BNA(NC) monomers bearing adenine, guanine, thymine, and 5-methylcytosine, and the properties of oligonucleotides fully modified with 2′,4′-BNA(NC). *Bioorg. Med. Chem.* **2019**, *27*, 1728–1741. [CrossRef]
32. Koshkin, A.A.; Nielsen, P.; Meldgaard, M.; Rajwanshi, V.K.; Singh, S.K.; Wengel, J. LNA (locked nucleic acid): An RNA mimic forming exceedingly stable LNA: LNA duplexes. *J. Am. Chem. Soc.* **1998**, *120*, 13252–13253. [CrossRef]
33. Koshkin, A.A.; Rajwanshi, V.K.; Wengel, J. Novel convenient syntheses of LNA [2.2.1] bicyclo nucleosides. *Tetrahedron Lett.* **1998**, *39*, 4381–4384. [CrossRef]
34. Koshkin, A.A.; Singh, S.K.; Nielsen, P.; Rajwanshi, V.K.; Kumar, R.; Meldgaard, M.; Olsen, C.E.; Wengel, J. LNA (Locked Nucleic Acids): Synthesis of the adenine, cytosine, guanine, 5-methylcytosine, thymine and uracil bicyclonucleoside monomers, oligomerisation, and unprecedented nucleic acid recognition. *Tetrahedron* **1998**, *54*, 3607–3630. [CrossRef]
35. Singh, S.K.; Kumar, R.; Wengel, J. Synthesis of novel bicyclo [2.2.1] ribonucleosides: 2′-amino- and 2′-thio-LNA monomeric nucleosides. *J. Org. Chem.* **1998**, *63*, 6078–6079. [CrossRef]
36. Wang, G.; Gunic, E.; Girardet, J.L.; Stoisavljevic, V. Conformationally locked nucleosides. Synthesis and hybridization properties of oligodeoxynucleotides containing 2′,4′-C-bridged 2′-deoxynucleosides. *Bioorg. Med. Chem. Lett.* **1999**, *9*, 1147–1150. [CrossRef]
37. Obika, S.; Nanbu, D.; Hari, Y.; Andoh, J.; Morio, K.; Doi, T.; Imanishi, T. Stability and structural features of the duplexes containing nucleoside analogues with a fixed N-type conformation, 2′-O,4′-C-methyleneribonucleosides. *Tetrahedron Lett.* **1998**, *39*, 5401–5404. [CrossRef]
38. Veedu, R.N.; Wengel, J. Locked nucleic acids: Promising nucleic acid analogs for therapeutic applications. *Chem. Biodivers.* **2010**, *7*, 536–542. [CrossRef]
39. Bhattacharyya, J.; Maiti, S.; Muhuri, S.; Nakano, S.; Miyoshi, D.; Sugimoto, N. Effect of locked nucleic acid modifications on the thermal stability of noncanonical DNA structure. *Biochemistry* **2011**, *50*, 7414–7425. [CrossRef]

40. Braasch, D.A.; Corey, D.R. Locked nucleic acid (LNA): Fine-tuning the recognition of DNA and RNA. *Chem. Biol.* **2001**, *8*, 1–7. [CrossRef]
41. Jackson, A.; Jani, S.; Sala, C.D.; Soler-Bistue, A.J.; Zorreguieta, A.; Tolmasky, M.E. Assessment of configurations and chemistries of bridged nucleic acids-containing oligomers as external guide sequences: A methodology for inhibition of expression of antibiotic resistance genes. *Biol. Methods Protoc.* **2016**, *1*, bpw001. [CrossRef]
42. Soler Bistue, A.J.; Martin, F.A.; Vozza, N.; Ha, H.; Joaquin, J.C.; Zorreguieta, A.; Tolmasky, M.E. Inhibition of *aac(6′)-Ib*-mediated amikacin resistance by nuclease-resistant external guide sequences in bacteria. *Proc. Natl. Acad. Sci. USA* **2009**, *106*, 13230–13235. [CrossRef]
43. Arzumanov, A.; Stetsenko, D.A.; Malakhov, A.D.; Reichelt, S.; Sorensen, M.D.; Babu, B.R.; Wengel, J.; Gait, M.J. A structure-activity study of the inhibition of HIV-1 Tat-dependent trans-activation by mixmer 2′-O-methyl oligoribonucleotides containing locked nucleic acid (LNA), alpha-L-LNA, or 2′-thio-LNA residues. *Oligonucleotides* **2003**, *13*, 435–453. [CrossRef]
44. Arzumanov, A.; Walsh, A.P.; Rajwanshi, V.K.; Kumar, R.; Wengel, J.; Gait, M.J. Inhibition of HIV-1 Tat-dependent trans activation by steric block chimeric 2′-O-methyl/LNA oligoribonucleotides. *Biochemistry* **2001**, *40*, 14645–14654. [CrossRef]
45. Singh, S.K.; Wengel, J. Universality of LNA-mediated high-affinity nucleic acid recognition. *Chem. Commun.* **1998**, 1247–1248. [CrossRef]
46. Stenvang, J.; Silahtaroglu, A.N.; Lindow, M.; Elmen, J.; Kauppinen, S. The utility of LNA in microRNA-based cancer diagnostics and therapeutics. *Semin. Cancer Biol.* **2008**, *18*, 89–102. [CrossRef]
47. Mouritzen, P.; Nielsen, A.T.; Pfundheller, H.M.; Choleva, Y.; Kongsbak, L.; Moller, S. Single nucleotide polymorphism genotyping using locked nucleic acid (LNA). *Expert Rev. Mol. Diagn.* **2003**, *3*, 27–38. [CrossRef]
48. Jakobsen, U.; Vogel, S. Mismatch discrimination of lipidated DNA and LNA-probes (LiNAs) in hybridization-controlled liposome assembly. *Org. Biomol. Chem.* **2016**, *14*, 6985–6995. [CrossRef]
49. Simon, L.; Probst, A.V. High-affinity LNA-DNA mixmer probes for detection of chromosome-specific polymorphisms of 5S rDNA repeats in *Arabidopsis thaliana*. *Methods Mol. Biol.* **2018**, *1675*, 481–491.
50. Ikenaga, M.; Katsuragi, S.; Handa, Y.; Katsumata, H.; Chishaki, N.; Kawauchi, T.; Sakai, M. Improvements in bacterial primers to enhance selective SSU rRNA gene amplification of plant-associated bacteria by applying the LNA oligonucleotide-PCR clamping technique. *Microbes Environ.* **2018**, *33*, 340–344. [CrossRef]
51. Levin, J.D.; Fiala, D.; Samala, M.F.; Kahn, J.D.; Peterson, R.J. Position-dependent effects of locked nucleic acid (LNA) on DNA sequencing and PCR primers. *Nucleic Acids Res.* **2006**, *34*, e142. [CrossRef]
52. Pakpour, N.; Cheung, K.W.; Souvannaseng, L.; Concordet, J.P.; Luckhart, S. Transfection and mutagenesis of target genes in mosquito cells by locked nucleic acid-modified oligonucleotides. *J. Vis. Exp.* **2010**, 2355. [CrossRef]
53. van Ravesteyn, T.W.; Dekker, M.; Fish, A.; Sixma, T.K.; Wolters, A.; Dekker, R.J.; Te Riele, H.P. LNA modification of single-stranded DNA oligonucleotides allows subtle gene modification in mismatch-repair-proficient cells. *Proc. Natl. Acad. Sci. USA* **2016**, *113*, 4122–4127. [CrossRef]
54. Parekh-Olmedo, H.; Drury, M.; Kmiec, E.B. Targeted nucleotide exchange in *Saccharomyces cerevisiae* directed by short oligonucleotides containing locked nucleic acids. *Chem. Biol.* **2002**, *9*, 1073–1084. [CrossRef]
55. Wojtkowiak-Szlachcic, A.; Taylor, K.; Stepniak-Konieczna, E.; Sznajder, L.J.; Mykowska, A.; Sroka, J.; Thornton, C.A.; Sobczak, K. Short antisense-locked nucleic acids (all-LNAs) correct alternative splicing abnormalities in myotonic dystrophy. *Nucleic Acids Res.* **2015**, *43*, 3318–3331. [CrossRef]
56. Elmen, J.; Lindow, M.; Schutz, S.; Lawrence, M.; Petri, A.; Obad, S.; Lindholm, M.; Hedtjarn, M.; Hansen, H.F.; Berger, U.; et al. LNA-mediated microRNA silencing in non-human primates. *Nature* **2008**, *452*, 896–899. [CrossRef]
57. Janssen, H.L.; Reesink, H.W.; Lawitz, E.J.; Zeuzem, S.; Rodriguez-Torres, M.; Patel, K.; van der Meer, A.J.; Patick, A.K.; Chen, A.; Zhou, Y.; et al. Treatment of HCV infection by targeting microRNA. *N. Engl. J. Med.* **2013**, *368*, 1685–1694. [CrossRef]
58. van der Ree, M.H.; de Vree, J.M.; Stelma, F.; Willemse, S.; van der Valk, M.; Rietdijk, S.; Molenkamp, R.; Schinkel, J.; van Nuenen, A.C.; Beuers, U.; et al. Safety, tolerability, and antiviral effect of RG-101 in patients with chronic hepatitis C: A phase 1B, double-blind, randomised controlled trial. *Lancet* **2017**, *389*, 709–717. [CrossRef]

59. van der Ree, M.H.; van der Meer, A.J.; de Bruijne, J.; Maan, R.; van Vliet, A.; Welzel, T.M.; Zeuzem, S.; Lawitz, E.J.; Rodriguez-Torres, M.; Kupcova, V.; et al. Long-term safety and efficacy of microRNA-targeted therapy in chronic hepatitis C patients. *Antivir. Res.* **2014**, *111*, 53–59. [CrossRef]
60. Guerard, M.; Andreas, Z.; Erich, K.; Christine, M.; Martina, M.B.; Christian, W.; Franz, S.; Thomas, S.; Yann, T. Locked nucleic acid (LNA): Based single-stranded oligonucleotides are not genotoxic. *Environ. Mol. Mutagen.* **2017**, *58*, 112–121. [CrossRef]
61. Bianchini, D.; Omlin, A.; Pezaro, C.; Lorente, D.; Ferraldeschi, R.; Mukherji, D.; Crespo, M.; Figueiredo, I.; Miranda, S.; Riisnaes, R.; et al. First-in-human Phase I study of EZN-4176, a locked nucleic acid antisense oligonucleotide to exon 4 of the androgen receptor mRNA in patients with castration-resistant prostate cancer. *Br. J. Cancer* **2013**, *109*, 2579–2586. [CrossRef]
62. Swayze, E.E.; Siwkowski, A.M.; Wancewicz, E.V.; Migawa, M.T.; Wyrzykiewicz, T.K.; Hung, G.; Monia, B.P.; Bennett, C.F. Antisense oligonucleotides containing locked nucleic acid improve potency but cause significant hepatotoxicity in animals. *Nucleic Acids Res.* **2007**, *35*, 687–700. [CrossRef]
63. Kakiuchi-Kiyota, S.; Koza-Taylor, P.H.; Mantena, S.R.; Nelms, L.F.; Enayetallah, A.E.; Hollingshead, B.D.; Burdick, A.D.; Reed, L.A.; Warneke, J.A.; Whiteley, L.O.; et al. Comparison of hepatic transcription profiles of locked ribonucleic acid antisense oligonucleotides: Evidence of distinct pathways contributing to non-target mediated toxicity in mice. *Toxicol. Sci.* **2014**, *138*, 234–248. [CrossRef]
64. Kasuya, T.; Hori, S.; Watanabe, A.; Nakajima, M.; Gahara, Y.; Rokushima, M.; Yanagimoto, T.; Kugimiya, A. Ribonuclease H1-dependent hepatotoxicity caused by locked nucleic acid-modified gapmer antisense oligonucleotides. *Sci. Rep.* **2016**, *6*, 30377. [CrossRef]
65. Stein, C.A.; Hansen, J.B.; Lai, J.; Wu, S.; Voskresenskiy, A.; Hog, A.; Worm, J.; Hedtjarn, M.; Souleimanian, N.; Miller, P.; et al. Efficient gene silencing by delivery of locked nucleic acid antisense oligonucleotides, unassisted by transfection reagents. *Nucleic Acids Res.* **2010**, *38*, e3. [CrossRef]
66. Traglia, G.M.; Sala, C.D.; Fuxman Bass, J.I.; Soler-Bistue, A.J.; Zorreguieta, A.; Ramirez, M.S.; Tolmasky, M.E. Internalization of locked nucleic acids/DNA hybrid oligomers into *Escherichia coli*. *Biores. Open Access* **2012**, *1*, 260–263. [CrossRef]
67. Soifer, H.S.; Koch, T.; Lai, J.; Hansen, B.; Hoeg, A.; Oerum, H.; Stein, C.A. Silencing of gene expression by gymnotic delivery of antisense oligonucleotides. *Methods Mol. Biol.* **2012**, *815*, 333–346.
68. Mettlen, M.; Pucadyil, T.; Ramachandran, R.; Schmid, S.L. Dissecting dynamin's role in clathrin-mediated endocytosis. *Biochem. Soc. Trans.* **2009**, *37*, 1022–1026. [CrossRef]
69. Lajoie, P.; Nabi, I.R. Lipid rafts, caveolae, and their endocytosis. *Int. Rev. Cell Mol. Biol.* **2010**, *282*, 135–163.
70. Howes, M.T.; Mayor, S.; Parton, R.G. Molecules, mechanisms, and cellular roles of clathrin-independent endocytosis. *Curr. Opin. Cell Biol.* **2010**, *22*, 519–527. [CrossRef]
71. Juliano, R.L. The delivery of therapeutic oligonucleotides. *Nucleic Acids Res.* **2016**, *44*, 6518–6548. [CrossRef]
72. Johannes, L.; Lucchino, M. Current challenges in delivery and cytosolic translocation of therapeutic RNAs. *Nucleic Acid Ther.* **2018**, *28*, 178–193. [CrossRef]
73. Fabani, M.M.; Gait, M.J. miR-122 targeting with LNA/2′-O-methyl oligonucleotide mixmers, peptide nucleic acids (PNA), and PNA-peptide conjugates. *RNA* **2008**, *14*, 336–346. [CrossRef]
74. Gupta, N.; Fisker, N.; Asselin, M.C.; Lindholm, M.; Rosenbohm, C.; Orum, H.; Elmen, J.; Seidah, N.G.; Straarup, E.M. A locked nucleic acid antisense oligonucleotide (LNA) silences PCSK9 and enhances LDLR expression in vitro and in vivo. *PLoS ONE* **2010**, *5*, e10682. [CrossRef]
75. Beane, R.; Gabillet, S.; Montaillier, C.; Arar, K.; Corey, D.R. Recognition of chromosomal DNA inside cells by locked nucleic acids. *Biochemistry* **2008**, *47*, 13147–13149. [CrossRef]
76. Grunweller, A.; Wyszko, E.; Bieber, B.; Jahnel, R.; Erdmann, V.A.; Kurreck, J. Comparison of different antisense strategies in mammalian cells using locked nucleic acids, 2′-O-methyl RNA, phosphorothioates and small interfering RNA. *Nucleic Acids Res.* **2003**, *31*, 3185–3193. [CrossRef]
77. Turner, J.J.; Jones, S.; Fabani, M.M.; Ivanova, G.; Arzumanov, A.A.; Gait, M.J. RNA targeting with peptide conjugates of oligonucleotides, siRNA and PNA. *Blood Cells Mol. Dis.* **2007**, *38*, 1–7. [CrossRef]
78. Jani, S.; Jackson, A.; Davies-Sala, C.; Chiem, K.; Soler-Bistue, A.; Zorreguieta, A.; Tolmasky, M.E. Assessment of external guide sequences' (EGS) efficiency as inducers of RNase P-mediated cleavage of mRNA target molecules. *Methods Mol. Biol.* **2018**, *1737*, 89–98.
79. Yin, H.; Wang, H.; Li, Z.; Shu, D.; Guo, P. RNA micelles for systemic delivery of anti-miRNA for cancer targeting and inhibition without ligand. *ACS Nano* **2018**, *13*, 706–717. [CrossRef]

80. Elmen, J.; Zhang, H.Y.; Zuber, B.; Ljungberg, K.; Wahren, B.; Wahlestedt, C.; Liang, Z. Locked nucleic acid containing antisense oligonucleotides enhance inhibition of HIV-1 genome dimerization and inhibit virus replication. *FEBS Lett.* **2004**, *578*, 285–290. [CrossRef]
81. Kurreck, J.; Wyszko, E.; Gillen, C.; Erdmann, V.A. Design of antisense oligonucleotides stabilized by locked nucleic acids. *Nucleic Acids Res.* **2002**, *30*, 1911–1918. [CrossRef]
82. Kaur, H.; Babu, B.R.; Maiti, S. Perspectives on chemistry and therapeutic applications of Locked Nucleic Acid (LNA). *Chem. Rev.* **2007**, *107*, 4672–4697. [CrossRef]
83. Hagedorn, P.H.; Persson, R.; Funder, E.D.; Albaek, N.; Diemer, S.L.; Hansen, D.J.; Moller, M.R.; Papargyri, N.; Christiansen, H.; Hansen, B.R.; et al. Locked nucleic acid: Modality, diversity, and drug discovery. *Drug Discov. Today* **2018**, *23*, 101–114. [CrossRef]
84. Grunweller, A.; Hartmann, R.K. Locked nucleic acid oligonucleotides: The next generation of antisense agents? *Biodrugs* **2007**, *21*, 235–243. [CrossRef]
85. Sadewasser, A.; Dietzel, E.; Michel, S.; Kluver, M.; Helfer, M.; Thelemann, T.; Klar, R.; Eickmann, M.; Becker, S.; Jaschinski, F. Anti-Niemann Pick C1 single-stranded oligonucleotides with locked nucleic acids potently reduce ebola virus infection in vitro. *Mol. Ther. Nucleic Acids* **2019**, *16*, 686–697. [CrossRef]
86. Hillebrand, F.; Ostermann, P.N.; Muller, L.; Degrandi, D.; Erkelenz, S.; Widera, M.; Pfeffer, K.; Schaal, H. Gymnotic delivery of LNA mixmers targeting viral SREs induces HIV-1 mRNA degradation. *Int. J. Mol. Sci.* **2019**, *20*, 1088. [CrossRef]
87. Kim, S.; Linse, K.; Retes, P.; Castro, P.; Castro, M. Bridged nucleic acids (BNAs) as molecular tools. *J. Biochem. Mol. Biol. Res.* **2015**, *1*, 67–71.
88. Morita, K.; Koizumi, M. Synthesis of ENA nucleotides and ENA oligonucleotides. *Curr. Protoc. Nucleic Acid Chem.* **2018**, *72*, 4.79.01–4.79.21. [CrossRef]
89. Mitsuoka, Y.; Kodama, T.; Ohnishi, R.; Hari, Y.; Imanishi, T.; Obika, S. A bridged nucleic acid, 2′,4′-BNA COC: Synthesis of fully modified oligonucleotides bearing thymine, 5-methylcytosine, adenine and guanine 2′,4′-BNA COC monomers and RNA-selective nucleic-acid recognition. *Nucleic Acids Res.* **2009**, *37*, 1225–1238. [CrossRef]
90. Kotkowiak, W.; Wengel, J.; Scotton, C.J.; Pasternak, A. Improved RE31 analogues containing modified nucleic acid monomers: Thermodynamic, structural, and biological effects. *J. Med. Chem.* **2019**, *62*, 2499–2507. [CrossRef]
91. Ferino, A.; Miglietta, G.; Picco, R.; Vogel, S.; Wengel, J.; Xodo, L.E. MicroRNA therapeutics: Design of single-stranded miR-216b mimics to target KRAS in pancreatic cancer cells. *RNA Biol.* **2018**, *15*, 1273–1285. [CrossRef]
92. Yamamoto, T.; Harada-Shiba, M.; Nakatani, M.; Wada, S.; Yasuhara, H.; Narukawa, K.; Sasaki, K.; Shibata, M.A.; Torigoe, H.; Yamaoka, T.; et al. Cholesterol-lowering action of BNA-based antisense oligonucleotides targeting PCSK9 in atherogenic diet-induced hypercholesterolemic mice. *Mol. Ther. Nucleic Acids* **2012**, *1*, e22. [CrossRef]
93. Rahman, S.M.; Seki, S.; Obika, S.; Haitani, S.; Miyashita, K.; Imanishi, T. Highly stable pyrimidine-motif triplex formation at physiological pH values by a bridged nucleic acid analogue. *Angew. Chem. Int. Ed. Engl.* **2007**, *46*, 4306–4309. [CrossRef]
94. Lopez, C.; Arivett, B.A.; Actis, L.A.; Tolmasky, M.E. Inhibition of AAC(6′)-Ib-mediated resistance to amikacin in *Acinetobacter baumannii* by an antisense peptide-conjugated 2′,4′-bridged nucleic acid-NC-DNA hybrid oligomer. *Antimicrob. Agents Chemother.* **2015**, *59*, 5798–5803. [CrossRef]
95. Manning, K.S.; Rao, A.N.; Castro, M.; Cooper, T.A. BNA(NC) gapmers revert splicing and reduce RNA foci with low toxicity in myotonic dystrophy cells. *ACS Chem. Biol.* **2017**, *12*, 2503–2509. [CrossRef]
96. Shivarov, V.; Ivanova, M.; Naumova, E. Rapid detection of DNMT3A R882 mutations in hematologic malignancies using a novel bead-based suspension assay with BNA(NC) probes. *PLoS ONE* **2014**, *9*, e99769. [CrossRef]
97. Cromwell, C.R.; Sung, K.; Park, J.; Krysler, A.R.; Jovel, J.; Kim, S.K.; Hubbard, B.P. Incorporation of bridged nucleic acids into CRISPR RNAs improves Cas9 endonuclease specificity. *Nat. Commun.* **2018**, *9*, 1448. [CrossRef]
98. Good, L.; Nielsen, P.E. Antisense inhibition of gene expression in bacteria by PNA targeted to mRNA. *Nat. Biotechnol.* **1998**, *16*, 355–358. [CrossRef]

99. Tolmasky, M.E. Strategies to prolong the useful life of existing antibiotics and help overcoming the antibiotic resistance crisis. In *Frontiers in Clinical Drug Research-Anti Infectives*; Atta-ur-Rhaman, Ed.; Bentham Books: Sharjah, United Arab Emirates, 2017; Volume 1, pp. 1–27.
100. Guerrier-Takada, C.; Salavati, R.; Altman, S. Phenotypic conversion of drug-resistant bacteria to drug sensitivity. *Proc. Natl. Acad. Sci. USA* **1997**, *94*, 8468–8472. [CrossRef]
101. Ayhan, D.H.; Tamer, Y.T.; Akbar, M.; Bailey, S.M.; Wong, M.; Daly, S.M.; Greenberg, D.E.; Toprak, E. Sequence-specific targeting of bacterial resistance genes increases antibiotic efficacy. *PLoS Biol.* **2016**, *14*, e1002552. [CrossRef]
102. Ju, L.C.; Cheng, Z.; Fast, W.; Bonomo, R.A.; Crowder, M.W. The continuing challenge of metallo-beta-lactamase inhibition: Mechanism matters. *Trends Pharmacol. Sci.* **2018**, *39*, 635–647. [CrossRef]
103. van den Akker, F.; Bonomo, R.A. Exploring additional dimensions of complexity in inhibitor design for serine beta-lactamases: Mechanistic and intra- and inter-molecular chemistry approaches. *Front. Microbiol.* **2018**, *9*, 622. [CrossRef]
104. Ramirez, M.S.; Tolmasky, M.E. Aminoglycoside modifying enzymes. *Drug Resist. Updates* **2010**, *13*, 151–171. [CrossRef]
105. Meng, J.; He, G.; Wang, H.; Jia, M.; Ma, X.; Da, F.; Wang, N.; Hou, Z.; Xue, X.; Li, M.; et al. Reversion of antibiotic resistance by inhibiting mecA in clinical methicillin-resistant Staphylococci by antisense phosphorothioate oligonucleotide. *J. Antibiot. (Tokyo)* **2015**, *68*, 158–164. [CrossRef]
106. Sully, E.K.; Geller, B.L.; Li, L.; Moody, C.M.; Bailey, S.M.; Moore, A.L.; Wong, M.; Nordmann, P.; Daly, S.M.; Sturge, C.R.; et al. Peptide-conjugated phosphorodiamidate morpholino oligomer (PPMO) restores carbapenem susceptibility to NDM-1-positive pathogens in vitro and in vivo. *J. Antimicrob. Chemother.* **2016**, *72*, 782–790.
107. Sarno, R.; Ha, H.; Weinsetel, N.; Tolmasky, M.E. Inhibition of aminoglycoside 6′-*N*-acetyltransferase type Ib-mediated amikacin resistance by antisense oligodeoxynucleotides. *Antimicrob. Agents Chemother.* **2003**, *47*, 3296–3304. [CrossRef]
108. Soler Bistue, A.J.; Ha, H.; Sarno, R.; Don, M.; Zorreguieta, A.; Tolmasky, M.E. External guide sequences targeting the *aac(6′)-Ib* mRNA induce inhibition of amikacin resistance. *Antimicrob. Agents Chemother.* **2007**, *51*, 1918–1925. [CrossRef]
109. Vakulenko, S.B.; Mobashery, S. Versatility of aminoglycosides and prospects for their future. *Clin. Microbiol. Rev.* **2003**, *16*, 430–450. [CrossRef]
110. Arivett, B.A.; Fiester, S.E.; Ream, D.C.; Centron, D.; Ramirez, M.S.; Tolmasky, M.E.; Actis, L.A. Draft genome of the multidrug-resistant *Acinetobacter baumannii* strain A155 clinical isolate. *Genome Announc.* **2015**, *3*, e00212-15. [CrossRef]
111. Lundblad, E.W.; Altman, S. Inhibition of gene expression by RNase P. *New Biotechnol.* **2010**, *27*, 212–221. [CrossRef]
112. Bird, T.D. Myotonic Dystrophy Type 1. In *GeneReviews*; Adam, M.P., Ardinger, H.H., Pagon, R.A., Wallace, S.E., Bean, L.J.H., Stephens, K., Amemiya, A., Eds.; University of Washington: Seattle, WA, USA, 1993.
113. Brook, J.D.; McCurrach, M.E.; Harley, H.G.; Buckler, A.J.; Church, D.; Aburatani, H.; Hunter, K.; Stanton, V.P.; Thirion, J.P.; Hudson, T.; et al. Molecular basis of myotonic dystrophy: Expansion of a trinucleotide (CTG) repeat at the 3′ end of a transcript encoding a protein kinase family member. *Cell* **1992**, *68*, 799–808. [CrossRef]
114. Mahadevan, M.; Tsilfidis, C.; Sabourin, L.; Shutler, G.; Amemiya, C.; Jansen, G.; Neville, C.; Narang, M.; Barcelo, J.; O'Hoy, K.; et al. Myotonic dystrophy mutation: An unstable CTG repeat in the 3′ untranslated region of the gene. *Science* **1992**, *255*, 1253–1255. [CrossRef]
115. Brouwer, J.R.; Willemsen, R.; Oostra, B.A. Microsatellite repeat instability and neurological disease. *Bioessays* **2009**, *31*, 71–83. [CrossRef]
116. Lee, J.E.; Cooper, T.A. Pathogenic mechanisms of myotonic dystrophy. *Biochem. Soc. Trans.* **2009**, *37*, 1281–1286. [CrossRef]
117. Thornton, C.A. Myotonic dystrophy. *Neurol. Clin.* **2014**, *32*, 705–719. [CrossRef]
118. Blanchard, V.; Khantalin, I.; Ramin-Mangata, S.; Chemello, K.; Nativel, B.; Lambert, G. PCSK9: From biology to clinical applications. *Pathology* **2019**, *51*, 177–183. [CrossRef]
119. Abifadel, M.; Varret, M.; Rabes, J.P.; Allard, D.; Ouguerram, K.; Devillers, M.; Cruaud, C.; Benjannet, S.; Wickham, L.; Erlich, D.; et al. Mutations in PCSK9 cause autosomal dominant hypercholesterolemia. *Nat. Genet.* **2003**, *34*, 154–156. [CrossRef]

120. Hallman, D.M.; Srinivasan, S.R.; Chen, W.; Boerwinkle, E.; Berenson, G.S. Relation of PCSK9 mutations to serum low-density lipoprotein cholesterol in childhood and adulthood (from The Bogalusa Heart Study). *Am. J. Cardiol.* **2007**, *100*, 69–72. [CrossRef]
121. Lambert, G.; Charlton, F.; Rye, K.A.; Piper, D.E. Molecular basis of PCSK9 function. *Atherosclerosis* **2009**, *203*, 1–7. [CrossRef]
122. Cameron, J.; Ranheim, T.; Kulseth, M.A.; Leren, T.P.; Berge, K.E. Berberine decreases PCSK9 expression in HepG2 cells. *Atherosclerosis* **2008**, *201*, 266–273. [CrossRef]
123. Kong, W.J.; Wei, J.; Zuo, Z.Y.; Wang, Y.M.; Song, D.Q.; You, X.F.; Zhao, L.X.; Pan, H.N.; Jiang, J.D. Combination of simvastatin with berberine improves the lipid-lowering efficacy. *Metabolism* **2008**, *57*, 1029–1037. [CrossRef]
124. Chan, J.C.; Piper, D.E.; Cao, Q.; Liu, D.; King, C.; Wang, W.; Tang, J.; Liu, Q.; Higbee, J.; Xia, Z.; et al. A proprotein convertase subtilisin/kexin type 9 neutralizing antibody reduces serum cholesterol in mice and nonhuman primates. *Proc. Natl. Acad. Sci. USA* **2009**, *106*, 9820–9825. [CrossRef]
125. Frank-Kamenetsky, M.; Grefhorst, A.; Anderson, N.N.; Racie, T.S.; Bramlage, B.; Akinc, A.; Butler, D.; Charisse, K.; Dorkin, R.; Fan, Y.; et al. Therapeutic RNAi targeting PCSK9 acutely lowers plasma cholesterol in rodents and LDL cholesterol in nonhuman primates. *Proc. Natl. Acad. Sci. USA* **2008**, *105*, 11915–11920. [CrossRef]
126. Chaudhary, R.; Garg, J.; Shah, N.; Sumner, A. PCSK9 inhibitors: A new era of lipid lowering therapy. *World J. Cardiol.* **2017**, *9*, 76–91. [CrossRef]
127. Graham, M.J.; Lemonidis, K.M.; Whipple, C.P.; Subramaniam, A.; Monia, B.P.; Crooke, S.T.; Crooke, R.M. Antisense inhibition of proprotein convertase subtilisin/kexin type 9 reduces serum LDL in hyperlipidemic mice. *J. Lipid Res.* **2007**, *48*, 763–767. [CrossRef]
128. Brunetti, L.; Gundry, M.C.; Goodell, M.A. DNMT3A in Leukemia. *Cold Spring Harb. Perspect. Med.* **2017**, *7*, a030320. [CrossRef]
129. Suetake, I.; Mishima, Y.; Kimura, H.; Lee, Y.H.; Goto, Y.; Takeshima, H.; Ikegami, T.; Tajima, S. Characterization of DNA-binding activity in the N-terminal domain of the DNA methyltransferase Dnmt3a. *Biochem. J.* **2011**, *437*, 141–148. [CrossRef]
130. Jurkowska, R.Z.; Rajavelu, A.; Anspach, N.; Urbanke, C.; Jankevicius, G.; Ragozin, S.; Nellen, W.; Jeltsch, A. Oligomerization and binding of the Dnmt3a DNA methyltransferase to parallel DNA molecules: Heterochromatic localization and role of Dnmt3L. *J. Biol. Chem.* **2011**, *286*, 24200–24207. [CrossRef]
131. Shivarov, V.; Gueorguieva, R.; Stoimenov, A.; Tiu, R. DNMT3A mutation is a poor prognosis biomarker in AML: Results of a meta-analysis of 4500 AML patients. *Leuk. Res.* **2013**, *37*, 1445–1450. [CrossRef]
132. Itzykson, R.; Kosmider, O.; Fenaux, P. Somatic mutations and epigenetic abnormalities in myelodysplastic syndromes. *Best Pract. Res. Clin. Haematol.* **2013**, *26*, 355–364. [CrossRef]
133. Jankowska, A.M.; Makishima, H.; Tiu, R.V.; Szpurka, H.; Huang, Y.; Traina, F.; Visconte, V.; Sugimoto, Y.; Prince, C.; O'Keefe, C.; et al. Mutational spectrum analysis of chronic myelomonocytic leukemia includes genes associated with epigenetic regulation: UTX, EZH2, and DNMT3A. *Blood* **2011**, *118*, 3932–3941. [CrossRef]
134. Vannucchi, A.M.; Lasho, T.L.; Guglielmelli, P.; Biamonte, F.; Pardanani, A.; Pereira, A.; Finke, C.; Score, J.; Gangat, N.; Mannarelli, C.; et al. Mutations and prognosis in primary myelofibrosis. *Leukemia* **2013**, *27*, 1861–1869. [CrossRef]
135. Traina, F.; Visconte, V.; Jankowska, A.M.; Makishima, H.; O'Keefe, C.L.; Elson, P.; Han, Y.; Hsieh, F.H.; Sekeres, M.A.; Mali, R.S.; et al. Single nucleotide polymorphism array lesions, TET2, DNMT3A, ASXL1 and CBL mutations are present in systemic mastocytosis. *PLoS ONE* **2012**, *7*, e43090. [CrossRef]
136. Grossmann, V.; Haferlach, C.; Weissmann, S.; Roller, A.; Schindela, S.; Poetzinger, F.; Stadler, K.; Bellos, F.; Kern, W.; Haferlach, T.; et al. The molecular profile of adult T-cell acute lymphoblastic leukemia: Mutations in RUNX1 and DNMT3A are associated with poor prognosis in T-ALL. *Genes Chromosom. Cancer* **2013**, *52*, 410–422. [CrossRef]
137. Gaidzik, V.I.; Schlenk, R.F.; Paschka, P.; Stolzle, A.; Spath, D.; Kuendgen, A.; von Lilienfeld-Toal, M.; Brugger, W.; Derigs, H.G.; Kremers, S.; et al. Clinical impact of DNMT3A mutations in younger adult patients with acute myeloid leukemia: Results of the AML Study Group (AMLSG). *Blood* **2013**, *121*, 4769–4777. [CrossRef]
138. Yuan, X.Q.; Peng, L.; Zeng, W.J.; Jiang, B.Y.; Li, G.C.; Chen, X.P. DNMT3A R882 Mutations Predict a Poor Prognosis in AML: A Meta-Analysis From 4474 Patients. *Medicine (Baltimore)* **2016**, *95*, e3519. [CrossRef]

139. Kihara, R.; Nagata, Y.; Kiyoi, H.; Kato, T.; Yamamoto, E.; Suzuki, K.; Chen, F.; Asou, N.; Ohtake, S.; Miyawaki, S.; et al. Comprehensive analysis of genetic alterations and their prognostic impacts in adult acute myeloid leukemia patients. *Leukemia* **2014**, *28*, 1586–1595. [CrossRef]
140. Snetsinger, B.; Ferrone, C.K.; Rauh, M.J. Targeted, amplicon-based, next-generation sequencing to detect age-related clonal hematopoiesis. *Methods Mol. Biol.* **2019**, in press.
141. Luthra, R.; Patel, K.P.; Reddy, N.G.; Haghshenas, V.; Routbort, M.J.; Harmon, M.A.; Barkoh, B.A.; Kanagal-Shamanna, R.; Ravandi, F.; Cortes, J.E.; et al. Next-generation sequencing-based multigene mutational screening for acute myeloid leukemia using MiSeq: Applicability for diagnostics and disease monitoring. *Haematologica* **2014**, *99*, 465–473. [CrossRef]
142. Marcucci, G.; Metzeler, K.H.; Schwind, S.; Becker, H.; Maharry, K.; Mrozek, K.; Radmacher, M.D.; Kohlschmidt, J.; Nicolet, D.; Whitman, S.P.; et al. Age-related prognostic impact of different types of DNMT3A mutations in adults with primary cytogenetically normal acute myeloid leukemia. *J. Clin. Oncol.* **2012**, *30*, 742–750. [CrossRef]
143. Brewin, J.N.; Horne, G.A.; Bisling, K.E.; Stewart, H.J.; Chevassut, T.J. Rapid detection of DNMT3A R882 codon mutations allows early identification of poor risk patients with acute myeloid leukemia. *Leuk. Lymphoma* **2013**, *54*, 1336–1339. [CrossRef]
144. Singh, R.R.; Bains, A.; Patel, K.P.; Rahimi, H.; Barkoh, B.A.; Paladugu, A.; Bisrat, T.; Ravandi-Kashani, F.; Cortes, J.E.; Kantarjian, H.M.; et al. Detection of high-frequency and novel DNMT3A mutations in acute myeloid leukemia by high-resolution melting curve analysis. *J. Mol. Diagn.* **2012**, *14*, 336–345. [CrossRef]
145. Shabbir, M.A.; Hao, H.; Shabbir, M.Z.; Wu, Q.; Sattar, A.; Yuan, Z. Bacteria vs. bacteriophages: Parallel evolution of immune arsenals. *Front. Microbiol.* **2016**, *7*, 1292. [CrossRef]
146. Dy, R.L.; Richter, C.; Salmond, G.P.; Fineran, P.C. Remarkable mechanisms in microbes to resist phage infections. *Annu. Rev. Virol.* **2014**, *1*, 307–331. [CrossRef]
147. Arutyunov, D.; Frost, L.S. F conjugation: Back to the beginning. *Plasmid* **2013**, *70*, 18–32. [CrossRef]
148. Ishino, Y.; Krupovic, M.; Forterre, P. History of CRISPR-Cas from encounter with a mysterious repeated sequence to genome editing technology. *J. Bacteriol.* **2018**, *200*. [CrossRef]
149. Hille, F.; Charpentier, E. CRISPR-Cas: Biology, mechanisms and relevance. *Philos. Trans. R. Soc. Lond. B Biol. Sci.* **2016**, *371*, 20150496. [CrossRef]
150. Strich, J.R.; Chertow, D.S. CRISPR-Cas Biology and Its Application to Infectious Diseases. *J. Clin. Microbiol.* **2019**, *57*, e01307-18. [CrossRef]
151. Wright, A.V.; Nunez, J.K.; Doudna, J.A. Biology and applications of CRISPR systems: Harnessing nature's toolbox for genome engineering. *Cell* **2016**, *164*, 29–44. [CrossRef]
152. Yu, J.S.L.; Yusa, K. Genome-wide CRISPR-Cas9 screening in mammalian cells. *Methods* **2019**, in press. [CrossRef]
153. Jinek, M.; Chylinski, K.; Fonfara, I.; Hauer, M.; Doudna, J.A.; Charpentier, E. A programmable dual-RNA-guided DNA endonuclease in adaptive bacterial immunity. *Science* **2012**, *337*, 816–821. [CrossRef]
154. Mali, P.; Esvelt, K.M.; Church, G.M. Cas9 as a versatile tool for engineering biology. *Nat. Methods* **2013**, *10*, 957–963. [CrossRef]
155. Cong, L.; Ran, F.A.; Cox, D.; Lin, S.; Barretto, R.; Habib, N.; Hsu, P.D.; Wu, X.; Jiang, W.; Marraffini, L.A.; et al. Multiplex genome engineering using CRISPR/Cas systems. *Science* **2013**, *339*, 819–823. [CrossRef]
156. Gasiunas, G.; Barrangou, R.; Horvath, P.; Siksnys, V. Cas9-crRNA ribonucleoprotein complex mediates specific DNA cleavage for adaptive immunity in bacteria. *Proc. Natl. Acad. Sci. USA* **2012**, *109*, E2579–E2586. [CrossRef]
157. Sternberg, S.H.; LaFrance, B.; Kaplan, M.; Doudna, J.A. Conformational control of DNA target cleavage by CRISPR-Cas9. *Nature* **2015**, *527*, 110–113. [CrossRef]
158. Sander, J.D.; Joung, J.K. CRISPR-Cas systems for editing, regulating and targeting genomes. *Nat. Biotechnol.* **2014**, *32*, 347–355. [CrossRef]
159. Joung, J.; Konermann, S.; Gootenberg, J.S.; Abudayyeh, O.O.; Platt, R.J.; Brigham, M.D.; Sanjana, N.E.; Zhang, F. Genome-scale CRISPR-Cas9 knockout and transcriptional activation screening. *Nat. Protoc.* **2017**, *12*, 828–863. [CrossRef]
160. Farhat, S.; Jain, N.; Singh, N.; Sreevathsa, R.; Dash, P.; Rai, R.; Yadav, S.; Kumar, P.; Sarkar, A.; Jain, A.; et al. CRISPR-cas 9 directed genome engineering for enhancing salt stress tolerance in rice. *Semin. Cell Dev. Biol.* **2019**, in press. [CrossRef]

161. Kaushik, I.; Ramachandran, S.; Srivastava, S.K. CRISPR-Cas9: A multifaceted therapeutic strategy for cancer treatment. *Semin. Cell Dev. Biol.* **2019**, in press. [CrossRef]
162. O'Geen, H.; Henry, I.M.; Bhakta, M.S.; Meckler, J.F.; Segal, D.J. A genome-wide analysis of Cas9 binding specificity using ChIP-seq and targeted sequence capture. *Nucleic Acids Res.* **2015**, *43*, 3389–3404. [CrossRef]
163. O'Geen, H.; Yu, A.S.; Segal, D.J. How specific is CRISPR/Cas9 really? *Curr. Opin. Chem. Biol.* **2015**, *29*, 72–78. [CrossRef]
164. Molla, K.A.; Yang, Y. CRISPR/Cas-mediated base editing: Technical considerations and practical applications. *Trends Biotechnol.* **2019**, in press. [CrossRef]
165. Tadic, V.; Josipovic, G.; Zoldos, V.; Vojta, A. CRISPR/Cas9-based epigenome editing: An overview of dCas9-based tools with special emphasis on off-target activity. *Methods* **2019**, in press.
166. Kimberland, M.L.; Hou, W.; Alfonso-Pecchio, A.; Wilson, S.; Rao, Y.; Zhang, S.; Lu, Q. Strategies for controlling CRISPR/Cas9 off-target effects and biological variations in mammalian genome editing experiments. *J. Biotechnol.* **2018**, *284*, 91–101. [CrossRef]
167. Guilinger, J.P.; Thompson, D.B.; Liu, D.R. Fusion of catalytically inactive Cas9 to FokI nuclease improves the specificity of genome modification. *Nat. Biotechnol.* **2014**, *32*, 577–582. [CrossRef]
168. Slaymaker, I.M.; Gao, L.; Zetsche, B.; Scott, D.A.; Yan, W.X.; Zhang, F. Rationally engineered Cas9 nucleases with improved specificity. *Science* **2016**, *351*, 84–88. [CrossRef]
169. Kleinstiver, B.P.; Pattanayak, V.; Prew, M.S.; Tsai, S.Q.; Nguyen, N.T.; Zheng, Z.; Joung, J.K. High-fidelity CRISPR-Cas9 nucleases with no detectable genome-wide off-target effects. *Nature* **2016**, *529*, 490–495. [CrossRef]
170. Tycko, J.; Myer, V.E.; Hsu, P.D. Methods for optimizing CRISPR-Cas9 genome editing specificity. *Mol. Cell* **2016**, *63*, 355–370. [CrossRef]
171. O'Reilly, D.; Kartje, Z.J.; Ageely, E.A.; Malek-Adamian, E.; Habibian, M.; Schofield, A.; Barkau, C.L.; Rohilla, K.J.; DeRossett, L.B.; Weigle, A.T.; et al. Extensive CRISPR RNA modification reveals chemical compatibility and structure-activity relationships for Cas9 biochemical activity. *Nucleic Acids Res.* **2019**, *47*, 546–558. [CrossRef]
172. Hendel, A.; Bak, R.O.; Clark, J.T.; Kennedy, A.B.; Ryan, D.E.; Roy, S.; Steinfeld, I.; Lunstad, B.D.; Kaiser, R.J.; Wilkens, A.B.; et al. Chemically modified guide RNAs enhance CRISPR-Cas genome editing in human primary cells. *Nat. Biotechnol.* **2015**, *33*, 985–989. [CrossRef]
173. Xiao, J.; Deng, Y.M.; Liu, X.R.; Cao, J.P.; Zhou, M.; Tang, Y.L.; Xiong, W.H.; Jiang, Z.S.; Tang, Z.H.; Liu, L.S. PCSK9: A new participant in lipophagy in regulating atherosclerosis? *Clin. Chim. Acta* **2019**, *495*, 358–364. [CrossRef]
174. Briata, P.; Di Blas, E.; Gulisano, M.; Mallamaci, A.; Iannone, R.; Boncinelli, E.; Corte, G. EMX1 homeoprotein is expressed in cell nuclei of the developing cerebral cortex and in the axons of the olfactory sensory neurons. *Mech. Dev.* **1996**, *57*, 169–180. [CrossRef]
175. Uehara, T.; Choong, C.J.; Nakamori, M.; Hayakawa, H.; Nishiyama, K.; Kasahara, Y.; Baba, K.; Nagata, T.; Yokota, T.; Tsuda, H.; et al. Amido-bridged nucleic acid (AmNA)-modified antisense oligonucleotides targeting alpha-synuclein as a novel therapy for Parkinson's disease. *Sci. Rep.* **2019**, *9*, 7567. [CrossRef]

© 2019 by the authors. Licensee MDPI, Basel, Switzerland. This article is an open access article distributed under the terms and conditions of the Creative Commons Attribution (CC BY) license (http://creativecommons.org/licenses/by/4.0/).

molecules

MDPI

Review

Cinnoline Scaffold—A Molecular Heart of Medicinal Chemistry?

Marta Szumilak [1,*] and Andrzej Stanczak [2]

[1] Department of Hospital Pharmacy, Faculty of Pharmacy, Medical University of Lodz, 1 Muszynskiego Street, 90-151 Lodz, Poland

[2] Department of Applied Pharmacy, Faculty of Pharmacy, Medical University of Lodz, 1 Muszynskiego Street, 90-151 Lodz, Poland; andrzej.stanczak@umed.lodz.pl

* Correspondence: marta.szumilak@umed.lodz.pl; Tel.: +48 426-779-252

Academic Editor: Josef Jampilek

Received: 31 May 2019; Accepted: 16 June 2019; Published: 18 June 2019

Abstract: The cinnoline nucleus is a very important bicyclic heterocycle that is used as the structural subunit of many compounds with interesting pharmaceutical properties. Cinnoline derivatives exhibit broad spectrum of pharmacological activities such as antibacterial, antifungal, antimalarial, anti-inflammatory, analgesic, anxiolytic and antitumor activities. Some of them are under evaluation in clinical trials. In the present review, we have compiled studies focused on the biological properties of cinnoline derivatives conducted by many research groups worldwide between 2005 and 2019. Comprehensive and target oriented information clearly indicate that the development of cinnoline based molecules constitute a significant contribution to the identification of lead compounds with optimized pharmacodynamic and pharmacokinetic properties.

Keywords: cinnoline; biological activity; heterocyclic compounds

1. Introduction

Cinnoline (1,2-benzodiazine) **1**, depicted in Figure 1, is present in many compounds of considerable pharmacological and chemical importance [1]. It is six-membered ring system with two nitrogen atoms, an isosteric relative to either quinoline or isoquinoline and isomeric with phthalazine [1,2].

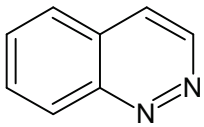

1

Figure 1. Structure of the cinnoline ring system.

Synthesis of cinnoline and its derivatives has been extensively discussed in many papers [2–9]. Until 2011, no compounds containing the cinnoline ring system were found in nature. The first natural cinnoline derivative 2-furanmethanol-(5′→11)-1,3-cyclopentadiene-[5,4-*c*]-1*H*-cinnoline **2** (Figure 2) was isolated from *Cichorium endivia* when investigating the in vitro and in vivo hepatoprotective properties of *Cichorium endivia* L. extract (CEE) [10]. Synthetic molecules bearing a cinnoline framework are extensively studied due to their various biological activities depending on the nature and position of their substituents. In addition, they are often designed as analogs of previously obtained quinoline or isoquinoline derivatives [11–14].

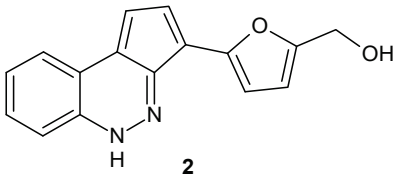

Figure 2. Structure of 2-furanmethanol-(5′→11)-1,3-cyclopentadiene-[5,4-*c*]-1*H*-cinnoline.

Cinnoline, together with other bicyclic scaffolds, is the subject of our special interest as the terminal moiety of symmetrical compounds designed in agreement with the bisintercalators' structural requirements [15,16]. Our previous review describing the biological properties of cinnoline derivatives included papers and patents published until 2004 [1]. Herein, we aimed to review documents published from 2005 to 2019, focusing on the compounds bearing a cinnoline nucleus, in particular with respect to their biological activity and potential therapeutic use.

2. Biological Activity of Cinnoline Derivatives

2.1. Antimicrobial Activity

Infectious diseases constitute a growing therapeutic challenge worldwide due to the developing resistance of pathogens to known drugs [17,18]. As a consequence, there is an urgent need to design new compounds with improved activity against drug-sensitive as well as drug-resistant pathogens. Cinnoline derivatives were widely studied as antimicrobial agents [1]. Cinoxacin **3** (Figure 3) is a common drug used in urinary tract infections [19]. Since it has a high phototoxicity index, Vargas et al. synthesized the naphthyl ester of cinoxacin **4** (Figure 3) in order to evaluate its possible application in antibacterial phototherapy. The ester derivative of cinoxacin **4** exhibited comparable photostability and antibacterial activity against *E. coli* to the parent drug but enhanced antibacterial activity upon irradiation [20].

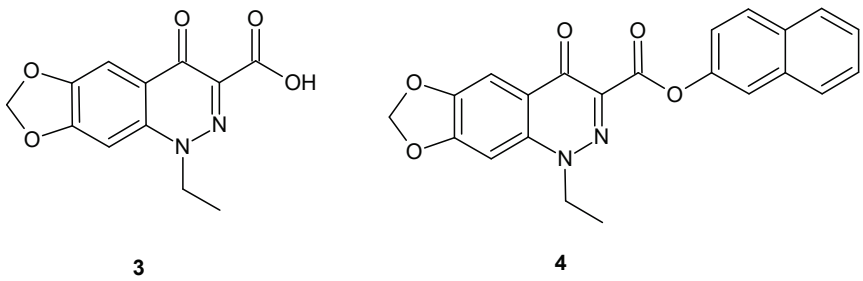

Figure 3. Cinoxacin and its naphthyl ester derivative.

Depicted in Figure 4, 6-hydroxycinnolines were synthesized and tested for in vitro antifungal activity against *Candida* and *Aspergillus* species. It was elucidated that most of the obtained compounds exhibited potent antifungal activity against *C. krusei*, *C. neoformans*, and *A. niger*, with the highest activity towards *C. neoformans* [21].

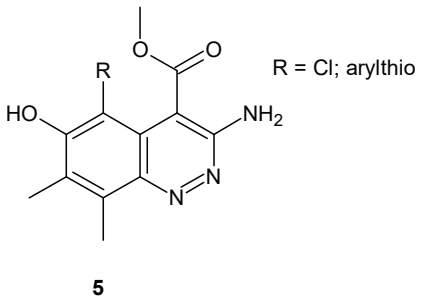

Figure 4. General structure of 6-hydroxycinnoline derivatives.

Cinnoline derivatives bearing sulphonamide moiety **6** (Figure 5) were synthesized as potential antimicrobial and antifungal agents. Evaluation of their activity against a panel of bacteria strains including *P. aeruginosa, E. coli, B. subtilis, S. aureus* and fungi *C. albicans* and *A. niger* revealed that the combination of two active moieties in one molecule resulted in significant activity improvement. Halogen substituted derivatives showed potent activity at lesser concentrations with approximately the same zone of inhibition as the reference drug [22].

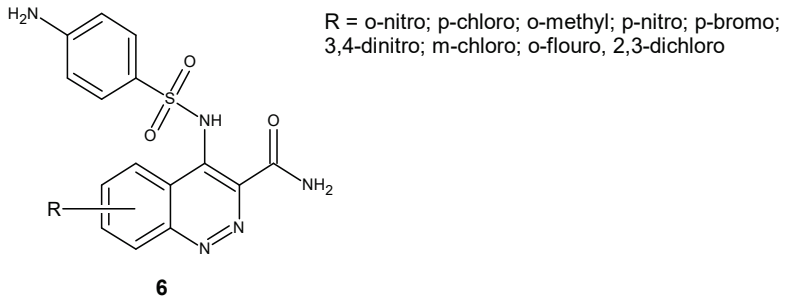

Figure 5. Cinnolines bearing a sulphonamide moiety with antibacterial and antifungal activity.

Some new cinnoline based chalcones **7** and cinnoline based pyrazoline derivatives **8** (Figure 6) were evaluated for their antibacterial activity against *B. subtilis*, *E. coli*, *S. aureus* and *K. pneumoniae*, antifungal activity against *A. flavus*, *F. oxysporum*, *A. niger* and *T. viridae* and insecticidal activity against *Periplaneta americana*. The most potent tested compounds were 4-Cl-, 2-NO_2-, 4-NO_2-substituted cinnoline based chalcones as well as 3-Cl-, 2-NO_2- and 4-OH-substituted cinnoline based pyrazolines. In addition, all chloro-substituted derivatives of series **7** and hydroxy-substituted derivatives of series **8** exhibited better insecticidal activity in comparison to the standard drug [23].

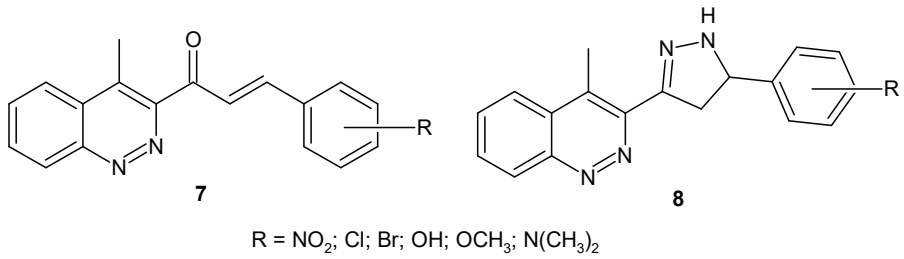

Figure 6. General structures of cinnoline based chalcones and cinnoline based pyrazoline derivatives.

In the search for potent antibacterial and antimalarial drugs, Unnissa and co-workers synthesized pyrazole based cinnoline derivatives **9** (Figure 7). All compounds demonstrated significant antitubercular and antifungal activity. Compound **10** 4-methyl-3-[5-(4-hydroxy-3-methoxyphenyl)-4,5-dihydro-1*H*-pyrazol-3-yl]cinnoline-6-sulphonamide (Figure 7) was found to be the most potent with promising activity against resistant strains of *M. tuberculosis* and various pathogenic fungi [24], as well as against protozoan parasite *P. falciparum* [25].

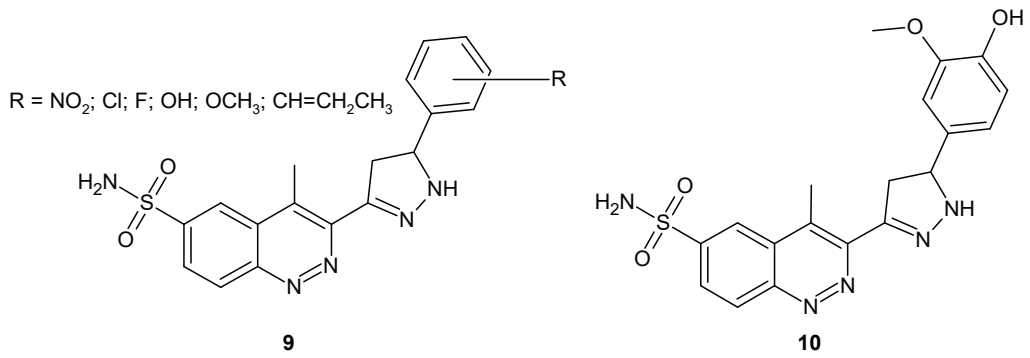

Figure 7. General structure of pyrazole based cinnoline-6-sulphonamides.

Parasuraman et al. described 7-substituted 4-aminocinnoline-3-carboxamide derivatives that were evaluated against a panel of Gram+ and Gram− bacteria. All the synthesized compounds exhibited moderate to good antibacterial activity. The MIC (Minimal inhibitory concentration) of tested compounds against *V. cholera, E. coli, B. substills, B. linctus, M. luteus, S. aureus, K. pneumoniae, Corynebacterium* and *S. albus* was found to be in the range of 6.25–25 μg/mL. The most active compounds, **11** and **12** (Figure 8), demonstrated larger or approximately the same zone of inhibition as the reference drug ciprofloxacin. In addition, the synthesized compounds exhibited moderate to good antifungal activity against *A. fumigatus, S. griseus, A. niger, A. parasitus, C. albicans* and *M. ruber*, with the zone of inhibition between 8–27 mm. MIC values were found to be in the range of 6.25–25 μg/mL [26].

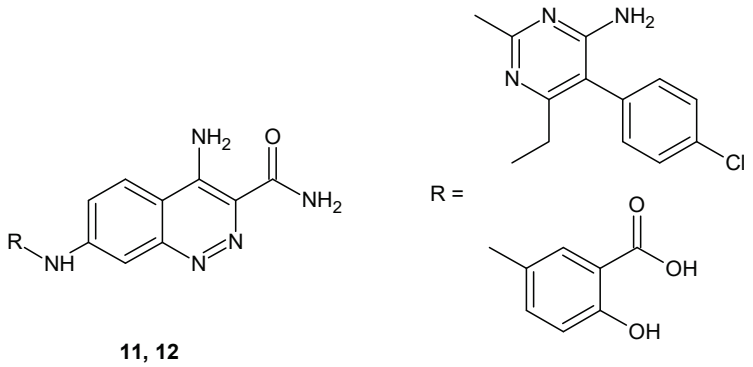

Figure 8. Selected 4-aminocinnoline-3-carboxamide derivatives with antibacterial and antifungal activity.

Saxena and co-workers obtained a series of substituted 4-(*p*-aminopiperazine)cinnoline-3-carboxamide derivatives **13** (Figure 9). The in vitro antimicrobial screening against G+ *B. subtilis* and *S. aureus* and G− *E. coli* and *P. aeruginosa* revealed the MIC of the synthesized compounds in the range of 12.5–50 μg/mL, whereas the zone of inhibition was between 6–29 mm. *A. niger* and *C. albicans* were used for evaluation of the antifungal activity. The MIC of the tested compounds was found to be in the range of 12.5–50 μg/mL, whereas the zone of inhibition was between 8–25 mm. The most potent antimicrobial agents in comparison to standard drugs were 6-chloro, 7-chloro and 7-bromo substituted derivatives [27].

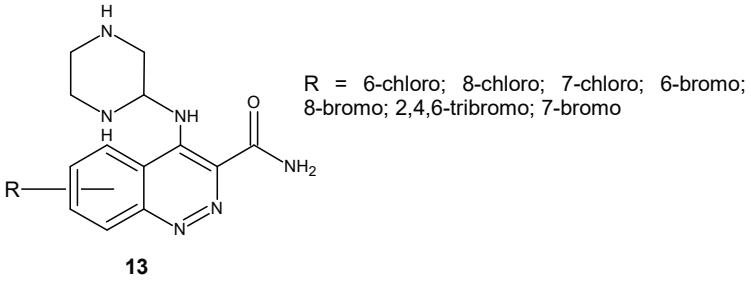

Figure 9. General structure of 4-(*p*-aminopiperazine)cinnoline-3-carboxamide derivatives.

As a continuation of previous studies, they obtained a new series of cinnoline-3-carboxamide derivatives with five-membered (thiophene **14**, furan **15**, pyrazole **16**, imidazole **17**) or six-membered heterocycle (piperazine **18**) substitutions at the 4-amino group of cinnoline core (Figure 10). Compounds were evaluated for antibacterial, antifungal and anti-inflammatory activity. They exhibited antibacterial activity against *B. subtilis, S. aureus, E. coli* and *P. aeruginosa.* However, the potency of tested compounds differed depending on the substituent at the cinnoline nucleus. The most potent compounds in comparison to the standard drug norfloxacin were 6-chloro substituted compounds. Antifungal activity against *C. albicans* and *A. niger* was observed for all series, but the most potent antifungal agents were the 7-chloro substituted cinnoline thiophene derivative and the 6-chloro substituted cinnoline furan derivative. In all five series, halogen substituted compounds were found to be the most active, followed by methyl substituted and nitro substituted derivatives [28].

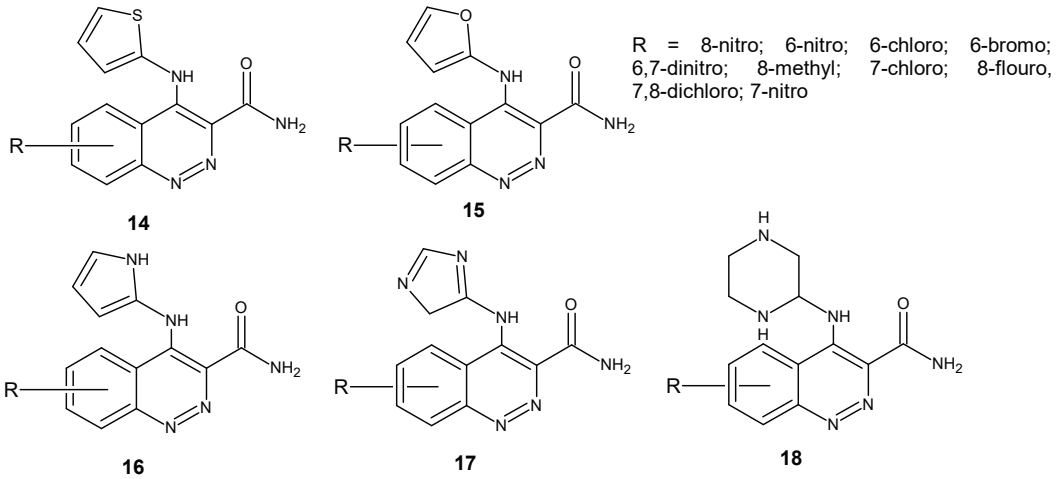

Figure 10. Structure of 4-aminocinnoline-3-carboxamides substituted with five- or six-membered heterocycles.

Looking for potent antitubercular compounds, Dawadi et al. obtained analogues of nucleoside antibiotics where the salicyl-sulfamate moiety was replaced by a cinnolinone-3-sulphonamide group. The most active compound **19** (Figure 11) demonstrated low nanomolar mycobacterial salicylate ligase (MbtA) inhibition and exhibited very good antimycobacterial activity under iron-deficient conditions (MIC = 2.3 μM) by blocking production of siderophores in whole *M. tuberculosis* cells [29].

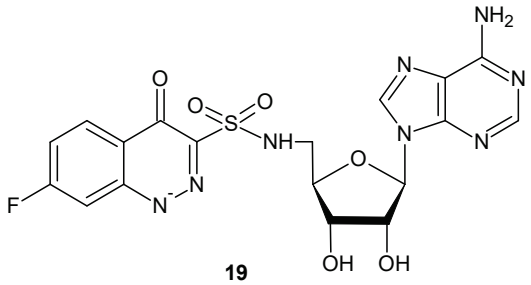

Figure 11. Cinnoline nucleoside analog acting as a siderophore biosynthesis inhibitor.

The cinnoline ring system was also used in designing compounds active against tropical protozoan infections. Devine and co-workers synthesized a panel of compounds with different heterocyclic scaffolds (quinoline, isoquinoline, cinnoline, phthalazine, 3-cyanoquinoline). Cinnoline derivative **20** (Figure 12) displayed potent proliferation inhibition for *L. major* and *P. falciparum* (Half maximal effective concentration EC_{50} value = 0.24 μM and 0.003 μM, respectively). In addition, the cinnoline derivative exhibited increased potency against amastigotes (0.24 μM) but with a significant decrease in potency against the promastigote form [12].

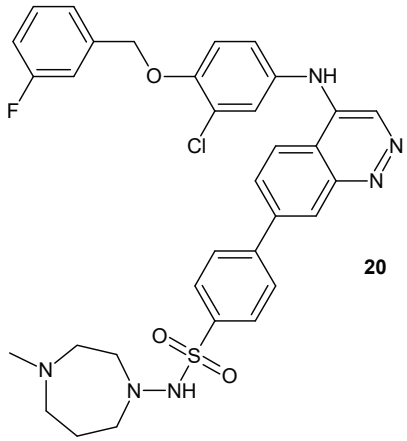

Figure 12. N-(3-chloro-4-((3-fluorobenzyl)oxy)phenyl)-7-(4-((4-methyl-1,4-diazepan-1-yl)sulfonyl) phenyl)cinnolin-4-amine (NEU-1017).

Some cinnoline derivatives **21** (Figure 13) were patented as compounds active against resistance developing bacteria. Glinka and co-workers described the invention related to efflux pump inhibitor (EPI) compounds having polybasic functionalities. The compounds inhibited bacterial efflux pumps and could be used in combination with an antibacterial agent to treat or prevent bacterial infections. [30].

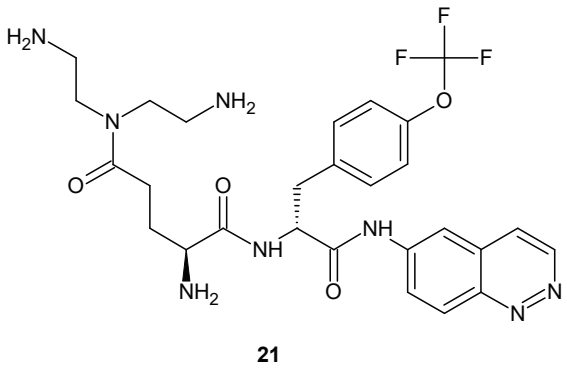

Figure 13. Example of a cinnoline derivative with polybasic functionalities patented as an efflux pump inhibitor.

2.2. Analgesic and Antiinflamatory Activities

In an effort to find dual acting compounds, Chaudhary et al. designed a series of cinnoline derivatives with pyrazoline **23** or without a pyrazoline nucleus **22** (Figure 14) as anti-inflammatory and antibacterial agents. It has been shown that cinnolines bearing pyrazoline ring **23** (Figure 14) and having electron donating functional groups at the phenyl moiety (methoxyl and hydroxyl) exhibited the highest anti-inflammatory activity. In case of antibacterial activity, an electron withdrawing substituent at the phenyl group of cinnoline derivatives without pyrazoline ring **22** (Figure 14), as well as hydroxyl substitution of the phenyl ring of cinnoline derivatives with a pyrazoline moiety, were associated with increased activity against G+ (*S. aureus*, *B. subtilis*) and G− bacteria (*E. coli*) [31].

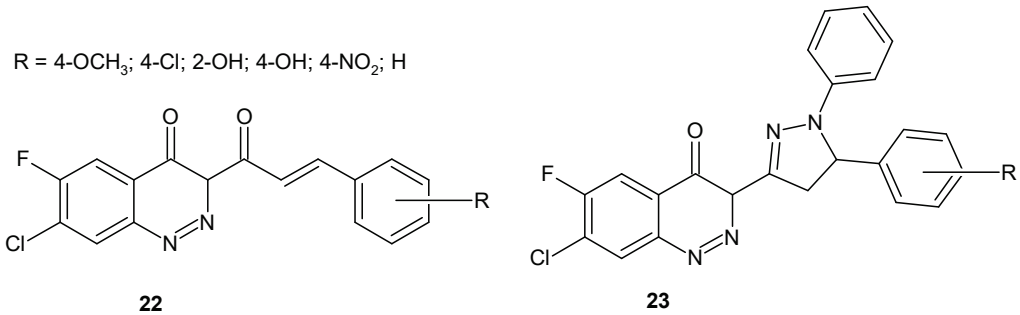

Figure 14. Cinnoline derivatives with dual anti-inflammatory and antibacterial activity.

A series of dual acting pyrazolo[4,3-*c*]cinnoline derivatives were also obtained by Tonk and co-workers. It was elucidated that compounds with an electron donating group in the benzoyl ring exhibited higher anti-inflammatory activity than compounds with a benzoyl ring substituted by electron withdrawing groups. Moreover, a methylene spacer between the phenyl group and the carbonyl carbon increased anti-inflammatory activity, whereas the O-CH_2 group caused a considerable decrease in activity. Compounds that exhibited excellent protection against inflammation **24** and **25,** depicted in Figure 15, also showed a strong cyclooxygenase-2 (COX-2) binding profile. They were considered safer in terms of gastric ulcerogenicity and lipid peroxidation activity than the standard drug naproxen. In case of antibacterial activity, compounds with a 4-nitro- (**26**) or 2,4-dichloro (**27**) substituent at the benzoyl group exhibited significant activity against G− (*E. coli* and *P. aeruginosa*) and G+ (*S. aureus*) bacterial strains. However, compounds with an unsubstituted phenyl ring and methylene spacer **28** (Figure 15) were found to be the best dual anti-inflammatory and antibacterial agent (with significant activity against all three strains) [32].

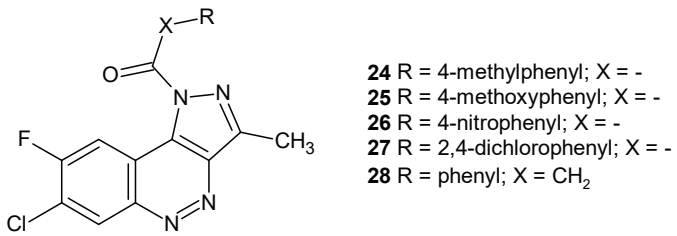

Figure 15. Selected pyrazolo[4,3-*c*]-cinnoline derivatives.

Cinnoline derivatives have been also reported as phosphodiesterase 4 (PDE4) inhibitors [33]. PDE4 is the predominant isoenzyme in almost all immune and inflammatory cells and is an important regulator of cyclic adenosine monophosphate (cAMP) content in airway smooth muscle. Inhibition of PDE4 leads to bronchodilation and the reduction in the production of inflammatory mediators such as tumor necrosis factor (TNF-α) by cAMP down regulation. A PDE4 inhibitor could be used as a potential anti-inflammatory agent in chronic obstructive pulmonary disease (COPD), asthma, rhinitis and

rheumatoid arthritis [34]. Structurally related to quinoline PDE4 inhibitors, 3-amido-4-anilinocinnoline **29** has been designed by Lunniss et al. in order to overcome the poor pharmacokinetic profile in the cynomolgus monkey [33]. Compound **29** (Figure 16) retained excellent in vitro potency and >100-fold selectivity versus other PDE isoenzymes with improved pharmacokinetics in the monkey in comparison to the quinoline analog [33].

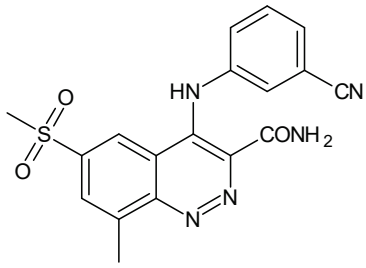

29

Figure 16. The most promising phosphodiesterase 4 (PDE4) inhibitor with a cinnoline nucleus.

Vanilloid receptor subtype VR1 (TRPV1) present in various brain regions, the spinal cord, peripheral sensory neurons and non-neuronal tissues is considered as a new target for pain management but all natural vanilloid receptor agonists such as capsaicin cause an initial burning effect. TRPV1 competitive antagonists, which lack excitatory effects, were designed and evaluated in vivo in animal pain models. Urea derivative bearing cinnoline group **30** (Figure 17) was synthesized among other compounds with various bicyclic heteroaromatic pharmacophores as novel potential analgesics acting through the TRPV1 receptor antagonism ([35] and references therein).

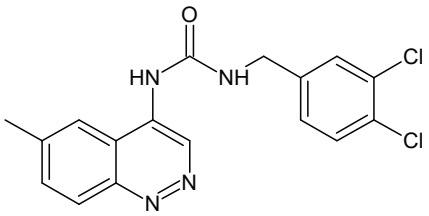

30

Figure 17. Urea derivative bearing a cinnoline nucleus evaluated as Vanilloid receptor subtype VR1 (TRPV1) receptor antagonist.

Since Bruton's tyrosine kinase (BTK) is a kinase implicated in autoimmune disorders, BTK inhibition is considered as an attractive approach for the treatment of autoimmune diseases such as rheumatoid arthritis [36]. In 2013, scientists from Takeda Pharmaceutical Company Ltd. patented cinnoline derivatives of general formula **31** depicted in Figure 18 as BTK inhibitors [37]. In addition, the discovery of a series of 4-aminocinnoline-3-carboxamides that exhibited BTK inhibition were reported by Smith et al. A fragment-based screening approach incorporating X-ray co-crystallography was used to identify a cinnoline fragment and characterize its binding mode. Optimization of the fragment hit resulted in the identification of compound **32** (Figure 18), an orally absorbed, noncovalent BTK inhibitor reducing paw swelling in a dose- and exposure-dependent fashion in a rat model of collagen-induced arthritis [38].

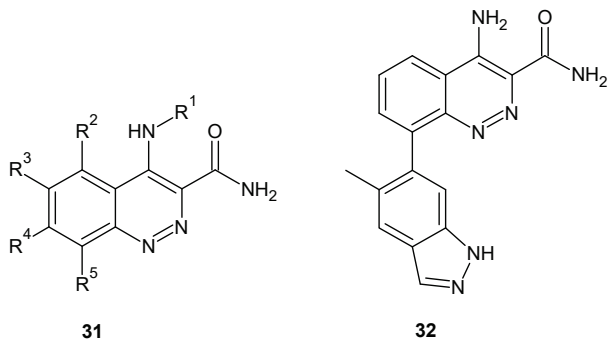

Figure 18. Structure of 4-aminocinnoline-3-carboxamide derivatives that exhibit Bruton's tyrosine kinase (BTK) inhibition activity.

Cinnoline derivatives were also evaluated as human neutrophil elastase (HNE) inhibitors. Excessive HNE activity is connected with many inflammatory disorders and compounds which are able to inhibit the proteolytic activity of HNE represent promising therapeutic agents for the treatment of diseases involving its excessive activity. Potential HNE inhibitors bearing cinnoline scaffolds were designed by transformation of indazole into the cinnoline by enlargement of the pyrazole ring of the *N*-benzoylindazoles reported earlier [39,40]. Studies revealed that although cinnoline derivatives (**33** and **34** were the most potent) (Figure 19) were reversible competitive inhibitors of HNE with increased stability in aqueous solution, they exhibited lower potency in comparison to *N*-benzoylindazoles ([41] and references therein).

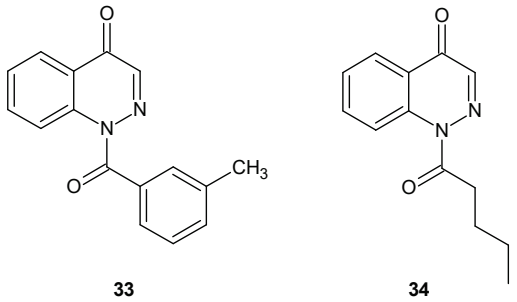

Figure 19. The most potent cinnoline human neutrophil elastase (HNE) reversible competitive inhibitors.

A cinnoline fused Mannich base with a large hydrophobic diphenyl substituent at amino group **35** (Figure 20) exhibited higher analgesic activity when compared to diclofenac at 120 min and 180 min. In addition, its dose level (50 mg/kg) resulted in similar anti-inflammatory activity in comparison to celecoxib (20 mg/kg). What is more, compound **35** as well as **36** (with a dicyclohexane moiety) (Figure 20) also exhibited antibacterial activity with a larger zone of inhibition when compared to streptomycin in *S. aureus* and *E. coli*, respectively [42].

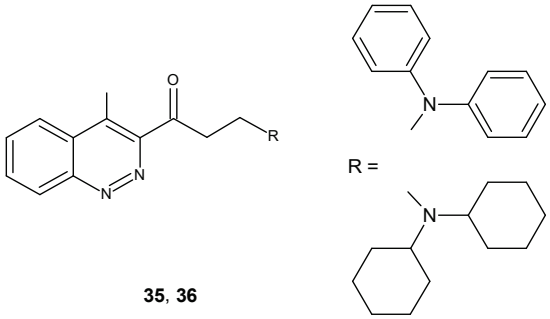

Figure 20. Cinnoline fused Mannich base derivatives.

2.3. Potential for Neurological Disorders

Compounds bearing a cinnoline nucleus fused with various heterocyclic scaffolds were also designed as potential therapeutic agents aiming at treating many neurological and psychiatric disorders e.g., Huntington's [43] or Alzheimer's disease [44].

Amer et al. synthesized dibenzopyrazolocinnolines and evaluated their antiparkinsonian activity. The pharmacological screening revealed that the most active compounds **37** and **38,** depicted in Figure 21, exhibited antiparkinsonian activity comparable to benzatropine [45].

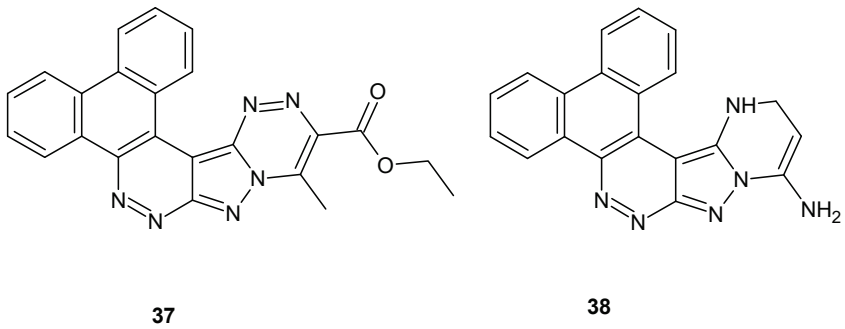

Figure 21. Dibenzopyrazolocinnolines with antiparkinsonian activity.

Mutations in the leucine-rich repeat kinase 2 (LRRK2) protein have been associated with Parkinson's disease. Inhibition of LRRK2 kinase activity by a selective small-molecule inhibitor has been proposed as a potential treatment for this disease [46]. Scientists from Elan Pharmaceuticals worked on a series of cinnoline LRRK2 small-molecule inhibitors identified from a kinase-focused high throughput screening (HTS) of an in-house library [47]. In addition, Garofalo et al. reported 4-aminocinnoline-3-carboxamide derivatives **39**, **40** (Figure 22) potent against both wild-type and mutant LRRK2 kinase activity in biochemical and cellular assays. In addition, these compounds exhibited excellent central nervous system penetration. Unfortunately, due to disappointing kinase specificity, they were no longer studied [48].

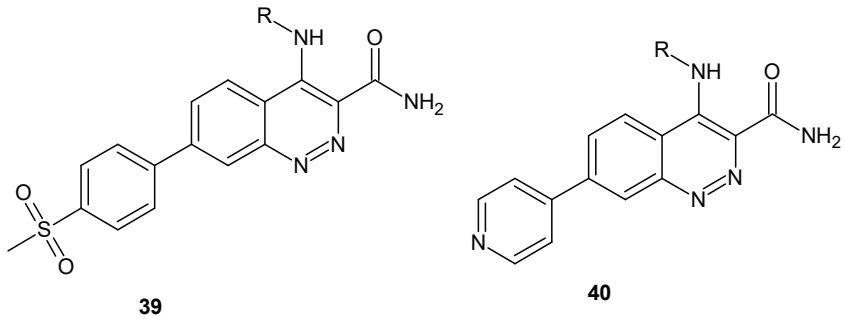

Figure 22. General structures of cinnoline leucine-rich repeat kinase 2 (LRRK2) inhibitors.

The phosphodiesterase 10A (PDE10A) enzyme is involved in cellular signaling pathways in schizophrenia. As a consequence, inhibitors of PDE10A offer a promising therapeutic approach for the treatment or prevention of psychiatric disorders, especially schizophrenia and related diseases [49].

Hu et al. described 6,7-dimethoxy-4-(pyridine-3-yl)cinnolines as novel phosphodiesterase 10A inhibitors. The mode of binding in the enzyme's catalytic domain was also elucidated. Selective inhibitor of PDE10A **41** (Figure 23) was selected. It demonstrated efficacy in a rodent behavioral model of schizophrenia and good in vivo metabolic stability in rats [50]. Yang et al. described high in vitro potency of compounds **41** and **42** (Figure 23) for PDE10A with the half maximal inhibitory concentration (IC_{50}) values of 1.52 ± 0.18 nM and 2.86 ± 0.10 nM, respectively and 1000-fold selectivity over

PDE3A/B and PDE4A/B. These compounds were also suitable for positron emission tomography (PET) radionuclide labelling [51].

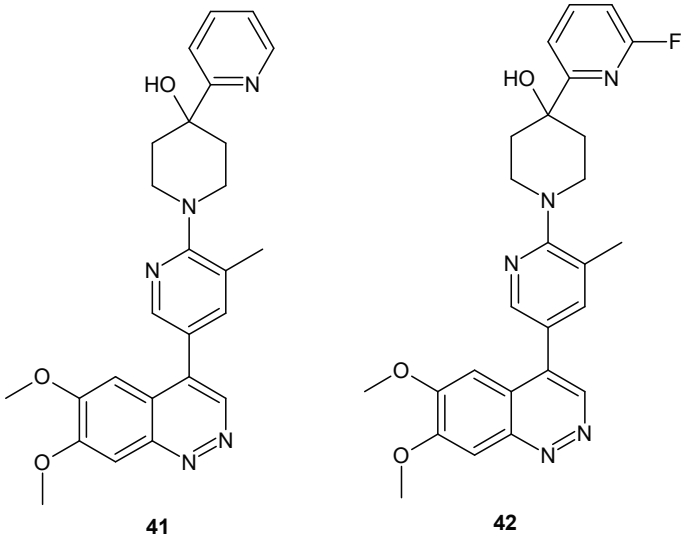

Figure 23. Structure of 6,7-dimethoxy-4-(pyridine-3-yl)cinnolines with potent phosphodiesterase 10A (PDE10A) inhibitory activity.

Since some 6,7-dimethoxy-4-(pyridine-3-yl)cinnolines also exhibited PDE3 activity (a risk of off-target effects), optimization of structure **43** (Figure 24) led to the discovery of compounds **44** and **45** (Figure 24) with significantly improved selectivity against PDE3 but maintaining their PDE10A inhibitory activity and in vivo metabolic stability comparable to **43** (Figure 24) [52].

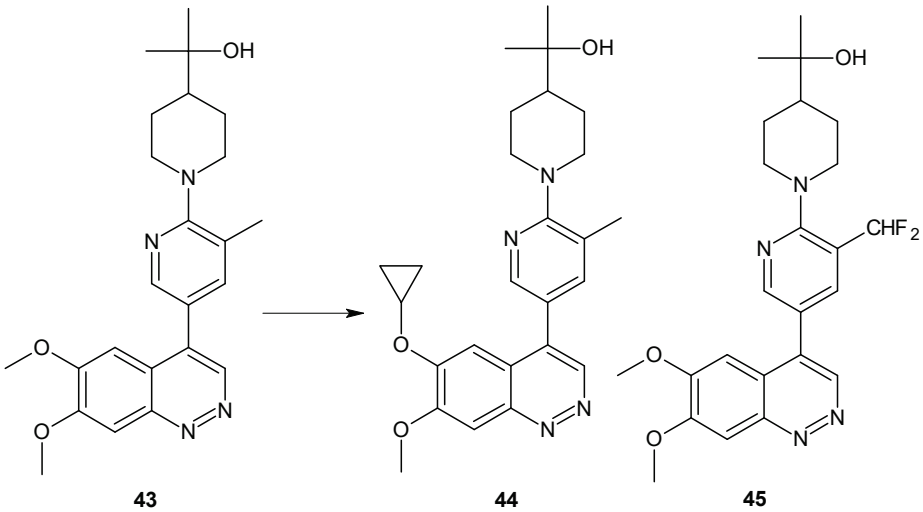

Figure 24. PDE10A inhibitors with improved selectivity.

Recently, Geneste et al. described the optimization of HTS hit structure **46** (Figure 25) supported by X-ray crystal structure analysis and molecular modeling which gave 3*H*-pyrazolo[3,4-*c*]cinnolines **47** and **48** (Figure 25), which are potent, selective and brain-penetrant PDE10A inhibitors with an improved pharmacokinetic profile in rats [53]. Preparation of 3*H*-pyrazolo[3,4-*c*]cinnoline derivatives as PDE10A inhibitors was also the subject of patent WO2014/027078 [54].

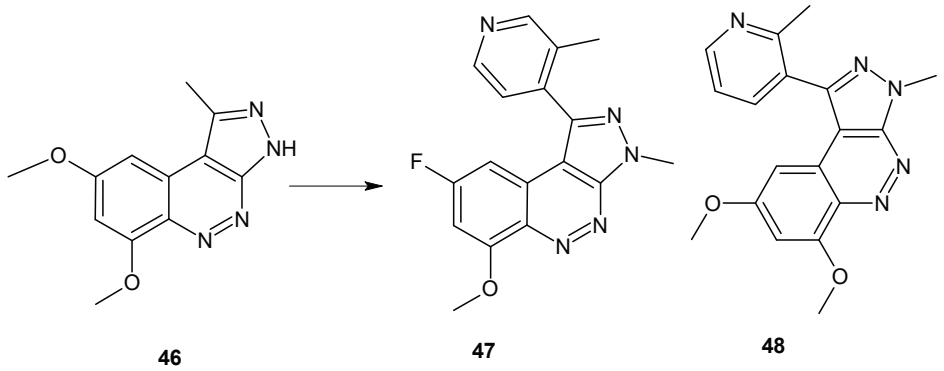

Figure 25. Selected 3*H*-pyrazolo[3,4-*c*]cinnolines that act as potent, selective and brain-penetrant PDE10A inhibitors.

The cinnoline scaffold turned out to be a useful building block in designing compounds targeting histamine receptor H_3. Involvement of the H_3 receptor subtype in the presynaptic regulation of the release of various neurotransmitters in the central nervous system makes it an attractive target for treating diseases such as attention-deficit hyperactivity disorder, Alzheimer's disease, mild cognitive impairment and schizophrenia. Josef and co-workers obtained compounds with the tricyclic benzocinnolinone pyridazinone core as analogues of irdabisant. The compounds 2*H*-benzo[*h*]cinnolin-3-ones and 3*H*-benzo[*f*]cinnolin-2-ones exhibited high H_3 receptor binding affinity with excellent selectivity against the H_1R, H_2R and H_4R subtypes of histamine receptor. Modification to the linker/amine region of the pharmacophore resulted in **±49** as a mixture of diastereoisomers (Figure 26), which showed improved metabolic stability and rat pharmacokinetics following oral administration ([55] and references therein).

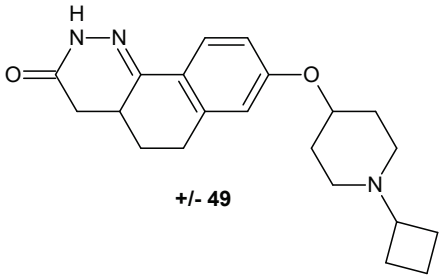

Figure 26. Potent benzocinnolinone analogue of irdabisant with high histamine receptor H_3 H_3R binding affinity.

Cinnoline derivatives are also enumerated among non-benzodiazepine modulators of γ-aminobutyric acid receptor A (GABA A) [56]. Astra Zeneca works on an orally bioavailable positive modulator of the GABA A α2 and α3 subunits and developed novel compound **50** depicted in Figure 27 as a possible treatment or prophylaxis of anxiety disorders, cognitive disorders, and/or mood disorders [57]. AZD7325 (**51**) and AZD6280 (**52**) depicted in Figure 27 were identified as positive modulators at α2/α3 and negative modulators at α5 GABA A receptors and exhibited a potent anxiolytic-like effect without sedation or cognitive impairment [13,58]. These compounds have undergone clinical trial phase I [59,60]. Moreover, AZD7325 was studied in two phase II proof-of-concept trials in patients with general anxiety disorders (NCT 00807937 and NCT00808249) as well as in a phase II proof-of-mechanism in patients with autism spectrum disorders (NCT01966679). In addition, the diverse metabolite profile of AZD7325 was investigated [61]. In vivo studies in rat and in vitro studies in human, rat, mouse, rabbit and dog liver microsomes were performed with radiolabeled AZD7325, revealing approximately 40 metabolites [61,62].

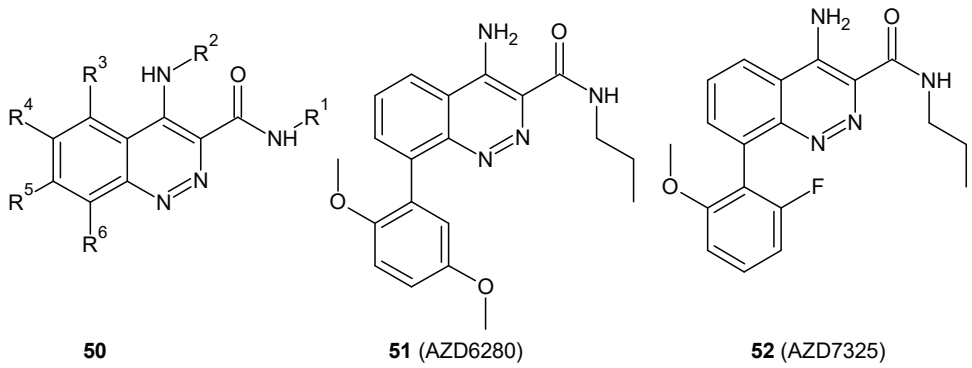

Figure 27. Cinnoline non-benzodiazepine modulators of γ-aminobutyric acid receptor A (GABA A).

Cinnolinones (**53**, **54**) (Figure 28) as diaza analogues of known aminobutyrophenones were designed as potential atypical psychotics. Determination of the binding affinities towards the serotonin receptors 5-HT_{2A} and 5-HT_{2C}, and the dopamine D_2 receptors revealed that these compounds lacked appreciable affinity for the dopamine D_2 receptors, and as a consequence, they were not suited as potential psychotics. However, they displayed the highest affinity for the 5-HT_{2C} receptor [63].

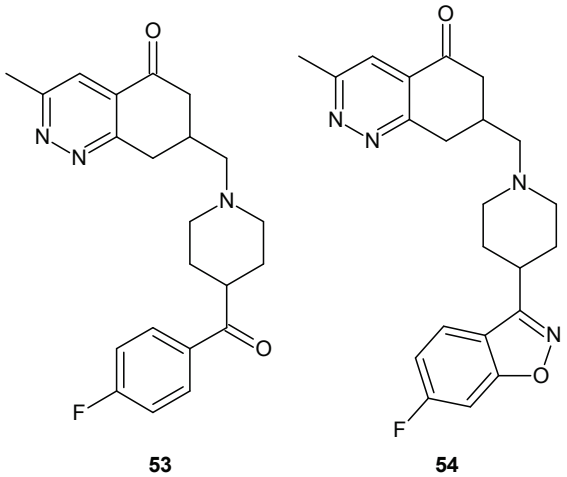

Figure 28. Cinnolinone-diaza analogs of known aminobutyrophenones.

2.4. Anticancer Properties

Cinnoline derivatives were also designed as potential anticancer drugs. Extensive studies have been performed to assess the topoisomerase 1-targeting (TOP1-targeting) activity and cytotoxicity of substituted dibenzo[*c*,*h*]cinnolines **55**, **56** (Figure 29) as non-CPT (camptothecin) TOP1 inhibitors. Structure-activity relationship (SAR) studies of dibenzo[*c*,*h*]cinnolines revealed that removal of the methylenedioxy group on the D ring or its replacement by other substituents (methoxy-, benzyloxy- or hydroxy- groups) resulted in a substantial loss of TOP1-targeting activity. The presence of 2,3-dimethoxy substituents in ring A was also determined as a crucial structural element for retaining TOP1 activity and cytotoxicity. Although the substituted dibenzo[*c*,*h*]cinnolines with significant TOP1-targeting activity exhibited cross-resistance in camptothecin-resistant cell lines, their cytotoxicity was not diminished in cells overexpressing multidrug resistance protein 1 MDR1 [64].

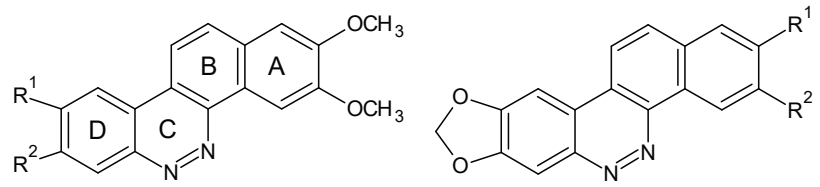

55 R_1 = H, OCH_3; R_2 = H, OCH_3, OBn, OH;

56 R_1 = H, OCH_3; R_2 = H, OCH_3 OBn, OH, CH_2OH;
57 R_1, R_2 = OCH_3

Figure 29. Dibenzo[*c*,*h*]cinnoline topoisomerase 1 (TOP1) inhibitors.

As a continuation of studies on the most potent derivative **57**, 5,6,11-triazachrysen-12-ones with various substituents at 11-position were synthesized [65]. Compound **58** (ARC-31, Figure 30) exhibited an enhanced ability to induce DNA cleavage in the presence of TOP1 and exceptional cytotoxic activity with IC_{50} values below 2 nM against the human lymphoblastoma cell line (RPMI8402) but dose limiting toxicity limited in vivo efficacy in the human tumor xenograft athymic nude mouse model (MDA-MB-435 breast tumor cell line) [66]. In an effort to obtain a less toxic analog with improved efficacy, a number of compounds related to **58** (Figure 30) were synthesized where the 11-ethyl group was substituted at its 2-position with various polar moieties (*N*-methylamino-, *N*-isopropylamino-, hydroxy- and hydroxylamino- groups). These analogs were prepared via the trimethylammonium derivatives of ARC-31 according to methods described in [67]. All analogs exhibited high cytotoxic activity. Although, derivatives with *N*-methylamine **59** and *N*-isopropylamine **60** (Figure 31) exhibited greater cytotoxic activity in vitro in comparison to ARC-31, evaluation in vivo in athymic nude mice showed minimal differences in efficacy in comparison to ARC-31 without therapeutic index improvement [11].

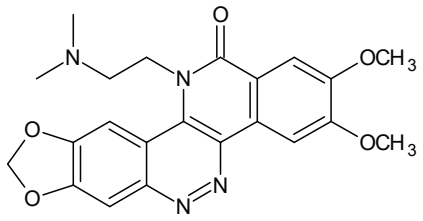

58

Figure 30. The structure of compound ARC-31.

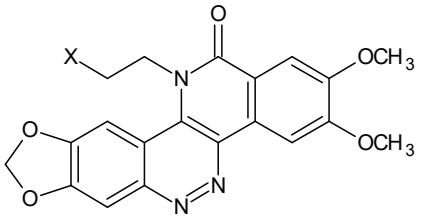

59 X = $NHCH_3$
60 X = $NHCH(CH_3)_2$

Figure 31. TOP1-acting agents related to ARC-31.

Zoidis and co-workers obtained tetra- and pentacyclic cinnoline based compounds indeno[1,2-*c*]cinnoline and benzo[*h*]indeno[1,2-*c*]cinnoline, respectively, bearing protonable amino groups. All tested compounds inhibited proliferation of human cervical carcinoma (HeLa) and human breast adenocarcinoma (MCF-7) cell lines as well as displayed intercalating properties on different nucleic acid strands, with preference for G-quadruplex sequences. The aminobutylamide derivative **61**

(Figure 32) exhibited the highest antiproliferative activity with IC_{50} values of 45 nM and 85 nM on HeLa and MCF-7, respectively, whereas the pentacyclic derivative with the same protonable moiety (*N*,*N*-dimethylamine) **62** (Figure 32) caused the highest thermal stabilization in melting studies and exerted acceptable inhibitory activity on human topoisomerase IIα [68].

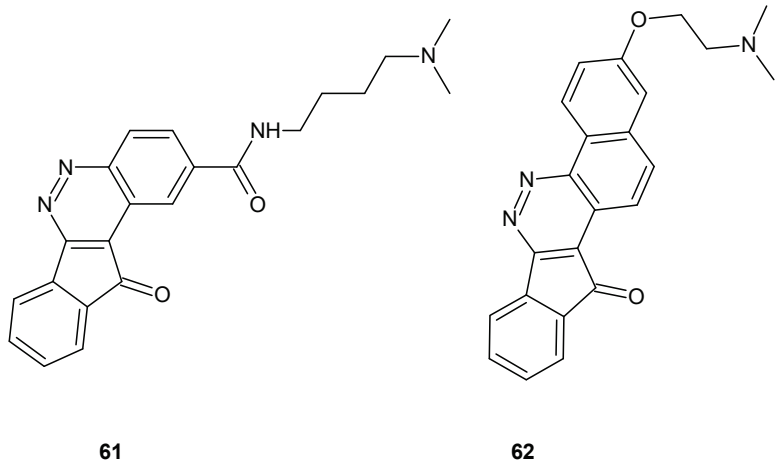

Figure 32. Selected indeno[1,2-*c*]cinnoline) and benzo[*h*]indeno[1,2-*c*]cinnoline derivatives.

Borowski and co-workers obtained a series of anthrapyridazone derivatives **63** (Figure 33) bearing one or two basic side chains at various positions of the tetracyclic core [69,70]. The compounds 2,7-dihydro-3*H*-dibenzo[*de,h*]cinnoline-3,7-diones **64** and **65** (Figure 33) exhibited in vitro cytotoxic activity against murine (L1210) and human (K562) leukemia cell lines. In addition, they were active against human leukemia multi-drug-resistant (K562/DX) cell lines. The most active compounds **64** and **65** (Figure 33) were also tested in vivo against murine P388 leukemia and showed activity comparable to mitoxantrone [71].

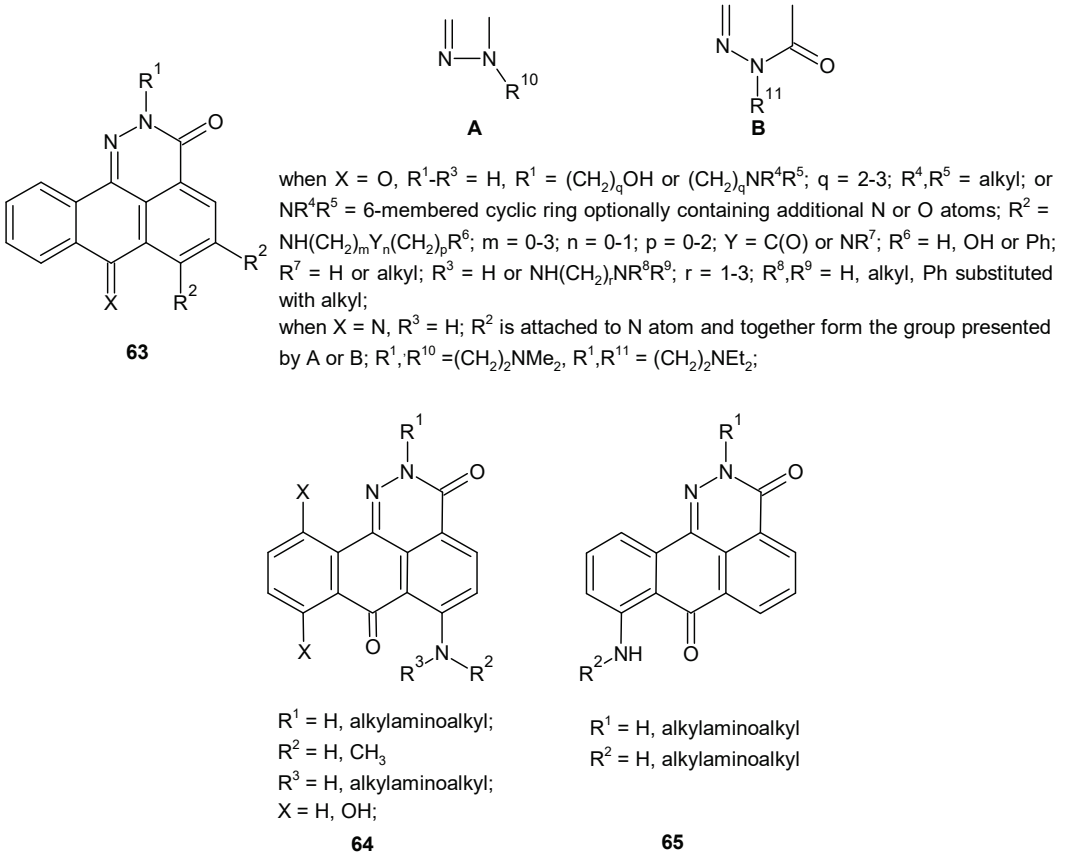

Figure 33. General structure of 2,7-dihydro-3*H*-dibenzo[*de*,*h*]cinnoline-3,7-diones.

Parrino et al. described 11*H*-pyrido[3′,2′:4,5]pyrrolo[3,2-*c*]cinnoline derivative **66** (Figure 34) which exhibited high cytotoxic activity against a panel of 60 human tumor cell lines screened by the National Cancer Institute (Bethesda, MD, USA). Particular efficacy of tested compounds was observed against the leukemia subpanel. In addition, they were also found to be active in cells overexpressing MDR1. The compounds caused apoptosis, mitochondrial depolarization, generation of reactive oxygen species, and the activation of caspase-3, caspase-8, and caspase-9. Moreover, they acted as topoisomerase I inhibitors [72].

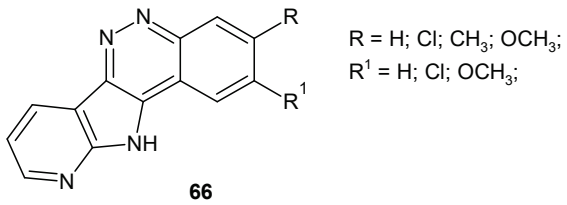

Figure 34. General structure of 11*H*-pyrido[3′,2′:4,5]pyrrolo[3,2-*c*]cinnolines.

Barlaam and co-workers, while working on the optimization of selective quinoline based inhibitors of ataxia teleangiectasia mutated (ATM) kinase involved in the repair of DNA double strand breaks, synthesized a series of cinnoline-3-carboxamides as suitable replacements of quinoline carboxamides. Compound **67** (Figure 35) was identified as a potent ATM inhibitor with excellent kinase selectivity and good physicochemical and pharmacokinetic properties. Monotherapy with ATM inhibitor **67** did not cause tumor regression in the SW620 colorectal tumor xenograft model, whereas combination with irinotecan resulted in significantly greater tumor growth inhibition in comparison to irinotecan alone [14,73]. The 1,3-dihydroimidazo[4,5-*c*]cinnoline-2-one derivatives of general formula **68** (Figure 35)

were patented as ATM modulators used to treat or prevent ATM mediated diseases, including cancer [74].

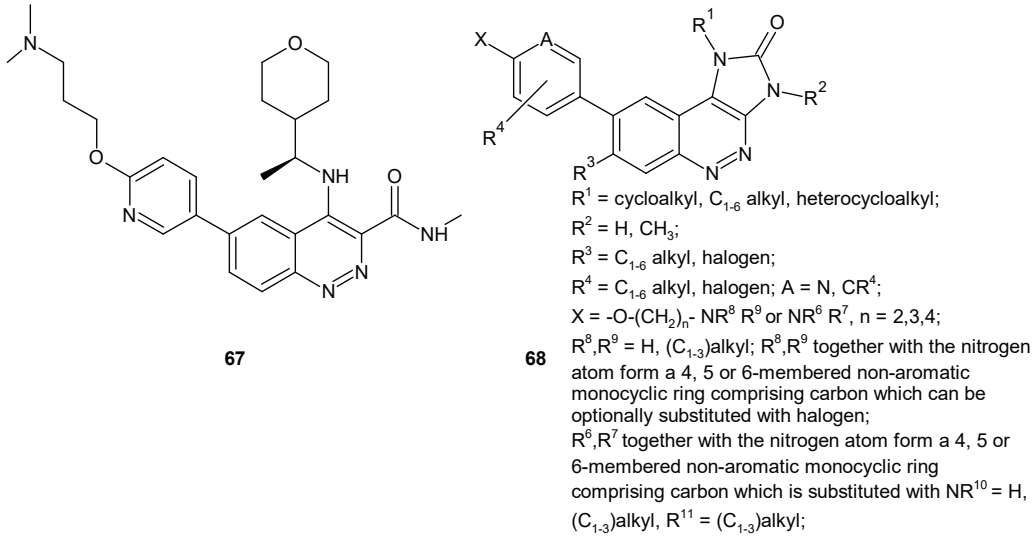

Figure 35. Cinnoline based ataxia teleangiectasia mutated (ATM) inhibitors.

Colony-stimulating factor-1 (CSF-1) through binding to its receptor (CSF-1R) regulates the migration, proliferation, function, and survival of macrophages [75]. Since CSF-1R is overexpressed in many tumors and at sites of inflammation, CSF-1R inhibitors seem to be an attractive therapeutic strategy for cancer as well as autoimmune and inflammatory diseases. The 3-amido-4-anilinocinnolines of general formula **69** (Figure 36) were reported as potent, highly selective CSF-1R inhibitors [76,77]. They were designed in order to overcome the cardiovascular liability of potent and selective 3-amido-4-anilinoquinoline CSF-1R inhibitor (AZ683), which was able to reduce the level of tumor-associated macrophages in a breast cancer xenograft model. The 3-amido-4-anilinocinnoline compound with 1-hydroxyethylpiperazine substituent at 7 position of cinnoline scaffold **70** (AZD7507, Figure 36) was a potent CSF-1R inhibitor demonstrating good oral pharmacokinetic profile as well as reduced risk of cardiotoxicity in comparison to AZ683 [78].

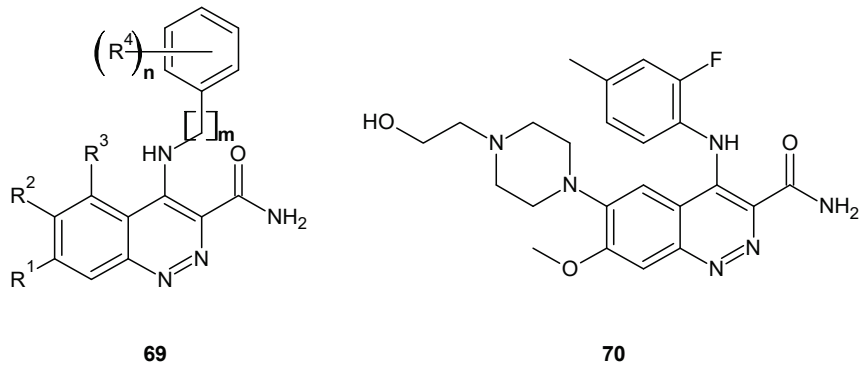

Figure 36. Structure of 3-amido-4-anilinocinnoline derivatives exhibiting colony-stimulating factor-1 receptor (CSF-1R) inhibition.

c-Met receptor tyrosine kinase is another cellular target for compounds designed as potential anticancer agents because it has been found to be overexpressed or mutated in various human cancer cells [79]. Some 4-(2-fluorophenoxy)quinoline derivatives bearing a 4-oxo-1,4-dihydrocinnoline-3-carboxamide moiety **71** (Figure 37) were designed as c-Met inhibitors and

evaluated against five c-Met-dependent cancer cell lines and one c-Met-independent cancer cell [80,81]. Most compounds were active against c-Met and the tested cell lines [82].

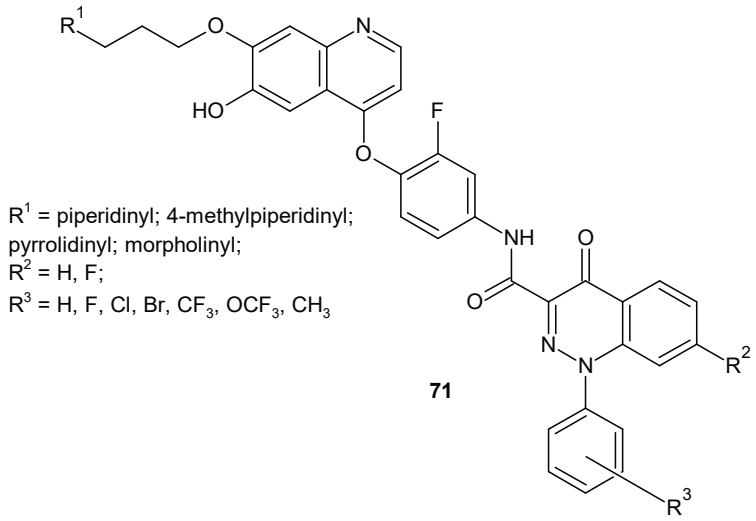

Figure 37. c-Met inhibitor with 4-oxo-1,4-dihydrocinnoline-3-carboxamide moiety.

New dihydrobenzo[*h*]cinnoline-5,6-dione derivatives **72** (Figure 38) were also prepared and evaluated as potential antitumor agents. The majority of tested derivatives exhibited at least moderate cytotoxic activity against a epidermoid carcinoma cell line (KB) and a hepatoma carcinoma cell line (Hep-G2). Nine of the new dihydrobenzo[*h*]cinnoline-5,6-diones displayed a considerable activity profile with IC_{50} values below 5μM against both cell lines. A compound with a 4-$NO_2C_6H_4$ substituent was identified as the most promising agent with IC_{50} values of 0.56 μM and 0.77 μM against the KB and Hep-G2 cell lines, respectively [83].

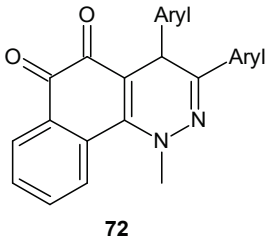

Figure 38. General structure of dihydrobenzo[*h*]cinnoline-5,6-diones.

Many cinnoline derivatives (Figure 39) such as 9-substituted-4,10-dimethylpyrano[2,3-*f*] cinnolin-2-ones with *N*-piperazinyl moieties at C-9 **73** **[84]**, 6-substituted-4-methyl-3-(4-arylpiperazin-1-yl)cinnolines **74** [85], hexahydrocinnolines **75** [86] and pyrazolo[4,3-*c*]cinnoline derivatives **76** [87] were synthesized and evaluated in vitro for their antitumor activity against breast cancer cell lines MCF-7 and MDA-231 for bicinnolines **77** [88].

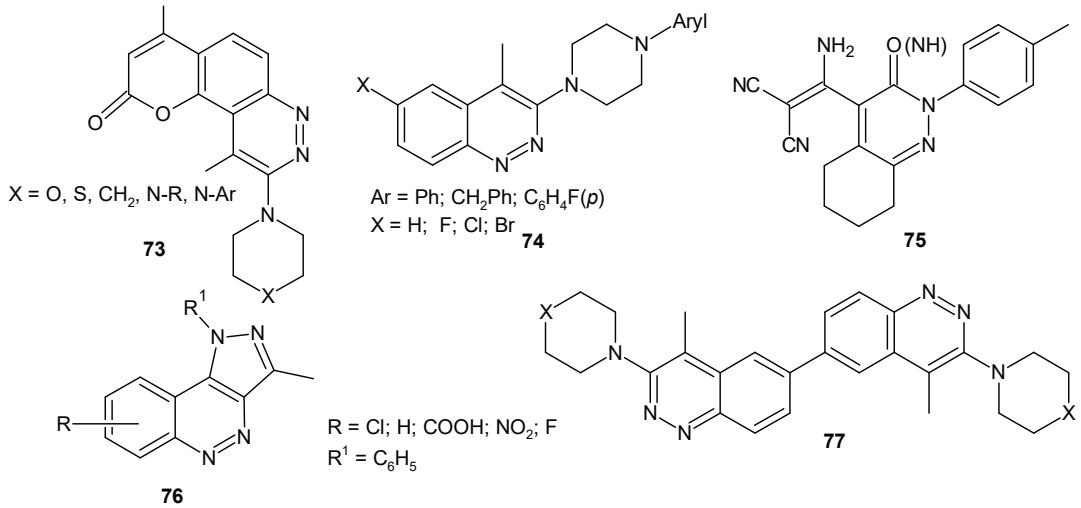

Figure 39. Compounds bearing cinnoline moieties evaluated against breast cancer cell lines.

2.5. Miscellaneous

A compound with cinnoline moiety **78** (Figure 40) is patented by Stein and co-authors for very interesting uses. Among other hydrazone derivatives, it was tested as inhibitor of a transient receptor potential cation channel, subfamily M, member 5 (TRPM5) protein which has been shown to be essential for taste transduction. Such compounds could be used as taste inhibitors when administered as a component of pharmaceutical or food products to improve acceptance. Moreover, these agents are intended for use in treating diabetes mellitus, obesity, insulin resistance syndrome and many more [89].

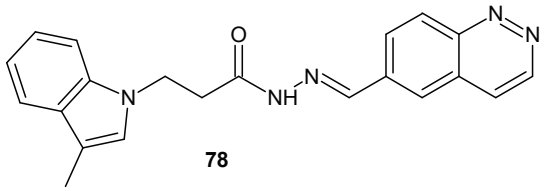

Figure 40. Cinnoline transient receptor potential cation channel, subfamily M, member 5 (TRPM5) inhibitor.

Cinnoline derivatives were also patented as thyroid hormone receptor agonists [90], orexin receptor antagonists [91–95], histone deacetylase (HDAC) inhibitors [96], liver X receptors β selective modulators for the treatment of atherosclerosis [97], somatostatin regulators [98] or cannabinoid-1 receptor inverse agonists [99] and many more.

3. Conclusions

In this paper, we have presented a review of studies focused on the biological activity of cinnoline derivatives conducted by many research groups worldwide between 2005 and 2019. The provided information clearly indicates the enormous significance of the cinnoline framework as a building block of many valuable compounds. Compounds bearing the cinnoline scaffold are able to interact with a variety of molecular targets including receptors such as GABA A, CSF-1R, H_3R and enzymes such as cyclooxygenase-2, topoisomerases, phosphodiesterase, human neutrophil elastase, Bruton's tyrosine kinase involved in pathogenesis of many diseases. As a consequence, they are intended to be used as antibacterial, antifungal, antimalarial, anti-inflammatory, analgesic, anxiolytic and antitumor agents. Some cinnoline derivatives are under evaluation in clinical trials. There is no doubt that development of cinnoline based molecules constitutes a significant contribution to the identification of lead compounds with optimized pharmacodynamic and pharmacokinetic properties.

Author Contributions: Conceptualization, M.S. Writing—Original Draft Preparation, M.S.; Writing—Review and Editing, M.S. and A.S.; Visualization, M.S.; All authors read and approved the final manuscript.

Funding: This review was funded by the Medical University of Lodz, Poland, Research Programme No. 503-03/3-011-03/503-31-001 and 503/3-011-03/503-36-001.

Conflicts of Interest: The authors declare no conflict of interest.

References

1. Lewgowd, W.; Stanczak, A. Cinnoline derivatives with biological activity. *Arch. Pharm.* **2007**, *340*, 65–80. [CrossRef] [PubMed]
2. Castle, N.R. *The Chemistry of Heterocyclic Compounds*; John Wiley & Sons: New York, NY, USA, 1973; Volume 27, Chapter 1; pp. 1–231.
3. Vinogradova, O.V.; Balova, I.A. Methods for the synthesis of cinnolines. *Chem. Heterocycl. Compd.* **2008**, *44*, 501–522. [CrossRef]
4. Kumari, S.; Kishore, D.; Paliwal, S.; Chauhan, R.; Dwivedi, J.; Mishra, A. Transition metal-free one-pot synthesis of nitrogen-containing heterocycles. *Mol. Diver.* **2016**, *20*, 185–232. [CrossRef] [PubMed]
5. Muralirajan, K.; Cheng, C.H. Rhodium(III)-catalyzed synthesis of cinnolinium salts from azobenzenes and alkynes: Application to the synthesis of indoles and cinnolines. *Chem. Eur. J.* **2013**, *19*, 6198–6202. [CrossRef] [PubMed]
6. Zhao, D.; Wu, Q.; Huang, X.; Song, F.; Lv, T.; You, J. A general method to diverse cinnolines and cinnolinium salts. *Chem. Eur. J.* **2013**, *19*, 6239–6244. [CrossRef] [PubMed]
7. Kiriazis, A.; Rüffer, T.; Jäntti, S.; Lang, H.; Yli-Kauhaluoma, J. Stereoselective aza Diels-Alder reaction on solid phase: A facile synthesis of hexahydrocinnoline derivatives. *J. Comb. Chem.* **2007**, *9*, 263–266. [CrossRef] [PubMed]
8. Mathew, T.; Papp, A.Á.; Paknia, F.; Fustero, S.; Surya Prakash, G.K. Benzodiazines: Recent synthetic advances. *Chem. Soc. Rev.* **2017**, *46*, 3060–3094. [CrossRef]
9. Haddadin, M.J.; Zerdan, R.M.B.; Kurth, M.J.; Fettinger, J.C. Efficient syntheses of the unknown quinolino [2,3-c] cinnolines; Synthesis of neocryptolepines. *Org. Lett.* **2010**, *12*, 5502–5505. [CrossRef]
10. Chen, C.J.; Deng, A.J.; Liu, C.; Shi, R.; Qin, H.L.; Wang, A.P. Hepatoprotective activity of cichorium endivia L. extract and its chemical constituents. *Molecules* **2011**, *16*, 9049–9066. [CrossRef]
11. Satyanarayana, M.; Feng, W.; Cheng, L.; Liu, A.A.; Tsai, Y.-C.; Liu, L.F.; LaVoie, E.J. Syntheses and biological evaluation of topoisomerase I-targeting agents related to 11-[2-(N, N-dimethylamino) ethyl]-2,3-dimethoxy-8,9-methylenedioxy-11H-isoquino [4,3-c] cinnolin-12-one (ARC-31). *Bioorg. Med. Chem.* **2008**, *16*, 7824–7831. [CrossRef]
12. Devine, W.; Woodring, J.L.; Swaminathan, U.; Amata, E.; Patel, G.; Erath, J.; Roncal, N.E.; Lee, P.J.; Leed, S.E.; Rodriguez, A.; et al. Protozoan parasite growth inhibitors discovered by cross-screening yield potent scaffolds for lead discovery. *J. Med. Chem.* **2015**, *58*, 5522–5537. [CrossRef] [PubMed]
13. Alhambra, C.; Becker, C.; Blake, T.; Chang, A.; Damewood, J.R.; Daniels, T.; Dembofsky, B.T.; Gurley, D.A.; Hall, J.E.; Herzog, K.J.; et al. Development and SAR of functionally selective allosteric modulators of GABAA receptors. *Bioorg. Med. Chem.* **2011**, *19*, 2927–2938. [CrossRef] [PubMed]
14. Barlaam, B.; Cadogan, E.; Campbell, A.; Colclough, N.; Dishington, A.; Durant, S.; Goldberg, K.; Hassall, L.A.; Hughes, G.D.; MacFaul, P.A.; et al. Discovery of a series of 3-cinnoline carboxamides as orally bioavailable, highly potent, and selective ATM inhibitors. *ACS Med. Chem. Lett.* **2018**, *9*, 809–814. [CrossRef] [PubMed]
15. Szumilak, M.; Szulawska-Mroczek, A.; Koprowska, K.; Stasiak, M.; Lewgowd, W.; Stanczak, A.; Czyz, M. Synthesis and in vitro biological evaluation of new polyamine conjugates as potential anticancer drugs. *Eur. J. Med. Chem.* **2010**, *45*, 5744–5751. [CrossRef] [PubMed]
16. Szumilak, M.; Lewgowd, W.; Stanczak, A. In silico ADME studies of polyamine conjugates as potential anticancer drugs. *Acta Pol. Pharm.* **2016**, *73*, 1190–1199.
17. Wiederhold, N.P. Antifungal resistance: Current trends and future strategies to combat. *Infect Drug Res.* **2017**, *10*, 249–259. [CrossRef]
18. Ventola, C.L. The antibiotic resistance crisis: Part 1: Causes and threats. *Pharm. Ther.* **2015**, *40*, 277–283.
19. Cinobac. Available online: https://www.rxlist.com/cinobac-drug.htm#clinpharm (accessed on 31 March 2019).

20. Vargas, F.; Zoltan, T.; Rivas, C.; Ramirez, A.; Cordero, T.; Díaz, Y.; Izzo, C.; Cárdenas, Y.M.; López, V.; Gómez, L.; et al. Synthesis, primary photophysical and antibacterial properties of naphthyl ester cinoxacin and nalidixic acid derivatives. *J. Photochem. Photobiol. B* **2008**, *92*, 83–90. [CrossRef]
21. Ryu, C.-K.; Lee, J.Y. Synthesis and antifungal activity of 6-hydroxycinnolines. *Bioorg. Med. Chem. Lett.* **2006**, *16*, 1850–1853. [CrossRef]
22. Vikas, S.; Darbhamulla, S. Synthesis, characterization and biological activities of substituted cinnoline sulphonamides. *Afr. Health Sci.* **2009**, *9*, 275–278.
23. Gautam, N.; Chourasia, O.P. Synthesis, antimicrobial and insecticidal activity of some new cinnoline based chalcones and cinnolinc based pyrazoline derivatives. *Indian J. Chem. B* **2010**, *49*, 830–835.
24. Unnissa, S.H.; Ravi, T.K. Synthesis and screening of pyrazole based cinnoline derivatives for its anti-tubercular and anti-fungal activity. *J. Chem. Pharm. Res.* **2015**, *7*, 957–963.
25. Unnissa, S.H.; Nisha, N.; Reddy, G.K. Synthesis and in vitro antimicrobial evaluation including anti-malarial activity of pyrazole based novel cinnoline derivatives. *J. Appl. Pharm. Sci.* **2015**, *15*, 121–126. [CrossRef]
26. Parasuraman, P.; Shanmugarajan, R.S.; Aravazhi, T.; Nehru, K.; Mathiazhaga, T.; Rajakumari, R. Synthesis, characterization and antimicrobial evaluation of some substituted 4-aminocinnoline-3- carboxamide derivatives. *Int. J. Pharm. Life Sci.* **2012**, *3*, 1430–1436.
27. Varshney, S.; Saxena, V. Design, synthesis, characterization and biological evaluation of some novel cinnolo piperazine derivatives. *Int. J. Pharm. Pharm. Sci.* **2014**, *6*, 245–248.
28. Mishra, P.; Middha, A.; Saxena, V.; Saxena, A. Synthesis, biological evaluation and comparative study of some cinnoline derivatives. *UK J. Pharm. Biosci.* **2016**, *4*, 74–80. [CrossRef]
29. Dawadi, S.; Boshoff, H.I.M.; Park, S.W.; Schnappinger, D.; Aldrich, C.C. Conformationally constrained cinnolinone nucleoside analogues as siderophore biosynthesis inhibitors for tuberculosis. *ACS Med. Chem. Lett.* **2018**, *9*, 386–391. [CrossRef]
30. Glinka, T.; Lomovskaya, O.; Bostian, K.; Wallace, D.M. Preparation of Peptide Polybasic Bacterial Efflux Pump Inhibitors for Enhancing Levofloxacin Potency in Treating Bacterial Infections. WO Patent 2008141010A2, 20 November 2008.
31. Chaudhary, J.; Patel, K.; Patel, C.N. Synthesis and biological screening of some cinnoline derivatives. *Int. J. Univers. Pharm. Biol. Sci.* **2014**, *3*, 128–140.
32. Tonk, R.K.; Bawa, S.; Chawla, G.; Deora, G.S.; Kumar, S.; Rathore, V.; Mulakayala, N.; Rajaram, A.; Kalle, A.M.; Afzal, O. Synthesis and pharmacological evaluation of pyrazolo[4,3-c]cinnoline derivatives as potential anti-inflammatory and antibacterial agents. *Eur. J. Med. Chem.* **2012**, *57*, 176–184. [CrossRef]
33. Lunniss, C.; Eldred, C.; Aston, N.; Craven, A.; Gohil, K.; Judkins, B.; Keeling, S.; Ranshaw, L.; Robinson, E.; Shipley, T.; et al. Addressing species specific metabolism and solubility issues in a quinoline series of oral PDE4 inhibitors. *Bioorg. Med. Chem. Lett.* **2010**, *20*, 137–140. [CrossRef]
34. Houslay, M.D.; Schafer, P.; Zhang, K.Y.J. Keynote review: Phosphodiesterase-4 as a therapeutic target. *Drug Discov. Today* **2005**, *10*, 1503–1519. [CrossRef]
35. Gomtsyan, A.; Bayburt, E.K.; Schmidt, R.G.; Zheng, G.Z.; Perner, R.J.; Didomenico, S.; Koenig, J.R.; Turner, S.; Jinkerson, T.; Drizin, I.; et al. Novel transient receptor potential vanilloid 1 receptor antagonists for the treatment of pain: structure−activity relationships for ureas with quinoline, isoquinoline, quinazoline, phthalazine, quinoxaline, and cinnoline moieties. *J. Med. Chem.* **2005**, *48*, 744–752. [CrossRef] [PubMed]
36. Di Paolo, J.A.; Huang, T.; Balazs, M.; Barbosa, J.; Barck, K.H.; Bravo, B.J.; Carano, R.A.D.; Darrow, J.; Davies, D.R.; DeForge, L.E.; et al. Specific Btk inhibition suppresses B cell- and myeloid cell-mediated arthritis. *Nat. Chem. Biol.* **2011**, *7*, 41–50. [CrossRef] [PubMed]
37. Lawson, J.D.; Sabat, M.; Smith, C.; Wang, H.; Chen, Y.K.; Kanouni, T. Preparation of Cinnolinecarboxamides as BKT Inhibitors. WO Patent 2013148603A1, 03 October 2013.
38. Smith, C.R.; Dougan, D.R.; Komandla, M.; Kanouni, T.; Knight, B.; Lawson, J.D.; Sabat, M.; Taylor, E.R.; Vu, P.; Wyrick, C. Fragment-based discovery of a small molecule inhibitor of Bruton's tyrosine kinase. *J. Med. Chem.* **2015**, *58*, 5437–5444. [CrossRef] [PubMed]
39. Crocetti, L.; Giovannoni, M.P.; Schepetkin, I.A.; Quinn, M.T.; Khlebnikov, A.I.; Cilibrizzi, A.; Dal Piaz, V.; Graziano, A.; Vergelli, C. Design, synthesis and evaluation of *N*-benzoylindazole derivatives and analogues as inhibitors of human neutrophil elastase. *Bioorg. Med. Chem.* **2011**, *19*, 4460–4472. [CrossRef] [PubMed]

40. Crocetti, L.; Schepetkin, I.A.; Cilibrizzi, A.; Graziano, A.; Vergelli, C.; Gionni, D.; Khlebnikov, A.I.; Quinn, M.T.; Giovannoni, M.P. Optimization of *N*-Benzoylindazole derivatives as inhibitors of human neutrophil elastase. *J. Med. Chem.* **2013**, *56*, 6259–6272. [CrossRef] [PubMed]
41. Giovannoni, M.P.; Schepetkin, I.A.; Crocetti, L.; Ciciani, G.; Cilibrizzi, A.; Guerrini, G.; Khlebnikov, A.I.; Quinn, M.T.; Vergelli, C. Cinnoline derivatives as human neutrophil elastase inhibitors. *J. Enzyme Inhib. Med. Chem.* **2016**, *31*, 628–639. [CrossRef] [PubMed]
42. Kalyani, G.; Srinivas, B.; Sastry, K.V.; Vijaya, K. Synthesis of novel cinnoline fused mannich bases: Pharmacological evaluation of antibacterial, analgesic and anti-inflammatory activity. *IJPCR* **2017**, *9*, 515–520. [CrossRef]
43. Woll, M.G.; Amedzo, L.; Babu, S.; Barraza, S.J.; Bhattacharyya, A.; Karp, G.M.; Mazzotti, A.R.; Narasimhan, J.; Patel, J.; Turpoff, A.; et al. Preparation of Heteroaryl Compounds for Treating Huntington's Disease. WO Patent 2018226622A1, 13 December 2018.
44. Beshore, D.C.; Kuduk, S.D. Pyrazolo [4,3-c] Cinnolin-3-One Derivatives as M1 Receptor Positive Allosteric Modulators and Their Preparation, Pharmaceutical Compositions and Use in the Treatment of Diseases. WO Patent 2010096338A1, 26 August 2010.
45. Amer, A.M.; El-Farargy, A.F.; Yousif, N.M.; Fayed, A.A. Synthesis and pharmacological activities of some dibenzopyrazolocinnolines and dibenzopyridazoquinoxalines. *Chem. Heterocycl. Compd.* **2011**, *47*, 101–107. [CrossRef]
46. Hatcher, J.M.; Choi, H.G.; Alessi, D.R.; Gray, N.S. Small-molecule inhibitors of LRRK2. *Adv. Neurobiol.* **2017**, *14*, 241–264. [CrossRef]
47. Aubele, D.L.; Usgarofalo, A.W.; Bowers, S.; Ustruong, A.P.; Usye, X.M.; Franzini, M.; Adler, M.; Usnietz, R.J.; Usprobst, G. Preparation of Cinnoline Derivatives as Inhibitors of LRRK2 Kinase Activity. WO Patent 2012162254A1, 29 November 2012.
48. Garofalo, A.W.; Adler, M.; Aubele, D.L.; Bowers, S.; Franzini, M.; Goldbach, E.; Lorentzen, C.; Neitz, R.J.; Probst, G.D.; Quinn, K.P.; et al. Novel cinnoline-based inhibitors of LRRK2 kinase activity. *Bioorg. Med. Chem. Lett.* **2013**, *23*, 71–74. [CrossRef] [PubMed]
49. Zagórska, A.; Partyka, A.; Bucki, A.; Gawalska, A.; Czopek, A.; Pawłowski, M. Phosphodiesterase 10 inhibitors–novel perspectives for psychiatric and neurodegenerative drug discovery. *Curr. Med. Chem.* **2018**, *25*, 3455–3481. [CrossRef] [PubMed]
50. Hu, E.; Kunz, R.K.; Rumfelt, S.; Chen, N.; Burli, R.; Li, C.; Andrews, K.L.; Zhang, J.D.; Chmait, S.; Kogan, J.; et al. Discovery of potent, selective, and metabolically stable 4-(pyridin-3-yl) cinnolines as novel phosphodiesterase 10A (PDE10A) inhibitors. *Bioorg. Med. Chem. Lett.* **2012**, *22*, 2262–2265. [CrossRef]
51. Yang, H.; Murigi, F.N.; Wang, Z.J.; Li, J.F.; Jin, H.J.; Tu, Z.D. Synthesis and in vitro characterization of cinnoline and benzimidazole analogues as phosphodiesterase 10A inhibitors. *Bioorg. Med. Chem. Lett.* **2015**, *25*, 919–924. [CrossRef] [PubMed]
52. Hu, E.; Kunz, R.K.; Rumfelt, S.; Andrews, K.L.; Li, C.; Hitchcock, S.A.; Lindstrom, M.; Treanor, J. Use of structure based design to increase selectivity of pyridyl-cinnoline phosphodiesterase 10A (PDE10A) inhibitors against phosphodiesterase 3 (PDE3). *Bioorg. Med. Chem. Lett.* **2012**, *22*, 6938–6942. [CrossRef] [PubMed]
53. Geneste, H.; Drescher, K.; Jakob, C.; Laplanche, L.; Ochse, M.; Torrent, M. Novel, potent, selective, and brain penetrant phosphodiesterase 10A inhibitors. *Bioorg. Med. Chem. Lett.* **2019**, *29*, 406–412. [CrossRef] [PubMed]
54. Geneste, H.; Ochse, M.; Drescher, K.; Jakob, C. Preparation of 3H-Pyrazolo [3,4-c] Cinnoline Derivatives as Phosphodiesterase Type 10A Inhibitors. WO Patent 2014027078A1, 20 February 2014.
55. Josef, K.A.; Aimone, L.D.; Lyons, J.; Raddatz, R.; Hudkins, R.L. Synthesis of constrained benzocinnolinone analogues of CEP-26401 (irdabisant) as potent, selective histamine H3 receptor inverse agonists. *Bioorg. Med. Chem. Lett.* **2012**, *22*, 4198–4202. [CrossRef] [PubMed]
56. Solomon, V.R.; Tallapragada, V.J.; Chebib, M.; Johnston, G.A.R.; Hanrahan, J.R. GABA allosteric modulators: An overview of recent developments in non-benzodiazepine modulators. *Eur. J. Med. Chem.* **2019**, *171*, 434–461. [CrossRef] [PubMed]
57. Chapdelaine, M.J.; Ohnmacht, C.J.; Becker, C.; Chang, H.-F.; Dembofsky, B.T. Preparation of Novel Cinnoline Compounds for Treating Anxiety, Depression and Cognition Disorders. U.S. Patent 20070142328A1, 16 September 2007.

58. Jucaite, A.; Cselenyi, Z.; Lappalainen, J.; McCarthy, D.J.; Lee, C.M.; Nyberg, S.; Varnas, K.; Stenkrona, P.; Halldin, C.; Cross, A.; et al. GABA(A) receptor occupancy by subtype selective GABA(A α 2,3) modulators: PET studies in humans. *Psychopharmacology* **2017**, *234*, 707–716. [CrossRef] [PubMed]
59. Chen, X.; Jacobs, G.; de Kam, M.; Jaeger, J.; Lappalainen, J.; Maruff, P.; Smith, M.A.; Cross, A.J.; Cohen, A.; van Gerven, J. The central nervous system effects of the partial GABA-A α (2,3)-selective receptor modulator AZD7325 in comparison with lorazepam in healthy males. *Br. J. Clin. Pharmacol.* **2014**, *78*, 1298–1314. [CrossRef]
60. Te Beek, E.T.; Chen, X.; Jacobs, G.E.; Nahon, K.J.; de Kam, M.L.; Lappalainen, J.; Cross, A.J.; van Gerven, J.M.A.; Hay, J.L. The effects of the nonselective benzodiazepine lorazepam and the α (2)/α (3) subunit-selective GABA(A) receptor modulators AZD7325 and AZD6280 on plasma prolactin levels. *Clin. Pharmacol. Ther.* **2015**, *4*, 149–154. [CrossRef]
61. Artelsmair, M.; Gu, C.; Lewis, R.J.; Elmore, C.S. Synthesis of C-14 labeled GABAA α2/α3 selective partial agonists and the investigation of late-occurring and long-circulating metabolites of GABAA receptor modulator AZD7325. *J. Label. Compd. Radiopharm.* **2018**, *61*, 415–426. [CrossRef] [PubMed]
62. Gu, C.; Artelsmair, M.; Elmore, C.S.; Lewis, R.J.; Davis, P.; Hall, J.E.; Dembofsky, B.T.; Christoph, G.; Smith, M.A.; Chapdelaine, M.; et al. Late-occurring and long-circulating metabolites of GABAAα2,3 receptor modulator AZD7325 involving metabolic cyclization and aromatization: Relevance to MIST analysis and application for patient compliance. *Drug Metab. Dispos.* **2018**, *46*, 303–315. [CrossRef] [PubMed]
63. Alvarado, M.; Barcelo, M.; Carro, L.; Masaguer, C.F.; Ravina, E. Synthesis and biological evaluation of new quinazoline and cinnoline derivatives as potential atypical antipsychotics. *Chem. Biodivers.* **2006**, *3*, 106–117. [CrossRef] [PubMed]
64. Yu, Y.; Singh, S.K.; Liu, A.; Li, T.-K.; Liu, L.F.; LaVoie, E.J. Substituted dibenzo [c,h] cinnolines: Topoisomerase I-targeting anticancer agents. *Bioorg. Med. Chem.* **2003**, *11*, 1475–1491. [CrossRef]
65. Ruchelman, A.L.; Singh, S.K.; Wu, X.; Ray, A.; Yang, J.-M.; Li, T.-K.; Liu, A.; Liu, L.F.; LaVoie, E.J. Diaza-and triazachrysenes: Potent topoisomerase-targeting agents with exceptional antitumor activity against the human tumor xenograft, MDA-MB-435. *Bioorg. Med. Chem. Lett.* **2002**, *12*, 3333–3336. [CrossRef]
66. Ruchelman, A.L.; Singh, S.K.; Ray, A.; Wu, X.; Yang, J.-M.; Zhou, N.; Liu, A.; Liu, L.F.; LaVoie, E.J. 11H-Isoquino [4,3-c] cinnolin-12-ones: Novel anticancer agents with potent topoisomerase I-targeting activity and cytotoxicity. *Bioorg. Med. Chem.* **2004**, *12*, 795–806. [CrossRef]
67. Feng, W.; Satyanarayana, M.; Tsai, Y.-C.; Liu, A.A.; Liu, L.F.; LaVoie, E.J. Facile formation of hydrophilic derivatives of 5H-8,9-dimethoxy-5- [2-(N,N-dimethylamino)ethyl]-2,3-methylenedioxydibenzo [c,h] [1,6]naphthyridin-6-one (ARC-111) and its 12-aza analog via quaternary ammonium intermediates. *Bioorg. Med. Chem. Lett.* **2008**, *18*, 3570–3572. [CrossRef]
68. Zoidis, G.; Sosic, A.; Da Ros, S.; Gatto, B.; Sissi, C.; Palluotto, F.; Carotti, A.; Catto, M. Indenocinnoline derivatives as G-quadruplex binders, topoisomerase Hoc inhibitors and antiproliferative agents. *Bioorg. Med. Chem.* **2017**, *25*, 2625–2634. [CrossRef]
69. Borowski, E.; Stefanska, B.; Dzieduszycka, M.; Cybulski, M.; Szelejewski, W.; Obukowicz, J.; Bontemps-Gracz, M. Preparation of Asymmetrically Substituted Anthrapyridazone Derivatives as Cytostatics. WO Patent 2012141604A1, 18 October 2012.
70. Borowski, E.; Stefanska, B.; Dzieduszycka, M.; Cybulski, M.; Szelejewski, W.; Obukowicz, J.; Bontemps-Gracz, M.; Wysocka, M.; Mazerski, J.; Punda, P.; et al. Asymmetrically Substituted Anthrapyridazone Derivatives as Cytostatics. U.S. Patent 9096536B2, 08 April 2015.
71. Stefańska, B.; Arciemiuk, M.; Bontemps-Gracz, M.M.; Dzieduszycka, M.; Kupiec, A.; Martelli, S.; Borowski, E. Synthesis and biological evaluation of 2,7-Dihydro-3H-dibenzo [de,h] cinnoline-3,7-dione derivatives, a novel group of anticancer agents active on a multidrug resistant cell line. *Bioorg. Med. Chem.* **2003**, *11*, 561–572. [CrossRef]
72. Parrino, B.; Carbone, A.; Muscarella, M.; Spano, V.; Montalbano, A.; Barraja, P.; Salvador, A.; Vedaldi, D.; Cirrincione, G.; Diana, P. 11*H*-Pyrido [3′,2′:4,5] pyrrolo [3,2-c] cinnoline and pyrido [3′,2′:4,5] pyrrolo [1,2-c][1,2,3] benzotriazine: Two new ring systems with antitumor activity. *J. Med. Chem.* **2014**, *57*, 9495–9511. [CrossRef] [PubMed]
73. Pike, K.G.; Barlaam, B.C. Preparation of Cinnolin-4-Amine Compounds as ATM Kinase Inhibitors and Their Use in Treating Cancer. WO Patent 2017162605A1, 28 September 2017.

74. Pike, K.G.; Barlaam, B.C. Preparation of 1,3-Dihydroimidazo [4,5-c] Cinnolin-2-Ones for the Treatment and Prevention of Cancer. WO Patent 2019057757A1, 28 March 2019.
75. Hume, D.A.; MacDonald, K.P.A. Therapeutic applications of macrophage colony-stimulating factor-1 (CSF-1) and antagonists of CSF-1 receptor (CSF-1R) signaling. *Blood* **2012**, *119*, 1810. [CrossRef] [PubMed]
76. Daly, K.; Del Valle, D.; Scott, D.; Ye, Q. Preparation of Cinnolinecarboxamides as Colony Stimulating Factor 1 Receptor (CSF-1R) Kinase Inhibitors. WO Patent 2009136191A1, 12 November 2009.
77. Scott, D.A.; Dakin, L.A.; Del Valle, D.J.; Bruce Diebold, R.; Drew, L.; Gero, T.W.; Ogoe, C.A.; Omer, C.A.; Repik, G.; Thakur, K.; et al. 3-Amido-4-anilinocinnolines as a novel class of CSF-1R inhibitor. *Bioorg. Med. Chem. Lett.* **2011**, *21*, 1382–1384. [CrossRef] [PubMed]
78. Scott, D.A.; Dakin, L.A.; Daly, K.; Del Valle, D.J.; Diebold, R.B.; Drew, L.; Ezhuthachan, J.; Gero, T.W.; Ogoe, C.A.; Omer, C.A.; et al. Mitigation of cardiovascular toxicity in a series of CSF-1R inhibitors, and the identification of AZD7507. *Bioorg. Med. Chem. Lett.* **2013**, *23*, 4591–4596. [CrossRef] [PubMed]
79. Parizadeh, S.M.; Jafarzadeh-Esfehani, R.; Fazilat-Panah, D.; Hassanian, S.M.; Shahidsales, S.; Khazaei, M.; Parizadeh, S.M.R.; Ghayour-Mobarhan, M.; Ferns, G.A.; Avan, A. The potential therapeutic and prognostic impacts of the c-MET/HGF signaling pathway in colorectal cancer. *IUBMB Life* **2019**. [CrossRef]
80. Gong, P.; Zhao, Y.; Liu, Y.; Zhai, X. Quinoline and cinnoline compounds as c-Met kinase inhibitors and their preparation, pharmaceutical compositions and use in the treatment of hyperplastic diseases. CN Patent 102643268A, 21 May 2012.
81. Li, S.; Zhao, Y.F.; Wang, K.W.; Gao, Y.L.; Han, J.M.; Cui, B.B.; Gong, P. Discovery of novel 4-(2-fluorophenoxy) quinoline derivatives bearing 4-oxo-1,4-dihydrocinnoline-3-carboxamide moiety as c-Met kinase inhibitors. *Bioorg. Med. Chem.* **2013**, *21*, 2843–2855. [CrossRef] [PubMed]
82. Mohareb, R.M.; Al Farouk, F.O.; Wardakhan, W.W. Uses of dimedone for the synthesis of new heterocyclic derivatives with anti-tumor, c-Met, tyrosine, and Pim-1 kinases inhibitions. *Med. Chem. Res.* **2018**, *27*, 1984–2003. [CrossRef]
83. Dang Thi, T.A.; Decuyper, L.; Thi Phuong, H.; Vu Ngoc, D.; Thanh Nguyen, H.; Thanh Nguyen, T.; Do Huy, T.; Huy Nguyen, H.; D'Hooghe, M.; Van Nguyen, T. Synthesis and cytotoxic evaluation of novel dihydrobenzo [h] cinnoline-5,6-diones. *Tetrahedron Lett.* **2015**, *56*, 5855–5858. [CrossRef]
84. Al-zagameem, A.S.; El-Abadelah, M.M.; Zihlif, M.A.; Naffa, R.G.; Al-Smadi, M.L.; Mubarak, M.S. Synthesis and bioassay of novel substituted pyrano [2,3-f] cinnoline-2-ones. *J. Heterocycl. Chem.* **2016**, *53*, 1771–1777. [CrossRef]
85. Awad, E.D.; El-Abadelah, M.M.; Matar, S.; Zihlif, M.A.; Naffa, R.G.; Al-Momani, E.Q.; Mubarak, M.S. Synthesis and biological activity of some 3-(4-(Substituted)-piperazin-1-yl) cinnolines. *Molecules* **2012**, *17*, 227–239. [CrossRef]
86. Mohareb, R.; Moustafa, H. Use of 2-aminoprop-1-ene-1,1,3-tricarbonitrile for the synthesis of tetrahydronaphthalene, hexahydroisoquinoline and hexahydrocinnoline derivatives with potential antitumor activities. *Acta Pharm.* **2011**, *61*, 51–62. [CrossRef] [PubMed]
87. Unnissa, S.H.; Rose, S. Drug design, development and screening of pyrazolo pyridazine as potential agent for treatment of breast cancer. *J. Chem. Pharm. Res.* **2015**, *7*, 966–971.
88. Al-Qtaitat, M.A.; El-Abadelah, M.M.; Sabri, S.S.; Matar, S.A.; Hammad, H.M.; Mubarak, M.S. Synthesis, characterization and bioactivity of novel bicinnolines having 1-piperazinyl moieties. *J. Heterocycl. Chem.* **2019**, *56*, 158–164. [CrossRef]
89. Stein, P.; Daines, R.; Sprous, D.; O'Grady, H. Preparation of Cyclic Hydrazone Compounds and Their Use in Inhibiting Taste and Treating Diabetes and Other Disorders. WO Patent 2010132615A1, 18 November 2010.
90. Garcia Collazo, A.M.; Koch, E.K.; Lofstedt, A.J.; Cheng, A.; Hansson, T.F.; Zamaratski, E. Preparation of Quinolines, Indazoles, and Their Analogs as Thyroid Receptor Agonists. WO Patent 2007003419A1, 11 January 2007.
91. Betschart, C.; Cotesta, S.; Hintermann, S.; Wagner, J.; Roy, B.L.; Gerspacher, M.; Von Matt, A. Preparation of 4-Aryl-Butane-1,3-Diamides as Orexin Receptors Antagonists. WO Patent 2011073316A1, 23 June 2011.
92. Aissaoui, H.; Boss, C.; Gude, M.; Koberstein, R.; Sifferlen, T. Preparation of Azetidine Compounds as Orexin Receptor Antagonists. WO Patent 2008020405A2, 21 February 2008.
93. Aissaoui, H.; Boss, C.; Brotschi, C.; Koberstein, R.; Siegrist, R.; Sifferlen, T.; Trachsel, D.; Williams, J.T. Preparation of Phenethylamide Derivatives and Their Heterocyclic Analogs as Orexin Receptor Antagonists. WO Patent 2010044054A1, 22 April 2010.

94. Chai, W.; Letavic, M.A.; Ly, K.S.; Pippel, D.J.; Rudolph, D.A.; Sappey, K.C.; Savall, B.M.; Shah, C.R.; Shireman, B.T.; Soyode-Johnson, A.; et al. Preparation of Disubstituted Octahydropyrrolo [3,4-c] Pyrroles as Orexin Receptor Modulators. WO Patent 2011050198A1, 28 April 2011.
95. Letavic, M.; Rudolph, D.A.; Savall, B.M.; Shireman, B.T.; Swanson, D. Disubstituted Octahydropyrrolo [3,4-c] Pyrroles as Orexin Receptor Modulators and Their Preparation. WO Patent 2012145581A1, 26 October 2012.
96. Rusche, J.R.; Peet, N.P.; Hopper, A.T. Preparation of 6-Aminohexanoic Acid Derivatives as HDAC Inhibitors. WO Patent 2010028192A1, 11 March 2010.
97. Hu, B.; Unwalla, R.; Collini, M.; Quinet, E.; Feingold, I.; Goos-Nilsson, A.; Wihelmsson, A.; Nambi, P.; Wrobel, J. Discovery and SAR of cinnolines/quinolines as liver X receptor (LXR) agonists with binding selectivity for LXRβ. *Bioorg. Med. Chem.* **2009**, *17*, 3519–3527. [CrossRef] [PubMed]
98. Zhao, J.; Han, S.; Kim, S.H.; Wang, S.; Zhu, Y. Preparation of Nitrogen Containing Bicyclic Compounds as Somatostatin Modulators, Especially SSTR2 Agonists, and Their Therapeutic Use. WO Patent 2018013676A1, 18 January 2018.
99. Abouzid, K.; Shouman, S. Design, synthesis and in vitro antitumor activity of 4-aminoquinoline and 4-aminoquinazoline derivatives targeting EGFR tyrosine kinase. *Bioorg. Med. Chem.* **2008**, *16*, 7543–7551. [CrossRef] [PubMed]

© 2019 by the authors. Licensee MDPI, Basel, Switzerland. This article is an open access article distributed under the terms and conditions of the Creative Commons Attribution (CC BY) license (http://creativecommons.org/licenses/by/4.0/).

molecules

MDPI

Article

Screening of Phenanthroquinolizidine Alkaloid Derivatives for Inducing Cell Death of L1210 Leukemia Cells with Negative and Positive P-glycoprotein Expression

Jana Kubíčková [1], Katarína Elefantová [1], Lucia Pavlikova [2], Martin Cagala [2], Mário Šereš [2], Peter Šafář [3], Štefan Marchalín [3], Kamila Ďurišová [1], Viera Boháčová [2], Zdena Sulova [2], Boris Lakatoš [1], Albert Breier [1,*] and Petra Olejníková [1,*]

1 Institute of Biochemistry and Microbiology, Faculty of Chemical and Food Technology, Slovak University of Technology in Bratislava, Radlinského 9, 812 37 Bratislava, Slovakia; jana.kubickova@stuba.sk (J.K.); katarina.elefantova@stuba.sk (K.E.); kamila.durisova@stuba.sk (K.Ď.); boris.lakatos@stuba.sk (B.L.)

2 Institute of Molecular Physiology and Genetics, Centre of Bioscience, Slovak Academy of Sciences, Dubravska Cesta 9, 840 05 Bratislava, Slovakia; lucia.pavlikova@savba.sk (L.P.); martin.cagala@savba.sk (M.C.); mario.seres@savba.sk (M.Š.); viera.bohacova@savba.sk (V.B.); zdena.sulova@savba.sk (Z.S.)

3 Institute of Organic chemistry, Faculty of Food and Chemical Technology, Slovak University of Technology in Bratislava, Radlinského 9, 812 37 Bratislava, Slovakia; peter.safar@stuba.sk (P.Š.); stefan.marchalin@stuba.sk (Š.M.)

* Correspondence: albert.breier@stuba.sk (A.B.); petra.olejnikova@stuba.sk (P.O.); Tel.: +421-259-325-514 (A.B.); +421-259-325-516 (P.O.)

Academic Editor: Josef Jampilek
Received: 24 May 2019; Accepted: 4 June 2019; Published: 5 June 2019

Abstract: We describe the screening of a set of cryptopleurine derivatives, namely thienoquinolizidine derivatives and (epi-)benzo analogs with bioactive phenanthroquinolizidine alkaloids that induce cytotoxic effects in the mouse lymphocytic leukemia cell line L1210. We used three variants of L1210 cells: i) parental cells (S) negative for P-glycoprotein (P-gp) expression; ii) P-glycoprotein positive cells (R), obtained by selection with vincristine; iii) P-glycoprotein positive cells (T), obtained by stable transfection with a human gene encoding P-glycoprotein. We identified the most effective derivative **11** with a median lethal concentration of ≈13 μM in all three L1210 cell variants. The analysis of the apoptosis/necrosis induced by derivative **11** revealed that cell death was the result of apoptosis with late apoptosis characteristics. Derivative **11** did not induce a strong alteration in the proportion of cells in the G_1, S or G_2/M phase of the cell cycle, but a strong increase in the number of S, R and T cells in the subG_1 phase was detected. These findings indicated that we identified the most effective inducer of cell death, derivative **11**, and this derivative effectively induced cell death in S, R and T cells at similar inhibitory concentrations independent of P-gp expression.

Keywords: L1210 cells; P-glycoprotein; multidrug resistance; phenanthroquinolizidine alkaloids; apoptosis

1. Introduction

While much attention has been paid to finding effective anticancer agents, these discoveries remain important for future improvements in cancer treatment. In order to find novel derivatives of naturally occurring compounds with potentiated cytotoxic effects, neoplastic cells are important for rational anticancer drug development [1]. Moreover, neoplastic cells can develop pleiotropic cell

resistance based on multifactorial inducement [2]. Such resistance leads to reduced drug-induced cytotoxicity, which enables cells to escape drug-induced death. This cell survival points to the necessity to include knowledge about the induction and/or development of this resistance when designing and preparing drugs with the potential for use as novel anticancer therapies [3].

Plant alkaloids represent a large but well-defined group of nitrogen-containing substances that have been used in both traditional and alternative medical practice to treat many diseases because of their wide range of biological activities. Currently, plant alkaloids are at the forefront of therapeutic discovery and serve mainly as suitable structures for the derivatization and development of new drugs with potential use in modern medicine. The derivatization of well-known natural compounds/plant metabolites with a wide range of biological activities is a promising way for focusing on their specific effectiveness [4]. A rich source of plant alkaloids with a wide range of biological activities is found in the *Leguminosae* family. Cryptopleurine, a phenanthroquinolizidine alkaloid, was isolated from *Cryptocarya* and *Boehmeria* species [5] as a compound with potent antiviral [6], anti-inflammatory [7] and antiproliferative activity [8,9]. It is representative of natural compounds with a common pentacyclic structure such that the phenanthrene ring is conjugated with quinolizidine. Phenanthroquinolizidines have gained renewed attention because of their described mode of action, which differs from that of currently used drugs [10]. Many potential biological targets of phenanthroquinolizidines have been reported. The antiproliferative action of phenanthroquinolizidines seems to be associated with the downregulation of cell cycle regulatory proteins such as cyclin and cyclin-dependent kinases [11]. Several other quinolizine structures have been reported as inhibitors of DNA topoisomerase I activity such that the cell cycle is arrested at the G0/G1 phase [12].

In the present paper, we report the cytotoxic effects of a set of cryptopleurine derivatives (thienoquinolizidine derivatives and (epi-)benzo analogs with bioactive phenanthroquinolizidine alkaloids) obtained by organic synthesis [13,14] on the lymphocytic leukemia cell line L1210. When looking for new active structures with potential antileukemic activity, it is important to think about the potential risks of multidrug resistance (MDR) development. The most often observed mechanism of neoplastic cell resistance stems from the enhanced expression or activity of plasma membrane efflux pumps, classified as ABC transporters [15], that are able to eliminate various unrelated chemicals with diverse structures from intracellular space. The overexpression of these efflux pumps is one of the molecular-based causes of MDR. Therefore, it is important to test new, active molecular structures as substrates for efflux pumps. The overexpression of P-glycoprotein (P-gp), the most frequently occurring drug efflux pump of the plasma membrane (an ABCB1 member of the ABC transporter gene family), in neoplastic cells is generally accepted as the molecular mechanism behind the dramatically reduced cell sensitivity to a well-defined group of anticancer drugs known as P-gp substrates [16]. Therefore, we aimed to test for the cytotoxic effects of thienoquinolizidine derivatives and the (epi-)benzo analogs of bioactive phenanthroquinolizidine alkaloids on cells with and without expression- or drug-induced P-gp efflux activity. The biological model used in the current study is based on three variants of L1210 cells: parental drug-sensitive cells that do not express P-gp (S) and two drug-resistant P-gp-positive cell variants obtained by either S cell adaptation to vincristine (R) or transfection of S cells with the human gene encoding P-gp (T) [17].

2. Results

2.1. Characterization of L1210 Cell Variants

The cytotoxic effects of a newly prepared set of quinolizidine derivatives QDs were evaluated on three variants of L1210 cells that differed in their expression of P-gp. These variants included parental P-gp-negative (S) cells and two P-gp-positive cell variants obtained either by selection with vincristine (R) [18] or by transfection with a gene encoding P-gp (T) [17]. We detected massive amounts of P-gp mRNA and protein by RT-PCR and Western blotting, respectively, in P-gp-positive R and T variants. In contrast, the detection of P-gp mRNA expression and protein levels gave only weak (if any) signals in

S cells [17]. Moreover, we also demonstrated that the P-gp efflux activities that led to decreased calcein retention within R and T cells were lacking in S cells. Consistent with this finding, R and T cells were much less sensitive to P-gp substrates, such as VCR, doxorubicin, and mitoxantrone, than S cells [19]. P-gp was detected by immunofluorescence confocal microscopy in R and T cells predominantly in the plasma membrane [20]. In contrast, no immunoreactive materials were visible in S cells. All these features are consistent with previously published data [17,19,21,22] and were periodically controlled in our laboratory in the experiments described in the current paper. Taken together, the characteristics of S, R and T cells make them a suitable cell model for studying the differences between the responses of P-gp-negative and P-gp-positive leukemia cells to various chemicals.

2.2. Characterization of QD Derivatives

Thirteen isomeric (epi)-thieno analogs of phenanthroquinolizidine (TQD, denoted as **cis10Aa**, **cis10Ab**, **trans10Aa**, trans**10Ab**, **trans10Bb**, **11Ba**, **11Bb**, **11Aa**, **11Ab**, **15a**, **15b**, **18Aa** and **18Ab**) with structural motifs similar to those of naturally occurring cryptopleurine and hydroxycryptopleurine were used in this study (Table 1).

Table 1. Structures of the assayed derivatives.

(epi)-thieno analogs of phenanthroquinolizidine alkaloids (TQDs)			
Derivative	**Structure**	**Derivative**	**Structure**
11Ba[1] M_w = 193.31 g/mol	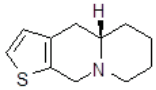	**11Bb**[1] M_w = 192.31 g/mol	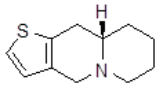
11Aa[1] M_w = 207.29 g/mol	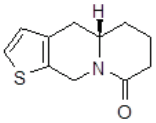	**11Ab**[1] M_w = 207.29 g/mol	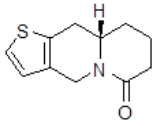
A4[2] M_w = 335.25 g/mol	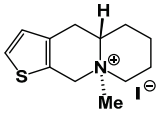	**B10**[2] M_w = 235.25 g/mol	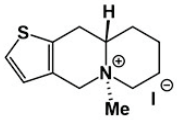
B9[2] M_w = 351.25 g/mol	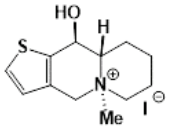	**trans10Bb**[1] M_w = 209.31 g/mol	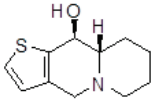
trans10Aa[1] M_w = 223.29 g/mol	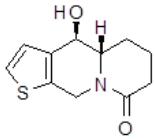	**trans10Ab**[1] Mw = 223.29 g/mol	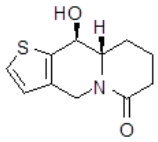
cis10Aa[1] M_w = 223.29 g/mol	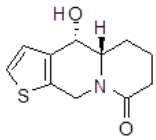	**cis10Ab**[1] M_w = 223.29 g/mol	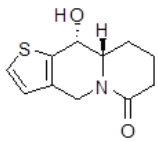
15a[1] M_w = 221.28 g/mol	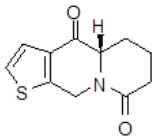	**15b**[1] M_w = 221.29 g/mol	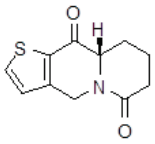
18Aa[1] M_w = 263.33 g/mol	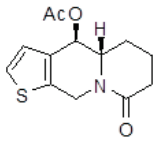	**18Ab**[1] M_w=265.33 g/mol	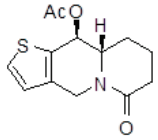

Table 1. *Cont.*

(epi)benzo analogs of phenanthroquinolizidine alkaloids (BQDs)			
5a[3] M_w = 217,27 g/mol	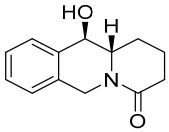	**5b**[3] M_w = 217.27 g/mol	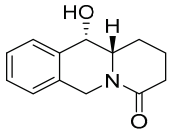
6b[3] M_w = 259.31 g/mol	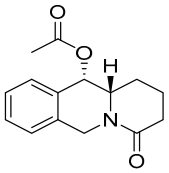	**9**[3] M_w = 307.43 g/mol	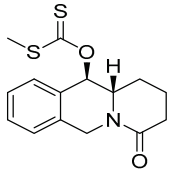
7a[3] M_w = 203.29 g/mol	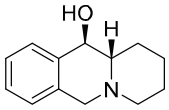	**7b**[3] M_w = 203.29	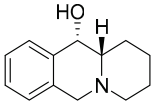
10[3] M_w = 201.27 g/mol	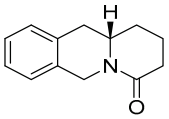	**11**[3] M_w = 187.29 g/mol	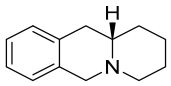

Synthesis and substance characterizations are described elsewhere: 1–[13]; 2–[23], 3–[14].

The analogs were synthesized from L-2-aminoadipic acid and the corresponding thiophen-2-carbaldehyde or thiophen-3-carbaldehyde. L-2-aminoadipic acid was used as a source of chirality as well as for the nitrogen necessary for further applications, specifically for the synthesis of these types of compounds. *N*-methylthienoquinolizinium iodides **A4**, **B9**, and **B10** were obtained by *N*-alkylation of the corresponding thienoquinolizidines **10Bb**, **11Ba**, and **11Bb** [23]. The asymmetric synthesis of (epi)-benzo analogs of the phenanthroquinolizidine bioactive alkaloids (-)-cryptopleurine and (-)-(15R)-hydroxycryptopleurine **5a**, **5b**, **6a**, **7a**, **7b**, **9**, **10** and **11** (BQD) (Table 1) was achieved from enantiopure L-2-aminoadipic acid and benzaldehyde [14]. Details about the synthesis, accepted structure and characterization are published elsewhere [13,14,23].

2.3. Effectiveness of QDs to Induce Cell Death of S, R and T Cells

All derivatives were assayed for their cytotoxic effects on leukemia cells. The IC_{50} (median of lethal concentration) values were calculated from growth inhibition curves and are presented in Table 2. Our results show that a higher cytotoxic effect was induced with the BQD derivatives compared to the TQD derivatives. In the TQD group, only derivative **11Ba** was effective on P-gp-negative S cells, and no measurable cytotoxic effect was found in R and T cells at derivative concentrations exceeding 100 μM. This finding was used to predict the resistance of P-gp-positive cell variants against **11Ba** (Table 2).

In the BQD group, four effective derivatives were identified; among them, cell death was more effectively induced in P-gp-negative S cells, compared to P-gp positive R and T cells, by derivative **6b** (the IC_{50} values were 192 μM for S cells and 385 μM for both R and T cells). Derivative **10** seems to be more effective in S than in R and T cells but only at much higher concentrations (the IC_{50} value was 490 μM). In contrast to previously tested derivatives, two BQD derivatives, **9** and **11**, induced almost similar levels of cell death on all three cell variants. Moreover, these derivatives were found to be very effective, with IC_{50} values of approximately 72–82 μM for derivative **9** and 13 μM for derivative **11** (Table 2). Due to their efficacy, both derivatives were assayed on the human acute myeloid leukemia SKM-1 and MOLM-13 cells, and their respective IC_{50} values were similar to those obtained for S, R and T cells, i.e., approximately 60–90 μM for derivative **9** and 10–15 μM for derivative **11**. In our previous paper [14], the cytotoxic effects induced by derivatives **9** and **11** were tested with two non-neoplastic cell lines (hamster kidney fibroblast cell line BHK-21 and African green monkey kidney fibroblast-like

cell line VERO). Derivative **11** reached the IC_{50} value in the higher concentration range of 213 μM for BHK-21 cells and 266 μM for VERO cells. Neither cell line was affected by derivative 9. Thus, it could be concluded that these two derivatives induced more effective cell death in neoplastic cells than in normal cells. The best antiproliferative activity found in S, R and T cells was induced by derivative **11**, and this effect was not influenced by the presence of P-gp in either the R or T cells. Therefore, additional studies of several features associated with the cell death of S, R and T were focused on derivative **11**.

Table 2. The IC_{50} values for the growth inhibition of S, R and T cells by quinolizidine derivatives.

(epi)-thieno analogs of phenanthroquinolizidine			
Derivative	**IC_{50} (μmol/l)**		
	S	R	T
11Ba	130 ± 9	na	na
11Bb	na	na	na
11Aa	na	na	na
11Ab	na	na	na
A4	na	na	na
B10	na	na	na
B9	na	na	na
trans10Bb	na	na	na
trans10Aa	na	na	na
trans10Ab	na	na	na
cis10Aa	na	na	na
cis10Ab	na	na	na
15a	na	na	na
15b	na	na	na
18Aa	na	na	na
18Ab	na	na	na
(epi)-benzo analogs of phenanthroquinolizidine alkaloids			
5a	na	na	na
5b	na	na	na
6b	192 ± 12	385 ± 16	385 ± 19
7a	na	na	na
7b	na	na	na
9	81 ± 5	81 ± 4	74 ± 3
10	490 ± 43	na	na
11	13.1 ± 2.5	13.4 ± 3.1	12.8 ± 2.7

na–not active.

2.4. Effectiveness of Derivative 11 on Expression and Efflux Activity of P-gp in R and T Cells

Derivative **11** induced a visible increase in transcripts encoding P-gp in R and T cells, namely, at a concentration of 13 μM, which is equal to that for inducing the IC_{50} value (Figure 1A). This amount was quantified by qRT-PCR, which revealed an approximate doubling of the cellular amount of this transcript (Figure 1B). The transport activity of P-gp was monitored by the retention of the calcein originating from calcein-AM (a P-gp substrate) after esterified carboxylic group liberation with intracellular esterases [20,24]. In S cells, we observed a massive retention of calcein within the cells that could not be influenced by verapamil (a known P-gp inhibitor) or derivative **11** (Figure 1C). In contrast, retention of calcein in both P-gp positive cell variants (R and T) was less pronounced, and could be achieved to an extent similar to that in S cells by verapamil. Contrary to verapamil, derivative **11** did not influence the retention of calcein in R and T cells.

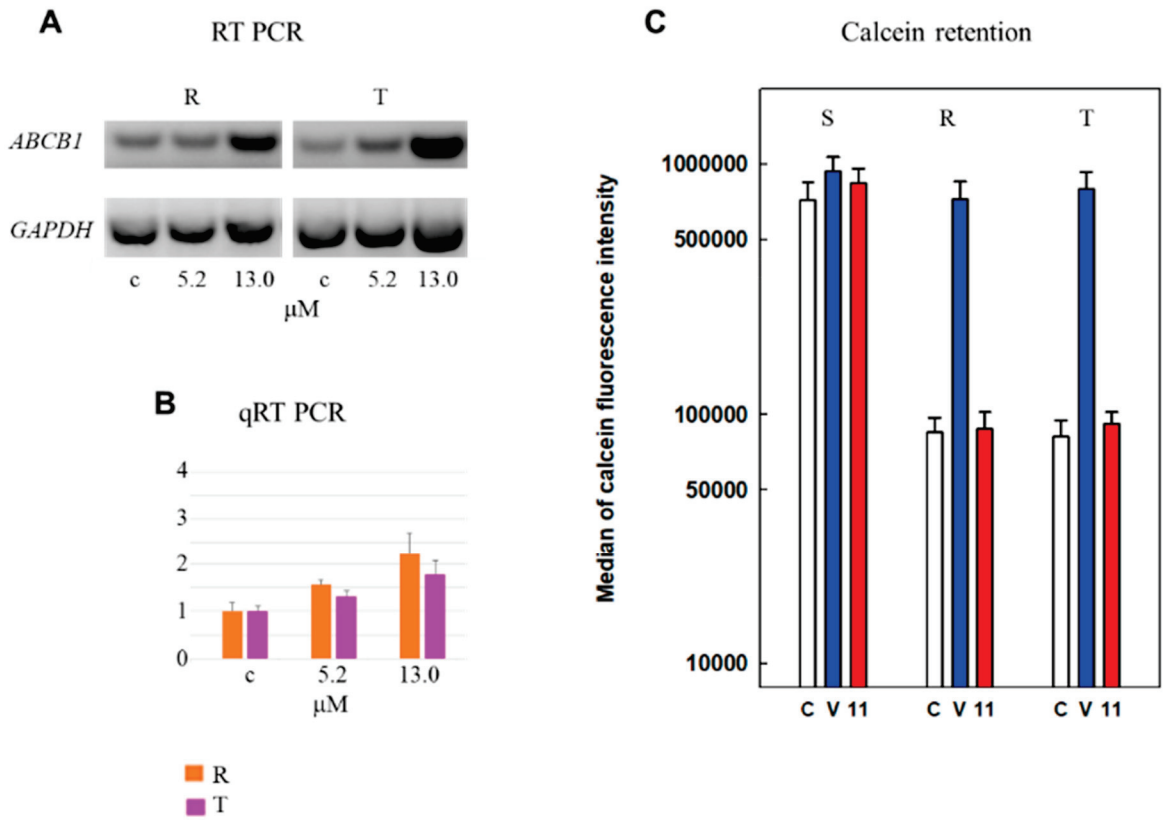

Figure 1. Effect of derivative **11**, applied at concentrations of 0.0 (c), 5.2 and 13.0 μM, on the expression and activity of P-gp. (**A**) Cell contents of ABCB1 gene transcripts encoding P-gp by RT-PCR (reverse transcription polymerase chain reaction). The results are representative of three independent measurements of triplicate experiments, and transcripts for GAPDH were used as housekeepers. (**B**) Quantification of mRNA content by qRT-PCR. Data represent the mean ± S.E.M. from three independent measurements. The amount of detected PCR product in R cells incubated in the presence of derivative **11** at a concentration of 13.0 μM differed significantly from the corresponding value in the absence of substance (c) at the level of $p<0.05$. Other results did not fulfill the criteria for statistical significance. (**C**) Median values of calcein retention in S, R and T cells in the presence or absence of verapamil (V, 10.0 μM) and derivative **11** (11.0, 13.0 μM). Median values were obtained from corresponding cytometry histograms of calcein fluorescence using BD-Accuri C6 software. Verapamil at this concentration fully restores calcein retention in R and T cells to the extent characteristic of S cells [17]. Data represent the mean ± S.E.M. from three independent measurements. Median values registered for R and T cells in the absence of inhibiting compounds or in the presence of derivative **11** differ significantly (at least on the level of $p < 0.02$) from median values obtained either from S cells independent of the presence of verapamil) or for R and T cells obtained in the presence of verapamil.

2.5. Measurements of the Effectiveness of Derivative 11 to Induce Cell Death Based on FITC-Annexin V and Propidium Iodide Double Staining

Annexin V linked with fluorescein isothiocyanate (FAV), which specifically labels externalized phosphatidylserine on the surface of apoptotic cells, and propidium iodide (PI), which labels DNA in necrotic cells with disrupted plasma membranes [25], were used as markers of apoptosis and necrosis, respectively. Proportions of viable S, R and T cells (i.e., cells that did not bind FAV or PI) after a 24 h incubation period in cultivation medium without derivative **11** (under standard cultivation conditions) consistently exceeded 90% (Figure 2).

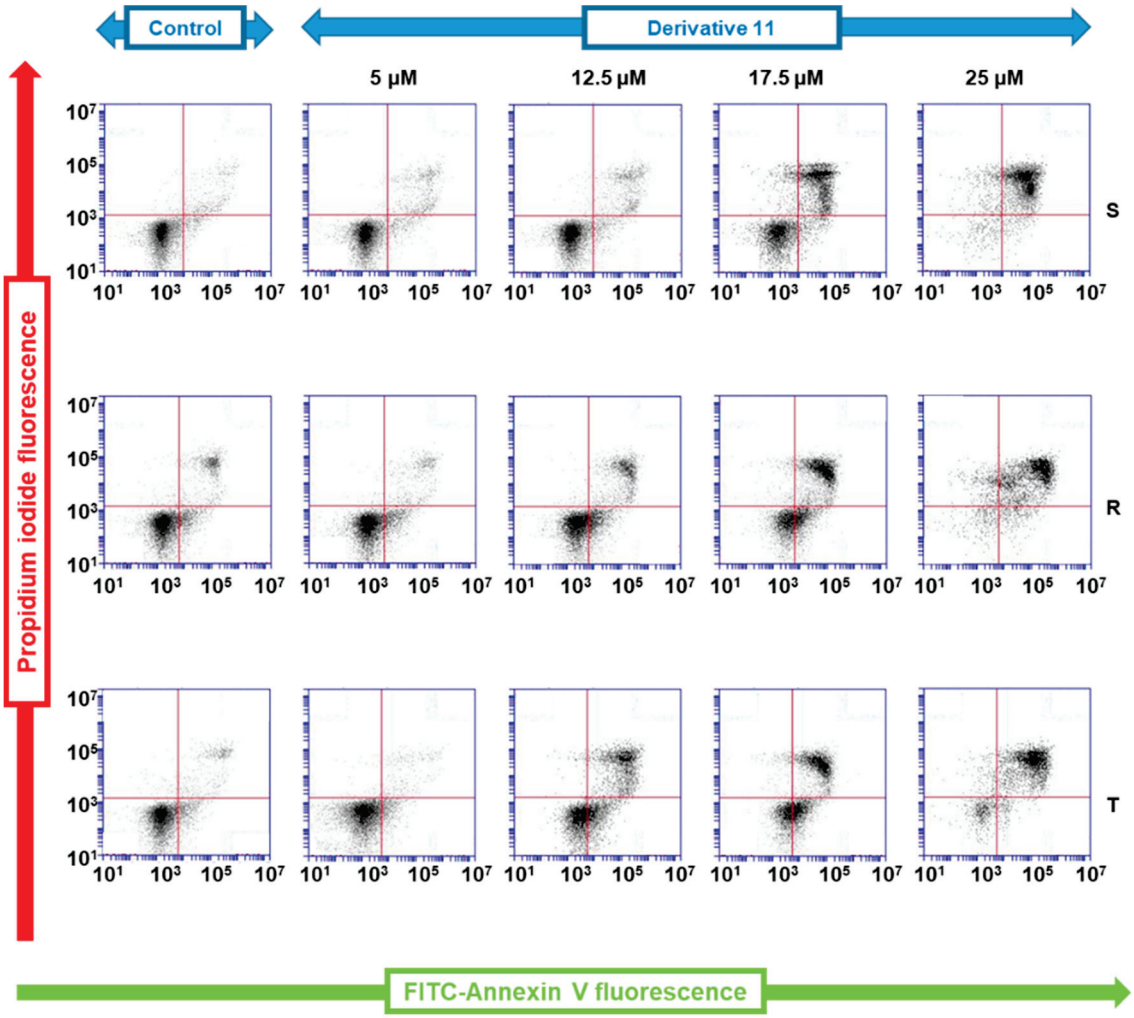

Figure 2. Measurement of S, R and T cell proportions during apoptosis and necrosis as measured using an FAV/PI apoptosis necrosis kit. The cells were cultivated for 24 h in cultivation medium in the presence or absence of derivative **11** at the given concentrations. The dot blots are representative of three independent measurements.

The presence of derivative **11** (at a concentration range of 5–25 µM) in the cultivation medium induced an increase in either the proportion of cells labeled with FAV (indicating apoptotic cells) or the proportion of cells labeled by both FAV and PI (indicating cells in late apoptosis). These effects seem to be concentration dependent. The labeling of cells by PI alone (i.e., necrotic cells) was not as pronounced (Figure 2).

2.6. Derivative 11 Induced Changes Expression of Bcl-2 and Bax as Well as Expression and Activation of Caspase-3

To study the mechanisms of cell death induced by derivative **11**, we further estimated cell expression of the proapoptotic Bax protein and the antiapoptotic Bcl-2 protein as well as cell content and activation of caspase-3 in S, R and T cells cultivated for 24 h in the absence or presence of 6.5 and 13.0 µM derivative **11** (Figure 3). The expression of Bcl-2 protein is considerably higher in R and T cells than in S cells, as measured by mRNA (Figure 3A) or protein (Figure 3B) levels. In contrast, no similar differences in proapoptotic Bax protein expression between P-gp-negative and P-gp-positive cells were observed either at the mRNA or protein level. The presence of derivative **11** in the cultivation medium did not induce changes in the expression of either protein in S, R or T cells. The massive protein content of procaspase-3 is present in S, R and T cells, and a small proportion of it is proteolytically activated to caspase-3 in all three variants of L1210 cells (Figure 3). However, no statistically significant changes in

procaspase-3 content or its cleavage products were detected after S R and T cells were incubated in medium containing derivative **11** at concentrations of 6.5 and 13.0 μM for 24 h.

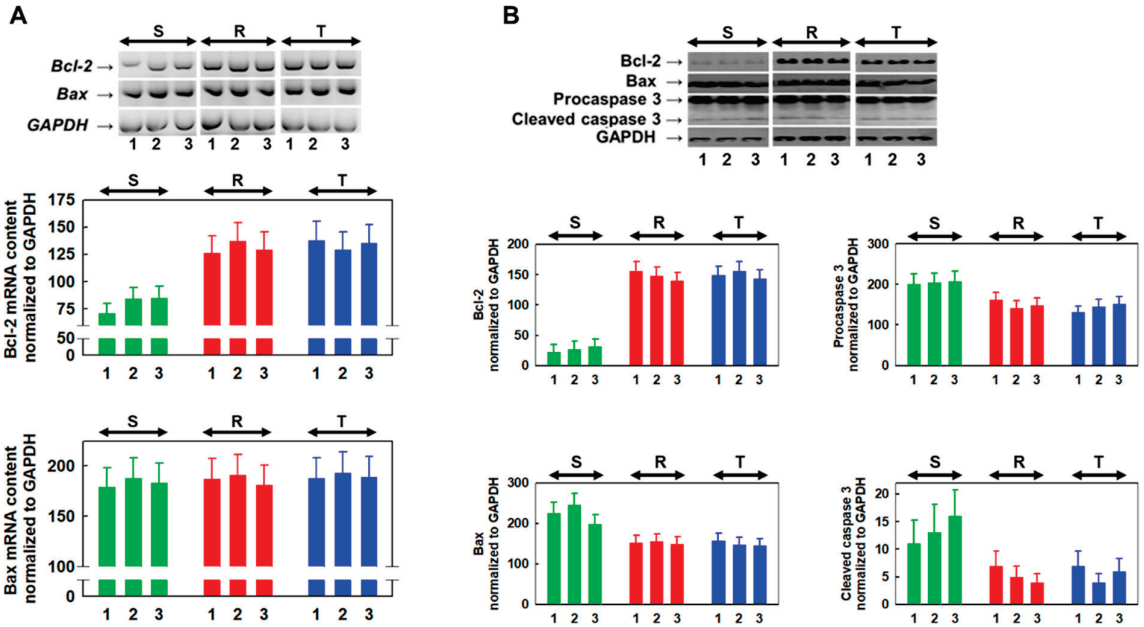

Figure 3. Detection of Bcl-2 and BAX expression as well as caspase-3 expression and activation in S, R and T cells incubated for 24 h in cultivation medium in the absence (1) or presence of derivative **11** at concentrations of 6.5 (2) and 13.0 (3) μM. (**A**) Detection of Bcl-2 and BAX transcripts using RT-PCR in gel (upper part, data are representative of three independent measurements) and its densitometric quantification values (lower part, data are expressed as the mean ± S.E.M. for three measurements). The amount of Bcl-2 transcript detected in S cells differed significantly from the corresponding values for R and T cells (at least at the level of $p<0.02$) independent of derivative **11**. (**B**) Western blot detection of Bcl-2, Bax, procaspase-3 and caspase-3 in S, R and T cells. The blot records are representative of three independent measurements (upper part), the protein bands were quantified using densitometry (lower part), and the data are expressed as the mean ± S.E.M. for three measurements. The quantities of Bcl-2 protein differ significantly from corresponding values for R and T cells (at least at the level of $p < 0.01$) independent of derivative **11**. GAPDH mRNA and protein were used as internal standards for RT-PCR and Western blotting.

2.7. Effect of Derivative 11 on Cell Cycle Progression of S, R and T Cells

The incubation of S, R and T cells for 24 h in the presence of derivative **11** at a concentration of 13.0 μM induced visible cell damage associated with an elevation of the proportion of cells in the subG_1 phase (Figure 4) when cell cycle progression was monitored by cytometry using DNA cell content detection by PI. Cells in the subG_1 phase represent the proportion of cells that have enter the progression of programmed cell death and have partially fragmented or degraded DNA. The proportions of S, R and T cells in the subG_1 phase increased depending on the concentration of derivative **11** (Figure 4B), with an almost identical median effective concentration in the range of 12-18 μM for all three variants of L1210 cells. This finding is consistent with the data documented in Table 2 as obtained using an MTT test of cell viability, in which the median effective concentration was approximately 13.0 μM. According to a previously published recommendation [19], only viable cells, i.e., cells that are not in subG_1 phase, were used for the analysis of the cell cycle (Figure 4C). Analysis of the cell cycle did not reveal differences between the proportions of S, R and T cells in the respective (G_1, S or G_2/M) cell cycle phases. Moreover, the incubation of S, R and T cells in the presence of derivative **11** did not induce an expressed alteration in the proportion of cells in the respective cell cycle phases. An exception of this cell cycle-related behavior, R cells incubated in the presence of derivative **11** at

a concentration of 13.0 μM showed an increased proportion of cells in the G_1 phase (approximately 25%), which was associated with corresponding decreases in the proportion of cells in the S and G_2/M phases (Figure 4C).

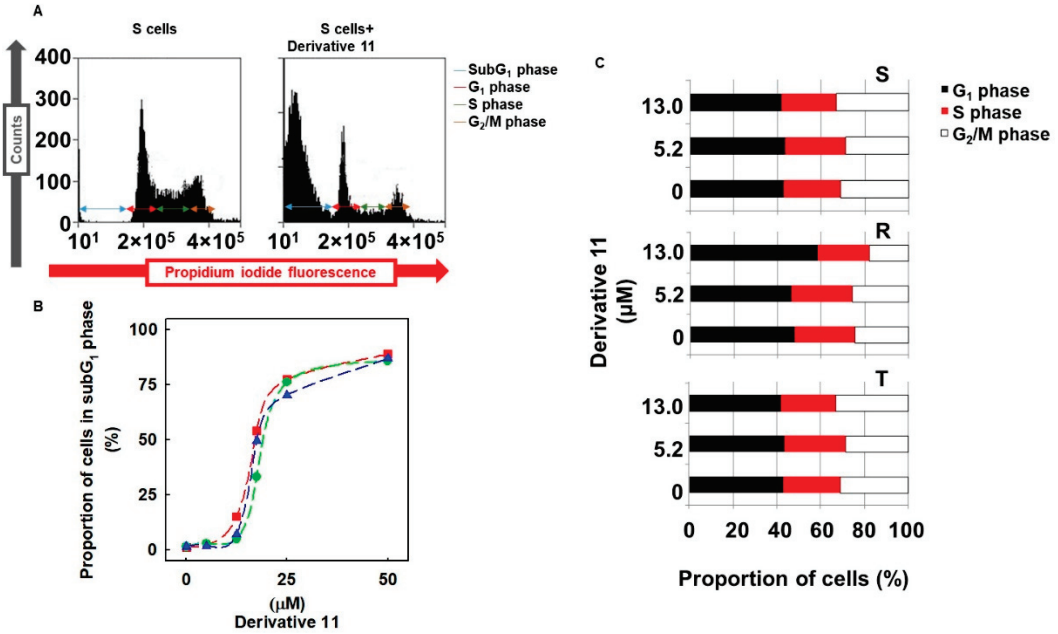

Figure 4. Effect of derivative **11** on cell cycle progression of S, R and T cells. (**A**) Measurement of the cell cycle documented as being in S independent of derivative **11** at a concentration of 13.0 μM. Data are representative of three independent measurements. Similar measurements were made for S, R and T cells in the absence or presence of derivative **11** at concentrations of 0–50 μM, and the resulting data were used for the construction of (**B**,**C**). (**B**) Relative levels of S, R and T cells in subG_1 phase by the concentration of derivative **11**. Data represent the mean ± S.E.M. of three independent measurements. (**C**) Summary of the effect of derivative **11** on the cell cycle progression of S, R and T cells. Data represent the means from three independent measurements.

3. Discussion

Multiple drug resistance of neoplastic cells leads to reduced cell sensitivity toward different drugs and represents a real obstacle in the effective chemotherapy of neoplastic diseases, including blood malignancies [26]. Until now, diverse but well-understood mechanisms of MDR have been identified [16] of which the efflux activity of overexpressed P-gp in the plasma membrane of neoplastic cells is the most frequently occurring [27]. Therefore, searching for substances that cannot be eliminated from the inner space of cells by overexpressed P-gp is a rational undertaking in medicinal chemistry. For this reason, we have oriented ourselves to study the effective means of cell death induced by phenanthroquinolizidine alkaloid derivatives related to P-gp expression in leukemia cells. We used sets of 13 TQDs, 3 of which are *N*-methylthienoquinolizinium iodides, and 8 BQDs (Table 1) for which the synthesis and chemical characterization have been described elsewhere [13,14,23]. Only derivative **11Ba** was effective from among all the TQD in S cells (with $IC_{50} \approx 130$ μM). This derivative did not induce cell death in R and T cells. The corresponding substance A4, with permanent quaternary nitrogen derived from **11Ba** by *N*-methylation, lost cell death effectiveness in S cells, indicating the importance of localized free electron pair on the nitrogen atom of the quinolizidine skeleton. However, permanent positive charge on nitrogen atom may depress ability of substance to enter the cell via passive diffusion, which may be responsible for lack of effectiveness. Derivative **11Bb**, which differs from derivative **11Ba** only in the orientation of the sulfur atom in the thienyl ring, also failed to induce cell death in S cells. Therefore, the proper structural orientation of the thienyl-ring seems to be another crucial feature important for TQD effectiveness in inducing cell death of S cells. It is reasonable to

expect that the position of the conjugated π-electron system of the thienyl ring may be important for effecting cell death. Similarities in the conjugated π-electron density at a similar position as in the thienyl-ring of derivative **11Ba** also exist on the benzene ring of BQD derivatives. Derivative **11** exhibits both of the features described above in relation to derivative **11Ba**, i.e., a localized free electron pair on the nitrogen atom of the quinolizidine skeleton and a π-electron system on the benzene ring. This derivative showed the most pronounced effectiveness for inducing cell death in all three variants of L1210 cells, with an $IC_{50} \approx 13$ μM independent of P-glycoprotein expression. Derivative **10** differs from derivative **11** by the existence of a formyl group located on carbon atom 3, i.e., in the position directly adjacent to the nitrogen atom of quinolizidine, thus inducing strong delocalization of the free electron pair associated with the nitrogen. This derivative induced only negligible cell death in S cells ($IC_{50} \approx 500$ μM) and was ineffective in R and T cells (Table 2). There are also two other effective derivatives, **9** with IC_{50} values 81, 81 and 74 μM for S, R and T cells, respectively, as well as **6b** with IC_{50} values of 192, 385 and 385 μM for S, R and T cells, respectively. Both of these derivatives contain the formyl group, described above, in position 3, and substituents (S-methyl xanthate or O-acetyl) in position 10 that could give the derivatives additional ability to cause cell death, most likely by inducing oxidative stress. The property attributed to the localized free electron pair on the nitrogen atom of the quinolizidine skeleton could be parametrized by the respective pK_a value of the respective derivative [28]. Therefore, we calculated pKa values for the derivatives **11Ba** and **11** using the online pK_a calculator at Instant Cheminformatics Solutions on web (Table 3). Other derivatives with the ability to induce cell death, at least in S cells (**6b**, **9** and **10**), due to the delocalization of free electrons around the nitrogen caused by the existence of a formyl group at position 3 did not have the same acid-base parameterizing characteristics as derivatives **11Ba** and **11**.

Table 3. Physicochemical properties of effective derivatives.

Derivative	Effective on (μM)			pK_a[1]	Log P[2]
	S	R	T		
11Ba	≈130	Na	Na	8.89	2.93 ± 0.35
6b	≈190	≈385	≈385	-	1.05 ± 0.62
9	≈80	≈80	≈74	-	2.52 ± 0.69
10	≈490	Na	Na	-	1.62 ± 0.56
11	≈13	≈13	≈13	9.20	3.25 ± 0.32

[1] Calculated using the online pK_a calculator Instant Cheminformatics Solutions on web. [2] Calculated using ACD/ChemSketch for academic and personal use (Advanced Chemistry Development, Inc. Toronto, Ontario, Canada).

Another important property that could be evaluated when predicting the effectiveness of substances to cause cell death is hydrophobicity, which enables them to enter the inner space of the cell through the plasma membrane by passive diffusion. These properties could be parametrized by the value of the partition coefficient in a two-phase system (frequently water: n-octanol, [29]). For this reason, we calculate the partition coefficient logarithm values in this two-phase system using ACD/ChemSketch for academic and personal use (Advanced Chemistry Development, Inc., Toronto, Ontario, Canada). The most effective at inducing cell death by this parameter, derivative **11** achieved the highest value of logP (3.25) among all derivatives studied (Table 3). Derivative **9** was effective at concentrations below 100 μM and has a logP value of 2.52. The only effective derivative from the TQD group in S cells, **11Ba**, had the second highest logP value (2.93). These facts enable us to propose rules for further design of such derivatives as potential agents for induction of cytotoxic effects in leukemia cells: i. to improve localization of the electron density associated with the nitrogen in the quinolizidine skeleton by introducing electron-donating groups (Figure 5); ii. to potentiate the conjugated π-electron system density on the benzene (thienyl-) part of molecule by introducing electron-donating groups (Figure 5); iii. to modify molecules with structures by improving the hydrophobicity of the substance.

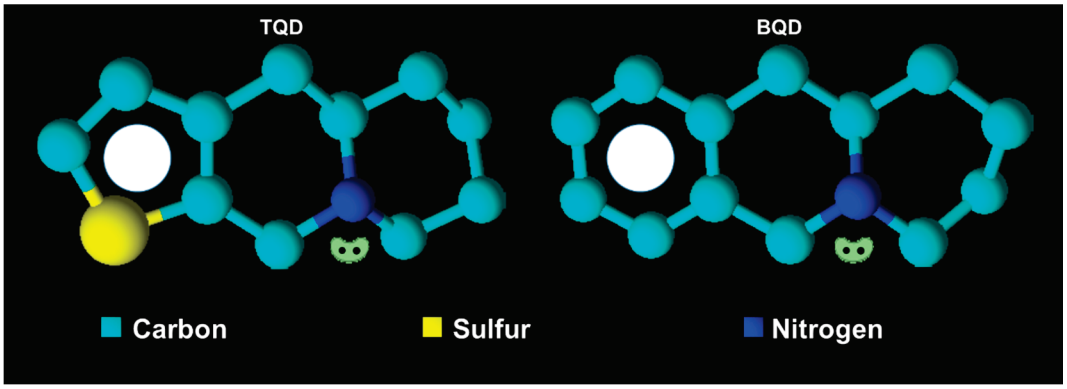

Figure 5. Features important for the effect TQD and BQD on cell death of S, R and T cells: i. Localized free electron pair on the nitrogen atom of derivatives; ii. aromatic character of the terminal left ring with conjugated π electron system; iii. lipophilic character of the substance.

Recently, phenanthroindolizidine alkaloids with similar localized free electron pairs on the nitrogen atom of the indolizidine skeleton and more complex side aromatic systems were shown to induce strong growth inhibitory activity toward a large panel of neoplastic cell lines, including P-gp-overexpressing cells [30].

Derivatives **6b**, **11Ba** and, to a lesser extent, derivative **10** induced cell death more effectively in S than in R and T cells. Differences between the effectiveness of substances on P-gp-negative S and P-gp-positive R and T cells could be caused by the efflux activity of this drug transporter and by simple elimination of substances from the inner space of P-gp-positive cells such that they cannot induce cell death processes [16,27,31]. However, P-gp seems to play a secondary role in silencing apoptosis, and this side effect of P-gp expression is independent of P-gp drug efflux activity [16,31,32]. Thus, this suspected secondary role of P-gp that operates against apoptosis progression may induce differences between the effectiveness of substances that are not substrates of this efflux pump [33].

The most effective cell death-inducing substance we registered was derivative **11**, which is effective at a 10^{-5} M concentration independent of the expression of P-gp. This finding indicated that the presence of P-gp in R and T cells did not protect cells against derivative **11**-induced cell death. Thus, derivative **11** does not seem to be a substrate for P-gp-mediated drug efflux. This derivative induced an elevation of *ABCB1* gene (encoding P-gp) transcription in both P-gp-positive L1210 cell variants (Figure 1). However, this derivative did not alter calcein retention in R and T cells. This finding indicated that derivative **11** does not alter P-gp-mediated substance efflux activity.

In subsequent sets of experiments, we examined the mode of cell death induced by this derivative using a FAV/PI detection kit, which enabled the cytometric quantification of apoptotic (labeled by FAV), necrotic (labeled by PI) and late apoptotic/necrotic cells (labeled by both these markers) [34]. This procedure revealed the elevation of cells labeled with either FAV alone or both FAV and PI and only a negligible proportion of cells labeled with PI alone (Figure 2). This outcome is consistent with apoptotic cell death. Both P-gp positive cell variants (R and T) cultivated in the absence of derivative **11** contained higher levels of antiapoptotic Bcl-2 protein than found in P-gp-negative S cells (Figure 3). The coexpression of Bcl-2 and P-gp confers resistance against the induction of apoptosis in leukemia cells originating from alterations in the lymphoid pathway of hematopoiesis [35]. This difference in Bcl-2 expression also persists in the presence of derivative **11**. We further observed a massive amount of procaspase-3, which was partially cleaved to the active 17 kDa form (Figure 3). This caspase activates caspase-dependent DNase, which fragments DNA as a result of both the intrinsic and extrinsic pathways of caspase-dependent apoptosis [36]. Therefore, our results indicated the readiness of S, R and T cells to initiate apoptosis. However, all three cell variants failed to upregulate this apoptotic marker after treatment with derivative **11**.

During the cultivation of S, R and T cells in medium containing derivative **11**, we observed an increase in the proportion of dead cells in subG_1 with fragmented/degraded DNA (when cell DNA content was quantified with PI), which is often attributed to initiation and progression of apoptosis [37]. Viable cells after incubation with derivative **11** did not differ significantly in cell proportion by position in the G1, S or G2/M phase of the cell cycle.

4. Materials and Methods

4.1. Chemicals

In the present paper, sets of previously synthesized and characterized quinolizidine derivatives were tested for cytotoxic effects on P-gp-negative and P-gp-positive L1210 cells (Table 1): i. 13 (epi)-thieno analogs of phenanthroquinolizidines with similar structural motifs as the naturally occurring cryptopleurine and hydroxycryptopleurine [13]; ii. three *N*-methylthienoquinolizinium iodides obtained by *N*-alkylation of corresponding thienoquinolizidines [23]; iii. eight benzo analogs and epi-benzo analogs of bioactive phenanthroquinolizidine alkaloids, which were prepared by asymmetric synthesis as described elsewhere [14].

4.1.1. Components of Cultivation Medium

RPMI 1640 medium with L-glutamine (1 mg/mL), 8% fetal bovine serum, 100,000 units/l of penicillin and 50 mg/l of streptomycin were from Merck in Slovakia (Bratislava, Slovakia) and 1 μg/mL gentamycin was from Thermo Fisher Scientific s.r.o.

4.1.2. Kits

The apoptosis/necrosis kit based on cell labeling with FAV and PI, the ProteomeExtract Subcellular Proteome Extraction Kit were from Calbiochem (San Diego, CA, USA) and GenElute™ Mammalian Total RNA Miniprep Kit (Sigma-Aldrich through Merck in Slovakia, Bratislava, Slovakia)

4.1.3. PCR Primers

The following primers were used for RT-PCR and qRT-PCR: GAPDH F: 5′-TGA ACG GGA AGC TCA CTG G-3′and R: 5′-TCC ACC ACC CTG TTG CTG TA-3′, which produced a 307 bp product; mouse P-gp F: 5′-GGC TGT TAA AGG TAA CTC C-3′ and R: 5′- TGT TCT CTT ATG AAT CAC GTA-3′, which produced a 152 bp product; human P-GP, F: 5′-CTC CTG TCG CAT TAT AGC-3′, R: 5′-AGA CAT GAC CAG GTA TGC-3′, which produced a 151 bp product; Bcl-2 F: 5′-GGC TGG GGA TGA CTT CTC TC-3´, R: 5´-GCA TGCT GGG GCC ATA TAG TT-3´, which produced a 323 bp product; and Bax F: 5´-ATC CAA GAC CAG GGT GGC T-3´, which produced a 197 bp product.

4.1.4. Antibodies

For visualization of protein bands on Western blots, the following antibodies were used: N-20 (sc-493) rabbit polyclonal antibody against Bax, C-2 (sc-7382) mouse monoclonal antibody from Santa Cruz Biotechnology (Dallas, TX, USA); rabbit polyclonal antibody (9662S) against caspase-3 from Cell Signaling Technology Europe (Leiden, The Netherlands); and mouse monoclonal antibody against GAPDH (MAM 374) from Merc in Slovakia. Antimouse recombination antibody (sc-516102) or mouse anti-rabbit affinity purified polyclonal antibody linked with horseradish peroxidase (HRP) were used as secondary antibodies and were purchased from Santa Cruz Biotechnology. HRP signals were visualized using an ECL detection system (GE Healthcare Europe GmbH, Vienna, Austria) and an Amersham Imager 600 (GE Healthcare Europe GmbH, Pittsburgh, PA, USA).

4.1.5. Other Chemicals

MTT ([3-(4,5-dimethyldiazol-2-yl)-2,5 diphenyltetrazolium bromide]), and calcein/AM, verapamil, vincristine, propidium iodide and Triton X-100 were purchased from Merck in Slovakia (Bratislava,

Slovakia). RNase A was from Thermo Fisher Scientific s.r.o. (Bratislava, Slovakia). All other chemicals were from Merck in Slovakia (previously Sigma Aldrich).

4.2. Cell Culture Conditions

We used three variants of the mouse lymphocytic leukemia cell line L1210: i. P-gp-negative drug-sensitive parental L1210 cells (ACC-123, S) obtained from Leibniz-Institut DSMZ-Deutsche Sammlung von Mikroorganismen und Zellkulturen GmbH (Braunschweig, Germany); ii. P-gp-positive, drug-resistant cells (R) overexpressing P-gp due to selection with vincristine [18]; P-gp-positive, drug-resistant cells (T) overexpressing P-gp due to stable transfection with Addgene plasmid 10957 (pHaMDRwt), and a retrovirus encoding full-length P-gp cDNA [38]). Transfection and cell characterization were completed as described elsewhere [17].

All variants of L1210 cells (S, R and T) were cultured in the RPMI medium described above at 37 °C in a humidified atmosphere with 5% CO_2. This procedure is termed passage and was repeated three times a week. R cells were periodically passaged each second in the presence of vincristine (250 nM), and were harvested for experiments during the second passage without vincristine. Cell viability was monitored using Countess™ II FL, Invitrogen through Thermo Fisher Scientific s.r.o. R cells were cultured for two passages without VCR prior to the experiments. The expression/activity/localization of P-gp was periodically analyzed by RT-PCR, Western blotting, calcein retention assay and confocal immunocytochemistry [24]). All cell variants (S, R and T) were cultivated in the absence or presence of the respective quinolizidine derivatives at a concentration range of 1-500 μM and were used for further examination.

4.3. Measurements of Cytotoxic Effects of Quinolizidine Derivatives on S, R and T Cells

S, R and T L1210 cells (5 × 104 cells/well) were incubated with TQD or BQD in a concentration range of 1–500 μM in 96-well culture plates for 48 h. Tested quinolizidine derivatives were added directly to 200 μL of RPMI culture media, and cell viability was assessed using an MTT assay [39]. In brief, after 48 h, the plates were centrifuged for 10 min at 2500 rpm; the cells were resuspended in 200 μL RPMI without fetal bovine serum, and MTT (0.25 mg/mL, i.e., 50 μg per well) was added for 2 h in the dark at 37 °C and then centrifuged for 10 min (3000 rpm); cell sediments were extracted with 150 μL dimethyl sulfoxide (DMSO), and absorbance at 540 nm was measured using the Universal Microplate Spectrophotometer mQuant (BioTek Instruments, Inc., Winooski, VT, USA). Dose-responsiveness curves were fitted according to an exponential decay equation (Eq. (1)) by nonlinear regression as previously described [21]:

$$N = 100\% \times \exp[\ln(0.5) \times (c/IC50)] \quad (1)$$

where N represents the percentage (from a control in the absence of drugs) of cell viability after culturing in the presence of the tested derivates at concentration c; IC50 is the concentration of a substance when N = 50%; IC50 values were calculated from three independent measurements. The significance of differences was analyzed using an unpaired Student's t-test.

4.4. Detection of the Effect of Derivative 11 on P-gp, Bcl-2 and Bax Transcription

4.4.1. RT-PCR

Total RNA was isolated from S, R and T L1210 cells using the GenElute™ Mammalian Total RNA Miniprep Kit (Sigma-Aldrich through Merck in Slovakia) according to the manufacturer's instructions. Reverse transcription was performed using 2 μg of template RNA, Random Hexamer primers (100 pmol) (Thermo Fisher Scientific s.r.o., Waltham, MA, USA) and DEPC-treated water at a total volume of 12.5 μL according to the manufacturer's protocol.

PCR was performed in a 25 μL total volume containing 4 μL of reaction buffer 250 mM Tris-HCl, 250 mM KCl, 20 mM MgCl2, 50 mM DTT, and 0.5 μL Thermo Scientific™ RiboLock™ RNase Inhibitor, 2 μL dNTP mix, 10 mM each and 1 μL RevertAid H Minus Reverse Transcriptase (all from Thermo

Fisher Scientific s.r.o., Waltham, MA, USA). After heating at 95 °C for 5 min to inactivate the reverse transcriptase, the samples were subjected to 35 cycles of denaturation (95 °C for 45 s), annealing (57 °C *Mus musculus* and *Homo sapiens* P-gp and 58 °C GAPDH, Bcl-2 and Bax for 30 s) and extension (72 °C, 90 s), followed by a final extension at 72 °C for 10 min. The PCR products were separated on a 2% agarose gel (Merck in Slovakia) and visualized with GelRed™ nucleic acid gel stain (Biotium, Fremont, CA, USA) using an Amersham™ Imager 600 (GE Healthcare Europe GmbH, Pittsburgh, PA, USA). The data were expressed as the relative level of each mRNA normalized to that of the housekeeping gene *GAPDH*. Statistical significance was analyzed using an unpaired Student's t-test.

4.4.2. qRT-PCR

Total RNA isolation, reverse transcription and the PCR primers were the same as described for RT-PCR. qPCR was run on a 96-well microtitration plate using a CFX96 TouchTM real-time PCR Detection System (Bio Rad, USA). PCR was run in a 10 μL solution containing 500 ng of cDNA, 5 μL of 2x iTaq Universal SYBR® Green Supermix (Bio-Rad), 1 μL of primer solution at a concentration of 5 μmol/L and 2.5 μL of RNase-free UltraPureTM DEPC-treated water for 39 cycles at 57 °C. The samples were measured in triplicate.

4.5. Western Blot Procedures

After incubation, the cells were harvested, and crude membrane fractions were prepared with a ProteomeExtract Subcellular Proteome Extraction Kit according to the manufacturer's instructions. The proteins from the samples were separated by sodium dodecyl sulfate-polyacrylamide electrophoresis using 10% polyacrylamide gels according to the classic Laemmli [40] protocol and then transferred by electroblotting to a polyvinylidene difluoride (PVDF) membrane (GE Healthcare Europe GmbH). Finally, proteins were detected with specific primary and secondary antibodies linked with horseradish peroxidase. Electroblotting and interaction with antibodies were performed using the classic Towbin protocol [41], and HRP signals were visualized with the ECL system.

4.6. Estimation of P-gp Transport Activity by Calcein/AM Retention Assay

P-gp transport activity was measured using a previously described protocol for the calcein retention assay [42]. After cultivation, S, R and T Ll1210 cells were harvested by centrifugation (500× *g*), and 5×10^5 cells were incubated with derivative **11** for 1 h at final concentrations of 5.2 and 13.0 μM. Then, the cells were centrifuged (500× *g*), washed three times with PBS containing 0.2% BSA and then resuspended in 500 μL of the same buffer. Calcein/AM (final concentration 0.1 μmol/L) was added directly to the buffer, and the samples were incubated for 20 min at 37 °C in a CO_2 incubator. Calcein retention assays were performed in the absence or presence of derivative **11** at final concentrations (5.2 and 13.0 μM). For an inhibitor of P-gp, we used verapamil (final concentration of 10 μM), which was added to the samples together with calcein/AM. Finally, cells were incubated with propidium iodide (final concentration 0.9 μmol/L, Sigma-Aldrich) for an additional 10 min and then washed twice with ice-cold PBS. Fluorescence was measured using an Accuri C6 flow cytometer (BD Bioscience, San Jose, CA, USA). Only viable, propidium iodide-negative cells were counted.

4.7. Measurement of Apoptosis/Necrosis Induced by Derivative 11 in S, R and T Cells

Cells ($1 \times 10^{6/mL}$) were incubated for a 24-h incubation with or without derivative **11** (5–50 μM) under standard culture conditions. The proportions of apoptotic and necrotic cells were then detected using an FAV and PI kit. According to the procedure described by the manufacturer, the cells were washed twice with PBS and gently resuspended in binding buffer (obtained from the manufacturer) containing 0.5 μg/mL FAV. The mixture was then incubated in the dark for 15 min at room temperature and centrifuged (500× *g*, 15 min). The resulting sediments were resuspended in binding buffer, and propidium iodide (final concentration 0.6 μg/mL) was added to each sample, which was analyzed by flow cytometry using an Accuri C6 flow cytometer.

4.8. Detection of Cell Proportions in Different Phases of the Cell Cycle

Cells (1×10^6/mL) were incubated for 24 in the absence or presence of derivative **11** (5–50 μM) under standard cultivation conditions. Then, the cells were washed with PBS, resuspended in 0.05% Triton X-100 (Sigma-Aldrich, St. Louis, MO, USA) dissolved in PBS containing 0.1 mg/mL RNase A and incubated for 20 min at 37 °C. The final mixtures were cooled on ice for 10 min, and propidium iodide (40 μg/mL) was added to each sample, which was then incubated on ice for another 30 min. Finally, the specimens were evaluated by flow cytometry on an Accuri C6 flow cytometer.

5. Conclusions

We identified derivative **11** as the most effective among those in a set of derivatized quinolizidines. The derivative-induced cell death in L1210 mice lymphocytic cells independent of the expression of P-glycoprotein at a concentration of 13 μM. This derivative is much less effective on the normal fibroblast VERO and BHK-21 cells, for which the effective concentration exceeded 200 μM. Therefore, derivative **11** represents a sufficient starting point for the future design of effective structures.

Author Contributions: J.K. and K.E. conceived and designed the experiments; L.P., M.C., M.Š., K.Ď., V.B. and B.L. performed the experiments and analyzed the data; P.Š. and Š.M synthesized and characterized the derivatives; Z.S. assisted with the final preparation of the manuscript; and P.O. and A.B. reviewed the final results and drafted the paper.

Funding: This research was funded by the Slovak Research and Development Agency, grant numbers: APVV-14-0334 and APVV-15-0303; Scientific Grant Agency of Slovak Ministry of Education and Slovak Academy of Sciences (VEGA), grant numbers: Vega 2/0122/17, 1/0697/18, 2/0157/18, 2/0070/19, 2/0159/19, 1/0262/19; Slovak research agency, grant number: ITMS 26230120009, 26240220084 and by an internal grant of the Slovak University of Technology in Bratislava for the scheme to Support Young Researchers' Excellent Teams.

Acknowledgments: The manuscript was edited for proper English language, grammar, punctuation, spelling, and overall style by one or more of the highly qualified native English speaking editors at American Journal Experts.

Conflicts of Interest: The authors declare no conflicts of interest.

References

1. Mangal, M.; Sagar, P.; Singh, H.; Raghava, G.P.; Agarwal, S.M. NPACT: Naturally Occurring Plant-based Anti-cancer Compound-Activity-Target database. *Nucleic Acids Res.* **2013**, *41*, D1124–D1129. [CrossRef] [PubMed]
2. Toffoli, G.; Viel, A.; Tumiotto, L.; Biscontin, G.; Rossi, C.; Boiocchi, M. Pleiotropic-resistant phenotype is a multifactorial phenomenon in human colon carcinoma cell lines. *Br. J. Cancer* **1991**, *63*, 51–56. [CrossRef] [PubMed]
3. Duvvuri, M.; Konkar, S.; Funk, R.S.; Krise, J.M.; Krise, J.P. A chemical strategy to manipulate the intracellular localization of drugs in resistant cancer cells. *Biochemistry* **2005**, *44*, 15743–15749. [CrossRef] [PubMed]
4. Genilloud, O. Current challenges in the discovery of novel antibacterials from microbial natural products. *Recent Pat. Antiinfect. Drug Discov.* **2012**, *7*, 189–204. [CrossRef] [PubMed]
5. Stoye, A.; Opatz, T. Synthesis of (–)-Cryptopleurine by Combining Gold (I) Catalysis with a Free Radical Cyclization. *Eur. J. Org. Chem.* **2015**, *2015*, 2149–2156. [CrossRef]
6. Wang, K.; Hu, Y.; Liu, Y.; Mi, N.; Fan, Z.; Wang, Q. Design, synthesis, and antiviral evaluation of phenanthrene-based tylophorine derivatives as potential antiviral agents. *J. Agric. Food Chem.* **2010**, *58*, 12337–12342. [CrossRef] [PubMed]
7. Wang, Z.; Wu, M.; Wang, Y.; Li, Z.; Wang, L.; Han, G.; Chen, F.; Liu, Y.; Wang, K.; Zhang, A.; et al. Synthesis and SAR studies of phenanthroindolizidine and phenanthroquinolizidine alkaloids as potent anti-tumor agents. *Eur. J. Med. Chem.* **2012**, *51*, 250–258. [CrossRef]
8. Jin, H.R.; Jin, S.Z.; Cai, X.F.; Li, D.; Wu, X.; Nan, J.X.; Lee, J.J.; Jin, X. Cryptopleurine targets NF-kappaB pathway, leading to inhibition of gene products associated with cell survival, proliferation, invasion, and angiogenesis. *PLoS ONE* **2012**, *7*, e40355.
9. Yang, C.W.; Lee, Y.Z.; Hsu, H.Y.; Wu, C.M.; Chang, H.Y.; Chao, Y.S.; Lee, S.J. c-Jun-mediated anticancer mechanisms of tylophorine. *Carcinogenesis* **2013**, *34*, 1304–1314. [CrossRef]

10. Kwon, Y.; Song, J.; Lee, H.; Kim, E.Y.; Lee, K.; Lee, S.K.; Kim, S. Design, Synthesis, and Biological Activity of Sulfonamide Analogues of Antofine and Cryptopleurine as Potent and Orally Active Antitumor Agents. *J. Med. Chem.* **2015**, *58*, 7749–7762. [CrossRef]
11. Yang, X.; Shi, Q.; Lai, C.Y.; Chen, C.Y.; Ohkoshi, E.; Yang, S.C.; Wang, C.Y.; Bastow, K.F.; Wu, T.S.; Pan, S.L.; et al. Antitumor agents 295. E-ring hydroxylated antofine and cryptopleurine analogues as antiproliferative agents: Design, synthesis, and mechanistic studies. *J. Med. Chem.* **2012**, *55*, 6751–6761. [CrossRef] [PubMed]
12. Tang, S.; Peng, Z.G.; Zhang, X.; Cheng, X.Y.; Li, W.J.; Jiang, J.D.; Li, Y.H.; Song, D.Q. Synthesis and biological evaluation of 12-benzyl matrinic amide derivatives as a novel family of anti-HCV agents. *Chin. Chem. Lett.* **2016**, *27*, 1052–1057. [CrossRef]
13. Olejníková, P.; Thomay, S.; Pagáč, T.; Ježíková, Z.; Marchalín, Š.; Šafař, P. Antimicrobial activity of newly synthesized thienoquinolizidines derivatives: Inspired by natural plant alkaloids. *Chem. Pap.* **2017**, *71*, 2375–2383. [CrossRef]
14. Pagáč, T.; Šafář, P.; Marchalín, Š.; Ježíková, Z.; Balónová, B.; Šupolíková, M.; Nováková, E.; Kubíčková, J.; Šoral, M.; Sivý, J.; et al. Asymmetric synthesis and study of biological activity of (epi-) benzoanalogues of bioactive phenanthroquinolizidine alkaloids. *Monatshefte Chem.-Chem. Mon.* **2018**, *149*, 1865–1876.
15. Dlugosz, A.; Janecka, A. ABC Transporters in the Development of Multidrug Resistance in Cancer Therapy. *Curr. Pharm. Des.* **2016**, *22*, 4705–4716. [CrossRef] [PubMed]
16. Breier, A.; Gibalova, L.; Seres, M.; Barancik, M.; Sulova, Z. New insight into p-glycoprotein as a drug target. *Anticancer Agents Med. Chem.* **2013**, *13*, 159–170. [CrossRef] [PubMed]
17. Sulova, Z.; Ditte, P.; Kurucova, T.; Polakova, E.; Rogozanova, K.; Gibalova, L.; Seres, M.; Skvarkova, L.; Sedlak, J.; Pastorek, J.; et al. The presence of P-glycoprotein in L1210 cells directly induces down-regulation of cell surface saccharide targets of concanavalin A. *Anticancer Res.* **2010**, *30*, 3661–3668. [PubMed]
18. Polekova, L.; Barancik, M.; Mrazova, T.; Pirker, R.; Wallner, J.; Sulova, Z.; Breier, A. Adaptation of mouse leukemia cells L1210 to vincristine. Evidence for expression of P-glycoprotein. *Neoplasma* **1992**, *39*, 73–77.
19. Pavlikova, L.; Seres, M.; Imrichova, D.; Hano, M.; Rusnak, A.; Zamorova, M.; Katrlik, J.; Breier, A.; Sulova, Z. The expression of P-gp in leukemia cells is associated with cross-resistance to protein *N*-glycosylation inhibitor tunicamycin. *Gen. Physiol. Biophys.* **2016**, *35*, 497–510. [CrossRef]
20. Elefantova, K.; Lakatos, B.; Kubickova, J.; Sulova, Z.; Breier, A. Detection of the Mitochondrial Membrane Potential by the Cationic Dye JC-1 in L1210 Cells with Massive Overexpression of the Plasma Membrane ABCB1 Drug Transporter. *Int. J. Mol. Sci.* **2018**, *19*, 1985. [CrossRef]
21. Bohacova, V.; Seres, M.; Pavlikova, L.; Kontar, S.; Cagala, M.; Bobal, P.; Otevrel, J.; Brtko, J.; Sulova, Z.; Breier, A. Triorganotin Derivatives Induce Cell Death Effects on L1210 Leukemia Cells at Submicromolar Concentrations Independently of P-glycoprotein Expression. *Molecules* **2018**, *23*, 1053. [CrossRef] [PubMed]
22. Pavlikova, L.; Seres, M.; Hano, M.; Bohacova, V.; Sevcikova, I.; Kyca, T.; Breier, A.; Sulova, Z. L1210 Cells Overexpressing ABCB1 Drug Transporters Are Resistant to Inhibitors of the *N*- and *O*-glycosylation of Proteins. *Molecules* **2017**, *22*, 1104. [CrossRef] [PubMed]
23. Šafař, P.; Marchalín, Š.; Prónayová, N.; Vrábel, V.; Lawson, A.M.; Othman, M.; Daich, A. Use of chiral-pool approach into epi-thieno analogues of the scarce bioactive phenanthroquinolizidine alkaloids. *Tetrahedron* **2016**, *72*, 3221–3231. [CrossRef]
24. Seres, M.; Cholujova, D.; Bubencikova, T.; Breier, A.; Sulova, Z. Tunicamycin depresses P-glycoprotein glycosylation without an effect on its membrane localization and drug efflux activity in L1210 cells. *Int. J. Mol. Sci.* **2011**, *12*, 7772–7784. [CrossRef] [PubMed]
25. Hingorani, R.; Deng, J.; Elia, J.; McIntyre, C.; Mittar, D. *Detection of Apoptosis Using the BD Annexin V FITC Assay on the BD FACSVerse™ System*; BD Bioscience Application Note; BD Bioscience: San Jose, CA, USA, 2011; pp. 1–12. Available online: https://www.bdbiosciences.com/documents/BD_FACSVerse_Apoptosis_Detection_AppNote.pdf (accessed on 05 June 2019).
26. Fruci, D.; Cho, W.C.; Nobili, V.; Locatelli, F.; Alisi, A. Drug Transporters and Multiple Drug Resistance in Pediatric Solid Tumors. *Curr. Drug Metab.* **2016**, *17*, 308–316. [CrossRef] [PubMed]
27. Abraham, J.; Salama, N.N.; Azab, A.K. The role of P-glycoprotein in drug resistance in multiple myeloma. *Leuk. Lymphoma* **2015**, *56*, 26–33. [CrossRef] [PubMed]
28. Manallack, D.T. The pK(a) Distribution of Drugs: Application to Drug Discovery. *Perspect. Med. Chem.* **2007**, *1*, 25–38.

29. Bennion, B.J.; Be, N.A.; McNerney, M.W.; Lao, V.; Carlson, E.M.; Valdez, C.A.; Malfatti, M.A.; Enright, H.A.; Nguyen, T.H.; Lightstone, F.C.; et al. Predicting a Drug's Membrane Permeability: A Computational Model Validated With in Vitro Permeability Assay Data. *J. Phys. Chem. B* **2017**, *121*, 5228–5237. [CrossRef]
30. Ueno, S.; Yamazaki, R.; Ikeda, T.; Yaegashi, T.; Matsuzaki, T. Antitumor effect of a novel phenanthroindolizidine alkaloid derivative through inhibition of protein synthesis. *Anticancer Res.* **2014**, *34*, 3391–3397. [PubMed]
31. Hano, M.; Tomasova, L.; Seres, M.; Pavlikova, L.; Breier, A.; Sulova, Z. Interplay between P-Glycoprotein Expression and Resistance to Endoplasmic Reticulum Stressors. *Molecules* **2018**, *23*, 337. [CrossRef] [PubMed]
32. Tainton, K.M.; Smyth, M.J.; Jackson, J.T.; Tanner, J.E.; Cerruti, L.; Jane, S.M.; Darcy, P.K.; Johnstone, R.W. Mutational analysis of P-glycoprotein: Suppression of caspase activation in the absence of ATP-dependent drug efflux. *Cell Death Differ.* **2004**, *11*, 1028–1037. [CrossRef] [PubMed]
33. Gibalova, L.; Seres, M.; Rusnak, A.; Ditte, P.; Labudova, M.; Uhrik, B.; Pastorek, J.; Sedlak, J.; Breier, A.; Sulova, Z. P-glycoprotein depresses cisplatin sensitivity in L1210 cells by inhibiting cisplatin-induced caspase-3 activation. *Toxicol. In Vitro* **2012**, *26*, 435–444. [CrossRef] [PubMed]
34. Crowley, L.C.; Marfell, B.J.; Scott, A.P.; Waterhouse, N.J. Quantitation of Apoptosis and Necrosis by Annexin V Binding, Propidium Iodide Uptake, and Flow Cytometry. *Cold Spring Harb. Protoc.* **2016**, *2016*. [CrossRef] [PubMed]
35. Del Principe, M.I.; Del Poeta, G.; Maurillo, L.; Buccisano, F.; Venditti, A.; Tamburini, A.; Bruno, A.; Cox, M.C.; Suppo, G.; Tendas, A.; et al. P-glycoprotein and BCL-2 levels predict outcome in adult acute lymphoblastic leukaemia. *Br. J. Haematol.* **2003**, *121*, 730–738. [CrossRef] [PubMed]
36. Redza-Dutordoir, M.; Averill-Bates, D.A. Activation of apoptosis signalling pathways by reactive oxygen species. *Biochim. Biophys. Acta* **2016**, *1863*, 2977–2992. [CrossRef] [PubMed]
37. Murad, H.; Hawat, M.; Ekhtiar, A.; AlJapawe, A.; Abbas, A.; Darwish, H.; Sbenati, O.; Ghannam, A. Induction of G1-phase cell cycle arrest and apoptosis pathway in MDA-MB-231 human breast cancer cells by sulfated polysaccharide extracted from Laurencia papillosa. *Cancer Cell Int.* **2016**, *16*, 39. [CrossRef] [PubMed]
38. Pastan, I.; Gottesman, M.M.; Ueda, K.; Lovelace, E.; Rutherford, A.V.; Willingham, M.C. A retrovirus carrying an MDR1 cDNA confers multidrug resistance and polarized expression of P-glycoprotein in MDCK cells. *Proc. Natl. Acad. Sci. USA* **1988**, *85*, 4486–4490. [CrossRef] [PubMed]
39. Gerlier, D.; Thomasset, N. Use of MTT colorimetric assay to measure cell activation. *J. Immunol. Methods* **1986**, *94*, 57–63. [CrossRef]
40. Laemmli, U.K. Cleavage of structural proteins during the assembly of the head of bacteriophage T4. *Nature* **1970**, *227*, 680–685. [CrossRef]
41. Towbin, H.; Staehelin, T.; Gordon, J. Electrophoretic transfer of proteins from polyacrylamide gels to nitrocellulose sheets: Procedure and some applications. *Proc. Natl. Acad. Sci. USA* **1979**, *76*, 4350–4354. [CrossRef]
42. Turakova, K.; Pavlikova, L.; Messingerova, L.; Lakatos, B.; Breier, A.; Sulova, Z. Reduced UDP-glucose Levels Are Associated with P-glycoprotein Over-expression in L1210 Cells and Limit Glucosylceramide Synthase Activity. *Anticancer Res.* **2015**, *35*, 2627–2634. [PubMed]

Sample Availability: Samples of the compounds are available from the authors.

© 2019 by the authors. Licensee MDPI, Basel, Switzerland. This article is an open access article distributed under the terms and conditions of the Creative Commons Attribution (CC BY) license (http://creativecommons.org/licenses/by/4.0/).

molecules

MDPI

Article

A Study of 5-Fluorouracil Desorption from Mesoporous Silica by RP-UHPLC

Monika Šuleková [1,*], Lucia Váhovská [2], Alexander Hudák [1], Lukáš Žid [3] and Vladimír Zeleňák [3]

1 Department of Chemistry, Biochemistry and Biophysics, Institute of Pharmaceutical Chemistry, The University of Veterinary Medicine and Pharmacy in Košice, 041 81 Košice, Slovakia; alexander.hudak@uvlf.sk

2 Department of Chemistry, Biochemistry and Biophysics, Institute of Biochemistry, The University of Veterinary Medicine and Pharmacy in Košice, 041 81 Košice, Slovakia; lucia.vahovska@uvlf.sk

3 Department of Inorganic Chemistry, Faculty of Sciences, P. J. Šafárik University, Moyzesova 11, SK-041 54 Košice, Slovakia; lukas.zid@student.upjs.sk (L.Ž.); vladimir.zelenak@upjs.sk (V.Z.)

* Correspondence: monika.sulekova@uvlf.sk; Tel.: +421-917-360-631

Academic Editor: Josef Jampilek
Received: 29 January 2019; Accepted: 1 April 2019; Published: 3 April 2019

Abstract: In cancer treatment, the safe delivery of the drug to the target tissue is an important task. 5-fluorouracil (5-FU), the well-known anticancer drug, was encapsulated into the pores of unmodified mesoporous silica SBA-15, as well as silica modified with 3-aminopropyl and cyclohexyl groups. The drug release studies were performed in two different media, in a simulated gastric fluid (pH = 2) and in a simulated body fluid (pH = 7) by RP-UHPLC. The simple and rapid RP-UHPLC method for quantitative determination of 5-fluorouracil released from unmodified and modified mesoporous silica SBA-15 was established on ODS Hypersil C18 column (150 × 4.6 mm, 5 μm) eluted with mobile phase consisted of methanol: phosphate buffer in volume ratio of 3:97 (v/v). Separation was achieved by isocratic elution. The flow rate was kept at 1 mL/min, the injection volume was set at 20 μL and the column oven temperature was maintained at 25 °C. The effluent was monitored at 268 nm. This paper provides information about the quantitative determination of the released 5-FU from silica. It was found out that larger amount of the drug was released in neutral pH in comparison with the acidic medium. In addition, surface functionalisation of silica SBA-15 influences the release properties of the drug.

Keywords: mesoporous silica; 5-fluorouracil; desorption; RP-UHPLC

1. Introduction

Over the past three decades, there has been rapid growth in the area of silica-based ordered mesoporous materials as drug delivery systems owing to the great versatility and stability of these mesoporous matrices. MCM-41, MCM-48 and SBA-15 are the most common mesoporous silica materials with the pore size ranging from 2–10 nm and 2D-hexagonal and 3D-cubic structural characteristics [1]. The high surface area, tunable pore diameter, good biocompatibility/biodegradation [2,3] and uniform mesoporous structure of the mesoporous silicas allow the adsorption of drugs and biomolecules into their mesostructures to be then locally released. There are also triggers that can activate the release of the guest molecules, such as heat, pH, light, chemicals, ultrasound or even magnetism [4]. In the family of mesoporous silica materials, SBA-15 silica was studied more than the others, due to its higher hydrothermal stability [5].

The use of silica-based ordered mesoporous materials as drug delivery systems was carried out for the first time in 2001. The first to describe the use of mesoporous silica as drug delivery support were Regí et al. [6], who enclosed ibuprofen in a MCM-41 matrix in an effort to design an

implantable delivery system. Three years later, controlled release of gentamicine sulphate as model drug from SBA-15 was studied by a HPLC method [7]. In addition, the antibiotic amoxicillin has been incorporated into the porous calcined SBA-15 by contacting a solution of the drug in an appropriate solvent with the porous solid. The drug release process from the matrix into a simulated body fluid solution has been studied [8]. In other works, the release of nimodipine from SBA-15 [9], naproxen from MCM-41 [10] and SBA-15 [11], as well as indomethacin from MCM-48 mesoporous silica were studied, too [12].

A great advantage of silica-based ordered mesoporous materials (SMMs) is that these materials can be modified by various functional groups. The surface of SMMs presents a high density of silanol groups, which are also susceptible of undergoing a chemical modification with a large variety of organic groups through functionalization process [13]. Thus, it is possible to modulate the chemical properties of the mesoporous surfaces to achieve the desired properties [14–17]. For example, modification by various functional groups lead to the decreasing release rate of the drug from the pores of silica matrix. Muňoz et al. [18] studied the rate of drug release from the amino-modified MCM-41 silicas with different pore sizes. Their study showed that amino functionalization lead to decreasing the rate of drug release. It can be thought that this delivery rate could be tuned by modifying the interaction between the drug molecule and the silica matrix. Moreover, the organic functionalization of the mesoporous silica materials can influence their biocompatibility [19].

The encapsulation and controlled release of the therapeutic drug into/from the drug delivery material has become still more important for the therapeutic system. The main advantages of this system is especially safety and efficiency and take control over the negative influence of the using drug. Moreover, the drug can be loaded into the pores in a preferably amorphous state, which can increase the drug dissolution properties dramatically [20]. The most of anticancer drugs are known for their low solubility, low stability, short plasma half-life and cytotoxicity to normal cells [21]. One of the problematic drugs that have been widely used in anticancer chemotherapy is 5-fluorouracil.

5-Fluorouracil (5-FU) is a water-soluble pyrimidine analogue (Figure 1), used in cancer treatment that has been particularly effective in the treatment of colorectal cancer [22,23], stomach, breast, and head and neck cancers [24,25]. Despite its water solubility, this antitumor agent suffers from several drawbacks: the oral use of 5-FU exhibits a short plasma half-life (30 min) as a result of its rapid enzymatic metabolism [26], which demands continuous high doses that simultaneously lead to high toxicity, incomplete and non-uniform oral absorption, the development of drug resistance by tumor cells, and nonselective action against normal cells [27,28].

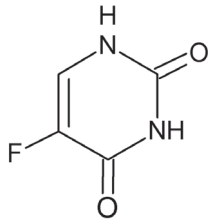

Figure 1. Chemical structure of 5-fluorouracil.

As can be seen from the abovementioned facts, there are several limitations to the use of 5-FU, thus, encapsulation in an appropriate delivery system might contribute to reduce these side effects and improve its oral bioavailability, preventing its premature degradation and decreasing its side effects, increasing concentrations at the target cell site, with lower cytotoxicity for normal cells. Moreover, encapsulation may allow drugs to be released in a controlled way to the cancer area, preventing degradation of the anticancer drug [29]. Until now, controlled loading and releasing of 5-fluorouracil has been studied from several matrices: organic-modified montmorillonite [30], hybrid TiO_2/ZnO nanotubes [31], layered inorganic nanocomposites [28], biodegradable polymers [32], hydrogels [33], mesoporous organosilica [34], magnetic nanocarriers [27], porous silica calcium

phosphate nanocomposites [35] and zeolites [36,37]. To the best of our knowledge, there are only three reports on using silicate nanoparticles, namely thiol-functionalized MCM-41 [38], MCM-48 nanoparticles [39] and magnetic iron oxide/mesoporous silica nanocomposites (*m*-MCM-41) with and without aminopropyl functionalization [40], as carriers for 5-FU. In this work, we report encapsulation and subsequent release of 5-FU from silica SBA-15.

For the characterization of the delivery system such as mesoporous silica, suitable and validated quantitation method is required to assess pharmaceutical parameters such as drug content. Various methods for the determination of 5-FU have been reported, but mostly in biological fluids [41–44]. To the best of our knowledge, the study of controlled loading and releasing of 5-FU from mesoporous silica SBA-15 using reversed-phase ultra-high performance liquid chromatography RP-UHPLC has been not investigated, up to now.

Therefore, the objective of this work was to develop a fast, simple and optimized HPLC method to determine the encapsulation efficiency of 5-FU incorporated in unmodified and modified mesoporous silica SBA-15 and its quantitative analysis. In this study, SBA-15 material was functionalized with 3-aminopropyl and cyclohexyl groups by grafting method. The analysis of 5-FU released from unmodified and modified silica SBA-15 in defined time interval during 48 h was performed in two different media: simulated gastric fluid (pH = 2) and simulated body fluid (pH = 7). This study can be useful in the biomedical applications. The encapsulation and subsequent release of the 5-FU from mesoporous silica should decrease the negative influence of the drug using. The present work describes simple, rapid and precise chromatographic method based on RP-UHPLC mechanism for the desorption study of 5-fluorouracil from mesoporous silica SBA-15.

2. Results and Discussion

2.1. Characterization of SBA-15

To evaluate the textural properties of prepared nanomaterials the method of nitrogen adsorption/desorption at 77 K was used. All measured isotherms are depicted at Figure 2.

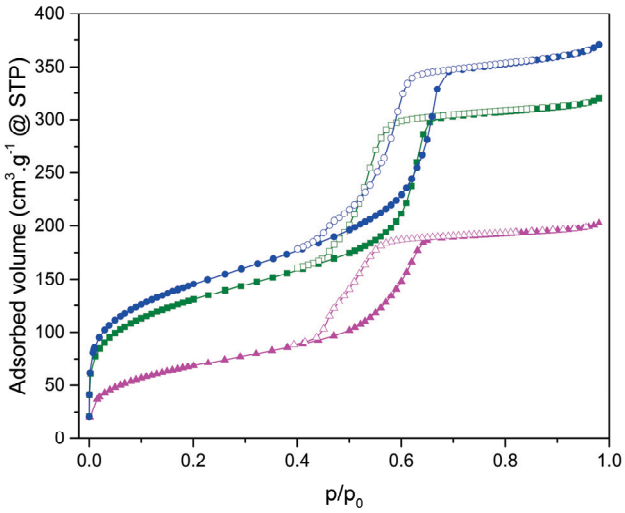

Figure 2. Isotherms of mesoporous silica SBA-15 before (blue) and after modification with 3-aminopropyl (cyan) and cyclohexyl (green) groups.

Isotherms are characterized by the presence of hysteresis loops. According to their shape, they are classified as IVb isotherms type. This type of isotherms is characteristic of mesoporous materials with 2D structure as SBA-15 [45]. The pure SBA-15 is shown in blue at Figure 2. In the range of relative pressure 0–0.05, there is a rapid increase in the adsorbed volume, which is associated with the filling of the micropores. The gradual increase of relative pressure to 0.5 is accompanied by the

steady increase of adsorbed volume caused by the multilayer formation. Capillary condensation, which is manifested by a sharp increase in the isotherm, occurs in the 0.6–0.7 relative pressure range. Above 0.7, no more N_2 was adsorbed because the pores are already filled until 0.95 where is the slight rise of isotherms caused by the condensation of N_2 on the external surface between nanoparticles. Desorption isotherms are shifted to lower relative pressures, which is characteristic nature of SBA-15 type of materials. The amount decreasing of adsorbed volume is proportional to the amount of bound organic groups on the surface and their bulkiness. All computed values are summarized in a Table 1. From the BJH graphs at Figure 3 is evident, that the nanomaterials are characteristic with narrow pore size distribution. Moreover, the nSBA-15 and cSBA-15 increase the number of pores with smaller radius. It is evident from the comparison of all computed values, that the least number of immobilized groups was attached to the surface of cSBA-15. This behaviour could be explained by the bulkiness and hydrophobic nature of cyclohexyl ligand in comparison to 3-aminopropyl group. Another possible explanation (Figure 4) is related to the type of precursor used in modification step. Cyclohexyltrimethoxysilane was used as a modifying agent (Figure 4A), which by bonding to the surface, releases methanol as a by-product (Figure 4B).

Table 1. Textural characteristics of SBA-15 mesoporous drug nanocarriers (S_{BET}—specific surface area, D_P—pore diameter, V_P—volume of pores).

Material	S_{BET} (m^2/g)	D_P (nm)	V_P (cm^3/g)
SBA-15 [1]	528	5	0.496
nSBA-15 [2]	250	4.7	0.289
cSBA-15 [3]	477	4.9	0.435

[1] SBA-15: unmodified silica; [2] nSBA-15: modified with 3-aminopropyl groups; [3] cSBA-15: modified with cyclohexyl groups.

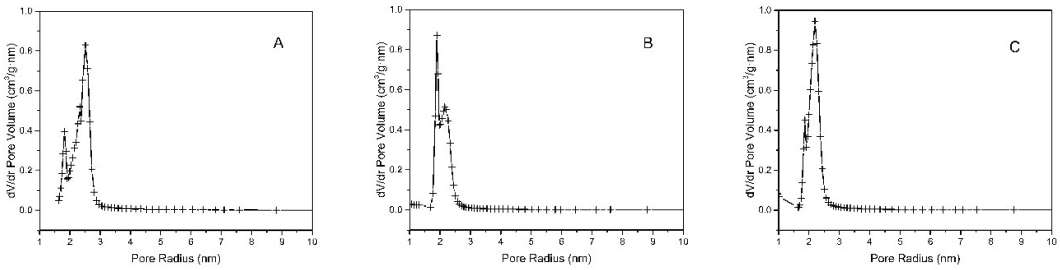

Figure 3. BJH pore size distribution for nanomaterials SBA-15 (**A**), nSBA-15 (**B**) and cSBA-15 (**C**) shows decrease in radius after modification step.

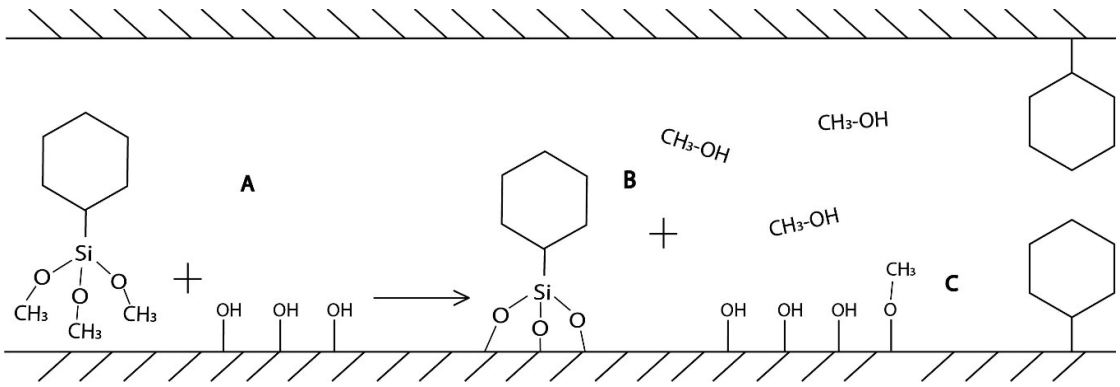

Figure 4. Schematic representation of possible reason for lower number of cyclohexyl groups in comparison to 3-aminopropyl groups. In the process of modification (**A**) the methanol was released as a by-product (**B**) and slowly diffuse into the reaction media. Alcohols can bind to the MPS surface and modify it (**C**), which results in the lower number of free hydroxyl groups.

The binding of chemical groups occurs primarily on the external surface of the MPS, which is associated with a better diffusion of reaction products to the reaction medium. However, if the cyclohexyl group is bonded inside the pores, the methanol is repelled by the cyclohexyl groups bounded to the external surface. Moreover, according to Björklund and Kocherbitov [46], alcohols can bind to the surface of silica and modify it (Figure 4C), which results in less free hydroxyl groups for modification. This synergic effect can reduce the amount of immobilized cyclohexyl groups on the surface of MPS.

A high-resolution transmission electron microscopy (HRTEM) micrograph was taken to prove the morphology of the prepared SBA-15 material. As can be seen at Figure 5, the mesoporous material SBA-15 has regular porous structure with a hexagonal array of uniform channels with average pore diameter about 5 nm. Average pore size suggested by HRTEM micrograph well agree with the result calculated by nitrogen adsorption/desorption measurement.

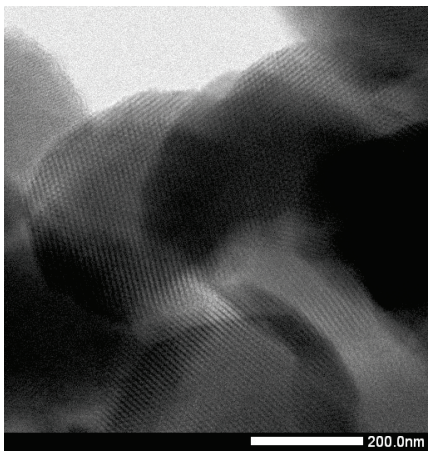

Figure 5. HRTEM micrograph of SBA-15.

Mesoporous materials are stable, and their regular porous structure does not change upon drug adsorption. Regular porous structure and stability of SBA-15 silica and other mesoporous matrices was proven by Small Angle X-ray Scattering (SAXS) in our previous works [10–12,47–50]. Wide Angle X-ray Scattering (WAXS) or XRD measurements do not give useful information, as mesoporous silica matrices have amorphous walls, so no diffraction from the matrix is observed and at high angles (15 to 70°) the XRD patterns of SBA-15 and the 5-flourouracil loaded sample only showed a broad peak at $2\theta = 23–26°$, which is characteristic of amorphous silica, and the characteristic XRD peaks of crystalline 5-fluorouracil were not observed. This finding indicates a good dispersion of 5-FU inside the support mesopores (Figure 6).

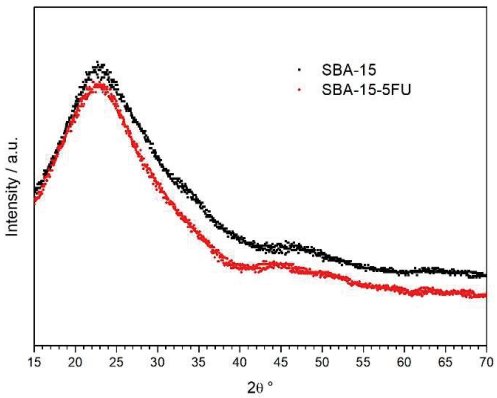

Figure 6. XRD pattern of samples SBA-15 (black) and SBA-15 with 5-fluorouracil loaded (red).

This behaviour is one of the advantages of mesoporous materials as drug delivery systems, which enhances the solubility of hydrophobic drugs. For this reason, these materials are very suitable for delivery of drugs with low water solubility, like 5-fluorouracil [51]. The amount of loaded 5-FU in each sample was obtained by analysing the change in concentration of the solutions before and after the adsorption step. 5-FU was loaded into the pores of the samples by the penetration method. Prior to experiment, a 10 mg/mL 5-FU solution was prepared, and the exact concentration was measured. To 10 mL of 5-FU solution was added 100 mg of nanomaterial. Consequently, the largest amount that can be loaded into the samples is 1 gram of 5-fluorouracil per gram of nanomaterial ($g_{5\text{-FU}}/g$). The loading capacity of pure SBA-15 is 142.3 $mg_{5\text{-FU}}/g$. Nanomaterial nSBA-15 has a loading capacity equals to 184.25 $mg_{5\text{-FU}}/g$. The observed gain can be explained by the improved interaction of 5-FU molecules with the modified surface via hydrogen bonds. The last sample cSBA-15 has loading capacity of 146 $mg_{5\text{-FU}}/g$. The loading capacity of 5-FU was calculated as following Equation (1):

$$\text{5-FU loading capacity} = \frac{\text{weight of loaded 5-FU in the pores}}{\text{weight of whole delivery system}} \quad (1)$$

The amount of drug loaded into the mesoporous samples was determined after subtracting the amount of unloaded drug from the initial amount of drug in loading medium. The exact concentration of 5-FU in media during sample preparation was measured using UV-VIS spectrophotometry.

The encapsulation efficiency for samples 5-FU-SBA-15, 5-FU-nSBA-15 and 5-FU-cSBA-15 was 14.23%, 18.425% and 14.6%, respectively. The encapsulation efficiency was calculated by the following Equation (2):

$$\text{encapsulation efficiency} = \frac{\text{weight of loaded 5-FU in the pores}}{\text{initial weight of 5-FU in loading media}} \times 100\% \quad (2)$$

An infrared spectroscopy method of was used to verify the success of SBA-15 surface modification and subsequent adsorption of 5-fluorouracil. The measured infrared spectra are depicted in Figure 7.

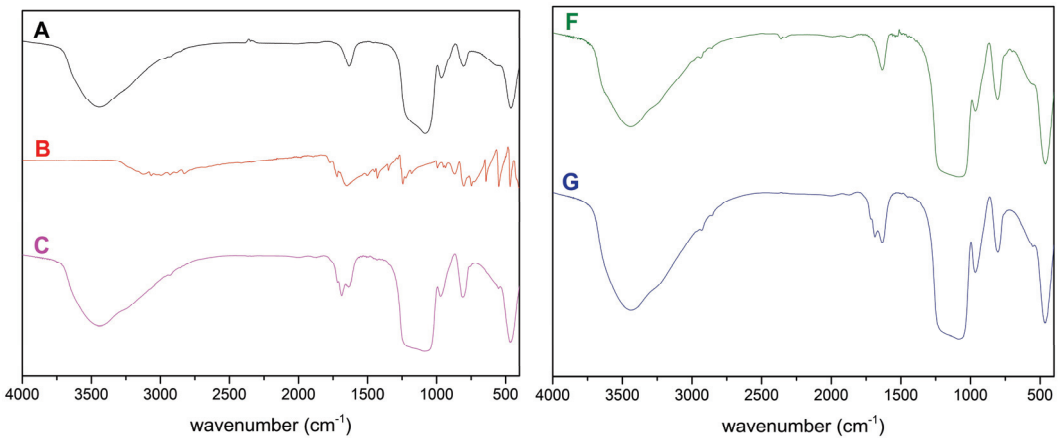

Figure 7. *Cont.*

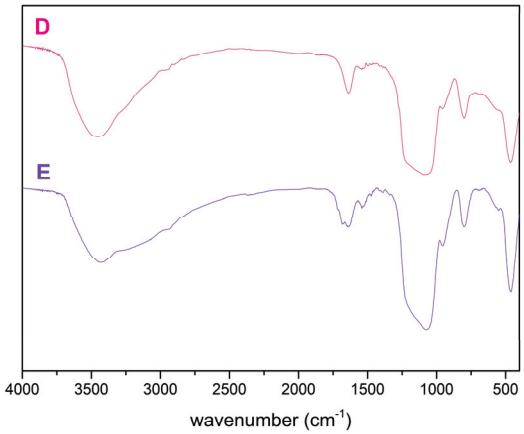

Figure 7. Infrared spectra of nanomaterials SBA-15 (**A**), 5-FU (**B**), 5-FU-SBA-15 (**C**), nSBA-15 (**D**), 5-FU-nSBA-15 (**E**), cSBA-15 (**F**) and 5-FU-cSBA-15 (**G**).

The presence of a broad band in the 3750–3100 cm^{-1} range, which is assigned to the stretching vibrations of O-H and Si-OH bonds, is characteristic of all mesoporous silica samples. Free silanol groups on the surface of mesoporous silica can be detected around 960 cm^{-1}. The presence of asymmetric vibration of the Si-O-Si group overlapping with the Si-O-C and Si-C vibrations is observed in the 1100–1200 cm^{-1} range. Another vibration is located around 790 cm^{-1}, which corresponds to the symmetrical Si-O-Si bond stretch. Because all modifying agents used in this work are organic, characteristic vibrations of organic groups such as the stretching vibration of the C-H group in the 2900 cm^{-1} region or the bending vibration of the CH_2 group in the 1520 cm^{-1} region are visible in the infrared spectra. Because the ligands are only bound to the surface, they occupy only a small portion of the mesoporous silica and the observed vibrations are therefore very weak, but strong enough to prove the success of surface modification. After loading of 5-FU into the pores the infrared spectrum of mesoporous systems slightly changed. Specifically, the most noticeable difference is presence of broader vibration (C, E, G) in the 1500–1750 cm^{-1} range. Most 5-FU is loaded into the pores of nSBA-15, which is evidenced by a broader and more intensive band between 2400–3400 cm^{-1} compared to clear nSBA-15 material.

2.2. Release Study of 5-Fluorouracil from Mesoporous Silica SBA-15 by RP-UHPLC

UHPLC with a photodiode array detector (PAD) was chosen as a simple, fast, and effective separation method for the determination of released 5-FU from studied mesoporous silica SBA-15 samples in defined time intervals (5 min, 15 min, 30 min, 1 h, 2 h, 4 h, 6 h, 24 h and 48 h). To optimize the operating conditions for isocratic RP-UHPLC detection of the released amount of 5-FU a number of parameters such as the column type, mobile phase composition, column temperature and the flow rate were varied. The effect of mobile phase composition on retention time of 5-FU was examined. For solvent A, the common reversed-phase solvents such as methanol and acetonitrile were compared. Methanol gave the best separation of the peaks. Phosphate buffer with pH = 6.9 was used for solvent B. The variations in mobile phase composition consisted of changes in the methanol to phosphate buffer (pH = 6.9) volume ratio. Good separation of 5-FU and short run time were obtained by using a mobile phase consisted of methanol: phosphate buffer (pH = 6.9) in volume ratio of 3:97 (v/v). Optimized chromatographic conditions for determination of released amount of 5-FU from mesoporous silica are summarized in Table 2. These chromatographic conditions were the same for both media: simulated gastric fluid (pH = 2), as well as simulated body fluid (pH = 7).

Table 2. Optimized chromatographic conditions for determination of released amount of 5-FU from mesoporous silica SBA-15.

Parameters	Conditions
Mobile phase	methanol: phosphate buffer, pH 6.9 (3:97, *v*/*v*)
Stationary phase	ODS Hypersil C18 column, (150 × 4.6 mm, 5 μm)
Column Temperature	25 °C
Detection Wavelength	268 nm
Flow rate	1.0 mL/min
Injection volume	20 μL
Retention time	2.9 min

The absorption spectrum of the drug was recorded between 190 and 800 nm. Peak identification was done by comparing the retention times and absorption spectra of the samples with 5-FU standard. The optimal absorption wavelength for 5-FU was determined by measuring the standard solutions. 5-FU exhibits two absorption maxima at 204 and 268 nm (Figure 8). UV radiation below 200 nm (vacuum area) is not used routinely because of the technical complexity of such measurements. Radiation in this region is strongly absorbed by atmospheric oxygen, thus the measurement of the absorption spectra near the 200 nm wavelength is very problematic. Therefore, a second absorption band with a wavelength 268 nm was selected as optimal for determination of the 5-FU released amount.

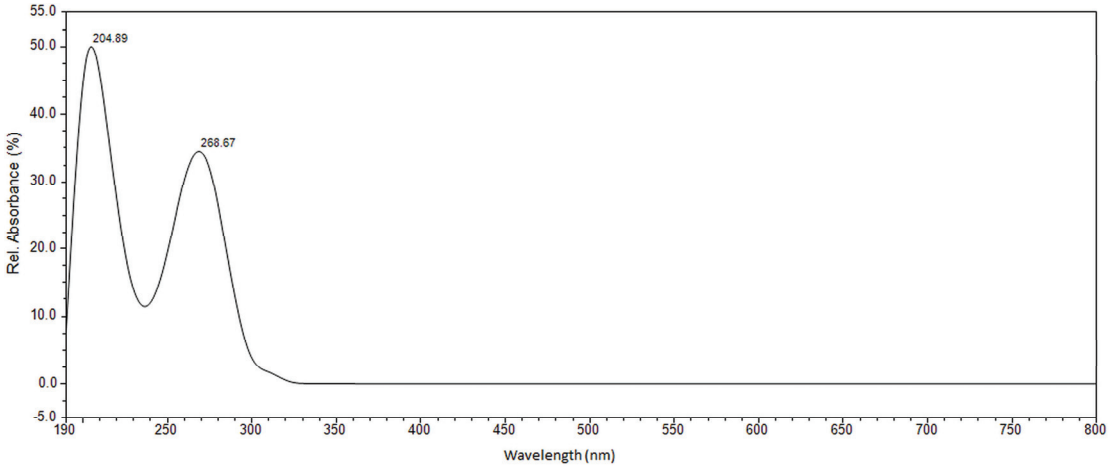

Figure 8. Absorption spectrum of 5-FU.

Under the experimental conditions, the chromatogram of a standard solution of 5-FU, with detection at the absorption maximum of 5-FU is shown in Figure 9, where the concentration of 5-FU is 25 μg/mL. 5-FU standard solution shows one peak at a retention time of 2.9 min.

The released amount of 5-FU was determined by plotting the calibration curve (Figure 9). Standard solutions of 5-FU were prepared and analysed with three replicates and the results were processed with the Chromeleon Version 7.2 software. The calibration curve was constructed by plotting the peak area against each 5-FU concentration for the five standard solutions in water. Under the above-described experimental chromatographic conditions, linear correlation between the peak area and applied concentration was found in the concentration range 1–100 μg/mL, as confirmed by the correlation coefficient of 0.99996. The value of correlation coefficient near 1 indicates very good linearity in the proposed range. The peak area (y) is proportional to the concentration of released 5-FU (x) following the regression equation $y = 0.6892\ x + 0.1062$. The sensitivity of HPLC method was determined by LOD and LOQ. LOD is the lowest concentration of the analyte the method can detect and LOQ is the lowest concentration that can be quantified accurately by the method. The experimentally derived LOD and LOQ for 5-FU were determined to be 0.1134 and 0.3742 μg/mL, respectively.

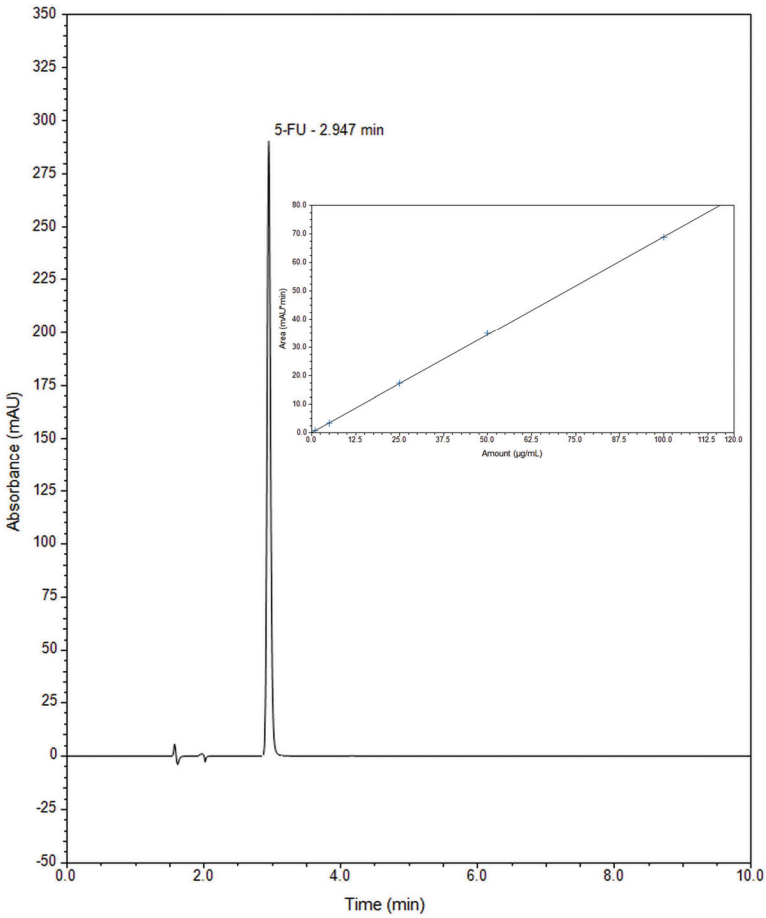

Figure 9. Chromatogram of 5-FU standard solution (25 µg/mL) and calibration curve for 5-FU.

5-FU was encapsulated into the pores of silica SBA-15 and consequently released out of the structure of this matrix during 48 h. The surface of mesoporous silica SBA-15 was modified with various organic groups, such as 3-aminopropyl group (nSBA-15) and cyclohexyl group (cSBA-15) (Figure 10).

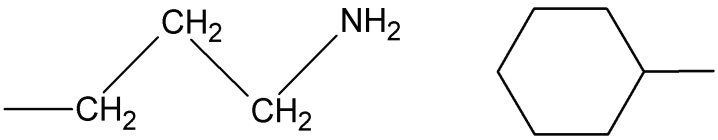

Figure 10. Chemical structure of the 3-aminopropyl (left) and cyclohexyl (right) groups.

The amounts of the drug released from samples were monitored in selected time intervals ranging from 5 min to 48 h by RP-UHPLC in two different media, which are as follows: simulated gastric fluid represented by buffer solution with pH = 2 and simulated body fluid represented by physiological solution with pH = 7. Under the optimized conditions of the present assay, the drug was eluted with optimum resolution at about 2.9 min in acidic and neutral medium. Figure 11 shows typical chromatograms of a working sample solution obtained under the optimized HPLC conditions described in the preceding for both media.

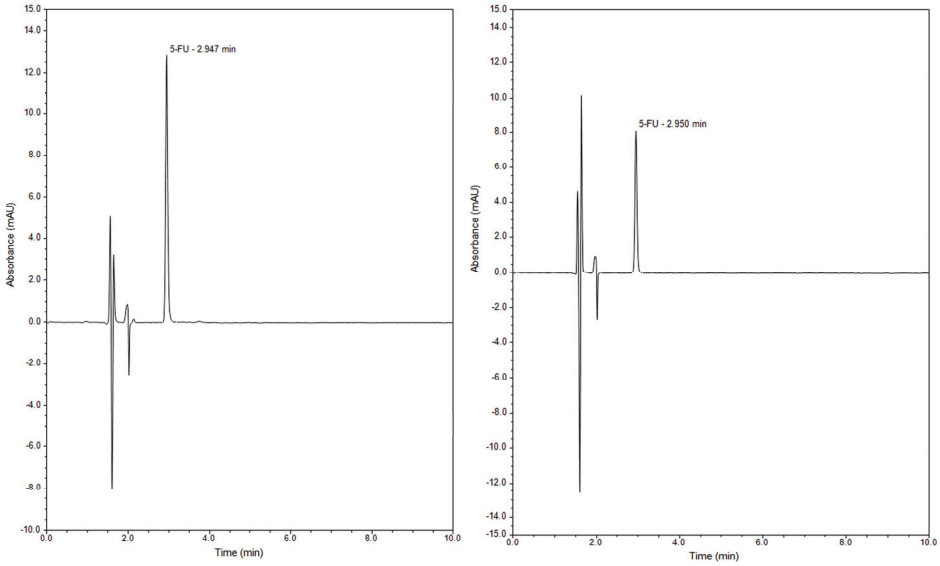

Figure 11. Representative chromatogram of 5-FU released during 4 h from SBA-15 into medium with pH = 2 (left) and medium with pH = 7 (right).

According to the chromatographic results, the curves of the time dependences of 5-FU were constructed. As can be seen from Table 3 and Figure 12, the release profile of 5-FU from prepared mesoporous nanomaterials is strongly dependent on the pH of the release media. Release of 5-FU to an acidic pH environment practically did not occur, as only up to 3.26% was released for unmodified SBA-15. A different situation occurs with the release of 5-fluorouracil in physiological saline. A higher pH significantly improved the solubility of 5-FU. Unmodified SBA-15 material interacts with 5-FU molecules only by the silanol groups on the surface, so nearly all 5-FU was released. Surface modification by 3-aminopropyl groups improve the wettability of the nanomaterial, so the release of 5-FU was faster in comparison to unmodified SBA-15. Moreover, interaction of 5-FU with 3-aminopropyl groups leads to lower released amounts. On the other hand, modification with cyclohexyl groups increases the hydrophobicity. Nanomaterial cSBA-15 cannot mix well with the release medium so the release occurs only from the external surface. All samples are characterized by their fast release profiles. Similar release profiles of 5-FU from mesoporous silica were observed in earlier studies. Egodawatte et al. studied the influence of the solvent in the preparation of 5-FU containing magnetic mesoporous nanoparticles and all release profiles were characterized by a fast initial release of 5-FU [40].

Table 3. Cumulative release of 5-FU from the samples in media with different pH.

Time	Cumulative Release of 5-FU (%)					
	pH 2			pH 7		
	SBA-15	nSBA-15	cSBA-15	SBA-15	nSBA-15	cSBA-15
5 min	3.06	2.26	1.92	31.40	62.82	7.27
15 min	3.20	2.27	1.94	38.77	63.09	10.53
30 min	3.23	2.29	1.94	43.83	64.34	13.94
1 h	3.23	2.32	1.98	50.08	65.43	14.82
2 h	3.24	2.33	1.99	57.76	67.68	15.35
4 h	3.24	2.34	2.00	73.51	71.74	15.57
6 h	3.25	2.36	2.00	87.42	72.99	15.94
24 h	3.26	2.44	2.01	98.48	74.93	16.13
48 h	3.26	2.49	2.03	98.69	75.16	16.81

The pH-dependent release behaviour of the prepared nanocarriers has many advances compared to free 5-FU. 5-FU is commonly given intravenously because of the complications associated with its oral administration. 5-FU is anticancer drug for treatment of various tumours such as colon,

stomach and lung [52]. Using mesoporous silica as drug carrier can improve the site specificity of 5-FU, for example, in colon cancer treatment. In gastrointestinal fluid with low pH, 5-FU stay in pores until the drug delivery system reaches neutral colon pH conditions.

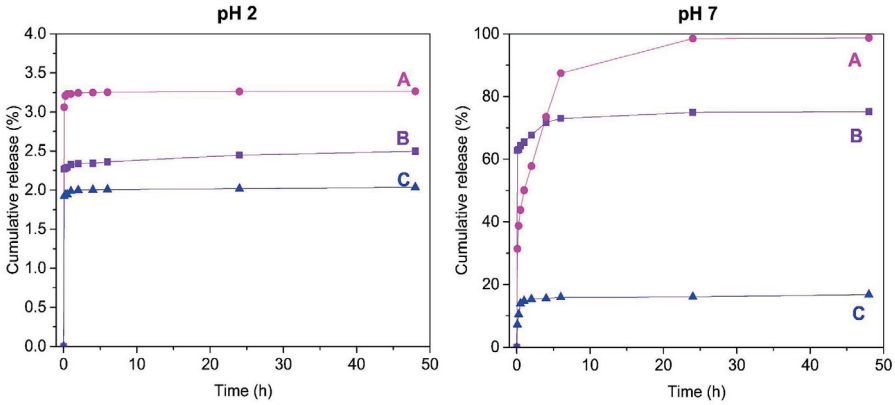

Figure 12. Release profiles of 5-fluorouracil from 5-FU-SBA-15 (**A**), 5-FU-nSBA-15 (**B**) and 5-FU-cSBA-15 (**C**) nanomaterials into the media with different pH.

3. Materials and Methods

3.1. Instruments

Chromatographic separation was carried out using a Dionex UltiMate 3000 RS HPLC system equipped with a Chromeleon Chromatography Data System, Version 7.2 (Thermo Fisher Scientific, Braunschweig, Germany) comprising a quaternary pump, degasser, automated injector, column oven, and photodiode array detector (PAD). Analyses was performed on a chromatographic column (150 × 4.6 mm) filled with the sorbent ODS Hypersil C18 with particle size of 5 µm (Thermo Fisher Scientific). A pH-meter inoLab pH7110 (WTW, Weilheim, Germany) equipped with a combined electrode SenTixR 41 (WTW, Weilheim, Germany) was employed for pH measurements. Syringe filters PVDF 0.45 µm (Fisher Scientific, Pardubice, Czech Republic) were used for solvents and sample filtration throughout the experiment. Infrared spectra of prepared samples were measured using Thermo Fisher Scientific Nicolet 6700 FT-IR spectrophotometer (Thermo Fisher, Madison, WI, USA). All FT-IR measurement was done using KBr pellet method. The concentration of 5-FU in media during sample preparation was measured on Spekord 350 UV-VIS spectrophotometer made by Analytic Jena (Jena, Germany). The texture characterization of mesoporous silica by adsorption/desorption of N_2 at 77 K was done using a Micromeritics ASAP 2020 plus instrument (Norcross, GA, USA). To calculate the specific surface area of prepared nanomaterials the Brunauer-Emmett-Teller (BET) equation was used. Volume of pores was compute using t-plot method and the pore size are calculated using Barrett-Halenda-Joyner method (BHJ). HRTEM images were taken with a JEOL TEM 2100F UHR microscope (Tokio, Japan) operated at 200 kV. A powder sample was sonicated in ethanol for 10 min. Copper grid covered with carbon was used as a support for sample.

3.2. Chemicals and Reagents

All reagents used, such as orthophosphoric acid 85% EMSURE®, potassium dihydrogenphosphate and disodium hydrogenphosphate dodecahydrate (Merck, Darmstadt, Germany), tetraethylorthosilicate (TEOS), cyclohexyltrimethoxysilane (CHTMS) (99%, pK_A = 7.55), (3-aminopropyl)triethoxysilane (APTES, 99%, pK_B = 3.63), poly(ethylene oxide)-poly(propylene oxide)-poly(ethylene oxide) triblock copolymer (Pluronic P-123) and 5-fluorouracil (5-FU, ≥ 99% by HPLC) (Sigma-Aldrich, St. Louis, MO, USA) were at least analytical grade and no further purification was done. Buffer solution with pH = 2 (hydrochloric acid/potassium chloride), according to Veibel was purchased from Honeywell Fluka (Steinheim, Switzerland) and physiological saline with pH = 7 was purchased from Centralchem

(Banská Bystrica, Slovak Republic). Toluene (>99%) was purchased from Sigma-Aldrich and dried over zeolite sieves. Methanol LiChrosolv® was of gradient grade for liquid chromatography (Merck). Water for chromatography LiChrosolv® (Merck) was used for the preparation of a mobile phase and all solutions.

3.3. Preparation of Samples and Standard Solutions

SBA-15 was used as a model mesoporous silica with narrow distribution of pore size and uniform structure. Preparation of SBA-15 material was done by the modified sol-gel process invented by Zhao et al. [5]. Specifically, SBA-15 was prepared by dissolving Pluronic P-123 (8 g) as a structure-directing agent in deionized water (60 g) and adding 2 M HCl (240 g) with continuous stirring (400 rpm) and constant temperature (35 °C) conditions. Then TEOS (17 g) was added dropwise to the mixture after complete dissolution of the Pluronic P-123. Than the mixture was left to stir at 400 rpm under constant temperature (35 °C) for 20 h. Subsequently, the mixture was moved to the furnace heated to 80 °C and left to mature for another 24 h. After that step, the solid product was filtered off, washed out with deionized water and left to dry at laboratory conditions. The final nanomaterial was obtained by calcination using slow temperature rise rate (1 °C/min) and two isothermal steps at 100 °C (3 h) and 550 °C (7 h) followed by slow cooling to laboratory temperature.

Modified SBA-15 was prepared by a grafting method. Prior to modification the SBA-15 was dried at furnace set to 150 °C for 3 h. Subsequently, the SBA-15 (0.5 g) was dispersed in dry toluene (50 mL) in a 100 mL flask and briefly ultrasonicated to break the silica clots into a uniform mixture. Next, APTES or CHTMS (3 mL) was added dropwise to the mixture and left to react under reflux for 24 h. The solid modified product was filtered off and washed with toluene. Soxhlet extraction with toluene as extraction medium was used to remove unreacted modification agent from the mesoporous silica. Finally the material was dried and denoted as nSBA-15 (modified with 3-aminopropyl groups) and cSBA-15 (modified with cyclohexyl groups), respectively.

The impregnation method was used to prepare mesoporous silicas containing 5-FU. 100 mg of each prepared material was immersed in 10 mL of a 10 mg/mL 5-fluorouracil aqueous solution and allowed to mix in closed container under laboratory conditions for 24 h. After 24 h each sample was centrifuged, and 1 mL sample was taken for concentration analysis. Subsequently, the all solid samples were vacuum filtered and dried under vacuum. Prepared samples were denoted as 5-FU-SBA-15, 5-FU-nSBA-15 and 5-FU-cSBA-15.

A stock standard solution of 1.0 mg/mL of 5-FU was prepared in water and subsequent dilutions were carried out to obtain five standard solutions (1.0, 5.0, 25.0, 50.0, 100.0 μg/mL). The standards and samples had previously been filtered through a syringe filter with a pore diameter of 0.45 μm prior to injection and chromatographed.

3.4. Release Study of 5-Fluorouracil from Mesoporous Silica by RP-UHPLC and Chromatographic Conditions

The release of drug from mesoporous silica nanocarriers was studied in two different media: a buffer solution with pH = 2 and a physiological saline solution with pH = 7. Specifically, 10 mg of each sample was immersed in 50 mL of release medium at constant stirring (300 rpm) and temperature (37 °C) conditions. The amount of the 5-FU released from the mesoporous silica SBA-15 was analysed using RP-UHPLC in defined time intervals. To determine the release profile, sampling for chromatographic analysis was performed at predetermined intervals after 5 min, 15 min, 30 min, 1 h, 2 h, 4 h, 6 h, 24 h and 48 h. ODS Hypersil C18 column (150 × 4.6 mm, 5 μm) was used as stationary phase. The HPLC operating mode was isocratic, the column temperature 25 °C. The mobile phase contains a mixture of methanol: phosphate buffer adjust to pH = 6.9 (3:97, *v*/*v*), which was pumped at a flow rate of 1.0 mL/min. The PAD detector was set to collect signals within the spectral range of 190–800 nm. The effluent was monitored at 268 nm and injection volume was set at 20 μL. The samples were filtered through a syringe filter with a pore diameter of 0.45 μm and chromatographed. Optimized chromatographic conditions for determination of released amount of 5-FU from mesoporous silica are

summarized in Table 1. Data acquisition, analysis, and reporting were performed using the Chromeleon Chromatography software, Version 7.2 (Thermo Fisher Scientific, Braunschweig, Germany).

4. Conclusions

An RP-UHPLC method for the determination of released 5-FU from studied mesoporous silica SBA-15 samples in defined time intervals has been developed and is presented here. The release amount of the drug was studied as a function of time in two different media, which are as follows, simulated gastric fluid represented by buffer solution with pH = 2 and simulated body fluid represented by physiological solution with pH = 7. The method uses isocratic elution and is shown to be selective, providing good accuracy and sensitivity. It was found out that surface functionalisation of silica SBA-15 influences the release properties of the drug. The functionalisation of the surface with more bulky ligands such as cyclohexyl led to lower drug release. According to the chromatographic results, larger amount of the drug was released in neutral pH in comparison with the acidic medium.

Author Contributions: L.Ž. performed synthesis of mesoporous silica and surface modification, adsorption of 5-FU into the mesoporous matrices, characterisations of prepared samples by FT-IR. L.Ž. and V.Z. performed characterisation of prepared samples by porosimetry. M.Š. and L.V. performed the release experiments with samples analysis; M.Š., L.V., L.Ž., A.H. and V.Z. analysed the measured data. All authors discussed the contents of the manuscript and approved the submission.

Funding: This research work was supported by Slovak Research and Development Agency under contract No. APVV-15-0520, Bratislava, Slovakia and by Slovak Grant Agency KEGA project No. 008UVLF-4/2017, Košice, Slovakia.

Conflicts of Interest: The authors declare no conflict of interest.

References

1. Yang, P.; Gai, S.; Lin, J. Functionalized mesoporous silica materials for controlled drug delivery. *Chem. Soc. Rev.* **2012**, *41*, 3679–3698. [CrossRef]
2. Böttcher, H.; Slowik, P.; Süβ, W. Sol-Gel Carrier Systems for Controlled Drug Delivery. *J. Sol–Gel Sci. Technol.* **1998**, *13*, 277. [CrossRef]
3. Wu, Z.; Joo, H.; Lee, T.G.; Lee, K. Controlled release of lidocaine hydrochloride from the surfactant-doped hybrid xerogels. *J. Control. Release* **2005**, *104*, 497. [CrossRef]
4. Manzano, M.; Vallet-Regí, M. New developments in ordered mesoporous materials for drug delivery. *J. Mater. Chem.* **2010**, *20*, 5593–5604. [CrossRef]
5. Zhao, D.; Feng, J.; Huo, Q.; Melosh, N.; Fredrickson, G.H.; Chmelka, B.F.; Stucky, G.D. Triblock copolymer syntheses of mesoporous silica with periodic 50 to 300 angstrom pores. *Science* **1998**, *279*, 548–552. [CrossRef] [PubMed]
6. Vallet-Regí, M.; Rámila, A.; Real, R.P.; Pérez-Pariente, J. A new property of MCM-41: Drug delivery system. *Chem. Mater.* **2001**, *13*, 308–311. [CrossRef]
7. Doadrio, A.L.; Sousa, E.M.B.; Doadrio, J.C.; Pérez-Pariente, J.; Izquierdo-Barba, I.; Vallet-Regí, M. Mesoporous SBA-15 HPLC evaluation for controlled gentamicin drug delivery. *J. Control. Release* **2004**, *97*, 125–132. [CrossRef]
8. Vallet-Regí, M.V.; Doadrio, J.C.; Doadrio, A.L.; Barba, I.I.; Pariente, J.P. Hexagonal ordered mesoporous materials as a matrix for the controlled release of amoxicillin. *Solid State Ion.* **2004**, *172*, 435–439. [CrossRef]
9. Yu, H.; Zhai, Q.Z. Mesoporous SBA- 15 molecular sieve as carrier for controlled release of nimodiphine. *Micropor. Mesopor. Mater.* **2009**, *123*, 298–305. [CrossRef]
10. Halamová, D.; Zeleňák, V. NSAID naproxen in mesoporous matrix MCM-41: Drug uptake and release properties. *J. Incl. Phenom. Macrocycl. Chem.* **2012**, *72*, 15–23. [CrossRef]
11. Halamová, D.; Badaničová, M.; Zeleňák, V.; Gondová, T.; Vainio, U. Naproxen drug delivery using periodic mesoporous silica SBA-15. *Appl. Surf. Sci.* **2010**, *256*, 6489–6494. [CrossRef]
12. Zeleňák, V.; Halamová, D.; Almáši, M.; Žid, L.; Zeleňáková, A.; Kapusta, O. Ordered cubic nanoporous silica support MCM-48 for delivery of poorly soluble drug indomethacin. *Appl. Surf. Sci.* **2018**, *443*, 525–534. [CrossRef]

13. Pagar, O.B.; Nagare, H.S.; Chine, Y.M.; Autade, R.R.; Narode, P.R.; Sanklecha, V.M. Mesoporous Silica: A Review. *Int. J. Pharm. Drug Anal.* **2018**, *6*, 1–12.
14. Han, Y.J.; Stucky, G.D.; Butle, A. Mesoporous silicate sequestration and release of proteins. *J. Am. Chem. Soc.* **1999**, *121*, 9897–9898. [CrossRef]
15. Lu, Y.; Fan, H.; Doke, N.; Loy, D.A.; Assink, R.A.; LaVan, D.A.; Brinker, C.J. Evaporation-induced self-assembly of hybrid bridged silsesquioxane film and particulate mesophases with integral organic functionality. *J. Am. Chem. Soc.* **2000**, *122*, 5258–5261. [CrossRef]
16. Hoffmann, F.; Cornelius, M.; Morell, J.; Froba, M. Silica-based mesoporous organic-inorganic hybrid materials. *Angew. Chem-Int. Edit.* **2006**, *45*, 3216–3225. [CrossRef]
17. Kecht, J.; Schlossbauer, A.; Bein, T. Selective functionalization of the outer and inner surfaces in mesoporous silica nanoparticles. *Chem. Mater.* **2008**, *20*, 7207–7214. [CrossRef]
18. Munoz, B.; Rámila, A.; Pérez-Pariente, J.; Díaz, I.; Vallet-Regí, M. MCM-41 Organic modification as drug delivery rate regulator. *Chem. Mater.* **2003**, *15*, 500–503. [CrossRef]
19. Wang, G.; Otuonye, A.N.; Blair, A.; Denton, K.; Tao, Z.; Asefa, T. Functionalized mesoporous materials for adsorption and release of different drug molecules: A comparative study. *J. Solid State Chem.* **2009**, *182*, 1649–1660. [CrossRef]
20. Maleki, A.; Kettiger, H.; Schoubben, A.; Rosenholm, J.M.; Ambrogi, V.; Hamidi, M. Mesoporous silica materials: From physico-chemical properties to enhanced dissolution of poorly water-soluble drugs. *J. Control. Release* **2017**, *262*, 329–347. [CrossRef]
21. Zhu, K.; Ye, T.; Liu, J.; Peng, Z.; Xu, S.; Lei, J.; Deng, H.; Li, B. Nanogels fabricated by lysozyme and sodium carboxymethyl cellulose for 5-fluorouracil controlled release. *Int. J. Pharm.* **2013**, *441*, 721–727. [CrossRef] [PubMed]
22. Meyerhardt, J.A.; Mayer, R.J. Systemic therapy for colorectal cancer. *N. Engl. J. Med.* **2005**, *352*, 476–487. [CrossRef]
23. Longley, D.B.; Harkin, D.P.; Johnston, P.G. 5-fluorouracil: Mechanisms of action and clinical strategies. *Nat. Rev. Cancer* **2003**, *3*, 330–338. [CrossRef] [PubMed]
24. Wang, X.; Lin, J.; Zhang, X.; Liu, Q.; Xu, Q.; Tan, R.-X.; Guo, Z. 5-Fluorouracil–cisplatin adducts with potential antitumor activity. *J. Inorg. Biochem.* **2003**, *94*, 186–192. [CrossRef]
25. Rich, T.A.; Shepard, R.C.; Mosley, S.T. Four decades of continuing innovation with fluorouracil: Current and future approaches to fluorouracil chemoradiation therapy. *J. Clin. Oncol.* **2004**, *22*, 2214–2232. [CrossRef]
26. Mundargi, R.C.; Rangaswamy, V.; Aminabhavi, T.M. A novel method to prepare 5-fluorouracil, an anti-cancer drug, loaded microspheres from poly(N-vinylcaprolactam-co-acrylamide) and controlled release studies. *Des. Monomers. Polym.* **2010**, *13*, 25–336. [CrossRef]
27. Arias, J.L.; López-Viota, M.; Delgado, Á.V.; Ruiz, M.A. Iron/ethylcellulose (core/shell) nanoplatform loaded with 5-fluorouracil for cancer targeting. *Colloid Surface B* **2010**, *77*, 111–116. [CrossRef]
28. Kevadiya, B.D.; Patel, T.A.; Jhala, D.D.; Thumbar, R.P.; Brahmbhatt, H.; Pandya, M.P.; Rajkumar, S.; Jena, P.K.; Joshi, G.V.; Gadhia, P.K.; et al. Layered inorganic nanocomposites: A promising carrier for 5-fluorouracil (5-FU). *Eur. J. Pharm. Biopharm.* **2012**, *81*, 91–101. [CrossRef] [PubMed]
29. Vilaça, N.; Machado, A.F.; Morais-Santos, F.; Amorim, R.; Neto, A.P.; Logodin, E.; Pereira, M.F.R.; Sardo, M.; Rocha, J.; Parpot, P.; et al. Comparison of different silica microporous structures as drug delivery systems for in vitro models of solid tumors. *RSC Adv.* **2017**, *7*, 13104–13111.
30. Gârea, S.; Mihai, A.; Ghebaur, A.; Nistor, C.; Sârbu, A. Porous clay heterostructures: A new inorganic host for 5-fluorouracil encapsulation. *Int. J. Pharm.* **2015**, *491*, 299–309. [CrossRef] [PubMed]
31. Faria, H.A.M.; de Queiroz, A.A.A. A novel drug delivery of 5-fluorouracil device based on TiO_2/ZnS nanotubes. *Mater. Sci. Eng. C.* **2015**, *56*, 260–268. [CrossRef] [PubMed]
32. Cai, X.; Zhao, Q.; Luan, Y.; Jiang, Y.; Shi, J.; Shao, W. Polymer fibrous materials composed of sodium carboxymethylcellulose and poly(vinyl alcohol) for a hydrophilic anticancer drug release. *J. Disper. Sci. Technol.* **2012**, *33*, 835–839. [CrossRef]
33. Bayramgil, N.P. Synthesis, characterization and drug release behavior of poly(1-vinyl 1,2,4-triazole) hydrogels prepared by gamma irradiation. *Colloid Surface B* **2012**, *97*, 182–189. [CrossRef] [PubMed]
34. Moorthy, M.S.; Park, S.S.; Fuping, D.; Hong, S.H.; Selvaraj, M.; Ha, C.S. Step-up synthesis of amidoxime-functionalised periodic mesoporous organosilicas with an amphoteric ligand in the framework for drug delivery. *J. Mater. Chem.* **2012**, *22*, 9100–9108. [CrossRef]

35. El-Ghannam, A.; Ricci, K.; Malkawi, A.; Jahed, K.; Vedantham, K.; Wyan, H.; Allen, L.D.; Dréau, D. A ceramic-based anticancer drug delivery system to treat breast cancer. *J. Mater. Sci. Mater. Med.* **2010**, *21*, 2701–2710. [CrossRef] [PubMed]
36. Larsen, S.C. Nanocrystalline zeolites and zeolite structures: Synthesis, characterization, and applications. *J. Phys. Chem. C* **2007**, *111*, 18464–18474. [CrossRef]
37. Petushkov, A.; Intra, J.; Graham, J.B.; Larsen, S.C.; Salem, A.K. Effect of crystal size and surface functionalization on the cytotoxicity of silicalite-1 nanoparticles. *Chem. Res. Toxicol.* **2009**, *22*, 1359–1368. [CrossRef] [PubMed]
38. Murugan, B.; Ramana, L.N.; Gandhi, S.; Sethuraman, S.; Krishnan, U.M. Engineered chemoswitchable mesoporous silica for tumor-specific cytotoxicity. *J. Mater. Chem. B* **2013**, *1*, 3494–3505. [CrossRef]
39. Hodali, H.A.; Marzouqa, D.M.; Tekfa, F.Z. Evaluation of mesoporous silicate nanoparticles for the sustained release of the anticancer drugs: 5-fluorouracil and 7-hydroxycoumarin. *J. Sol-Gel Sci. Technol.* **2016**, *80*, 417–425. [CrossRef]
40. Egodawatte, S.; Dominguez, S., Jr.; Larsen, S.C. Solvent effects in the development of a drug delivery system for 5-fluorouracil using magnetic mesoporous silica nanoparticles. *Micropor. Mesopor. Mater.* **2017**, *237*, 108–116. [CrossRef]
41. Yang, L.; Chu, J.S.; Fix, J.A. Colon-specific drug delivery: New approaches and in vitro/in vivo evaluation. *Int. J. Pharm.* **2002**, *235*, 1–15. [CrossRef]
42. Anderson, D.; Kerr, D.J.; Blesing, C.; Seymour, L.W. Simultaneous gas chromatographic-mass spectrophotometric determination of alpha-fluoro-beta-alanine and 5-fluorouracil in plasma. *J. Chromatogr. B Biomed. Sci. Appl.* **1997**, *688*, 87–93. [CrossRef]
43. Barberi-Heyob, M.; Merlin, J.L.; Weber, B. Analysis of 5-fluorouracil in plasma and urine by high-performance liquid chromatography. *J. Chromatogr.* **1992**, *581*, 281–286. [CrossRef]
44. Iwamoto, M.; Yoshida, S.; Hirose, S. Fluorescence determination of 5-fluorouracil and 1-(tetrahydro-2-furanyl)-5-fluorouracil in blood serum by high-performance liquid chromatography. *J. Chromatogr.* **1984**, *310*, 151–157. [CrossRef]
45. Sing, K.S.W. Reporting physisorption data for gas/solid systems with special reference to the determination of surface area and porosity. *Pure Appl. Chem.* **1985**, *57*, 603–619. [CrossRef]
46. Björklund, S.; Kocherbitov, V. Alcohols react with MCM-41 at room temperature and chemically modify mesoporous silica. *Sci. Rep.* **2017**, *7*, 9960. [CrossRef] [PubMed]
47. Beňová, E.; Zeleňák, V.; Halamová, D.; Almáši, M.; Petruľová, V.; Psotka, M.; Zeleňáková, A.; Bačkor, M.; Hornebecq, V. A drug delivery system based on switchable photo-controlled p-coumaric acid derivatives anchored on mesoporous silica. *J. Mater. Chem. B* **2017**, *5*, 817–825. [CrossRef]
48. Zeleňák, V.; Beňová, E.; Almáši, M.; Halamová, D.; Hornebecq, V.; Hronský, V. Photo-switchable nanoporous silica supports for controlled drug delivery. *New J. Chem.* **2018**, *42*, 13263–13271. [CrossRef]
49. Zeleňák, V.; Halamová, D.; Zeleňáková, A.; Girman, V. Periodic 3D nanoporous silica modified by amine or SPION nanoparticles as NSAID delivery system. *J. Porous Mater.* **2016**, *23*, 1633–1645. [CrossRef]
50. Zeleňák, V.; Hornebecq, V.; Llewellyn, P. Zinc(II)-benzoato complexes immobilised in mesoporous silica host. *Micropor. Mesopor. Mater.* **2005**, *83*, 125–135. [CrossRef]
51. Tzankov, B.; Voycheva, C.; Aluani, D.; Yordanov, Y.; Avramova, K.; Tzankova, V.; Spassova, I.; Kovacheva, D.; Yoncheva, K. Improvement of dissolution of poorly soluble glimepiride by loading on two types of mesoporous silica carriers. *J. Solid State Chem.* **2019**, *271*, 253–259. [CrossRef]
52. Shishu; Gupta, N.; Aggarwal, N. Stomach-specific drug delivery of 5-fluorouracil using floating alginate beads. *AAPS Pharm. Sci. Tech.* **2007**, *8*, E143–E149. [CrossRef] [PubMed]

Sample Availability: Samples nSBA-15, cSBA-15, 5-FU-SBA-15, 5-FU-nSBA-15 and 5-FU-cSBA-15 are available from the authors.

© 2019 by the authors. Licensee MDPI, Basel, Switzerland. This article is an open access article distributed under the terms and conditions of the Creative Commons Attribution (CC BY) license (http://creativecommons.org/licenses/by/4.0/).

molecules

MDPI

Article

Design, Synthesis, and Biological Evaluation of Novel Nitrogen Heterocycle-Containing Ursolic Acid Analogs as Antitumor Agents

Wenzhi Wang †, Lei Lei †, Zhi Liu, Hongbo Wang * and Qingguo Meng *

School of Pharmacy, Key Laboratory of Molecular Pharmacology and Drug Evaluation (Yantai University), Ministry of Education, Collaborative Innovation Center of Advanced Drug Delivery System and Biotech Drugs in Universities of Shandong, Yantai University, Yantai 264005, China; wxwnx123@163.com (W.W.); 18363855773@163.com (L.L.); zhi_liu0812@163.com (Z.L.)

* Correspondence: hongbowangyt@163.com (H.W.) qinggmeng@163.com (Q.M.); Tel.: +86-535-6706022 (Q.M.); Fax: +86-535-6706066 (H.W.)

† Authors contributed equally.

Received: 21 January 2019; Accepted: 19 February 2019; Published: 1 March 2019

Abstract: Nineteen ursolic acid analogues were designed, synthesized, and evaluated for their antiproliferative activity against the Hela and MKN45 cell lines. Some compounds containing a piperazine moiety displayed moderate to high levels of antitumor activities against the tested cancer cell lines. The most potent compound shares the IC_{50} value of 2.1 μM and 2.6 μM for the Hela and MKN45 cell lines, respectively. Further mechanism studies and in vivo antitumor studies have shown that it decreased the apoptosis regulator (BCL2/BAX) ratio, disrupted mitochondrial potential and induced apoptosis, and suppressed the growth of Hela xenografts in nude mice.

Keywords: ursolic acid analogues; synthesis; nitrogen heterocycles; apoptosis; antitumor activity

1. Introduction

Ursolic acid (3*β*-hydroxy-12-urs-12-en-28-oic acid, UA) is a pentacyclic triterpenoid that occurs naturally in many vegetables, fruits, and Chinese medicinal herbs [1,2]. UA and its derivatives possess extensive pharmacological effects, including antiviral [3], antibacterial [4,5], anticancer [6,7], antiosteoporosis [8], antidiabetic [9,10], anti-inflammatory, and hepatoprotective activity [11,12]. In recent years, increasing attention has been focused on the antitumor activity and the possible mechanisms of UA and its derivatives. It has been reported that they exert antitumor activity by a number of different mechanisms. These include inducing apoptosis and differentiation, inhibition of proliferation and angiogenesis, promotion of chemosensitization, and induction of cell cycle arrest [13]. Intense efforts have been made to endow UA with higher water solubility and to achieve an improved antineoplastic effect [2,14–16].

Nitrogen heterocycles are significant structural components of most new synthetic molecules that are endowed with significant biological activity [17,18] and pharmaceuticals. More than 59% of unique small molecule drugs that are approved by the FDA contain nitrogen heterocycles [19]. Studies showed that 3-oxo-UA-triazolyl derivatives with *o*-bromo, *o*-chloro, or *o*-methoxy substitution on the aromatic ring more potently inhibit the growth of MCF-7 and THP-1 cancer cell lines [20]. UA analogues containing an acyl piperazine moiety at C-28 exhibit high inhibitory activity against MGC-803 and Bcap-37 cancer cell lines and promote apoptosis [21]. In addition, some UA derivatives containing quinoline displayed potent antitumor activity against MDA-MB-231, Hela, and SMMC-7721 cell lines [22].

Using a drug discovery strategy that is based on nitrogen heterocycles, nineteen UA analogues containing nitrogen heterocycles were designed and synthesized (Schemes 1–3). Their antitumor activities were evaluated and the possible mechanism of Hela cell growth inhibition was also investigated.

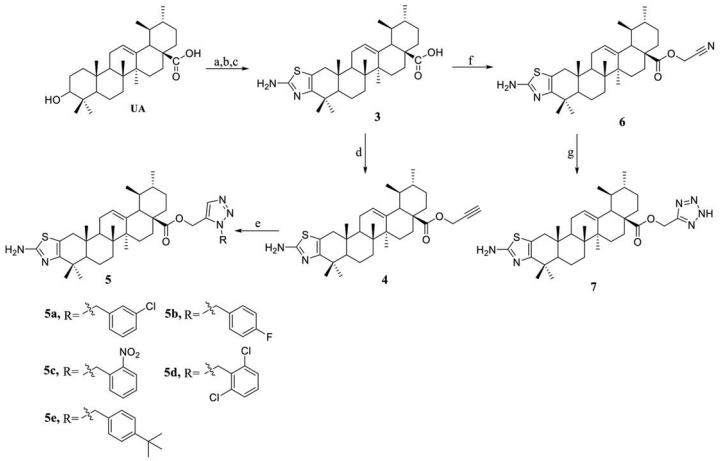

Scheme 1. Synthesis of compounds **3–7.** Reagents and conditions: (**a**) PCC, $CHCl_3$, rt, 6 h (**b**) pyridinium tribromide, HOAc, rt, 6 h (**c**) thiourea, 80 °C, 10 h (**d**) 3-bromo-propyne, K_2CO_3, *N*,*N*-dimethylformamide (DMF), 60 °C 1 h (**e**) N_3-R, $CuSO_4 \cdot 5H_2O$, sodium ascorbate, EtOH, H_2O, rt, 4 h (**f**) chloroacetonitrile, K_2CO_3, DMF, 60 °C 1 h (**g**) NaN_3, $ZnCl_2$, isopropanol/H_2O, 85 °C, 6 h.

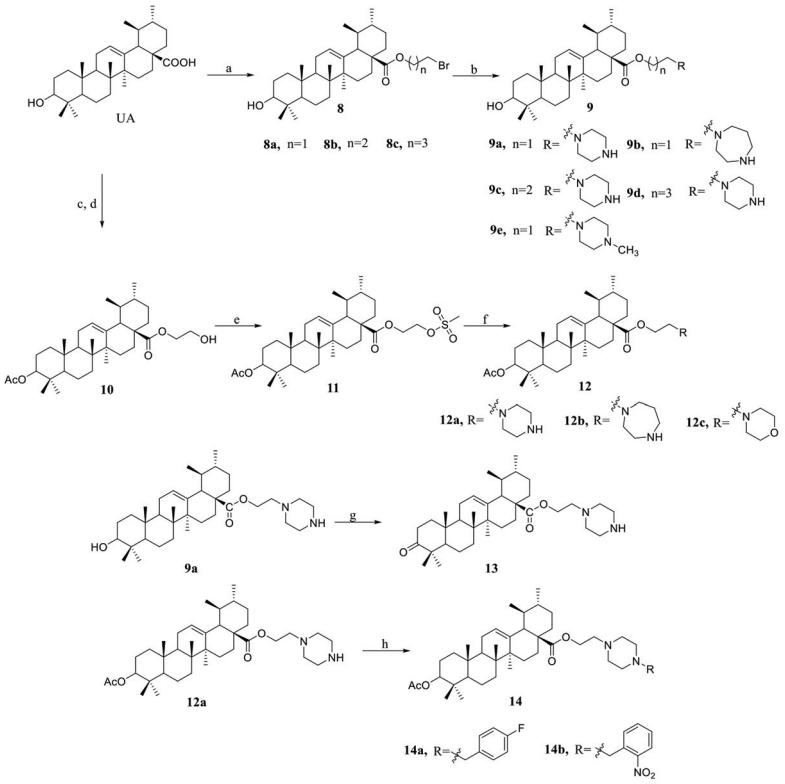

Scheme 2. Synthetic pathways of compounds **8–14**. Reagents and conditions: (**a**) 1,2-dibromoethane or 1,3-dibromopropane or 1,4-dibromobutane, K_2CO_3, DMF, 60 °C, 1 h (**b**) piperazine or homopiperazine or 1-methylpiperazine, K_2CO_3, DMF, 80 °C, 30–60 min (**c**) Ac_2O, pyridine, 0 °C~r.t, 15 h (**d**) 2-chloroethanol, K_2CO_3, DMF 60 °C, 3 h (**e**) MsCl, pyridine, 10 °C~r.t, 3 h (**f**) piperazine or homopiperazine or morpholine, K_2CO_3, DMF, 60 °C, 30 min (**g**) PCC, $CHCl_3$, 0 °C, 10 h (**h**) 4-fluorobenzyl bromide or 2-nitrobenzyl bromide, K_2CO_3, DMF, 60 °C 1 h.

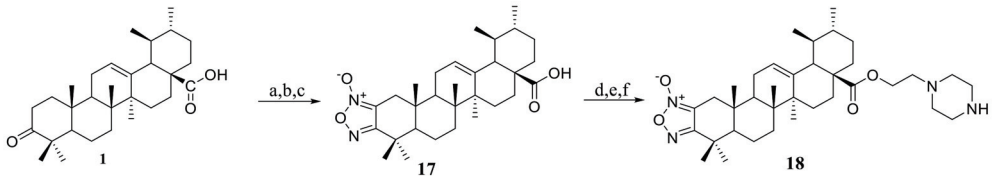

Scheme 3. Synthesis of **17** and **18**. Reagents and conditions: (**a**) isoamyl nitrite, *t*-BuOK, *t*-BuOH, r.t, 2.5 h (**b**) hydroxylamine hydrochloride, pyridine, 110 °C, 2 h (**c**) EtOH, NaOH, NaOCl, rt, 2 min (**d**) 2-chloroethanol, K_2CO_3, DMF, 60 °C, 3 h (**e**) MsCl, pyridine, 10 °C~r.t, 3 h (**f**) piperazine, K_2CO_3, DMF, 60 °C, 30 min.

2. Results and Discussion

2.1. Chemistry

The compounds were synthesized, as outlined in the Schemes 1–3. The initial key intermediate **3** was synthesized according to published protocols [23]. As shown in Scheme 1, compound **3** was treated with 3-bromo-1-propyne or chloroacetonitrile in *N*,*N*-dimethylformamide (DMF), followed by a click reaction with corresponding azides to introduce a triazole or tetrazole moiety (**5a**–**e** and **7**). Compounds **8a**–**c** were synthesized from UA and dibromoalkane, and then treated with piperazine, homopiperazine, or 1-methylpiperazine to gain derivatives **9a**–**e** with a moderate yield (38–43%). Among them, compounds **9a** and **9c** have been reported as antitumor agents by M.C. Liu and X. Li, respectively [21,24]. UA was subjected to acetylation and reacted with 2-chloroethanol to obtain compound **10**, followed by sulfonylation to generate derivative **11**. Subsequently, compound **11** was treated with piperazine, homopiperazine, or morpholine to afford derivatives **12a**–**c** with a yield of 71–75%. Compound **13** was synthesized from compound **9a** by oxidation with PCC in chloroform. Compound **12a** was treated with 4-fluorobenzyl or 2-nitrobenzyl bromide to generate derivatives **14a**–**b** (Scheme 2).

Compound **17**, bearing a furazan moiety at C-2 and C-3 of UA, was synthesized according to the published method [25]. It was further spliced with an ethyl-piperazine to yield compound **18** (Scheme 3). All of the target compounds were purified by silica gel column chromatography. ^{1}H-NMR, ^{13}C-NMR and HR-MS spectra of compounds are shown in Supplementary Materials.

2.2. Biological Evaluation

The target compounds were screened for antiproliferative activity against Hela and MKN45 cancer cell lines using an MTT assay. Cisplatin and UA were used as positive controls and the preliminary results are presented in Table 1. Compounds **5a**–**e** and **7** shared low to moderate antiproliferative activity (inhibition rates from 1–45%) against Hela and MKN45 cancer cells at the tested concentration (10 μM). Compounds **9a**, **9c**, **12a**, **12b**, **13**, **14a,** and **18** displayed much higher activity than UA and possessed IC_{50} values that were lower than 10 μM. Nevertheless, derivatives **9e**, **12c, 14b,** and **17** showed moderate to low activity against the two cancer cell lines.

The structure activity relationship studies revealed that the introduction of thiazole on A ring and triazole or tetrazole moiety on C-28 have little help to improve antitumor activities. The introduction of piperazine or homopiperazine can significantly improve the antitumor activity. The length of the carbon chains between the carboxyl and piperazine moiety of compounds **9a**, **9c,** and **9d** could have affected the antiproliferative activity. The two- or three-carbon chain linker appears to the optimum, **9a** and **9c** with a straight two- and three -carbon chain showed good antitumor activities against the two cell lines. Compounds **12a** and **12b** possess more potent anticancer activity when compared with **9a** and **9b**, which may be attributed to the introduced acetyl group. **14a** showed much higher antiproliferative activity than both UA and cisplatin with IC_{50} values of 2.1 μM and 2.6 μM for Hela and MKN45, respectively. Compound **14b** displayed weaker antiproliferative activity as compared

with UA. These results demonstrated that 4-fluorobenzyl and piperazine moieties are the crucial anticancer functional groups of these compounds.

Table 1. Cytotoxic activities of the compounds against Hela and MKN45 cell lines.

Compound	Inhibition Rates [a]		IC_{50} (μM) [b]	
	Hela	MKN45	Hela	MKN45
UA	13%	18%	15.1 ± 2.7	16.7 ± 1.4
5a	1%	31%	>20	>20
5b	2%	35%	>20	>20
5c	16%	45%	>20	>20
5d	3%	31%	NT[c]	NT
5e	2%	32%	NT	NT
7	1%	35%	NT	NT
9a	59%	51%	9.8 ± 1.8	7.4 ± 1.9
9b	34%	29%	>20	>20
9c	61%	55%	9.3 ± 0.5	7.9 ± 0.2
9d	9%	10%	16.2 ± 0.8	19.3 ± 0.3
9e	24%	27%	NT	NT
12a	81%	77%	6.4 ± 0.3	6.4 ± 0.1
12b	89%	75%	7.3 ± 0.2	6.2 ± 0.5
12c	8%	0%	NT	NT
13	58%	61%	8.5 ± 0.3	8.9 ± 0.1
14a	89%	84%	2.6 ± 1.1	2.1 ± 0.3
14b	16%	7%	NT	NT
17	3%	3%	NT	NT
18	90%	86%	3.9 ± 0.6	4.5 ± 0.2
CDDP [d]	77%	62%	15.1 ± 0.9	2.8 ± 0.1

[a] Inhibition rate of cells treated with 10 μM concentration for 72 h. [b] The concentration (μM) of compound that inhibited 50% of cell growth at 72 h after treatment. [c] Not tested. [d] Cisplatin, positive control.

Since the inhibition of apoptosis is one of hallmarks of cancer, the effects of compound **14a** on cell cycle progression were examined by the propidium iodide staining method. The results showed that compound **14a**, but not UA, at a concentration of 5 μM increased the proportion of cells in the sub-G1 phase (Figure 1A). This indicated that **14a** induced cell death. Consistent with this, western blotting showed that **14a** increased the abundance of cleaved poly-ADP ribose polymerase (PARP), which is a biomarker of apoptosis (Figure 1B). The disruption of the mitochondrial membrane potential, regulated by BCL2 family of proteins, such as BCL2 and BAX, is a mechanism that triggers apoptosis following treatment by anticancer drugs. Our results showed that treatment with **14a** decreased the expression of BCL2, one of the main mitochondrial-associated antiapoptotic proteins. **14a** also increased the expression of BAX, a key mitochondrial-associated apoptotic protein, in a dose-dependent manner (Figure 1C). Therefore, our results suggest that compound **14a** induces apoptosis via the intrinsic mitochondrial pathway.

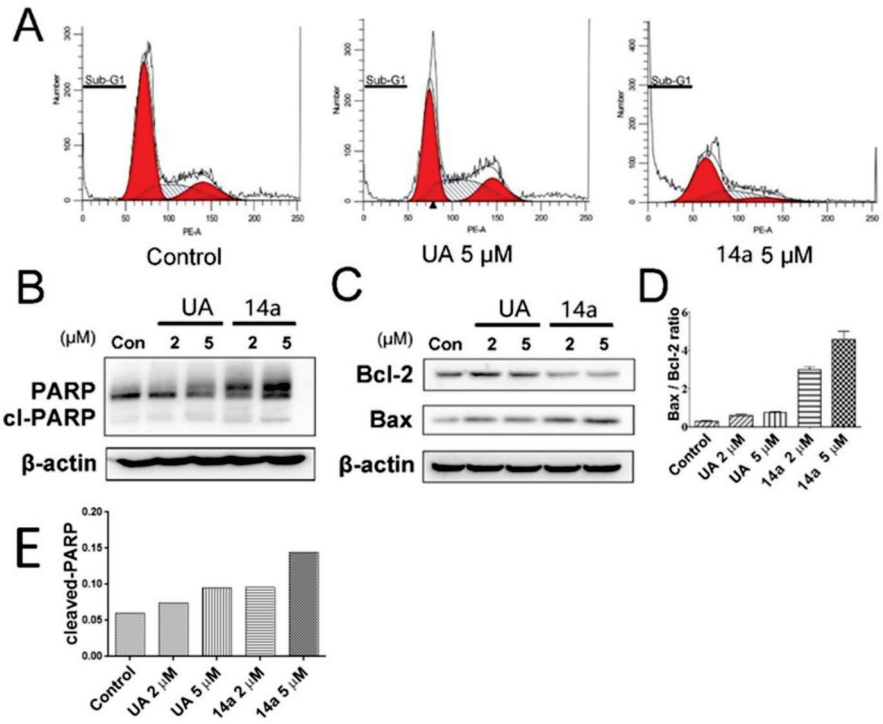

Figure 1. Apoptotic profile of compound **14a** in Hela cells. (**A**) DNA cell cycle analyses of Hela cells exposed to **14a**. The cells were treated with indicated concentrations of **14a** for 24 h and stained with propidium iodide (PI, 50 μg/mL) to determine DNA fluorescence and cell cycle phase distribution. (**B**) and (**C**) Effect of **14a** on the expression of key apoptotic-related proteins. Cells (2×10^5) were treated with 2 μM or 5 μM of **14a** for 24 h before cell lysates were prepared and analyzed. β-actin was used as an internal control. (**D**) The relative density of BCL2 and BAX was measured as arbitrary units by ImageJ software and was used to calculate the BAX/BCL2 ratio. (**E**) The relative density of cleaved poly-ADP ribose polymerase also was measured as arbitrary units by ImageJ software. Data are representative of three experiments.

A xenograft model in nude mice was established and used to evaluate the in vivo antitumor activity of **14a**. The mice were treated with vehicle, cisplatin (3 mg/kg, i.p.) and 50 mg/kg of **14a**. Our results showed that **14a** could significantly suppress growth of Hela xenograft tumors and had a similar effect to cisplatin treatment (Figure 2 and Table 2).

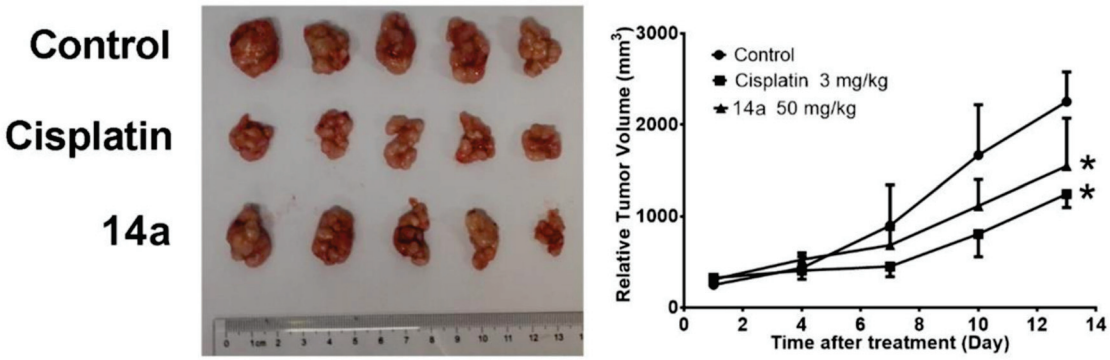

Figure 2. Effect of **14a** on the growth of Hela in nude mice. Tumor diameter was serially measured with a vernier caliper to calculate the relative tumor volume. Each experiment was conducted using 5 mice per group. Vehicle (●); 50 mg/kg **14a** (▲); and, 3 mg/kg cisplatin (■). The statistical difference between the drug-treated group and the vehicle was determined by one-way ANOVA (* $p < 0.05$).

Table 2. The anti-tumor activity of **14a** against the growth of Hela in nude mice[a].

Group (mg/kg)	Number (Initial/End)	Body Weight (g)		Tumor Weight (g)	
		Initial	End	g	IR (%)
Control	5/5	20.52 ± 0.99	20.56 ± 2.11	2.12 ± 0.40	
Cisplatin 3	5/5	20.80 ± 1.34	21.70 ± 1.32	0.88 ± 0.12 *	58.49
14a 50	5/5	21.08 ± 1.04	20.48 ± 0.89	1.20 ± 0.59 *	43.40

[a] Data are expressed as the mean ±SD (n = 5). *$p < 0.05$, compared with control.

3. Materials and Methods

3.1. Materials

Ursolic acid (>95%) was purchased from Shaanxi Pioneer Biotech Co., Ltd (Hanzhong, China). Reagents and solvents were either analytical or chemical purity. The silica gel GF_{254} plates and silica gel (200 to 300 mesh, Qingdao, Shandong, China) were used. The melting points were determined using an XT3A micro-melting point apparatus and are uncorrected (Beijing Keyi Company, Beijing, China). ^{1}H NMR and ^{13}C NMR were recorded on the Avance-400 spectrometer (Bruker, Ettlingen, Germany). High resolution mass spectra (HR-MS) were obtained on an AutoSpec Ultima-Tof spectrometer with an electrospray ionization (ESI) source (Micromass, Manchester, UK).

3.2. Chemistry

3.2.1. Preparation of Compounds **3**, **4** and **6**

Compound **3** was synthesized by the literature method with slight modifications [21]. The solution of **3** (500 mg, 0.98 mmol), K_2CO_3 (135 mg, 0.98 mmol), and 3-bromopropyne (0.11 mL, 1.28 mmol) or chloroacetonitrile (0.08 mL, 1.26 mmol) in DMF (20 mL) was stirred at 60 °C for 1 h. After cooled to room temperature, the mixture was poured into ice-cold water and filtered. The solid was dissolved with ethyl acetate (100 mL) and washed with water (50 mL) and brine (50 mL × 2), dried over Na_2SO_4 anhydrous, filtered, and concentrated to obtain **4** and **6**, as yellowish-white powder, in 92% and 95% yield, respectively.

3.2.2. General Procedure for the Synthesis of Compounds **5a–e**

To a solution of compound **4** (200 mg, 0.36 mmol) in anhydrous alcohol (5 mL), $CuSO_4 \cdot 5H_2O$ (37 mg, 0.15 mmol), sodium ascorbate (18 mg, 0.09 mmol), and corresponding benzyl azide (0.6 mmol) were added. The mixture was stirred at room temperature for 4 h and then concentrated. The residue was dissolved with ethyl acetate (80 mL), washed with water (40 mL) and brine (40 mL × 2), and then dried over Na_2SO_4 anhydrous. After filtration, concentration and purification by silica gel column chromatography with cyclohexane/methanol (3:1), compounds **5a–e** were afforded.

*[1-(3-chlorobenzyl)-1H-1,2,3-triazol-5-yl]methyl-urs-12-en-[(3,2-d)thiazol-2-amino]-28-oate (**5a**).* 26%, off-white powder. mp: 120.1–122.5 °C. ^{1}H NMR (400 MHz, $CDCl_3$): δ 7.51 (1H, s), 7.36–7.27 (2H, m), 7.23 (1H, s), 7.14 (1H, d, J = 7.0 Hz), 5.53–5.42 (2H, m), 5.22 (1H, s), 5.19–5.09 (2H, m), 2.47 (1H, d, J = 15.4 Hz), 2.21 (1H, d, J = 11.5 Hz), 2.16 (1H, d, J = 15.6 Hz), 1.25 (6H, s), 1.20 (3H, s), 1.12 (3H, s), 1.06 (3H, s), 0.92 (6H, s); ^{13}C NMR (100 MHz, $CDCl_3$): δ 177.64, 164.78, 152.08, 143.92, 138.17, 136.52, 135.20, 130.54, 129.20, 128.20, 126.21, 125.57, 124.04, 116.04, 57.45, 53.54, 53.04, 52.68, 48.32, 46.14, 42.34, 39.68, 39.26, 38.94, 38.89, 38.33, 36.95, 36.63, 32.50, 30.75, 30.49, 28.09, 24.30, 23.43, 23.31, 22.29, 21.25, 19.66, 17.08, 16.79, 15.72. HR-MS *m/z* calcd. for $C_{41}H_{55}ClN_5O_2S$ $[M + H]^+$ 716.37595, found 716.37531.

*[1-(4-fluorobenzyl)-1H-1,2,3-triazol-5-yl]methyl-urs-12-en-[(3,2-d)thiazol-2-amino]-28-oate (**5b**).* 26%, off-white powder. mp: 115.0–116.9 °C; ^{1}H NMR (400 MHz, $CDCl_3$): δ 7.47 (1H, s), 7.30–7.22 (2H, m), 7.05 (2H, t, J = 8.5 Hz), 5.46 (2H, s), 5.21 (1H, s), 5.18–5.06 (2H, m), 2.47 (1H, d, J = 15.4 Hz), 2.20 (1H, d, J = 12.7 Hz), 2.16 (1H, s), 1.24 (3H, s), 1.20 (3H, s), 1.11 (3H, s), 1.06 (3H, s), 0.92 (6H, s), 0.83 (3H, d, J = 6.4 Hz), 0.59

(3H, s); ^{13}C NMR (100 MHz, $CDCl_3$): δ 177.64, 164.75, 163.01 (d, J = 248.4 Hz), 152.13, 143.81, 138.17, 130.45 (d, J = 3.3 Hz), 130.13 (d, J = 8.4 Hz), 125.56, 123.84, 116.30 (d, J = 21.8 Hz), 57.47, 53.53, 53.05, 52.68, 48.32, 46.14, 42.34, 39.68, 39.26, 38.94, 38.91, 38.34, 36.96, 36.65, 32.51, 31.08, 30.76, 30.49, 28.08, 24.30, 23.44, 23.34, 22.26, 21.26, 19.64, 17.09, 16.77, 15.72. HR-MS *m/z* calcd. for $C_{41}H_{55}FN_5O_2S$ [M + H]$^+$ 700.40550, found 700.40482.

*[1-(2-nitrobenzyl)-1H-1,2,3-triazol-5-yl]methyl-urs-12-en-[(3,2-d)thiazol-2-amino]-28-oate (**5c**)*. 28%, off-white powder. mp: 130.3-132.5 °C; ^{1}H NMR (400 MHz, $CDCl_3$): δ 8.15 (1H, d, J = 8.1 Hz), 7.71 (1H, s), 7.53–7.60 (2H, m), 7.09 (1H, d, J = 7.7 Hz), 5.91 (2H, s), 5.25 (1H, s), 5.23–5.13 (2H, m), 2.48 (1H, d, J = 15.3 Hz), 2.23 (1H, d, J = 11.4 Hz), 2.17 (1H, d, J = 14.8 Hz), 1.20 (3H, s), 1.12 (3H, s), 1.07 (3H, s), 0.93 (6H, d, J = 1.0 Hz), 0.65 (3H, s); ^{13}C NMR (100 MHz, $CDCl_3$): δ 177.55, 164.60, 147.58, 143.85, 138.12, 134.44, 130.57, 129.88, 125.64, 125.54, 124.99, 116.11, 57.45, ^{53}.06, 52.66, 50.92, 48.32, 46.13, 42.32, 39.68, 39.24, 38.94, 38.89, 38.33, 36.95, 36.65, 32.49, 30.75, 30.53, 28.08, 24.28, 23.45, 23.34, 22.30, 21.24, 19.66, 17.07, 16.84, 15.70. HR-MS *m/z* calcd. for $C_{41}H_{55}N_6O_4S$ [M + H]$^+$ 727.40000, found 727.39938.

*[1-(2,6-dichlorobenzyl)-1H-1,2,3-triazol-5-yl]methyl-urs-12-en-[(3,2-d)thiazol-2-amino]-28-oate (**5d**)*. 260%, off-white powder. mp: 136.0–138.8 °C; ^{1}H NMR (400 MHz, $CDCl_3$): δ 7.50 (1H, s), 7.40 (2H, d, J = 7.9 Hz), 7.33–7.27 (1H, m), 5.83 (2H, s), 5.22 (1H, s), 5.17–5.07 (2H, m), 4.92 (2H, s), 2.48 (1H, d, J = 15.4 Hz), 2.20 (1H, d, J = 11.7 Hz), 2.19–2.14 (2H, m), 1.20 (3H, s), 1.12 (3H, s), 1.06 (3H, s), 0.93 (6H, s), 0.83 (3H, d, J = 6.4 Hz), 0.58 (3H, s); ^{13}C NMR (100 MHz, $CDCl_3$): δ 177.58, 164.64, 152.24, 143.14, 138.19, 136.95, 131.26, 130.05, 129.03, 125.55, 123.75, 116.09, 57.43, 53.03, 52.67, 49.15, 48.29, 46.13, 42.30, 39.66, 39.24, 38.96, 38.90, 38.33, 36.96, 36.65, 32.47, 30.76, 30.50, 28.06, 24.25, 23.45, 23.36, 22.28, 21.25, 19.68, 17.08, 16.67, 15.73. HR-MS *m/z* calcd. for $C_{41}H_{54}Cl_2N_5O_2S$ [M + H]$^+$ 750.33698, found 750.33651.

*{1-[4-(tert-butyl)benzyl]-1H-1,2,3-triazol-5-yl}methyl-urs-12-en-[(3,2-d)thiazol-2-amino]-28-oate (**5e**)*. 26%, off-white powder. mp: 149.1–151.3 °C; ^{1}H NMR (400 MHz, $CDCl_3$): δ 7.46 (1H, s), 7.38 (2H, d, J = 8.3 Hz), 7.18 (2H, d, J = 8.3 Hz), 5.53–5.39 (2H, m), 5.22 (1H, s), 5.09–5.17 (2H, m), 4.86 (2H, s), 2.50 (1H, d, J = 15.4 Hz), 1.30 (9H, s), 1.21 (3H, s), 1.12 (3H, s), 1.07 (3H, s), 0.97 (3H, s), 0.92 (3H, s), 0.83 (3H, d, J = 6.4 Hz), 0.66 (3H, s); ^{13}C NMR (100 MHz, $CDCl_3$): δ 177.59, 164.59, 152.19, 152.10, 143.58, 138.17, 131.50, 128.04, 126.17, 125.59, 123.89, 116.19, 57.50, 54.00, 53.06, 52.70, 48.29, 46.18, 42.35, 39.71, 39.26, 39.00, 38.91, 38.37, 36.97, 36.61, 32.53, 31.39, 30.77, 30.53, 28.10, 24.29, 23.46, 23.36, 22.32, 21.26, 19.68, 17.09, 16.85, 15.77. HR-MS *m/z* calcd. for $C_{45}H_{64}N_5O_2S$ [M + H]$^+$ 738.47752, found 738.48079.

*(2H-tetrazol-5-yl) methyl-urs-12-en-[(3,2-d)thiazol-2-amino]-28-oate (**7**)*. The solution of **6** (200 mg, 0.36 mmol), sodium azide (48 mg, 0.74 mmol) and $ZnCl_2$ (196 mg, 1.4 mmol) in isopropanol/water (3:1, 8 mL) was added and stirred at 85 °C for 6 h. After concentration, the residue was dissolved with *n*-butanol (60 mL) and washed with water (30 mL) and brine (30 mL × 2), dried over Na_2SO_4 anhydrous, filtered, evaporated and purified by silica gel column chromatography with chloroform/methanol (10:1) to give **7**. 31%, white powder. mp: 256.0–258.0 °C; ^{1}H NMR (400 MHz, DMSO-d_6): δ 6.70 (2H, s), 5.28 (2H, s), 5.15 (1H, s), 2.40 (1H, d, J = 15.4 Hz), 2.16 (1H, d, J = 11.3 Hz), 2.08 (1H, d, J = 15.5 Hz), 1.10 (3H, s), 1.04 (3H, s), 1.02 (3H, s), 0.91 (3H, s), 0.86 (3H, d, J = 7.7 Hz), 0.81 (2H, d, J = 6.3 Hz), 0.51 (3H, s); ^{13}C NMR (100 MHz, DMSO-d_6): δ 175.83, 165.29, 153.23, 150.88, 137.41, 125.21, 112.23, 54.61, 52.58, 52.04, 47.63, 45.35, 39.00, 38.38, 38.36, 38.21, 37.78, 36.43, 35.98, 32.02, 30.39, 30.01, 27.45, 23.73, 23.10, 22.76, 22.12, 20.95, 19.14, 16.92, 16.30, 15.41. HR-MS *m/z* calcd. for $C_{33}H_{49}N_6O_2S$ [M + H]$^+$ 593.36322, found 593.36123.

3.2.3. General Procedure for Compounds **8a–c**

To a solution of UA (1.10 g, 2.41 mmol), K_2CO_3 (0.49 g, 3.55 mmol) and corresponding dibromoalkane (8.0 mmol) in 15 mL DMF, the mixture was stirred at 60 °C for 1 h. This was followed by the similar post-reaction treatment of compounds **4** or **5**, purified by silica gel column chromatography with petroleum ether/ethyl acetate (5:1) to afford derivatives **8a–c**, as yellowish-white powder, 61–63% yield.

3.2.4. General Procedure for Compounds **9a–e**

K_2CO_3 (1 equiv) and the corresponding nitric heterocyclic compounds (2–6 equiv) were added to the solution of **8a**, **8b,** or **8c** (1 equiv) in DMF. The mixture was stirred at 80 °C for 30–60 min and then poured into ice-cold water, stirred, and filtered. The crude product was dissolved in ethyl acetate, washed with water and brine, dried over Na_2SO_4 anhydrous, filtered, evaporated, and purified by silica gel column chromatography to yield **9a–e**.

*[2-(Piperazin-1-yl)ethyl] 3-hydroxy-urs-12-en-28-oate (**9a**).* 40% (purified by silica gel column chromatography with dichloromethane/methanol, 10:1), white solid. mp: 180.0–182.0 °C; ^{1}H NMR (400 MHz, $CDCl_3$): δ 5.23 (1H, s), 4.19–4.07 (2H, m), 3.22 (1H, dd, J = 10.8, 4.6 Hz), 3.14 (4H, s), 2.75 (4H, s), 2.65 (2H, t, J = 5.6 Hz), 2.20 (1H, d, J = 11.3 Hz), 1.08 (3H, s), 0.99 (3H, s), 0.95 (3H, d, J = 5.5 Hz), 0.92 (3H, s), 0.86 (3H, d, J = 6.3 Hz), 0.79 (3H, s), 0.74 (3H, s); ^{13}C NMR (100 MHz, $CDCl_3$): δ 176.89, 137.61, 125.09, 78.47, 61.24, 56.67, 54.70, 54.06, 52.34, 47.48, 47.03, 45.52, 41.52, 39.04, 38.56, 38.37, 38.25, 38.10, 36.46, 36.18, 32.53, 30.17, 27.65, 27.47, 26.73, 23.71, 23.05, 22.78, 20.70, 17.81, 16.65, 16.54, 15.15, 14.97. HR-MS *m/z* calcd. for $C_{36}H_{61}N_2O_3$ $[M + H]^+$ 569.46767, found 569.46555.

*[2-(homopiperazine-1-yl)ethyl] 3-hydroxy-urs-12-en-28-oate (**9b**).* 39% (purified by silica gel column chromatography with dichloromethane/methanol, 10:1), white solid. mp: 189.2–192.0 °C; ^{1}H NMR (400 MHz, $CDCl_3$): δ 5.22 (1H, s), 4.14–4.02 (2H, m), 3.27–2.78 (9H, m), 2.18 (1H, d), 1.07 (3H, s), 0.98 (3H, s), 0.93 (3H, d, J = 5.7 Hz), 0.91 (3H, s), 0.84 (3H, d, J = 6.4 Hz), 0.77 (3H, s), 0.73 (3H, s); ^{13}C NMR (100 MHz, $CDCl_3$): δ 177.51, 138.17, 125.72, 79.09, 61.92, 56.43, 55.29, 54.00, 53.01, 51.03, 48.15, 47.61, 46.97, 44.67, 42.15, 39.63, 39.14, 38.96, 38.84, 38.70, 37.06, 36.86, 33.15, 30.72, 28.26, 28.09, 27.31, 25.36, 24.35, 23.62, 23.40, 21.26, 18.41, 17.27, 17.13, 15.77, 15.60. HR-MS *m/z* calcd. for $C_{37}H_{63}N_2O_3$ $[M + H]^+$ 583.48332, found 583.48116.

*[3-(piperazin-1-yl)propyl] 3-hydroxy-urs-12-en-28-oate (**9c**).* 39% (purified by silica gel column chromatography with dichloromethane/methanol, 10:1), white solid. mp: 99.1–101.0 °C; ^{1}H NMR (400 MHz, $CDCl_3$): δ 5.22 (1H, s), 4.11–3.90 (2H, m), 3.21 (1H, dd, J = 10.8, 4.6 Hz), 3.15 (4H, s), 2.68 (4H, s), 2.53–2.38 (2H, m), 2.20 (1H, d, J = 11.2 Hz), 1.07 (3H, s), 0.98 (3H, s), 0.93 (3H, d, J = 5.6 Hz), 0.90 (3H, s), 0.84 (3H, d, J = 6.3 Hz), 0.77 (3H, s), 0.72 (3H, s); ^{13}C NMR (100 MHz, $CDCl_3$): δ 177.66, 138.37, 125.62, 79.14, 62.20, 55.31, 54.82, 52.97, 50.17, 48.21, 47.61, 43.76, 42.17, 39.65, 39.18, 38.99, 38.87, 38.71, 37.08, 36.88, 33.14, 30.76, 28.27, 28.08, 27.31, 25.95, 24.34, 23.66, 23.42, 21.31, 18.43, 17.24, 17.15, 15.79, 15.62. HR-MS *m/z* calcd. for $C_{37}H_{63}N_2O_3$ $[M + H]^+$ 583.48332, found 583.48103.

*[4-(piperazin-1-yl)butyl] 3-hydroxy-urs-12-en-28-oate (**9d**).* 38% (purified by silica gel column chromatography with dichloromethane/methanol, 10:1), white solid. mp: 100.0–102.5 °C; ^{1}H NMR (400 MHz, $CDCl_3$): δ 5.21 (1H, s), 4.06–3.91 (2H, m), 3.19–3.21 (5H, m), 2.70 (4H, s), 2.41 (2H, t, J = 7.0 Hz), 2.20 (1H, d, J = 11.2 Hz), 1.07 (3H, s), 0.98 (3H, s), 0.93 (3H, d, J = 5.8 Hz), 0.90 (3H, s), 0.84 (3H, d, J = 6.4 Hz), 0.77 (3H, s), 0.73 (3H, s); ^{13}C NMR (100 MHz, $CDCl_3$): δ 177.69, 138.31, 125.62, 79.10, 63.88, 57.60, 55.29, 52.99, 49.92, 48.17, 47.61, 43.76, 42.16, 39.63, 39.16, 38.98, 38.85, 38.71, 37.06, 36.87, 33.16, 30.76, 28.26, 28.08, 27.30, 26.42, 24.33, 23.65, 23.40, 23.27, 21.30, 18.41, 17.24, 17.15, 15.78, 15.60. HR-MS *m/z* calcd. for $C_{38}H_{65}N_2O_3$ $[M + H]^+$597.49897, found 597.49693.

*[2-(4-methylpiperazin-1-yl)ethyl] 3-hydroxy-urs-12-en-28-oate (**9e**).* 43% (purified by silica gel column chromatography with petroleum ether/ethyl acetate, 3:1), white solid. mp: 100.0–103.0 °C; ^{1}H NMR (400 MHz, $CDCl_3$): δ 5.22 (1H, s), 4.12 (2H, t, J = 6.0 Hz), 3.21 (1H, dd, J = 10.8, 4.7 Hz), 2.60 (10H, m), 2.33 (3H, d, J = 9.8 Hz), 2.20 (1H, d, J = 11.2 Hz), 1.07 (3H, s), 0.98 (3H, s), 0.93 (3H, d, J = 6.1 Hz), 0.90 (3H, s), 0.84 (3H, d, J = 6.4 Hz), 0.77 (3H, s), 0.74 (3H, s); ^{13}C NMR (100 MHz, $CDCl_3$): δ 177.48, 138.22, 125.72, 79.10, 61.97, 56.65, 55.33, 55.17, 53.29, 52.96, 48.10, 47.66, 46.05, 42.15, 39.67, 39.19, 39.00, 38.87, 38.74, 37.09, 36.79, 33.15, 30.79, 28.27, 28.10, 27.36, 24.34, 23.67, 23.41, 21.31, 18.43, 17.27, 17.16, 15.77, 15.59. HR-MS *m/z* calcd. for $C_{37}H_{63}N_2O_3$ $[M + H]^+$583.48332, found 583.48100.

3.2.5. General Procedure for Compounds **10** and **11**

Acetic anhydride (1.0 mL, 10.58 mmol) was added dropwise to the solution of UA (2.0 g, 4.38 mmol) in 15 mL pyridine under 0 °C. Subsequently, the mixture was stirred at room

temperature for 15 h, poured into ice-cold water and filtered to give a white semisolid, 95% yield. The semisolid was dissolved with ethyl acetate (150 mL) and washed with 1 mol/L hydrochloric acid (60 mL), water (60 mL) and brine (60 mL), dried over Na_2SO_4 anhydrous, filtered, and then concentrated to afford 3-acetyl-UA. The mixture of 3-acetyl-UA (1.16 g, 2.33 mmol), K_2CO_3 (0.49 g, 3.55 mmol), and 2-chloroethanol (0.17 mL, 2.53 mmol) in 15 mL DMF was stirred at 60 °C for 3 h. Following the similar post-processing steps of **6, 10** was obtained as white powder, in 86% yield. Methanesulfonyl chloride (0.5 mL, 6.46 mmol) in pyridine (5 mL) was dropwise added to the solution of **10** (1.10 g, 2.03 mmol) in 15 mL pyridine under 10 °C. The mixture was stirred at room temperature for 3 h and treated with the similar post reaction treatment of 3-acetyl-UA to provide **11**, as off-white powder, in 94% yield.

3.2.6. General Procedure for the Synthesis of Compounds **12a–c**

The mixture of **11** (1 equiv), K_2CO_3 (1 equiv), and piperazine (6 equiv), homopiperazine (6 equiv) or morpholine (2 equiv) in DMF was stirred at 60 °C for 30 min, poured into ice-cold water, stirred, and filtered. The off-white solid was dissolved in ethyl acetate and washed with water and brine, dried over Na_2SO_4 anhydrous, filtered, evaporated, and purified by silica gel column chromatography to yield **12a–c**.

*[2-(piperazin-1-yl)ethyl] 3-acetoxy-urs-12-en-28-oate (**12a**).* 73% (purified by silica gel column chromatography with dichloromethane/methanol, 10:1), white solid. mp: 80.1–82.9 °C; ^{1}H NMR (400 MHz, $CDCl_3$): δ 5.21 (1H, s), 4.52–4.44 (1H, m), 4.16–4.04 (2H, m), 3.10 (4H, s), 2.72 (4H, s), 2.63 (2H, t, J = 5.6 Hz), 2.18 (1H, d, J = 12.5 Hz), 2.04 (3H, s), 1.06 (3H, s), 0.93 (6H, d, J = 5.8 Hz), 0.85 (9H, d, J = 4.9 Hz), 0.72 (3H, s); ^{13}C NMR (100 MHz, $CDCl_3$) δ 177.51, 171.19, 138.26, 125.62, 81.03, 61.59, 58.52, 56.94, 55.39, 52.97, 52.78, 48.13, 47.56, 45.13, 42.14, 39.67, 39.16, 38.99, 38.39, 37.79, 36.97, 36.83, 33.07, 30.75, 28.19, 28.07, 24.32, 23.66, 23.62, 23.41, 21.46, 21.29, 18.56, 18.31, 17.25, 17.18, 16.86, 15.65. HR-MS *m/z* calcd. for $C_{38}H_{63}N_2O_4$ $[M + H]^+$ 611.47823, found 611.47836.

*[2-(Homopiperazine-1-yl)ethyl] 3-acetoxy-urs-12-en-28-oate (**12b**).* 71% (purified by silica gel column chromatography with dichloromethane/methanol, 10:1), white solid. mp: 76.5–78.0 °C. ^{1}H NMR (400 MHz, $CDCl_3$): δ 5.22 (1H, s), 4.53–4.44 (1H, m), 4.16 (2H, s), 3.38 (4H, s), 3.20 (2H, s), 2.94–3.00 (4H, m), 2.04 (3H, s), 1.06 (3H, s, CH), 0.94 (6H, d, J = 3.8 Hz), 0.85 (9H, d, J = 4.6 Hz), 0.72 (3H, s); ^{13}C NMR (100 MHz, $CDCl_3$): δ 177.52, 171.17, 138.22, 125.64, 81.01, 61.84, 56.44, 55.38, 53.97, 53.00, 51.16, 48.16, 47.55, 46.85, 44.47, 42.15, 39.65, 39.14, 38.97, 38.38, 37.79, 36.97, 36.87, 33.08, 30.72, 28.19, 28.08, 25.31, 24.35, 23.65, 23.60, 23.41, 21.45, 21.28, 18.31, 17.27, 17.18, 16.86, 15.67. HR-MS *m/z* calcd. for $C_{39}H_{65}N_2O_4$ $[M + H]^+$ 625.49388, found 625.49126.

*(2-morpholinoethyl) 3-acetoxy-urs-12-en-28-oate (**12c**).* 75% (purified by silica gel column chromatography with petroleum ether/ ethyl acetate, 3:1), white solid. mp: 63.1–65.1 °C. ^{1}H NMR (400 MHz, $CDCl_3$): δ 5.22 (1H, s), 4.54–4.44 (1H, m), 4.27 (2H, s), 3.82 (4H, s), 2.19 (1H, d, J = 11.2 Hz), 2.04 (3H, s), 1.07 (3H, s), 0.94 (6H, d, J = 5.5 Hz), 0.85 (9H, d, J = 4.9 Hz), 0.74 (3H, s); ^{13}C NMR (100 MHz, $CDCl_3$): δ 177.37, 171.16, 138.24, 125.72, 81.00, 66.21, 56.95, 55.39, 53.52, 52.97, 48.17, 47.54, 42.15, 39.69, 39.16, 38.99, 38.38, 37.79, 36.98, 36.82, 33.06, 30.72, 29.82, 28.19, 28.04, 24.34, 23.65, 23.63, 23.39, 21.45, 21.28, 18.30, 17.32, 17.18, 16.86, 15.64. HR-MS *m/z* calcd. for $C_{38}H_{62}NO_5$ $[M + H]^+$ 612.46225, found 612.45986.

3.2.7. Preparation of Compound **13**

The mixture of **9a** (500 mg, 0.88 mmol) and PCC (190 mg, 0.88 mmol) in 80 mL chloroform was stirred at 0 °C for 10 h, then isopropanol (1.0 mL, 13.1 mmol) was added and stirred at room temperature for 1 h. The mixture was washed with water (40 mL) and brine (2 × 40 mL), dried over Na_2SO_4 anhydrous, filtered, concentrated, and purified by silica gel column chromatography with dichloromethane/methanol (10:1) to obtain *[2-(Piperazin-1-yl)ethyl] 3-oxo-urs-12-en-28-oate (**13**).* 69%, off-white powder. mp:144.4–146.8 °C; ^{1}H NMR (400 MHz, $CDCl_3$): δ 5.24 (1H, s), 4.18–4.04 (2H, m), 3.19 (4H, s), 2.81 (4H, s), 2.65 (2H, t, J = 5.4 Hz), 2.59-2.47 (1H, m), 2.34–2.39 (1H, m), 2.23–2.14 (1H, m), 1.08 (6H, s), 1.03 (6H, s), 0.94 (3H, d, J = 5.5 Hz), 0.85 (3H, d, J = 6.3 Hz), 0.77 (3H, s);

^{13}C NMR (100 MHz, $CDCl_3$): δ 218.00, 177.42, 138.33, 125.48, 61.20, 56.39, 55.33, 53.06, 49.91, 48.20, 47.52, 46.82, 43.72, 42.27, 39.60, 39.38, 39.15, 38.95, 36.83, 36.77, 34.29, 32.65, 30.70, 28.06, 26.67, 24.30, 23.56, 21.62, 21.24, 19.69, 17.23, 17.13, 15.36. HR-MS *m/z* calcd. for $C_{36}H_{59}N_2O_3$ [M + H]$^+$567.45202, found 567.44977.

3.2.8. General Procedure for Synthesizing Compounds **14a** and **14b**

The mixture of **12a** (300 mg, 0.49 mmol), K_2CO_3 (70 mg, 0.51 mmol), and 4-fluorobenzyl bromide (120 mg, 0.63 mmol) or 2-nitrobenzyl bromide (130 mg, 0.60 mmol) in DMF (10 mL) was stirred at 60 °C for 1 h, the mixture was poured into 50 mL ice-cold water and then filtered. The white solid was dissolved in ethyl acetate (100 mL) and washed with water (50 mL) and brine (2 × 50 mL), dried over Na_2SO_4 anhydrous, filtered, evaporated, and purified by silica gel column chromatography with dichloromethane/methanol (20:1) to obtain **14a** and **14b**.

*{2-[4-(4-fluorobenzyl)piperazin-1-yl]ethyl} 3-acetoxy-urs-12-en-28-oate (**14a**).* 45% as white solid. mp: 140.0–141.8 °C; ^{1}H NMR (400 MHz, $CDCl_3$): δ 7.76–7.58 (2H, m), 7.12 (2H t, *J* = 8.2 Hz), 5.16 (1H, s), 4.51–4.43 (1H, m), 4.08 (2H, s), 2.73–3.90 (10H, m), 2.09 (1H, d, *J* = 11.3 Hz), 2.04 (3H, s), 1.04 (3H, d, *J* = 7.4 Hz), 0.92 (6H, d, *J* = 10.4 Hz), 0.88–0.81 (9H, m), 0.65 (3H, d, *J* = 13.5 Hz); ^{13}C NMR (100 MHz, $CDCl_3$): δ 176.88, 171.17, 164.24 (d, *J* = 252.6 Hz), 138.14, 136.01 (d, *J* = 8.5 Hz), 130.81 (d, *J* = 7.6 Hz), 125.92, 122.57, 116.74 (d, *J* = 21.6 Hz), 115.67 (d, *J* = 21.4 Hz), 80.89, 61.04, 57.23, 56.48, 55.33, 53.12, 48.38, 47.42, 46.25, 46.17, 42.18, 39.65, 39.08, 39.04, 38.35, 37.77, 36.93, 36.78, 32.96, 30.50, 28.17, 27.97, 24.36, 23.56 (d, *J* = 4.5 Hz), 23.38, 21.43, 21.16, 18.22, 17.47, 17.17, 16.84, 15.62. HR-MS *m/z* calcd. for $C_{45}H_{68}FN_2O_4$ [M + H]$^+$ 719.51576, found 719.51562.

*{2-[4-(2-nitrobenzyl)piperazin-1-yl]ethyl} 3-acetoxy-urs-12-en-28-oate (**14b**).* 43%, white solid. mp: 83.0–85.0 °C; ^{1}H NMR (400 MHz, $CDCl_3$): δ 7.80 (1H, d, *J* = 7.9 Hz), 7.60–7.47 (2H, m), 7.40 (1H, t, *J* = 7.5 Hz), 5.21 (1H, s), 4.55–4.41 (1H, m), 4.17 (2H, s), 3.80 (2H, s), 2.61 (8H, m), 2.19 (1H, d, *J* = 11.3 Hz), 2.04 (3H, s), 1.06 (3H, s), 0.94 (6H, d, *J* = 4.9 Hz), 0.86 (9H, d, *J* = 4.0 Hz), 0.74 (3H, d, *J* = 10.5 Hz); ^{13}C NMR (100 MHz, $CDCl_3$): δ 177.44, 171.19, 149.98, 138.23, 132.49, 131.16, 128.21, 125.67, 124.57, 118.04, 81.04, 59.05, 56.49, 55.40, 53.35, 52.94, 48.12, 47.57, 42.14, 39.68, 39.17, 38.97, 38.39, 37.80, 36.98, 36.79, 33.07, 30.75, 28.21, 28.06, 24.32, 23.67, 23.63, 23.41, 21.48, 21.31, 18.31, 17.29, 17.19, 16.88, 15.66. HR-MS *m/z* calcd. for $C_{45}H_{68}N_3O_6$ [M + H]$^+$ 746.51062, found 746.51035.

3.2.9. General Procedure for Synthesizing Compounds **17** and **18**

Compound **17** was synthesized from compound **1** according to the literature method [25]. **18** was prepared from **17** according to the synthetic procedure of **12a** and then purified by silica gel column chromatography with dichloromethane/methanol (15:1) to afford **18**.

Urs-12-en-[2,3-c][1,2,5]*oxadiazole oxide-28-oic acid (**17**).* 60%, white solid. mp: >286 °C; ^{1}H NMR (400 MHz, $CDCl_3$): δ 5.29 (1H, s), 2.72 (1H, d, *J* = 16.6 Hz), 2.23 (1H, d, *J* = 11.6 Hz), 2.17 (3H, s), 1.41 (3H, s), 1.30 (3H, s), 1.10 (3H, s), 0.95 (3H, d, *J* = 5.9 Hz), 0.91 (3H, s), 0.86 (3H d, *J* = 6.3 Hz), 0.82 (1H, s); ^{13}C NMR (100 MHz, $CDCl_3$): δ 184.01, 163.66, 138.25, 125.04, 112.03, 52.71, 52.65, 48.14, 46.01, 42.27, 39.63, 39.20, 38.90, 38.40, 36.75, 35.17, 34.72, 32.04, 30.71, 28.08, 24.10, 23.92, 23.55, 23.29, 21.27, 18.91, 17.09, 16.72, 16.30.HR-MS *m/z* calcd. for $C_{30}H_{45}O_4N_2$ [M + H]$^+$ 497.33738, found 497.33572.

[2-(Piperazin-1-yl)ethyl)] urs-12-en-[2,3-c][1,2,5]*oxadiazole oxide-28-oate (**18**).* 47%, white powder. mp: 134.1–136.8 °C; ^{1}H NMR (400 MHz, $CDCl_3$): δ 5.29 (1H, s, H-12), 4.12 (2H, t, *J* = 5.7 Hz, CH_2), 3.02–3.05 (4H, m), 2.64 (4H, d, *J* = 4.1 Hz), 2.62 (2H, d, *J* = 5.8 Hz), 2.24 (1H, d, *J* = 11.1 Hz), 1.41 (3H, s), 1.33 (3H, s), 1.09 (3H, s), 0.94 (3H, d, *J* = 5.7 Hz), 0.91 (3H, s), 0.86 (3H, d, *J* = 6.3 Hz), 0.79 (3H, s); ^{13}C NMR (100 MHz, $CDCl_3$): δ 177.38, 163.72, 138.49, 124.84, 112.02, 61.77, 57.17, 54.01, 53.02, 52.77, 48.16, 46.01, 45.79, 42.36, 39.69, 39.26, 38.96, 38.39, 36.72, 35.20, 34.73, 32.16, 30.75, 28.07, 24.27, 23.96, 23.48, 23.33, 21.26, 18.97, 17.13, 16.92, 16.32. HR-MS *m/z* calcd. for $C_{36}H_{57}O_4N_4$ [M + H]$^+$ 609.43743, found 609.43526.

3.3. Biology

3.3.1. Cell Culture and Treatment

MKN45, Hela cell (the Shanghai Institute of Life Sciences) were cultivated in DMEM media (Hyclone, Thermo Fisher Scientific, Waltham, MA, USA) supplemented with 10% fetal bovine serum (Life Technology, Thermo Fisher Scientific, Waltham, MA, USA), 100 U/mL penicillin, and l00 μg/mL streptomycin, and grown in a humidified incubator (37 °C, 5% CO_2). All of the cells were harvested in the exponential growth phase for assays.

3.3.2. MTT Assay

All of the tested compounds were dissolved in DMSO and subsequently diluted in the culture medium before treatment of the cultured cells. When the cells were 80–90% confluent, they were harvested by treatment with a solution containing 0.25% trypsin, thoroughly washed, and resuspended in supplemented growth medium. Cells (2×10^3/well) were plated in 100 μL of medium/well in 96-well plate. After incubations overnight, the cells were treated with different concentrations of the compounds in DMEM with 10% FBS for 72 h. In parallel, the cells that were treated with DMSO served as negative control and CDDP (cisplatin) as positive control. Finally, 20 μL of MTT was added and the cells were incubated for 4 h. The MTT-formazan that formed by metabolically viable cells was dissolved in 100 μL of DMSO for 10 min. The absorbance was then measured at 570 nm with a microplate reader, in which the cell survival rates were calculated and the IC_{50} was calculated following our previous method [26,27].

3.3.3. Flow Cytometric Analysis

To determine the effect of compound **14a** on the cell cycle, the cells were seeded in six-well plates at a density of 2×10^5 cells/mL for 24 h. After incubation, the cells were treated with indicated concentrations of compound **14a** for 24 h. Subsequently, the cells were collected, washed, and fixed in 70% ethanol in PBS at −20 °C. After overnight, fixed cells were pelleted and stained with cell cycle analysis reagent propidium iodide solution as per the manufacturer instructions for 30 min at 37 °C in dark, and about 5000 events were analysed on a FACScan cytometry(C6 Plus, Becton Dickinson, San Jose, CA, USA) following published protocol [28].

3.3.4. Western Blotting Assay

The Hela cell were treated with **14a** at three concentrations: 0, 2, 5 μM. After treatment, the cells were washed with PBS and kept in −80 °C until further handing. Western blotting was then performed, as previously described. Briefly, total cell extracts were collected by RIPA buffer and electrophoresed on 8% or 10% SDS-polyacrylamide gels and then transferred to PVDF membranes (Millipore, Temecula, CA, USA). The membranes were blocked and then incubated overnight at 4 °C with primary antibodies to Bax (2772, Cell Signaling Technology, Boston, MA, USA), Bcl2 (2876, Cell Signaling Technology, Boston, MA, USA), PARP (46D11, Cell Signaling Technology, Boston, MA, USA), and β-actin (C4, Santa Cruz Biotechnology, Dallas, TX, USA). The member was developed and visualized by Image Quant LAS4000 (GE Healthcare, Boston, MA, USA) [29].

3.3.5. Xenograft Studies

Nude mice (6−8 weeks old, BALB/c, female) were used to establish the xenograft tumors following the published protocol [30]. Briefly, Hela cells (5×10^6) were implanted in the dorsal region of recipient mice by means of subcutaneous injection. Once a tumor had reached around 300 mm^3 in size, the mice were randomized into three groups as control, **14a** (50 mg/kg) and cisplatin (3 mg/kg) with five mice per group. The animals were administrated by intraperitoneal injection for cisplatin and administrated by gavage for **14a**. Tumor growth and body weight were measured every three days

during the treatment. At the end of the treatment, the mice were sacrificed and tumors were removed and weighed. The use of animals was approved by the Animal Experimentation Ethics Committee of Yantai University in accordance with the guidelines for ethical conduct in the care and use of animals (Ethical code YT-YX-1817).

4. Conclusions

In summary, nineteen nitrogen-bearing heterocyclic UA analogues have been synthesized in this work. The antiproliferative activity against Hela and MKN45 cell lines in vitro were evaluated. The results showed that compounds bearing thiazole, triazole or tetrazole groups (**5a**–**e** and **7**) displayed moderate antitumor activity. **9a**, **9c**, **12a**, **12b**, **13**, **14a**, **18** (containing a piperazine or homopiperazine moiety) exhibited promising results against the cancer cell lines that were tested here, with IC_{50} values from 2.1–9.8 μM. In addition, an analysis of the structure-activity relationships revealed that a number of factors remarkably affected the cytotoxicity. These included acetylation of 3-OH, the type of nitrogen heterocycle, the linkers' length between 28-COOH and nitrogen heterocycles, as well as different substituents in the piperazine. **14a**, which is one of the most active compounds, decreased the apoptosis regulator (BCL2/BAX) ratio, which subsequently disrupted the mitochondrial potential and induced apoptosis and significantly suppressed the growth of Hela xenografts in nude mice.

The anti-cancer activity of the newly synthesized ursolic acid analogs is encouraging and may provide a starting point for further structural optimization. Further pharmacokinetic study for these compounds is planned.

Supplementary Materials: The following are available online at http://www.mdpi.com/1420-3049/24//877/s1, ^{1}H-NMR, ^{13}C-NMR and HR-MS spectra of compounds.

Author Contributions: W.W., L.L., H.W. and Q.M. conceived and designed the experiments; W.W., L.L., and Z.L. performed the experiments; H.W and Q.M. analyzed the data; W.W. and L.L. wrote the paper.

Funding: This work was supported by the National Natural Science Foundation of China (No. 81473104), Taishan Scholar Project (No. 81728020), Key Research Project of Shandong Province (2017GSF18177), Shandong Graduate Education Innovation Program (SDYY16132), Yantai University Graduate Innovation Fund (YDYB1825).

Conflicts of Interest: The authors have declared no conflict of interest.

References

1. Yin, M.C.; Lin, M.C.; Mong, M.C.; Lin, C.Y. Bioavailability, Distribution, and Antioxidative Effects of Selected Triterpenes in Mice. *J. Agric. Food. Chem.* **2012**, *60*, 7697–7701. [CrossRef] [PubMed]
2. Chen, H.J.; Gao, Y.; Wang, A.L.; Zhou, X.B.; Zheng, Y.Q.; Zhou, J. Evolution in medicinal chemistry of ursolic acid derivatives as anticancer agents. *Eur. J. Med. Chem.* **2015**, *92*, 648–655. [CrossRef] [PubMed]
3. Kazakova, O.B.; Giniyatullina, G.V.Y.; Amansarov, E.Y.; Tolstikov, G.A. Betulin and ursolic acid synthetic derivatives as inhibitors of Papilloma virus. *Bioorg. Med. Chem. Lett.* **2010**, *20*, 4088–4090. [CrossRef] [PubMed]
4. Kurek, A.; Nadkowska, P.; Pliszka, S.; Wolska, K.I. Modulation of antibiotic resistance in bacterial pathogens by oleanolic acid and ursolic acid. *Phytomedicine* **2012**, *19*, 515–519. [CrossRef] [PubMed]
5. Cunha, W.R.; de Matos, G.X.; Souza, M.G.; Tozatti, M.G.; Andrade e Silva, M.L.; Martins, C.H.; da Silva, R. Evaluation of the antibacterial activity of the methylene chloride extract of Miconia ligustroides, isolated triterpene acids, and ursolic acid derivatives. *Pharm. Biol.* **2010**, *48*, 166–169. [CrossRef] [PubMed]
6. Hua, S.X.; Huang, R.Z.; Ye, M.Y.; Pan, Y.M.; Yao, G.Y.; Zhang, Y.; Wang, H.S. Design, synthesis and invitro evaluation of novel ursolic acid derivatives as potential anticancer agents. *Eur. J. Med. Chem.* **2015**, *95*, 435–452. [CrossRef] [PubMed]
7. Wu, C.C.; Cheng, C.H.; Lee, Y.H.; Chang, I.L.; Chen, H.Y.; Hsieh, C.P.; Chueh, P.J. Ursolic acid triggers apoptosis in human osteosarcoma cells via caspase activation and the ERK1/2 MAPK pathway. *J. Agric. Food. Chem.* **2016**, *64*, 4220–4226. [CrossRef] [PubMed]

8. Fu, H.J.; Zhou, Y.R.; Bao, B.H.; Jia, M.X.; Zhao, Y.; Zhang, L.; Li, J.X.; He, H.L.; Zhou, X.M. Tryptophan hydroxylase 1 (Tph-1)-targeted bone anabolic agents for osteoporosis. *J. Med. Chem.* **2014**, *57*, 4692–4709. [CrossRef] [PubMed]
9. Gutiérrez, R.M.P.; Vargas, S.R.; Garcia, B.E.; Gallardo, N.Y. Hypoglycemic activity of constituents from Astianthus viminalis in normal and streptozotocin-induced diabetic mice. *J. Nat. Med.* **2009**, *63*, 393–401. [CrossRef] [PubMed]
10. Zhang, W.; Hong, D.; Zhou, Y.; Zhang, Y.; Shen, Q.; Li, J.Y.; Hu, L.H.; Li, J. Ursolic acid and its derivative inhibit protein tyrosine phosphatase 1B, enhancing insulin receptor phosphorylation and stimulating glucose uptake. *Biochem. Biophis. Acta* **2006**, *1760*, 1505–1512. [CrossRef] [PubMed]
11. Ali, M.S.; Ibrahim, S.A.; Jalil, S.; Choudhary, M.I. Ursolic acid: A potent Inhibitor of superoxides produced in the cellular system. *Phytother. Res.* **2007**, *21*, 558–561. [CrossRef] [PubMed]
12. Jin, Y.R.; Jin, J.L.; Li, C.H.; Piao, X.X.; Jin, N.G. Ursolic acid enhances mouse liver regeneration after partial hepatectomy. *Pharm Biol.* **2012**, *50*, 523–528. [CrossRef] [PubMed]
13. Mendes, V.I.S.; Rtholomeusz, G.A.; Ayres, M.; Gandhi, V.; Salvador, J.A.R. Synthesis and cytotoxic activity of novel A-ring cleaved ursolic acid derivatives in human non-small cell lung cancer cells. *Eur. J. Med. Chem.* **2016**, *123*, 317–331. [CrossRef] [PubMed]
14. Wang, X.H.; Zhou, S.Y.; Qian, Z.Z.; Zhang, H.L.; Qiu, L.H.; Song, Z.; Zhao, J.; Wang, P.; Hao, X.S.; Wang, H.Q. Evaluation of toxicity and single-dose pharmacokinetics of intravenous ursolic acid liposomes in healthy adult volunteers and patients with advanced solid tumors. *Expert Opin. Drug Metab. Toxicol.* **2013**, *9*, 117–125. [CrossRef] [PubMed]
15. Gao, Y.; Li, Z.; Xie, X.; Wang, C.; You, J.; Mo, F.; Jin, B.; Chen, J.; Shao, J.; Chen, H.; et al. Dendrimeric anticancer prodrugs for targeted delivery of ursolic acid to folate receptor-expressing cancer cells: Synthesis and biological evaluation. *Eur. J. Pharm. Sci.* **2015**, *70*, 55–63. [CrossRef] [PubMed]
16. Sun, L.; Li, B.; Su, X.; Chen, G.; Li, Y.; Yu, L.; Li, L.; Wei, W. An Ursolic Acid Derived Small Molecule Triggers Cancer Cell Death through Hyperstimulation of Macropinocytosis. *J. Med. Chem.* **2017**, *60*, 6638–6648. [CrossRef] [PubMed]
17. Parrino, B.; Carbone, A.; Spano, V.; Montalbano, A.; Giallombardo, D.; Barraja, P.; Attanzio, A.; Tesoriere, L.; Sissi, C.; Palumbo, M.; et al. Aza-isoindolo and isoindolo-azaquinoxaline derivatives with antiproliferative activity. *Eur. J. Med. Chem.* **2015**, *94*, 367–377. [CrossRef] [PubMed]
18. Parrino, B.; Carbone, A.; Ciancimino, C.; Spano, V.; Montalbano, A.; Barraja, P.; Cirrincione, G.; Diana, P.; Sissi, C.; Palumbo, M.; et al. Water-soluble isoindolo[2,1-a]quinoxalin-6-imines: In vitro antiproliferative activity and molecular mechanism(s) of action. *Eur. J. Med. Chem.* **2015**, *94*, 149–162. [CrossRef] [PubMed]
19. Vitaku, E.; Smith, D.T.; Njardarson, J.T. Analysis of the structural diversity, substitution patterns, and frequency of nitrogen heterocycles among U.S. FDA approved pharmaceuticals. *J. Med. Chem.* **2014**, *57*, 10257–10274. [CrossRef] [PubMed]
20. Rashid, S.; Dar, B.A.; Majeed, R.; Hamid, A.; Bhat, B.A. Synthesis and biological evaluation of ursolic acid-triazolyl derivatives as potential anti-cancer agents. *Eur. J. Med. Chem.* **2013**, *66*, 238–245. [CrossRef] [PubMed]
21. Liu, M.C.; Yang, S.J.; Jin, L.H.; Hu, D.Y.; Xue, W.; Song, B.A.; Yang, S. Synthesis and cytotoxicity of novel ursolic acid derivatives containing an acyl piperazine moiety. *Eur. J. Med. Chem.* **2012**, *58*, 128–135. [CrossRef] [PubMed]
22. Gu, W.; Jin, X.Y.; Li, D.D.; Wang, S.F.; Tao, X.B.; Chen, H. Design, synthesis and in vitro anticancer activity of novel quinoline and oxadiazole derivatives of ursolic acid. *Bioorg. Med. Chem. Lett.* **2017**, *27*, 4128–4132. [CrossRef] [PubMed]
23. Qiu, W.W.; Shen, Q.; Yang, F.; Wang, B.; Zou, H.; Li, J.Y.; Li, J.; Tang, J. Synthesis and biological evaluation of heterocyclic ring-substituted maslinic acid derivatives as novel inhibitors of protein tyrosine phosphatase 1B. *Bioorg. Med. Chem. Lett.* **2009**, *19*, 6618–6622. [CrossRef] [PubMed]
24. Li, X.; Bai, X.; Wu, K.; Wang, Y.; Shi, W.; Li, Y.; Yin, S. Synthesis and Antitumor Activities of 3′-Substituted Propanolursolates. *Chin. J. Org. Chem.* **2012**, *32*, 703–708. [CrossRef]
25. Khan, M.S.Y.; Ahmad, S.; Yadav, M.R.; Jindal, D.P. Synthesis and study of azatriterpenes. *J. Indian Chem. Soc.* **1990**, *67*, 330–331.

26. Ma, Y.-T.; Yang, Y.; Cai, P.; Sun, D.-Y.; Sánchez-Murcia, P.A.; Zhang, X.-Y.; Jia, W.-Q.; Lei, L.; Guo, M.; Gago, F.; et al. A Series of Enthalpically Optimized Docetaxel Analogues Exhibiting Enhanced Antitumor Activity and Water Solubility. *J. Nat. Prod.* **2018**, *81*, 524–533. [CrossRef] [PubMed]
27. Zhang, D.; Xu, Q.; Wang, N.; Yang, Y.; Liu, J.; Yu, G.; Yang, X.; Xu, H.; Wang, H. A complex micellar system co-delivering curcumin with doxorubicin against cardiotoxicity and tumor growth. *Int. J. Nanomed.* **2018**, *13*, 4549–4561. [CrossRef] [PubMed]
28. Lv, G.; Sun, D.; Zhang, J.; Xie, X.; Wu, X.; Fang, W.; Tian, J.; Yan, C.; Wang, H.; Fu, F. Lx2-32c, a novel semi-synthetic taxane, exerts antitumor activity against prostate cancer cells in vitro and in vivo. *Acta Pharm. Sin. B* **2017**, *7*, 52–58. [CrossRef] [PubMed]
29. Li, D.J.; Tong, J.; Zeng, F.Y.; Guo, M.; Li, Y.H.; Wang, H.; Wang, P. Nicotinic ACh receptor α7 inhibits PDGF-induced migration of vascular smooth muscle cells by activating mitochondrial deacetylase sirtuin 3. *Br. J. Pharmacol.* **2018**. [CrossRef] [PubMed]
30. Yang, Y.; Guan, D.; Lei, L.; Lu, J.; Liu, J.Q.; Yang, G.; Yan, C.; Zhai, R.; Tian, J.; Bi, Y.; et al. H6, a novel hederagenin derivative, reverses multidrug resistance in vitro and in vivo. *Toxicol. Appl. Pharm.* **2018**, *341*, 98–105. [CrossRef] [PubMed]

Sample Availability: Samples of the compounds are available from the authors.

© 2019 by the authors. Licensee MDPI, Basel, Switzerland. This article is an open access article distributed under the terms and conditions of the Creative Commons Attribution (CC BY) license (http://creativecommons.org/licenses/by/4.0/).

molecules

MDPI

Article

Synthesis and Biological Evaluation of Novel Thiazolyl-Coumarin Derivatives as Potent Histone Deacetylase Inhibitors with Antifibrotic Activity

Viviana Pardo-Jiménez [1,2,*], Patricio Navarrete-Encina [1] and Guillermo Díaz-Araya [2,3,*]

1 Laboratory of Advanced Organic Chemistry, Department of Organic Chemistry and Physical Chemistry, Faculty of Chemical and Pharmaceutical Sciences; University of Chile, Santiago 8380000, Chile; pnavarre@ciq.uchile.cl

2 Laboratory of Molecular Pharmacology, Department of Pharmacological & Toxicological Chemistry, Faculty of Chemical and Pharmaceutical Sciences; University of Chile, Santiago 8380000, Chile

3 Advanced Center of Chronic Diseases (ACCDiS), Faculty of Chemical and Pharmaceutical Sciences, University of Chile, Santiago 8380000, Chile

* Correspondence: vivianapardo@ug.uchile.cl (V.P.-J.); gadiaz@ciq.uchile.cl (G.D.-A.); Tel.: +56-2-2-978-2873 (V.P.-J.); +56-2-2-978-2975 (G.D.-A.)

Academic Editor: Josef Jampilek
Received: 31 December 2018; Accepted: 14 February 2019; Published: 19 February 2019

Abstract: New histone deacetylases (HDAC) inhibitors with low toxicity to non-cancerous cells, are a prevalent issue at present because these enzymes are actively involved in fibrotic diseases. We designed and synthesized a novel series of thiazolyl-coumarins, substituted at position 6 (R = H, Br, OCH_3), linked to classic zinc binding groups, such as hydroxamic and carboxylic acid moieties and alternative zinc binding groups such as disulfide and catechol. Their in vitro inhibitory activities against HDACs were evaluated. Disulfide and hydroxamic acid derivatives were the most potent ones. Assays with neonatal rat cardiac fibroblasts demonstrated low cytotoxic effects for all compounds. Regarding the parameters associated to cardiac fibrosis development, the compounds showed antiproliferative effects, and triggered a strong decrease on the expression levels of both α-SMA and procollagen I. In conclusion, the new thiazolyl-coumarin derivatives inhibit HDAC activity and decrease profibrotic effects on cardiac fibroblasts.

Keywords: thiazolyl-coumarin; HDACs inhibitor; cardiac fibroblasts; antifibrotic

1. Introduction

Cardiac fibrosis is characterized by the excessive deposition of collagens and extracellular matrix (ECM) proteins that lead to impaired organ function, and is the major factor in the progression of myocardial infarction and heart failure [1]. Cardiac fibroblasts (CFs) play a key role in the homeostatic maintenance of ECM and healing after injury [2]. By the use of transforming growth factor beta1 (TGF–β1) they are differentiated to cardiac myofibroblasts (CMFs), which are cells characterized by increased collagen synthesis, expression and assembly in stress fiber of the α–smooth muscle actin (α–SMA), a contractile protein and marker of CMFs [2]. Recent investigations have shown that the expression and activity of distinct histone deacetylases (HDACs) are strongly correlated to the cardiac fibrosis development. The pattern expression analysis of HDAC1 and HDAC2 in hearts showed that HDAC1 is expressed mainly by fibroblasts/interstitial cells, whereas HDAC2 is more prominent in cardiomyocytes with low levels of expression in fibroblasts/interstitial cells. Moreover, in hearts with heart failure, both HDAC1 and HDAC2 showed strong expression in CFs, although HDAC2 maintained its expression in cardiomyocytes. Together, these data suggest that HDAC1 and HDAC2 are mainly associated with the regulation of the biology of CFs in the heart [3–5].

HDACs are enzymes that remove acetyl groups from an ε–N–acetyllysine amino acid on a histone and restore the positive charge to lysine residues [6]. Additionally, non-histone proteins such as transcription factors (e.g., p53, FOXP3), Hsp90, tubulin and other cytoplasmic proteins that play a role in regulatory processes can also be deacetylated by HDACs [7–9]. HDACs are a family of 18 enzymes categorized into four classes: class I (HDAC1, 2, 3 and 8); class II (HDAC4, 5, 6, 7, 9 and 10); class III (SIRT1–7), also known as sirtuins; and class IV (HDAC11). Classes I, II and IV are zinc dependent enzymes, and class III are NAD^+ dependent [10].

HDAC inhibitors (iHDACs) block the access to the active site of HDACs and thus produce hyperacetylation of histones and non-histone proteins. Their effects vary according to cell type and stimulus [11,12]. Hydroxamic acid-based HDAC pan-inhibitors have long been recognized for their antifibrotic action on the heart and, more recently, selective inhibitors of the HDAC class I isoform have been shown to block cardiac fibrosis [13–16]. In the heart, iHDACs have been shown to reduce interstitial cardiac fibrosis by multiple mechanisms, including inhibition of proliferation and/or migration of CFs, induction of genes that suppress ECM protein synthesis of fibroblast, deletion of proinflammatory signals for fibrosis, and blockade of the endothelial-mesenchymal transition [13–16].

iHDACs are compounds either of natural origin or obtained by synthesis and they constitute a very diverse group in terms of structure, biological activity and specificity [17,18]. iHDACs known at present are classified according to their chemical structure in the following groups: hydroxamic acid derivatives, aliphatic acids, benzamides, epoxides, cyclic peptides and sulfonamides containing peptide structures. There are three common characteristics present in these inhibitors: a zinc binding group (ZBG) to coordinate the catalytic metal ion, a hydrophobic spacer that normally has a chain of 5 to 6 methylenes and a surface recognition group (CAP, see Figure 1), which interacts with the outer surface of the enzyme [18,19]. The searching for novel iHDAC compounds with high affinity for these enzymes, but of less structural complexity, low toxicity and easier syntheses remains a challenge for researchers.

Coumarins and their analogues are an important class of compounds of natural and synthetic origin [20]. These compounds belong to the lactone family and are composed of benzene rings condensed onto an α–pyrone ring. In recent years the use of the coumarin ring as a scaffold molecule has occupied an important place in the investigation of new drugs possessing different pharmacological activities such as antibacterial, antiviral, anticancer, anticoagulant, anti-inflammatory, antioxidant and analgesic effects [21,22]. Moreover, coumarin–based benzamides and osthole have been used successfully as CAP in new iHDACs synthesis [23,24]. Coumarin derivatives having various substituted thiazole rings at C-3 exhibit promising biological activities [25]. Recently, syntheses of some new thiazolyl–coumarin derivatives with good anticonvulsivante [26], antimicrobial [27], analgesic and anti-inflammatory activities [28] were also reported. Some thiazolyl–coumarin analogues are found to bepotential anticancer and antimicrobial agents [29], with selective cytotoxicity towards tumor cell lines but not on normal cells [30,31], making them interesting for their evaluation as iHDACs in non-cancer cells.

Another important aspect to consider is that compounds with antifibrotic activity are scarce and nowadays the use of iHDACs has attracted the interest of medicinal chemists due to their participation on avoiding fibrotic disorders [32,33]. This study reports the synthesis, characterization, in vitro inhibitory activity of HDACs and antifibrotic activities of new 3-(2-amino-thiazol-4-yl)-coumarin (CTz) derivatives.

2. Results and Discussion

2.1. Chemistry

To mimic the structural features of the natural compound trichostatin A (TSA) and the three characteristic sites of the enzyme, i.e., the edge, the tubular pocket and the active site that

contains the Zn^{2+} [18,19], the final synthesized compounds are made up of four components: a3-(4-thiazolyl)coumaringroup (CAP), hydrophobic spacer and a ZBG (Figure 1).

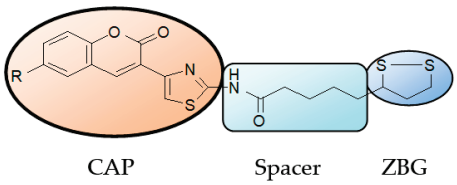

Figure 1. General schematic assembly of the derivatives showing the CAP, spacer and a disulfide ZBG.

2.1.1. Scaffold CAP Synthesis

The CTz ensemble establishes a scaffold that allows us to obtain derivatives easily by substitutions in the coumarin benzene ring and also allow us to form amide bonds with the amino group at position 2 of the thiazole to subsequently incorporate the spacer. The general structure of the scaffold CAP is shown in Figure 2.

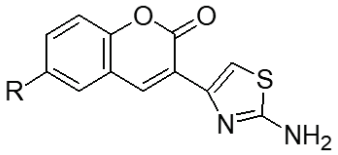

Figure 2. Structure of the CTz derivative scaffold CAP (**4a**, R= H; **4b**,R= Br; **4c**, R= OCH_3).

Starting from 5-substituted-salicylaldehydes **1a**–**c**, compounds **4a**–**c** were synthesized in three steps (Scheme 1).

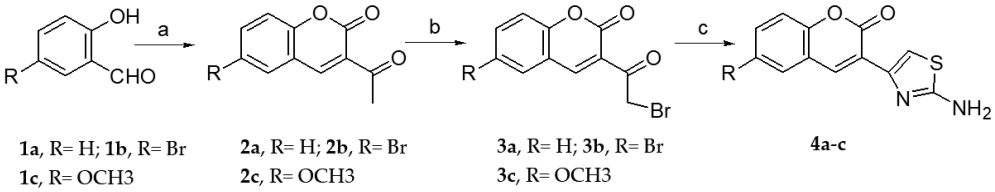

Scheme 1. Reagents and conditions: (a) ethyl acetoacetate, piperidine (drops), 50 °C, 0.5–2 h (depending on R) (**2a**, yield= 85%;**2b**,yield= 84%;**2c**, yield= 88%)(b) Br_2, $CHCl_3/CH_3COOH$, 40–60 °C, 3 h; (**3a**, yield= 80%; **3b**, yield= 86%; **3c**, yield= 66%) (c) (c.1)$SC(NH_2)_2$, EtOH, 78 °C (reflux), 15 min,(c.2) CH_3COONa, H_2O, 50 °C (**4a**, yield= 91%; **4b**, yield= 73%;**4c**, yield= 82%).

The first step corresponding to the synthesis of the substituted acetylcoumarin, was carried out by means of a Knoevenagel-type condensation between the corresponding salicylaldehyde (R = H, OCH_3 and Br) and ethyl acetoacetate in the presence of piperidine as a catalyst. After bromination of the coumarin acetyl group, the last stage of the CAP synthesis was accomplished by using the Hantzsch thiazole synthesis [34]. Fast and easy condensation of bromoacetylcoumarins with thiourea led to the synthesis of derivatives **4a**–**c**.

2.1.2. Adding the Spacer and the ZBG

In this manuscript we study the use of CTz derivatives linked to a spacer which in turn has a ZBG group chosen for its recognized zinc chelating ability. Four different ZBG groups were tested: disulfide, carboxylic acid, catechol and hydroxamic acid. Synthesis of the final derivatives obtained are described in Scheme 2.

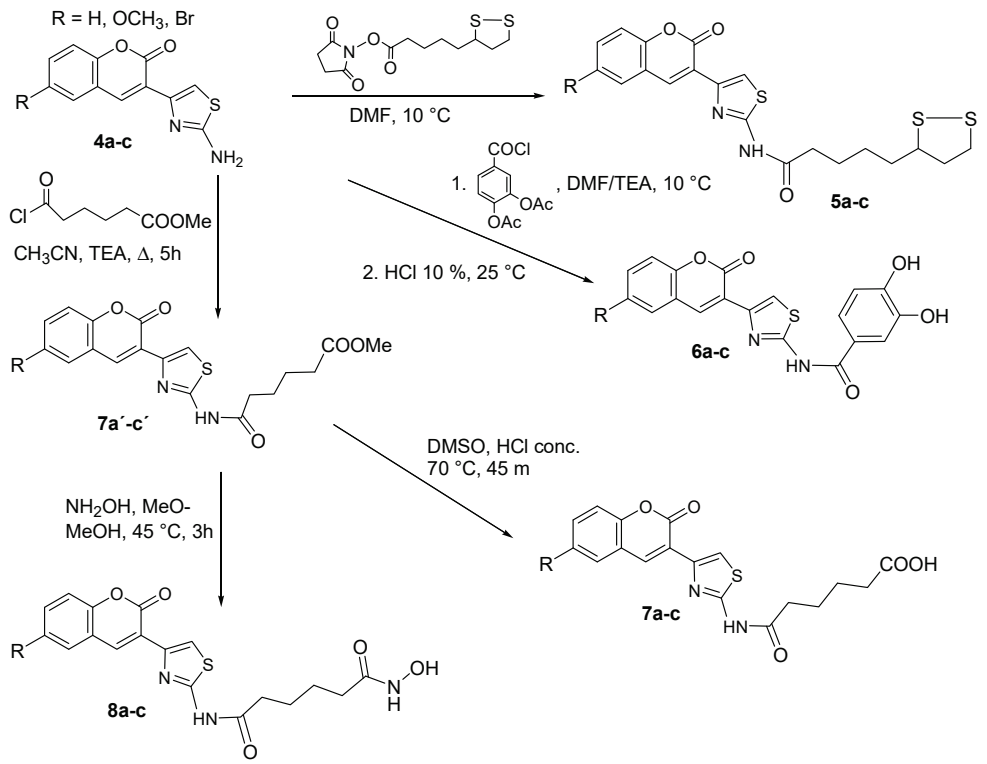

Scheme 2. General scheme of the reactions leading to the final derivatives.

α–Lipoic acid (ALA, 5-(1,2-dithiolan-3-yl) pentanoic acid), has a fivecarbon chain and a disulfide ZBG group. Studies in vitro and in vivo have shown that ALA is able to chelate Zn^{2+}, Cu^{2+} and Fe^{3+} ions [35–38]. The biological effects of ALA are primarily associated with their antioxidant properties [35,36] although it also exhibits antimutagenic, anticarcinogenic activities [37] and produces an increase in normal cell survival [39,40].

3,4–Dihydroxybenzoic acid, is a polyphenol broadly distributed in Nature, forming part of the secondary metabolites of a wide variety of plants and fruits [41]. These phenols are strong transition metal chelating agents for Fe^{3+} and Cu^{2+}, also forming complexes with Zn^{2+} through their hydroxyl groups [42,43]. Polyphenols are also recognized for their antioxidant activity in addition to exhibiting antimicrobial and anticancer properties [41,44].

Valproic and butyric acids are known iHDACs. The inhibitory potency of these compounds is in the low mM range, compared with compounds such as suberoylanilide hydroxamic acid (SAHA) and trapoxin, among others. In most HDAC inhibitory activity studies, short alkyl chain acid derivatives are used [45] and the experimental facts highlight the importance of a voluminous substituent group which must interact with the external surface of the enzyme [18,45]. Therefore, the presence of the CTz as group head could increase the inhibitory potency of the proposed compounds.

The compounds that contain the hydroxamic acid group as a ligand for Zn^{2+}, are those that show the highest inhibitory potency of HDACs [15,45]. This functional group has been widely used in the synthetic strategy of compound inhibitors of matrix metalloproteinases, exhibiting inhibitory concentrations (in vitro) in the nM range [35] but hydroxamic acid derivatives have poor oral bioavailability and are rapidly metabolized in vivo to the corresponding carboxylic acid group [44,46]. In Table 1 we show a summary of the final synthesized and tested compounds.

Table 1. Summary of the synthesized and tested compounds (CTz derivatives).

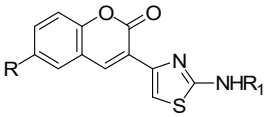

Compound	R_1	R	Yield (%)
5a	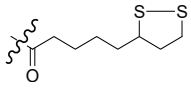	H	80.6
5b	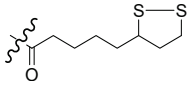	Br	70.5
5c	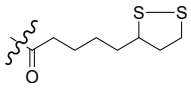	OCH_3	72.5
6a	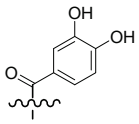	H	71.0
6b	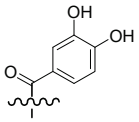	Br	82.0
6c	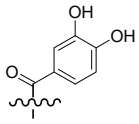	OCH_3	78.0
7a	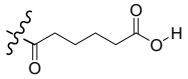	H	81.0
7b	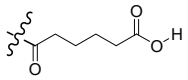	Br	85.0
7c	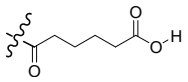	OCH_3	77.0
8a	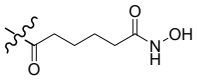	H	64.0
8b	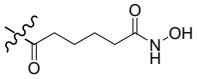	Br	57.0
8c	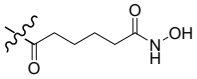	OCH_3	68.0

2.2. HDACs Enzyme Inhibition

The assays of the HDAC inhibitory activity of each of the CTz derivatives were carried out using HeLa cell nuclear extract, HDAC1 and HDAC6 human recombinant as HDAC source. We evaluated the ability of the CTz derivatives, each one in a broad concentration range (10–5000 nM), to inhibit HDACs activity using TSA as positive control. Results were expressed as IC_{50} values and tabulated in Table 2. All compounds showed inhibitory activities against HDACs. Among them, the derivatives **5a–c** and **8a–c** were the most active inhibitory compounds of HDACs nuclear HeLa cells, HDAC1 and HDAC6 isoforms. Among the **5a–c** derivatives, compound **5c** exhibited the highest inhibitory activity with IC_{50} values of 50.0 nM for HeLa cells nuclear HDACs and 39.7 nM for HDAC1, while for

HDAC6 IC_{50} value increases to 84.1 nM. In general, compounds belonging to series 1 displayed modest selectivity towards HDAC1 with a 2.3–fold preference for HDAC1 versus HDAC6. It should be noted that the HeLa cells nuclear extract as well as the isoforms HDACs 1 and 6 used in the assay do not present enzymes that can reduce the disulfide to the corresponding thiol; therefore, we suppose that the disulfide acts per se as ZBG. This behavior has been also observed in diallyl disulfide derivatives which have HDAC inhibitory activity without being previously reduced to thiol [47].

Table 2. Half maximal inhibitory concentration of HDACs activity.

Compounds	Nuclear HeLa Cells Extract IC_{50} (nM)	Class I	Class II
		HDAC1 IC_{50} (nM)	HDAC6 IC_{50} (nM)
5a	66.7 ± 2.9	60.4 ± 1.7	153.4 ± 5.3
5b	62.1 ± 2.5	47.6 ± 2.3	122.8 ± 5.1
5c	50.0 ± 1.7	39.7 ± 1.3	84.1 ± 2.9
6a	573.5 ± 24.4	422.8 ± 30.2	276.1 ± 20.9
6b	508.7 ± 23.3	612.7 ± 32.8	449.5 ± 20.7
6c	476.7 ± 27.5	504.4 ± 31.4	580.5 ± 27.5
7a	6100 ± 390	7689 ± 328	5589 ± 184
7b	5400 ± 400	4666 ± 362	6336 ± 466
7c	4700 ± 310	3382 ± 302	2427 ± 157
8a	66.9 ± 1.8	50.6 ± 2.1	98.3 ± 3.5
8b	57.1 ± 4.5	45.4 ± 2.6	80.2 ± 3.7
8c	41.5 ± 2.7	46.5 ± 2.2	62.6 ± 2.3
TSA	5.0 ± 0.12	2.1 ± 0.06	48.0 ± 4.4

Among the derivatives **8a–c**, compound **8c** exhibited the highest inhibitory activity with IC_{50} values of 41.5 nM for HeLa cells nuclear HDACs and 46.5 nM for HDAC1, while for HDAC6 the IC_{50} value increases to 62.6 nM. Same tendency was observed for compounds **8a** and **8b**. In comparison with the derivatives of series **5** (**5a–c**), those of series **8** (**8a–c**) showed less selectivity towards HDAC class I. This result agrees with the literature, since the selectivity of hydroxamic acid group is often questioned in the drug design, because of its high binding affinity to the zinc and other ions [48].

Compounds **6a–c** possessing a catechol as ZBG, have lower potency in HDACs inhibition than the compounds of series **5** and **8**, probably because they do not have the spacer length corresponding to 5 to 6 methylenes as described in the literature for optimal interaction with the enzyme [18,19]. It is also observed that the compounds of this series are not selective in the inhibition of class I and class II HADCs. With respect to the compounds **7a–c** having a carboxylic acid as ZBG, a weak HDACs inhibitory activity was observed.

These results demonstrated that CTz group is an effective surface recognition CAP for HDACs inhibition. Since the IC_{50} values of the acid derivatives (4.7–6.1 μM) are higher than the values of short chain fatty acid, such as valproic acid (140 μM) and phenylbutyric acid (620 μM) [49], is indicative that the inclusion of a 6–carbon spacer and CTz is responsible of the improvement in the inhibitory activity.The same is observed with the catecholic derivatives (IC_{50}= 477–574 nM) which are more potent inhibitors than catecholic derivatives such as chlorogenic acid (IC_{50}= 375 μM) and caffeic acid (2.54 mM) [50]. However, the CTz capping group did not have a significant impact on the selectivity of the HDAC inhibitors for class I and class II.

2.3. Cellular Assays

2.3.1. Cytotoxicity Assay

CFs were treated for 48 h with all the new CTz derivatives in a broad concentration range (100 μM^{-1} mM), and their cytotoxicity was then evaluated. In Table 3 cytotoxic concentration 50 (CC_{50}) values for each of the synthesized compounds are shown. The data show that all the derivatives have a cytotoxic effect of the same order of magnitude. In each series, the Br derivatives were the

ones that caused an increasein cell death, being **8b** the most cytotoxic compound (CC_{50}= 72.4 μM). The non-substituted derivatives caused less cell death, being compound **5a** the less cytotoxic one (CC_{50}= 200.9 μM). When comparing the different ZBG the series 5 is the least cytotoxic for CFs, while series 8 was the most cytotoxic.

It has been described that HDACs activity has a key role on viability on cancer cells [18,19]. In this study we found no correlation between the HDACs inhibitory activity and cytotoxicity for each series of compounds. These results have also been seen in other studies where iHDACs have been synthesized with alternative ZBG to the hydroxamate, such as mercaptoacetamide and ortho-aminoanilides with higher selectivity towards class I HDACs and less cytotoxic [51].

Table 3. Half maximal inhibitory concentration cytotoxic.(CC_{50}) of new CTz derivatives.

Compound	CC_{50} (μM)
5a	200.9 ± 20.3
5b	127.2 ± 19.2
5c	170.7 ± 6.1
6a	140.2 ± 11.7
6b	102.2 ± 10.3
6c	124.5 ± 12.8
7a	111.4 ± 4.4
7b	80.0 ± 23.6
7c	99.5 ±6.3
8a	90.5 ± 5.1
8b	72.5 ± 11.6
8c	86.5 ± 5.9

2.3.2. Cell Proliferation

CFs were treated for 48 h with 10% fetal bovine serum (FBS), to induce CFs proliferation in presence/absence of each new CTz derivatives in a concentration range of 1–10 μM. In Table 4, the inhibition percentage of cell proliferation for each concentration of the synthesized compounds are shown. All derivatives inhibited CFs proliferation induce by serum.

Table 4. Inhibition percentage of cell proliferation.

Compound	1 μM	5 μM	10 μM
5a	57.3 ± 6.7	70.7 ± 7.1	92.8 ± 6.4
5b	71.5 ± 3.8	89.1 ± 9.5	96.4 ± 4.7
5c	67.0 ± 8.3	83.2 ± 6.8	91.2 ± 3.2
6a	3.0 ± 3.9	35.0 ± 1.9	60.6 ± 1.9
6b	15.8 ± 3.6	40.0± 1.8	64.1 ± 1.7
6c	10.9 ± 3.6	42.2 ± 1.8	64.9 ± 2.3
7a	0.5 ± 0.1	26.8 ± 5.9	45.0 ± 5.1
7b	2.4 ± 1.1	36.1 ± 5.4	48.0 ± 4.8
7c	6.0 ± 0.4	33.0 ± 4.1	48.8 ± 5.2
8a	59.4 ± 6.1	79.9 ± 9.7	94.4 ± 3.8
8b	72.7 ± 3.9	94.4 ± 7.0	104.0 ± 2.8
8c	69.7 ± 9.1	81.8 ± 5.5	97.7 ± 4.7

The derivatives **5a–c** and **8a–c** already has a proliferation inhibition percentage of more than 50% at a concentration of 1 μM, the most powerful in inhibition being compounds **5b** and **8b**. While derivatives **6a–c** and **7a–c** shows a slight inhibition of proliferation at concentrations 1 and 5 μM. These results agree with the results obtained from HDACs inhibitory activity. The derivatives **5a–c** and **8a–c** shows the highest HDAC inhibitory activity, maintaining the trend of greater activity for these two series in inhibiting the proliferation of CFs. The results also show that at concentrations where serum-induced proliferation is inhibited by more than 50%, these compounds are not cytotoxic.

It is important to highlight that CF proliferation playsa key role in cardiac fibrosis development [48]. Therefore, inhibition of CF proliferation by novel CTz derivatives could be important to prevent cardiac fibrosis. Our results showed that at lower concentration, derivatives **5a**–**c** and **8a**–**c** prevent FBS-induced CFs proliferation. Other iHDACs have been shown to inhibit the proliferation of CFs at similar concentrations found for our derivatives, mocetinostat (1 μM), SAHA (10 μM) and apicidin (3 μM) [3,15]. From these results we can conclude that CTz derivatives (**5a**–**c** and **8a**–**c**) at lower concentration could have important effect on cardiac fibrosis by inhibiting CFs proliferation, a key step in active fibrotic disorders.

2.3.3. Cardiac Fibroblast HDACs Inhibition

Our next step was to demonstrate the inhibitory effect on histone deacetylase activity in CFs. For this purpose, CFs of neonatal rats were incubated in the presence/absence of the **5a**, **6a**, **7a** and **8a** derivatives, and the expression of histone H4–acetylated was measured using the western blot technique. Inhibition of HDACs was studied at non-cytotoxic concentrations and TSA was used as a control and also for comparative purposes. In the upper panel of Figure 3, a representative image of the expression of histone H4–acetylated is exhibited, whereas in the lower panel we show the corresponding graphical analysis. The results demonstrate that at anuclear level, CFs expresses detectable levels of H4–acetylated protein. Also, we observed that the **5a**, **6a** and **8a** derivatives increase in a statistically significant manner the histone H4–acetylated expression, while the derivative **7a** had no effect.

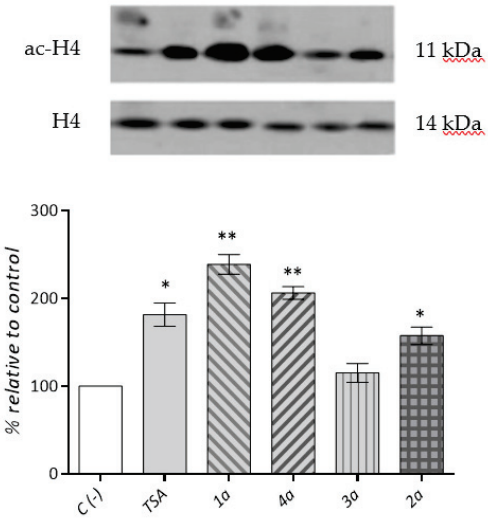

Figure 3. CTz non–substituted derivatives inhibit histone H4 acetylation. CFs were exposed to **5a**, **7a**, **6a** and **8a** at 5 μM for 8 h. TSA at 0.1μM was used as positive control. Nuclear extracts were isolated and histone H4 acetylation expression levels were measured by western blot. Histone H4 was used as control load. The results are showed as Mean +/− SD for three independent experiments. $^{**}p < 0.01$ and $^{*}p < 0.05$ vs. control.

Derivatives **5a** and **8a** showed higher histone H4-acetylated expression levels. These results were complementary and coincident within vitro HDAC inhibition and show that the derivatives increased histone H4–acetylated expression levels, indicative of HDACs inhibition in CFs. These results are quite significant, since no cytotoxic effects were observed at working concentration.

2.3.4. Cardiac Fibroblast α-SMA Expression Levels

It has been indicated that HDACs are important in CFs–to–CMFs differentiation, an important features of cardiac fibrosis development. Thus our objective was to demonstrate that in the CFs the

CTz derivatives reduce α–SMA expression levels and prevent those induced by TGF–β1, therefore inhibiting the differentiation process.

For this purpose, a fixed concentration of **5a**, **6a**, **7a** and **8a** derivatives in the presence/absence of TGF–β1 (a strong inducer of CFs–to–CMFs differentiation), was studied, and α–SMA expression levels were measured by using the western blot technique. TSA was used as a control and also for comparative purposes. In the upper panels of Figure 4 (A and B), representative photographs of α-SMA expression level and glyceraldehyde 3-phosphate dehydrogenase(GAPDH) (used as charge control) are exhibited, while in the lower panel the graphic analyses are shown. In Figure 4A, the results show significant α–SMA expression levels in CFs, and TGF–β1 significantly increased α-SMA expression levels with respect to control levels. In absence of TGF–β1, **5a**, **6a** and **8a** derivatives decreased in a statistically significant manner α-SMA expression levels being **5a** and **8a** derivatives the compounds that strongly decreased α-SMA expression levels, while compound **7a** had no effect. In Figure 4B it can be seen that TGF-β1 significantly increased the expression levels of α-SMA with respect to control levels. Pretreatment of CFs with **5a**, **6a**, **8a** and TSA produce a decrease close to control levels on α-SMA expression levels induced by TGF–β1.

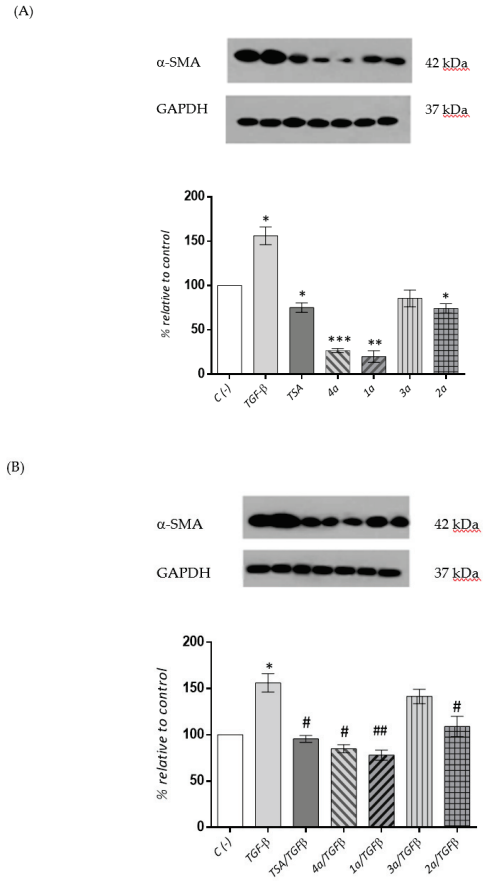

Figure 4. CTz non–substituted inhibit α-SMA expression in cardiac fibroblasts. (**A**) CFs were exposed to **5a**, **6a**, **7a** and **8a** at 5 μM for 48 h. TSA (0.1 μM) and TGF–β1 (5 μg/mL) were used as positive control. (**B**) CFs were exposed to **5a**, **6a**, **7a** and **8a** at 5 μM for 48 h in presence of TGF–β1 (5 μg/mL). α-SMA expression levels were measured by western blot. GAPDH was used as control load. The results are showed as Mean +/− SD for three independent experiments. *$p < 0.05$, **$p < 0.01$ and ***$p < 0.001$ vs. control, #$p < 0.05$ and ##$p < 0.01$ vs. TGF-β1.

2.3.5. Cardiac Fibroblast Procollagen Type I Expression Levels

In CFs collagen type I secretion is a hallmark of cardiac fibrosis development, which is regulated by HDACs. Thus our objective was to demonstrate that in CFs the CTz derivatives reduce procollagen

type I expression levels and prevent those induced by TGF–β1. For this purpose, a fixed concentration of **5a**, **6a**, **7a** and **8a** derivatives in presence/absence of TGF-β1 were studied, and procollagen type I expression levels were measured by using the western blot technique. TSA was used as control and also for comparative purposes. In Figure 5 (A and B), in the upper panel representative photographs of procollagen type I expression level and GAPDH (used as charge control) are shown, whereas in the lower panel the graphic analyses are observed. In Figure 5A, it can be seen that there is significant procollagen type I expression levels in CFs, and TGF–β1 significantly increased procollagen type I expression levels with respect to control. In absence of TGF–β1, **5a**, **6a**, and **8a** derivatives decreased in a statistically significant manner procollagen type I expression levels with respect to control, being **5a** derivative the most potent compound, while compound **7a** had no effect. In Figure 5B, the results show that TGF–β1 significantly increased procollagen type I expression levels with respect to control levels. Pretreatment of CFs with **5a**, **6a**, and **8a** derivatives and TSA decreased, close to control levels, procollagen type I expression levels induced by TGF–β1.

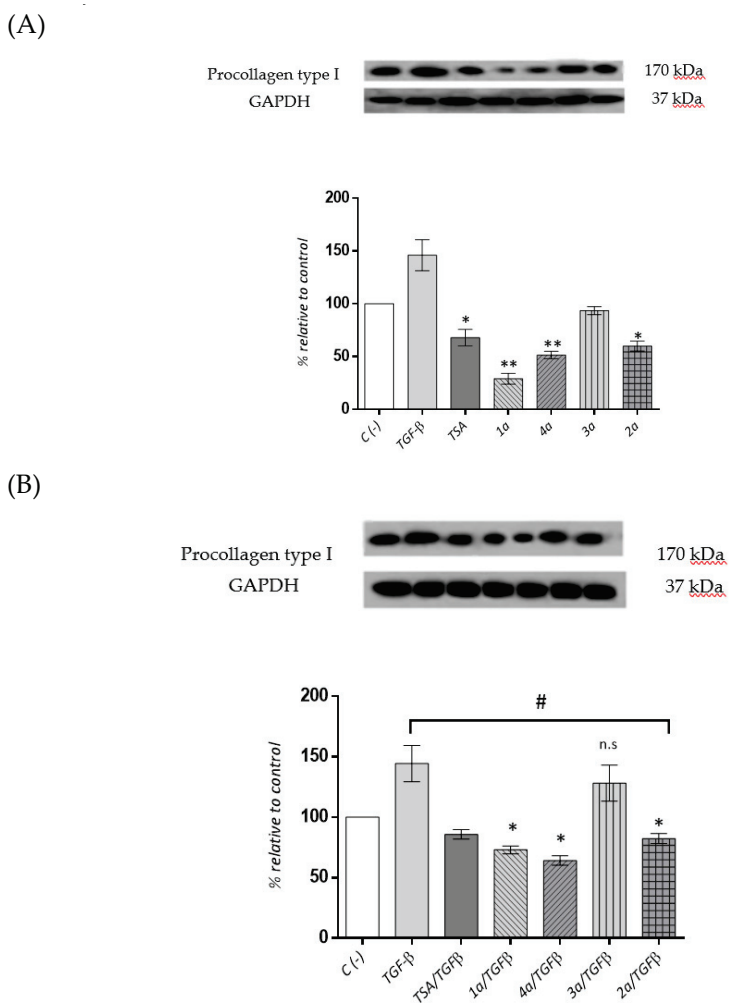

Figure 5. CTz non–substituted inhibit procollagen type I expression levels in cardiac fibroblasts. (**A**) CFs were exposed to **5a**, **6a**, **7a** and **8a** at 5 μM for 48 h.TSA (0.1μM) and TGF–β1 (5 μg/mL) were used as positive control. (**B**) CFs were exposed to **5a**, **6a**, **7a** and **8a** at 5 μM for 48 h in presence of TGF–β1. Procollagen type I expression levels were measured by western blot. GAPDH was used as control load. The results are showed as mean +/− SD for three independent experiments. *$p < 0.05$ and **$p < 0.01$ vs. control, #$p < 0.05$ vs. TGF–β1.

α–SMA is a protein marker of CFs–to–CMF differentiation, a key process in cardiac fibrosis development, whereas collagen type I is the main extracellular matrix protein secreted by CFs, and

it is the main ECM protein involved in cardiac fibrosis development. TGF–β1 is the main growth factor responsible for this differentiation process, and also for collagen synthesis and secretion. Our results showed that **5a**, **6a** and **8a** derivatives decreased both α–SMA and procollagen type I expression levels, either under basal conditions (not stimulated) or under TGF–β1 stimulation, being **5a** and **8a** the most potent inhibitors. These results are consistent with our previous results in which we showed that **5a** and **8a** derivatives were the best HDAC activity inhibitors and those that mostly increased the histone H4-acetylated expression levels. In general terms, our results are consistent with those reported in cardiac and lung fibroblasts where TSA and SAHA inhibit the expression of contractile protein α–SMA [52] as well as, those found in cultured rat CFs, in which TSA blocks TGF–β1–induced collagen synthesis [52,53]. However, we cannot rule out the possibility that our CTz compounds as iHDACs prevent α–SMA and procollagen expression levels through additional mechanisms [54].

Collectively, our results highlight the importance of the disulfide–derivatives and hydroxamic acid ones as the most potent iHDACs. The disadvantages of hydroxamic acids are the biological limitations associated with poor HDACs selectivity and cytotoxicity.

2.4. ADMET Analysis

We cannot ignore the influence of the physicochemical characteristics of each synthesized compounds on the results obtained in the assays carried out in CFs, for this reason a theoretical analysis of the absorption, distribution, metabolism, excretion and toxicity (ADMET) parameters of each CTz was carried out.

The ADMET parameters of CTz derivatives were measured using QikProp software (Table 5). Compounds of the series **5**,**6** and **8** have partition coefficient (QplogPo/w) values in the permeable range 1.8–5.0. The Caco-2 cell permeability (QPPCaco) was in the permissible range of 29–1177. The percentage human oral absorption for the series 1 compounds is 100%, while for the others compounds ranged from 58 to 79%. Compounds belonging to series 7 are out of range of acceptable partition coefficient values. In consequence this may explain the poor effects obtained on CFs assays.

Parameters of the compounds belonging to series **5**,**6** and **8** were all within the acceptable range defined for human use and therefore these compounds may exhibit significant pharmacokinetic and drug likeness properties.

Table 5. ADMET parameters prediction for the thiazolyl–coumarin compounds using QikProp.

Compounds	QlogPo/w [a]	QPPCaco [b]	QPlogBB [c]	Percent Human Oral Absorption [d]	QPlogKp [e]	#metab [f]
5a	4.4	1177	−0.5	100	−1.8	2
5b	5.0	1173	−0.4	100	−2.0	2
5c	4.5	1171	−0.6	100	−1.9	3
6a	1.8	134	−1.5	75	−3.4	3
6b	2.4	134	−1.4	78	−3.6	3
6c	1.9	129	−1.6	76	−3.6	4
7a	0.3	38	−2.1	57	−4.1	3
7b	0.8	37	−2.0	60	−4.3	3
7c	0.4	38	−2.2	58	−4.2	4
8a	2.3	29	−1.8	66	−3.8	3
8b	2.9	29	−1.7	70	−4.0	3
8c	2.4	29	−1.9	67	−3.9	4

[a] Predicted octanol/water partition coefficient (acceptable range: 2.0–6.5).[b] Predicted Caco-2 cell permeability in nm/s (acceptable range: <25 is poor, >500 is great).[c] Predicted brain/blood partition coefficient (Concern value is −3.0 to −1.2).[d] Predicted human oral absorption on 0–100% scale (acceptable range: <25% is poor, >80% is high).[e] Predicted skin permeability, log Kp (acceptable range: −8.0 to −1.0).[f] Number of likely metabolic reactions (acceptable range: 1–8).

3. Experimental Section

3.1. Chemistry

3.1.1. General Information

Nuclear magnetic spectra (^{1}H-NMR, 300 MHz and ^{13}C-NMR, 75.47MHz) were recorded on an Avance DRX 300 spectrometer (Bruker, Billerica, MA, USA) at ambient temperature. Fourier-transform infrared spectroscopy (FTIR) spectra were recorded with a Bruker IFS 55 spectrophotometer in the 600–4000 cm^{-1} range. Matrix-assisted laser desorption/ionization mass spectrometry (MALDI-MS) mass spectra were recorded on a MALDI-time of flight (MALDI-TOF) Microflexsystem (Bruker Daltonics GmbH, Leipzig, Germany) in positive ion mode. Electrospray ionization mass spectra (ESI-MS) were obtained on an electrospray-ion trap type ESI-IT Esquire 4000 mass spectrometer (Bruker Daltonik GmbH, Leipzig, Germany). Melting points were measured on a Electrothermal IA9000 Series Digital Melting Point Apparatus (Rochford, UK) and are uncorrected. Silica gel 60 (0.040–0.063 mm) for column chromatography (Merck, Darmstadt, Germany) was employed. All solvents were purified by routine techniques prior to use.

2-Hydroxybenzaldehyde p.a., ethyl acetoacetate (AcOEt) p.a., acetone p.a., glacial acetic acid p.a., 98% sulfuric acid, sodium acetate p.a., acetic anhydride p.a., chloroform p.a., dimethylsulfoxide (DMSO) p.a., ethanol p.a., sodium hydroxide p.a., sodium sulfate p.a., toluene p.a., were purchased from Merck. 5-methoxy-salicylaldehyde p.a., 5-bromo-salicylaldehyde p.a., 99.9% acetone d6, 3,4-dihydroxybenzoic acid., methyl adipoyl chloride p.a., 99.9% chloroform d6, 99.9% dimethylsulfoxide d6, were from Sigma-Aldrich (St Louis, MO, USA). Methanol p.a., *N,N*-dimethylformamide (DMF), p.a., 37% hydrochloric acid p.a., were from J.T.Baker (Phillipsburg, NJ, USA). Nitrogen 99.995% extra pure was purchased from Linde Gas (Santiago, R.M. Chile).

3.1.2. General Synthesis of 6-substituted-3-acetylcoumarins **2a**–**c**

These derivatives were synthesized in accordance with the Knoevenagel procedure [55]. In a 100 mL Erlenmeyer flask, 82 mmol of the corresponding salicylaldehyde **1a**–**c**, 82 mmol of ethyl acetoacetate and three drops of piperidine as catalyst were added. The solution is stirred at 50 °C. After 15 min the appearance of a yellow precipitate was observed and heating was continued for another 30 min. The reaction conditions varied depending on the substituent, with the 5-methoxy-salicylaldehyde the reaction was carried out at room temperature for 1 h, while using the 5-bromo-salicylaldehyde the reaction was refluxed with ethanol for 2 h. The products of the reactions were monitored by thin layer chromatography (silica gel 60 F254), using EtOAc/hexane 1:2 mixtures as the mobile phase. All pure coumarins were obtained by recrystallization from ethanol. The compounds were characterized by their melting points, ^{1}H-NMR, ^{13}C-NMR and FTIR.

3.1.3. General Synthesis of 3-bromoacetylcoumarins **3a**–**c**

6-Substituted-3-acetylcoumarins **2a**–**c** (15.9 mmol) were dissolved in chloroform (40 mL) and glacial acetic acid (10 mL), then Br_2 (15.9 mmol) was carefully added dropwise while stirring the solution at room temperature. Once the addition of Br_2 was finished, the mixture was heated between 40–60 °C thus facilitating the emission of hydrobromic acid fumes. After 3 h of reaction, precipitation of 3-bromoacetylcoumarin was observed. The solution was allowed to cool to room temperature, filtered and the precipitate washed with three 10 mL portions of cold ethanol. All brominated derivatives were recrystallized from an 80:20 ethanol/chloroform mixture and characterized by their melting points, ^{1}H-NMR, ^{13}C-NMR, and FTIR [56,57].

3.1.4. General Synthesis of 6-substituted-3-(2-amino-thiazol-4-yl)-coumarins **4a**–**c**

To an ethanol solution (150 mL) of 6-substituted-3-bromoacetilcoumarin **3a**–**c** (6.3 mmol) at 50 °C an equimolar amount of thiourea was added with vigorous stirring and maintained at 70 °C. Ten min

after the addition of thiourea, the mixture turned to an intense orange-yellow color and further precipitation of a yellow solid was observed. After evaporation of the solvent to 50% of the initial volume, the mixture was cooled, the solid filtered out and washed with cold ethanol. The yellow solid was dissolved in 200 mL of a hot solution of 10% ammonium acetate in water, stirred for 10 min and then allowed to cool to room temperature. The solids corresponding to **4a–c** were filtered. All compounds were recrystallized from ethanol and characterized by their melting points, ^{1}H-NMR, ^{13}C-NMR and FTIR.

3.1.5. Synthesis of *N*-hydroxysuccinimide (NHS)-lipoate (**9**)

Lipoic acid (1.0 g, 5 mmol) was dissolved in dry DMF (10 mL) in a 50 mL Erlenmayer flask, the solution was cooled to 10 °C in an ice bath and NHS (0.6 g, 5 mmol) was added. The mixture was stirred for 15 min and dicyclohexylcarbodiimide (DCC, 1.0 g, 5 mmol) was added. The solution was stirred for 3 h in an ice bath and further maintained for 9 h at room temperature. The white solid dicyclohexylurea (DCU) was filtered off. The solution was cooled to 8 °C for 5 h and the remaining DCU precipitate was filtered again. The procedure was repeated until no DCU crystals were observed. The solution in DMF containing the activated lipoic (Figure 6) acid was used directly in the formation of compounds **5a–c.**

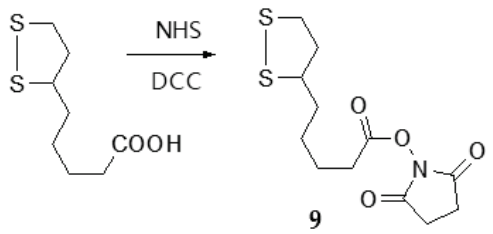

Figure 6. Synthesis of *N*-hydroxysuccinimide (NHS)-lipoate.

3.1.6. General Synthesis of 6-substituted-5-[1,2]-dithiolan-3-yl-pentanoic acid [4-(2-oxo-2*H*-chromen-3-yl)-thiazol-2-yl]-amides **5a–c**

Compounds **4a–c** (4.80 mmol) were added to compound **9** (4.35 mmol) dissolved in dry DMF (25 mL) at 10 °C. The mixture was stirred for 12 h at room temperature (Figure 7). The DMF solution was slowly poured into 100 mL H_2O/ice. A pale yellow solid precipitated. The solid was filtered off and washed with H_2O and then added to a cold concentrated HCl (37%) solution to dissolve the unreacted **4a–c**. The remaining solid was filtered and neutralized with a 10% aqueous sodium bicarbonate solution. The obtained precipitate was purified by using a Merck 60 silica gel column (70–230mesh) and EtOAc/chloroform 1:1 as mobile phase. The yellow color solids were characterized by their melting point, ^{1}H-NMR, ^{13}C-NMR, FTIR and mass spectrometry.

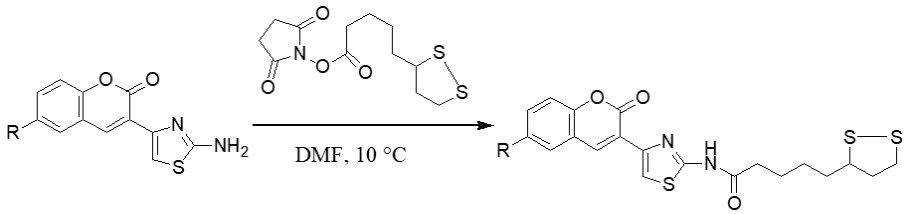

Figure 7. General synthesis of 6-substituted-5-[1,2]-dithiolan-3-yl-pentanoic acid [4-(2-oxo-2*H*-chromen-3-yl)-thiazol-2-yl]-amides.

3.1.7. General Synthesis of 6-substituted-*N*-[4-(2-oxo-2*H*-chromen-3-yl)-thiazol-2-yl]-3,4-dihydroxy-acetylbenzamide Coumarins **6a′–c′**

3,4-Diacetylbenzoic acid chloride (1.2 mmol) was dissolved in dry DMF (10 mL), cooled to 10 °C and **1a–c** (R = H, OCH_3 and Br, 1.7 mmol) dissolved in dry DMF (6 mL) was added dropwise. After

20 min of stirring, triethylamine (Et_3N, 1 mL) was added, and the mixture stirred for 16 h from 10 °C to room temperature (Figure 8). The formed salt was filtered off and the DMF solution was slowly poured into 50 mL H_2O/ice forming a yellow colored precipitate. The solid was filtered and washed with H_2O, then it was added to aqueous cold HCl (37%) to dissolve the compounds **4a**–**c** that did not react, the remaining solid was filtered and neutralized with a solution of sodium bicarbonate. The precipitate obtained was purified by using a Merck 60 silica gel column (70–230 mesh), using the mobile phase EtOAc/dichloromethane 2:1 obtaining a yellow-brown solid which was characterized by their melting point, ^{1}H-NMR, ^{13}C-NMR, FTIR and mass spectrometry.

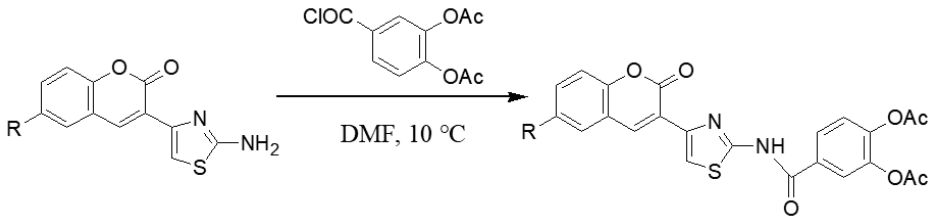

Figure 8. General synthesis of 6-substituted *N*-[4-(2-oxo-2*H*-chromen-3-yl)-thiazol-2-yl]-3,4-dihydroxy-acetylbenzamide coumarins.

3.1.8. General Synthesis of 6-substituted *N*-[4-(2-oxo-2*H*-chromen-3-yl)-thiazol-2-yl]-3,4-dihydroxy-benzamide Coumarins **6a**–**c**

Each derivative **6a′**–**c′** (1.2 mmol) was dissolved in DMF (10 mL) and added to 20% HCl (10 mL). The mixture was stirred at room temperature for 30 min. The formed precipitate was washed with 10% sodium bicarbonate solution and purified using a Merck 60 silica gel column (70–230mesh), using as mobile phase EtOAc/dichloromethane 2:1. Yellow-brown solids corresponding to compounds **6a**–**c**, were obtained, recrystallized in ethanol and characterized by their melting points, ^{1}H-NMR, ^{13}C-NMR and FTIR.

3.1.9. General Synthesis of 6-substituted methyl 5-[4-(2-oxo-2*H*-chromen-3-yl)-thiazol-2-yl-carbamoyl]-pentanoate Coumarins **7a′**–**c′**

In a 100 mL round bottom flask each compound **4a**–**c** (6 mmol) was dissolved in dry acetonitrile (30 mL), adipoyl acid monomethyl ester chloride (6 mmol) and Et_3N (1 mL) were added and the mixture was stirred at reflux for 5 h (Figure 9). A pale yellow solid precipitated, was filtered off and washed with cold acetonitrile and further purified by recrystallization from glacial acetic acid and column chromatography using silica gel Merck 60 (70–230 mesh) and EtOAc/dichloromethane 1:1 as mobile phase. The solid obtained was characterized by their melting point, ^{1}H-NMR, ^{13}C-NMR, FTIR and mass spectrometry. Mild hydrolysis of the methyl esters yields the corresponding pentanoic acid derivatives **7a**–**c**.

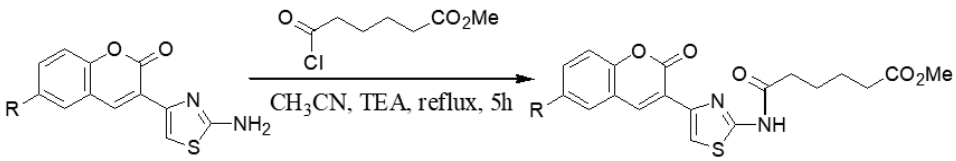

Figure 9. General synthesis of 6-substituted methyl 5-[4-(2-oxo-2*H*-chromen-3-yl)-thiazol-2-yl-carbamoyl]-pentanoate coumarins.

3.1.10. General synthesis of 6-substituted5-[4-(2-oxo-2*H*-chromen-3-yl)-thiazol-2-yl-carbamoyl]-pentanoicacidcoumarins **7a**–**c**

Each compound **7a′**–**c′** (2.6 mmol) was dissolved in DMSO (10 mL) and slowly added to a solution of 37% HCl (20 mL). The mixture was heated to 70 °C with stirring for 45 min. Subsequently the solution was cooled to form a precipitate, which was filtered off and washed with cold water.

The products were purified by using Merck 60 silica gel column (70–230mesh), using the mobile phase EtOAc/dichloromethane 1:3. The whitish yellow solids were characterized by their melting point, FTIR and ^{1}H-NMR. Due to its insolubility it was not possible to characterize these acid derivatives by ^{13}C-NMR or MS.

3.1.11. General synthesis of 6-substituted-5-[4-(2-oxo-2*H*-chromen-3-yl)-thiazol-2-yl-carbamoyl] –pentanoate hydroxamic acid derivatives **8a–c**

Each compound **7a′–c′** (3.9 mmol) was added to a solution with hydroxylamine (3.9 mmol) in 10% sodium methoxide in methanol (100 mL). The mixture was heated to 45 °C for 3 h (Figure 10). Methanol was removed using a rotavapor at room temperature. The residue was neutralized with a cold solution of 10% HCl in methanol. The NaCl formed was filtered off and the methanol was removed again with a rotary evaporator, forming a waxy yellow precipitate. The products were purified by using Merck 60 silica gel column (70–230 mesh), using the mobile phase methanol/dichloromethane 1:3. The yellow solids obtained were characterized by their melting point, ^{1}H-NMR, ^{13}C-NMR, FTIR and mass spectrometry.

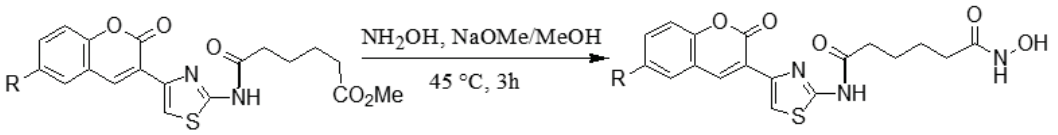

Figure 10. General synthesis of 6-substituted-5-[4-(2-oxo-2*H*-chromen-3-yl)-thiazol-2-yl-carbamoyl]–pentanoate hydroxamic acid derivatives.

3.1.12. Physical Characterization of the Main Precursors and Final Synthesized Compounds

3-(2-Aminothiazol-4-yl)-coumarin (**4a**). Yellow crystals, m.p.: 228–230 °C. Yield: 91%. FTIR (cm^{-1}): 3311 (-NH$_2$); 3148 (aromatic); 1700 (O-C=O, lactone); 1643 (-C=N-); 1602 (-C=C-). ^{1}H-NMR (δ, DMSO-d$_6$): 5.00 (s, 2H, -NH-); 7.20–7.70 (m, 4H, -ArH); 7.85 (s, 1H, -CH=, thiazole); 8.72 (s, 1H, -CH =, coumarin). ^{13}C-NMR (δ, DMSO-d$_6$):112.0; 115.8; 117.5; 124.6; 125.0; 127.1; 133.2; 137.4; 145.3; 154.4; 157.3; 170.2.

3-(2-Aminothiazol-4-yl)-6-bromocoumarin (**4b**). Yellow-pale crystals, m.p.: 224 °C. Yield: 73%. FTIR (cm^{-1}): 3341 (-NH$_2$); 3157 (aromatic); 1710 (O-C=O, lactone). ^{1}H-NMR (δ, DMSO-d$_6$): 5.10 (s, 1 H, -NH-); 7.20 (d, 1H, *J* = 8.4 Hz, -ArH); 7.80 (d, 1H, *J* = 8.47 Hz, -ArH); 7.95 (s, 1H, -ArH); 7.85 (s, 1H, -CH=, thiazole); 8.92 (s, 1H, -CH=, coumarin). ^{13}C-NMR (δ, DMSO-d$_6$): 112.5; 115.9; 118.0; 121.2; 125.3; 128.4; 135.3; 138.6; 146.1; 155.8; 158.7; 172.2.

3-(2-Aminothiazol-4-yl)-6-methoxycoumarin (**4c**). Yellow-orange crystals, m.p.: 201–203 °C. Yield: 82%. FTIR (cm^{-1}): 3300 (-NH$_2$); 3133 (aromatic); 1705 (O-C=O, lactone). ^{1}H-NMR (δ, DMSO-d$_6$): 3.74 (s, 3H, -OCH$_3$); 5.00 (s, 1H, -NH-); 7.08 (s, 1H, -ArH$_5$); 7.4 (d, 1H, *J* = 8.5 Hz, -ArH); 7.7 (d, 1H, *J* = 8.5Hz, -ArH); 7.80 (s, 1H, -CH=, thiazole); 8.7 (s, 1H, -CH=, coumarin). ^{13}C-NMR (δ, DMSO-d$_6$): 56.3; 108.5; 113. 6; 115.0; 115.8; 117.9; 128.5; 133.2; 135.3; 143.2; 152.0; 154.8; 168.9.

5-[1,2]-Dithiolan-3-yl-N-[4-(2-oxo-2H-chromen-3-yl)-thiazol-2-yl]-pentanamide (**5a**). Pale yellow solid, m.p.: 91–92 °C. Yield: 80.6%. FTIR (cm^{-1}): 3155 (aromatic); 2931 (-CH-); 1726 (O-C = O, lactone); 1648 (-C= N-); 1540 (-C=C-). ^{1}H-NMR (δ, DMSO-d$_6$): 1.60 (m, 4H, -CH$_2$-); 1.94 (m, 2H, -CH$_2$-); 2.42 (m, 4H, -CH$_2$-); 2.67 (m, 2H, -CH$_2$-); 3.65 (m, 1H, -CH=); 7.3–7.8 (m, 4H, -ArH); 7.5 (s, 1H, -CH=, thiazole); 8.55 (s, 1H, -CH=, coumarin). ^{13}C-NMR (δ, DMSO-d$_6$): 25.5; 27.0; 33.2; 37.6; 39.3; 40.2; 55.1; 107.0; 117.3; 118.1; 122.4; 124.2; 127.5; 133.7; 139.3; 148.2; 154.5; 157.6; 160.4; 175.1. MALDI-MS theoretical *m*/*z*: 433.0714; *m*/*z* experimental: 433.0694; error (ppm): −4.6. ESI-MS: *m*/*z*: 433.0 [M + H]$^{+}$; 431.0 [M − H]$^{-}$. 306 [M-H$_2$O + C$_3$H$_6$S$_2$ + H]$^{+}$; 245 [M-CO-C$_4$H$_7$-C$_3$H$_5$S$_2$ + H]$^{+}$; 225 [M-H$_2$O + CO + C$_4$H$_9$-C$_3$H$_5$S$_2$ + H]$^{+}$; 207 n.d. 397 [M-H$_2$S − H]$^{-}$. Molecular formula: C$_{20}$H$_{20}$O$_3$N$_2$S$_3$. Molecular weight (monoisotopic): 432.0636 g/mol

5-[1,2]-Dithiolan-3-yl-N-[4-(6-bromo-2-oxo-2H-chromen-3-yl)-thiazol-2-yl]-pentanamide (**5b**). Pale yellow solid, m.p.: 150–153 °C. Yield: 70.5%. FTIR (cm^{-1}): 3197 (aromatic); 2945 (-CH-); 1697 (O-C = O, lactone); 1625 (-C = N-); 1538 (-C = C-). ^{1}H-NMR (δ, DMSO-d_6):1.56 (m, 4 H, -CH_2 -); 1.88 (m, 2H, -CH_2-); 2.42 (m, 4H, -CH_2-); 2.67 (m, 2H, -CH_2-); 3.62 (m, 1H, -CH=); 7.15 (s, 1H, -NH-); 7.20–7.62 (m, 3H, -ArH); 7.53 (s, 1H, -CH=, thiazole); 8.49 (s, 1H, -CH=, coumarin). ^{13}C-NMR(δ,DMSO-d_6): 25.7; 27.3; 33.0; 36.9; 38.7; 40.8; 56.1; 107.8; 117.6; 119.0; 122.6; 124.7; 128.5; 134.2; 140.2; 149.5; 155.5; 158.4; 160.9; 176.3. MALDI-MS: theoretical *m/z*: 510.9819; *m/z*experimental: 510.9796; error (ppm): -4.5. ESI-MS: *m/z*: 513.0 $[M + H]^+$; 511.0 $[M + H]^+$; 511 $[M - H]^-$. 397 [M-HBr + H2S + H]$^+$; 325 [M-CO-C_4H_7-$C_3H_5S_2$ + H]$^+$; 306 [M-HBr + H_2O + $C_3H_6S_2$ + H]$^+$; 189 [M-Br-$C_9H_4O_2$-C_3HNS-NH_2 + H]$^+$. 498 n.d; 396 [M-HBr + H_2S + H]$^+$; 323 [M-CO-C_4H_7-$C_3H_5S_2$ + H]$^+$; 189 [M-Br-$C_9H_4O_2$-C_3HNS-NH_2+H]$^+$. 477 [M-H_2S − H]$^-$. Molecular Formula: $C_{20}H_{19}O_3N_2S_3Br$. Molecular weight (monoisotopic): 509.9741 g/mol.

5-[1,2]-Dithiolan-3-yl-N-[4-(6-methoxy-2-oxo-2H-chromen-3-yl)-thiazol-2-yl]-pentanamide (**5c**). Yellow solid, m.p.: 83–84 °C. Yield: 70.5%. FTIR (cm^{-1}): 3083 (aromatic); 2922 (-CH-); 1702 (O-C = O, lactone); 1640 (-C = N-); 1556 (-C=C-). ^{1}H-NMR (δ, DMSO-d_6): 1.55 (m, 4H, -CH_2-); 1.88 (m, 2H, -CH_2-); 2.41 (m, 4H, -CH_2-); 2.68 (m, 2H, -CH_2-); 3.62 (m, 1H, -CH=); 7.15 (s, 1H, -NH-); 7.4 (d, 1H, *J* = 8.5 Hz, -ArH) 7.55 (s, 1H, -CH=, thiazole); 7.7 (d, 1H, *J* = 8.5 Hz, -ArH); 8.1 (s, 1H, -ArH); 8.45 (s, 1H, -CH=, coumarin). ^{13}C-NMR (δ, DMSO-d_6): 25.3; 27.15; 31.7; 36.3; 39.5; 40.9; 54.3 55.1; 108.2; 110.5; 117.1; 117.4; 117.7; 119.1; 139.7; 146.3; 146.4; 153.3; 154.5; 158.2; 177.1. MALDI-MS theoretical *m/z*: 463.0820; *m/z*experimental: 463.0797; error (ppm): −5.0. ESI-MS: *m/z*: 463.0 $[M + H]^+$; n.d $[M - H]^-$. 398 [M-C_3OH + H_2S_2 + H]$^+$; 275 [M-CO-C_4H_7-$C_3H_5S_2$ + H]$^+$. Molecular formula: $C_{21}H_{22}O_4N_2S_3$. Molecular weight (monoisotopic): 462.0742 g/mol.

N-[4-(2-Oxo-2 H-chromen-3-yl) -thiazol-2-yl]-3,4-dihydroxyacetyl-benzamide (**6a′**). Pale yellow solid, m.p.: 175–177 °C. Yield: 75%. FTIR (cm^{-1}): 3064 (aromatic); 2926 (-CH-); 1707 (O-C=O, lactone); 1609 (-C=N-); 1485 (-C=C-). ^{1}H-NMR (δ, DMSO-d_6):3.00 (s, 3H, -CH_3); 3.17 (s, 3H, -CH_3); 7.18 (s, 1H, -NH); 7.30–7.98 (m, 7H, -ArH); 7.85 (s, 1H, -CH=, thiazole); 8.73 (s, 1H, -CH=, coumarin). ^{13}C-NMR (δ, DMSO-d_6): 25.3 (d); 109.2; 113.9; 116.3; 119.7 (d); 121.0; 125.2; 129.2; 131.9; 132.0; 138.5; 139.3; 137.4; 143.7; 144.5; 152.6; 152.8; 157.3; 159.4 (d); 167.9; 173.6. MALDI-MS theoretical *m/z*: 465.0756; *m/z* experimental: 465.0737; error (ppm): −4.0. ESI-MS: *m/z*: 465.0 $[M + H]^+$; n.d $[M - H]^-$. 424 [M-CH_3CHO +H]$^+$; 387 [M-H_2O + HO-$COCH_3$ + H]$^+$; 258 n.d; 136 [M-H-$C_9H_4O_2$-C_3H-NS-NH-CO + CO-CH_2O + H]$^+$. Molecular Formula: $C_{23}H_{16}O_7N_2S$. Molecular weight (monoisotopic): 464.0678 g/mol.

N-[4-(6-Bromo-2-oxo-2H-chromen-3-yl)-thiazol-2-yl]-3,4-dihydroxyacetyl-benzamide (**6b′**). Pale yellow solid, m.p.: 214–217 °C. Yield: 70%. FTIR (cm^{-1}): 3068 (aromatic); 2931 (-CH-); 1727 (O-C=O, lactone); 1631 (-C=N-); 1504 (-C=C-). ^{1}H-NMR (δ, DMSO-$_{d6}$):3.05 (s, 3H, -CH_3); 3.19 (s, 3H, -CH_3); 7.18 (s, 1H, -NH); 7.35-8.00 (m, 6H, -ArH); 7.92 (s, 1H, -CH=, thiazole); 8.91 (s, 1H, -CH=, coumarin). ^{13}C-NMR (δ, DMSO-d_6):26.4 (d); 109.5; 114.0; 116.5; 119.8; 119.4121.0; 126.6; 130.0; 133.2; 133.4; 139.0; 140.3; 144.1; 144.8; 153.4; 154.1; 157.9; 162.4 (d); 169.8; 177.3. MALDI-MS theoretical *m/z*: 542.9862; experimental *m/z*: 542.9839; error (ppm): −4.2. ESI-MS: *m/z*: n.d. $[M + H]^+$; n.d. [M − H]. Due to the low intensity of the signals, fragmentation characterization at low resolution could not be performed. Molecular Formula: $C_{23}H_{15}O_7N_2SBr$. Molecular weight (monoisotopic): 541.9783 g/mol.

N-[4-(6-Methoxy-2-oxo-2H-chromen-3-yl)-thiazol-2-yl]-3,4-dihydroxyacetyl-benzamide (**6c′**). Yellow solid, m.p.: 118–120 °C. Yield: 68.2%.FTIR (cm^{-1}): 3116 (aromatic); 2927 (-CH-); 1714 (O-C=O, lactone); 1611 (-C=N-); 1572 (-C=C-).^{1}H-NMR (δ, DMSO-d_6):3.00 (s, 3H, -CH_3); 3.16 (s, 3H, -CH_3); 3.83 (s, 3H, -OCH_3); 7.00–8.10 (m, 6H, -ArH); 7.80 (s, 1H, -CH =, thiazole); 8.41 (s, 1H, -NH); 8.72 (s, 1H, -CH=, coumarin). ^{13}C-NMR (δ, DMSO-d_6):25.3 (d); 58.8; 108.1; 112.7; 115.3; 118.6; 120.9; 124.5; 128.7; 130.8; 131.7; 137.5; 138.3; 142.5; 144.3; 151.3; 152.0; 156.1; 158.5 (d); 166.6; 172.8. MALDI-MS theoretical *m/z*: 495.0862; experimental *m/z*: 495.0840; error (ppm): −4.4. ESI-MS: *m/z*: 495.0 $[M + H]^+$; 493.0 $[M - H]^-$. 450 [M-CH_3 CHO + H]$^+$; 401 [M-H_2O + CO_2 + CH_3OH + H]$^+$; 372 [M-H_2O + HO-$COCH_3$ + CH_3CHO

+ H]$^+$; 270 [M-CH_2O + C_6H_4-(O-CO-CH_3)$_2$]$^+$; 452 [M-CH_2CO− H]$^-$; 479 [M-CH_3− H]$^-$. Molecular formula: $C_{24}H_{18}O_8N_2S$. Molecular weight (monoisotopic): 494.0784 g/mol.

5-[4-(2-Oxo-2H-chromen-3-yl)-thiazol-2-yl-carbamoyl]-pentanoic acid methyl ester (**7a′**). Pale yellow solid, m.p.: 165–166 °C. Yield: 75%. FTIR (cm^{-1}): 3185 (aromatic); 2981 (-CH-); 1687 (O-C = O, lactone); 1643 (-C= N-); 1539 (-C=C-). ^{1}H-NMR (δ, DMSO-d$_6$):1.60 (m, 4H, -CH_2-); 2.35 (t, 2H, -CH_2-); 2.49 (t, 2H, -CH_2-) 3.59 (s, 3H, -OCH_3); 7.05–7.47 (m, 4H, Ar-H); 7.51 (s, 1H, -CH=, thiazole); 8.2 (s, 1H, -NH); 8.48 (s, 1H, -CH=, coumarin). ^{13}C-NMR (δ, DMSO-d$_6$):24.7; 25.7; 32.2; 33.7; 49.9; 109.1; 116.3; 119.5; 120.4; 125.0; 129.1; 132.2; 138.7; 152.7; 154.1; 159.2; 168.2; 169.8; 173.0. MALDI-MS theoretical *m/z:* 387.1015; experimental *m/z*: 387.0996; error (ppm): −4.9. ESI-MS: *m/z*: 387.0 [M + H]$^+$; 385.0 [M − H]$^-$. 355 [M-CH_3OH + H]$^+$; 311 [M-H_2O + $COOCH_2$ + H]$^+$; 271 [M-C_4H_9-$COOCH_3$ + H]$^+$; 245 [M-CO-C_4H_7-$COOCH_3$ + H]$^+$. 353 [M-CH_3OH − H]$^-$; 310 [M-H_2O + $COOCH_2$− H]$^-$; 243 [M-CO-C_4H_7-$COOCH_3$− H]$^-$. Molecular formula: $C_{19}H_{18}O_5N_2S$. Molecular weight (monoisotopic): 386.0936 g/mol.

5-[4-(6-Bromo-2-oxo-2H-chromen-3-yl)-thiazol-2-yl-carbamoyl]-pentanoic acid methyl ester (**7b′**). Yellow solid, m.p.: 182–185 °C. Yield: 61.4%. FTIR (cm^{-1}): 3067 (aromatic); 2943 (-CH-); 1704 (O-C=O, lactone); 1639 (-C= N-); 1536 (-C= C-). ^{1}H-NMR (δ, DMSO-d$_6$):1.70 (m, 4H, -CH_2-); 2.38 (t, 2H, -CH_2-); 2.56 (t, 2H, -CH_2-); 3.61 (s, 3H, -OCH_3); 7.30 (d, 1H, *J* = 8.4 Hz, Ar-H); 7.80 (d, 1H, *J* = 8.4 Hz, Ar-H); 7.83 (s, 1H, Ar-H); 8.00 (s, 1H-CH=, thiazole); 8.92 (s, 1H, -CH =, coumarin). ^{13}C-NMR (δ, DMSO-d$_6$):24.9; 25.8; 32.9; 34.5; 51.8; 110.0; 119.7; 120.3; 121.4; 125.5; 129.8; 135.2; 140.6; 153.7; 155.6; 160.0; 170.3; 173.1; 173.9. MALDI-MS theoretical *m/z*: 465.0120; experimental *m/z*: 465.0103; error (ppm): −3.7. ESI-MS: *m/z*: 467.0 [M + H]$^+$; 465.0 [M − H]$^+$; 463.0 [M − H]$^-$. 435 [M-CH_3OH + H]$^+$; 325 [M-CO-C_4H_7-$COOCH_3$ + H]$^+$; 433 [M-CH_3OH + H]$^+$; 409 n.d; 323 [M-CO-C_4H_7-$COOCH_3$ + H]$^+$; 431 [M-CH_3OH-H]$^-$; 321 [M-CO-C_4H_7-$COOCH_3$− H]$^-$. Molecular formula: $C_{19}H_{17}O_5N_2SBr$. Molecular weight (monoisotopic): 464. 0042 g/mol.

5-[4-(6-Methoxy-2-oxo-2H-chromen-3-yl)-thiazol-2-yl-carbamoyl]-pentanoic acid methyl ester (**7c′**). Yellow solid, m.p.: 163–164 °C. Yield: 64%. FTIR (cm^{-1}): 3188 (aromatic); 2935 (-CH-); 1705 (O-C=O, lactone); 1614 (-C = N-); 1540 (-C=C-). ^{1}H-NMR (δ, DMSO-d$_6$):1.75 (m, 4H, -CH_2-); 2.36 (m, 2H, -CH_2-); 2.50 (m, 2H, -CH_2-); 3.68 (s, 3H, -OCH_3); 6.96 (s, 1H, -NH); 7.06 (d, 1H, *J* = 8.5 Hz -ArH); 7.30 (d, 1H, *J* = 8.5 Hz -ArH); 7.75 (s, 1H, -CH =, thiazole); 8.23 (s, 1H, -ArH); 8.44 (s, 1H, -CH =, coumarin). ^{13}C-NMR (δ, DMSO-$_{d6}$):24.5; 25.3; 33.1; 35.0; 49.3; 55.1; 109.0; 116.0; 116.4; 117.0; 119.5; 124.0; 138.5; 151.1; 152.5; 158.6; 166.3; 169.8; 173.0. MALDI-MS theoretical *m/z*: 417.1120; experimental *m/z*: 417.1102; error (ppm): −4.3. ESI-MS: *m/z*: 417.0 [M + H]$^+$; 415.0 [M − H]$^-$. 385 [M-CH_3OH + H]$^+$; 341 [M-H_2O + $COOCH_2$ + H]$^+$; 301 [M-C_4H_9-$COOCH_3$ + H]$^+$; 275 [M-CO-C_4H_7-$COOCH_3$ + H]$^+$. 383 [M-CH_3OH − H]$^-$; 273 [M-CO-C_4H_7-$COOCH_3$− H]$^-$. Molecular formula: $C_{20}H_{20}O_6N_2S$. Molecular weight (monoisotopic): 416.1042 g/mol.

5-[4-(2-Oxo-2H-chromen-3-yl)-thiazol-2-yl-carbamoyl]-N-hydroxypentanamide (**8a**). Pale yellow solid, m.p.: 150–152 °C (d). Yield: 64%. FTIR (cm^{-1}): 3057 (aromatic); 2925 (-CH-); 1699 (O-C=O, lactone); 1640 (-C=N-); 1539 (-C=C-).^{1}H-NMR (δ, DMSO-d$_6$): 1.50 (m, 4 H, -CH_2-); 2.02 (m, 4H, -CH_2-); 5.50 (s, 1H, -CONH-); 6.50-7.30 (m, 4H, Ar-H); 7.97 (s, 1H, -CH =, thiazole); 8.50 (s, 1H, -CONHOH); 8.60 (s, 1H, -CH=, coumarin). ^{13}C-NMR (δ, DMSO-d$_6$):24.7; 25.7; 32.2; 33.7; 49.9; 109.1; 116.3; 119.5; 120.4; 125.0; 129.1; 132.2; 138.7; 152.7; 154.1; 159.2; 168.2; 169.8; 173.0. MALDI-MS theoretical m/z: 388.0967; experimental m/z: 388.0953; error (ppm): −3.6. ESI-MS: *m/z:* 388.0 [M + H]$^+$; 386.0 [M − H]$^-$. 370 [M-H_2O + H]$^+$; 355 [M-NH_2OH + H]$^+$; 271 [M-C_4H_9-CONHOH + H]$^+$; 245 [M-CO-C_4H_7-CONHOH + H]$^+$. 353 [M-NH_2OH − H]$^-$; 259 n.d.; 243 [M- CO-C_4H_7-CONHOH − H]$^-$; 141 [M-H-$C_9H_4O_2$-C_3HNSNH_2− H]$^-$. Molecular Formula: $C_{18}H_{17}O_5N_3S$. Molecular weight (monoisotopic): 387.0889 g/mol.

5-[4-(6-Bromo-2-oxo-2H-chromen-3-yl)-thiazol-2-yl-carbamoyl]-N-hydroxypentanamide (**8b**). Pale yellow solid, m.p.: 106–110 °C (d). Yield: 57%. FTIR (cm^{-1}): 3032 (aromatic); 2951 (-CH-); 1698 (O-C=O,

lactone); 1648 (-C=N-); 1537 (-C=C-). ^{1}H-NMR (δ, DMSO-$_{d6}$):1.50 (m, 4H, -CH2-); 2.50 (m, 4H, -CH_2-); 7.24 (s, 1H, -CONH-); 7.52 (s, 1H, -CH=, thiazole); 7.39 (d, 1H, *J* = 9.0 Hz, ArH); 7.40 (s, 1H, ArH); 7.73 (d, 1H, *J* = 9.0 Hz, ArH); 8.10 (s, 1H, -CONHOH); 8.50 (s, 1H, -CH= coumarin). ^{13}C-NMR (δ, DMSO-d_6): 31.5; 32.4; 34.4 (d); 110.1; 116.8; 118.5; 121.7; 121.8; 131.3; 134.1; 131.0; 134.1; 137.1; 143.5; 151.5; 158.7; 168.0. Due to the insolubility of the compound it was not possible to perform mass spectrometry analysis. Molecular Formula: $C_{18}H_{16}O_7N_2SBr$.

5-[4-(6-Methoxy-2-oxo-2H-chromen-3-yl)-thiazol-2-yl-carbamoyl]-N-hydroxypentanamide (**8c**). Pale yellow solid, m.p.: 125–127 °C (d). Yield: 68%.FTIR (cm^{-1}): 3136 (aromatic); 2916 (-CH-); 1721 (O-C=O, lactone); 1631 (-C=N-); 1555 (-C=C-).1H-NMR (δ, DMSO-d_6):1.56 (m, 4H, -CH_2-); 1.97 (m, 4H, -CH_2-); 3.82 (s, 3H, -OCH_3); 7.20 (d, 1H, *J* = 9.0 Hz, ArH); 7.53 (s, 1H, ArH); 7.34 (s, 1H, -CONH-); 7.38 (d, 1H, *J* = 9.0 Hz, ArH); 7.98 (s, 1H, -CH =, thiazole); 8.50 (s, 1H, -CONHOH); 8.53 (s, 1H, -CH= coumarin). ^{13}C-NMR (δ, DMSO-d_6): 24.8; 25.2; 32.6; 35.2; 56.3; 109.4; 111.1; 111.5; 117.4; 119.7; 120.1; 121.0; 139.0; 147.0; 155.3; 159.2; 168.3; 169.3; 172.1. MALDI-MS theoretical m/z: 418.1073; m/z experimental: 418.1053; error (ppm): −4.8. ESI-MS: *m/z*: 418.0 $[M + H]^+$; 416.0 $[M - H]^-$. 400 $[M\text{-}H_2O + H]^+$; 385 $[M\text{-}CH_3OH + H]^+$; 301 $[M\text{-}C_4H_9\text{-}CONHOH + H]^+$; 275 $[M\text{-}CO\text{-}C_4H_7\text{-}CONHOH + H]^+$. 383 $[M\text{-}CH_3OH - H]^-$; 288 n.d.; 273 $[M\text{-}CO\text{-}C_4H_7\text{-}CONHOH - H]^-$; 141 $[M\text{-}H\text{-}CH_3O\text{-}C_9H_4O_2\text{-}C_3HNS\text{-}NH_2 - H]^-$. Molecular Formula: $C_{19}H_{19}O_6N_3S$. Molecular weight (monoisotopic): 417.0995 g/mol.

3.2. Biology

3.2.1. Reagents

Fetal bovine serum (FBS), trypsin/ethylenediaminetetraacetic acid (EDTA), molecular weight standard and organic and inorganic compounds were purchased from Merck (Darmstadt, Germany). Reagents for enhanced chemiluminescence (ECL) were purchased from PerkinElmer Life Sciences (Boston, MA, USA). Sterile plastic material was obtained from Corning Inc. (Corning, NY, USA). Primary anti-histone H4–acetylated antibody and total histone H4 were purchased from R & D Systems (Minneapolis, MN, USA). Primary anti–collagen type I and anti–α–SMA were purchased from Sigma-Aldrich (St. Louis, MO, USA). Primary anti–GAPDH antibody and secondary antibodies conjugated to horseradish peroxidase (HRP) were obtained at Santa Cruz Biotechnology (Dallas, TX, USA). Alamar Blue® from Invitrogen was purchased to Thermo Fisher (Waltham, MA, USA).

3.2.2. Cell Culture.

Sprague Dawley rats were obtained from the Animal Breeding Facility of the School of Chemical and Pharmaceutical Sciences at the University of Chile. All studies followed the Guide for the Care and Use of Laboratory Animals published by the US National Institutes of Health (NIH Publication 8th, 2011), and experimental protocols were approved by the University of Chile Institutional Ethics Review Committee. CF were isolated from of 2 or 3–day–old Sprague-Dawley rats and cultured as described previously [58]. Briefly, the neonatal rats were decapitated and their hearts were extracted under aseptic environment. Atria were removed and ventricles were cut into small pieces (~1–2 mm) for posterior colagenase II digestion. The digestion yield was separated by 10 min centrifugation at 89×*g*. The pellet was resuspended in 10 mL of Dulbecco's Modified Eagle's Medium/Nutrient F-12 (DMEM-F12) supplemented with 10% FBS and antibiotics (100 μg/mL streptomycin and 100 units/mL penicillin) and cultured in a humid atmosphere of 5% CO_2 and 95% O_2 at 37°C until confluence (5 days). The purity of the CFs population was assessed through the expression of several markers. CFs had positive staining against vimentin (Santa Cruz Biotechnology), while being negative against sarcomeric actin and desmin (Sigma-Aldrich). Experiments were performed on cells at passage 1. Cells were cultured in 35-mm well plates and serum starved for 24 h prior to stimulation.

3.2.3. Cytotoxicity and Cell Proliferation Assay

To evaluate cytotoxicity, CFs were seeded in 12 microwell plates at a ratio of 2×10^4 cell/cm^2, cultured in DMEM–F12 medium + 10% FBS, which was subsequently replaced by DMEM–F12. After 24 h of serum starvation derivatives were applied at proper times and concentrations in accordance to experimental procedures. Cell viability assays were carried out using Alamar Blue®, a nontoxic, cell permeable non fluorescent compound that is blue in color. Viable cells reduce resazurin to resorufin, which produces very bright red fluorescence which is used as a quantitative cell viability measure. 10 μL of 0.2 mg/mL Alamar Blue® was added into each well followed by incubation for 24 h. The fluorescence of Alamar Blue® was read using microplate reader at 570 excitation and emission to 595 nm. Cell survival was expressed as percentage over the untreated cells. To evaluate CFs proliferation assay, cells were seeded as mentioned before, and after serum starvation, they were stimulated by 10% fetal bovine serum (FBS), in presence/absence of CTz derivatives for 24 h, at concentrations according to experiment. Cell proliferation was quantified by Alamar Blue®, according to protocol mentioned before. Cell proliferation was expressed as percentage over the control FBS treated cells.

3.2.4. HDACs Inhibitory Activity Assay

The inhibitory activity of the synthesized compounds against HDACs Hela cells nuclear extract, HDAC1 (class I) and HDAC6 (class II) were measured utilizing the Fluorometric Drug Discovery Assay Kit BML-AK500-0001 (HeLa cells nuclear extract), BML-AK511 (HDAC1), and BML-AK516 (HDAC6) (Enzo Life Science, Farmingdale, NY, USA). The HDACs fluorometric substrate and assay buffer were added to HeLa nuclear extracts and also to HDACs 1 and 2 substrates in a 96–wellplate and incubated at 37 °C for 30 min. TSA at 5 nM served as the positive control. The fluorophore produced was detected in a plate spectrofluorimeter, with an excitation of 360 nm and an emission of 460 nm. The assay was performed according to the manufacturer's instructions, at various concentrations of the synthesized compounds.

3.2.5. Preparation of the Cell Lysate

For the analysis of the protein expression of histone H4–acetylated (ac–H4) and total H4 histone, a number of 1×10^6 of CFs seeded in 60 mm plates was used, which were incubated with the inhibitory compounds at a concentration of 10 μM, in the absence/presence of TGF–β1(5ng/mL) for 4 h. Subsequently, total histones were extracted by the technique of saline precipitation (high salt extraction). Briefly, CFs were scraped from the plates with 1 mL of cold PBS transferring their contents to Eppendorf tubes to be centrifuged for 60 s at 1500 rpm at 4 °C and re–suspended in 400 μL of cold buffer A (10 mM 4-(2-hydroxyethyl)-1-piperazineethanesulfonic acid-KOH (HEPES-KOH) adjusted to pH 7.9, 1.5 mM $MgCl_2$, 10 mM KCl, 0.5 mM dithiothreitol and 0.2 mM phenylmethylsulfonyl fluoride (PMSF). The suspension is left on ice for 10 min and then placed in the vortex for 10 s. The samples were centrifuged for 60 s, subsequently discarding the supernatant fraction. The obtained pellet was re-suspended in 60 μL of cold C buffer (20 mM HEPES-KOH adjusted to pH 7.9, 25% glycerol, 420 mM NaCl, 1.5 mM $MgCl_2$, 0.2 mM EDTA, dithiothreitol 0.5 mM and 0.2 mM PMSF) and placed on ice for 20 min for saline precipitation. Cell debris is removed by centrifugation for 120 s at 1500 rpm at 4 °C and the supernatant fraction, which contains the DNA binding proteins, is stored at minus 20 °C. For the analysis of α–SMA and procollagen type I expression levels, 3×10^5 CFs seeded in 35 mm plates were used, which were incubated together with inhibitor compounds at a 5 μM, in the absence/presence of TGF–β1 (5 ng/mL) for 48 h. To obtain the total proteins, the CFs were washed three times with cold PBS, then scraped and lysed with 50 μL of radio inmuno-precipitation assay (RIPA) lysis buffer (10 mM Tris–HCl pH 7.2, 5 mM EDTA, 150 mM NaCl, Triton X–100 1%, sodium dodecyl sulfate (SDS) 0.1%, deoxycholate 1%, leupeptin 2 μg/mL, aprotinin 10mM, PMSF 1mM and Na_3VO_4 100μM). The solution was centrifuged for 15 min at 10,000 rpm and at 4 °C. The supernatant

fraction containing the total proteins was stored at minus 20 °C. The concentration of proteins obtained was determined by spectrophotometry at 570 nm, using the Bradford method (Bio-Rad, Hercules, CA, USA).

3.2.6. Western Blot Analysis

CFs proteins (25 μg), were subjected to 10% sodium dodecyl sulfate-polyacrylamide gel electrophoresis and finally transferred onto a nitrocellulose membrane (Millipore, Billerica, MA, USA). The membrane was washed twice with tris–buffered saline solution containing 0.1% Tween 20 (TBST). After being blocked with TBST containing 5% nonfat milk for 40 min, the membrane was incubated with primary antibodies in TBST/1% nonfat milk at 4 °C overnight. The membrane was washed three times with TBST for a total of 15 min and then incubated with primary antibodies (ac–H4, H4 total, α-SMA, procollagen type I and GAPDH). Then the membrane was incubated with goat anti–rabbit or anti-mouse IgG antibodies conjugated with horseradish (diluted 1:1000) for 1 h at room temperature. Signals were developed with ECL reagents and exposure to photographic film.

3.2.7. Prediction of ADMET Properties

The ADMET properties of the thiazolyl–coumarin derivatives as drug candidate were predicted using the software QikProp (Schrödinger Release2018-4: QikProp, Schrödinger, LLC, New York, NY, USA, 2018).

4. Conclusions

Synthesis and evaluation of different ZBGs linked to thiazolyl–coumarin moieties shows that the series **5** and series **8** derivatives are potent HDAC inhibitors. All derivatives inhibit HDAC enzymatic activity (to a greater or lesser degree), suggesting that the thiazolyl–coumarin group is an effective surface recognition CAP. All compounds at lower concentration display diminished cytotoxicity. Regarding the parameters associated to cardiac fibrosis development, compounds **5a** and **8a** show significant inhibition on CFs proliferation at 1 μM and also showed better decrease of procollagen type I and α–SMA expression levels.

These results confirm that series **5** and **8** derivatives could be considered as leads to develop drugs with strong antifibrotic activity and are consistent with published reports where HDAC inhibitors could be useful pharmacological tools to prevent cardiac fibrosis development. Finally, the advantage of thiazolyl–coumarin disulfide over hydroxamic acid derivatives is their low cytotoxicity and better ADMET parameters.

Author Contributions: Conceptualization, V.P.-J., P.N.-E. and G.D.-A.; methodology, V.P.-J., P.N.-E. and G.D.-A.; software, V.P.-J.; validation, V.P.-J. and P.N.-E.; formal analysis, V.P.-J., P.N.-E. and G.D.-A.; investigation, V.P.-J., P.N.-E. and G.D.-A.; resources, V.P.-J., P.N.-E. and G.D.-A.; data curation, V.P.-J., P.N.-E. and G.D.-A.; writing—original draft preparation, V.P.-J., P.N.-E. and G.D.-A.; writing—review and editing, V.P.-J., P.N.-E. and G.D.-A.; visualization, V.P.-J., P.N.-E. and G.D.-A.; supervision, V.P.-J., P.N.-E. and G.D.-A.; project administration, V.P.-J., P.N.-E. and G.D.-A.; funding acquisition, V.P.-J. and G.D.-A.

Funding: This work was supported by CONICYT fellowship N° 21140371 to Viviana Pardo Jiménez and FONDECYT Grant N° 1130300 and N° 1170425 to Guillermo Díaz Araya.

Conflicts of Interest: The authors declare no conflict of interest.

References

1. Weber, K.T.; Sun, Y.; Díez, J. Fibrosis: A living tissue and the infarcted heart. *J. Am. Coll. Cardiol.* **2008**, *52*, 2029–2031. [CrossRef] [PubMed]
2. Gourdie, R.G.; Dimmeler, S.; Kohl, P. Novel therapeutic strategies targeting fibroblasts and fibrosis in heart disease. *Nat. Rev. Drug Discov.* **2016**, *15*, 620–638. [CrossRef] [PubMed]
3. Schuetze, K.B.; McKinsey, T.A.; Long, C.S. Targeting cardiac fibroblasts to treat fibrosis of the heart: Focus on HDACs. *J. Mol. Cell. Cardiol.* **2014**, *70*, 100–107. [CrossRef] [PubMed]

4. Tao, H.; Shi, K.H.; Yang, J.J.; Huang, C.; Zhan, H.Y.; Li, J. Histone deacetylases in cardiac fibrosis: Current perspectives for therapy. *Cell. Signal.* **2014**, *26*, 521–527. [CrossRef] [PubMed]
5. Xie, M.; Hill, J.A. HDAC-dependent ventricular remodeling. *Trends Cardiovasc. Med.* **2013**, *23*, 229–235. [CrossRef] [PubMed]
6. Thiagalingam, S.; Cheng, K.H.; Lee, H.J.; Mineva, N.; Thiagalingam, A.; Ponte, J.F. Histone deacetylases: Unique players in shaping the epigenetic histone code. *Ann. N. Y. Acad. Sci.* **2003**, *983*, 84–100. [CrossRef] [PubMed]
7. Sadoul, K.; Boyault, C.; Pabion, M.; Khochbin, S. Regulation of protein turnover by acetyltransferases and deacetylases. *Biochimie* **2008**, *90*, 306–312. [CrossRef] [PubMed]
8. Bolden, J.E.; Peart, M.J.; Johnstone, R.W. Anticancer activities of histone deacetylase inhibitors. *Nat. Rev. Drug Discov.* **2006**, *5*, 769–784. [CrossRef] [PubMed]
9. Spange, S.; Wagner, T.; Heinzel, T.; Krame, O.H. Acetylation of non-histone proteins modulates cellular signaling at multiple levels. *Int. J. Biochem. Cell Biol.* **2009**, *41*, 185–198. [CrossRef] [PubMed]
10. McKinsey, T.A. Isoform-selective HDAC inhibitors: Closing in on translational medicine for the heart. *J. Mol. Cell. Cardiol.* **2011**, *51*, 491–496. [CrossRef] [PubMed]
11. McKinsey, T.A. Therapeutic potential for HDAC inhibitors in the heart. *Annu. Rev. Pharmacol. Toxicol.* **2012**, *52*, 303–319. [CrossRef]
12. Tang, J.; Yan, H.; Zhuang, S. Histone deacetylases as targets for treatment of multiple diseases. *Clin. Sci.* **2013**, *124*, 651–662. [CrossRef] [PubMed]
13. Bush, E.W.; McKinsey, T.A. Protein acetylation in the cardiorenal axis: The promise of histone deacetylase inhibitors. *Circ. Res.* **2010**, *106*, 272–284. [CrossRef] [PubMed]
14. Nural-Guvener, H.F.; Zakharova, L.; Nimlos, J.; Popovic, S.; Mastroeni, D.; Gaballa, M.A. HDAC class I inhibitor, Mocetinostat, reverses cardiac fibrosis in heart failure and diminishes CD90+ cardiac myofibroblast activation. *Fibrogenesis Tissue Repair* **2014**, *7*, 10. [CrossRef] [PubMed]
15. Williams, S.M.; Golden-Mason, L.; Ferguson, B.S.; Schuetze, K.B.; Cavasin, M.A.; Demos-Davies, K.; Yeager, M.E.; Stenmark, K.R.; McKinsey, T.A. Class I HDACs regulate angiotensin II-dependent cardiac fibrosis via fibroblasts and circulating fibrocytes. *J. Mol. Cell. Cardiol.* **2014**, *67*, 112–125. [CrossRef] [PubMed]
16. Stratton, M.S.; McKinsey, T.A. Epigenetic regulation of cardiac fibrosis. *J. Mol. Cell. Cardiol.* **2016**, *92*, 206–213. [CrossRef]
17. Roche, J.; Bertrand, P. Inside HDACs with more selective HDAC inhibitors. *Eur. J. Med. Chem.* **2016**, *121*, 451–483. [CrossRef]
18. Monneret, C. Histone deacetylase inhibitors. *Eur. J. Med. Chem.* **2005**, *40*, 1–13. [CrossRef] [PubMed]
19. Bertrand, P. Inside HDAC with HDAC inhibitors. *Eur. J. Med. Chem.* **2010**, *45*, 2095–2116. [CrossRef]
20. DellaGreca, M.; Fiorentino, A.; Isidori, M.; Previtera, L.; Temussi, F.; Zarrelli, A. Benzocoumarins from the rhizomes of Juncus acutus. *Tetrahedron* **2003**, *59*, 4821–4825. [CrossRef]
21. Iaroshenko, V.O.; Ali, S.; Babar, T.M.; Dudkin, S.; Mkrtchyan, S.; Rama, N.H.; Villinger, A.; Langer, P. 4-Chloro-3-(trifluoroacetyl)coumarin as a novel building block for the synthesis of 7-(trifluoromethyl)-6H-chromeno[4,3-b]quinolin-6-ones. *Tetrahedron Lett.* **2011**, *52*, 3373–3376. [CrossRef]
22. Temitope Olomola, O.; Klein, R.; Kevin Lobb, A.; Sayed, Y.; Kaye Perry, T. Towards the synthesis of coumarin derivatives as potential dual-action HIV-1 protease and reverse transcriptase inhibitors. *Tetrahedron Lett.* **2010**, *51*, 6325–6328. [CrossRef]
23. Huang, W.J.; Chen, C.C.; Chao, S.W.; Yu, C.C.; Yang, C.Y.; Guh, J.H.; Lin, Y.C.; Kuo, C.I.; Yang, P.; Chang, C.I. Synthesis and evaluation of aliphatic-chain hydroxamates capped with osthole derivatives as histone deacetylase inhibitors. *Eur. J. Med. Chem.* **2011**, *46*, 4042–4049. [CrossRef] [PubMed]
24. Abdizadeh, T.; Kalani, M.R.; Abnous, K.; Tayarani-Najaran, Z.; Khashyarmanesh, B.Z.; Abdizadeh, R.; Ghodsi, R.; Hadizadeh, F. Design, synthesis and biological evaluation of novel coumarin-based benzamides as potent histone deacetylase inhibitors and anticancer agents. *Eur. J. Med. Chem.* **2017**, *132*, 42–62. [CrossRef]
25. Kumar, P.V.; Reddy, K.M.; Rao, V.R. Synthesis of Some 7-Methyl3-(2-oxo-2H-chromen-3-yl)-5H-[1,3]thiazolo-[3,2-a]pyrimidin-5-ones. *Indian, J. Chem. Sect. B* **2008**, *47*, 759–763. [CrossRef]
26. Siddiqui, N.; Arshad, M.; Khan, S.A. Synthesis of some new coumarin incorporated thiazolylsemicarbazones as anticonvulsants. *Acta Pol. Pharm. Drug Res.* **2009**, *66*, 161–167.

27. Arshad, A.; Osman, H.; Bagley, M.C.; Lam, C.K.; Mohamad, S.; Zahariluddin, A.S. Synthesis and antimicrobial properties of some new thiazolyl-coumarin derivatives. *Eur. J. Med. Chem.* **2011**, *46*, 3788–3794. [CrossRef]
28. Kalkhambkar, R.; Kulkarni, G.; Shivkumar, H.; Rao, R. Synthesis of novel tri heterocyclic thiazoles as anti-inflammatory and analgesic agents. *Eur. J. Med. Chem.* **2007**, *42*, 1272–1276. [CrossRef]
29. Kamal, A.; Adil, S.; Tamboli, J.; Siddardha, B.; Murthy, U. Synthesis of coumarin linked naphthalimide conjugates as potential anticancer and antimicrobial agents. *Lett. Drug Des. Discov.* **2009**, *6*, 201–209. [CrossRef]
30. Suhaily, F.; Rahman, A.; Yusufzai, S.K.; Osman, H.; Mohamad, D. Synthesis, Characterisation and Cytotoxicity Activity of Thiazole Substitution of Coumarin Derivatives. *J. Phys. Sci.* **2016**, *27*, 77–87.
31. Mohareb, R.M.; Megally Abdo, N.Y. Synthesis and Cytotoxic Evaluation of Pyran, Dihydropyridine and Thiophene Derivatives of 3-Acetylcoumarin. *Chem. Pharm. Bull.* **2015**, *63*, 678–687. [CrossRef] [PubMed]
32. Pang, M.; Zhuang, S. Histone Deacetylase: A Potential Therapeutic Target for Fibrotic Disorders. *J. Pharmacol. Exp. Ther.* **2010**, *335*, 266–272. [CrossRef] [PubMed]
33. Bulow, R.; Fitzner, B.; Sparmann, G.; Emmrich, J.; Liebe, S.; Jaster, R. Antifibrogenic effects of histone deacetylase inhibitors on pancreatic stellate cells. *Biochem. Pharmacol.* **2007**, *74*, 1747–1757. [CrossRef] [PubMed]
34. Hantzsch, A.; Weber, J.H. Ueber Verbindungen des Thiazols (Pyridins der Thiophenreihe). *Ber. Dtsch. Chem. Ges.* **1887**, *20*, 3118–3132. [CrossRef]
35. Nichols, T.W. alpha-lipoic acid: Biological effects and Clinical Implications. *Alt. Med. Rev.* **1997**, *2*, 177–183.
36. Islam, M.T. Antioxidant activities of dithiol alpha-lipoic acid. *Bangladesh J. Med. Sci.* **2009**, *8*, 46–51. [CrossRef]
37. Goraca, A.; Huk-Kolega, H.; Piechota, A.; Kleniewska, P.; Skibska, B. Lipoic acid—Biological activity and therapeutic potential. *Pharmacol. Rep.* **2011**, *63*, 849–858. [CrossRef]
38. Jia, L.; Zhang, Z.; Zhai, L.; Bai, Y. Prottective effect of lipoic acid against acrolein-induced cytotoxicity in IMR-90 human fibroblast. *J. Nutr. Sci. Vitaminol.* **2009**, *55*, 126–130. [CrossRef]
39. Leppert, U.; Gillespie, A.; Orphal, M.; Böhme, K.; Plum, C.; Nagorsen, K.; Berkholz, J.; Kreutz, R.; Eisenreich, A. The impact of α-Lipoic acid on cell viability and expression of nephrin and ZNF580 in normal human podocytes. *Eur. J. Pharmacol.* **2017**, *810*, 1–8. [CrossRef]
40. Shay, K.P.; Moreau, R.F.; Smith, E.J.; Hagen, T.M. Alpha-lipoic acid as a dietary supplement: Molecular mechanisms and therapeutic potential. *Biochim. Biophys. Acta* **2009**, *1790*, 1149–1160. [CrossRef]
41. Li, X.; Wang, X.; Chen, D.; Chen, S. Antioxidant Activity and Mechanism of Protocatechuic Acid in vitro. *Funct. Foods Health Dis.* **2011**, *7*, 232–244. [CrossRef]
42. Masoud, M.S.; Hagagg, S.S.; Ali, A.E.; Nasr, N.M. Synthesis and spectroscopic characterization of gallic acid and some of its azo complexes. *J. Mol. Struct.* **2012**, *1014*, 17–25. [CrossRef]
43. Schweigert, N.; Zehnder, A.J.; Eggen, R.I. Chemical properties of catechols and their molecular modes of toxic action in cells, from microorganisms to mammals. *Environ. Microbiol.* **2001**, *3*, 81–91. [CrossRef] [PubMed]
44. Jacobsen, F.E.; Lewis, J.A.; Cohen, S.M. The Design of Inhibitors for Medicinally Relevant Metalloproteins. *Chem. Med. Chem.* **2007**, *2*, 152–171. [CrossRef] [PubMed]
45. Miller, T.A.; Witter, D.J.; Belvedere, S. Histone Deacetylase Inhibitors. *J. Med. Chem.* **2003**, *46*, 5097–5116. [CrossRef]
46. Elaut, G.; Laus, G.; Alexandre, E.; Richert, L.; Bachellier, P.; Tourwe, D.; Rogiers, V.; Vanhaecke, T. A Metabolic Screening Study of Trichostatin A (TSA) and TSA Like Histone Deacetylase Inhibitors in Rat and Human Primary Hepatocyte Cultures. *J. Pharmacol. Exp. Ther.* **2007**, *321*, 400–408. [CrossRef]
47. Tan, S.; Liu, Z.P. Natural products as zinc-dependent histone deacetylase inhibitors. *Chem. Med. Chem.* **2015**, *10*, 441–450. [CrossRef]
48. Shen, S.; Kozikowski, A.P. Why Hydroxamates May Not Be the Best Histone Deacetylase Inhibitors–What Some May Have Forgotten or Would Rather Forget? *Chem. Med. Chem.* **2016**, *11*, 15–21. [CrossRef]
49. Suzuki, T.; Miyata, N. Non-hydroxamate histone deacetylase inhibitors. *Curr. Med. Chem.* **2005**, *12*, 2867–2880. [CrossRef]
50. Bora-Tatar, G.; Dayangaç-Erden, D.; Demir, A.S.; Dalkara, S.; Yelekçi, K.; Erdem-Yurter, H. Molecular modifications on carboxylic acid derivatives as potent histone deacetylase inhibitors: Activity and docking studies. *Bioorg. Med. Chem.* **2009**, *17*, 5219–5228. [CrossRef]

51. Zhang, L.; Zhang, J.; Jiang, Q.; Zhang, L.; Song, W. Zinc binding groups for histone deacetylase inhibitors. *J. Enzyme Inhib. Med. Chem.* **2018**, *33*, 714–721. [CrossRef] [PubMed]
52. Kong, Y.; Tannous, P.; Lu, G.; Berenji, K.; Rothermel, B.A.; Olson, E.N.; Hill, J.A. Suppression of class I and II histone deacetylases blunts pressure-overload cardiac hypertrophy. *Circulation* **2006**, *113*, 2579–2588. [CrossRef] [PubMed]
53. Rombouts, K.; Niki, T.; Greenwel, P.; Vandermonde, A.; Wielant, A.; Hellemans, K.; De Bleser, P.; Yoshida, M.; Schuppan, D.; Rojkind, M.; et al. Trichostatin A, a histone deacetylase inhibitor, suppresses collagen synthesis and prevents TGF-beta(1)-induced fibrogenesis in skin fibroblasts. *Exp. Cell. Res.* **2002**, *278*, 184–197. [CrossRef] [PubMed]
54. Liu, N.; He, S.; Ma, L.; Ponnusamy, M.; Tang, J.; Tolbert, E.; Bayliss, G.; Zhao, T.C.; Yan, H.; Zhuang, S. Blocking the class I histone deacetylase ameliorates renal fibrosis and inhibits renal fibroblast activation via modulating TGF-beta and EGFR signaling. *PLoS ONE* **2013**, *8*, e54001. [CrossRef] [PubMed]
55. Brufola, G.; Fringuelli, F.; Piermatti, O.; Pizzo, F. Simple and Efficient One-Pot Preparation of 3-Substituted Coumarins in Water. *Heterocycles* **1996**, *43*, 1257–1266. [CrossRef]
56. Zhuravel, I.O.; Kovalenko, M.S.; Vlasov, S.V.; Chernykh, P.V. Solution-phase Synthesis of a Combinatorial Library of 3-[4-(Coumarin-3-yl)-1,3-thiazol-2-ylcarbamoyl]propanoic acid Amides. *Molecules* **2005**, *10*, 444–456. [CrossRef] [PubMed]
57. Parameshwar, R.; Sri Ranganath, Y.; HarinadhaBabu, V.; Sandeep, G. Synthesis and Antifungal Screening of Some Novel Coumarin Linked Imidazole Derivatives. *Res. J. Pharm. Biol. Chem. Sci.* **2011**, *2*, 514–520.
58. Boza, P.; Ayala, P.; Vivar, R.; Humeres, C.; Cáceres, F.T.; Muñoz, C.; García, L.; Hermoso, M.A.; Díaz-Araya, G. Expression and function of toll-like receptor 4 and inflammasomes in cardiac fibroblasts and myofibroblasts: IL-1β synthesis, secretion, and degradation. *Mol. Immunol.* **2016**, *74*, 96–105. [CrossRef] [PubMed]

Sample Availability: Samples of the compounds are not available from the authors.

© 2019 by the authors. Licensee MDPI, Basel, Switzerland. This article is an open access article distributed under the terms and conditions of the Creative Commons Attribution (CC BY) license (http://creativecommons.org/licenses/by/4.0/).

molecules

MDPI

Article

Position-Selective Synthesis and Biological Evaluation of Four Isomeric A-Ring Amino Derivatives of the Alkaloid Luotonin A

Amra Ibric [1], Stefan Eckerstorfer [1], Martin Eder [1], Ivan Louko [1], Leopold Tunjic [1], Petra Heffeter [2], Hemma Henrike Schueffl [2], Brigitte Marian [2] and Norbert Haider [1,*]

1 Department of Pharmaceutical Chemistry, University of Vienna, Althanstraße 14, A-1090 Vienna, Austria; amra.ibric@univie.ac.at (A.I.); stefan.eckerstorfer@me.com (S.E.); semrad@gmx.at (M.E.); ivan_louko@yahoo.com (I.L.); leopold.tunjic@gmail.com (L.T.)

2 Institute of Cancer Research and Comprehensive Cancer Center, Medical University of Vienna, Borschkegasse 8a, A-1090 Vienna, Austria; petra.heffeter@meduniwien.ac.at (P.H.); hemma.schueffl@meduniwien.ac.at (H.H.S.); brigitte.marian@meduniwien.ac.at (B.M.)

* Correspondence: norbert.haider@univie.ac.at; Tel.: +43-1-4277-55624

Academic Editor: Josef Jampilek
Received: 25 January 2019; Accepted: 14 February 2019; Published: 16 February 2019

Abstract: Following two orthogonal synthetic routes, a series of all four possible A-ring amino derivatives of the natural product Luotonin A (a known Topoisomerase I inhibitor) was synthesized. In both strategies, intramolecular cycloaddition reactions are the key step. The target compounds were obtained in good yields by mild catalytic transfer hydrogenation of the corresponding nitro precursors. In-vitro evaluation of the antiproliferative activity towards human tumor cell lines revealed the 4-amino compound (**5b**) to be the most effective agent, showing an interesting profile of cytotoxic activity. Among other effects, a significant G2/M cell cycle arrest was observed for this compound, suggesting that either Topoisomerase I is not the only biological target, or that some atypical mechanism is responsible for inhibition of this enzyme.

Keywords: Luotonin A; quinazoline; quinoline; cycloaddition; catalytic transfer hydrogenation; Topoisomerase I; cytotoxic activity

1. Introduction

DNA Topoisomerase I (Top1) represents an attractive target for cancer chemotherapy [1], as this enzyme plays a crucial role in the DNA replication process by relaxing the nucleic acid's supercoiled structure. Based on the natural product, Camptothecin (CPT) as lead structure (Figure 1), highly effective Top1 inhibitors have been developed [2] that are clinically used for the treatment of various malignancies: Topotecan [3] has been approved as a drug against ovarian cancers and small-cell lung cancers, and Irinotecan [4] is therapeutically used against colorectal tumors [2]. With regard to their biochemical mode of action, drugs of this type are known to form a stable ternary complex with the covalent adduct of DNA and Top1 [5,6], thus blocking DNA replication efficiently by causing irreversible DNA damage upon collision of the ternary complex with the progressing replication fork [7].

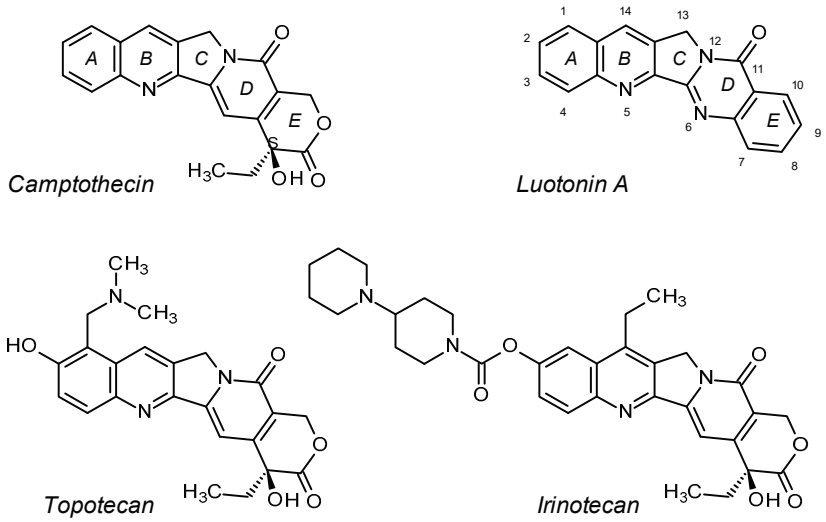

Figure 1. Structures of Camptothecin (CPT), Luotonin A (with IUPAC-conformant numbering scheme) and the CPT-derived drugs, Topotecan and Irinotecan.

Among various efforts to circumvent severe side-effects of these drugs, especially their bladder toxicity due to labile lactone motif, through chemical stabilization of the E-ring [1], the discovery of the alkaloid Luotonin A and its Top1-inhibitory activity [8] has opened a new perspective for the development of potentially useful new members of this drug family. As shown in Figure 1, the structures of CPT and Luotonin A are quite similar, differing mainly in the nature of ring E, which is a simple benzene ring in Luotonin A. Despite lacking the lactone functionality of CPT, Luotonin A is able to stabilize the DNA/Top1 covalent complex in an analogous manner as CPT, albeit at a significantly lower level of activity [9]. Thus, the search for new Luotonin A derivatives with a higher Top1-poisoning activity (comparable to that of CPT) has become a challenging topic for various research groups and it has stimulated the development of different synthetic strategies to access compounds of the quino[2′,3′:3,4] pyrrolo[2,1-*b*]quinazolin-11(13*H*)-one type.

In this context, it should be noted that there are indications that Topoisomerase I may not be the only biological target that is involved in the cytotoxic activity of Luotonin-A-derived compounds [10,11]. Also for Evodiamine [12], a pentacyclic alkaloid with high structural similarity to Luotonin A, there have been reports describing Top1 inhibition as well as other cytotoxic effects that are associ-ated with a G2/M cell cycle arrest rather than with the CPT-typical effect on the S-phase [13–15].

A systematic overview of the main synthetic routes to Luotonin A is given in a review article by Liang et al. [8]. Among the more recent approaches, two orthogonal pathways have been shown by our group to be suitable for the specific placement of substituents at all possible positions of ring A: the "southern route" gives access to either 2- or 4-substituted Luotonin A derivatives [16–18] whereas the "northern route" leads to either 1- or 3-susbtituted congeners [19]. In both reaction sequences, intramolecular [4 + 2] cycloadditions represent the key step.

As observed previously [11,20], many derivatives of the large and planar quino[2′,3′:3,4] pyrrolo[2,1-*b*]quinazolin-11(13*H*)-one system are characterized by low solubility in common solvents (especially in water) and thus we frequently encountered solubility problems on attempted biological evaluation of such compounds. Therefore, we decided to focus on Luotonin A derivatives with substituents capable of improving water solubility. In this context, the NH_2 group appears particularly interesting, not only for its hydrophilic nature, but also for its potential to enhance drug/target binding affinity by enabling additional contacts (e.g., via hydrogen bonding). So far, only two Luotonin A derivatives with a primary amino group at ring E have been described in literature (7-amino-Luotonin A [11], 8-amino-Luotonin A [20]). In the present article, we report the synthesis and biological evaluation of four novel isomeric congeners bearing an amino group at ring A, namely at positions 1, 2, 3, and 4.

2. Results and Discussion

2.1. Chemistry

For the synthesis of the target Luotonin A derivatives featuring a primary amino function at ring A, the corresponding nitro compounds were envisaged as suitable precursors. Out of the four possible A-ring nitro isomers, only the 2-nitro compound [16] has been known to date: our group had prepared this Luotonin A derivative via a pathway that was based on the cycloaddition strategy previously reported by Zhou et al. [21] for the synthesis of the parent natural product. As outlined in Scheme 1, this pathway (referred to as the "southern route") should be principally suitable to give access also to the hitherto unknown 4-nitro derivative as a pure isomer, starting from a 2-nitroaniline building block instead of a 4-nitroaniline synthon. Indeed, this proved to be the case: although acylation of a 2-nitroaniline NH_2 group is somewhat challenging for both electronic and steric reasons, the $AlMe_3$-mediated coupling reaction known as Weinreb amidation [22] permitted the smooth transformation of the quinazolinone ester **1** [23] (representing the D and E ring fragment of the target structure) into the ortho-substituted anilide **2b**. This intermediate, however, turned out to be almost insoluble in common solvents (in contrast to its known isomer **2a** [16]) and thus required some optimization in the subsequent alkylation reaction with propargyl bromide, which is necessary to introduce the requisite three-carbon fragment containing the dienophile for the following step. We succeeded in this alkylation to obtain compound **3b** by applying a protocol that we had recently used for similarly insoluble substrates [17] (DMSO as solvent, finely powdered potassium hydroxide, tetrabutylammonium bromide as phase-transfer catalyst, ultrasound irradiation at room temperature). Assembly of the pentacyclic skeleton (**4b**) then was easily accomplished by intramolecular [4 + 2] cycloaddition, mediated by bis(triphenyl)oxodiphosphonium triflate (Hendrickson's reagent) [24] in dry dichloromethane at room temperature, conditions that had been previously applied for analogous transformations [16–18,21].

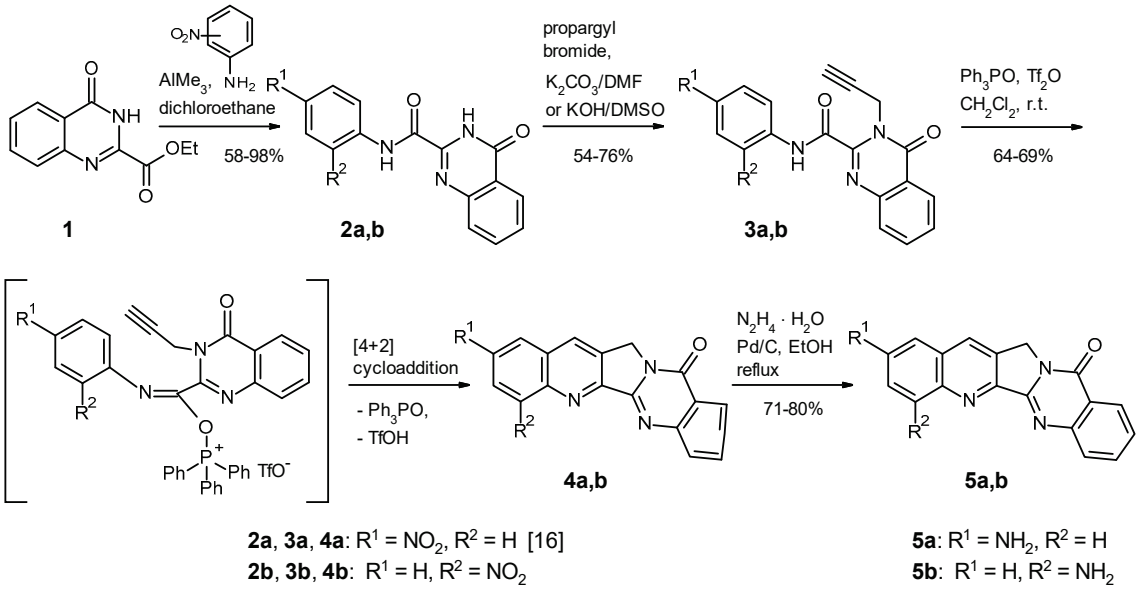

Scheme 1. Synthesis of 2-nitro-Luotonin A (**4a**) [16] and 4-nitro-Luotonin A (**4b**) and their reduction into 2-amino-Luotonin A (**5a**) and 4-amino-Luotonin A (**5b**).

With the 2-nitro compound **4a** [16] and the new 4-nitro isomer **4b** in hands, preparation of the corresponding two amino-substituted Luotonin A derivatives should be feasible in a straightforward manner by reduction of the NO_2 group. While Cagir et al. [20] had obtained 8-amino-Luotonin A from the 8-nitro precursor by reduction with $SnCl_2$ in moderate yield (40%) and Dallavalle et al. [25] had reported an unsuccessful attempt to selectively reduce the nitro group in 9-nitro-Luotinin A by

catalytic hydrogenation in acetic acid, we decided to apply a protocol that had been successfully used for the reduction of nitrocarbazoles into aminocarbazoles [26,27]. This method makes use of hydrazine hydrate as hydrogen source in a catalytic transfer hydrogenation reaction in alcoholic solution or suspension at elevated temperature. Indeed, when **4a** or **4b**, respectively, were subjected to these conditions, the target amino compounds **5a** or **5b**, respectively, were formed very cleanly in good yields (70–80%). It should be noted that this transformation works very well despite the low solubility of the substrate (**4a**,**b**) in boiling ethanol. As there are no non-volatile reagents involved and no non-volatile by-products formed, work-up requires only removal of the catalyst by filtration after an ethanol/DMF solvent exchange, followed by precipitation upon dilution with water (see Experimental Section).

For the synthesis of the other two amino-substituted target compounds (**10a,b**), the "northern route" seemed ideally suited, again making use of an intramolecular cycloaddition reaction to assemble the polycyclic skeleton. As demonstrated previously [19], the requisite arylpropargyl-substituted quinazolinonecarbonitriles as cycloaddition substrates are accessible in two steps from the carboxamide **6** (which can be prepared by ammonolysis of the ester **1** [28], followed by selective quinazolinone N-3 propargylation [29]) via Sonogashira coupling of the terminal alkyne with an appropriate aryl iodide and subsequent dehydration of the amide function into a nitrile. The latter step turned out to be unexpectedly challenging for the nitro compounds **7a**,**b** that were obtained from the propargyl compound **6**. In contrast to our previous experiences with structurally related compounds [19], employment of a dehydrating agent in combination with a base (trifluoroacetic anhydride/triethylamine [30] or ethyl dichlorophosphate/DBU [31]) resulted in rapid resinification. However, heating of the primary amides **7a**,**b** with phosphorus oxychloride in chloroform solution under carefully controlled conditions finally afforded the desired carbonitriles **8a**,**b** in good yields (Scheme 2). For both isomers, ring closure into the target quino[2′,3′:3,4]pyrrolo[2,1-*b*]quinazoline system was smoothly accomplished by a thermally induced intramolecular [4 + 2] cycloaddition reaction in the presence of catalytic amounts of DBU in analogy to lit. [19,32].

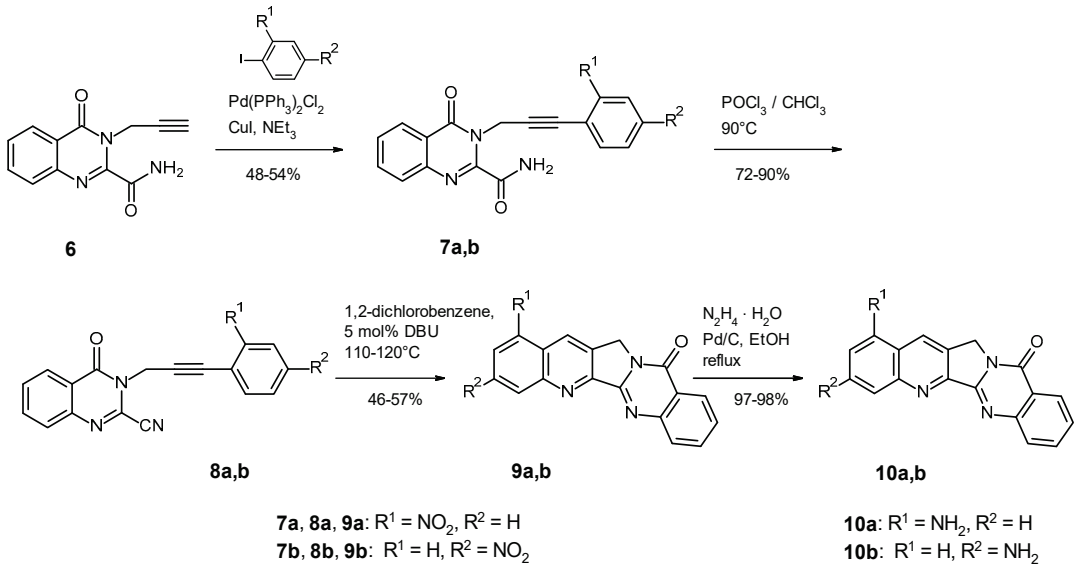

Scheme 2. Synthesis of 1-nitro-Luotonin A (**9a**) and 3-nitro-Luotonin A (**9b**) and their reduction into 1-amino-Luotonin A (**10a**) and 3-amino-Luotonin A (**10b**).

The resulting nitro-substituted Luotonin A derivatives **9a**,**b** precipitated from the reaction solvent (1,2-dichlorobenzene) and were isolated simply by filtration. Reduction of the nitro group, applying the same method as described above for **5a**,**b**, afforded the target 1-amino or 3-amino-substituted Luotonin A derivatives **10a**,**b** in nearly quantitative yields.

All new compounds are fully characterized with ^{1}H-NMR, ^{13}C-NMR, EI-MS and elemental analyses or high-resolution MS (ESI-TOF). In all final compounds (**5a**,**b** and **10a**,**b**), the presence of

an amino group at ring A instead of a nitro group is reflected in their ^{1}H-NMR spectra by a marked upfield shift that is observed for the proton signals belonging to rings A and B, as compared to the spectra of the nitro compounds (**4a**,**b** and **9a**,**b**). Assignment of all proton signals rests on COSY and 1D-NOE or NOESY spectra. The carbon signals of compounds **5a**,**b** and **10a**,**b** (which are much better soluble in DMSO-d_6 than their precursors) were assigned by means of HSQC and HMBC experiments; for a complete signal listing, see Table 1.

Table 1. ^{1}H-NMR (400 MHz) and ^{13}C-NMR (100 MHz) signals of the amino-substituted Luotonin A derivatives **5a**,**b** and **10a**,**b** (DMSO-d_6 solutions, chemical shifts in ppm, coupling constants in Hz).

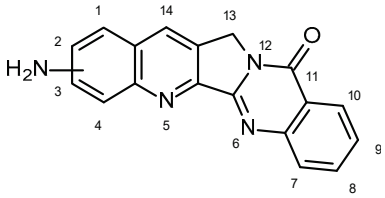

Signal	10a (1-amino)	5a (2-amino)	10b (3-amino)	5b (4-amino)
1-H	–	6.91 (d, *J* = 2.3)	7.81 (d, *J* = 8.0)	7.22 (dd, *J* = 8.2, 1.0)
1-C	149.7	104.1	128.9	113.8
2-H	6.86 (dd, *J* = 7.6)	–	7.16 (dd, *J* = 8.8, 2.0)	7.45 (t, *J* = 7.8)
2-C	108.8	149.0	120-9	129.7
3-H	7.57 (t, *J* = 8.1)	7.31 (dd, *J* = 9.1, 2.4)	–	6.98 (dd, *J* = 7.6, 1.1)
3-C	131.3	123.0	151.1 [a]	109.1
4-H	7.43 (d, *J* = 8.2)	7.93 (d, *J* = 9.3)	7.12 (d, unresolved)	–
4-C	116.7	130.7	105.9	146.2
4a-C	145.7	142.8	151.0 [a]	138.1
5a-C	150.7	145.5	150.6	147.9
5b-C	153.4	153.6	153.7	153.2
6a-C	149.1	149.3	149.2	149.1
7-H	7.97–7.90 (m)	7.90–7.86 (m)	7.95–7.91 (m)	7.96–7.90 (m)
7-C	128.0	127.7	127.9	127.8
8-H	7.97–7.90 (m)	7.90–7.86 (m)	7.95–7.91 (m)	7.96–7.90 (m)
8-C	134.5	134.3	134.4	134.5
9-H	7.66–7.61 (m)	7.58 (ddd, *J* = 8.0, 6.1, 2.2)	7.63–7.59 (m)	7.62 (ddd, *J* = 7.7, 5.7, 2.5)
9-C	127.1	126.5	126.9	127.0
10-H	8.30 (dd, *J* = 7.8, 1.0)	8.26 (d, *J* = 7.1)	8.28 (d, *J* = 8.0)	8.30 (d, *J* = 7.7)
10-C	125.9	125.8	125.9	125.9
10a-C	121.0	120.7	121.0	121.0
11-C	159.7	159.7	159.8	159.7
13-H	5.30 (s)	5.20 (s)	5.19 (s)	5.28 (s)
13-C	47.5	47.3	47.3	47.4
13a-C	128.4	131.2 [b]	126.4	131.1
14-H	8.92 (s)	8.25 (s)	8.41 (s)	8.55 (s)
14-C	126.8	127.3	131.0	131.3
14a-C	118.2	131.1 [b]	121.6	129.3
NH_2	6.17 (br s)	6.07 (br s)	6.06 (br s)	6.18 (br s)

[a,b] assignment ambiguous.

2.2. Biological Evaluation

While the nitro compounds of type **4** and **9** were not considered for any biological evaluation because of their very low water solubility, the new amino-substituted Luotonin A derivatives **5a**,**b** and **10a**,**b** were examined with respect to their cytotoxic activity towards human tumor and normal cell lines. For any compound with significant activity, cell cycle specificity was to be clarified as well as the question if DNA Top1 is indeed the biological target.

2.2.1. Evaluation of Cell Viability and Toxicity

All four A-ring amino derivatives of Luotonin A were subjected to the MTT viability assay. Two standard cell lines were used: a human colon adenocarcinoma (SW480) and a human leukemia cell line (HL60). Because of insufficient medium solubility, compound **10b** had to be excluded. Out of the three remaining candidates, two compounds showed stronger activity than Luotonin A in solid tumor cells (SW480), whereas in leukemia cells (HL60), compound **5b** was found to be significantly more potent

than its isomers (**5a** and **10a**) as well as the reference, Luotonin A (Figure 2). Thus, **5b** was selected for more in-depth investigations regarding its biological effects.

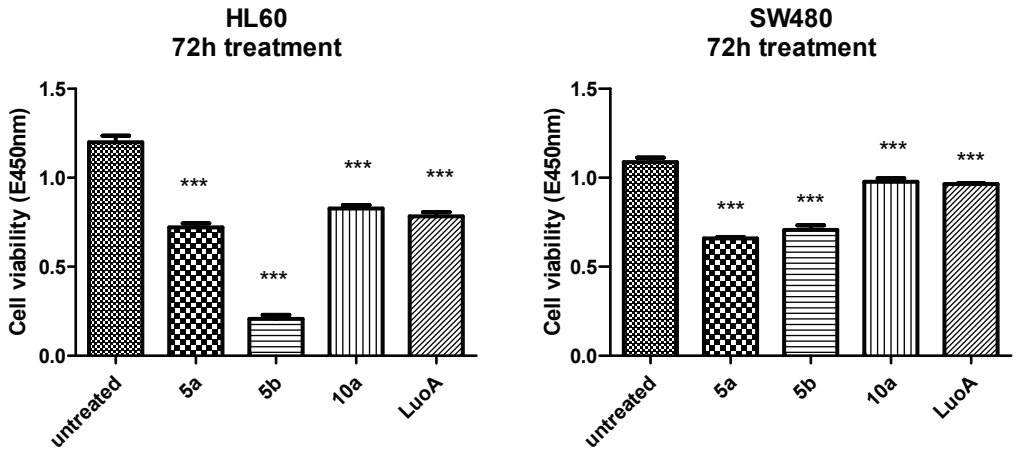

Figure 2. Cell viability screening; cells were treated with the indicated compounds at 40 μM, after 72 h of incubation the MTT assay was conducted, showing compound **5b** as significantly most potent in HL60 cells. Significance was designated as *** for $P < 0.001$. Error bars depict ± SD.

A dose-response relationship was examined for both Luotonin A and **5b** for the two examined cell lines. An IC_{50} of 7.17 ± 1.07 μM was calculated for **5b** in HL60 cells, whereas an IC_{50} for SW480 could not be determined due to solubility limitations, with 100 μM being the upper solubility limit. For both cell lines (HL60 and SW480), it was estimated that an IC_{50} of Luotonin A is not reached at 100 μM and 60 μM, respectively, which were the highest usable concentrations under the experiment conditions.

These results of the MTT assay should be interpreted with some caution due to the observed enlarged morphology of treated cells, which might shift the photometric readout of the assay towards higher values, mistakenly indicating too high cell viability. Furthermore, the results of the FACS analysis (see below) show that most of the treated cancer cells—while still alive—are trapped in an irrecoverable state, which is triggered by relatively low concentrations of **5b**, compared to the concentrations indicated by the MTT assay (for further discussion, see Section 2.2.3).

Toxicological viability assays, using two different fibroblast cell lines, including colon fibroblasts F331 and lung fibroblasts HLF, show low toxicity of the examined compound (Figure 3).

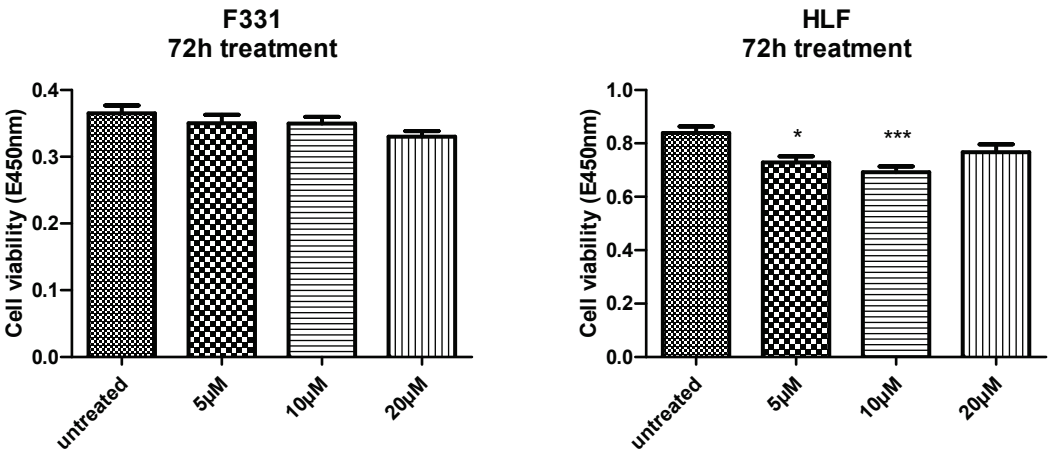

Figure 3. Toxicological profile of compound **5b** was examined on two fibroblast cell lines, as relative rapidly proliferating non-tumor human cells. Result of the MTT assay after exposure to **5b** for 72 h, no significant difference in cell growth in F331, some inhibitory activity could be statistically speculated for 10 μM at HLF, but not for 20 μM. Significance was designated as * for $P < 0.05$ and *** for $P < 0.001$. Error bars depict ± SD.

2.2.2. Top1 Inhibition

In order to evaluate the Top1 inhibition potential of our compounds, we performed DNA relaxation assays using Luotonin A and a known Topoisomerase I inhibitor, Camptothecin, as references. Supercoiled plasmid DNA EGFP was incubated with human Topoisomerase I and with the test compounds at a concentration range of 1 to 100 μM. Agarose gel electrophoresis was used to monitor the plasmid unwinding (Figure 4). These experiments revealed that the intensities of the lowest migrating band (corresponding to the supercoiled DNA) visibly increase with **5a**, **5b** and **10b** when compared to the original Luotonin A in a dose-dependent manner, partially indicating stronger activity than CPT. In contrast, **10a** showed no Topoisomerase I inhibition.

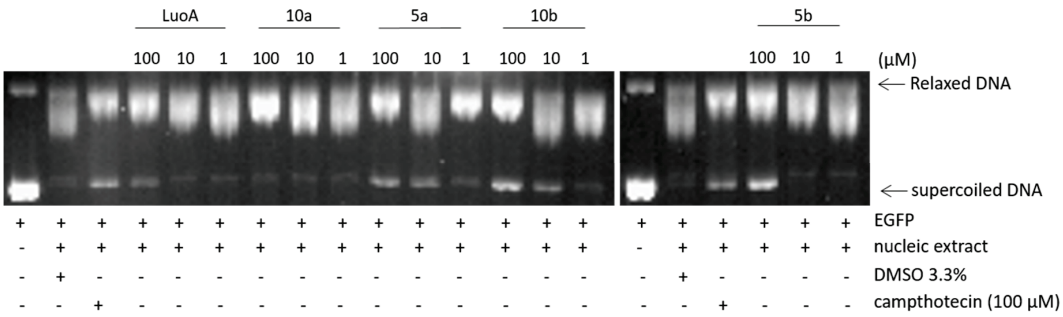

Figure 4. Effects of examined compounds on relaxation of supercoiled EGFP plasmid DNA by Top1. Three independent experiments were accomplished, showing concordant result. Top1-inhibitory activity was observed under exposure to **5a**, **5b** and **10b** ("+" and "−" signs indicate the exact composition of the individual gel traces).

2.2.3. Morphological Alterations and Cell Cycle Analysis: Induction of G2/M Arrest

In the course of our viability assay studies, we noticed some unexpected morphological alterations in both cell lines when treated with the investigated compounds, particularly in the case of compound **5b**. After incubation, cells treated with this compound show an enlarged and flattened morphology, involving uncommon nuclear changes that could be characterized as multi-nucleation and even macro-nucleation. This observation was analyzed in more detail by nuclear staining with the Hoechst 33285 dye [33], using adherent SW480 cells, as more convenient for this assay (see Figure 5). Neither clear apoptotic nor necrotic elements could be ascertained.

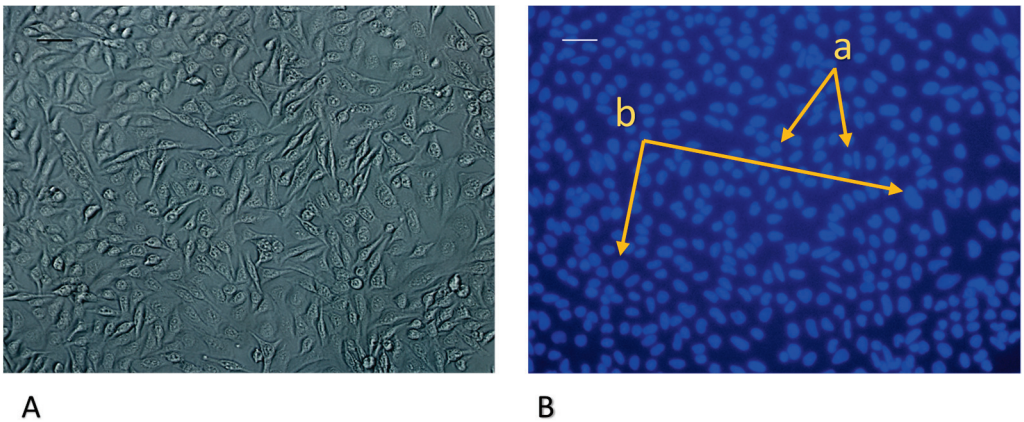

Figure 5. *Cont.*

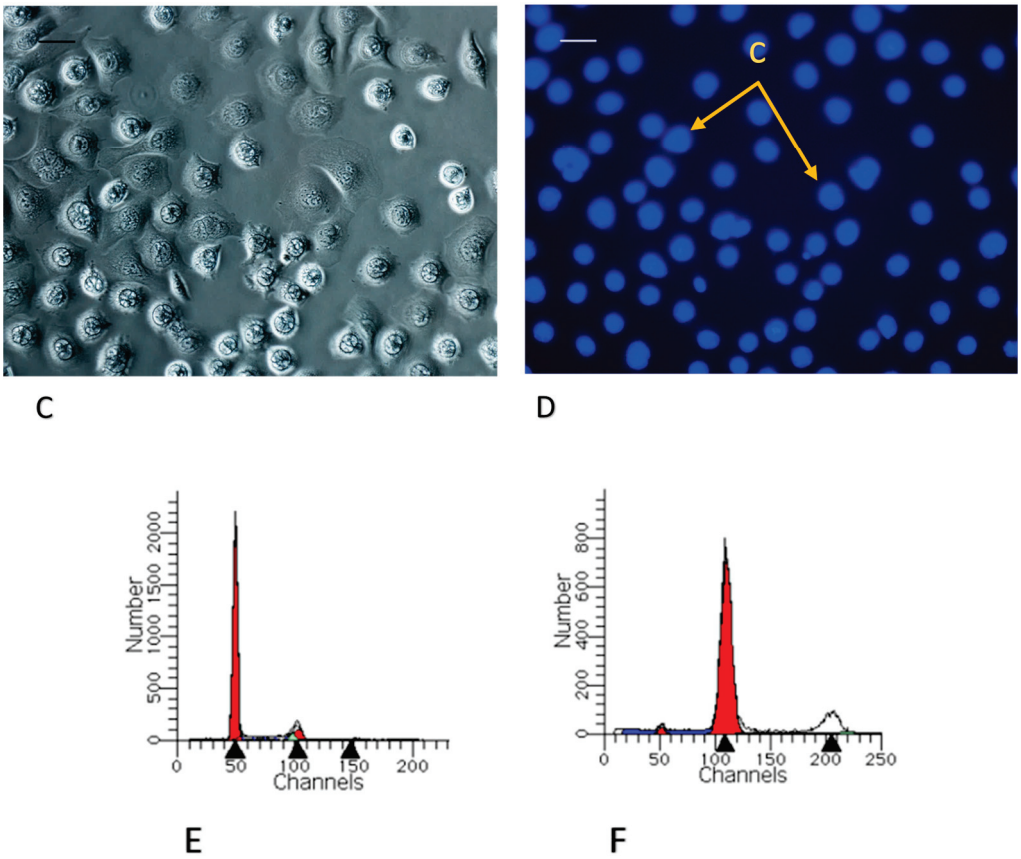

Figure 5. Results of nuclear staining with Hoechst 33285: SW480, untreated, 72 h incubation, phase contrast (**A**), UV excitation with blue/cyan filter (**B**): normal nucleus G1 (a), normal nucleus G2 (b); SW480, treated with **5b** (10 μM), 72 h incubation, phase contrast (**C**), UV excitation with blue/cyan filter (**D**): giant nucleus (c). The bars in the upper left corner of each panel represent a length of 25 μm. The subfigures E and F show representative histograms of control (**E**) and 10 μM **5b** exposed (**F**) SW480 cells. The 8n peak appears at an intensity of approx. 200.

As the morphological changes indicated a G2 cell cycle arrest, we investigated the cell cycle state of treated cells using flow cytometry. Both cell lines (HL60 and SW480) demonstrated a strong cell cycle arrest in the G2 phase, when treated with **5b**, compared to untreated cells (see Figure 6). HL60 cells seem to respond faster, and the described effect could already be measured after 24 h of treatment. For SW480, 72 h were needed to obtain a comparable readout. Based on the results of the viability assays, the extent of the cell cycle block was surprising. A wash-out experiment that was conducted by substituting the treatment medium with a growth medium showed no recovery and massive loss of cells after incubation for further 48 h (Figure 7). This result demonstrates that the cells fragment even after removal of **5b**, indicating that the examined compound was indeed much more potent than the result of the MTT assay implies.

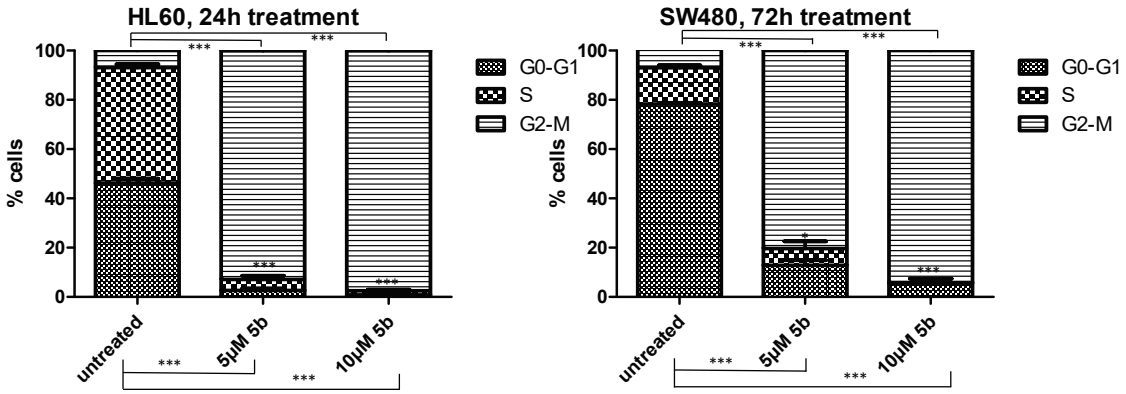

Figure 6. Cell cycle analysis of HL60 and SW480 cells treated with compound **5b**. A massive G2/M arrest was detected, showing at 10 µM almost no cell dividing. Significance was designated as * for $P < 0.05$ and *** for $P < 0.001$. Error bars depict ± SD.

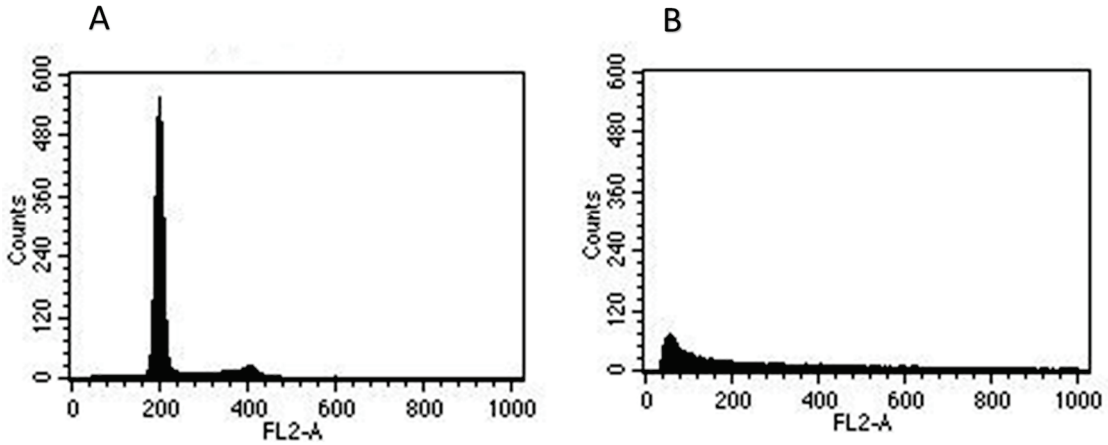

Figure 7. Results of the wash-out experiment: (**A**) SW480, non-treated, the scan shows a regular growing cell culture; (**B**) SW480, wash-out experiment, 48 h after removal of the examined compound; no recovery of cells, main peak in sub-G1 domain indicates cell death.

The G2 phase is a subphase of interphase, immediately followed by mitosis. Due to the particular sensitivity of the cell cycle during interphase, the G2 phase can be regarded as a very interesting target for diverse cytotoxic or cytostatic agents. If reparatory mechanisms fail to accomplish their work, a G2/M-arrest will be initiated and cell death pathways are induced. In their research, Bible et al., Tyagi et al., Ling et al. and Potter et al. demonstrated synergy of such cell-cycle checkpoint arrest with multiple chemotherapeutic agents, including irradiation [34–37]. G2/M-arrest-causing agents are therefore of interest as an alternative or subsidiary therapy option, in order to reduce the dosage and to mitigate side effects [35,38,39]. In view of the results obtained in the FACS analysis with **5b**, a potential use of this compound in combination with another cytostatic drug should be more closely investigated.

Morphological anomalies, induced by treatment with compound **5b**, combined with a massive G2/M arrest permit the assumption that some 'mitotic catastrophe' elements could also be considered as responsible for the observed cytotoxicity. A similar model was discussed by Kainz et al. in 2013, referring to the natural compound, 2-Deprenyl-Rheediaxanthone B [40]. Furthermore, mitotic catastrophe following a G2/M arrest was described recently by Gu and coworkers: cells that initiate a G2/M arrest often miscarry mitosis and execute mitotic catastrophe, which results in the formation of enlarged cells usually bearing tetraploid DNA content [41]. However, this assumption requires further investigation.

2.2.4. Stimulation of Caspase Activity by Compound **5b**

To determine if caspase activation is also involved in the observed cell death pathway, an assessment of caspase activity was conducted, following the protocol of Werner et al. [42]. In both cell lines, an increase of caspase activity was detected. For SW480 cells, the increase of caspase activity under treatment with **5b** was not as strong as for HL60 cells. However, it was already observed with the 5 μM concentration. In the HL60 cultures, 5 μM **5b** did not affect caspase activity, but a 6-fold increase at the 10 μM concentration was observed (Figure 8).

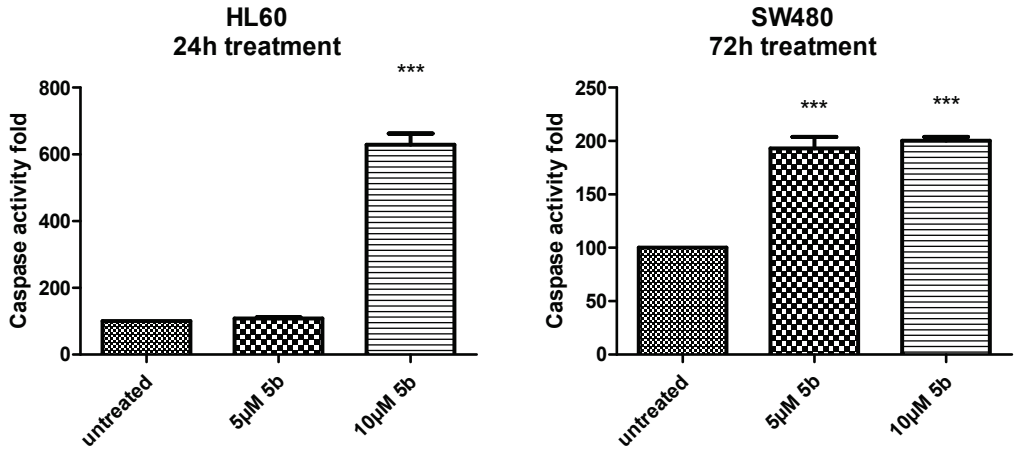

Figure 8. Caspase assay of HL60 and SW480 cells after treatment. Particularly strong activation of caspases was observed in HL60 cells treated with 10 μM of compound **5b**. Significance was designated as *** for $P < 0.001$. Error bars depict ± SD.

We assume that some metabolic and genetic differences between the investigated cell lines could be the cause for such a difference in caspase activation. Furthermore, confirmation of caspase activity, based on this result, implies that cells treated with **5b** could terminate in apoptotic cell death.

Caspases are also crucial for termination of mitotic death, which implicates that involvement of the above-mentioned mitotic catastrophe elements may result in an activation of apoptotic elements. Ho et al. suggest that apoptotic and mitotic death pathways may occur simultaneously, following a G2/M arrest [43–45]. Based on these results, we believe that in our experiment, mitotic catastrophe might be associated with apoptosis, or at least end up in an apoptosis-related cell execution. For this assumption, some confirmations would be needed.

3. Conclusions

In this work, four novel A-ring amino derivatives of the alkaloid Luotonin A were synthesized via two orthogonal pathways involving intramolecular cycloaddition reactions as the key step. The target compounds were obtained in good yields by mild catalytic transfer hydrogenation of the corresponding nitro precursors. In the biological evaluation, we detected at least one compound that showed convincingly stronger antiproliferative activity than the lead compound, Luotonin A. Similar to CPT, three of four examined compounds were clearly superior to Luotonin A, inhibiting the Top1 enzyme. Surprisingly, the most active compound in the viability assay, **5b**, showed no activity of Top1 inhibition in a DNA relaxation assay at lower antiproliferative concentrations. Furthermore, under exposure to compound **5b** in such concentrations, we observed a massive G2/M arrest, as well as elements of both mitotic catastrophe and apoptosis. This behavior is, although under certain conditions observed in some other cases [46–48], not typical for CPT-related Topoisomerase I inhibitors, which usually exhibit an S phase arrest rather than a G2/M arrest. Therefore, some other biological targets for our compound might be relevant, or another effect on the enzyme could be speculated. Considering the detected G2/M arrest of tumor cells under exposure to **5b**, we suggest the observed G2 checkpoint inhibition to be a mitotic disruptor that leads either to apoptotic or (also possible) mitotic cell death.

Hence, we hope that our work might contribute to complementing the efforts of developing new therapy approaches in which using one G2/M-arrest-inducing agent and/or mitotic cell death initiator could eventually lead to some alternative therapy options and milden the side effects of conventional therapy.

4. Experimental Section

4.1. Chemistry

4.1.1. General

Melting points (uncorrected) were determined on a Kofler hot-stage microscope (Leica GmbH, Wetzlar, Germany). ^{1}H-NMR and ^{13}C-NMR spectra (see Supplementary Materials) were recorded on a Bruker Avance III 400 spectrometer (Bruker BioSpin GmbH, Rheinstetten, Germany) at 400 MHz and 100 MHz, respectively; chemical shifts (ppm) were referenced to residual amounts of undeuterated solvents. Mass spectra (EI) were obtained on a Shimadzu QP5050A DI 50 instrument (Shimadzu Corp., Kyoto, Japan); high-resolution mass spectra (ESI-TOF) were recorded on a Bruker maXis HD spectrometer (Bruker Daltonics GmbH, Bremen, Germany). Column chromatography was carried out on Merck Kieselgel 60, 0.063–0.200 mm. Thin layer chromatography was done on Merck aluminium sheets pre-coated with Kieselgel 60 F_{254} (Merck, Darmstadt, Germany). Microanalyses were performed at the Microanalytical Laboratory, Faculty of Chemistry, University of Vienna. Ethyl 4-oxo-3,4-dihydroquinazoline-2-carboxylate (**1**) was prepared according to a literature procedure [23].

4.1.2. Syntheses

N-(2-Nitrophenyl)-4-oxo-3,4-dihydroquinazoline-2-carboxamide (**2b**). To a solution of 2-nitroaniline (1105 mg, 8 mmol) in dry 1,2-dichloroethane (20 mL) under argon was added dropwise a 2 M solution of $AlMe_3$ (4.0 mL, 8 mmol) in heptane. The mixture was stirred for 30 min at room temperature, then the ester **1** (1091 mg, 5 mmol) was added in one portion, and the mixture was refluxed for 2 h. After cooling to 0 °C, it was then quenched by slow addition of 2 N HCl (20 mL), followed by water (80 mL). The resulting liquid/liquid/solid system was filtered and the filter cake was washed with 70% EtOH and dried to give compound **2b** (903 mg, 58%) in sufficient purity for the next reaction step. Analytically pure material can be obtained by recrystallization from EtOH as pale yellow crystals, m.p. > 315 °C. MS (EI, 70 eV): m/z = 310 (M^+, 25%), 264 (84), 146 (78), 145 (22), 119 (100), 118 (21), 91 (18), 90 (49); ^{1}H-NMR (DMSO-d_6) δ: 12.76 (br s, 1H, 3-H), 12.15 (br s, 1H, amide NH), 8.54 (d, J = 8.4 Hz, 1H, phenyl 6′-H), 8.26 (dd, J = 8.4 Hz, 1.5 Hz, 1H, phenyl 3′-H), 8.22 (d, J = 7.8 Hz, 1H, 5-H), 7.98–7.93 (m, 1H, 7-H), 7.89–7.85 (m, 2H, 8-H, phenyl 5′-H), 7.68 (t, J = 7.8 Hz, 1H, 6-H), 7.46–7.42 (m, 1H, phenyl 4′-H); ^{13}C-NMR (DMSO-d_6) δ: 161.0, 158.0, 146.4, 145.1, 138.7, 135.7, 135.1, 132.3, 128.7, 127.9, 126.3, 125.9, 125.1, 122.9, 122.7. Anal. calcd. for $C_{15}H_{10}N_4O_4 \cdot 0.1\ H_2O$: C, 57.73; H, 3.29; N, 17.95. Found: 57.87; H, 2.96; N, 17.56. HRMS (ESI-TOF) calcd. for $C_{15}H_{11}N_4O_4$ ([M + H]$^+$): 311.0775. Found: 311.0775.

N-(2-Nitrophenyl)-4-oxo-3-(prop-2-yn-1-yl)-3,4-dihydroquinazoline-2-carboxamide (**3b**). In a round-bottomed flask, finely ground anilide **2b** (155 mg, 0.5 mmol) was added to DMSO (20 mL) and the resulting suspension was stirred at room temperature for 30 min. Then, finely powdered KOH (34 mg, 0.5 mmol) and tetrabutylammonium bromide (10 mg) were added and the mixture was sonicated in an ultrasound cleaning bath for 10 min. While the mixture was vigorously stirred, a solution of propargyl bromide (80% in toluene; 82 mg, 0.5 mmol) in DMSO (10 mL) was dropwise added over a period of 2 h. Stirring was continued at room temperature for 24 h (TLC monitoring: CH_2Cl_2/ethyl acetate, 19:1), then the solution was poured into water (100 mL) and the precipitate was collected by filtration, washed with water, and dried. This material was subjected to column chromatography (eluent: CH_2Cl_2/ethyl acetate, 19:1). Evaporation of the main fraction, followed by recrystallization from ethyl acetate/light petroleum afforded compound **3b** (133 mg, 76%) as yellow crystals, m.p.

207–208 °C. MS (EI, 70 eV): m/z = 348 (M^+, 16%), 347 (39), 331 (30), 330 (25), 303 (49), 302 (100), 300 (42), 273 (26), 156 (37), 155 (49), 145 (75), 130 (39), 129 (61), 119 (58), 102 (37), 90 (78);); ^{1}H-NMR ($CDCl_3$) δ: 12.72 (br s, 1H, NH), 8.92 (dd, *J* = 8.5 Hz, 1.2 Hz, 1H, phenyl 6′-H), 8.41–8.35 (m, 1H, 5-H), 8.32 (dd, *J* = 8.4 Hz, 1.5 Hz, 1H, phenyl 3′-H), 7.95–7.90 (m, 1H, 8-H), 7.87 (ddd, *J* = 8.2 Hz, 7.0 Hz, 1.5 Hz, 1H, 7-H), 7.79–7.70 (m, 1H, phenyl 5′-H), 7.64 (ddd, *J* = 8.2 Hz, 7.0 Hz, 1.4 Hz, 1H, 6-H), 7.31 (ddd, *J* = 8.5 Hz, 7.3 Hz, 1.3 Hz, 1H, phenyl 4′-H), 5.59 (d, *J* = 2.5 Hz, 2H, CH_2), 2.27 (t, *J* = 2.5 Hz, 1H, acetylene H); ^{13}C-NMR ($CDCl_3$) δ: 161.4, 159.4, 144.9, 144.5, 137.3, 136.1, 135.3, 133.8, 129.6, 128.6, 127.6, 126.2, 124.4, 122.1, 121.9, 78.9, 72.2, 33.7. Anal. calcd. for $C_{18}H_{12}N_4O_4$: C, 62.07; H, 3.47; N, 16.08. Found: C, 61.81; H, 3.13; N, 15.71.

4-Nitroquinolino[2′,3′:3,4]pyrrolo[2,1-b]quinazolin-11(13H)-one (**4b**). To a solution of triphenyl-phosphine oxide (835 mg, 3 mmol) in dry CH_2Cl_2 (22 mL) was dropwise added trifluoro-methanesulfonic anhydride (0.25 mL, 1.5 mmol) at 0 °C under argon, and the mixture was stirred at the same temperature for 15 min. Then, the educt **3b** (348 mg, 1 mmol) was added in one portion at 0 °C, and the mixture was stirred for 24 h while slowly warming to room temperature. The mixture was evaporated under reduced pressure and the solid residue was re-suspended in 10% aq. $NaHCO_3$ solution and stirred for 1 h. The product was collected by filtration and washed consecutively with water, EtOH and cold $CHCl_3$. Recrystallization from $CHCl_3$ afforded **4b** (211 mg, 64%) as pale yellow crystals, m.p. 263–264 °C. MS (EI, 70 eV): m/z = 330 (M^+, 12%), 300 (10), 284 (6), 81 (8), 69 (100), 65 (39), 64 (15), 57 (9); ^{1}H-NMR (DMSO-d_6) δ: 8.99 (s, 1H, 14-H),8.49 (d, *J* = 8.7 Hz, 1H, 1-H),8.43 (d, *J* = 7.7 Hz, 1H, 3-H), 8.32 (d, *J* = 7.6 Hz, 1H, 10-H), 8.03 (d, *J* = 8.3 Hz, 1H, 7-H), 8.00–7.85 (m, 2H, 2-H, 8-H), 7.67 (t, *J* = 7.4 Hz, 1H, 9-H), 5.36 (s, 2H, 13-CH_2); ^{13}C-NMR (DMSO-d_6) δ: 159.6, 153.6, 152.3, 148.8, 148.4, 139.0, 134.6, 133.1, 132.5, 132.3, 129.0, 128.2, 127.6, 127.4, 125.9, 124.0, 121.2, 47.6. HRMS (ESI-TOF) calcd. for $C_{18}H_{11}N_4O_3$ ([M + H]$^+$): 331.0826. Found: 331.0824.

2-Aminoquinolino[2′,3′:3,4]pyrrolo[2,1-b]quinazolin-11(13H)-one (**5a**). To a suspension of the nitro compound **4a** [16] (165 mg, 0.503 mmol) in EtOH (50 mL) were added hydrazine hydrate (350 mg, 7 mmol) and 10% palladium on carbon (30 mg) and the mixture was refluxed under an argon atmosphere for 2 h (TLC monitoring: CH_2Cl_2/EtOH, 30:1). The solvent was evaporated under reduced pressure (max. bath temperature: 25 °C) and the residue was taken up in DMF (15 mL). The catalyst was removed by filtration and the filtrate was concentrated to approx. 5 mL under reduced pressure, then it was diluted with water (5 mL). The precipitate was collected by filtration and washed with 70% EtOH to give the amino compound **5a** (120 mg, 80%) as yellow crystals, m.p. >350 °C (decomp.). MS (EI, 70 eV): m/z = 300 (M^+, 13%), 231 (100), 71 (57), 70 (79), 69 (44), 57 (93), 55 (42), 44 (39), 43 (88); for ^{1}H-NMR and ^{13}C-NMR data, see Table 1. HRMS (ESI-TOF) calcd. for $C_{18}H_{13}N_4O$ ([M + H]$^+$): 301.1084. Found: 301.1083.

4-Aminoquinolino[2′,3′:3,4]pyrrolo[2,1-b]quinazolin-11(13H)-one (**5b**). To a suspension of the nitro compound **4b** (165 mg, 0.503 mmol) in EtOH (50 mL) were added hydrazine hydrate (350 mg, 7 mmol) and 10% palladium on carbon (30 mg) and the mixture was refluxed under an argon atmosphere for 2 h (TLC monitoring: CH_2Cl_2/EtOH, 30:1). The solution was filtered while hot and then cooled to room temperature. The red crystals were collected by filtration and washed with cold EtOH. The filtrate was evaporated to dryness under reduced pressure and the residue was dissolved in DMF (15 mL). The solution was filtered twice to remove traces of colloidal Pd/C, then it was diluted with water (20 mL). The red precipitate was collected by filtration and washed with cold EtOH. The combined crops were recrystallized from $CHCl_3$ to afford **5b** (107 mg, 71%) as red crystals, m.p. >315 °C (decomp.). MS (EI, 70 eV): m/z = 300 (M^+, 44%), 215 (18), 204 (18), 203 (40), 178 (81), 145 (24), 57 (100), 41 (25); for ^{1}H-NMR and ^{13}C-NMR data, see Table 1. HRMS (ESI-TOF) calcd. for $C_{18}H_{13}N_4O$ ([M + H]$^+$): 301.1084. Found: 301.1081.

3-[3-(2-Nitrophenyl)prop-2-yn-1-yl]-4-oxo-3,4-dihydroquinazoline-2-carboxamide (**7a**). To a stirred suspension of the amide **6** [29] (454 mg, 2 mmol) in dry CH_2Cl_2 (30 mL) was added 2-iodonitrobenzene (746 mg, 3 mmol), 2,6-di-tert-butyl-4-methylphenol (110 mg, 0.5 mmol), CuI (76 mg, 0.4 mmol), $Pd(PPh_3)Cl_2$ (140 mg, 0.2 mmol) and triethylamine (486 mg, 4.8 mmol). The mixture was flushed

with argon and stirred in a closed vessel at room temperature for 2 h (TLC monitoring: CH_2Cl_2/ethyl acetate, 2:1). It was then diluted with CH_2Cl_2 (80 mL) and filtered. The filtrate was concentrated under reduced pressure and the residue was subjected to column chromatography (eluent: CH_2Cl_2/ethyl acetate, 2:1). Evaporation of the main fraction, followed by recrystallization from toluene/ethyl acetate and subsequently from EtOH gave the product **7a** (328 mg, 48%) as light-brown crystals, m.p. 193–194 °C. MS (EI, 70 eV): m/z = 349 ([M + 1]$^+$, 2%), 331 (36), 288 (88), 146 (100), 145 (86), 130 (96), 119 (37), 102 (66), 90 (43), 76 (64), 63 (33); ^{1}H-NMR (DMSO-d_6) δ: 8.52 (br s, 1H, NH), 8.23 (dd, J = 8.2 Hz, 1.4 Hz, 1H, 5-H), 8.22 (br s, 1H, NH), 8.09 (d, J = 8.2 Hz, 1H, phenyl 3′-H), 7.93 (td, J = 7.5 Hz, 1.5 Hz, 1H, 7-H, shows positive NOE on irradiation at 7.78 ppm), 7.78 (d, J = 7.8 Hz, 1H, 8-H, shows positive NOE on irradiation at 7.93 ppm), 7.73–7.69 (m, 2H, phenyl 5′-H, 6′-H), 7.68–7.60 (m, 2H, 6-H, phenyl 4′-H, shows positive NOE on irradiation at 8.09 ppm or at 7.93 ppm), 5.37 (s, 2H, CH_2); ^{13}C-NMR (DMSO-d_6) δ: 163.2, 160.0, 149.3, 148.6, 145.8, 135.2, 134.8, 133.6, 130.0, 128.4, 127.6, 126.6, 124.6, 120.9, 116.3, 92.0, 78.3, 33.9. Anal. calcd. for $C_{18}H_{12}N_4O_4 \cdot 0.3\ H_2O$: C, 61.12; H, 3.59; N, 15.84. Found: C, 61.11; H, 3.24; N, 15.73.

3-[3-(4-Nitrophenyl)prop-2-yn-1-yl]-4-oxo-3,4-dihydroquinazoline-2-carboxamide (**7b**). A solution/suspension of the amide **6** [29] (227 mg, 1 mmol) in dry DMF (1 mL) was diluted with dry CH_2Cl_2 (15 mL). Then, 4-iodonitrobenzene (373 mg, 1.5 mmol), 2,6-di-tert-butyl-4-methylphenol (55 mg, 0.25 mmol), CuI (38 mg, 0.2 mmol), $Pd(PPh_3)Cl_2$ (70 mg, 0.1 mmol) and triethylamine (243 mg, 2.4 mmol) were added consecutively. The mixture was flushed with argon and stirred in a closed vessel at room temperature for 2 h (TLC monitoring: CH_2Cl_2/ethyl acetate, 2:1). It was then diluted with CH_2Cl_2 (40 mL) and filtered. The filtrate was concentrated under reduced pressure and the residue was subjected to column chromatography (eluent: CH_2Cl_2/ethyl acetate, 2:1). Evaporation of the main fraction, followed by recrystallization from toluene/ethyl acetate and subsequently from EtOH gave the product **7b** (188 mg, 54%) as colorless needles, m.p. 224–225 °C. MS (EI, 70 eV): m/z = 348 (M$^+$, 100%), 305 (16), 258 (27), 229 (22), 198 (14), 175 (32), 160 (14), 146 (38), 130 (40), 129 (39), 114 (35), 102 (50), 76 (38), 63 (51); ^{1}H-NMR (DMSO-d_6) δ: 8.58 (br s, 1H, NH), 8.26–8.18 (m, 4H, NH, 5-H, phenyl 3′-H, 5′-H), 7.95–7.90 (m, 1H, 7-H), 7.77 (d, J = 9.0 Hz, 1H, 8-H), 7.70–7.63 (m, 3H, 6-H, phenyl 2′-H, 6′-H), 5.34 (s, 2H,CH_2); ^{13}C-NMR (DMSO-d_6) δ: 163.2, 160.0, 148.7, 147.0, 145.8, 135.2, 132.7, 128.4, 128.3, 127.6, 126.5, 123.7, 120.9, 89.9, 81.4, 33.8. Anal. calcd. for $C_{18}H_{12}N_4O_4$: C, 62.07; H, 3.47; N, 16.08. Found: C, 61.74; H, 3.25; N, 15.73.

3-[3-(2-Nitrophenyl)prop-2-yn-1-yl]-4-oxo-3,4-dihydroquinazoline-2-carbonitrile (**8a**). In an oven- dried 50 mL round-bottomed flask, the amide **7a** (100 mg, 0.287 mmol) was dissolved in dry $CHCl_3$ (10 mL). To this solution was added freshly distilled $POCl_3$ (1 mL) and the mixture was heated to 90 °C under exclusion of moisture for 24 h (TLC monitoring: CH_2Cl_2/EtOH, 30:1). The dark suspension was dropwise added to ice-water (50 mL) with stirring. After 30 min, the phases were separated and the aqueous layer was extracted with $CHCl_3$ (3 × 15 mL). The combined organic layers were washed with water and brine, dried over Na_2SO_4 and concentrated under reduced pressure. The residue was purified by column chromatography (eluent: CH_2Cl_2), followed by recrystallization from EtOH to afford the nitrile **8a** (68 mg, 72%) as colorless crystals, m.p. 170–172 °C. MS (EI, 70 eV): m/z = 330 (M$^+$, 5%), 313 (65), 160 (48), 154 (70), 146 (61), 130 (46), 104 (100), 102 (69), 89 (59), 76 (89), 63 (50); ^{1}H-NMR ($CDCl_3$) δ: 8.37 (dd, J = 8.0, 1.1 Hz, 1H, 5-H), 8.07 (dd, J = 8.3, 1.1 Hz, 1H, phenyl 3′-H, shows positive NOE on irradiation at 7.49 ppm), 7.90–7.82 (m, 2H, 7-H, 8-H), 7.69–7.64 (m, 2H, 6-H, phenyl 6′-H, shows positive NOE on irradiation at 8.37 ppm), 7.58 (td, J = 7.7, 1.3 Hz, 1H, phenyl 4′-H), 7.49 (td, J = 7.7, 1.5 Hz, 1H, phenyl 5′-H, shows positive NOE on irradiation at 8.07 ppm), 5.37 (s, 2H, CH_2); ^{13}C-NMR ($CDCl_3$) δ: 159.3, 146.4, 135.6, 135.2, 133.1, 130.8, 130.5, 129.6, 128.9, 127.6, 124.9, 122.8, 117.3, 111.4, 89.1, 81.3, 36.0. Anal. calcd. for $C_{18}H_{10}N_4O_3$: C, 65.45M H, 3.05; N, 16.96. Found: C, 65.05; H, 2.92; N, 16.81.

3-[3-(4-Nitrophenyl)prop-2-yn-1-yl]-4-oxo-3,4-dihydroquinazoline-2-carbonitrile (**8b**). This compound was prepared and isolated as described for compound **8a**, starting from the amide **7b** (100 mg, 0.287 mmol). Recrystallization from EtOH gave the nitrile **8b** (88 mg, 90%) as colorless needles, m.p.

188–190 °C. MS (EI, 70 eV): m/z = 330 (M^+, 100%), 284 (45), 256 (21), 230 (7), 208 (12), 160 (79), 130 (27), 114 (73), 113 (75), 102 (80), 88 (38), 76 (53), 63 (92), 50 (36); ^{1}H-NMR ($CDCl_3$) δ: 8.39–8.36 (m, 1H, 5-H), 8.20–8.16 (m, 2H, phenyl 3′-H, 5′-H), 7.93–7.87 (m, 1H, 7-H), 7.86–7.82 (m, 1H, 8-H), 7.72–7.67 (m, 1H, 6-H), 7.64–7.69 (m, 2H, phenyl 2′-H, 6′-H), 5.34 (s, 2H, CH_2); ^{13}C-NMR ($CDCl_3$) δ: 159.3, 147.9, 146.4, 135.7, 133.1, 130.7, 130.6, 129.0, 128.5, 127.6, 123.7, 122.8, 111.4, 86.4, 83.9, 35.8. Anal. calcd. for $C_{18}H_{10}N_4O_3 \cdot 0.5\ H_2O$: C, 63.72; H, 3.27; N, 16.51. Found: C, 63.96; H, 3.01; N, 16.20.

1-Nitroquinolino[2′,3′:3,4]pyrrolo[2,1-b]quinazolin-11(13H)-one (**9a**). To a solution of the nitrile **8a** (100 mg, 0.303 mmol) in 1,2-dichlorobenzene (8 mL) was added a 0.1 M solution of DBU in 1,2-dichlorobenzene (0.15 mL, 5 mol%). After flushing with argon, the vessel was closed and the mixture was heated to 110–120 °C for 24 h. If TLC (CH_2Cl_2/EtOH, 30:1) indicated incomplete conversion, another portion of the base (0.15 mL of 0.1 M DBU solution) was added and heating was continued for another 24 h. The resulting suspension was chilled and diluted with Et_2O (55 mL). The precipitate was collected by filtration, washed with Et_2O and recrystallized from $CHCl_3$ to afford compound **9a** (46 mg, 46%) as almost colorless crystals, m.p. 325–327 °C. MS (EI, 70 eV): m/z = 330 (M^+, 100%), 284 (47), 262 (31), 183 (33), 108 (28), 77 (36), 69 (31), 57 (51), 55 (36), 43 (47); ^{1}H-NMR (DMSO-d_6) δ: 9.24 (s, 1H, 14-H), 8.66 (d, J = 8.5 Hz, 1H, 4-H), 8.58 (d, J = 7.4 Hz, 1H, 2-H), 8.27 (d, J = 8.0 Hz, 1H, 10-H), 8.08 (t, J = 8.1 Hz, 1H, 3-H), 7.98–7.91 (m, 2H, 7-H, 8-H), 7.66–7.61 (m, 1H, 9-H), 5.36 (s, 2H, 13-CH_2); ^{13}C-NMR (DMSO-d_6) δ: 159.6, 153.2, 152.5, 148.9, 145.9, 145.4, 139.7, 136.6, 134.7, 134.0, 129.1, 128.2, 127.6, 126.2, 126.0, 121.3, 120.7, 48.1. HRMS (ESI-TOF) calcd. for $C_{18}H_{11}N_4O_3$ ([M + H]$^+$): 331.0826. Found: 331.0818.

3-Nitroquinolino[2′,3′:3,4]pyrrolo[2,1-b]quinazolin-11(13H)-one (**9b**). This compound was pre-pared as described for compound **9a**, starting from the nitrile **8b** (100 mg, 0.303 mmol). Recrystallization from DMF/$CHCl_3$ afforded **9b** (57 mg, 57%) as yellow crystals, m.p. > 310 °C (decomp.). MS (EI, 70 eV): m/z = 330 (M^+, 100%), 300 (14), 284 (59), 254 (14), 228 (10), 142 (17), 114 (13), 77 (15), 76 (20), 63 (25), 50 (18); ^{1}H-NMR (DMSO-d_6) δ: 9.06 (s, 1H, 4-H), 8.96 (s, 1H, 14-H, shows positive NOE on irradiation at 5.37 ppm), 8.47–8.45 (m, 2H, 1-H, 2-H), 8.30 (d, J = 8.0 Hz, 1H, 10-H), 7.98–7.95 (m, 2H, 7-H, 8-H), 7.68–7.64 (m, 1H, 9-H), 5.37 (s, 2H, 13-CH_2); ^{13}C-NMR (DMSO-d_6) δ: 160.2, 159.6, 154.3, 152.4, 151.5, 148.9, 148.3, 147.0, 134.7, 134.2, 132.2, 131.6, 128.2, 126.0, 125.4, 121.3, 121.2, 47.8. HRMS (ESI-TOF) calcd. for $C_{18}H_{11}N_4O_3$ ([M + H]$^+$): 331.0826. Found: 331.0827.

1-Aminoquinolino[2′,3′:3,4]pyrrolo[2,1-b]quinazolin-11(13H)-one (**10a**). To a suspension of the nitro compound **9a** (100 mg, 0.303 mmol) in EtOH (20 mL) was added hydrazine hydrate (240 mg, 4.8 mmol) and 10% palladium on carbon (10 mg) and the mixture was refluxed under an argon atmosphere for 1 h (TLC monitoring: CH_2Cl_2/EtOH, 30:1). The mixture was diluted with EtOH (300 mL), refluxed for a few minutes and filtered hot to remove the catalyst. The filter cake was re-suspended in EtOH (300 mL), refluxed for a few minutes and again filtered while still hot. This procedure was repeated until the last filtrate did not show any fluorescence under UV_{366} light. The combined filtrates were evaporated under reduced pressure to afford the amino compound **10a** (89 mg, 98%) as reddish crystals, m.p. 315–317 °C (decomp.). MS (EI, 70 eV): m/z = 300 (M^+, 100%), 272 (14), 150 (13), 111 (16), 97 (22), 83 (21), 77 (19), 71 (27), 57 (41), 43 (26); for ^{1}H-NMR and ^{13}C-NMR data, see Table 1. HRMS (ESI-TOF) calcd. for $C_{18}H_{13}N_4O$ ([M + H]$^+$): 301.1084. Found: 301.1075.

3-Aminoquinolino[2′,3′:3,4]pyrrolo[2,1-b]quinazolin-11(13H)-one (**10b**). This compound was prepared and isolated as described for compound **10a**, starting from the nitro compound **9b** (100 mg, 0.303 mmol). Evaporation of the combined ethanolic filtrates afforded **10b** (88 mg, 97%) as yellow crystals, m.p. > 310 °C (decomp.). MS (EI, 70 eV): m/z = 300 (M^+, 100%), 272 (9), 244 (5), 223 (9), 150 (11), 122 (7), 102 (7), 77 (16), 64 (10), 63 (11), 51 (9); for ^{1}H-NMR and ^{13}C-NMR data, see Table 1. HRMS (ESI-TOF) calcd. for $C_{18}H_{13}N_4O$ ([M + H]$^+$): 301.1084. Found: 301.1084.

4.2. Biology

4.2.1. Cell Culture

SW480 (ATCC®CCl-228™) as representative for solid tumors, and HL60 (ATCC®CCl-240™) for non-solid tumors as well as human primary lung fibroblasts, normal, HLF (ATCC®PCS-201-013™), were obtained from the American Type Culture Collection (ATCC®). Colon-associated fibroblasts F331 have been isolated from human fetal colon [49].

All cell lines were kept under standard tissue culture conditions and passaged when dense. Media used were Minimal Essential Medium (MEM) for SW480; RPMI-1640 for HL60 and Dulbecco's medium for fibroblasts. The media were supplemented with 10% fetal calf serum.

4.2.2. Cell Viability Assay

Cells were seeded at a density of 5×10^4 cells per mL (SW480) and 10^5 cells per mL (HL60) in a 96-well plate. Compounds were diluted from DMSO stock solutions into MEM-BSA or serum-free RPMI-1640 medium to defined concentrations and added to the cells. Concentration of DMSO was limited with 0.6%, because higher DMSO concentration had influence on cell growth. Treated cells were incubated for 72 h at 37 °C and 5% CO_2. After incubation, MTT viability assay was performed using EZ4U®Cell proliferation & Cytotoxicity Assay (Biomedica). For photometric evaluation, a plate reader TECAN Infinite®200 PRO was used. IC_{50} values were determined as follows: HL60 cells were exposed to the test compound **5b** at a concentration range of 1 μM to 100 μM for 72 h and cell viability was measured using the MTT assay. The data from three independent experiments were pooled and IC_{50} was calculated using a nonlinear regression model of GraphPad Prism (see Section 4.2.7).

4.2.3. DNA Relaxation Assay

The relaxation of the supercoiled EGFP plasmid DNA by the nucleic extract from MCF-7 cells was determined as previously described [50]. Concisely, plasmid DNA (EGFP) was incubated for 30 min at 37 °C with decreasing concentrations of the test compound dissolved in DMSO in a final volume of 30 μL nucleic extract (1:55), 10 mM Tris (pH 7.9), 100 mM KCl, 10 mM MgCl2, 0.5 mM dithiothreitol (DTT), 0.5 mM EDTA, and 0.03 mg/mL bovine serum albumin (BSA). Camptothecin, dissolved in DMSO, was used as positive control. The reaction was stopped by incubation with 5% SDS containing 1 mg/mL proteinase K at 37 °C for 30 min. Subsequently, samples were separated by submarine 1% agarose gel electrophoresis (55 V, 2 h) and gels were stained with 10 μL/100 mL ethidium bromide for 30 min. UV-transilluminated gels (Gel Doc™ XR, BioRad) were documented by Quantity One analysis software.

4.2.4. Cell Cycle Distribution Assay (FACS)

HL60 cells were seeded at a density of 5×10^5 cells per mL in a suspension culture flask. SW480 cells were seeded at a density of 3×10^5 cells per mL in a 6 cm petri dish. 24 h later, compounds were added in defined concentration diluted into serum-free media. Incubation was done for 24 h for HL60 and 72 h for SW480 cultures. After this, the cells were harvested and nuclei isolated and stained with propidium iodide as described before [40]. Cell cycle distribution was evaluated using BD science FACSCalibur®.

4.2.5. Caspase Assay

For determination of caspase activity under influence of experimental substance, the cells were seeded at appropriate density incubated with the compounds for 24 h (for HL60) or 72 h (for SW480). Cell proteins were then isolated and prepared for caspase assay. Caspase reaction solution was prepared fresh and added to protein lysate. After 90 min of incubation at 37 °C under light excision, TECAN Infinite®200 PRO plate reader was used to measure a caspase activity at 405Ex/535Em.

4.2.6. Nuclear Staining

SW480 cells were cultured in 24-well plates at a density of 10^5 cells per mL for 24 h. After 72 h of treatment, the cells were washed, fixed in ice-cold acetone-methanol (1:1), then washed again with PBS and stained with Hoechst 33285, incubating cells for 15 min in dark at room temperature. Photos were captured with a fluorescence microscope equipped with UV light source and a blue/cyan filter.

4.2.7. Statistics

Statistical analysis was performed using GraphPad Prism 5.00, GraphPad Software, California, USA. Conducted was one-way analysis of variance (ANOVA) with Dunnett's post or Bonferroni test and two-way ANOVA, as appropriate. Significance was designated as * for $P < 0.05$, ** for $P < 0.01$, and *** for $P < 0.001$. Error bars depict ± SD.

Supplementary Materials: Spectra (^{1}H-NMR, ^{13}C-NMR, EI-MS) of all new compounds are available online.

Author Contributions: A.I. planned and performed synthetic work and biological testing; S.E., M.E., I.L and L.T. performed synthetic work; P.H., H.H.S., and B.M. designed, performed and supervised the biological testing and helped to interpret the in-vitro experiments; N.H. designed the synthetic part, recorded and interpreted the NMR spectra, and coordinated manuscript writing.

Funding: This research received no external funding.

Acknowledgments: We are grateful to Martin Zehl, Judith Wackerlig, and Daniel Dobusch, MSc, for recording the high-resolution mass spectra and to Leopold Jirovetz for recording the low-resolution mass spectra. We also wish to thank Irene Herbacek from the Institute of Cancer Research, Medical University of Vienna, for performing the fluorescence-activated cell sorting analysis.

Conflicts of Interest: The authors declare no conflict of interest.

References

1. Pommier, Y. DNA Topoisomerase I Inhibitors: Chemistry, Biology, and Interfacial Inhibition. *Chem. Rev.* **2009**, *109*, 2894–2902. [CrossRef] [PubMed]
2. Pizzolato, J.F.; Saltz, L.B. The camptothecins. *Lancet* **2003**, *361*, 2235–2242. [CrossRef]
3. Kollmannsberger, C.; Mross, K.; Jakob, A.; Kanz, L.; Bokemeyer, C. Topotecan—A novel topoisomerase I inhibitor: Pharmacology and clinical experience. *Oncology* **1999**, *56*, 1–12. [CrossRef] [PubMed]
4. Ramesh, M.; Ahlawat, P.; Srinivas, N.R. Irinotecan and its active metabolite, SN-38: Review of bioanalytical methods and recent update from clinical pharmacology perspectives. *Biomed. Chromatogr.* **2010**, *24*, 104–123. [CrossRef]
5. Staker, B.L.; Hjerrild, K.; Feese, M.D.; Behnke, C.A.; Burgin, A.B., Jr.; Stewart, L. The mechanism of topoisomerase I poisoning by a camptothecin analog. *Proc. Natl. Acad. Sci. USA* **2002**, *99*, 15387–15392. [CrossRef]
6. Staker, B.L.; Feese, M.D.; Cushman, M.; Pommier, Y.; Zembower, D.; Stewart, L.; Burgin, A.B. Structures of three classes of anticancer agents bound to the human topoisomerase I-DNA covalent complex. *J. Med. Chem.* **2005**, *48*, 2336–2345. [CrossRef] [PubMed]
7. Strumberg, D.; Pilon, A.A.; Smith, M.; Hickey, R.; Malkas, L.; Pommier, Y. Conversion of topoisomerase 1 cleavage complexes on the leading strand of ribosomal DNA into 5′-phosphorylated DNA double-strand breaks by replication runoff. *Mol. Cell. Biol.* **2000**, *20*, 3977–3987. [CrossRef] [PubMed]
8. Liang, J.L.; Cha, H.C.; Jahng, Y. Recent advances in the studies on luotonins. *Molecules* **2011**, *16*, 4861–4883. [CrossRef]
9. Cagir, A.; Jones, S.H.; Gao, R.; Eisenhauer, B.M.; Hecht, S.M. Luotonin A. A naturally occurring human DNA topoisomerase I poison. *J. Am. Chem. Soc.* **2003**, *125*, 13628–13629. [CrossRef]
10. Ma, Z.Z.; Hano, Y.S.; Nomura, T.; Chen, Y.J. Novel quinazoline-quinoline alkaloids with cytotoxic and DNA topoisomerase II inhibitory activities. *Bioorg. Med. Chem. Lett.* **2004**, *14*, 1193–1196. [CrossRef]
11. Nacro, K.; Zha, C.C.; Guzzo, P.R.; Jason Herr, R.; Peace, D.; Friedrich, T.D. Synthesis and topoisomerase poisoning activity of A-ring and E-ring substituted luotonin A derivatives. *Bioorg. Med. Chem.* **2007**, *15*, 4237–4246. [CrossRef] [PubMed]

12. Lu, J.J.; Bao, J.L.; Chen, X.P.; Huang, M.; Wang, Y.T. Alkaloids isolated from natural herbs as the anticancer agents. *Evid.-Based Complement. Alternat. Med.* **2012**, *2012*, 485042. [CrossRef] [PubMed]
13. Liao, C.H.; Pan, S.L.; Guh, J.H.; Chang, Y.L.; Pai, H.C.; Lin, C.H.; Teng, C.M. Antitumor mechanism of evodiamine, a constituent from Chinese herb Evodiae fructus, in human multiple-drug resistant breast cancer NCI/ADR-RES cells in vitro and in vivo. *Carcinogenesis* **2005**, *26*, 968–975. [CrossRef] [PubMed]
14. Kan, S.F.; Huang, W.J.; Lin, L.C.; Wang, P.S. Inhibitory effects of evodiamine on the growth of human prostate cancer cell line LNCaP. *Int. J. Cancer* **2004**, *110*, 641–651. [CrossRef] [PubMed]
15. Huang, Y.C.; Guh, J.H.; Teng, C.M. Induction of mitotic arrest and apoptosis by evodiamine in human leukemic T-lymphocytes. *Life Sci.* **2004**, *75*, 35–49. [CrossRef] [PubMed]
16. Haider, N.; Nuss, S. Weinreb amidation as the cornerstone of an improved synthetic route to A-ring-modified derivatives of luotonin A. *Molecules* **2012**, *17*, 11363–11378. [CrossRef]
17. Atia, M.; Bogdan, D.; Brugger, M.; Haider, N.; Matyus, P. Remarkable regioselectivities in the course of the synthesis of two new Luotonin A derivatives. *Tetrahedron* **2017**, *73*, 3231–3239. [CrossRef]
18. Ibric, A.; Dutter, K.; Marian, B.; Haider, N. A Facile Oxidative Opening of the C-Ring in Luotonin A and Derivatives. *Molecules* **2017**, *22*, 1540. [CrossRef]
19. Haider, N.; Meng, G.; Roger, S.; Wank, S. An efficient and selective access to 1-substituted and 3-substituted derivatives of luotonin A. *Tetrahedron* **2013**, *69*, 7066–7072. [CrossRef]
20. Cagir, A.; Eisenhauer, B.M.; Gao, R.; Thomas, S.J.; Hecht, S.M. Synthesis and topoisomerase I inhibitory properties of luotonin A analogues. *Bioorg. Med. Chem.* **2004**, *12*, 6287–6299. [CrossRef]
21. Zhou, H.B.; Liu, G.S.; Yao, Z.J. Short and efficient total synthesis of luotonin a and 22-hydroxyacuminatine using a common cascade strategy. *J. Org. Chem.* **2007**, *72*, 6270–6272. [CrossRef] [PubMed]
22. Basha, A.; Lipton, M.; Weinreb, S.M. Mild, General Method for Conversion of Esters to Amides. *Tetrahedron Lett.* **1977**, 4171–4174. [CrossRef]
23. Baker, B.R.; Almaula, P.I. Nonclassical Antimetabolites .10. Facile Synthesis of 4-Quinazolone-2-Carboxylic Acid and Structure of Bogerts Ammonium Salt. *J. Org. Chem.* **1962**, *27*, 4672–4674. [CrossRef]
24. Hendrickson, J.B.; Singer, M.; Hussoin, M.S. Direct Borohydride Reduction of Alcohols to Alkanes with Phosphonium Anhydride Activation. *J. Org. Chem.* **1993**, *58*, 6913–6914. [CrossRef]
25. Dallavalle, S.; Merlini, L.; Beretta, G.L.; Tinelli, S.; Zunino, F. Synthesis and cytotoxic activity of substituted luotonin A derivatives. *Bioorg. Med. Chem. Lett.* **2004**, *14*, 5757–5761. [CrossRef] [PubMed]
26. Deady, L.W.; Sette, R.M.D. Lithiation of pivaloylamino derivatives of dibenzofuran and 9-methylcarbazole. *Aust. J. Chem.* **2001**, *54*, 177–180. [CrossRef]
27. Haider, N.; Tropper, K. Dimethyl 6-Amino-1-methyl-9H-carbazole-2,3-dicarboxylate. *Molbank* **2015**, M849. [CrossRef]
28. Varadi, A.; Horvath, P.; Kurtan, T.; Mandi, A.; Toth, G.; Gergely, A.; Kokosi, J. Synthesis and configurational assignment of 1,2-dihydroimidazo[5,1-*b*] quinazoline-3,9-diones: Novel NMDA receptor antagonists. *Tetrahedron* **2012**, *68*, 10365–10371. [CrossRef]
29. Usifoh, C.O.; Scriba, G.K.E. Synthesis and anticonvulsant activity of acetylenic quinazolinone derivatives. *Arch Pharm* **2000**, *333*, 261–266. [CrossRef]
30. Khanna, I.K.; Yu, Y.; Huff, R.M.; Weier, R.M.; Xu, X.D.; Koszyk, F.J.; Collins, P.W.; Cogburn, J.N.; Isakson, P.C.; Koboldt, C.M.; et al. Selective cyclooxygenase-2 inhibitors: Heteroaryl modified 1,2-diarylimidazoles are potent, orally active antiinflammatory agents. *J. Med. Chem.* **2000**, *43*, 3168–3185. [CrossRef]
31. Kuo, C.W.; Zhu, J.L.; Wu, J.D.; Chu, C.M.; Yao, C.F.; Shia, K.S. A convenient new procedure for converting primary amides into nitriles. *Chem. Commun.* **2007**, 301–303. [CrossRef] [PubMed]
32. Dai, W.X.; Petersen, J.L.; Wang, K.K. Synthesis of the parent and substituted tetracyclic ABCD ring cores of camptothecins via 1-(3-aryl-2-propynyl)-1,6-dihydro-6-oxo-2-pyridinecarbonitriles. *Org. Lett.* **2006**, *8*, 4665–4667. [CrossRef] [PubMed]
33. Crowley, L.C.; Marfell, B.J.; Waterhouse, N.J. Analyzing Cell Death by Nuclear Staining with Hoechst 33342. *Cold Spring Harbor Protocols* **2016**, *2016*. [CrossRef] [PubMed]
34. Bible, K.C.; Kaufmann, S.H. Cytotoxic synergy between flavopiridol (NSC 649890, L86-8275) and various antineoplastic agents: The importance of sequence of administration. *Cancer Res.* **1997**, *57*, 3375–3380. [PubMed]

35. Tyagi, A.K.; Singh, R.P.; Agarwal, C.; Chan, D.C.F.; Agarwal, R. Silibinin strongly synergizes human prostate carcinoma DU145 cells to doxorubicin-induced growth inhibition, G(2)-M arrest, and apoptosis. *Clin. Cancer Res.* **2002**, *8*, 3512–3519. [PubMed]
36. Ling, Y.H.; ElNaggar, A.K.; Priebe, W.; PerezSoler, R. Cell cycle-dependent cytotoxicity, G2/M phase arrest, and disruption of p34(cdc2)/cyclin B-1 activity induced by doxorubicin in synchronized P388 cells. *Mol. Pharmacol.* **1996**, *49*, 832–841.
37. Potter, A.J.; Gollahon, K.A.; Palanca, B.J.A.; Harbert, M.J.; Choi, Y.M.; Moskovitz, A.H.; Potter, J.D.; Rabinovitch, P.S. Flow cytometric analysis of the cell cycle phase specificity of DNA damage induced by radiation, hydrogen peroxide and doxorubicin. *Carcinogenesis* **2002**, *23*, 389–401. [CrossRef]
38. DiPaola, R.S. To arrest or not to G(2)-M cell-cycle arrest. *Clin. Cancer Res.* **2002**, *8*, 3311–3314.
39. Bucher, N.; Britten, C.D. G2 checkpoint abrogation and checkpoint kinase-1 targeting in the treatment of cancer. *Brit. J. Cancer* **2008**, *98*, 523–528. [CrossRef]
40. Kainz, K.P.; Krenn, L.; Erdem, Z.; Kaehlig, H.; Zehl, M.; Bursch, W.; Berger, W.; Marian, B. 2-Deprenyl-Rheediaxanthone B Isolated from Metaxya rostrata Induces Active Cell Death in Colorectal Tumor Cells. *PLoS ONE* **2013**, *8*, e65745. [CrossRef]
41. Gu, J.J.; Kaufman, G.P.; Mavis, C.; Czuczman, M.S.; Hernandez-Ilizaliturri, F.J. Mitotic catastrophe and cell cycle arrest are alternative cell death pathways executed by bortezomib in rituximab resistant B-cell lymphoma cells. *Oncotarget* **2017**, *8*, 12741–12753. [CrossRef] [PubMed]
42. Werner, M.; Sacher, J.; Hohenegger, M. Mutual amplification of apoptosis by statin-induced mitochondrial stress and doxorubicin toxicity in human rhabdomyosarcoma cells. *Brit. J. Pharmacol.* **2004**, *143*, 715–724. [CrossRef] [PubMed]
43. Vakifahmetoglu, H.; Olsson, M.; Zhivotovsky, B. Death through a tragedy: Mitotic catastrophe. *Cell Death Differ.* **2008**, *15*, 1153–1162. [CrossRef] [PubMed]
44. Vakifahmetoglu, H.; Olsson, M.; Tamm, C.; Heidari, N.; Orrenius, S.; Zhivotovsky, B. DNA damage induces two distinct modes of cell death in ovarian carcinomas. *Cell Death Differ.* **2008**, *15*, 555–566. [CrossRef]
45. Skwarska, A.; Augustin, E.; Konopa, J. Sequential induction of mitotic catastrophe followed by apoptosis in human leukemia MOLT4 cells by imidazoacridinone C-1311. *Apoptosis* **2007**, *12*, 2245–2257. [CrossRef]
46. Cliby, W.A.; Lewis, K.A.; Lilly, K.K.; Kaufmann, S.H. S phase and G(2) arrests induced by topoisomerase I poisons are dependent on ATR kinase function. *J. Biol. Chem.* **2002**, *277*, 1599–1606. [CrossRef] [PubMed]
47. Goldwasser, F.; Shimizu, T.; Jackman, J.; Hoki, Y.; OConnor, P.M.; Kohn, K.W.; Pommier, Y. Correlations between S and G(2) arrest and the cytotoxicity of camptothecin in human colon carcinoma cells. *Cancer Res.* **1996**, *56*, 4430–4437.
48. Wu, N.; Wu, X.W.; Agama, K.; Pommier, Y.; Du, J.; Li, D.; Gu, L.Q.; Huang, Z.S.; An, L.K. A Novel DNA Topoisomerase I Inhibitor with Different Mechanism from Camptothecin Induces G2/M Phase Cell Cycle Arrest to K562 Cells. *Biochemistry* **2010**, *49*, 10131–10136. [CrossRef]
49. Kalabis, J.; Patterson, M.J.; Enders, G.H.; Marian, B.; Iozzo, R.V.; Rogler, G.; Gimotty, P.A.; Herlyn, M. Stimulation of human colonic epithelial cells by leukemia inhibitory factor is dependent on collagen-embedded fibroblasts in organotypic culture. *Faseb J.* **2003**, *17*, 1115–1117. [CrossRef]
50. Dornetshuber, R.; Heffeter, P.; Lemmens-Gruber, R.; Elbling, L.; Marko, D.; Micksche, M.; Berger, W. Oxidative stress and DNA interactions are not involved in Enniatin- and Beauvericin-mediated apoptosis induction. *Mol. Nutr. Food Res.* **2009**, *53*, 1112–1122. [CrossRef]

Sample Availability: Not available.

© 2019 by the authors. Licensee MDPI, Basel, Switzerland. This article is an open access article distributed under the terms and conditions of the Creative Commons Attribution (CC BY) license (http://creativecommons.org/licenses/by/4.0/).

molecules

MDPI

Article

Investigation of Permeation of Theophylline through Skin Using Selected Piperazine-2,5-Diones

Aneta Pokorna [1], Pavel Bobal [1,*], Michal Oravec [2], Lucie Rarova [3,4], Janette Bobalova [5] and Josef Jampilek [6,*]

1 Department of Chemical Drugs, Faculty of Pharmacy, University of Veterinary and Pharmaceutical Sciences Brno, Palackeho 1946/1, 612 42 Brno, Czech Republic; pokorna.anetaa@gmail.com
2 Global Change Research Institute CAS, Belidla 986/4a, 603 00 Brno, Czech Republic; oravec.m@czechglobe.cz
3 Department of Chemical Biology and Genetics, Centre of the Region Hana for Biotechnological and Agricultural Research, Faculty of Science, Palacky University, Slechtitelu 27, 783 71 Olomouc, Czech Republic; lucie.rarova@upol.cz
4 Department of Neurology, University Hospital in Olomouc, I. P. Pavlova 6, 775 20 Olomouc, Czech Republic
5 Institute of Analytical Chemistry of the CAS, Veveri 97, 602 00 Brno, Czech Republic; bobalova@iach.cz
6 Regional Centre of Advanced Technologies and Materials, Palacky University, Slechtitelu 27, 783 71 Olomouc, Czech Republic
* Correspondence: pavelbobal@yahoo.com (P.B.); josef.jampilek@gmail.com (J.J.)

Academic Editor: Maria Emília De Sousa
Received: 19 January 2019; Accepted: 1 February 2019; Published: 4 February 2019

Abstract: Transdermal administration of drugs that penetrate, in this case directly into the blood circulation, has many advantages and is promising for many drugs thanks to its easy application and good patient compliance. (*S*)-8-Methyl-6,9-diazaspiro[4.5]decan-7,10-dione (alaptide), has been studied as a potential chemical permeation enhancer. Based on its structure, four selected piperazine-2,5-diones were synthesized by means of multi-step synthetic pathways. All the compounds were investigated on their ability to enhance the permeation of the model drug theophylline from the hydrophilic medium propylene glycol:water (1:1). In vitro experiments were performed using vertical Franz diffusion cells at constant temperature 34 ± 0.5 °C and using full-thickness pig (*Sus scrofa* f. *domestica*) ear skin. Withdrawn samples were analyzed by RP-HPLC for determination of the permeated amount of theophylline. All the compounds were applied in ratio 1:10 (*w*/*w*) relative to the amount of theophylline. One hour after application, the permeated amount of theophylline from formulations with alaptide and (3*S*,6*S*)-3,6-dimethylpiperazine-2,5-dione, was ca. 15- and 12-fold higher, respectively, than from the formulation without the tested compounds. Despite the enhancement ratio of both enhancers in a steady state was ca. 2.3, the pseudo-enhancement ratio in the time range from 1 to 3 h was 4.4. These enhancement ratios indicate that the compounds are able to enhance the permeation of agents through the skin; however, the short-term application of both compound formulations seems to be more advantageous. In addition, the screening of the cytotoxicity of all the prepared compounds was performed using three cell lines, and the compounds did not show any significant toxic effect.

Keywords: piperazine-2,5-diones; theophylline; permeation; skin; Franz diffusion cell; HPLC determination; cytotoxicity

1. Introduction

Pharmaceutics can be administered in different ways depending on their physicochemical properties and pharmacokinetic profile (in general, based on their ADME profile) [1]. The use

of skin for the transdermal administration of drugs that can penetrate directly into the system circulation has many advantages, and thus, it is a promising way for administration of many drugs. Unfortunately, transdermal drug delivery frequently encounters the problem of limited penetration of active pharmaceutical ingredients through the skin [2,3]. The skin consists of three basic functional layers: the upper layer (epidermis), curium (dermis), and subcutaneous tissue (hypodermis). The most important and critical for the permeation of all compounds through the skin is the outermost layer of epidermis, the horny layer (stratum corneum, SC), which is, in fact, the real skin barrier [4].

Many different approaches to overcome the skin barrier can be found; from chemical and/or physical modifications of drugs [5] to the specific composition of final drug formulations or application of electrically assisted methods [3,6,7]. The use of chemical permeation enhancers (CPEs), specific pharmaceutical excipients, is one of the possibilities to facilitate drug delivery through the skin. A number of compounds from various chemical classes were investigated as CPEs, many of structurally different compounds expressed transdermal enhancement effect; thus, different sites and mechanisms of actions are supposed [7,8]. In general, all these CPEs are able to modify the SC, and a complex mechanism of action is expected. Many CPEs are particularly small molecules containing characteristic fragments of heteroatoms X−CO−N=, where X is $-CH_2-$, $-NH_2$, or −NH−, by which they can break intermolecular *H*-bonds among individual components of the SC [7,9,10].

Based on the structural similarity to CPEs [10], (*S*)-8-methyl-6,9-diazaspiro-[4.5]decan-7,10-dione (alaptide, **1**), an original Czech compound prepared by Kasafirek et al. in the 1980s [11,12], was investigated as a CPE with very good results [13–18]. Unfortunately, alaptide is very poorly soluble [12,19] and therefore selected "non-spirocyclic" derivatives of alaptide were designed, synthesized, and their transdermal enhancement effects as potential CPEs on the permeation of the model drug theophylline through the skin were investigated.

2. Results and Discussion

2.1. Chemistry and Physicochemical Properties

Alaptide, originally developed by Kasafirek, was prepared according to Scheme 1 from protected (*S*)-alanine and the ethyl ester of cycloleucine [20].

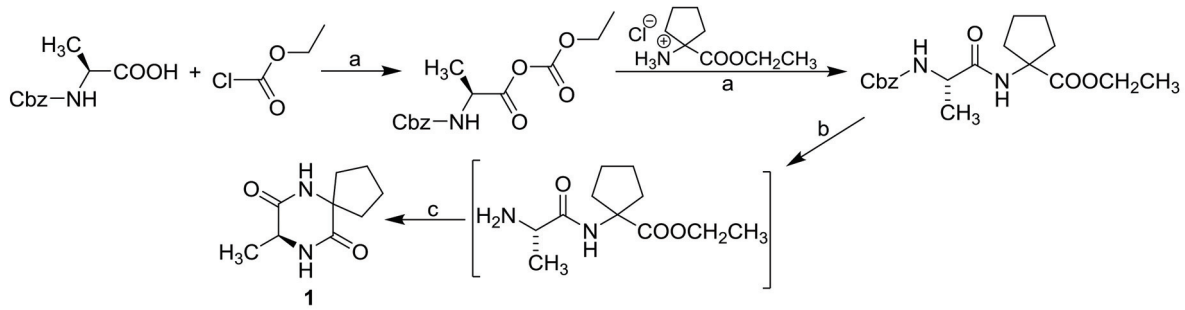

Scheme 1. Synthesis of (*S*)-alaptide (**1**). Reagents and conditions: a, 1-ethylpiperidine, dichloromethane; b, H_2, Pd/C, methanol; c, toluene, acetic acid [20].

The syntheses of non-spirocyclic derivatives **2**–**5** are illustrated in Schemes 2–4. A thermal cyclocondensation of glycine provided piperazine-2,5-dione (**2**) according to the literature procedure [21], see Scheme 2.

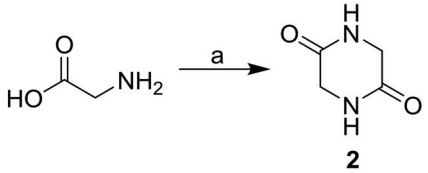

Scheme 2. Piperazine-2,5-dione (**2**) synthesis. Reagents and conditions: a, ethylene glycol, 170 °C [21].

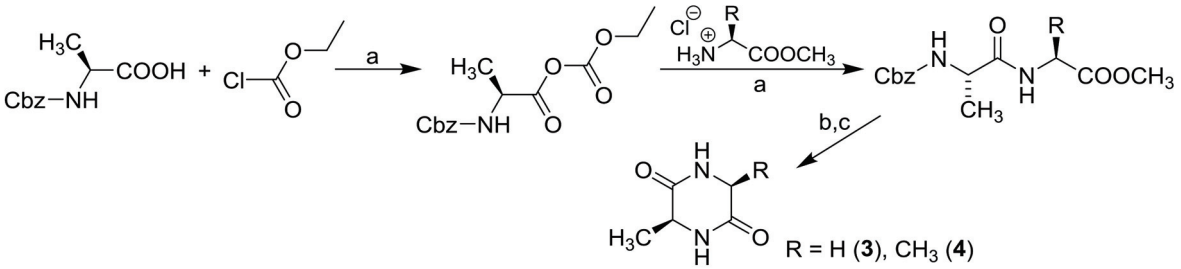

Scheme 3. Synthesis of (3*S*)-3-methylpiperazine-2,5-dione (**3**) and (3*S*,6*S*)-3,6-dimethylpiperazine-2,5-dione (**4**). Reagents and conditions: a, 1-ethylpiperidine, dichloromethane; b, H_2, Pd/C, methanol; c, toluene, acetic acid.

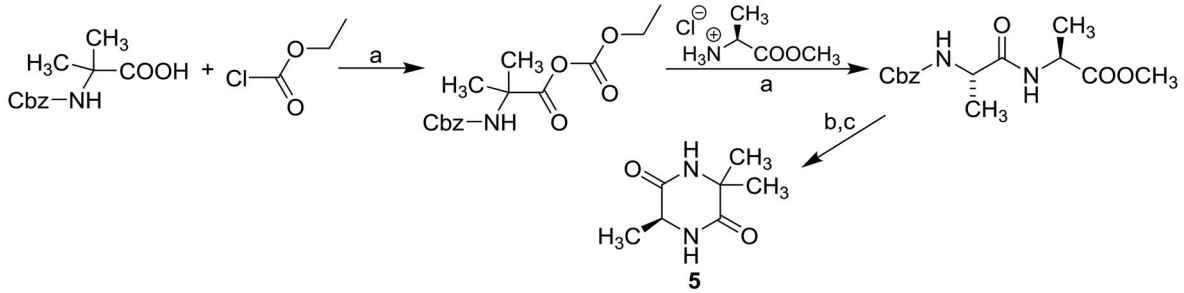

Scheme 4. Synthesis of (6*S*)-3,3,6-trimethylpiperazine-2,5-dione (**5**). Reagents and conditions: a, 1-ethylpiperidine, dichloromethane; b, H_2, Pd/C, methanol; c, toluene, acetic acid.

The cyclocondensation of the (*S*)-alanine derivative with glycine ester gave (3*S*)-3-methyl-piperazine-2,5-dione (**3**), while with (*S*)-alanine ester, (3*S*,6*S*)-3,6-dimethylpiperazine-2,5-dione (**4**) was obtained. The condensation of 2-methylalanine derivative with (*S*)-alanine ester yielded (6*S*)-3,3,6-trimethylpiperazine-2,5-dione (**5**). For the activation of the benzyloxycarbonyl moiety, the protected amino acids method using the in situ formation of a mixed anhydride with ethyl chloroformate and *N*-ethylpiperidine was applied, similar to the synthesis of alaptide [22]. The attempts to avoid the use of ethyl chloroformate by replacement with benign propylphosphonic anhydride (T3P®) were unsuccessful [23,24]. Generated mixed anhydrides were directly used without isolation for a coupling reaction with hydrochlorides of methyl glycinate or methyl L-alaninate to give benzyloxycarbonyl protected dipeptides with an ester at *C*-terminus. The dipeptide-coupled products at deprotection via hydrogenolysis on Pd/C at 3 atm in Parr reactor gave amino dipeptide esters, which then were cyclized in boiling toluene in the presence of acetic acid to form desired molecules **3**–**5**, see Schemes 3 and 4.

For the synthesis of (3*S*)-3-methylpiperazine-2,5-dione (**3**), [(benzyloxy)carbonyl]-L-alanine and hydrochloride of methyl glycinate were used as starting materials. In case of (3*S*,6*S*)-3,6-dimethyl-piperazine-2,5-dione (**4**), methyl glycinate was replaced by methyl L-alaninate. Finally, (6*S*)-3,3,6-trimethyl-piperazine-2,5-dione (**5**) was prepared from 2-{[(benzyloxy)carbonyl]-amino}-2-methylpropanoic acid and hydrochloride of methyl L-alaninate.

Physicochemical descriptors, such as lipophilicity, solubility, polar surface area, molar volume, parachor, etc., are often used to analyze structure-activity relationships within series of compounds [10,25–31]; therefore, in many studies dealing with the modification of skin permeation,

the effect of these descriptors on permeation was investigated as well (e.g., [7,10] and references therein). Thus, selected characteristics/descriptors were calculated using ACD/Percepta ver. 2012 (Advanced Chemistry Development, Toronto, ON, Canada) and are mentioned in Table 1. In this work, the effect of the following parameters is especially discussed: lipophilicity (expressed as log *P*) and solubility of CPEs in water (expressed as log S_W at pH 7.4). The accuracy of calculations for simple structures by the ACD/Percepta software used is usually better than 0.2–0.5 logarithmic units. Solubility is not derived primarily from log *P* and not only takes into account pH (solubility as a function of pH) but also compares fragmentary estimates [32] with experimental material from databases of about 6000 compounds. However, it is important to note that the algorithms used for the calculation of the descriptors, in particular, log *P* and log *S*, basically do not take into account configuration and conformation aspects. The positions of substituents are implemented in the calculation protocol; however, the prediction depends on the number of similar compounds in the database. With respect to the importance of permeability and solubility (polarity) for biological activity [33], it is necessary to understand all log *P* and log *S* values predicted by various programs as approximate. In addition, surface tension (ST [dyne/cm]), parachor [cm^3], and molar volumes (MV [cm^3]) were calculated as other characteristics of potential CPEs important for affecting the skin.

Table 1. Structure and calculated (ACD/Percepta ver. 2012) physicochemical properties of alaptide (**1**) and its derivatives **2**–**5**: lipophilicity (log *P*), water solubility (log S_w), molar volume (MV [cm^3]), parachor [cm^3], and surface tension (ST [dyne/cm]).

Comp.

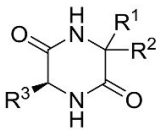

	R^1	R^2	R^3	log *P*	log S_w	MV [cm^3]	Parachor [cm^3]	ST [dyne/cm]
1	$-(CH_2)_4-$		$-CH_3$	−0.15	−1.09	156.64	392.52	45.88
2	−H	−H	−H	−1.94	0.10	91.5	227.40	38.12
3	−H	−H	$-CH_3$	−1.53	−0.23	109.04	265.43	32.10
4	$-CH_3$	−H	$-CH_3$	−1.15	−0.55	126.22	303.45	28.36
5	$-CH_3$	$-CH_3$	$-CH_3$	−0.79	−0.75	142.53	341.84	27.03

As mentioned above, the solubility of individually tested compounds is important. The dependence of lipophilicity on solubility is illustrated in Figure 1A. The second "spiro" cycle has great influence on lipophilicity as well as solubility, as it is shown by the large distance of compound **1** from the rest of investigated compounds **2**–**5**. Logically, lipophilicity increases (and solubility decreases) with an increasing number of methyl moieties/substituents on the piperazine-2,5-dione scaffold, see Figure 1A. On the other hand, physicochemical and structural similarity of the investigated compounds is evidenced by the high correlation coefficient of the linear dependence log *P* vs. log S_w ($r = 0.9930$, $n = 5$, the equation of the dependence: $\log P = -1.4846 \log S_w - 1.8602$). Similar dependences were also provided by relationships between molar volume or parachor and solubility; therefore, they are not illustrated. Figure 1B shows the dependence of surface tension (ST [dyne/cm]) on solubility (log S_w). Surface tension is inversely related to the surface activity of compounds, i.e., the ability of compounds to act as a detergent (surfactant). The greater the surface tension, the lower the surface activity (the ability of the compound to reduce the surface tension) and the lower the ability of the compound to act as a surfactant. The linear dependence of ST on log S_w of non-spirocyclic derivatives **2**–**5** shown in Figure 1B can be expressed by the following equation: $ST = 13.114 \log S_w + 36.091$, $r = 0.9841$, $n = 4$. An increase of surface tension (a decreasing number of methyl substituents on the piperazine-2,5-dione scaffold) increases solubility (log S_w). These discussed parameters play an important role in structure-activity relationships of the investigated piperazine-2,5-diones, as discussed below.

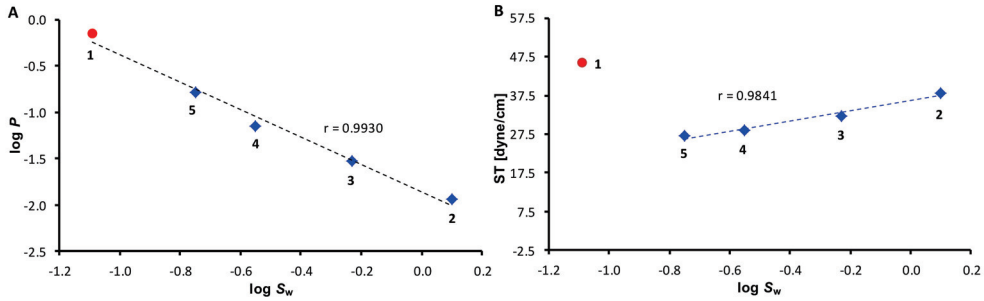

Figure 1. Dependences of lipophilicity (log *P*) (**A**) and surface tension (ST) (**B**) on water solubility (log S_w).

2.2. Permeation Experiments

The permeation of theophylline through the skin without and with alaptide (**1**) as a model molecule and with other prepared non-spirocyclic derivatives of alaptide **2–5** was tested from the propylene glycol/water (1:1) system as a donor vehicle using static Franz diffusion cells [34] within 24 h. It should be noted that recently reported studies demonstrated that propylene glycol or a propylene glycol/water system does not interfere with membranes [35,36]. Theophylline was used as a model penetrant/drug of medium polarity (log $P = -0.06$) [37,38], as it has been comprehensively investigated in transdermal penetration experiments [39–41]. Full-thickness pig ear skin was chosen for the In vitro evaluation of permeation. This tissue is considered as a suitable in vitro model of the human skin [42–44], as pig skin is histologically and biochemically similar to the human skin [45]. The values obtained from the permeation experiments were expressed as the cumulative permeated amount of the drug (Q_t [μg]) per unit of skin surface area, see Table 2. The dependences of the cumulative permeated amount of the drug per unit of skin surface area in time for the control and the most effective compounds **1** and **4** are illustrated in Figure 2, which is divided into parts A and B for better lucidity.

Table 2. Cumulative permeated amounts Q_t of theophylline per unit area [μg/cm^2] from propylene glycol:water 1:1 without (control) and with CPEs **1–5** achieved in In vitro transdermal permeation experiments using Franz diffusion cell. Q_t values are expressed as mean ± SD (n = 5 experiments).

Time [h]	Control	Compounds				
		1 (alaptide)	2	3	4	5
0.5	0.00 ± 0.00	0.79 ± 0.58	0.40 ± 0.24	0.39 ± 0.13	0.93 ± 0.18	0.32 ± 0.17
1	0.53 ± 0.12	7.92 ± 2.18	4.70 ± 1.17	2.52 ± 1.37	6.29 ± 1.01	2.44 ± 1.69
1.5	1.89 ± 0.33	20.53 ± 4.88	12.92 ± 2.08	7.54 ± 3.43	17.29 ± 2.37	8.22 ± 4.42
2	4.62 ± 0.60	33.66 ± 7.04	23.76 ± 3.04	14.77 ± 6.20	30.83 ± 3.59	16.16 ± 7.21
3	13.36 ± 1.63	68.73 ± 12.20	52.62 ± 5.18	34.41 ± 11.47	67.37 ± 6.53	39.36 ± 14.07
4	26.07 ± 3.31	114.08 ± 17.92	86.13 ± 7.16	59.64 ± 17.67	110.57 ± 9.03	69.44 ± 21.40
6	62.00 ± 8.40	212.49 ± 3062	168.24 ± 11.85	125.63 ± 28.83	216.87 ± 14.89	151.18 ± 37.41
8	112.06 ± 14.78	341.30 ± 45.25	270.85 ± 16.94	191.59 ± 37.56	319.76 ± 17.95	234.74 ± 49.44
12	235.20 ± 34.88	616.34 ± 72.86	496.43 ± 32.00	368.53 ± 56.04	595.79 ± 31.81	460.21 ± 77.54
24	684.56 ± 87.05	1439.30 ± 127.94	1253.20 ± 108.70	998.62 ± 120.08	1482.83 ± 74.42	1273.10 ± 144.46

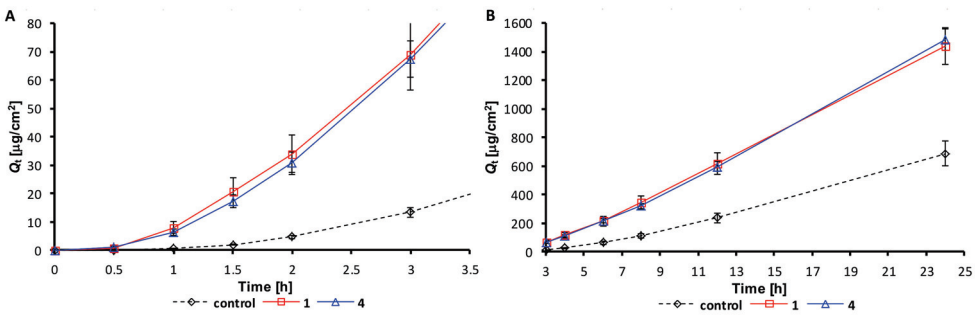

Figure 2. In vitro profile of cumulative permeated amounts Q_t per unit area [µg/cm^2] of theophylline alone (control) and after addition of alaptide (**1**) and other tested non-spirocyclic compounds **2**–**5** in ratio 10:1 from propylene glycol/water 1:1 system through the skin in time. Q_t values are expressed as mean ± SD (n = 5 experiments).

It is evident that the addition of piperazine-2,5-diones **1**–**5** caused the enhancement of theophylline permeation. Based on the above-mentioned results, the permeated amount of theophylline with all the tested CPEs increased rapidly already at minute 30. The permeated amount of theophylline with the CPEs at minute 60 reached approx. 5- to 15-fold higher values than from the formulation without the CPEs, see Table 2, and compounds **1** and **4** were the most effective. Similarly, a sharp enhancement of transdermal permeation was found at permeation of other drugs from different classes [13–18]. On the other hand, the enhancement effect (the slope of permeation) of all the tested CPEs began to decrease from the 4th hour, see Figure 2B. Nevertheless, it can be stated that theophylline without the CPEs permeated moderately in comparison with theophylline with added CPEs. Within the whole investigated time range, the corresponding Q_t values of samples with CPEs **1**–**5** were considerably higher in every time than those estimated in the system without CPEs (control sample), see Table 2. The Q_t values related to propylene glycol:water systems with alaptide (**1**) and compound **4** were within experimental error, see Figure 2, and the mean values of the permeated amount of theophylline with derivative **3** demonstrated that the enhancement activity of compound **3** was the lowest.

The effectivity of alaptide (**1**) and (3*S*,6*S*)-3,6-dimethylpiperazine-2,5-dione (**4**) as potential CPEs can also be confirmed by other calculated permeation parameters of theophylline without and with enhancers from propylene glycol:water (1:1), such as steady-state permeation fluxes (J [µg/h/cm^2]), lag times (t_{lag} [h]), permeability coefficients (K_p [cm/h]), and enhancement ratios (ER) that are mentioned in Table 3 (for the time period 1–3 h, pseudo-steady state values marked by an apostrophe) and in Table 4 (for the time period 6–12 h, real steady state).

Table 3. Pseudo-permeation parameters of theophylline in range 1–3 h without (control) and with tested CPEs **1**–**5** from propylene glycol:water (1:1): steady-state permeation fluxes (J'), corresponding lag times (t_{lag}'), permeability coefficients (K_p'), and enhancement ratios (ERs'). All values are expressed as mean ± SD (n = 5 experiments).

Comp.	$J'_{1\text{-}3h}$ [µg/cm^2/h]	$t_{lag}'_{1\text{-}3h}$ [h]	$K_p'_{1\text{-}3h} \times 10^{-3}$ [cm/h]	$ERs'_{1\text{-}3h}$
control (theophylline)	6.60 ± 0.80	1.10 ± 0.02	0.66 ± 0.08	1.00 ± 0.05
1	29.84 ± 7.02	0.77 ± 0.14	2.98 ± 0.70	4.52 ± 1.06
2	24.33 ± 2.05	0.91 ± 0.04	2.43 ± 0.20	3.68 ± 0.31
3	16.55 ± 3.92	0.87 ± 0.13	1.66 ± 0.39	2.51 ± 0.59
4	28.70 ± 1.73	0.80 ± 0.12	2.87 ± 0.17	4.35 ± 0.26
5	17.49 ± 5.48	0.91 ± 0.16	1.75 ± 0.55	2.65 ± 0.83

Table 4. Permeation parameters of theophylline in range 6–12 h without (control) and with tested CPEs **1**–**5** from propylene glycol:water (1:1): steady-state permeation fluxes (J), corresponding lag times (t_{lag}), permeability coefficients (K_p), and enhancement ratios (*ERs*). All values are expressed as mean ± SD (n = 5 experiments).

Comp.	J_{ss} [μg/cm^2/h]	t_{lag} [h]	$K_p \times 10^{-3}$ [cm/h]	*ERs*
control (theophylline)	29.12 ± 3.93	3.74 ± 0.41	2.91 ± 0.39	1.00 ± 0.05
1	67.52 ± 9.19	2.91 ± 0.17	6.75 ± 0.92	2.32 ± 0.32
2	54.94 ± 3.46	2.99 ± 0.06	5.49 ± 0.35	1.89 ± 0.12
3	41.02 ± 4.77	3.13 ± 0.41	4.10 ± 0.48	1.41 ± 0.16
4	63.99 ± 3.25	2.77 ± 0.16	6.40 ± 0.33	2.20 ± 0.11
5	52.20 ± 6.74	3.31 ± 0.33	5.22 ± 0.67	1.79 ± 0.23

Parameters calculated for the time period 1–3 h mentioned in Table 3 are more important than the standard steady-state parameters calculated for the time period 6–12 h (Table 4), because they reflect a significantly increased observed enhancement ratio (*ERs′* ca. 4.4) immediately after application (*ERs* compared with *ERs′* are approx. half: 51.3% (**1**), 51.4% (**2**), 56.2% (**3**), 50.6% (**4**), 67.5% (**5**)), which is more favorable than long-term application due to the stability of semi-solid drug dosage forms and compliance of patients. These facts indicate that not only the pattern alaptide (**1**) but also dimethylpiperazine-2,5-dione derivative **4** is able to enhance the permeation of theophylline through the skin.

It can be assumed that the enhancement activity of individually tested compounds is dependent on their physicochemical properties, as mentioned above. Within non-spirocyclic derivatives **2**–**5**, it is evident that the enhancement effect is negatively influenced by asymmetric substitution of the basic scaffold, i.e., 3-methylpiperazine-2,5-dione (**3**) showed the lowest activity followed by 3,3,6-trimethylpiperazine-2,5-dione (**5**). It seems that the position and number of methyl moieties is crucial for the activity. Besides these structural parameters, the activity of effective compounds is partially affected by lipophilicity and by molar volume; activity increases with increasing log P and bulkiness and is inversely influenced by solubility, see Tables 1 and 2. Thus, it can be stated that the same as for all drugs, also for these types of excipients, lipo-hydrophilic properties must be balanced. On the other hand, alaptide (**1**) has significantly higher surface tension value than comparable effective derivative **4**. Unsubstituted derivative **2** with medium activity is between them. It can be only hypothesized if these "opposite" values of compound **1** and **4** have strong impact on their enhancement activity, which may result in a different mode of action. Similarly, it can be speculated about the enhancement effect of piperazine-2,5-diones substituted by a longer alkyl tail(s), as, for example, is discussed for similar compounds in [10]. On the other hand, toxicity, skin irritability, and hydrophobicity increase, while solubility decreases with increasing surface activity [7].

2.3. In Vitro Cytotoxicity Assay

The cytotoxicity of the tested compounds was evaluated using a normal human skin fibroblast cells (BJ), a T-lymphoblastic leukaemia cell line (CEM), and a breast adenocarcinoma cell line (MCF7). The cytotoxicity was expressed as the IC_{50} value (compound concentration causing 50% inhibition of cell population proliferation). A compound is considered as cytotoxic when it demonstrates a toxic effect on cells at the concentration up to 10 μM [46], and the highest tested concentration that was used for the toxicity assay was five times this value. Treatment with 50 μM of the discussed compounds did not express any cytotoxic effect on any of the tested cell lines. Based on the results of these observations, it can be concluded that the discussed alaptide (**1**) as well as other piperazine-2,5-diones **2**–**5** can be considered as non-toxic agents.

3. Materials and Methods

3.1. General Information

All reagents were purchased from Merck (Sigma-Aldrich, St. Louis, MO, USA) and Acros Organics (Thermo Fisher Scientific, Geel, Belgium). The melting points were determined on a Kofler hot-plate apparatus HMK (Franz Kustner Nacht KG, Dresden, Germany) and are uncorrected. The measurement of optical rotations was carried on Automatic polarimeter AA-10 (Optical Activity, Ramsey, UK). The concentration of samples is given in 10 mg/mL. Infrared (IR) spectra were recorded on a Smart MIRacle™ ATR ZnSe for Nicolet™ Impact 410 Fourier-transform IR spectrometer (Thermo Scientific, West Palm Beach, FL, USA). The spectra were obtained by the accumulation of 256 scans with 2 cm^{-1} resolution in the region of 4000–650 cm^{-1}. All ^{1}H- and ^{13}C-NMR spectra were recorded on a JEOL ECZR 400 MHz NMR spectrometer (400 MHz for ^{1}H and 101 MHz for ^{13}C, Jeol, Tokyo, Japan) in dimethyl sulfoxide-d_6 (DMSO-d_6). ^{1}H and ^{13}C chemical shifts (δ) are reported in ppm. The signal of the residual solvent (DMSO-d_6) was used as a reference. High-resolution mass spectra were measured using a high-performance liquid chromatograph Dionex UltiMate® 3000 (Thermo Scientific) coupled with an LTQ Orbitrap XL™ Hybrid Ion Trap-Orbitrap Fourier Transform Mass Spectrometer (Thermo Scientific) equipped with a HESI II (heated electrospray ionization) source in the positive mode.

3.2. Synthesis

Alaptide, (*S*)-8-methyl-6,9-diazaspiro[4.5]decan-7,10-dione, (**1**) was prepared according to Kasafirek et al. [20].

Piperazine-2,5-dione (**2**) [21]. Glycine (7.5 g, 0.1 mol) was suspended in 50 mL of anhydrous ethylene glycol, and the mixture was stirred and heated at 170–180 °C for 6 h. After cooling and standing in a refrigerator overnight, the precipitate was filtered off and washed with methanol. Crude product was purified by recrystallization from hot water and dried under reduced pressure. Yield 62%; Mp >280 °C; IR (cm^{-1}): 3047, 2914, 2873, 1673, 1468, 1441, 1338, 1073, 914, 835, 806, 669; ^{1}H-NMR (DMSO-d_6), δ: 7.95 (br. s., 2H), 3.71 (d, J = 2.1 Hz, 4H); ^{13}C-NMR (DMSO-d_6), δ: 166.1, 44.3; HR-MS: for $C_4H_7N_2O_2$ $[M + H]^+$ calculated 115.0502 m/z, found 115.0495 m/z.

General procedure for preparation of piperazine-2,5-diones **3**–**5**. In a 3-neck round bottom flask equipped with a septum, a thermometer and an adapter for a balloon with argon, Cbz-aminoacid (1.0 equiv., 5.0 mM) and *N*-ethylpiperidine (1.1 equiv., 5.5 mM) were dissolved in anhydrous methylene chloride (25 mL) and cooled to −10 °C. Ethyl chloroformate (1.1 equiv., 5.5 mM) was added at the same temperature, and the mixture protected from ingress of moisture was stirred for 2 h. Hydrochloride of methyl L-alaninate or methyl glycinate (1.0 equiv., 5.0 mM) was dissolved in the second flask in anhydrous methylene chloride (10 mL) and cooled to 0 °C, and then *N*-ethylpiperidine (1.0 equiv., 5.0 mM) was added. The whole volume of the second flask was immediately transferred to a 3-neck round bottom flask with the help of syringe, and additional *N*-ethylpiperidine (1.0 equiv., 5.0 mM) was added. The solution was stirred at the same temperature for 2 h and then left at 5 °C overnight. After that, the reaction mixture was quenched with water (35 mL). The aqueous phase was extracted with methylene chloride (3 × 15 mL). Combined organic phases were washed with 2M HCl solution (3 × 10 mL), water (10 mL), saturated sodium hydrogen carbonate solution (3 × 10 mL), and brine (10 mL) and dried over anhydrous sodium sulfate. After filtration, the solvent was removed under reduced pressure to give Cbz-amino dipeptide esters. The crude Cbz-amino dipeptide esters were hydrogenated with 60 mL of methanol and 10% Pd/C as a catalyst (0.5 g of Pd/C per 3 mM of intermediate dipeptide esters) at room temperature. The reactor (250 mL capacity Parr reactor) was pressurized with hydrogen to 3 bars at ambient temperature. Reactor pressure remained unchanged during the reaction period of 1 h. After releasing the pressure, the catalyst was removed by filtration through Celite, and the solvent was removed under reduced pressure. The crude amino dipeptide esters were placed into a 250 mL round-bottomed flask equipped with an egg-shaped, Teflon-coated

magnetic stirring bar and a reflux condenser, and toluene (100 mL) containing 5 mL of acetic acid was added. The reaction mixture was stirred and refluxed for 2 h, then the reflux condenser was removed, and the amount of the solvent was reduced to 10% at atmospheric pressure. The remaining solvent was removed under reduced pressure and the residue was recrystallized from propane-2-ol. Pure piperazine-2,5-diones **3**–**5** were dried at 40 °C under reduced pressure.

(3S)-3-Methylpiperazine-2,5-dione (**3**) [47] was prepared according to the general procedure described above from [(benzyloxy)carbonyl]-L-alanine and hydrochloride of methyl glycinate. Yield 54%; Mp 278–280 °C; $[\alpha]^{25}_{D}$: −4.0 (CH_3OH), −5 (H_2O) [48] or −3.78 (H_2O) [49]; IR (cm^{-1}): 3047, 2879, 1663, 1456, 1327, 1094, 1044, 802, 669; ^{1}H-NMR (DMSO-d_6), δ: 8.09 (br. s., 1H), 7.90 (br. s., 1H), 3.84 (dq, *J* = 0.9, 7.0 Hz, 1H), 3.78–3.67 (m, 2H), 1.26 (d, *J* = 7.0 Hz, 3H); ^{13}C-NMR (DMSO-d_6), δ: 168.8, 166.2, 49.7, 44.5, 18.6; HR-MS: for $C_5H_9N_2O_2$ $[M + H]^+$ calculated 129.0659 *m*/*z*, found 129.0652 *m*/*z*.

(3S,6S)-3,6-Dimethylpiperazine-2,5-dione (**4**) [50] was prepared according to the general procedure described above from [(benzyloxy)carbonyl]-L-alanine and hydrochloride of methyl L-alaninate. Yield 58%; Mp 282–284 °C; $[\alpha]^{25}_{D}$: −20.0 (CH_3OH), −24 (H_2O)[48]; IR (cm^{-1}): 3084, 2987, 1665, 1450, 1375, 1307, 1091, 945, 831, 672; ^{1}H-NMR (DMSO-d_6), δ: 8.05 (br. s., 1H), 3.91 (dq, *J* = 1.0, 7.0 Hz, 1H), 1.26 (d, *J* = 7.0 Hz, 3H); ^{13}C-NMR (DMSO-d_6), δ: 168.0, 49.8, 18.8; HR-MS: for $C_6H_{11}N_2O_2$ $[M + H]^+$ calculated 143.0815 *m*/*z*, found 143.0803 *m*/*z*.

(6S)-3,3,6-Trimethylpiperazine-2,5-dione (**5**) [51] was prepared according to the general procedure described above from 2-{[(benzyloxy)carbonyl]amino}-2-methylpropanoic acid and hydrochloride of methyl L-alaninate. Yield 49%; Mp 271–273 °C; $[\alpha]^{25}_{D}$: +1.0 (CH_3OH); IR (cm^{-1}): 3181, 3043, 1666, 1438, 1381, 1311, 1241, 1199, 1164, 1098, 932, 835, 771, 683 ^{1}H-NMR (DMSO-d_6), δ: 8.10 (br. s., 1H), 7.97 (br. s., 1H), 3.93 (dq, *J* = 1.2, 6.9 Hz, 1H), 1.30 (s, 6H), 1.27 (d, *J* = 7.0 Hz, 3H); ^{13}C-NMR (DMSO-d_6), δ: 170.7, 168.1, 55.0, 49.9, 27.4, 27.4, 19.0; HR-MS: for $C_7H_{13}N_2O_2$ $[M + H]^+$ calculated 157.0972 *m*/*z*, found 157.0964 *m*/*z*.

3.3. In Vitro Transdermal Permeation Experiments

Skin samples were obtained from porcine ear. Full-thickness pig (*Sus scrofa* f. *domestica*) ear skin was cut in fragments and stored at −20 °C until utilized. Skin samples were slowly thawed (at 4 °C overnight and then at ambient temperature) before each experiment [52,53]. The penetration enhancing effect of alaptide was evaluated In vitro, using a vertical Franz diffusion cell (SES-Analytical Systems, Bechenheim, Germany) with a donor surface area of 0.6359 cm^2 and a receptor volume of 5.2 mL, see Figure 1. The skin was mounted between the donor and receptor compartments of the Franz diffusion cell with the epidermal side up. The receptor compartment was filled with phosphate buffered saline (pH 7.4) and maintained at 34.0 ± 0.5 °C [34,52] using a circulating water bath. The receptor compartment content was continuously stirred using a magnetic stirring bar. The skin was kept in contact with the receptor phase for 0.5 h prior to the experiment. Theophylline was purchased from Sigma-Aldrich; all other reagents and solvents were purchased from Merck (Darmstadt, Germany). Donor samples were prepared by dissolving theophylline (10 mg) and the tested CPE (1 mg) in propylene glycol (0.5 mL), to which water (0.5 mL) was added consequently to create a mixture of propylene glycol/water 1:1. These mixtures were shaken vigorously and then sonicated for 10 min at 40 °C; then these stable systems (dissolved theophylline in the enhancer emulsion) were applied to the skin surface, and the donor compartment of the cell was covered by Parafilm®. Control samples were prepared in the same manner without the tested CPE. Samples (0.5 mL) of the receptor phase were withdrawn at pre-determined time intervals (30, 60, 90, 120, 180, 240, 360, 480, 720 and 1440 min), and the cell was refilled with an equivalent amount of fresh buffer solution. A minimum of five determinations were performed using skin fragments from at least 2 animals for each compound, and the data was expressed as means ± SD.

The analysis of the samples was performed using an Agilent 1200 series HPLC system, equipped with a diode array detection system, a quaternary model pump, and an automatic injector (Agilent Technologies, Santa Clara, CA, USA). Data acquisition was performed using ChemStation

chromatography software (B.04.01 LC 1200, Agilent Technologies). A Gemini C6-Phenyl 110A 5 μm, 250 × 4.6 mm (Phenomenex, Torrance, CA, USA) chromatographic column was used. The total flow of the column was 1.0 mL/min; injection was 10 μL; column temperature was 40 °C; and sample temperature was 20 °C. The detection wavelength of 272 nm was chosen; the time of analysis was 7 min. A mixture of acetonitrile (HPLC grade, 10.0%), methanol (HPLC grade, 15.0%), and H_2O (HPLC—Mili-Q Grade, 75.0%) was used as the mobile phase. The retention time (t_R) of theophylline was 4.36 ± 0.05 min; the limit of detection (LOD) was 0.0063 μg/mL; and the limit of quantification (LOQ) was 0.0209 μg/mL. An equation of calibration curve was y = 30.59585x, and the correlation coefficient was r = 0.9998 (n = 7).

As a result of the sampling, the receptor compartment concentration of the tested CPEs was corrected for sample removal and replenishment using equation: $C'_n = C_n\ (V_t/V_t - V_s)\ (C'_{n-1}/C_{n-1})$, where C'_n = corrected drug concentration in the nth sample, C_n = measured drug concentration in the nth sample, $C'_{n\text{-}1}$ = corrected drug concentration in the $(n-1)^{th}$ sample, C_{n-1} = measured drug concentration in the $(n-1)^{th}$ sample, V_t = total volume of receptor solution, V_s = volume of the sample, and $C'_1 = C_1$. The corrected data were expressed as the cumulative drug permeation (Q_t) per unit of skin surface area using the equation: $Q_t = C'_n/A$, where A = 0.6359 cm^2 in the experiment. From the slope of the linear portion of the curve representing the dependence of the cumulative amount of the drug (Q_t [μg]) per unit area on time (t [h]), steady-state permeation flux (J [μg/h/cm^2]) was determined. Similarly, the lag time (t_{lag} [h]) was determined by extrapolating the linear portion of the cumulative amount of permeation per unit area (Q_t) versus time (t [h]) curve to the abscissa. The permeability coefficient (K_p [cm/h]) can be calculated according to $K_p = J/C_d$, where C_d = drug concentration in the donor compartment. It is assumed that under sink conditions, drug concentration in the receptor compartment is negligible compared to that in the donor compartment. The enhancement effect was expressed as an enhancement ratio (ER) that was calculated by the formula $ER = J_{ss-x}/J_{ss-k}$, where J_{ss-x} = steady-state permeation flux with CPE, J_{ss-k} = steady-state permeation flux without CPE [1,54,55]. All the calculated data are listed in Tables 1–3 and illustrated in Figure 2.

3.4. In Vitro Cytotoxicity Assay

Dulbecco's modified Eagle's medium (DMEM), L-glutamine, trypsin, penicillin, and streptomycin were purchased from Sigma (St. Louis, MO, USA); fetal bovine serum (FBS) and Calcein AM were purchased from Invitrogen (Carlsbad, CA, USA). The cell lines used for screening, T-lymphoblastic leukemia CEM, breast adenocarcinoma MCF7, and human foreskin fibroblasts BJ, were obtained from the American Type Culture Collection (Manassas, VA, USA). Cells were cultured in DMEM medium (Sigma). All media used were supplemented with 10% heat-inactivated fetal bovine serum, 2 mM L-glutamine, 10,000 U penicillin, and 10 mg/ml streptomycin. The cell lines were maintained under standard cell culture conditions at 37 °C and 5% CO_2 in a humid environment. Cells were subcultured two or three times a week using the standard trypsinization procedure. Suspensions with approximately 1.0×10^5 cells/mL (0.5×10^5 cells/mL for BJ) were distributed in 96-well microtiter plates, and after 12 h of stabilization, the tested compounds were added at desired concentrations in Lutrol F 127. Control cultures were treated with Lutrol F 127 alone, and the final concentration of Lutrol F 127 in the reaction mixture never exceeded 0.5%. In most cases, six serial 3-fold dilutions of the test substances were added at time zero in 20 μL aliquots to the microtiter plate wells, and the highest final concentration in the wells was 50 μM. After incubation for 72 h, Calcein AM solution (2 μM, Molecular Probes, Invitrogen, CA, USA) was added, and the cells were incubated for a further hour. The fluorescence from viable cells was then quantified, using a Fluoroskan Ascent fluorometer (Labsystems, Vantaa, Finland). The percentage of surviving cells in each well was calculated by dividing the intensity of the fluorescence signals from the exposed wells by the intensity of signals from control wells and multiplying by 100. These ratios were then used to construct dose-response curves from which IC_{50} values were calculated.

4. Conclusions

A series of four selected piperazine-2,5-diones as non-spirocyclic analogues of the pattern compound named alaptide (**1**, (*S*)-8-methyl-6,9-diazaspiro[4.5]decan-7,10-dione) were synthesized and characterized. The ability of all the compounds to enhance the permeation of the model drug theophylline from the medium of propylene glycol:water (1:1) was investigated using vertical Franz diffusion cells and a full-thickness pig (*Sus scrofa* f. *domestica*) ear skin. All the compounds were tested on their cytotoxic effect using human foreskin fibroblasts and two cancer cell lines, and none of the compounds expressed any toxic effect. All the compounds enhanced the permeation of theophylline through the skin, e.g., the permeated amount of theophylline was already at the 1st h after application approx. 1500% and 1200% higher at the application of alaptide (**1**) and (3*S*,6*S*)-3,6-dimethylpiperazine-2,5-dione (**4**), respectively, than from the formulation without the tested compounds. The position and number of methyl moieties as well as balanced lipo-hydrophilic properties seem to be crucial for the activity. The contributions of compounds **1** and **4** to the enhanced permeation of theophylline through the skin is significant not only in case of long-term application but especially immediately after application, which is favorable in terms of the stability of semi-solid drug dosage forms and compliance of patients. The exact mechanisms of actions of these piperazine-2,5-diones have not been known but have been under investigation.

Author Contributions: J.J. designed the compounds. P.B. synthesized the compounds. J.B. and M.O. characterized the compounds. A.P. performed permeation experiments. L.R. performed cytotoxicity screening. J.J. and P.B. wrote the paper.

Funding: This study was supported by the institutional support (RVO:68081715) of the Institute of Analytical Chemistry of the CAS. M.O. was supported by the National Sustainability Program (NPU I; Grant No. LO1415). L.R. was supported by project CZ.02.1.01/0.0/0.0/16_019/0000868 of the Ministry of Education of the Czech Republic, and J.J. gratefully thanks the National Program of Sustainability I (LO1305) of the Ministry of Education of the Czech Republic for the financial support.

Conflicts of Interest: The authors declare no conflict of interest.

References

1. Shargel, L.; Yu, A.B.C. *Applied Biopharmaceutics and Pharmacokinetics*, 7th ed.; McGraw-Hill: New York, NY, USA, 2016.
2. Watkinson, A.C.; Kearney, M.C.; Quinn, H.L.; Courtenay, A.J.; Donnelly, R.F. Future of the transdermal drug delivery market—Have we barely touched the surface? *Expert Opin. Drug Deliv.* **2016**, *13*, 523–532. [CrossRef] [PubMed]
3. Alkilani, A.Z.; McCrudden, M.T.C.; Donnelly, R.F. Transdermal drug delivery: Innovative pharmaceutical developments based on disruption of the barrier properties of the stratum corneum. *Pharmaceutics* **2015**, *7*, 438–470. [CrossRef] [PubMed]
4. Forslind, B.; Lindberg, M. *Skin, Hair, Nails: Structure and Function*; Marcel & Dekker: New York, NY, USA, 2004.
5. Cernikova, A.; Jampilek, J. Structure modification of drugs influencing their bioavailability and therapeutic effect. *Chem. Listy* **2014**, *108*, 7–16.
6. Jampilek, J. Transdermal application of drugs and techniques affecting skin barrier. *J. Bioequiv. Availab.* **2013**, *5*, 233–235. [CrossRef]
7. Jampilek, J.; Brychtova, K. Azone analogues: Classification, design, and transdermal penetration principles. *Med. Res. Rev.* **2012**, *32*, 907–947. [CrossRef] [PubMed]
8. Patil, U.K.; Saraogi, R. Natural products as potential drug permeation enhancer in transdermal drug delivery system. *Arch. Dermatol. Res.* **2014**, *306*, 419–426. [CrossRef] [PubMed]
9. Thong, H.Y.; Zhai, H.; Maibach, H.I. Percutaneous penetration enhancers: An overview. *Skin Pharmacol. Physiol.* **2007**, *20*, 272–282. [CrossRef] [PubMed]
10. Jampilek, J. Azone and its analogues. In *Percutaneous Penetration Enhancers—Chemical Methods in Penetration Enhancement: Modification of the Stratum Corneum*; Dragicevic-Curic, N., Maibach, H.I., Eds.; Springer: Berlin/Heidelberg, Germany, 2015; pp. 69–106.
11. Kasafirek, E.; Vanzura, J.; Krejci, I.; Krepelka, J.; Dlabac, A.; Valchar, M. 2,5-Piperazinedione Derivs. Belgian Patent 897843, 20 May 1984; Czechoslovakian Patent CS 231227, 26 January 1986.

12. Radl, S.; Kasafirek, E.; Krejci, I. Alaptide. *Drug. Future* **1990**, *15*, 445–447. [CrossRef]
13. Jampilek, J.; Opatrilova, R.; Coufalova, L.; Cernikova, A.; Dohnal, J. Utilization of Alaptide as Transdermal Penetration Modifier in Pharmaceutical Compositions for Human and Veterinary Applications Containing Anti-Inflammatory Drugs and/or Antimicrobial Chemotherapeutics. WO/2013/020527 A1, 14 February 2013.
14. Jampilek, J.; Opatrilova, R.; Dvorakova, L.; Brychtova, K.; Dohnal, J. Utilization of Alaptide as Transdermal Penetration Modifier in Pharmaceutical Compositions for Human and Veterinary Applications Containing Non-Steroidal Anti-Inflammatory and/or Antipyretic-Analgesic Drugs. Czech Patent CZ 304915 B6, 10 December 2014.
15. Jampilek, J.; Opatrilova, R.; Dvorakova, L.; Cernikova, A.; Dohnal, J. Utilization of Alaptide as Transdermal Penetration Modifier in Pharmaceutical Compositions for Human and Veterinary Applications Containing Antimicrobial Chemotherapeutics. Czech Patent CZ 306686 B6, 29 March 2017.
16. Jampilek, J.; Opatrilova, R.; Dvorakova, L.; Dohnal, J. Utilization of Alaptide as Transdermal Penetration Modifier in Pharmaceutical Compositions for human and Veterinary Applications Containing Glucocorticoids. Czech Patent CZ 306770 B6, 17 May 2017.
17. Jampilek, J.; Dohnal, J. Alaptide as transdermal permeation modifier. In *Percutaneous Penetration Enhancers—Chemical Methods in Penetration Enhancement: Modification of the Stratum Corneum*; Dragicevic-Curic, N., Maibach, H.I., Eds.; Springer: Berlin/Heidelberg, Germany, 2015; pp. 115–132.
18. Cernikova, A.; Bobal, P.; Bobalova, J.; Dohnal, J.; Jampilek, J. Investigation of permeation of acyclovir through skin using alaptide. *Acta Chromatogr.* **2018**, *30*, 62–65. [CrossRef]
19. Jampilek, J.; Opatrilova, R.; Rezacova, A.; Oktabec, Z.; Dohnal, J. Alaptide: Methods of Effecting Its Solubility, Membrane Permeation and Pharmaceutical Compositions for Human and/or Veterinary Applications. WO/2014/019556 A1, 6 February 2014.
20. Kasafirek, E.; Rybak, M.; Krejci, I.; Sturs, A.; Krepela, E.; Sedo, A. Two-step generation of spirocyclic dipeptides from linear peptide ethyl ester precursors. *Life Sci.* **1992**, *50*, 187–193. [CrossRef]
21. Vallejos, S.; Estevez, P.; Ibeas, S.; Munoz, A.; Garcia, F.C.; Serna, F.; Garcia, J.M. Selective and highly sensitive fluorescent probe of Hg2+ in organic and aqueous media: The role of a polymer network in extending the sensing phenomena to water environments. *Sens. Actuators B Chem.* **2011**, *157*, 686–690. [CrossRef]
22. Chen, F.M.F.; Stainauer, R.; Benoiton, N.L. Mixed anhydrides in peptide synthesis. Reduction of urethane formation and racemization using N-methylpiperidine as the tertiary amine base. *J. Org. Chem.* **1983**, *48*, 2939–2941. [CrossRef]
23. Pizova, H.; Bobal, P. Optimized and scalable synthesis of propylphosphonic anhydride for general use. *Tetrahedron Lett.* **2015**, *56*, 2014–2017. [CrossRef]
24. Pizova, H.; Havelkova, M.; Stepankova, S.; Bak, A.; Kauerova, T.; Kozik, V.; Oravec, M.; Imramovsky, A.; Kollar, P.; Bobal, P.; et al. Proline-based carbamates as cholinesterase inhibitors. *Molecules* **2017**, *22*, 1969. [CrossRef] [PubMed]
25. Lipinski, C.A.; Lombardo, F.; Dominy, B.W.; Feeney, P.J. Experimental and computational approaches to estimate solubility and permeability in drug discovery and development settings. *Adv. Drug Deliv. Rev.* **2001**, *46*, 3–26. [CrossRef]
26. Bak, A.; Kozik, V.; Smolinski, A.; Jampilek, J. Multidimensional (3D/4D-QSAR) probability-guided pharmacophore mapping: Investigation of activity profile for a series of drug absorption promoters. *RSC Adv.* **2016**, *6*, 76183–76205. [CrossRef]
27. Bak, A.; Kozik, V.; Smolinski, S.; Jampilek, J. In silico estimation of basic activity-relevant parameters for a set of drug absorption promoters. *SAR QSAR Environ. Res.* **2017**, *28*, 427–449. [CrossRef]
28. Kapustikova, I.; Bak, A.; Gonec, T.; Kos, J.; Kozik, V.; Jampilek, J. Investigation of hydro-lipophilic properties of *N*-alkoxyphenylhydroxynaphthalenecarboxamides. *Molecules* **2018**, *23*, 1635. [CrossRef]
29. Bąk, A.; Kozik, V.; Walczak, M.; Fraczyk, J.; Kaminski, Z.; Kolesinska, B.; Smolinski, A.; Jampilek, J. Towards intelligent drug design system: Application of artificial dipeptide receptor library in QSAR-oriented study. *Molecules* **2018**, *23*, 1964. [CrossRef]
30. Malik, I.; Csollei, J.; Solovic, I.; Pospisilova, S.; Michnova, H.; Jampilek, J.; Cizek, A.; Kapustikova, I.; Curillova, J.; Pechacova, M.; et al. Dibasic derivatives of phenylcarbamic acid against mycobacterial strains: Old drugs and new tricks? *Molecules* **2018**, *23*, 2493. [CrossRef]
31. Bak, A.; Kozik, V.; Malik, I.; Jampilek, J.; Smolinski, S. Probability-driven 3D pharmacophore mapping of antimycobacterial potential of hybrid molecules combining phenylcarbamoyloxy and N-arylpiperazine fragments. *SAR QSAR Environ. Res.* **2018**, *29*, 801–821. [CrossRef] [PubMed]

32. Japertas, P.; Didziapetris, R.; Petrauskas, A. Fragmental methods in the analysis of biological activities of diverse compound sets. *Mini-Rev. Med. Chem.* **2003**, *3*, 797–808. [CrossRef] [PubMed]
33. DeWitte, R.S. Understanding polyelectrolytes. *Mod. Drug Discov.* **2004**, *7*, 41–44.
34. Franz, T.J. Percutaneous absorption. On the relevance of In vitro data. *J. Investig. Dermatol.* **1975**, *64*, 190–195. [CrossRef] [PubMed]
35. Williams, A.C.; Barry, B.W. Urea analogues in propylene glycol as penetration enhancers in human skin. *Int. J. Pharm.* **1989**, *56*, 43–50. [CrossRef]
36. Yamane, M.A.; Williams, A.C.; Barry, B.W. Terpene penetration enhancers in propylene glycol/water co-solvent systems: Effectiveness and mechanism of action. *J. Pharm. Pharmacol.* **1995**, *47*, 978–989. [CrossRef] [PubMed]
37. Ni, N.; El-Sayed, M.M.; Sanghvi, T.; Yalkowsky, S.H. Estimation of the effect of NaCl on the solubility of organic compounds in aqueous solutions. *J. Pharm. Sci.* **2000**, *89*, 1620–1625. [CrossRef]
38. Katz, M.; Ben-Shlush, I.; Kolusheva, S.; Jelinek, R. Rapid colorimetric screening of drug interaction and penetration through lipid barriers. *Pharm. Res.* **2006**, *23*, 580–588. [CrossRef]
39. Fang, J.Y.; Tsai, T.H.; Hung, C.F.; Wong, W.W. Development and evaluation of the essential oil from Magnolia fargesii for enhancing the transdermal absorption of theophylline and cianidanol. *J. Pharm. Pharmacol.* **2004**, *56*, 1493–1500. [CrossRef]
40. Sloan, K.B.; Beall, H.D.; Taylor, H.E.; Getz, J.J.; Villaneuva, R.; Nipper, R.; Smith, K. Transdermal delivery of theophylline from alcohol vehicles. *Int. J. Pharm.* **1998**, *171*, 185–193. [CrossRef]
41. Abd, E.; Yousef, S.A.; Pastore, M.N.; Telaprolu, K.; Mohammed, Y.H.; Namjoshi, S.; Grice, J.E.; Roberts, M.S. Skin models for the testing of transdermal drugs. *Clin. Pharmacol.* **2016**, *8*, 163–176. [CrossRef] [PubMed]
42. Jacobi, U.; Kaiser, M.; Toll, R.; Mangelsdorf, S.; Audring, H.; Otberg, N.; Sterry, W.; Lademann, J. Porcine ear skin: An In vitro model for human skin. *Skin Res. Technol.* **2007**, *13*, 19–24. [CrossRef] [PubMed]
43. Herkenne, C.; Naik, A.; Kalia, Y.N.; Hadgraft, J.; Guy, R.H. Pig ear skin ex vivo as a model for in vivo dermatopharmacokinetic studies in man. *Pharm. Res.* **2006**, *23*, 1850–1856. [CrossRef] [PubMed]
44. Todo, H. Transdermal permeation of drugs in various animal species. *Pharmaceutics* **2017**, *9*, 33. [CrossRef] [PubMed]
45. Meyer, W.; Schwarz, K.; Neurand, K.T. The skin of domestic mammals as a model for the human skin, with special reference to the domestic pig. *Curr. Probl. Dermatol.* **1978**, *7*, 39–52. [PubMed]
46. Suffness, M.; Douros, J. Current status of the NCI plant and animal product program. *J. Nat. Prod.* **1982**, *45*, 1–14. [CrossRef] [PubMed]
47. Beagle, L.K.; Hansen, F.K.; Monbaliu, J.C.M.; DesRosiers, M.P.; Phillips, A.M.; Stevens, C.V.; Katritzky, A.R. Efficient Synthesis of 2,5-diketopiperazines by Staudinger-mediated cyclization. *Synlett* **2012**, *23*, 2337–2340.
48. Ishibashi, N.; Kouge, K.; Shinoda, I.; Kanehisa, H.; Okai, H. Studies on flavored peptides. Part V. A mechanism for bitter taste sensibility in peptides. *Agric. Biol. Chem.* **1988**, *52*, 819–827.
49. Chu, D.T.W.; Nordeen, C.W.; Hardy, D.J.; Swanson, R.N.; Giardina, W.J.; Pernet, A.G.; Plattner, J.J. Synthesis, antibacterial activities, and pharmacological properties of enantiomers of temafloxacin hydrochloride. *J. Med. Chem.* **1991**, *34*, 168–174. [CrossRef]
50. Campbell, T.D.; Hart, C.A.; Febrian, R.; Cheneler, M.L.; Bracher, P.J. The opposite effect of K+ and Na+ on the hydrolysis of linear and cyclic dipeptides. *Tetrahedron Lett.* **2018**, *59*, 2264–2267. [CrossRef]
51. Woodard, R.W. Stereochemistry of cyclic dipeptides. Assignment of the prochiral methylenes of 1-aminocyclopropane-1-carboxylic acid. *J. Org. Chem.* **1985**, *50*, 4796–4799. [CrossRef]
52. *OECD Guidelines for the Testing of Chemicals, Section 4, Test No. 428: Skin Absorption: In Vitro Method*; OECD Publishing: Paris, France, 2004.
53. WHO. *Environmental Health Criteria (EHC 235)—Dermal Absorption*; WHO Press: Geneva, Switzerland, 2006.

54. Shah, J.C. Application of kinetic model to In vitro percutaneous permeation of drugs. *Int. J. Pharm.* **1996**, *133*, 179–189. [CrossRef]
55. Steffansen, B.; Brodin, B.; Uhd Nielsen, C. *Molecular Biopharmaceutics: Aspects of Drug Characterisation, Drug Delivery and Dosage Form Evaluation*; Pharmaceutical Press: London, UK, 2010.

Sample Availability: Samples of compounds are available from authors.

© 2019 by the authors. Licensee MDPI, Basel, Switzerland. This article is an open access article distributed under the terms and conditions of the Creative Commons Attribution (CC BY) license (http://creativecommons.org/licenses/by/4.0/).

molecules

MDPI

Article

Synthesis, In Silico, and In Vitro Evaluation of Long Chain Alkyl Amides from 2-Amino-4-Quinolone Derivatives as Biofilm Inhibitors

Mariana Paola Espinosa-Valdés [1,†], Sara Borbolla-Alvarez [1,†], Ana Elena Delgado-Espinosa [1,†], Juan Francisco Sánchez-Tejeda [1], Anabelle Cerón-Nava [1], Osvaldo Javier Quintana-Romero [2], Armando Ariza-Castolo [2], Diego Fernando García-Del Río [1] and Marco A. Loza-Mejía [1,*]

1 Facultad de Ciencias Químicas, Universidad La Salle-México. Av. Benjamin Franklin 45, Cuauhtémoc, Mexico City 06140, Mexico; mariana-espinosa@lasallistas.org.mx (M.P.E.-V.); sara.borbolla@lasallistas.org.mx (S.B.-A.); ana.delgado@lasallistas.org.mx (A.E.D.-E.); juansanchez@lasallistas.org.mx (J.F.S.-T.); anabelle.ceron@lasalle.mx (A.C.-N.); diegodoku@gmail.com (D.F.G.-D.R.)

2 Departamento de Química Orgánica, Centro de Investigación y de Estudios Avanzados del Instituto Politécnico Nacional (CINVESTAV-IPN), Av. Instituto Politécnico Nacional 2508, Mexico City 07360, Mexico; javo_omnosnoa@hotmail.com (O.J.Q.-R.); aariza@cinvestav.mx (A.A.-C.)

* Correspondence: marcoantonio.loza@lasalle.mx; Tel.: +52-55-5278-9500 (ext. 2433)

† These authors made equal contribution to this work.

Academic Editor: Josef Jampilek

Received: 18 December 2018; Accepted: 16 January 2019; Published: 17 January 2019

Abstract: Infection from multidrug resistant bacteria has become a growing health concern worldwide, increasing the need for developing new antibacterial agents. Among the strategies that have been studied, biofilm inhibitors have acquired relevance as a potential source of drugs that could act as a complement for current and new antibacterial therapies. Based on the structure of 2-alkyl-3-hydroxy-4-quinolone and *N*-acylhomoserine lactone, molecules that act as mediators of quorum sensing and biofilm formation in *Pseudomonas aeruginosa,* we designed, prepared, and evaluated the biofilm inhibition properties of long chain amide derivatives of 2-amino-4-quinolone in *Staphylococcus aureus* and *P. aeruginosa*. All compounds had higher biofilm inhibition activity in *P. aeruginosa* than in *S. aureus.* Particularly, compounds with an alkyl chain of 12 carbons exhibited the highest inhibition of biofilm formation. Docking scores and molecular dynamics simulations of the complexes of the tested compounds within the active sites of proteins related to quorum sensing had good correlation with the experimental results, suggesting the diminution of biofilm formation induced by these compounds could be related to the inhibition of these proteins.

Keywords: quorum sensing; biofilm; quinolones; molecular docking; molecular dynamics

1. Introduction

One of the major health issues is the emergence of multidrug resistant (MDR) bacterial strains. Infection and contamination from MDR bacteria could compromise major surgeries and can be life-threating to children and elderly or immunocompromised persons, increasing the risk of complications and treatment costs. This situation creates a need to intensify the efforts directed at the development of new antibacterial agents with different approaches distinct from current therapies. The study of the intercellular communication systems in bacteria, known as quorum sensing (QS) systems, has emerged as an attractive biotarget for the development of new antibacterials [1,2]. QS is a cell density-dependent chemical signaling process that regulates several changes in gene expression, which lead to phenotypes, including bioluminescence, plasmid transfer, synthesis of

secondary metabolites, and biofilm formation [3]. The latter plays an important role in animal and human infections and food contamination, as well as in the implant of medical devices [1,4]. A biofilm is defined as a bacterial community that fixes and grows on surfaces through a polysaccharide matrix [5,6]. It has been reported that between 65–80% of infectious diseases are linked to bacterial communities whose proliferation is related to biofilms and that they are more resistant to host defense mechanisms and antimicrobials by approximately 10–1000-fold compared to nonbiofilm forming cultures [7–9]. Thus, the disruption of biofilm formation by quorum-sensing inhibitors (QSIs) represents an attractive option for the development of drugs that act as a complement for current and new therapies, as it has been reported that QSIs increase the susceptibility of bacteria to the action of antimicrobials [1,10,11].

QS is mediated by several signaling molecules (Figure 1), such as oligopeptides (like AIP-1, generally in Gram-positive bacteria), *N*-acyl homoserine lactones (AHLs, most common in Gram-negative bacteria), furanosyl borate (like AI-2, used by *S. typhimurium*), long chain acid esters, and 2-alkyl-3-hydroxy-4-quinolone in *Pseudonomas aeruginosa*, known as Pseudomonas quinoline signaling (PQS) system [12,13]. The biosynthesis of PQS is mediated by several proteins. In this pathway, anthranilic acid is activated by PqsA, while PqsB, PqsC, and PqsD mediate the conversion to 2-heptyl-4-quinolone (known as HHQ), which is converted into PQS by the participation of PqsH [14]. The transcription of the latter is controlled by LasR, which is one of the major regulators of the virulence factors of *P. aeruginosa*. Thus, inhibition of some of the proteins that participate in this pathway would have an impact on the biofilm formation of *Pseudomonas*. In fact, PqsD and LasR have been evaluated and validated as anti-biofilm targets [15–20].

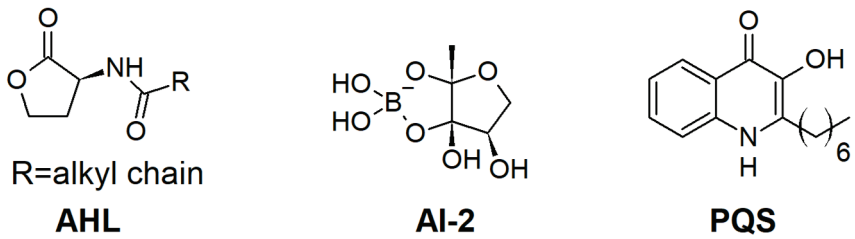

Figure 1. Examples of signaling molecules that mediate quorum sensing.

Some structural requirements have been proposed for the design of biofilm formation inhibitors, which are based primarily on the structure of AHL. It has been proposed that biofilm inhibitors should include a hydrophilic group with hydrogen bond donor (HBD) atoms and a lipophilic alkyl chain (Figure 2). Among the hydrophilic heterocyclic templates that have been studied for the design of biofilm inhibitors [21], some quinolones are described to possess high bioactivity [22–27]. We have previously reported a direct route for the synthesis of 2-amino-4-quinolone (compound **1**, Figure 2) and 2,3-diamino-4-quinoline (compound **2**) as key synthons for the preparation of tricyclic compounds [28]. The obvious structural similarity of compounds **1** and **2** with quinolones from the PQS system prompted us to determine if the long chain amide derivatives of **1** and **2** could interfere with bacterial biofilm formation in *P. aeruginosa*. Synthesis, in vitro evaluation of biofilm inhibition, and in silico studies are presented.

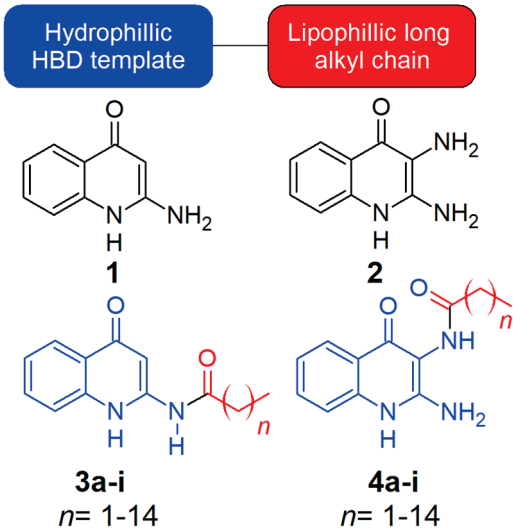

Figure 2. General structural requirements for biofilm inhibitors based on AHL and quinolone derivatives proposed as QSIs.

2. Results

2.1. Chemistry

Scheme 1 describes the synthetic route for the preparation of the target compounds. The 2-amino-4-quinolone derivatives **1** and **2** were prepared from isatoic anhydride as previously reported [28]. Acylation of **1** and **2** was easily performed from commercially available acid chlorides in pyridine at 0 °C in relatively good yields (70–85%). Variation of these conditions resulted in formation of subproducts (presumably diacylated compounds) or no reaction at all.

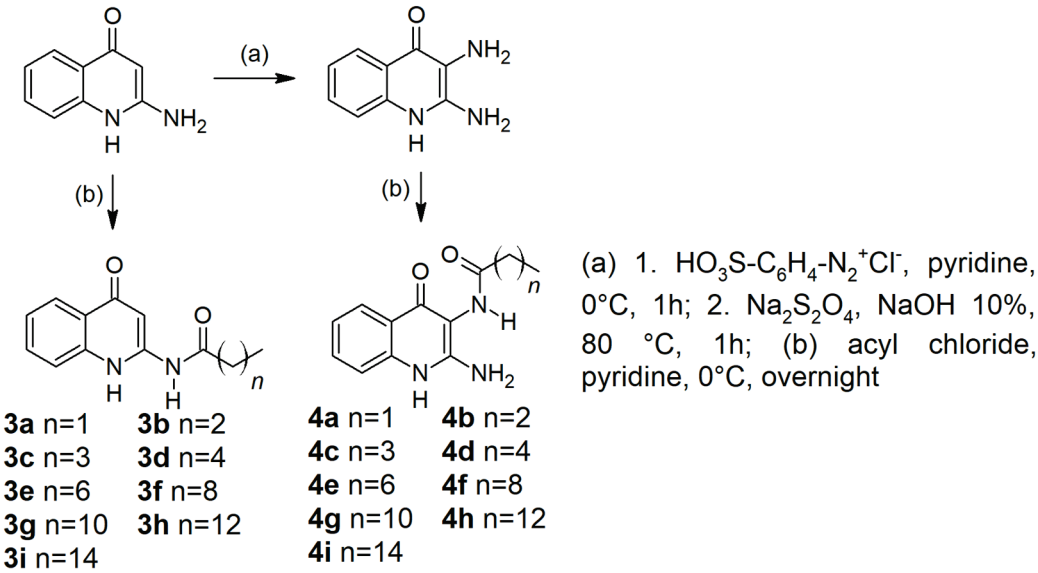

Scheme 1. Synthetic route for the preparation of target compounds, **3a-i** and **4a-i**.

Acylation of the 3-amino group in compound **2** was expected as it seems to be the most reactive group. Selective incorporation of the acyl groups was confirmed by analysis of NMR spectra of compounds **1**, **2** and **4a**. The signal of the protons of 2-amino group in compound **1** appears as a simple signal that integrates for two protons at 6.18 ppm, while in compound **2**, the signal for the protons of the amino group in position 2 appears at 5.99 ppm. For the compounds **4a-i**, a signal that integrates for two protons appears between 5.98 and 6.14 ppm, which allowed us to suppose that

the acylation occurred in position 3. Further evidence came from 1D NOE experiments, where the selective irradiation of the protons of the 2-amino group at δ 5.98 ppm in compound **4a** yielded NOEs on the proton of the 3-amide group (δ 11.06 ppm) and the proton bound to the heterocyclic nitrogen atom (δ 8.42 ppm). Additional evidence was provided by the presence of the long-range correlation between the 2-amino group protons and the heterocyclic nitrogen atom in the ^{1}H-^{15}N long-range HMQC spectra. Figure 3 summarizes these findings.

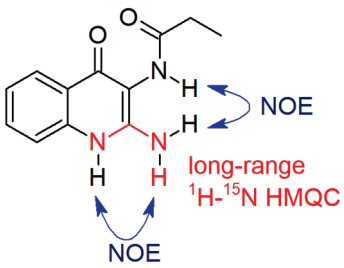

Figure 3. NOE and long-range ^{1}H-^{15}N-HMQC correlations that confirmed acylation in position 3.

2.2. Biofilm Inhibition

Table 1 shows the results of biofilm inhibition studies of compounds **3a-i** and **4a-i** at 20 M. Results obtained at higher concentrations were considered not reliable due to the poor solubility of the compounds. It is interesting to note that none of the compounds affected bacteria growth, indicating that the decrease of the biofilm formation is not related to bacteriostatic or bactericide activities. An ANOVA analysis using Dunnett's multiple comparison test showed that compounds with an alkyl chain with 12 carbon atoms or more were the most active and exhibited higher biofilm inhibition activity than tannic acid, which was used as the control [29] (BIC_{50} = 38.4 μM, BIC_{50} = concentration of compound required to reduce biofilm formation to 50%). Compounds **3g** and **4g** also decreased the synthesis of pyocyanin to 68.2% and 62.6% compared to the control, respectively. Values of the percentage efficiency index (PEI), which are derived from the measure of percentage inhibition at a specific concentration divided by the molecular weight [30], are also shown in Table 1. Figure 4 shows the plot of the biofilm inhibition percentage against the alkyl chain length.

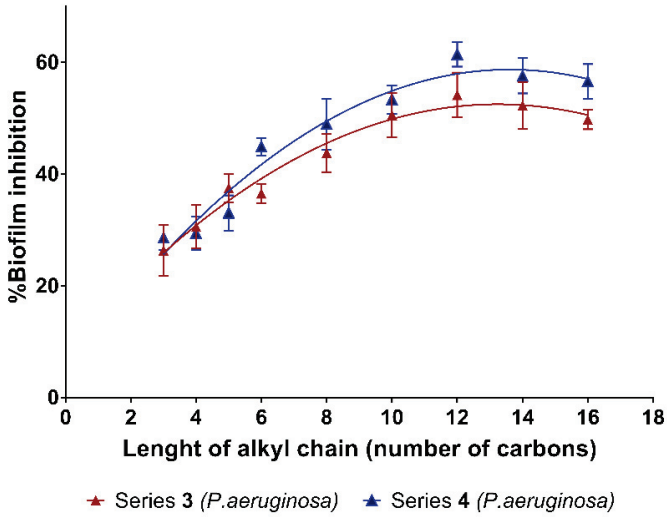

Figure 4. Plot of the percentage of biofilm inhibition in *P.aeruginosa* against the number of carbons in the alkyl chain.

Table 1. Biofilm inhibition (at 20 μM) of compounds **3a-i** and **4a-i** in *S. aureus* and *P. aeruginosa* studies.

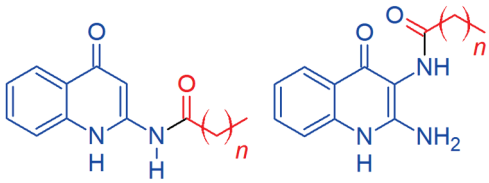

3a-i *n*= 1-14 **4a-i** *n*= 1-14

		BI (%) (±s.d.)					BI (%) (±s.d.)		
Cmp	***n***	***S.a***	***P.a***	**PEI**	**Cmp**	***n***	***S.a***	***P.a***	**PEI**
3a	1	15.3 (±2.8)	26.4 (±4.6)	1.22	**4a**	1	< 5	28.65 (±2.2)	1.24
3b	2	31.2 (±3.6)	30.6 (±3.9)	1.33	**4b**	2	29.8 (±5.1)	29.43 (±3.1)	1.20
3c	3	<5	37.5 (±2.6)	1.54	**4c**	3	<5	33.09 (±3.2)	1.28
3d	4	<5	36.6 (±1.7)	1.42	**4d**	4	<5	44.95 (±1.6)	1.64
3e	6	22.6 (±5.7)	43.8 (±3.4)	1.53	**4e**	6	<5	48.97 (±4.6)	1.62
3f	8	24.8 (±1.5)	50.6 (±4.0)	1.61	**4f**	8	11.9 (±4.2)	53.38 (±2.5)	1.62
3g	10	18.0 (±1.2)	54.2 (±4.0)	1.46	**4g**	10	15.7 (±5.8)	61.45 (±2.2)	1.72
3h	12	25.7 (±1.1)	52.3 (±4.2)	1.41	**4h**	12	16.8 (±4.4)	57.63 (±3.2)	1.49
3i	14	34.7 (±2.0)	49.8 (±1.8)	1.25	**4i**	14	14.2 (±5.4)	56.62 (±3.1)	1.37

BI (%) = percentage of biofilm inhibition in comparison to the control, S.a = *S.aureus*, P.a. = *P.aeruginosa*, percentage efficiency index.

2.3. Molecular Docking Studies

Table 2 show the docking scores (MolDock score, lower values are related with higher affinity) obtained during the in silico studies carried out on the LasR and PqsD active sites. Interestingly, MolDock scores had good correlation with biofilm inhibition activity as shown in Figure 5. The values of logP were computed using ChemSketch from ACD/Labs [31] and are also shown in Table 2

Table 2. Docking scores and *c*logP values calculated for compounds **3a-i** and **4a-i**.

		MolDock Score					MolDock Score		
Ligand	**BI (%)**	**PqsD**	**LasR**	**logP**	**Ligand**	**BI (%)**	**PqsD**	**LasR**	**logP**
3a	26.36	−99.478	−101.21	2.53	**4a**	28.65	−96.4705	−104.98	1.11
3b	30.61	−103.646	−109.25	3.06	**4b**	29.43	−104.784	−110.48	1.64
3c	37.54	−105.508	−113.46	3.59	**4c**	33.09	−110.356	−116.89	2.17
3d	36.56	−111.982	−114.62	4.12	**4d**	44.95	−117.802	−125.21	2.70
3e	43.84	−125.746	−137.16	5.18	**4e**	48.97	−129.125	−142.73	3.76
3f	50.57	−131.982	−152.30	6.24	**4f**	53.38	−136.142	−145.82	4.82
3g	54.20	−124.547	−151.66	6.77	**4g**	61.45	−139.494	−152.81	5.35
3h	52.27	−125.681	−146.32	7.30	**4h**	57.63	−133.275	−159.79	5.88
3i	49.82	−147.112	−156.07	7.83	**4i**	56.62	−150.072	−181.92	6.41

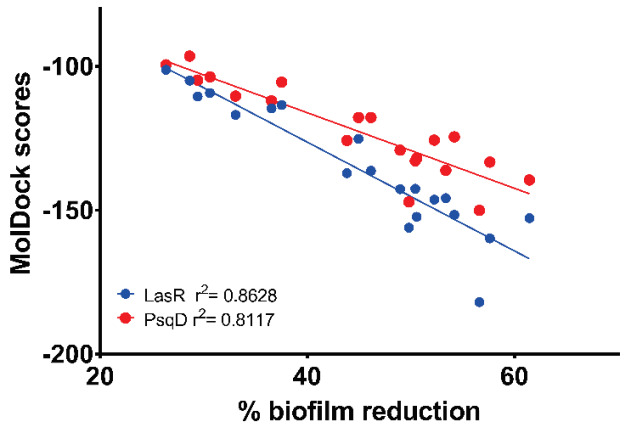

Figure 5. Correlation of the percentage of biofilm inhibition against the docking scores.

2.4. Molecular Dynamics Simulations

Molecular dynamics (MD) simulations were carried out to evaluate if the length of the alkyl chain affects the stability of the complexes. Three main parameters were analyzed, the root-median square deviation (RMSD), root-median square fluctuation (RMSF), and the ligand-protein binding energy. The set of Figure 6a,b shows the RMSD and RMSF around Loop 3 of LasR plots of the complexes of **4a**, **4g** and **4i** with LasR, while the set of Figure 7a,b shows the same plots of the complexes of those compounds with PqsD. Table 3 shows the ligand binding energy (LBE) values computed using MM-PBSA approximation. Using these LBE values, an in silico group efficiency (GE) [32,33] was calculated using the following formula:

$$GE_i = \frac{\Delta LBE}{\Delta HA} = \frac{LBE_i - LBE_{4a}}{HA_i - HA_{4a}} \quad (1)$$

where HA is the heavy atom (non-hydrogen) count.

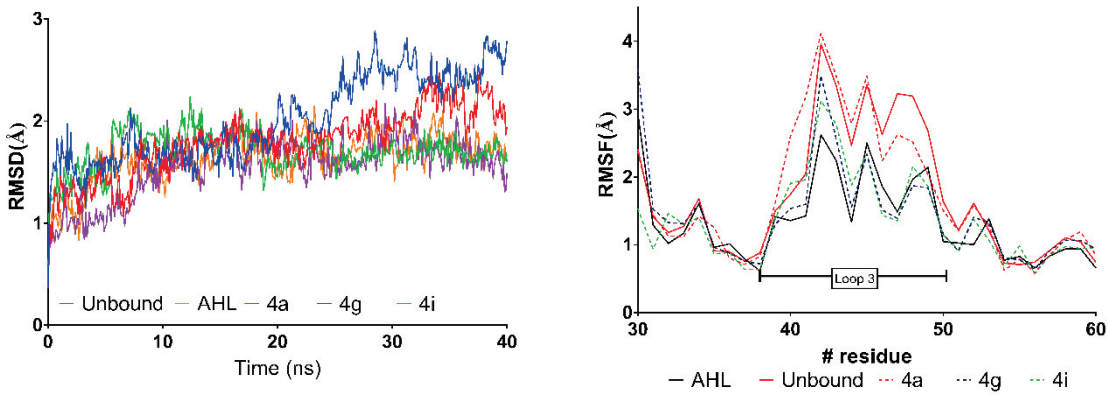

(a) (b)

Figure 6. (**a**) RMSD along simulation time plot and (**b**) RMSF of residues of Loop 3 plots generated from data from MD simulations of complexes of **4a**, **4g**, and **4i** with LasR.

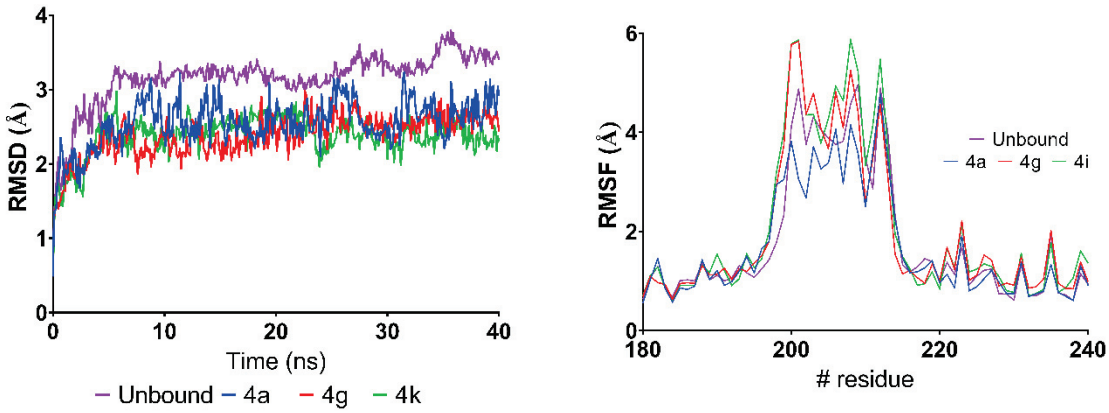

Figure 7. (**a**) RMSD along simulation time plot and (**b**) RMSF of residues along dimer interface (residues 180-240) plots generated from data from MD simulations of complexes of **4a**, **4g**, and **4i** with PqsD.

Table 3. Average RMSD values and ligand binding energy (LBE) [1] calculated during MD simulations.

	LasR			PqsD		
	Average RMSD (Å)	LBE (KJ/mol)	GE [2]	Average RMSD (Å)	LBE (KJ/mol)	GE [2]
4a	1.79	7.09	–	2.55	75.69	–
4g	2.01	2.01	−0.56	2.38	200.44	13.86
4i	1.70	−11.26	−1.41	2.37	229.30	11.81
AHL	1.76	3.29	–	3.26	—-	–

[1] Higher values of LBE indicate better binding, [2] Group Efficiency relative to LBE of **4a**.

3. Discussion

Most of the tested compounds reduced biofilm formation. Table 1 shows the results of biofilm inhibition studies of compounds **3a-i** and **4a-i** at 20 μM. In general, the tested compounds were more active against biofilm formation in *P. aeruginosa* than in *S. aureus*. The most active compounds were those with an alkyl chain of more than 12 carbon atoms (compounds **3g-i** and **4g-i**). This observation coincides with previous reports of biofilm inhibition activities of aminoquinolines, 4-(alkyloxy)-6-methyl-2*H*-pyran-2-one, and aniline derivatives, in which the compounds with an alkyl chain of 12 carbon atoms were the most active [27,34,35], suggesting that alkyl chain length is important for optimal biofilm inhibition. Compounds **3g** and **4g** also decreased the formation of pyocyanin to 68.2% and 62.6% compared to the control, respectively. These findings suggest that these compounds could affect the mechanisms related to virulence of *P. aeruginosa*, including QS.

Derivatives of series **4** were slightly more active than their corresponding analogues of series **3**, but with no significant difference ($p = 0.44$), indicating that the length of alkyl chain is the most important structural factor for biofilm inhibition. One way to evaluate the effect of the increase of the molecular weight (or in our case, the increase in the number of carbons of the alkyl chain) is the measurement of ligand efficiency. We calculated the percentage efficiency index (PEI), which is derived from the measure of percentage inhibition at a specific concentration. Compounds with PEI values higher than 1.5 have a good proportion of potency per molecular weight and are attractive as leads [30]. The PEI values of compounds of series **3** and **4** are shown in Table 2. Compound **4g** exhibited the highest value (1.72) among all the tested compounds, suggesting that it is the most promising molecule in the set. Other parameters of ligand efficiency, like lipophilic ligand efficiency (LLE = $pIC_{50} - logP$, [36]), could be applied. However, low solubility of most active compounds made the construction of a reliable dose-response curve to calculate the BIC_{50} difficult. This experimental

difficulty reveals that low solubility and high logP values (shown in Table 2) are physicochemical factors to consider for the improvement of the bioactivity of this class of compounds.

The plot of the percentage of biofilm decrease vs the alkyl length suggests a quadratic relationship between these parameters as shown in Figure 4. A parabolic model correlates the number of carbons in the alkyl chain and biofilm inhibition: $y = -0.2704x^2 + 7.2998x + 6.3152$, $r^2 = 0.9232$, where x is the number of carbons in the aliphatic chain and y is the biofilm reduction percentage. Parabolic models in QSAR equations are sometimes related to the influence of logP in membrane permeability, which would be a very important aspect to take in consideration due the presence of a double membrane in *P. aeruginosa* and the hydrophobic nature of the tested compounds. However, only a modest correlation was found between biofilm reduction and clogP using parabolic ($r^2 = 0.61$) or linear models. We speculated if the positioning of the alkyl chain within the binding site with proteins of QS signaling system could explain the experimental results better. Among the proteins related to the biofilm formation and other virulence factors, we selected LasR and PqsD as potential targets. LasR is one the major regulators of the quorum sensing signaling systems that controls virulence factors and biofilm formation in *P. aeruginosa,* while PqsD is an enzyme needed for biosynthesis of the signaling molecule PQS.

Figure 5 and Table 2 show the relationship between the docking scores results with biofilm inhibition activity in *P. aeruginosa*. The biofilm inhibition percentage had a good correlation with docking scores calculated during the studies with LasR and PqsD. Analysis of the PDB structure of the complex of AHL within the active site of LasR shows that the hydrophilic lactone moiety forms hydrogen bonds with Trp60 and the amide group forms hydrogen bonds with Tyr56, Asp73, and Ser129, while the 12-carbon chain is accommodated inside a hydrophobic pocket (see Figure S1 in the Supplemental Information). A closer observation of the interaction of the alkyl chain within this pocket shows that residues Gly38, Leu39, and Ala40 form a curve that obliges the aliphatic chain of AHL to make a turn [37]. This turn is significant, as it is the beginning of Loop 3 of LasR and it has been recently reported that the dynamics of Loop 3 (formed by residues between Leu40 and Phe51) are relevant to establish whether a ligand could act as an agonist or antagonist of LasR [38].

Figure 8 shows the docking pose obtained for compound **4g** within the active site of LasR. As expected, the heterocycle occupies almost the same site as the lactone ring of AHL. This occurs for the rest of the compounds of series **3** and **4**. The carbonyl groups of the quinolone and the amide form hydrogen bonds with Tyr64 (Arg61 in case of compounds of series **3**), Thr75, Thr115, and Ser129. The aliphatic chain of **4g** also "makes a turn" close to Leu39 and Ala40 just as AHL. The filling of this hydrophobic pocket in the same mode as AHL is probably important for LasR inhibition as compounds with shorter alkyl chains are less active while compounds with longer chains have torsional strains that make the formation of the complex inside the pocket more difficult.

MD simulations could help to understand and evaluate whether the length of the alkyl chain affects the stability of the complexes. Three main parameters were analyzed, RMSD, RMSF, and the ligand-protein binding energy. Figure 6a shows the RMSD plot of the complexes of **4a**, **4g**, and **4i** with LasR. A smaller value of RMSD indicates higher protein stability. All three complexes exhibited low RMSD variations after 5 ns of simulation, with values lower than 2.8 Å, suggesting that the three complexes are stable. Figure 6b shows the RMSF profile around residues that conform to Loop 3. Around this region, the RMSF values were higher than in the rest of the protein for the five structures analyzed (unbound LasR, LasR-AHL, LasR-**4a**, LasR-**4g**, and LasR-**4i**). Loop 3 exhibited higher flexibility in the absence of any ligands and in the complex with **4a** compared with complexes with AHL, **4g**, and **4i**, particularly around residues 42 to 48, suggesting that the length of the alkyl chain has an important effect on Loop 3. Table 3 shows the ligand binding energy. Interestingly, compound **4a** with the shortest alkyl chain had the better binding, even better than the natural agonist AHL. Compound **4g** and AHL had similar LBE (2.01 KJ/mol and 3.29 KJ/mol), but **4i** had significantly lower LBE, indicating that an increase of the alkyl chain above 12 carbons decreases the efficiency

of binding to LasR. It should be noted that with the algorithm implemented in YASARA, the more positive the MM-PBSA binding energy, the better the binding of the ligand.

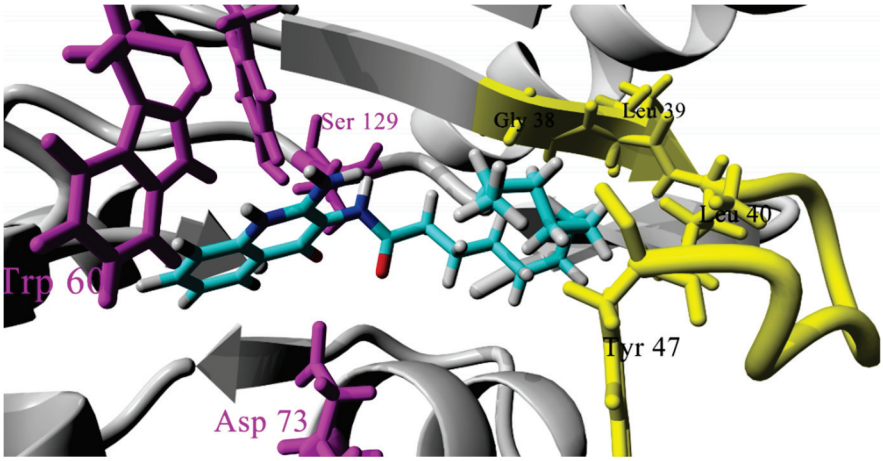

Figure 8. Docking pose for compound **4g** in the active site of LasR. Residues of the hydrophilic pocket that form hydrogen bonds with natural ligand AHL are shown in magenta and those of Loop 3 are in yellow.

Analysis of the available structures of PqsD in the complex with some anthranilate derivatives shows that residues Cys112 and Ser317 are important to bind the anthranilate nucleus. Moreover, as part of the proposed mechanism for PqsD, two important "tunnels" have been proposed, one for CoA binding (shown in green in Figure 9) and the other for the β-ketodecanoate (shown in yellow in Figure 9), with kinetics and SPR experiments suggesting a ping-pong mechanism and Acetyl CoA being the first substrate to enter [39,40]. In this mechanism, Ser317 plays a key role, as it is important not only for the binding of the anthranilate ring, but also for binding to the CoA and β-ketodecanoate chains through hydrogen bonding [40]. The docking pose of **4g** within the active site of PqsD shows that the heterocyclic nucleus interacts with Cys112 and Ser317 through the amine group in position 2 and the amide group of position 3 (see Figure S2 in the Supplemental Information), possibly limiting the access of anthranilate to its binding site. All compounds share similar interaction patterns.

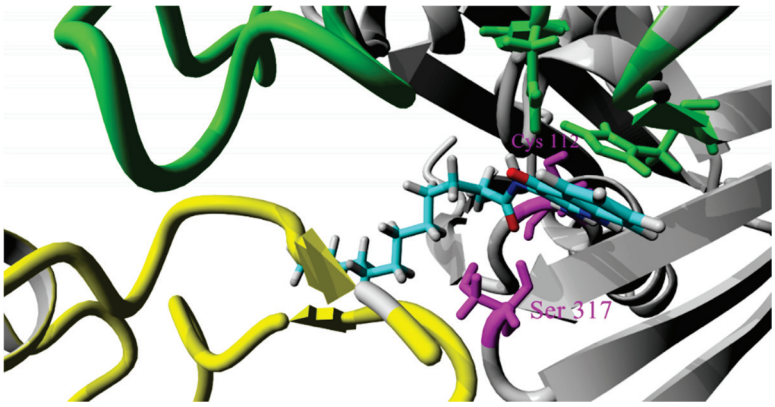

Figure 9. Docking pose of compound **4g** within the active site of PqsD. Key residues for anthranilate binding of Cys112 and Ser317 are shown in magenta.

To study the effect of the alkyl chain in the stability of the complexes of the tested compounds with PqsD and variations of distance to Ser317 along time, MD simulation of the complexes of **4a**, **4g**, and **4i** were carried out in a similar fashion as those of carried out with LasR. Figure 7a shows the RMSD plot of the complexes of **4a**, **4g**, and **4i** with LasR. From these plots it can be concluded that the

three complexes are stable, with minor variations in RMSD. Figure 7b shows the residue RMSF plot. The major variations were observed in the region between residues 195 to 213, which correspond to the hairpin loop of the dimer interface, which coincides with previous studies [40]. Flexibility around this region is increased by the presence of ligands **4g** and **4i**, but decreased by the presence of **4a**, thus it could suggest that in addition to blocking the entrance of anthranilate, this class of compounds could interfere in the formation of the dimer of PqsD. Results of the calculation of the ligand binding energy are shown in Table 3. Compounds **4g** and **4i** clearly exhibit better theoretical binding than **4a**, indicating that inhibition of PqsD is probably a good candidate for the mechanism of action of this class of compounds.

Additionally, group efficiency (GE) was introduced as a metric to evaluate the impact of an added moiety, with higher values indicating a higher potential for development. The values of in silico GE (Table 2), derived from LBE values, suggest that a length of 12 carbon atoms in the alkyl chain has a higher impact than the elongation to 16 atoms. This data suggests that a length of 12 carbon atoms is optimal for biofilm inhibition, and structural modification that leads to compounds with better bioactivity profile should be pursued in the heterocyclic template.

4. Materials and Methods

4.1. Chemistry

All reagents were purchased from Sigma-Aldrich and used without further purification. TLC analysis was carried out using silica gel 60 on aluminum foil from Sigma-Aldrich (St. Louis, MO, USA). Melting points were determined on a Fisher-Johns apparatus and are uncorrected. The IR spectra were obtained with a Perkin-Elmer FT IR-670 Plus spectrophotometer in KBr disk. NMR spectra were recorded at room temperature using a Bruker 400 Avance Nanobay (B_0 = 9.4 T) or a Jeol ECA-500 (B_0 = 11.7 T), both spectrometers equipped with a 5-mm multinuclear and pulse field gradient probe. The samples were determined in DMSO-d_6 solution. ^{1}H-NMR spectra were recorded at 399.7832 MHz and 500.1599 MHz, respectively (spectra width 15 ppm, acquisition time ~2.8 s, pulse width 45°, 16 scans, and recycle delay of 1 s). ^{13}C-NMR spectra were recorded at 75.47 MHz or a 125 MHz (spectral with 250 ppm, acquisition time >0.83 s, equivalent 30° pulse duration, scans 3000, and recycle delay of 0.1 s). The following abbreviations are used: s, singlet; br, broad signal; d, doublet; dd, doublet of doublet; t, triplet; m, multiplet. The FAB-MS analyses were obtained on a JEOL Sx102 mass spectrometer. Elemental analyses were performed in a Perkin-Elmer 2400 Series II instrument.

A typical procedure preparation was as follows: 0.12 mmol of the corresponding acid chloride was added to 3 mL of dry pyridine at 0 °C, then 0.1 mmol of the compound **1** or **2** was added, a yellowish suspension was formed, and the mixture was stirred at room temperature overnight. At the end of reaction time, a white precipitate was formed, which was filtered off in vacuum and washed with cold water and cold ethanol to give the target compounds as white solids.

N-(4-oxo-1,4-dihydroquinolin-2-yl)propanamide (**3a**). White solid. mp > 250 °C. IR (cm^{-1}): 3208 (br, NH), 2957, 2915, 2850 (CH_2), 1726, 1655 (C=O). ^{1}H-NMR (500.16 MHz) δ 13.35 (s, 1H, NH), 8.15 (br, 1H, NH), 7.94 (dd, *J* = 8.1, 0.7 Hz, 1H, H5), 7.70 (td, *J* = 8.1, 1.4 Hz, 1H, H7), 7.57 (dd, *J* = 8.1, 1.4 Hz, 1H, H8), 7.38 (td, *J* = 8.1, 0.7 Hz, 1H, H6), 6.47 (s, 1H, CH), 2.16 (q, *J* = 7.4 Hz, 2H, CH_2), 0.93 (t, *J* = 7.4 Hz, 3H, CH_3). ^{13}C-NMR (125.77 MHz) δ 175.76 (NCO), 165.73 (C4O), 156.25 (NCN), 137.76 (C10), 133.32(C7), 124.69 (C6), 123.63 (C5), 117.59 (C8), 116.54 (C9), 92.03 (CH), 27.42 (CH_2), 9.61 (CH_3). MS (FAB, *m/z*): 217 (M^+ + 1, 100%); Elemental analysis: C 66.53%, H 5.81%, N 12.59% Calc. for $C_{12}H_{12}N_2O_2$, C 66.65%, H 5.59%, N 12.96%

N-(4-oxo-1,4-dihydroquinolin-2-yl)butanamide (**3b**) White solid. mp > 250 °C. IR (cm^{-1}): 3204 (br, NH), 2958, 2910, 2842 (CH_2), 1725, 1650 (C=O). ^{1}H-NMR (500.16 MHz, DMSO-d_6) δ 14.39 (br, 1H, NH) 13.51 (br, 1H, NH), 7.93 (d, *J* = 8.0 Hz, 1H, H5), 7.69 (t, *J* = 8.0 Hz, 1H, H7), 7.57 (d, *J* = 8.0, 1H, H8), 7.37 (t, *J* = 8.0 Hz, 1H, H6), 6.53 (s, 1H, CH), 2.13 (t, *J* = 7.4 Hz, 2H, CH_2b), 1.45 (sext, *J* = 7.4 Hz, 2H, CH_2c),

0.82 (t, *J* = 7.4 Hz, 3H, CH_3d). ^{13}C-NMR (125.77 MHz) δ 174.88 (NCO), 165.73 (C4O), 156.32 (NCN), 137.73 (C10), 133.27 (C7), 124.62 (C6), 123.61 (C5), 117.55(C8), 116.57 (C9), 92.06 (C3H), 36.10 (CH_2 b), 18.44 (CH_2 c), 14.03 (CH_3). MS (FAB, *m*/*z*): 231 (M^+ + 1, 100%); Elemental analysis: C 67.75%, H 6.48%, N 11.93% Calc. for $C_{13}H_{14}N_2O_2$, C 67.81%, H 6.13%, N 12.17%

N-(4-oxo-1,4-dihydroquinolin-2-yl)pentanamide (**3c**) White solid. mp > 250 °C. IR (cm^{-1}): 3198 (br, NH), 2967, 2908, 2852 (CH_2), 1727, 1653 (C=O) ^{1}H-NMR (399.78 MHz, DMSO-d_6) δ 13.52 (br, 1H, NH), 8.18 (br, 1H, NH), 7.98 (d, *J* = 8.1 Hz, 1H, H5), 7.73 (dt, *J* = 8.1 Hz, 1H, H7), 7.62 (d, *J* = 8.1, 1H, H8), 7.42 (t, *J* = 8.1 Hz, 1H, H6), 6.53 (s, 1H, CH), 2.18 (t, *J* = 7.4 Hz, 2H, CH_2b), 1.46 (quint, *J* = 7.4 Hz, 2H, CH_2c), 1.26 (sext, *J* = 7.4 Hz, 2H, CH_2d), 0.84 (t, *J* = 7.4 Hz, 3H, CH_3). ^{13}C-NMR (100.52 MHz) δ 174.97 (NCO), 165.68 (C4O), 156.20 (NCN), 137.68 (C10), 133.22 (C7), 124.58 (C6), 123.55 (C5), 117.50(C8), 116.50 (C9), 92.97 (C3H), 33.85 (CH_2 b), 27.07 (CH_2), 22.13 (CH_2), 14.09 (CH_3). MS (FAB, *m*/*z*): 245 (M^+ + 1, 100%) Elemental analysis: C 69.05%, H 6.98%, N 11.11% Calc. for $C_{14}H_{16}N_2O_2$, C 68.83%, H 6.60%, N 11.47%

N-(4-oxo-1,4-dihydroquinolin-2-yl)hexanamide (**3d**) White solid. mp > 250 °C. IR (cm^{-1}): 3201 (br, NH), 2957, 2918, 2862 (CH_2), 1724, 1650 (C=O) ^{1}H-NMR (399.78 MHz, DMSO-d_6) δ 13.41 (br, 1H, NH), 8.16 (br, 1H, NH), 7.98 (dd, *J* = 8.1, 1.1 Hz, 1H, H5), 7.74 (ddd, *J* = 8.4, 7.9, 1.1 Hz, 1H, H7), 7.62 (dd, *J* = 7.9, 1.1 Hz, 1H, H8), 7.42 (ddd, *J* = 8.4, 8.1, 1.1 Hz, 1H, H6), 6.52 (s, 1H, CH), 2.17 (t, *J* = 7.4 Hz, 2H, CH_2b), 1.47 (quint, *J* = 7.4, Hz, 2H, CH_2c), 1.24 (sext, *J* = 7.4 Hz, 2H, CH_2), 1.22 (sext, *J* = 7.4 Hz, 2H, CH_2), 0.84 (t, *J* = 7.0 Hz, 3H, CH_3).^{13}C-NMR (100.52 MHz) δ 174.97 (NCO), 165.69 (C4O), 156.19 (NCN), 137.69 (C10), 133.23 (C7), 124.59 (C6), 123.55 (C5), 117.52 (C8), 116.50 (C9), 91.97 (C3H), 34.09 (CH_2 b), 31.20 (CH_2), 24.63 (CH_2), 22.28 (CH_2), 14.26 (CH_3).MS (FAB, *m*/*z*): 259 (M^+ + 1, 100%); Elemental analysis: C 69.65%, H 7.38%, N 10.63% Calc. for $C_{15}H_{18}N_2O_2$, C 69.74%, H 7.02%, N 10.84%

N-(4-oxo-1,4-dihydroquinolin-2-yl)octanamide (**3e**) White solid. mp > 250 °C. IR (cm^{-1}): 3203 (br, NH), 2953, 2912, 2857 (CH_2), 1729, 1655 (C=O). ^{1}H-NMR (500.16 MHz, DMSO-d_6) 14.23 (br, 1H, NH), 13.39 (br, 1H, NH), 7.95 (d, *J* = 8.1 Hz, 1H, H5), 7.71 (t, *J* = 8.1 Hz, 1H, H7), 7.58 (d, *J* = 8.1 Hz, 1H, H8), 7.39 (t, *J* = 8.1 Hz, 1H, H6), 6.48 (s, 1H, CH), 2.14 (t, *J* = 7.4 Hz, 2H, CH_2b), 1.43 (quint, *J* = 6.3 Hz, 2H, CH_2c), 1.38-1.13 (m, 8H, CH_2), 0.81 (t, *J* = 7.4 Hz, 3H, CH_3). ^{13}C-NMR (125.77 MHz) δ 175.03 (NCO), 165.76 (C4O), 156.28 (NCN), 137.83 (C10), 133.91 (C7), 124.68 (C6), 123.63 (C5), 117.61 (C8), 116.57 (C9), 92.05 (C3H), 34.20 (CH_2 b), 29.03 (CH_2), 28.93 (CH_2), 25.02 (CH_2), 24.51 (CH_2), 22.57 (CH_2), 14.47 (CH_3). MS (FAB, *m*/*z*): 287 (M^+ + 1, 100%); Elemental analysis: C 71.67%, H 7.97%, N 9.59% Calc. for $C_{17}H_{22}N_2O_2$, C 71.30%, H 7.74%, N 9.78%

N-(4-oxo-1,4-dihydroquinolin-2-yl)decanamide (**3f**) White solid. mp > 250 °C. IR (cm^{-1}): 3198 (br, NH), 2960, 2920, 2858 (CH_2), 1721, 1652 (C=O). ^{1}H-NMR (500.16 MHz, DMSO-d_6) δ 13.35 (br, 1H, NH), 8.12 (br, 1H, NH), 7.95 (dd, *J* = 8.1, 1.0 Hz, 1H, H5), 7.70 (ddd, *J* = 8.4, 7.1, 1.1 Hz, 1H, H7), 7.58 (d, *J* = 8.1, 1.0 Hz, 1H, H8), 7.38 (ddd, *J* = 8.1, 7.1 1.1 Hz, 1H, H6), 6.46 (s, 1H, CH), 2.14 (t, *J* = 7.4 Hz, 2H, CH_2b), 1.43 (quint, *J* = 7.0, 6.71 Hz, 2H, CH_2c), 1.23-1.13 (s, 12H, CH_2), 0.80 (t, *J* = 7.0 Hz, 3H, CH_3).^{13}C-NMR (125.77 MHz) δ 175.05 (NCO), 165.78 (C4O), 156.25 (NCN), 137.79 (C10), 133.32 (C7), 124.67 (C6), 123.63 (C5), 117.61 (C8), 116.59 (C9), 92.02 (C3H), 34.19 (CH_2 b), 31.80 (CH_2), 29.40 (CH_2), 29.28 (CH_2), 29.18 (CH_2), 29.07 (CH_2), 25.014 (CH_2), 22.62 (CH_2), 14.47 (CH_3). MS (FAB, *m*/*z*): 315 (M^+ + 1, 100%); Elemental analysis: C 72.59%, H 8.68%, N 8.56% Calc. for $C_{19}H_{26}N_2O_2$, C 72.58%, H 8.33%, N 8.91%

N-(4-oxo-1,4-dihydroquinolin-2-yl)dodecanamide (**3g**). White solid. mp > 250 °C. IR (cm^{-1}): 3203 (br, NH), 2957, 2918, 2854 (CH_2), 1722, 1653 (C=O). ^{1}H-NMR (500.16 MHz, DMSO-d_6) 13.23 (br, 1H, NH), 8.08 (br, 1H, NH), 7.94 (d, *J* = 8.1 Hz, 1H, H5), 7.70 (t, *J* = 8.1 Hz, 1H, H7), 7.57 (d, *J* = 8.1 Hz, 1H, H8), 7.38 (t, *J* = 8.1 Hz, 1H, H6), 6.42 (s, 1H, CH), 2.13 (t, *J* = 7.4 Hz, 2H, CH_2b), 1.43 (m, 2H, CH_2c), 1.30-1.10 (m, 14H, CH_2), 0.80 (t, *J* = 6.7 Hz, 3H, CH_3). ^{13}C-NMR (125.77 MHz) δ 175.05 (NCO), 165.77 (C4O), 156.27 (NCN), 137.85 (C10), 133.29 (C7), 124.66 (C6), 123.62 (C5), 117.60 (C8), 116.58 (C9), 92.02 (C3H), 34.20 (CH_2 b), 31.83 (CH_2), 29.52 (CH_2), 29.43 (CH_2) 29.28 (CH_2), 29.20 (CH_3), 29.08 (CH_2), 28.84 (CH_2), 25.01 (CH_2), 22.63 (CH_2), 14.47 (CH_3). MS (FAB, *m*/*z*): 343 (M^+ + 1, 100%); Elemental analysis: C 73.96%, H 9.01%, N 7.87% Calc. for $C_{21}H_{30}N_2O_2$, C 73.65%, H 8.83%, N 8.18%

N-(4-oxo-1,4-dihydroquinolin-2-yl)tetradecanamide (**3h**) White solid. mp: > 250 °C. IR (cm^{-1}): 3205 (br, NH), 2956, 2914, 2849 (CH_2), 1720, 1655 (C=O). ^{1}H-NMR (399.78 MHz, DMSO-d_6) δ 13.16 (br, 1H, NH), 8.10 (br, 1H, NH), 7.99 (dd, *J* = 8.1, 1.0 Hz, 1H, H5), 7.75 (ddd, *J* = 8.4, 7.1, 1.4 Hz, 1H, H7), 7.62 (dd, *J* = 8.0, 1.0 Hz, 1H, H8), 7.43 (ddd, *J* = 8.1, 7.1, 1.0 Hz, 1H, H6), 6.44 (s, 1H, CH), 2.18 (t, *J* = 7.4 Hz, 2H, CH_2b), 1.47 (quint, *J* = 7.4 Hz, 2H, CH_2c), 1.29-1.17 (m, 20H, CH_2), 0.84 (t, *J* = 7.0 Hz, 3H, CH_3).^{13}C-NMR (100.52 MHz) δ 175.03 (NCO), 165.75 (C4O), 156.14 (NCN), 137.75 (C10), 133.29 (C7), 124.67 (C6), 123.59 (C5), 117.59 (C8), 116.54 (C9), 91.94 (C3H), 34.12 (CH_2 b), 31.74 (CH_2), 29.49 (CH_2), 29.47 (CH_2), 29.45 (CH_2), 29.43 (CH_2), 29.35 (CH_2), 29.18 (CH_2), 29.15 (CH_2), 28.99 (CH_2), 24.94 (CH_2), 22.55 (CH_2), 14.40 (CH_3). MS (FAB, *m/z*): 371 (M^+ + 1, 100%); Elemental analysis: C 74.94%, H 9.58%, N 7.21% Calc. for $C_{23}H_{34}N_2O_2$, C 74.55%, H 9.25%, N 7.56%

N-(4-oxo-1,4-dihydroquinolin-2-yl)hexadecanamide (**3i**) White solid. mp > 250 °C. IR (cm^{-1}): 3204 (br, NH), 2957, 2918, 2851 (CH_2), 1726, 1655 (C=O) ^{1}H-NMR (399.78 MHz, DMSO-d_6) δ 13.21 (br, 1H, NH), 8.07 (br, 1H, NH), 8.00 (dd, *J* = 8.1, 1.1 Hz, 1H, H5), 7.75 (ddd, *J* = 8.4, 7.1, 1.1 Hz, 1H, H7), 7.61 (d, *J* = 8.4 Hz, 1H, H8), 7.43 (ddd, *J* = 8.1, 7.1, 0.8 Hz, 1H, H6), 6.43 (s, 1H, CH), 2.18 (t, *J* = 7.4 Hz, 2H, CH_2b), 1.47 (quint, *J* = 7.4 Hz, 2H, CH_2c), 1.29-1.17 (m, 24H, CH_2), 0.85 (t, *J* = 7.0 Hz, 3H, CH_3).^{13}C-NMR (100.52 MHz) δ 174.99 (NCO), 165.90 (C4O), 156.15 (NCN), 137.75 (C10), 133.28 (C7), 124.65 (C6), 123.60 (C5), 117.60 (C8), 116.66 (C9), 91.93 (C3H), 34.11 (CH_2 b), 31.74 (CH_2), 29.49 (2CH_2), 29.47 (2CH_2), 29.47 (CH_2), 29.43 (CH_2), 29.36 (CH_2), 29.19 (CH_2), 29.16 (CH_2), 29.00 (CH_2), 24.95 (CH_2), 22.56 (CH_2), 14.41 (CH_3). MS (FAB, *m/z*): 399 (M^+ + 1, 100%); Elemental analysis: C 75.17%, H 9.97%, N 6.77% Calc. for $C_{25}H_{36}N_2O_2$, C 75.33%, H 9.61%, N 7.03%

N-(2-amino-4-oxo-1,4-dihydroquinolin-2-yl)propanamide (**4a**). White solid. mp > 250 °C. IR (cm^{-1}): 3315 (NH_2), 2960, 2934, 2871 (CH_2), 1706, 1655 (C=O). ^{1}H-NMR (500.16 MHz, DMSO-d_6) δ 11.06 (br, 1H, NH), 8.42 (s, 1H, NH), 7.94 (d, *J* = 9.2 Hz, 1H, H5), 7.47 (t, *J* = 9.2 Hz, 1H, H7), 7.28 (d, *J* = 9.2 Hz, 1H, H8), 7.15 (t, *J* = 9.2 Hz, 1H, H6), 5.98 (s, 2H, NH_2), 2.30 (t, *J* = 6.9 Hz, 2H, CH_2), 1.02 (t, *J* = 6.9 Hz, 3H, CH_3). ^{13}C-NMR (100.52 MHz) δ 172.25 (NCO), 171.40 (C4O), 150.28 (NC2N), 148.57 (C3N), 137.66 (C10), 131.66 (C7), 125.62 (C6), 123.35 (C5), 122.21(C8), 116.86 (C9), 28.94 (CH_2b), 10.19 (CH_3). MS (FAB, *m/z*): 232 (M^+ + 1, 100%); Elemental analysis: C 62.04%, H 5.89%, N 17.92% Calc. for $C_{12}H_{13}N_3O_2$, C 62.33%, H 5.67%, N 18.17%

N-(2-amino-4-oxo-1,4-dihydroquinolin-2-yl)butanamide (**4b**) White solid. mp > 250 °C. IR(cm^{-1}): 3305 (NH_2), 2956, 2932, 2852 (CH_2), 1708, 1655 (C=O). ^{1}H-NMR (500.16 MHz, DMSO-d_6) δ 10.82 (br, 1H, NH), 8.42 (s, 1H, NH), 7.88 (d, *J* = 8.1 Hz, 1H, H5), 7.74 (t, *J* = 8.0 Hz, 1H, H7), 7.47 (d, *J* = 9.2 Hz, 1H, H8), 7.13 (t, *J* = 9.2 Hz, 1H, H6), 6.12 (s, 2H, NH_2), 2.13 (t, *J* = 6.9 Hz, 2H, CH_2), 1.67 (q, *J* = 7.2 Hz, 2H), 0.95 (t, *J* = 7.3 Hz, 3H, CH_3). ^{13}C-NMR (100.52 MHz) δ 172.42 (NCO), 168.75 (C4O), 150.43 (NC2N), 147.57 (C3N), 137.60 (C10), 131.09 (C7), 125.43 (C6), 123.54 (C5), 122.12(C8), 116.80 (C9), 36.22 (CH_2 b), 18.94 (CH_2 c), 14.40 (CH_3). MS (FAB, *m/z*): 246 (M^+ + 1, 100%); Elemental analysis: C 64.01%, H 6.37%, N 16.97% Calc. for $C_{13}H_{15}N_3O_2$, C 63.66%, H 6.16%, N 17.13%

N-(2-amino-4-oxo-1,4-dihydroquinolin-2-yl)pentanamide (**4c**) White solid. mp > 250 °C. IR (cm^{-1}): 3305 (NH_2), 2954, 2921, 2851 (CH_2), 1705, 1653 (C=O). ^{1}H-NMR (500.16 MHz, DMSO-d_6) δ 10.79 (br, 1H, NH), 8.54 (s, 1H, NH), 7.93 (d, *J* = 8.1 Hz, 1H, H5), 7.44 (t, *J* = 8.0 Hz, 1H, H7), 7.28 (d, *J* = 9.2 Hz, 1H, H8), 7.12 (t, *J* = 9.2 Hz, 1H, H6), 6.13 (s, 2H, NH_2), 2.27 (t, *J* = 7.4 Hz, 2H, CH_2b), 1.51 (quint, *J* = 7.4 Hz, 2H, CH_2c), 1.30 (m, *J* = 7.4 Hz, 2H, CH_2d), 0.86 (t, *J* = 7.4 Hz, 3H, CH_3). ^{13}C-NMR (100.52 MHz) δ 172.72 (NCO), 168.93 (C4O), 150.58 (NC2N), 149.95 (C3N), 137.58 (C10), 130.89 (C7), 125.33 (C6), 123.90 (C5), 122.02(C8), 116.74 (C9), 35.64 (CH_2 b), 27.95 (CH_2), 22.48 (CH_2), 14.43 (CH_3). MS (FAB, *m/z*): 260 (M^+ + 1, 100%); Elemental analysis: C 65.06%, H 6.85%, N 16.03% Calc. for $C_{14}H_{17}N_3O_2$, C 64.85%, H 6.61%, N 16.20%

N-(2-amino-4-oxo-1,4-dihydroquinolin-2-yl)hexanamide (**4d**) White solid. mp > 250 °C. IR (cm^{-1}): 3307 (NH_2), 2958, 2916, 2870 (CH_2), 1701, 1654 (C=O). ^{1}H-NMR (500.16 MHz, DMSO-d_6) δ 10.71 (br, 1H, NH), 8.51 (s, 1H, NH), 7.66 (d, *J* = 8.1 Hz, 1H, H5), 7.45 (t, *J* = 8.0 Hz, 1H, H7), 7.27 (d, *J* = 9.2 Hz, 1H,

H8), 7.13 (t, *J* = 9.2 Hz, 1H, H6), 6.11 (s, 2H, NH_2), 2.36 (t, *J* = 7.4 Hz, 2H, CH_2b), 1.56 (m, 2H, CH_2c), 1.27-1.22 (4H, 2CH_2), 0.83 (t, *J* = 7.0 Hz, 3H, CH_3). ^{13}C-NMR (100.52 MHz) δ 172.93 (NCO), 164.70 (C4O), 151.61 (NC2N), 147.75 (C3N), 137.92 (C10), 131.85 (C7), 125.48 (C6), 124.54 (C5), 123.80(C8), 116.90 (C9), 35.89 (CH_2 b), 31.57 (CH2), 25.38 (CH_2), 22.51 (CH_2), 14.39 (CH_3). MS (FAB, *m*/*z*): 274 (M^+ + 1, 100%); Elemental analysis: C 66.16%, H 7.34%, N 15.13% Calc. for $C_{15}H_{19}N_3O_2$, C 65.91%, H 7.01%, N 15.37%

N-(2-amino-4-oxo-1,4-dihydroquinolin-2-yl)octanamide (**4e**) White solid. mp > 250 °C. IR (cm^{-1}): 3308 (NH_2), 2955, 2934, 2860 (CH_2), 1702, 1658 (C=O). ^{1}H-NMR (500.16 MHz, DMSO-d_6): δ 10.69 (br, 1H, NH), 8.38 (s, 1H, NH), 7.93 (d, *J* = 8.1 Hz, 1H, H5), 7.47 (t, *J* = 8.0 Hz, 1H, H7), 7.20 (d, *J* = 9.2 Hz, 1H, H8), 7.04 (t, *J* = 9.2 Hz, 1H, H6), 6.19 (s, 2H, NH_2), 2.04 (t, *J* = 7.4 Hz, 2H, CH_2b), 1.41 (m, 2H, CH_2c), 1.30-1.04 (m, 8H, CH_2), 0.79 (t, *J* = 7.4 Hz, 3H, CH_3). ^{13}C-NMR (100.52 MHz) δ 171.53 (NCO), 157.90 (C4O), 150.83 (NC2N), 148.19 (C3N), 137.98 (C10), 130.90 (C7), 126.01 (C6), 124.25 (C5), 122.57 (C8), 116.05 (C9), 34.18 (CH_2 b), 29.02 (CH_2), 28.88 (CH_2), 24.98 (CH_2), 24.49 (CH_2), 22.53 (CH_2), 14.45 (CH_3). MS (FAB, *m*/*z*): 302 (M^+ + 1, 100%); Elemental analysis: C 68.01%, H 7.99%, N 13.55% Calc. for $C_{17}H_{23}N_3O_2$, C 67.75%, H 7.69%, N 13.94%

N-(2-amino-4-oxo-1,4-dihydroquinolin-2-yl)decanamide (**4f**) White solid. mp > 250 °C. IR (cm^{-1}): 3312 (NH_2), 2953, 2931, 2862, 2822 (CH_2), 1702, 1657 (C=O). ^{1}H-NMR (500.16 MHz, DMSO-d_6): δ 10.80 (br, 1H, NH), 9.08 (s, 1H, NH), 8.05 (d, *J* = 8.1 Hz, 1H, H5), 7.65 (t, *J* = 8.0 Hz, 1H, H7), 7.28 (d, *J* = 9.2 Hz, 1H, H8), 7.11 (t, *J* = 9.2 Hz, 1H, H6), 6.20 (s, 2H, NH_2), 2.35 (t, *J* = 7.4 Hz, 2H, CH_2b), 1.55 (m, 2H, CH_2c), 1.31-1.14 (m, 12H, CH_2), 0.82 (t, *J* = 7.0 Hz, 3H, CH_3). ^{13}C-NMR (100.52 MHz) δ 172.45 (NCO), 167.72 (C4O), 150.68 (NC2N), 148.97 (C3N), 137.70 (C10), 129.89 (C7), 124.93 (C6), 123.94 (C5), 122.64 (C8), 116.24 (C9), 35.09 (CH_2 b), 31.92 (CH_2), 29.68 (CH_2), 29.31 (CH_2), 29.21 (CH_2), 29.17 (CH_2), 25.14 (CH_2), 22.97 (CH_2), 14.45 (CH_3). MS (FAB, *m*/*z*): 330 (M^+ + 1, 100%); Elemental analysis: C 69.61%, H 8.37%, N 12.38% Calc. for $C_{19}H_{27}N_3O_2$, C 69.27%, H 8.26%, N 12.76%

N-(2-amino-4-oxo-1,4-dihydroquinolin-2-yl)dodecanamide (**4g**). White solid. mp > 250 °C. IR (cm^{-1}): 3311 (NH_2), 2951, 2929, 2858 (CH_2), 1703, 1655 (C=O). ^{1}H-NMR (500.16 MHz, DMSO-d_6): δ 10.88 (br, 1H, NH), 8.05 (s, 1H, NH), 7.82 (d, *J* = 8.1 Hz, 1H, H5), 7.65 (t, *J* = 8.0 Hz, 1H, H7), 7.40 (d, *J* = 9.2 Hz, 1H, H8), 7.28 (t, *J* = 9.2 Hz, 1H, H6), 6.19 (s, 2H, NH_2), 2.05 (t, *J* = 7.4 Hz, 2H, CH_2b), 1.54 (m, 2H, CH_2c), 1.31-1.13 (m, 16H, CH_2), 0.81 (t, *J* = 7.4 Hz, 3H, CH_3). ^{13}C-NMR (100.52 MHz) δ 172.45 (NCO), 167.97 (C4O), 150.68 (NC2N), 148.97 (C3N), 137.70 (C10), 129.35 (C7), 124.97 (C6), 123.94 (C5), 122.64 (C8), 116.4 (C9), 35.10 (CH_2 b), 32.03 (CH_2), 29.75 (CH_2), 29.51 (CH_2) 29.37 (CH_2), 29.27 (CH_3), 29.19 (CH_2), 28.94 (CH_2), 25.31 (CH_2), 22.93 (CH_2), 14.43 (CH_3). MS (FAB, *m*/*z*): 358 (M^+ + 1, 100%); Elemental analysis: C 70.88%, H 9.01%, N 11.53% Calc. for $C_{21}H_{31}N_3O_2$, C 70.55%, H 8.74%, N 11.75%

N-(2-amino-4-oxo-1,4-dihydroquinolin-2-yl)tetradecanamide (**4h**) White solid. mp > 250 °C. IR (cm^{-1}): 3314 (NH_2), 2949, 2930, 2858 (CH_2), 1702, 1654 (C=O). ^{1}H-NMR (500.16 MHz, DMSO-d_6): δ 10.85 (br, 1H, NH), 8.45 (s, 1H, NH), 7.92 (d, *J* = 8.1 Hz, 1H, H5), 7.43 (t, *J* = 8.0 Hz, 1H, H7), 7.27 (d, *J* = 9.2 Hz, 1H, H8), 7.14 (t, *J* = 9.2 Hz, 1H, H6), 6.17 (s, 2H, NH_2), 2.05 (br, 2H, CH_2b), 1.44 (m, 2H, CH_2c), 1.33-1.11 (m, 20H, CH_2), 0.75 (br, 3H, CH_3). ^{13}C-NMR (100.52 MHz) δ 170.72 (NCO), 166.88 (C4O), 148.85 (NC2N), 145.59 (C3N), 134.81 (C10), 131.09 (C7), 125.13 (C6), 123.42 (C5), 121.92(C8), 116.48 (C9), 34.21 (CH_2 b), 31.88 (CH_2), 29.94 (CH_2), 29.71 (CH_2), 29.41 (CH_2), 29.39 (CH_2), 29.31 (CH_2), 28.98 (CH_2), 28.95 (CH_2), 28.89 (CH_2), 24.85 (CH_2), 22.35 (CH_2), 14.31 (CH_3).MS (FAB, *m*/*z*): 386 (M^+ + 1, 100%); Elemental analysis: C 71.61%, H 9.27%, N 10.72 % Calc. for $C_{23}H_{35}N_3O_2$, C 71.65%, H 9.15%, N 10.90%

N-(2-amino-4-oxo-1,4-dihydroquinolin-2-yl)hexadecanamide (**4i**) White solid. mp > 250 °C. IR (cm^{-1}): 3334 (NH_2), 2960, 2934, 2870 (CH_2), 1701, 1654 (C=O). ^{1}H-NMR (500.16 MHz, DMSO-d_6): δ 10.94 (s, 1H, NH)8.47 (s, 1H, NH), 7.92 (s, 1H, H5), 7.43 (br, 1H, H7), 7.40 (s, 1H, H8), 7.27 (t, *J* = 9.2 Hz, 1H, H6), 6.14 (s, 2H, NH), 2.05 (s, 2H, CH_2b), 1.54 (m, 2H, CH_2c), 1.36-1.03 (m, 24H, CH_2), 0.81 (br, 3H, CH_3). ^{13}C-NMR (100.52 MHz) δ 171.27 (NCO), 164.91 (C4O), 149.25 (NC2N), 144.94 (C3N), 134.61 (C10),

130.94 (C7), 125.02 (C6), 123.22 (C5), 121.78(C8), 116.56 (C9), 34.01 (CH_2 b), 31.47 (CH_2), 29.45 ($2CH_2$), 29.44 ($2CH_2$), 29.41 (CH_2), 29.40 (CH_2), 29.36 (CH_2), 29.29 (CH_2), 29.06 (CH_2), 28.99 (CH_2), 24.85 (CH_2), 22.54 (CH_2), 14.39 (CH_3). MS (FAB, *m*/*z*): 414 (M^+ + 1, 100%); Elemental analysis: C 72.41%, H 9.57%, N 10.28% Calc. for $C_{25}H_{39}N_3O_2$, C 72.60%, H 9.50%, N 10.16%

4.2. Evaluation of Biofilm Inhibition

Biofilm inhibition studies were carried out on *Staphylococcus aureus* (ATCC 33862) and *Pseudomonas aeruginosa* (ATCC 10145), which have been characterized as biofilm forming strains [41,42] using a previously reported method [43,44] and tannic acid as the known biofilm inhibitorv [29]. Briefly, preinoculums of the bacteria strains were grown in trypticase soy broth (TSB) overnight. Then, 5 mL of cultured broth was diluted with sterile TSB to an optical density of 0.1 at 600 nm, and 200 μL of this mixture was transferred to a well of a flat-bottomed polystyrene 96-well microplate (Costar 3370). 10 μL of a stock solution of the test compound dissolved in DMSO was added and mixed into the well to give the desired final concentration of compound per well. All compounds were tested in triplicate at concentrations of 20, 100, and 250 μM. Wells with only cultured TSB and sterile TSB and 10 μL of DMSO were included as positive and negative controls, respectively. Microplates were incubated for 24 h at 37 °C. Growth inhibition was determined by measuring the OD_{600} of compound-treated wells and control wells in a Biotek Epoch™ absorbance microplate reader (BioTek Instruments, Inc., Winooski, VT). Liquid culture was discarded, and non-adherent bacteria were removed by washing 3 times with distilled water. Remnant biofilm was fixed with methanol and was stained with 200 μL of crystal violet (CV) at 0.1% in water for 10 min, excess CV was removed, and wells were washed again 3 times with distilled water. 100 μL of DMSO was added to dissolve CV and absorbance was quantified at 620 nm. Biofilm inhibition was determined by comparison of the absorbance of compound-treated wells to the absorbance of untreated wells as follows:

$$\%\text{biofilm inhibition} = \frac{(A_{\text{control}} - A_{\text{treated}})}{A_{\text{control}}} \times 100 \quad (2)$$

where A_{control} is the absorbance of untreated wells and A_{treated} is the absorbance of compound-treated wells.

4.3. Inhibition of Pyocyanin Formation

The effect of compounds **3g** and **4g** on pyocyanin biosynthesis was evaluated using a previously reported methodology in triplicate [45]. Briefly, preinoculums of the bacteria strains were added to 50 mL of sterile TSB to an optical density at 600 nm (OD_{600}) of 0.1. To 6 mL of this last suspension, 100 μL of a solution of **3i** or **4g** in dissolved DMSO was added to obtain a final concentration of 20 μM of the tested compound, which was incubated for 24 hrs. Cultured broth without **3g** or **4g** was used as the control. After incubation, 2 mL of chloroform was added, and the mixture was centrifuged (5000 g for 5 min). The bluish bottom layer was transferred to a new tube and 1.5 mL of 0.2 M HCl was added. The aqueous layer was separated and the absorbance at 520 μm was determined using 0.2 M HCl as the blank. The A_{520} of the untreated cultured broth was set to be 100% of the pyocyanin formation.

4.4. Molecular Docking

The structures of compounds **3a-i** and **4a-i** were constructed using ChemSketch (Advanced Chemistry Development, Inc., Toronto, ON, Canada) [31] and their geometry optimized using Spartan'10 [46] using MMFF//HF 6-31 G*. The docking studies were carried out using the crystal structures of PqsD (PDB code: 3H78 [39]) and LasR (PDB code: 2UV0 [37]) from *P. aeruginosa*. In the case of PqsD, the 3H78 structure is a complex of anthranilic acid with a C112A mutation of PqsD, then the alanine residue was changed to original cysteine using the mutation protocol included as part of Molegro Virtual Docker v.6.0.1 (Qiagen Bioinformatics, Aarhus, Denmark) [47,48], which interchanges the residues and performs an energy minimization to consider the potential changes induced by the

amino acid mutation. Protein structures were retrieved from the Protein Data Bank [49]. All water molecules and cocrystallized ligands were removed from the downloaded structures. Docking studies were carried out in Molegro Virtual Docker v.6.0.1 (Qiagen Bioinformatics, Aarhus, Denmark) using the standard protocol referred by the fabricant. Active sites of each protein were selected as the searching sites and delimited in a 15 Å sphere. The assignments of charges on each protein and the analyzed ligands were based on standard templates as part of the program. *MolDock Optimizer* was selected as a searching algorithm with 50 runs and *Moldock score* as the scoring scheme. The poses with the lowest score (higher theoretical affinity) of each compound were selected for further analysis. To evaluate the efficacy of this procedure, the cocrystallized ligand in LasR was also included in the docking study of its respective receptor; the RMSD of the pose of the lowest energy was lower than 2 Å.

4.5. Molecular Dynamics Simulations

The docking poses of **4a**, **4g**, and **4i** with both PqsD and LasR were further analyzed using molecular dynamics (MD) to analyze the stability and conformational changes of the predicted complexes. The MD simulations were run using YASARA v.18.4.24 [50,51] using the AMBER 14 force field [52]. The initial structures were taken from the poses with the lowest docking score of each complex and were placed in a cell box that had an extension of 10 Å larger on each side of the protein and was filed with water molecules. Periodic boundary conditions were applied. The temperature was set at 298 K, water density to 0.997 g/cm^3, and pH to a value of 7.4. Sodium (Na^+) and chlorine (Cl^-) ions were included to provide conditions that simulate a physiological solution (NaCl 0.9%). The cutoff for van der Waals interactions was 8 Å and the Particle Mesh Ewald algorithm was applied to evaluate long range electrostatic interactions. A multiple step of 2.5 fs was set, and data were collected per 100 ps to a final simulation time of 40 ns. The results were analyzed with a script included as part of the YASARA software and included the root mean square deviation (RMSD), root mean square fluctuations (RMSF), and ligand binding energy variations (using MM-PBSA calculations) along the simulation time.

5. Conclusions

In conclusion, we prepared some long chain amide derivatives of 2-amino-4-quinolone and 2,3-diamino-4-quinolone that inhibited biofilm formation in *P. aeruginosa.* The activity increased with the number of carbons present in the aliphatic chain, the compounds with 12 carbon atoms being the most active. This could be explained in terms of the potential affinity to LasR and PqsD as suggested from molecular docking and MD simulations. Compound **4g** is an attractive new starting point for the development of QSIs, however, solubility issues are a concern. Additional in vitro experiments to validate our hypothesis and the design of more soluble derivatives are currently underway in our research group.

Supplementary Materials: The following are available online at http://www.mdpi.com/1420-3049/24//327/s1, Figures S1 and S2: 2D ligand interaction diagrams of **4g** with PqsD and LasR; Figure S3: Representative NMR spectra.

Author Contributions: Conceptualization and methodology: M.A.L-M., A.C.-N., A.A.-C.; investigation and validation: M.P.E.-V., S.B.-A., A.E.D.-E., J.F.S.-T, D.F.G.D.-R., O.J.Q.-R.; formal analysis: M.A.L.-M., M.P.E.-V., S.A.-B., A.E.D.-E., J.F.S.-T., D.F.G-R., O.J.Q.-R, A.C.-N; writing-original draft preparation: M.A.L.-M., A.C.-N.; writing-review and editing: all authors; visualization: M.A.L.-M., J.F.S.-T.; funding acquisition and project administration: M.A.L.-M., A.A.-C.; supervision: M.A.L.-M.

Funding: This research was funded by UNIVERSIDAD LA SALLE, grant number SAL 05/16.

Acknowledgments: Authors wish to thank Dirección de Posgrado e Investigación of Universidad La Salle for additional computational resources.

Conflicts of Interest: The authors declare no conflict of interest. The funders had no role in the design of the study; in the collection, analyses, or interpretation of data; in the writing of the manuscript, or in the decision to publish the results.

References

1. Kalia, V.C. Quorum sensing inhibitors: An overview. *Biotechnol. Adv.* **2013**, *31*, 224–245. [CrossRef]
2. Defoirdt, T.; Brackman, G.; Coenye, T. Quorum sensing inhibitors: How strong is the evidence? *Trends Microbiol.* **2013**, *21*, 619–624. [CrossRef] [PubMed]
3. Solano, C.; Echeverz, M.; Lasa, I. Biofilm dispersion and quorum sensing. *Curr. Opin. Microbiol.* **2014**, *18*, 96–104. [CrossRef] [PubMed]
4. Bjarnsholt, T. The role of bacterial biofilms in chronic infections. *APMIS* **2013**, *121*, 1–58. [CrossRef] [PubMed]
5. Dickschat, J.S. Quorum sensing and bacterial biofilms. *Nat. Prod. Rep.* **2010**, *27*, 343. [CrossRef] [PubMed]
6. De la Fuente-Núñez, C.; Reffuveille, F.; Fernández, L.; Hancock, R.E. Bacterial biofilm development as a multicellular adaptation: Antibiotic resistance and new therapeutic strategies. *Curr. Opin. Microbiol.* **2013**, *16*, 580–589. [CrossRef] [PubMed]
7. Majik, M.S.; Parvatkar, P.T. Next generation biofilm inhibitors for Pseudomonas aeruginosa: Synthesis and rational design approaches. *Curr. Top. Med. Chem.* **2014**, *14*, 81–109. [CrossRef]
8. Wilson, M. Bacterial biofilms and human disease. *Sci. Prog.* **2001**, *84*, 235–254. [CrossRef]
9. Sharma, G.; Rao, S.; Bansal, A.; Dang, S.; Gupta, S.; Gabrani, R. Pseudomonas aeruginosa biofilm: Potential therapeutic targets. *Biologicals* **2014**, *42*, 1–7. [CrossRef]
10. Brackman, G.; Coenye, T. Quorum sensing inhibitors as anti-biofilm agents. *Curr. Pharm. Des.* **2015**, *21*, 5–11. [CrossRef]
11. Brackman, G.; Cos, P.; Maes, L.; Nelis, H.J.; Coenye, T. Quorum sensing inhibitors increase the susceptibility of bacterial biofilms to antibiotics in vitro and in vivo. *Antimicrob. Agents Chemother.* **2011**, *55*, 2655–2661. [CrossRef] [PubMed]
12. Zhu, J.; Kaufmann, G.F. Quo vadis quorum quenching? *Curr. Opin. Pharmacol.* **2013**, *13*, 688–698. [CrossRef]
13. Blackwell, H.E.; Fuqua, C. Introduction to Bacterial Signals and Chemical Communication. *Chem. Rev.* **2011**, *111*, 1–3. [CrossRef]
14. Lee, J.; Zhang, L. The hierarchy quorum sensing network in Pseudomonas aeruginosa. *Protein Cell* **2015**, *6*, 26–41. [CrossRef] [PubMed]
15. Storz, M.P.; Maurer, C.K.; Zimmer, C.; Wagner, N.; Brengel, C.; de Jong, J.C.; Lucas, S.; Müsken, M.; Häussler, S.; Steinbach, A.; et al. Validation of PqsD as an Anti-biofilm Target in Pseudomonas aeruginosa by Development of Small-Molecule Inhibitors. *J. Am. Chem. Soc.* **2012**, *134*, 16143–16146. [CrossRef] [PubMed]
16. O'Brien, K.T.; Noto, J.G.; Nichols-O'Neill, L.; Perez, L.J. Potent Irreversible Inhibitors of LasR Quorum Sensing in *Pseudomonas aeruginosa*. *ACS Med. Chem. Lett.* **2015**, *6*, 162–167. [CrossRef]
17. Kalia, M.; Singh, P.K.; Yadav, V.K.; Yadav, B.S.; Sharma, D.; Narvi, S.S.; Mani, A.; Agarwal, V. Structure based virtual screening for identification of potential quorum sensing inhibitors against LasR master regulator in Pseudomonas aeruginosa. *Microb. Pathog.* **2017**, *107*, 136–143. [CrossRef]
18. Sahner, J.H.; Empting, M.; Kamal, A.; Weidel, E.; Groh, M.; Börger, C.; Hartmann, R.W. Exploring the chemical space of ureidothiophene-2-carboxylic acids as inhibitors of the quorum sensing enzyme PqsD from Pseudomonas aeruginosa. *Eur. J. Med. Chem.* **2015**, *96*, 14–21. [CrossRef]
19. Sahner, J.H.; Brengel, C.; Storz, M.P.; Groh, M.; Plaza, A.; Müller, R.; Hartmann, R.W. Combining in Silico and Biophysical Methods for the Development of Pseudomonas aeruginosa Quorum Sensing Inhibitors: An Alternative Approach for Structure-Based Drug Design. *J. Med. Chem.* **2013**, *56*, 8656–8664. [CrossRef]
20. Zhou, Z.; Ma, S. Recent Advances in the Discovery of PqsD Inhibitors as Antimicrobial Agents. *ChemMedChem* **2017**, *12*, 420–425. [CrossRef]
21. Schütz, C.; Empting, M. Targeting the *Pseudomonas* quinolone signal quorum sensing system for the discovery of novel anti-infective pathoblockers. *Beilstein J. Org. Chem.* **2018**, *14*, 2627–2645. [CrossRef] [PubMed]
22. Basak, A.; Abouelhassan, Y.; Kim, Y.S.; Norwood, V.M.; Jin, S.; Huigens, R.W. Halogenated quinolines bearing polar functionality at the 2-position: Identification of new antibacterial agents with enhanced activity against Staphylococcus epidermidis. *Eur. J. Med. Chem.* **2018**, *155*, 705–713. [CrossRef] [PubMed]
23. Zaheer, Z.; Khan, F.A.K.; Sangshetti, J.N.; Patil, R.H.; Lohar, K.S. Novel amalgamation of phthalazine–quinolines as biofilm inhibitors: One-pot synthesis, biological evaluation and in silico ADME prediction with favorable metabolic fate. *Bioorg. Med. Chem. Lett.* **2016**, *26*, 1696–1703. [CrossRef] [PubMed]

24. Zuo, R.; Garrison, A.T.; Basak, A.; Zhang, P.; Huigens, R.W.; Ding, Y. In vitro antifungal and antibiofilm activities of halogenated quinoline analogues against Candida albicans and Cryptococcus neoformans. *Int. J. Antimicrob. Agents* **2016**, *48*, 208–211. [CrossRef] [PubMed]
25. Abouelhassan, Y.; Garrison, A.T.; Burch, G.M.; Wong, W.; Norwood, V.M.; Huigens, R.W. Discovery of quinoline small molecules with potent dispersal activity against methicillin-resistant Staphylococcus aureus and Staphylococcus epidermidis biofilms using a scaffold hopping strategy. *Bioorg. Med. Chem. Lett.* **2014**, *24*, 5076–5080. [CrossRef] [PubMed]
26. Speck-Planche, A.; Kleandrova, V.V.; Scotti, M.T. Fragment-based approach for the in silico discovery of multi-target insecticides. *Chemom. Intell. Lab. Syst.* **2012**, *111*, 39–45. [CrossRef]
27. Aleksić, I.; Šegan, S.; Andrić, F.; Zlatović, M.; Moric, I.; Opsenica, D.M.; Senerovic, L. Long-Chain 4-Aminoquinolines as Quorum Sensing Inhibitors in *Serratia marcescens* and *Pseudomonas aeruginosa*. *ACS Chem. Biol.* **2017**, *12*, 1425–1434. [CrossRef]
28. Maurino-Reyes, E.D.J.; Gonzalez-Rodriguez, E.; Reyes-Rangel, F.; Lira-Rocha, A.; Loza-Mejia, M.A. A direct synthetic route to fused tricyclic quinolones from 2,3-diaminoquinolin-4(1H)one. *Heterocycl. Commun.* **2016**, *22*, 169–173. [CrossRef]
29. Peeters, E.; Hooyberghs, G.; Robijns, S.; Waldrant, K.; De Weerdt, A.; Delattin, N.; Liebens, V.; Kucharíková, S.; Tournu, H.; Verstraeten, N.; et al. Modulation of the Substitution Pattern of 5-Aryl-2-Aminoimidazoles Allows Fine-Tuning of Their Antibiofilm Activity Spectrum and Toxicity. *Antimicrob. Agents Chemother.* **2016**, *60*, 6483–6497. [CrossRef]
30. Abad-Zapatero, C.; Metz, J.T. Ligand efficiency indices as guideposts for drug discovery. *Drug Discov. Today* **2005**, *10*, 464–469. [CrossRef]
31. Advanced Chemistry Development ChemSketch. Available online: www.acdlabs.com (accessed on 1 December 2018).
32. Verdonk, M.L.; Rees, D.C. Group Efficiency: A Guideline for Hits-to-Leads Chemistry. *ChemMedChem* **2008**, *3*, 1179–1180. [CrossRef] [PubMed]
33. Cavalluzzi, M.M.; Mangiatordi, G.F.; Nicolotti, O.; Lentini, G. Ligand efficiency metrics in drug discovery: The pros and cons from a practical perspective. *Expert Opin. Drug Discov.* **2017**, *12*, 1087–1104. [CrossRef] [PubMed]
34. Park, S.; Kim, H.-S.; Ok, K.; Kim, Y.; Park, H.-D.; Byun, Y. Design, synthesis and biological evaluation of 4-(alkyloxy)-6-methyl-2H-pyran-2-one derivatives as quorum sensing inhibitors. *Bioorg. Med. Chem. Lett.* **2015**, *25*, 2913–2917. [CrossRef] [PubMed]
35. Hodgkinson, J.T.; Galloway, W.R.J.D.; Wright, M.; Mati, I.K.; Nicholson, R.L.; Welch, M.; Spring, D.R. Design, synthesis and biological evaluation of non-natural modulators of quorum sensing in Pseudomonas aeruginosa. *Org. Biomol. Chem.* **2012**, *10*, 6032–6044. [CrossRef] [PubMed]
36. Leeson, P.D.; Springthorpe, B. The influence of drug-like concepts on decision-making in medicinal chemistry. *Nat. Rev. Drug Discov.* **2007**, *6*, 881–890. [CrossRef] [PubMed]
37. Bottomley, M.J.; Muraglia, E.; Bazzo, R.; Carfi, A. Molecular insights into quorum sensing in the human pathogen Pseudomonas aeruginosa from the structure of the virulence regulator LasR bound to its autoinducer. *J. Biol. Chem.* **2007**, *282*, 13592–13600. [CrossRef] [PubMed]
38. O'Reilly, M.C.; Dong, S.-H.; Rossi, F.M.; Karlen, K.M.; Kumar, R.S.; Nair, S.K.; Blackwell, H.E. Structural and Biochemical Studies of Non-native Agonists of the LasR Quorum-Sensing Receptor Reveal an L3 Loop "Out" Conformation for LasR. *Cell Chem. Biol.* **2018**, *25*, 1128–1139.e3. [CrossRef]
39. Bera, A.K.; Atanasova, V.; Robinson, H.; Eisenstein, E.; Coleman, J.P.; Pesci, E.C.; Parsons, J.F. Structure of PqsD, a *Pseudomonas* Quinolone Signal Biosynthetic Enzyme, in Complex with Anthranilate. *Biochemistry* **2009**, *48*, 8644–8655. [CrossRef]
40. Steinbach, A.; Maurer, C.K.; Weidel, E.; Henn, C.; Brengel, C.; Hartmann, R.W.; Negri, M. Molecular basis of HHQ biosynthesis: Molecular dynamics simulations, enzyme kinetic and surface plasmon resonance studies. *BMC Biophys.* **2013**, *6*, 10. [CrossRef]
41. Cruciata, M.; Gaglio, R.; Scatassa, M.L.; Sala, G.; Cardamone, C.; Palmeri, M.; Moschetti, G.; La Mantia, T.; Settanni, L. Formation and Characterization of Early Bacterial Biofilms on Different Wood Typologies Applied in Dairy Production. *Appl. Environ. Microbiol.* **2018**, *84*, e02107-17. [CrossRef]
42. Pires, D.; Sillankorva, S.; Faustino, A.; Azeredo, J. Use of newly isolated phages for control of Pseudomonas aeruginosa PAO1 and ATCC 10145 biofilms. *Res. Microbiol.* **2011**, *162*, 798–806. [CrossRef]

43. Kwasny, S.M.; Opperman, T.J. Static biofilm cultures of Gram-positive pathogens grown in a microtiter format used for anti-biofilm drug discovery. *Curr. Protoc. Pharmacol.* **2010**, *50*, 13A.8.1–13A.8.23. [CrossRef]
44. Martínez Díaz, Y.; Vanegas Laverde, G.; Reina Gamba, L.; Mayorga Wandurraga, H.; Arévalo-Ferro, C.; Ramos Rodríguez, F.; Duque Beltrán, C.; Castellanos Hernández, L. Biofilm inhibition activity of compounds isolated from two Eunicea species collected at the Caribbean Sea. *Rev. Bras. Farmacogn.* **2015**, *25*, 605–611. [CrossRef]
45. Tapia-Rodriguez, M.R.; Hernandez-Mendoza, A.; Gonzalez-Aguilar, G.A.; Martinez-Tellez, M.A.; Martins, C.M.; Ayala-Zavala, J.F. Carvacrol as potential quorum sensing inhibitor of Pseudomonas aeruginosa and biofilm production on stainless steel surfaces. *Food Control.* **2017**, *75*, 255–261. [CrossRef]
46. Wavefunction Inc Spartan '10. Available online: www.wavefun.com (accessed on 1 December 2018).
47. Thomsen, R.; Christensen, M.H. MolDock: A New Technique for High-Accuracy Molecular Docking. *J. Med. Chem.* **2006**, *49*, 3315–3321. [CrossRef]
48. CLC Bio Molegro Virtual Docker. Available online: https://www.qiagenbioinformatics.com/ (accessed on 1 December 2018).
49. Berman, H.M.; Westbrook, J.; Feng, Z.; Gilliland, G.; Bhat, T.N.; Weissig, H.; Shindyalov, I.N.; Bourne, P.E. The Protein Data Bank. *Nucleic Acids Res.* **2000**, *28*, 235–242. [CrossRef]
50. Krieger, E.; Vriend, G. New ways to boost molecular dynamics simulations. *J. Comput. Chem.* **2015**, *36*, 996–1007. [CrossRef] [PubMed]
51. Yasara Dynamics. Available online: www.yasara.org (accessed on 1 December 2018).
52. Maier, J.A.; Martinez, C.; Kasavajhala, K.; Wickstrom, L.; Hauser, K.E.; Simmerling, C. ff14SB: Improving the Accuracy of Protein Side Chain and Backbone Parameters from ff99SB. *J. Chem. Theory Comput.* **2015**, *11*, 3696–3713. [CrossRef] [PubMed]

Sample Availability: Samples of the compounds **3a-i** and **4a-i** are available from the authors.

© 2019 by the authors. Licensee MDPI, Basel, Switzerland. This article is an open access article distributed under the terms and conditions of the Creative Commons Attribution (CC BY) license (http://creativecommons.org/licenses/by/4.0/).

molecules

MDPI

Article

Design, Synthesis, Molecular Modeling, and Biological Evaluation of Novel Thiouracil Derivatives as Potential Antithyroid Agents

Samir M. Awad [1], Yasser M. Zohny [1,2], Sahar A. Ali [3], Shahenda Mahgoub [3] and Ahmed M. Said [1,4,*]

1 Pharmaceutical Organic Chemistry Department, Faculty of Pharmacy, Helwan University, Ein-Helwan, Helwan, Cairo 11795, Egypt; samirawad2000@yahoo.com (S.M.A.); dryasserzohny@su.edu.sa (Y.M.Z.)
2 Pharmaceutical Sciences Department, School of Pharmacy, Shaqra University, P.O. Box 11961, Dawadmi 11911, Saudi Arabia
3 Biochemistry and Molecular Biology Department, Faculty of Pharmacy, Helwan University, Ein-Helwan, Helwan, Cairo 11795, Egypt; ganah_nour@yahoo.com (S.A.A.); shahenda.mahgoub@pharm.helwan.edu.eg (S.M.)
4 Department of Chemistry, University at Buffalo, The State University of New York, Buffalo, NY 14260, USA
* Correspondence: ahmedmoh@buffalo.edu; Tel.: +1-716-907-5016

Received: 10 September 2018; Accepted: 30 October 2018; Published: 8 November 2018

Abstract: Hyperthyroidism is the result of uncontrolled overproduction of the thyroid hormones. One of the mostly used antithyroid agents is 6-*n*-propyl-2-thiouracil (PTU). The previously solved X-ray crystal structure of the PTU bound to mammalian lactoperoxidase (LPO) reveals that the LPO-PTU binding site is basically a hydrophobic channel. There are two hydrophobic side chains directed towards the oxygen atom in the C-4 position of the thiouracil ring. In the current study, the structural activity relationship (SAR) was performed on the thiouracil nucleus of PTU to target these hydrophobic side chains and gain more favorable interactions and, in return, more antithyroid activity. Most of the designed compounds show superiority over PTU in reducing the mean serum T4 levels of hyperthyroid rats by 3% to 60%. In addition, the effect of these compounds on the levels of serum T3 was found to be comparable to the effect of PTU treatment. The designed compounds in this study showed a promising activity profile in reducing levels of thyroid hormones and follow up experiments will be needed to confirm the use of the designed compounds as new potential antithyroid agents.

Keywords: hyperthyroidism; thiouracil; pyrimidine; antithyroid; PTU; LPO

1. Introduction

Hyperthyroidism is the abnormal excessive production of the T3 and T4 thyroid hormones by the thyroid gland [1–3]. This uncontrolled production of thyroid hormones could be due to the presence of autoantibodies (Graves' disease) that results in overactivation of the thyroid stimulating hormones (TSH) and, subsequently, overproduction of thyroid hormones [4–7]. In addition, these antibodies stimulate the deiodinases that are responsible for the transformation of prohormone thyroxine (T4) to the triiodothyronine (T3) thyroid hormone. Other causes for the uncontrolled overproduction of thyroid hormones may be inflammation of the thyroid gland or thyroid adenoma [8]. The overproduction of T4 and T3 thyroid hormones can be controlled by either blocking the biosynthesis of the thyroid hormones or by decreasing the conversion of T4 to the active T3 thyroid hormone. These processes could be controlled by specific inhibitors called antithyroid agents [9–13].

Antithyroid agents are relatively simple molecules that are thiourea-based (thionamides) compounds with a thione moiety within a heterocyclic structure. The widely used antithyroid agents

are 6-*n*-propyl-2-thiouracil (PTU), methimazole (MMI), 6-methyl-2-thiouracil (MTU), and carbimazole (CBZ) as well as their selenium analogues [14–17]. The mechanistic details of these agents on how they affect the production of the thyroid hormones are unclear. However, according to the initially proposed mechanism, these agents work by inhibiting the thyroid hormones biosynthesis by interfering with the peroxidase (thyroid peroxidase or lactoperoxidase) mediated iodination of the thyroglobulin tyrosyl residues [18–20]. This is usually done by either forming a stable electron donor-acceptor complex with diiodine or coordinating to the metal center of the thyroid peroxidase. The superfamily of mammalian peroxidases consists of four peroxidases: thyroid peroxidase (TPO), lactoperoxidase (LPO), myeloperoxidase (MPO), and eosinophil peroxidase (EPO) [21]. These peroxidases are covalently linked to a heme (iron containing) group and they use hydrogen peroxide (H_2O_2) as the electron acceptor, which catalyzes various oxidative reactions. TPO is a transmembrane homodimer that plays an important role in the biosynthesis of the thyroid hormones. The inhibition of TPO seems to be an excellent approach to treat hyperthyroidism. Since 6-*n*-propyl-2-thiouracil or its derivatives can inhibit TPO, a complete understanding of how PTU or its derivatives bind to the TPO catalytic binding site is very important. Although low-resolution crystals of TPO were reported over the years, its structure remains to be determined. The closest known homology of TPO is that of LPO, which shares 48% sequence identity with TPO's MPO-like domain [22]. In addition, TPO and LPO share similarity in functional properties. This means that the substrate binding sites are high likely to be similar in both TPO and LPO. This was preliminary proven when PTU was tested against LPO and was found to produce a similar effect to that against TPO, which indicates that PTU have similar binding modes with TPO and LPO. The x-ray crystal structure of LPO revealed a substrate-specific binding mode [19–26]. The LPO has its substrate-binding cleft located on the distal heme side. This will be the site where the PTU or any close derivative proposed will bind. In the current study, five different series of thiouracil derivatives were designed, synthesized, and biologically tested (PTU was used as the control drug) to provide more biologically active thiourea-pyrimidine based analogues (Thiouracil) that could be developed further as antithyroid agents. In addition, the binding mode of some analogues to the mammalian LPO was compared to the binding mode of PTU using molecular modeling. The structural differences between the new derivatives and the PTU are changes at positions 4- and 5- of the thiouracil nucleus in the new analogues. In addition, a fused ring (5- or 6- membered) with the pyrimidine ring of the thiouracil was added. These structural changes were performed to investigate how further changes on the thiouracil nucleus could affect the antithyroid activity of these compounds against the excessive secretions of the thyroid hormones T3 and T4 in rats.

2. Results and Discussion

2.1. Chemistry

The pyrimidine nucleus itself is unreactive toward electrophilic substitution reactions due to the -I and -M effects of the two nitrogen atoms while 2-thiouracil nucleus (**1**) is active due to the electron releasing effect of -OH and -SH groups [27,28]. Thus, 2-thiouracil could be chlorosulphonated in a good yield, which was reported by Fathalla et al. [29] to give an active sulphonyl chloride (**2**). A positive Lassaigne's test confirmed this transformation and the appearance of a doublet peak at C6 in its H-NMR spectrum. The sulphonyl chloride (Scheme 1) was reacted with isomers of anisidine (*o*, *m*, and *p*-anisidine) in the presence of a base such as pyridine in ethanol yielding 2-thiouracil-5-sulphonamide derivatives (**3A**–**3C**).

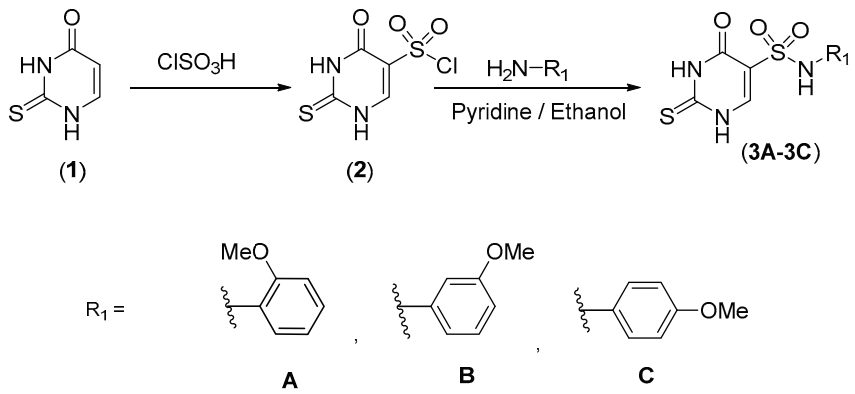

Scheme 1. Synthesis of intermediates **3A**–**3C**.

The thiouracil intermediates (**3A**–**3C**) were then chlorinated (Scheme 2) using the $POCl_3/PCl_5$ mixture giving active chloropyrimidine derivatives (**4A**–**4C**). These chloro compounds reacted with *p*-aminoacetophenone in pyridine as a solvent and base yielding aniline compounds **5A**–**5C**. The chlorinated compounds were also hydrazinolysed by NH_2NH_2 and gave hydrazinopyrimidines **6A**–**6C**. In another pathway, they were cyclo-condensed with glycine in butanol, which gave imidazopyrimidines (**7A**–**7C**).

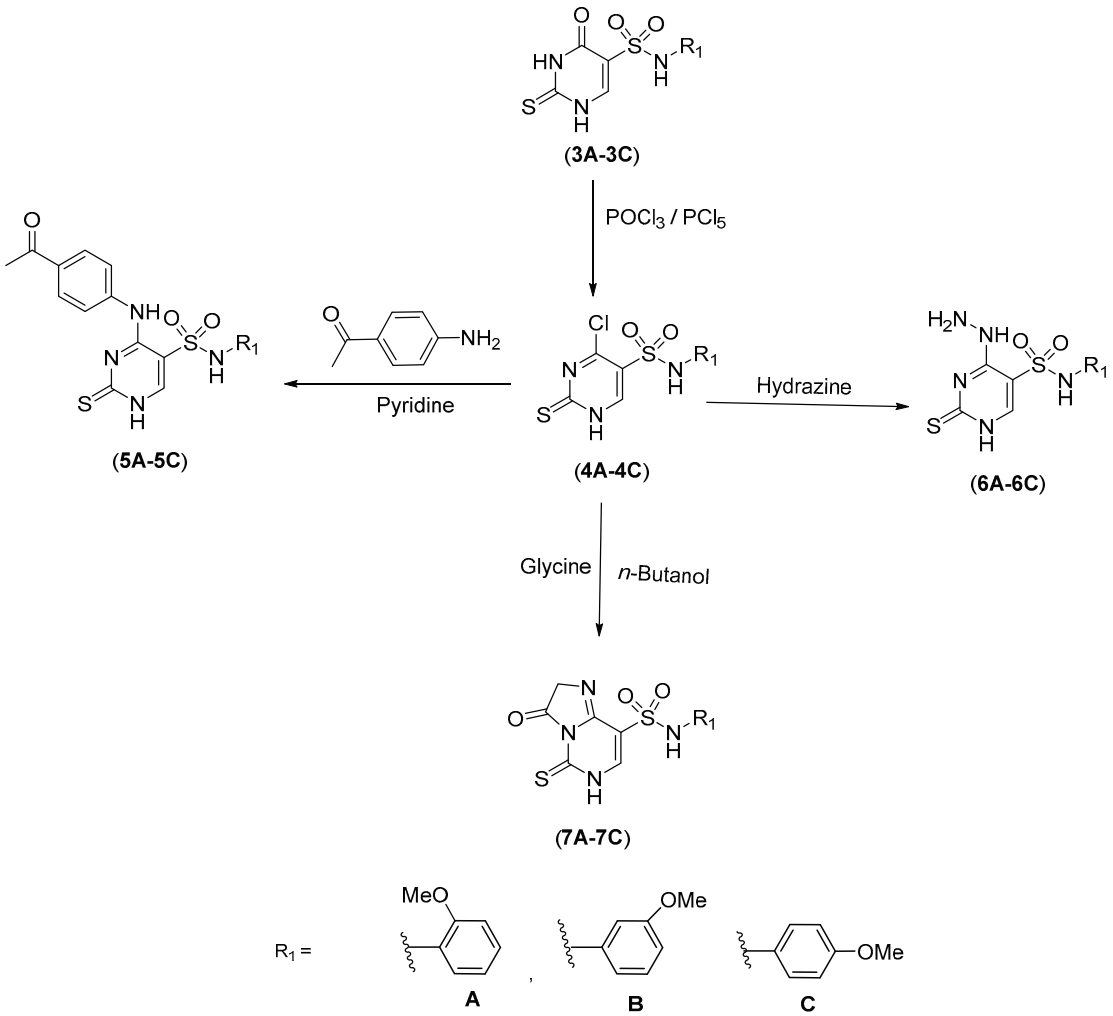

Scheme 2. Synthesis of compounds **4A**–**4C**, **5A**–**5C**, **6A**–**6C,** and **7A**–**7C**.

The formed hydrazinopyrimidines (**6A–6C**) were used in several pathways. The first pathway had these compounds further cyclo-condensed (Scheme 3) with Ac_2O into triazolopyrimidines (**8A–8C**). The second pathway reacted with the hydrazinopyrimidines with trimethyl orthoformate giving triazolopyrimidines (**9A–9C**). The third pathway gave pyrimidotriazines **10A–10C** by reaction with diethyl oxalate. The fourth pathway had these compounds condensed with *p*-nitro benzaldehyde and gave the corresponding Schiff's bases (**11A–11C**).

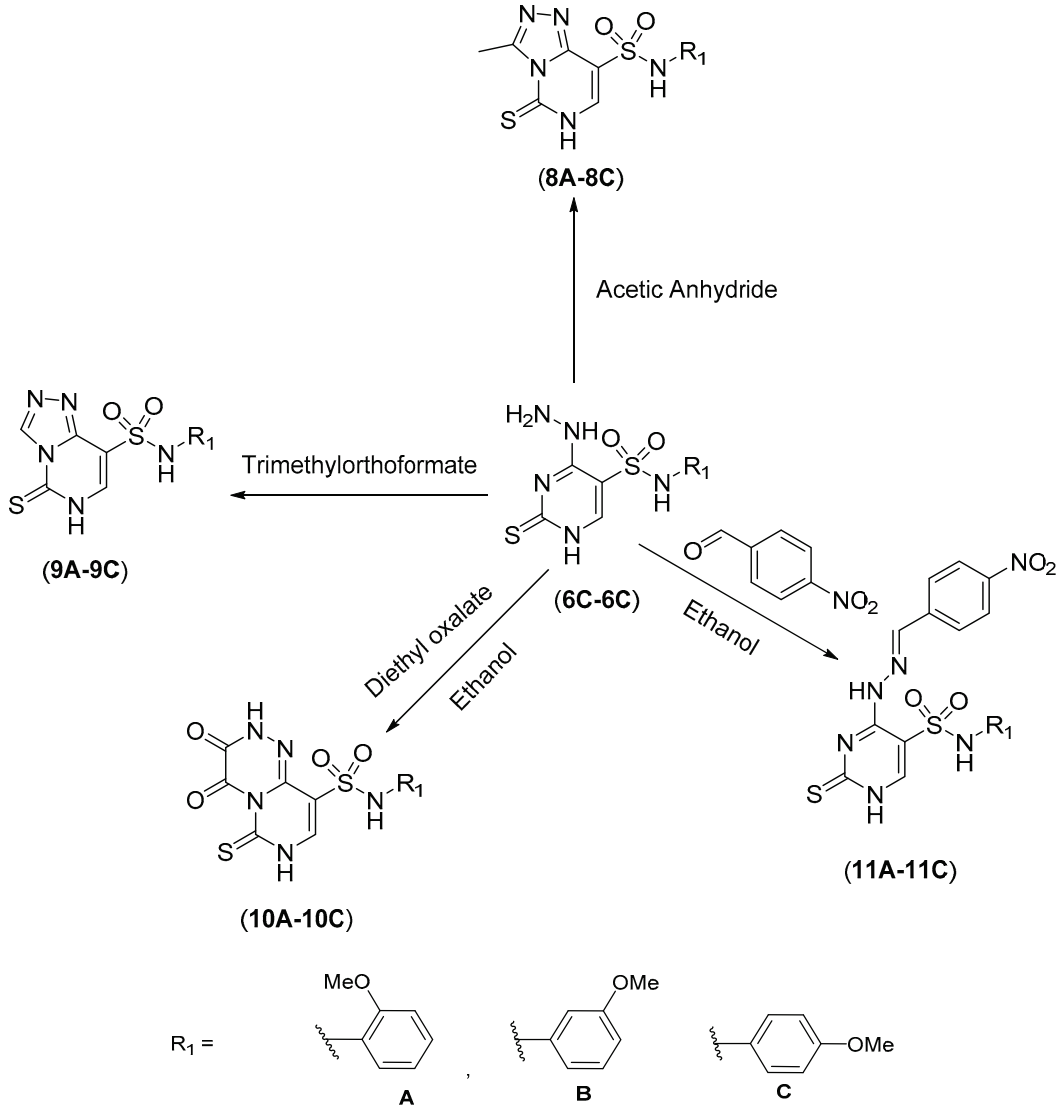

Scheme 3. Synthesis of compounds **8A–8C**, **9A–9C**, **10A–10C**, and **11A–11C**.

2.2. Molecular Modeling and Binding Mode Prediction

One way to overcome the undesirable state of hyperthyroidism is by inhibiting the function of the mammalian peroxidases TPO and LPO, which catalyze the biosynthesis of thyroid hormones. In a recent study, PTU was shown to have similar IC_{50} values against TPO (30 μM) and LPO (47 μM), respectively [19–26]. This suggests that the PTU binds similarly to both TPO and LPO substrate binding sites. The crystal structure of PTU bound to LPO was recently solved and the binding mode was revealed [22]. To predict and understand the binding mode and the interactions of the designed compounds inside the active site of LPO, the crystal structure (PDB: 5HPW) was used. All the modeling (docking) experiments described here were performed by using the Discovery Studio version 4.5 (Accelrys Inc., San Diego, CA, USA). The required LPO bound to PTU coordinates were

downloaded from the Brookhaven website (www.rcsb.org). The hydrogen atoms were then added to both the small molecule and the enzyme. The atom and bond types as well as the protonation state for the small molecule and the binding site residues were checked and corrected when needed. Water molecules were deleted. This was followed by minimizing the complex with the Discovery Studio (DS) force field by using the default parameters. The co-crystal structure (Figure 1a) reveals that PTU binds in the substrate-binding site on the distal heme side of LPO. The orientation of the S-atom of PTU was found to be directed towards the iron center of the heme side. The *n*-propyl hydrophobic side chain on the six-position engages in van der Waals interactions with atoms of neighboring amino acids in the binding site such as Gln 105, His 109, Ala 114, Arg 255, and Glu 258 [23]. These interactions were found to be responsible for the strong binding of PTU to the LPO binding site. The structure of the substrate-binding site where the PTU binds revealed that there are two hydrophobic side chains protruding into the binding site. These side chains are Phe 381 and Pro 424. These side chains were found to be directed towards the O-atom of PTU. As such, the synthesized analogues were designed to target these additional interactions. The modeling studies were performed by using the PTU co-crystal structure with LPO as a starting point and structural changes were performed case by case. The resulting modeled complexes were minimized to convergence by using the DS applied force field. The binding mode for the modeled structures was compared to the binding mode of PTU (Figure 1b) by overlaying the crystal structure of PTU bound to LPO with the modeled structures of the designed compounds. All the modeled structures maintained the same binding mode of PTU.

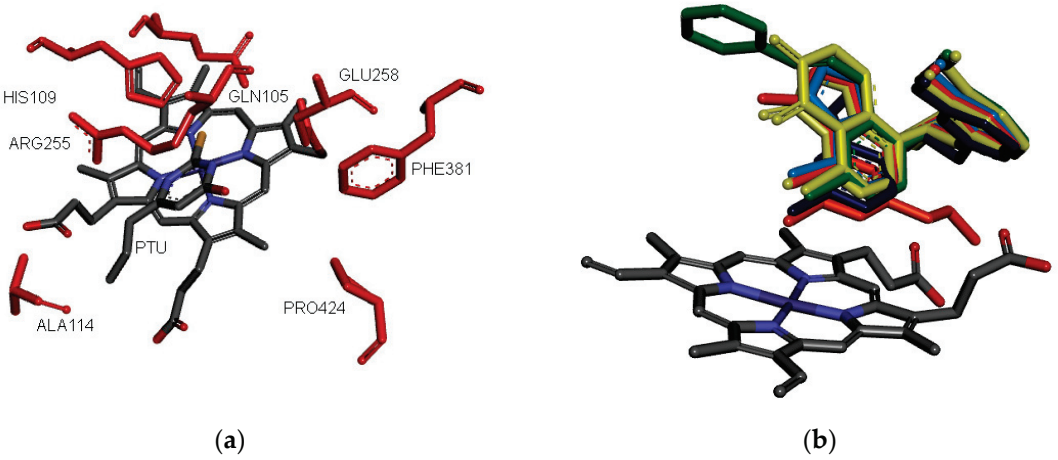

Figure 1. (**a**) Structure of the complex of 6-*n*-propyl-2-thiouracil (PTU) inbound to lactoperoxidase (LPO). (**b**) The overlaying of the modeled structure of inhibitors **6B**, **7B**, **9B**, **10B**, **11B**, and the crystal structure of PTU.

The designed inhibitors bind similarly to PTU by occupying the hydrophobic channel that is near the heme residue. The binding mode of the designed inhibitors inbound to the LPO binding site are included in the Supplementary Material. It is expected that these compounds will have a similar antithyroid mechanism of action as PTU [25,26]. These compounds, like PTU, are expected to block the synthesis of thyroid hormones by inhibiting the heme containing peroxidases that catalyzes the iodination and coupling of tyrosyl residues on thyroglobulin. In addition, these compounds like PTU could inhibit the iodothyronine deiodinase (ID-1) and, thereby, block the conversion of thyroxine (T4) to 3,3′,5-triiodothyronine (T3) within the thyroid and in peripheral tissues. It should be noted that the designed compounds as well as PTU will only inhibit the formation of new thyroid hormones and will not remove thyroid hormones, which are already in the thyroid or in the blood stream. Further investigation and experiments will be performed in the future to determine the exact antithyroid mechanism of action of these compounds and determine any direct or indirect antithyroid effect for these compounds.

2.3. Biological Screening

The synthesized thiouracil derivatives were evaluated for their antihyperthyroid activity by using a thyroxine-induced hyperthyroid model [30]. The antithyroid activity was obtained by comparing the mean serum T3 and T4 levels in hyperthyroid rats after treatment by using the synthesized thiouracil derivatives as well as the standard PTU. The synthesized compounds (10 mg/kg) were assessed for their anti-thyroid activity using the thyroxine-induced hyperthyroid model, which was comparable to PTU used as the standard antithyroid drug when comparing the mean serum T3 and T4 levels between the different studied groups. Administration of Thyroxine (600 μg/kg) to euthyroid animals significantly increased mean serum levels of T3 and T4 hormones. These results matched with what was observed earlier [31–35]. All rat groups treated with the designed inhibitors (10 mg/kg) showed a significant decrease in the mean serum T4 levels in the hyperthyroid model (except for drugs **5A** and **4B**) compared to the hyperthyroid untreated group, which is depicted in Table 1. Moreover, derivatives **3A**, **4A**, **5A**, **8A**, **10A**, **7B**, **3C**, and **6C** also showed a comparable decrease in the mean serum level of T3 compared to the hyperthyroid untreated group. Comparing the antithyroid activity of these compounds to that of the reference antithyroid drug PTU showed that nearly all the synthesized derivatives showed a significant decrease in the mean serum T4 level (except for drugs **5A** and **4B**), which is shown in Figure 2. However, they were not able to reach this significant reduction in the mean T3 level when compared to PTU. Previous studies [34,35] showed that patients treated with thionamides take three to eight weeks to become euthyroid since they block new hormone synthesis and any already formed thyroxine T4 and T3 stored in the colloid must be secreted and metabolized for clinical improvement to occur. Thus, antithyroid drugs typically reduce levels of both T3 and T4, but levels of T3 may take longer to return to normal. There are several possible explanations for the development of simultaneously high serum T3 and low serum T4 levels in patients with hyperthyroid disease during or after treatment. Iodide organification is impaired by thionamide antithyroid drugs. The resulting increase in iodide leakage from the gland creates a state of intrathyroidal iodine deficiency, which favors T3 production. Furthermore, hyperthyroidism is associated with increased T4 5′-deiodinase activity in both the thyroid gland and extrathyroidal tissues, which leads to increased T4 to T3 conversion. This agrees with the study results, which showed that the designed compounds reduced the serum T4 more than T3 levels in hyperthyroid rats.

Table 1. Effect of various treatments on the mean serum levels of T3 and T4 in rats.

Groups	Serum T3 (ng/mL)	Serum T4 (μg/dL)
Control	60.5 ± 5.08	4.45 ± 1.1
Hyperthyroid group	115.5 ± 22.47 *	9.96 ± 1.28 **
Standard (PTU 10 mg/kg)	42.4 ± 1.44 ##	6.06 ± 0.58 #
Compound **3A**	57.43 ± 1.43 ##	4.86 ± 0.48 ##
Compound **4A**	64.57 ± 3.96 #	4.60 ± 0.24 ###
Compound **5A**	52.67 ± 2.42 ##	7.88 ± 0.29
Compound **6A**	67.4 ± 1.86 #	4.63 ± 0.67 ##
Compound **8A**	58 ± 3.72 #	5.3 ± 0.4 ##
Compound **10A**	58 ± 4.16 #	4.92 ± 0.28 ##
Compound **3B**	76 ± 2.77	6.03 ± 0.36 #
Compound **4B**	73.67 ± 3.43	6.43 ±1.25
Compound **5B**	83.71 ± 4.61	5.41 ± 0.51 ##
Compound **6B**	91.83 ± 6.84	5.06 ± 0.502 ##
Compound **7B**	58.83 ± 3.49 #	5.28 ± 0.63 #
Compound **9B**	70.67 ± 3.35	5.92 ± 0.61 #
Compound **3C**	64.57 ± 1.94 #	5.62 ± 0.83 #
Compound **5C**	67.6 ± 3.91 #	3.58 ± 0.35 ###
Compound **6C**	57.14 ± 2.52 ##	5.97 ± 0.69 #
Compound **7C**	79.29 ± 4.79	5.31 ± 0.49 ##
Compound **9C**	74.13 ± 3.91	4.19 ± 0.61 ###

*: significant from the control group at $p < 0.05$. **: significant from the control group at $p < 0.01$ and 0.001. #, ## and ###: significant from hyperthyroidism group at $p < 0.05$, 0.01 and 0.001, respectively.

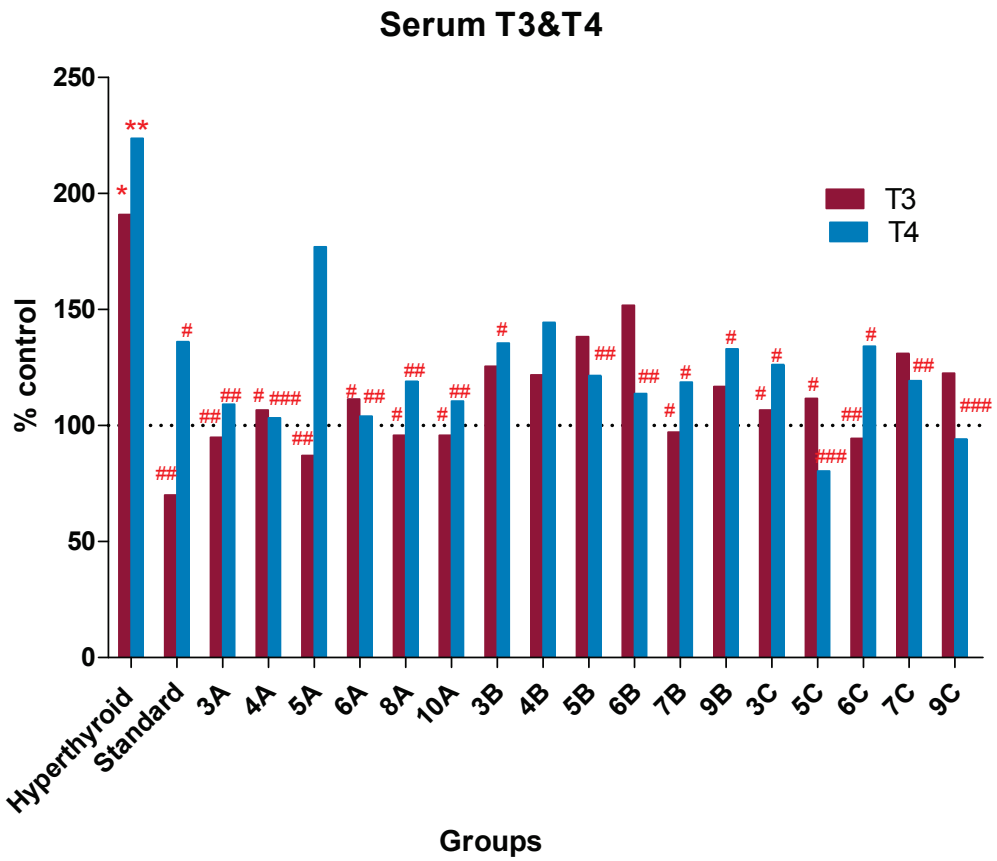

Figure 2. Effect of antithyroid derivatives on the mean serum levels of T3 and T4 in rats. Data are presented as the percentage in the control group. *: significant from the control group at $p < 0.05$. **: significant from the control group at $p < 0.01$ and 0.001. #, ## and ###: significant from Hyperthyroidism group at $p < 0.05$, 0.01 and 0.001, respectively.

As shown in Figures 2 and 3, the effect of the designed inhibitors on the mean serum level of T4 is significantly more potent (3% to 60% more) than the effect exerted by PTU except drugs **5A** and **4B**, which suggests an anti-thyroid role for these derivatives. However, only drugs (**3A**, **4A**, **5A**, **8A**, **10A**, **7B**, **3C**, and **6C** showed a comparable decrease in the mean serum level of T3 (Figure 3) compared to the hyperthyroid untreated group. In addition, lower potency was compared to the standard PTU drug. Our observations, therefore, revealed that the antithyroid effect produced by the treatment of the hyperthyroid rats with the thiouracil derivatives for 14 days was more significant on serum T4 levels than serum T3 levels.

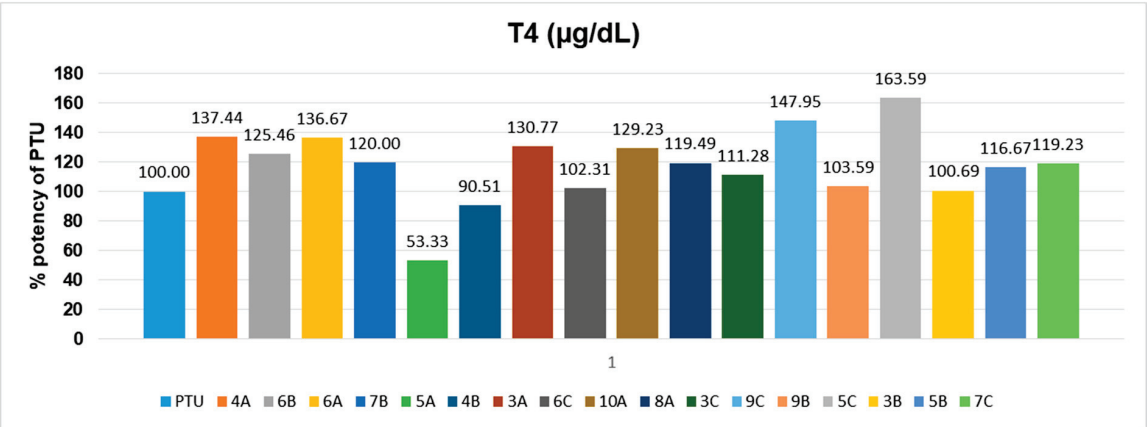

Figure 3. *Cont.*

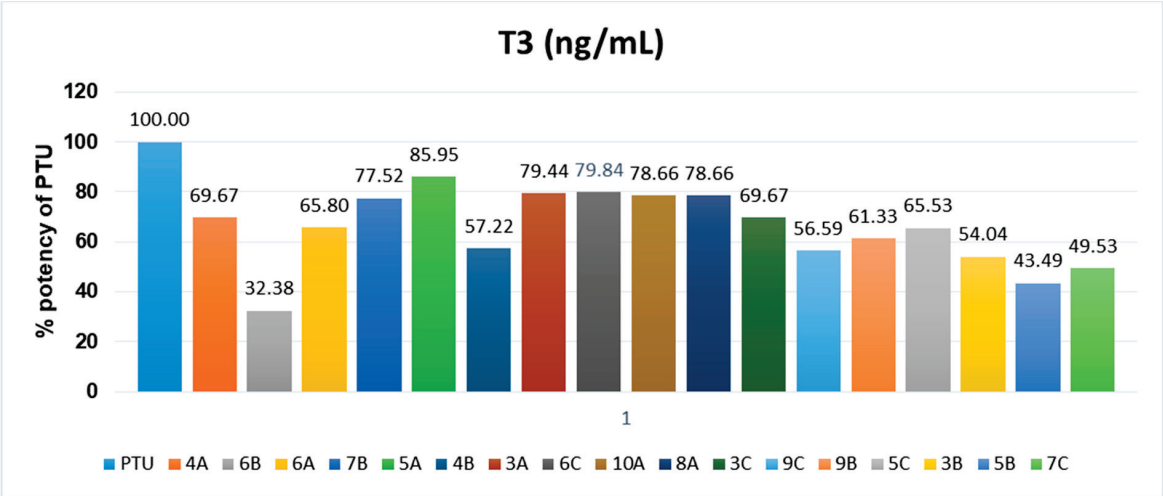

Figure 3. Potency of antithyroid derivatives compared to 6-*n*-propyl-2-thiouracil (PTU).

In addition, SAR strategies performed in this study involved replacement of =O (C4) with –Cl, which is shown in compounds **4A**–**4C**. This strategy slightly improved activity against T4 hormone levels (comparing **3A** to **4A**, 5% improvement). However, the activity against T3 hormone levels was not improved. Our second strategy was to replace =O with a *p*-acetyl aniline side chain as in compounds **5A**–**5C**. This strategy significantly improved the activity of the compounds against T4 hormone levels (Comparing **3C** to **5C**, 36% improvement). The activity against T3 hormone levels was also maintained. Our third strategy was to replace =O with the -$NHNH_2$ group. This strategy-maintained activity against both T3 and T4 hormones levels (compare **3A** to **6A**). The final strategy was to form a fused ring (five or six membered) to the thiouracil ring. This strategy somewhat maintains activity against T3 and T4 hormone levels.

In general, the data of selected pyrimidine derivatives **3A**, **4A**, **5A**, **6A**, **7A**, **8A**, **9A**, **10A**, and **11A** showed that 2-thiouracil-5-sulphonamide is active. When chlorinated, it is still active, but when chlorine is replaced by the NH group, the activity is reduced such as in compounds **5A**, **6A**, and **11A**. Cyclo-condensation of chloro derivative **4A** retains the activity such as in compounds **7A**, **8A**, **9A**, and **10A**.

3. Materials and Methods

3.1. General Experimental Methods

All melting points were measured by using an Electrothermal IA 9100 apparatus (Shimadzu, Kyoto, Japan). IR spectra were recorded as potassium bromide pellets on a Perkin-Elmer 1650 spectrophotometer (Perkin-Elmer, Boston, MA, USA). ^{1}H-NMR spectra (300MHz) were recorded in dimethyl sulfoxide (DMSO) by employing tetramethyl silane (TMS) as an internal standard on Varian Mercury 300 MHz NMR Spectrometer (Varian, Crawley, West Sussex, UK) and the chemical shifts (δ) were expressed as ppm against TMS as an internal standard. Electron impact mass spectra (EI) were recorded on a Shimadzu QP–2010 instrument (Shimadzu, Japan) at 70 eV. Microanalyses were operated by using the vario, Elementar apparatus (Shimadzu, Japan). Thin layer Chromatography plates (TLC) (Merck, Kenilworth, NJ, USA) was used to monitor the progress of all the reactions using chloroform-methanol (3:1) as a mobile phase and spots were visualized by iodine vapors or by irradiation with UV-light (254 nm).

*3.2. Synthesis of N-(2,3 or 4-Methoxyphenyl)-4-oxo-2-thioxo-1,2,3,4-tetrahydropyrimidine-5-sulphonamides (**3A–3C**)*

A mixture of 2-thiouracil-5-sulphonamide **2** (1.13 g, 0.005 mol), isomers of anisidine (0.6 g, 0.005 mol), and pyridine (0.4 mL, 0.005 mol) in absolute ethanol (50 mL) was heated under reflux for 12 h and then cooled, filtered off, dried, and recrystallized from dimethyl formamide (DMF)/water.

Yield, **3A** (0.8 g, 67%), m.p. 273 °C to 275 °C. **3B** (0.6 g, 61%), m.p. 256 °C to 258 °C. **3C** (0.5 g, 58%), m.p. 282–284 °C. IR (KBr): 3300–3020 (3 NH, very broad), 1660 (CO), 1320, 1140 (SO_2) cm^{-1}. ^{1}H-NMR (DMSO-d_6): δ 4.1 (s, 3H, OCH_3), 7.1–7.3 (m, 4H, ArH), 8.2 (s, 1H, pyrimidine), 9.8, 10.2, 10.5 (s, 3NH, D_2O-exchangeable). MS (EI) *m/z* (10.43%) 313.12 [M^+]. Analysis for C, H, and N, $C_{11}H_{11}N_3O_4S_2$ Calcd: C, 42.17, H, 3.51, N, 13.42. Found: C, 42.31, H, 3.7, N, 13.55.

*3.3. Synthesis of 4-Chloro-N-(2,3 or 4-methoxyphenyl)-2-thioxo-1,2-dihydropyrimidine-5-sulphonamide (**4A–4C**)*

A mixture of **3A–3C** (0.01 mol) and phosphorus pentachloride (0.01 mol) in phosphorus oxychloride (20 mL) was heated on a steam bath for 3 h and the reaction mixture was poured gradually on crushed ice. The precipitate was filtered off, dried, and then crystallized from DMF/water.

Yield, **4A** (0.6 g, 61%), m.p. 283–284 °C. **4B** (0.7 g, 64%), m.p. 267–268 °C. **4C** (0.8 g, 69%), m.p. 262–264 °C. IR (KBr): 3310–3026 (3 NH, very broad), 1670 (CO), 1325, 1135 (SO_2) cm^{-1}. ^{1}H-NMR (DMSO-d_6): δ 4.2 (s, 3H, OCH_3), 7.1–7.2 (m, 4H, ArH), 8.1 (s, 1H, pyrimidine), 9.7, 10.6 (s, 2NH, D_2O-exchangeable). MS (EI) *m/z* (1.74%) 331.57 [M^+], (0.57%) $[M + 2H]^+$, Analysis for C, H, and N, $C_{11}H_{10}N_3O_3S_2Cl$, Calcd: C, 39.82, H, 3.02, N, 12.67. Found: C, 39.71, H, 3.29, N, 12.45.

*3.4. Synthesis of 4-(4-acetylphenyl) amino]-N-(2,3or4-methoxyphenyl)-2-thioxo-1,2-dihydropyrimidine-5-sulphonamides (**5A–5C**)*

A mixture of **4A–AC** (1 mol) and *p*-aminoacetophenone (1 mol) in pyridine (30 mL) was refluxed for 8 to 10 h and the reaction mixture poured gradually on water and then neutralized until acidification. The precipitate was filtered off, dried, and then crystallized from DMF/water.

Yield, **5A** (0.7 g, 66%), m.p. 243–245 °C. **5B** (0.8 g, 73%), m.p. 286 to 288 °C. **5C** (0.8 g, 65%), m.p. 277–279 °C. IR(KBr): 3315–3028 (3 NH, very broad), 1670 (CO), 1690 (CO) 1322,1145 (SO_2) cm^{-1}. ^{1}H-NMR (DMSO-d_6): δ 2.2 (s, 3H, CH_3), 4.2 (s, 3H, OCH_3), 7.2–7.9 (m, 8H, ArH), 8.3 (s, 1H, pyrimidine), 6.7, 9.6, 10.6 (s, 3NH, D_2O-exchangeable). MS (EI) *m/z* (9.85%) 430.32 [M^+]. Analysis for C, H, and N, $C_{19}H_{18}N_4O_4S_2$ Calcd: C, 53.02, H, 4.19, N, 13.02. Found: C, 53.19, H, 3.99, N, 13.42.

*3.5. Synthesis of 4-Hydrazinyl-N-(2,3 or 4-methoxyphenyl)-2-thioxo-1,2-dihydropyrimidine-5-sulphonamides (**6A–6C**)*

A mixture of **4A–4C** (0.01 mol) and hydrazine hydrate (0.01 mol) in methanol (10 mL) was stirred for 8 h. The precipitate was filtered off, dried, and then crystallized from DMF/water.

Yield, **6A** (0.5 g, 55%), m.p. 263 °C to 265 °C. **6B** (0.6 g, 62%), m.p. 294 °C to 296 °C. **6C** (0.8 g, 68%), m.p. 280 °C to 282 °C. IR(KBr): 3340–3044 (3NH, NH_2 very broad), 1681 (CO), 1320, 1148 (SO_2) cm^{-1}. ^{1}H-NMR (DMSO-d_6): δ, 4.1 (s, 3H, OCH_3), 7.2–7.4 (m, 4H, ArH), 8.1 (s, 1H, pyrimidine), 6.7, 9.6, 10.6, 10.4 (s, NH_2, 3NH, D_2O-exchangeable). MS (EI) *m/z* (18.45%) 325.13 [M^+]. Analysis for C, H, and N, $C_{11}H_{13}N_5O_3S_2$, Calcd: C, 40.62, H, 3.39, N, 21.54. Found: C, 40.47.19, H, 3.41, N, 21.42.

*3.6. Synthesis of N-(2,3 or 4-methoxyphenyl)-3-oxo-5-thioxo-1,2,3,5,6,8a-hexahydroimidazo[1,2-c] pyrimidine-8-sulphonamides (**7A–7C**)*

A mixture of **4A–4C** (0.01 mol) and glycine (0.01 mol) in *n*-butanol (30 mL) was heated under reflux for 3 h. The solid separated was refluxed with anhydrous acetic acid (5 mL) for 2 h. The precipitate was filtered off, dried, and then crystallized from DMF/water.

Yield, **7A** (0.6 g, 57%), m.p. 243–245 °C. **7B** (0.7 g, 64%), m.p. 267 °C to 269 °C. **7C** (0.8 g, 66%), m.p. 287°C to 289 °C. IR (KBr): 3345–3034 (3 NH, very broad), 1687 (CO), 1320, 1140 (SO_2) cm^{-1}.^{1}H-NMR

(DMSO-d_6): δ 2.1(s, 2H, CH_2), 4.2 (s, 3H, OCH_3), 7.1–7.4 (m, 4H, ArH), 8.2 (s, 1H, pyrimidine), 9.7, 10.4, 10.5 (s, 3NH, D_2O-exchangeable). MS (EI) m/z (11.45%) 352.08 [M^+]. Analysis for C, H and N, $C_{13}H_{12}N_4O_4S_2$ Calcd: C, 44.32, H, 3.41, N, 15.91. Found: C, 44.19, H, 3.48, N, 16.02.

*3.7. Synthesis of N-(2,3 or 4-methoxyphenyl)-3-methyl-5-thioxo-5,6-dihydro [1,2,4] triazolo[4,3-c] pyrimidine-8-sulphonamides (**8A–8C**)*

A mixture of **6A–6C** (0.01 mol) and acetic anhydride (30 mL) was heated under reflux for 4 h. The solid obtained was filtered off, dried, and crystallized from DMF/water.

Yield, **8A** (0.6 g, 58%), m.p. 277 °C to 279 °C. **8B** (0.7 g, 68%), m.p. 244 °C to 246 °C. **8C** (0.8 g, 67%), m.p. 276 °C to 278 °C. IR (KBr): 3350–3037 (2NH, very broad), 1320, 1140 (SO_2) cm^{-1}. ^{1}H-NMR (DMSO-d_6): δ 2.3(s, 3H, CH_3), 4.1 (s, 3H, OCH_3), 7.1–7.4 (m, 4H, ArH), 8.1 (s, 1H, pyrimidine), 10.2, 10.5 (s, 2NH, D_2O-exchangeable). MS (EI) m/z (11.45%) 352.08 [M^+]. Analysis for C, H, and N, $C_{13}H_{13}N_5O_3S_2$, Calcd: C, 44.44, H, 3.70, N, 19.94. Found: C, 44.19, H, 3.68, N, 19.77.

*3.8. Synthesis of 8-(N-(2,3 or 4-methoxyphenyl)-5-thioxo-5,6-dihydro [1,2,4] triazolo [4,3-c] pyrimidine-8-sulphonamides (**9A–9C**)*

A mixture of **6A–6C** (0.01 mol) and trimethyl orthoformate (30 mL) was heated under reflux for 6 h. The solid obtained was filtered off, dried, and crystallized from DMF/water.

Yield, **9A** (0.6 g, 58%), m.p. 283 to 285 °C. **9B** (0.8 g, 69%), m.p. 276 to 278 °C. **9C** (0.8 g, 68%), m.p. 297 to 299 °C. IR (KBr): 3335–3027 (2NH, very broad), 1320, 1140 (SO_2) cm^{-1}. ^{1}H-NMR (DMSO-d_6): δ 2.1(s, 1H, CH), 4.1 (s, 3H, OCH_3), 7.2–7.4 (m, 4H, ArH), 8.1 (s, 1H, pyrimidine), 10.2, 10.4 (s, 2NH, D_2O-exchangeable). MS (EI) m/z (11.45%) 337.24 [M^+]. Analysis for C, H, and N, $C_{12}H_{11}N_5O_3S_2$, Calcd: C, 42.73, H, 3.26, N, 20.77. Found: C, 42.87, H, 3.38, N, 20.67.

*3.9. Synthesis of N-(2,3 or 4-methoxyphenyl)-3,4-dioxo-6-thioxo-3,4,6,7-tetrahydro-2H-pyrimido[6,1-c] [1,2,4] triazine-5-sulphonamides (**10A–10C**)*

A solution of **6A–6C** (0.01 mol) and diethyl oxalate (0.01 mol) in absolute ethanol (40 mL) was heated under reflux for 12 h. The solid obtained was filtered off, dried, and crystallized from DMF/water.

Yield, **10A** (0.5 g, 52%), m.p. 267 to 269 °C. **10B** (0.6 g, 64%), m.p. 256 to 258 °C. **10C** (0.6 g, 66%), m.p. 277 to 279 °C. IR (KBr): 3322–3037 (2NH, very broad), 1680, 1687 (2 CO), 1320, 1140 (SO_2) cm^{-1}. ^{1}H-NMR (DMSO-d_6): δ 4.1 (s, 3H, OCH_3), 7.2–7.5 (m, 4H, ArH), 8.2 (s, 1H, pyrimidine), 6.8 10.2, 10.3 (s, 3NH, D_2O-exchangeable). MS (EI) m/z (1.38%) 381.24 [M^+]. Analysis for C, H, and N, $C_{13}H_{11}N_5O_5S_2$, Calcd: C, 40.94, H, 2.89, N, 18.37. Found: C, 40.87, H, 2.99, N, 18.45.

*3.10. Synthesis of N-(2,3 or 4-Methoxyphenyl)-4-[(2E)-2-(4-nitrobenzylidene) hydrazinyl]-2-thioxo-1,2,3,4-tetrahydropyrimidine-5-ulphonamides (**11A–11C**)*

A mixture of **6A–6C** (0.01 mol) and *p*-nitro benzaldehyde (0.01 mol) in ethanol (30 mL) was heated under reflux for 8 h. The solid obtained was filtered off, dried, and crystallized from DMF/water.

Yield, **11A** (0.7 g, 70%), m.p. 257 to 259 °C. **11B** (0.5 g, 54%), m.p. 277 to 278 °C. **11C** (0.8 g, 78%), m.p. 258 to 259 °C. IR (KBr): 3332–3027 (3NH, very broad), 1320, 1140 (SO_2) cm^{-1}. ^{1}H-NMR (DMSO-d_6): δ 4.1 (s, 3H, OCH_3), 6.8 (s, 1H), 7.2–7.4 (m, 8H, ArH), 8.2 (s, 1H, pyrimidine), 6.9, 10.3, 10.5 (s, 3NH, D_2O-exchangeable). MS (EI) m/z (0.837%) 460.12 [M^+]. Analysis for C, H, and N, $C_{18}H_{16}N_6O_5S_2$, Calcd: C, 46.96, H, 3.48, N, 18.26. Found: C, 46.85, H, 3.56, N, 18.33.

3.11. Animals

The complete course of the experiment was conducted by using male Wistar albino rats (200–250 g), reared and maintained in the animal house of the institution, and provided free access to pelleted food and water ad libitum. The rats were maintained in a controlled environment (12 h light and dark cycle) for about a week for acclimatization. The animal ethics committee of the Faculty of Pharmacy,

Helwan University (1 October 2016) approved the protocol of the study. The study was conducted in accordance with the EC, directive 86/609/EEC for animal experiments [32]. (Ethical code number: 0011A-16; Date: 6 December 2016) [32]. After the course of treatment, the rats were still alive and showed no signs of toxicity.

3.12. Induction of Hyperthyroidism

Hyperthyroidism was induced in experimental rats by administrating Thyroxine (600 μg/kg) orally for 14 days, which was previously reported [33] and induction of hyperthyroidism was confirmed by analyzing the serum thyroid hormone levels. Propylthiouracil (PTU (10 mg/kg)) was used as a standard antithyroid drug and administered orally in compliance with literature experiments [34,35]. Equivalent doses from the selected thiouracil derivatives were given orally to the corresponding rat groups. Prior to the main study, a pilot study was done on a few numbers of rats of different groups to compare the changes of their thyroid gland weight (details are in the Supplementary Material) that is assumed to reflect the alteration in thyroid status. Comparison showed no significant difference in the mean weight of thyroid gland between the groups used.

3.13. Experimental Design

One hundred and forty rats (20 groups of 7 rats each) were available to investigate the antithyroid effect of the selected thiouracil derivatives. These rat groups were divided as follows: Group 1 was the normal control and Group 2 included the hyperthyroid induced rats (Thyroxine (600 μg/kg)), which served as a positive control group. Group 3 included hyperthyroid induced rats (Thyroxine (600 μg/kg)) treated with a standard drug (PTU (10 mg/kg)). As in group 3, the hyperthyroid induced rats were used in groups 4–20 (thiouracil derivatives used are **3A**, **4A**, **5A**, **6A**, **8A**, **10A**, **3B**, **4B**, **5B**, **6B**,**7B**, **9B**, **3C**, **5C**, **6C**, **7C**, and **9C**, resp.). The treated groups administered PTU and different derivatives orally for 14 days. For each group, body weights were determined, and blood was collected by a retro-orbital puncture under light ether anesthesia. Serum was separated by centrifugation at 3000 rpm for 10 min and serum produced was used for the biochemical analysis. Serum T3 and T4 levels were analyzed by using Mouse/Rat Triiodothyronine (T3) and Mouse/Rat Thyroxine (T4) ELISA Kits (Sigma-Aldrich Co., St Louis, MO, USA).

3.14. Data Presentation and Statistical Analysis

The data were represented as mean ± SEM. Significant differences between groups were tested by using GraphPad InStat software version 3.05 (GraphPad Inc., La Jolla, CA, USA). Appropriate graphs were plotted when needed using GraphPad Prism version 5 for Windows (GraphPad Inc., USA). A P value less than 0.05 was considered statistically significant.

4. Conclusions

In this study, we have utilized medicinal chemistry coupled with structure-based design strategies to identify more potent thiouracil derivatives that can lower the levels of T4 and T3 thyroid hormones in hyperthyroid rats more than what the standard treatment using PTU can do. The data revealed that we have managed to establish a SAR by doing several modifications to the thiouracil nucleus. All the designed inhibitors significantly reduced the mean serum level of T4 more than the PTU treated group except for compounds **5A** and **4B**. In addition, inhibitors **3A**, **4A**, **5A**, **6A**, **8A**, **10A**, **7B**, **3C**, **5C**, and **6C** showed a comparable effect in decreasing the mean serum level of T3 to that of PTU.

Supplementary Materials: The supplementary materials are available online. Supplementary data includes molecular modeling and binding mode evaluation to representative inhibitors as well as their spectral data.

Author Contributions: S.M.A., Y.M.Z. and A.M.S. synthesized, characterized and analyzed spectral data of all compounds; S.A.A. and S.M. performed the biological testing for all compounds; A.M.S. performed molecular modeling for chosen compounds; S.M.A., Y.M.Z., S.A.A., S.M. and A.M.S. contributed to early manuscript drafts; A.M.S. contributed to writing and finalizing the manuscript and its supplementary materials in their final versions;

S.M.A., Y.M.Z., S.A.A., S.M. and A.M.S. analyzed and interpreted the data for all compounds and contributed equally to the design of this study.

Funding: This research received no external funding.

Acknowledgments: We would like to thank colleagues from the Faculty of Pharmacy, Helwan University for help and support. The corresponding author A.M.S would like to thank David G. Hangauer, University at Buffalo for helpful discussions.

Conflicts of Interest: The authors declare no conflict of interest.

Abbreviations

PTU	6-*n*-propyl-2-thiouracil
LPO	mammalian lactoperoxidase
TPO	thyroid peroxidase
T4	prohormone thyroxine
T3	triiodothyronine thyroid hormone
$POCl_3$	phosphorus oxychloride
PCl_5	Phosphorus pentachloride
Ac_2O	Acetic anhydride

References

1. Gillam, M.P.; Sidhaye, A.R.; Lee, E.J.; Rutishauser, J.; Stephan, C.W.; Kopp, P. Functional Characterization of Pendrin in a Polarized Cell System: Evidence for Pendrin-mediated Apical Iodide Efflux. *J. Biol. Chem.* **2004**, *279*, 13004–13010. [CrossRef] [PubMed]
2. Kopp, P. Mutations in the Pendred Syndrome (PDS/SLC26A) Gene: An Increasingly Complex Phenotypic Spectrum from Goiter to Thyroid Hypoplasia. *J. Clin. Endocrinol. Metab.* **2014**, *99*, 67–69. [CrossRef] [PubMed]
3. Soldin, O.P.; Aschner, M. Effects of Manganese on Thyroid Hormone Homeostasis: Potential Links. *Neurotoxicology* **2007**, *28*, 951–956. [CrossRef] [PubMed]
4. Brent, G.A. Mechanisms of Thyroid Hormone Action. *J. Clin. Invest.* **2012**, *122*, 3035–3043. [CrossRef] [PubMed]
5. Brix, K.; Führer, D.; Biebermann, H. Molecules Important for Thyroid Hormone Synthesis and action—Known Facts and Future Perspectives. *Thyroid Res.* **2011**, *4*, S9. [CrossRef] [PubMed]
6. Klein, J.R. The Immune System as a Regulator of Thyroid Hormone Activity. *Exp. Biol. Med. (Maywood)* **2006**, *231*, 229–236. [CrossRef] [PubMed]
7. Fekete, C.; Lechan, R.M. Negative Feedback Regulation of Hypophysiotropic thyrotropin-releasing Hormone (TRH) Synthesizing Neurons: Role of Neuronal Afferents and Type 2 Deiodinase. *Front. Neuroendocrinol.* **2007**, *28*, 97–114. [CrossRef] [PubMed]
8. Hashizume, K.; Ichikawa, K.; Sakurai, A.; Suzuki, S.; Takeda, T.; Kobayashi, M.; Miyamoto, T.; Arai, M.; Nagasawa, T. Administration of Thyroxine in Treated Graves' Disease. Effects on the Level of Antibodies to thyroid-stimulating Hormone Receptors and on the Risk of Recurrence of Hyperthyroidism. *N. Engl. J. Med.* **1991**, *324*, 947–953. [CrossRef] [PubMed]
9. Nayak, B.; Hodak, S.P. Hyperthyroidism. *Endocrin. Metab. Clin.* **2007**, *36*, 617–656. [CrossRef] [PubMed]
10. Cooper, D.S. Antithyroid drugs. *N. Engl. J. Med.* **2005**, *352*, 905–917. [CrossRef] [PubMed]
11. Magnusson, R.P.; Taurog, A.; Dorris, M.L. Mechanism of iodide-dependent Catalytic Activity of Thyroid Peroxidase and Lactoperoxidase. *J. Biol. Chem.* **1984**, *259*, 197–205. [PubMed]
12. Davidson, B.; Soodak, M.; Neary, J.T.; Strout, H.V.; Kieffer, J.D.; Mover, H.; Maloof, F. The Irreversible Inactivation of Thyroid Peroxidase by Methylmercaptoimidazole, Thiouracil, and Propylthiouracil in Vitro and Its Relationship to in Vivo Findings. *Endocrinology* **1978**, *103*, 871–882. [CrossRef] [PubMed]
13. Basosi, R.; Niccolai, N.; Rossi, C. Coordination Behaviour of Antithyroid Drugs Against the Fe(I)(NO)2 Group in Solution: ESR and FT-NMR Study. *Biophys. Chem.* **1978**, *8*, 61–69. [CrossRef]

14. Azizi, F.; Amouzegar, A.; Mehran, L.; Alamdari, S.; Subekti, I.; Vaidya, B.; Poppe, K.; Sarvghadi, F.; Luis, T.S., Jr.; Akamizu, T. Management of Hyperthyroidism During Pregnancy in Asia. *Endocr. J.* **2014**, *61*, 751–758. [CrossRef] [PubMed]
15. Burch, H.B.; Burman, K.D.; Cooper, D.S. A 2011 Survey of Clinical Practice Patterns in the Management of Graves' Disease. *J. Clin. Endocrinol. Metab.* **2012**, *97*, 4549–4558. [CrossRef] [PubMed]
16. Andersson, L.A.; Bylkas, S.A.; Wilson, A.E. Spectral Analysis of Lactoperoxidase: Evidence a Common Heme in Mmammalian Peroxidases. *J. Biol. Chem.* **1996**, *271*, 3406–3412. [CrossRef] [PubMed]
17. Fiedler, T.J.; Davey, C.A.; Fenna, R.E. X-ray Crystal Structure and Characterization of Halide-binding Sites of Human Myeloperoxidase at 1.8 Å Resolution. *J. Biol. Chem.* **2000**, *275*, 11964–11971. [CrossRef] [PubMed]
18. Jones, T.A.; Zou, J.Y.; Cowan, S.W.; Kjeldgaard, M. Improved methods for building protein models in electron density maps and the location of errors in these models. *Acta Crystallogr.* **1991**, *47*, 110–119. [CrossRef]
19. Singh, A.K.; Singh, N.; Sharma, S.; Shin, K.; Takase, M.; Kaur, P.; Srinivasan, A.; Singh, T.P. Inhibition of Lactoperoxidase by Its Own Catalytic Product: Crystal Structure of the Hypothiocyanate-Inhibited Bovine Lactoperoxidase at 2.3-Å Resolution. *Biophys. J.* **2009**, *96*, 646–654. [CrossRef] [PubMed]
20. Sheikh, I.A.; Singh, A.K.; Singh, N.; Sinha, M.; Singh, S.B.; Bhushan, A.; Kaur, P.; Srinivasan, A.; Sharma, S.; Singh, T.P. Structural Evidence of Substrate Specificity in Mammalian Peroxidases: Structure of the Thiocyanate Complex with Lactoperoxidase and Its Interactions at 2.4 Å Resolution. *J. Biol. Chem.* **2009**, *284*, 14849–14856. [CrossRef] [PubMed]
21. Singh, A.; Singh, N.; Sinha, M.; Bhushan, A.; Kaur, P.; Srinivasan, A.; Sharma, S.; Singh, T. Binding Modes of Aromatic Ligands to Mammalian Heme Peroxidases with Associated Functional Implications: Crystal Structures of Lactoperoxidase Complexes with Acetylsalicylic Acid, Salicylhydroxamic Acid, and Benzylhydroxamic Acid. *J. Biol. Chem.* **2009**, *284*, 203–208. [CrossRef] [PubMed]
22. Singh, R.P.; Singh, A.; Kushwaha, G.S.; Singh, A.K.; Kaur, P.; Sharma, S.; Singh, T.P. Mode of Binding of the Antithyroid Drug Propylthiouracil to Mammalian Haem Peroxidases. Erratum. *Acta Crystallogr. F Struct. Biol. Commun.* **2015**, *71*, 804. [CrossRef] [PubMed]
23. Sing, R.P.; Singh, A.; Sirohi, H.V.; Singh, A.K.; Kaur, P.; Sharma, S.; Singh, T.P. Dual binding mode of antithyroid drug methimazole to mammalian heme peroxidases—Structural determination of the lactoperoxidase–methimazole complex at 1.97 Å resolution. *FEBS Open Biol.* **2016**, *6*, 640–650. [CrossRef] [PubMed]
24. Singh, A.K.; Singh, N.; Tiwari, A.; Sinha, M.; Kushwaha, G.S.; Kaur, P.; Srinivasan, A.; Sharma, S.; Singh, T.P. First Structural Evidence for the Mode of Diffusion of Aromatic Ligands and Ligand-Induced Closure of the Hydrophobic Channel in Heme Peroxidases. *J. Biol. Inorg. Chem.* **2010**, *15*, 1099–1107. [CrossRef] [PubMed]
25. Mondal, S.; Mugesh, G. Novel Thyroid Hormone Analogues, Enzyme Inhibitors and Mimetics, and Their Action. *Mol. Cell. Endocrinol.* **2017**, *458*, 91–104. [CrossRef] [PubMed]
26. Manna, D.; Roy, G.; Mugesh, G. Antithyroid Drugs and Their Analogues: Synthesis, Structure, and Mechanism of Action. *Acc. Chem. Res.* **2013**, *46*, 2706–2715. [CrossRef] [PubMed]
27. Langer, M.; Kratz, F.; Rothen-Rutishauser, B.; Wunderli-Allenspach, H.; Beck-Sickinger, A.G. Novel Peptide Conjugates for Tumor-Specific Chemotherapy. *J. Med. Chem.* **2001**, *44*, 1341–1348. [CrossRef] [PubMed]
28. Alyar, S.; Karacan, N. Synthesis, Characterization, Antimicrobial Activity and structure-activity Relationships of New Aryldisulfonamides. *J. Enzyme Inhib. Med. Chem.* **2009**, *24*, 986–992. [CrossRef] [PubMed]
29. Fathalla, O.A.; Zaghary, W.A.; Radwan, H.H.; Awad, S.M.; Mohamed, M.S. Synthesis of New 2-thiouracil-5-sulfonamide derivatives with Biological Activity. *Arch. Pharm. Res.* **2002**, *25*, 258–269. [CrossRef] [PubMed]
30. Panda, S.; Kar, A. Evaluation of the Antithyroid, Antioxidative and Antihyperglycemic Activity of Scopoletin from Aegle marmelos leaves in Hyperthyroid Rats. *Phytother. Res.* **2006**, *20*, 1103–1105. [CrossRef] [PubMed]
31. Panda, S.; Kar, A. Synergistic interactions of Aegle marmelos leaf, Emblica officinalis fruit and Ocimum sanctum leaf extracts in the regulation of hyperthyroidism and/or hyperglycemia. *Orient. Pharm. Exp. Med.* **2004**, *4*, 37–43.
32. Nakashima, T.; Taurog, A.; Riesco, G. Mechanism of Action of Thioureylene Antithyroid Drugs: Factors Affecting Intrathyroidal Metabolism of Propylthiouracil and Methimazole in Rats. *Endocrinology* **1978**, *103*, 2187–2197. [CrossRef] [PubMed]
33. Abrams, G.M.; Larsen, P.R. Triiodothyronine and Thyroxine in the Serum and Thyroid Glands of Iodine-Deficient Rats. *J. Clin. Investig.* **1973**, *52*, 2522–2531. [CrossRef] [PubMed]

34. Sugawara, M.; Lau, R.; Wasser, H.L.; Nelson, A.M.; Kuma, K.; Hershman, J.M. Thyroid T4 5′-deiodinase Activity in Normal and Abnormal Human Thyroid Glands. *Metabolism* **1984**, *33*, 332–336. [CrossRef]
35. Braverman, L.E.; Ingbar, S.H.; Sterling, K. Conversion of Thyroxine (T4) to triiodothyronine (T3) in Athyreotic Human Subjects. *J. Clin. Investig.* **1970**, *49*, 855–864. [CrossRef] [PubMed]

Sample Availability: Samples of the compounds listed in the main text of the manuscript are available from the authors.

© 2018 by the authors. Licensee MDPI, Basel, Switzerland. This article is an open access article distributed under the terms and conditions of the Creative Commons Attribution (CC BY) license (http://creativecommons.org/licenses/by/4.0/).

molecules

MDPI

Article

Synthesis of New Furothiazolo Pyrimido Quinazolinones from Visnagenone or Khellinone and Antimicrobial Activity

Ameen Ali Abu-Hashem [1,2]

[1] Photochemistry Department (Heterocyclic Unit), National Research Centre, Dokki, Giza1 2622, Egypt; aminaliabuhashem@yahoo.com; Tel.: +2-01225211700 or +966-591363915; Fax: + 202-33370931

[2] Chemistry Department, Faculty of Science, Jazan University, 2097 Jazan, Saudi Arabia

Academic Editor: Josef Jampilek

Received: 5 October 2018; Accepted: 24 October 2018; Published: 27 October 2018

Abstract: Substituted-6-methyl-1-thioxo-1,2-dihydro-3*H*-furo[3,2-g]pyrimido[1,6-a]quinazolin-3-ones (**5a**,**b**) were synthesized from condensation of visnagenone (**2a**) or khellinone (**2b**) with 6-amino-thiouracil (**3**) in dimethylformamide or refluxing of (**4a**) or (**4b**) in dimethylformamide. Hence, compounds (**5a**,**b**) were used as the starting materials for preparing many new heterocyclic compounds such as; furo[3,2-g]pyrimido[1,6-a]quinazoline (**6a**,**b**), furo[3,2-g]thiazolo[2′,3′:2,3] pyrimido[1,6-a]quinazolinone (**7a**,**b**), substituted-benzylidene-furo[3,2-g]thiazolo[2′,3′:2,3]pyrimido [1,6-a]quinazoline-3,5-dione (**8a**–**f**), 3-oxo-furo[3,2-g]pyrimido[1,6-a]quinazoline-pentane-2,4-dione (**9a**,**b**), 1-(pyrazole)-furo[3,2-g]pyrimido[1,6-a]quinazolinone (**10a**,**b**), 2-(oxo or thioxo)-pyrimidine-furo[3,2-g]pyrimido[1,6-a]quinazolinone (**11a**–**d**), 1-(methylthio)-furo[3,2-g]pyrimido[1,6-a] quinazolinone (**12a**,**b**), 1-(methyl-sulfonyl)-furo[3,2-g]pyrimido[1,6-a]quinazolinone (**13a**,**b**) and 6-methyl-1-((piperazine) or morpholino)-3*H*-furo[3,2-g]pyrimido[1,6-a]quinazolin-3-one (**14a**–**d**). The structures of the prepared compounds were elucidated on the basis of spectral data (IR, ^{1}H-NMR, ^{13}C-NMR, MS) and elemental analysis. Antimicrobial activity was evaluated for the synthesized compounds against Gram-positive, Gram-negative bacteria and fungi. The new compounds, furothiazolo pyrimido quinazolines **8a**–**f** and **11a**–**d** displayed results excellent for growth inhibition of bacteria and fungi.

Keywords: visnagenone; khellinone; quinazolinone; pyrimidine; thiazole; pyrazole; furane; antimicrobial activity

1. Introduction

Physicians confirm the usefulness of adding many naturally occurring drugs. Furochromones (visnagin and khellin) compounds are natural products extracted from the plant of *Ammi visnaga Lam*. and visnagin and khellin are used as therapy for kidney, bladder stones, diuretic infusions [1,2] and are considered essential components of many drugs [3]. As well, furochromone derivatives are reported as anti-atherosclerotic, antineoplastic, anti-gastric, anti-anaphylactic and are used in the treatment of urolithiasis, hypertriglyceridemia [4,5] and vitiligo [6]. Also, the visnaginone derivatives were synthesized using different procedures and elucidated efficient antimicrobial activities [7,8]. Furthermore, furochromones have been used to treat pain in the renal colic [9] and possesses coronary vasodilating activity [10,11]. Moreover, khellin and visnagin have been used in the photo-chemotherapeutic treatment of vitiligo and psoriasis [12], photoreaction with DNA [13] and Khellin displayed important epidermal growth factor receptor (EGFR) inhibitory activity [14]. Benzofurans and furochromones [15–18] are very exciting heterocycles, which are omnipresent in nature and display a wide range of pharmacological activities. Recently, furochromones

and benzofurans derivatives are used as in antiviral and anticancer activities [19,20]. When fused of furochromones with pyrimidine, quinoxaline and pyrazole derivatives showed anti-inflammatory and analgesic activities [21], the cytotoxic activity [22] and used in the protection of DNA [23]. Additionally, some of the moieties heterocyclic such as, chalcones [24], thiazolidinones [25], Mannich bases [26], sulfonamides [27], and isoxazole [28], too, showed several of biological activity with benzofuran derivatives (visnagenone, khellinone) (Figure 1).

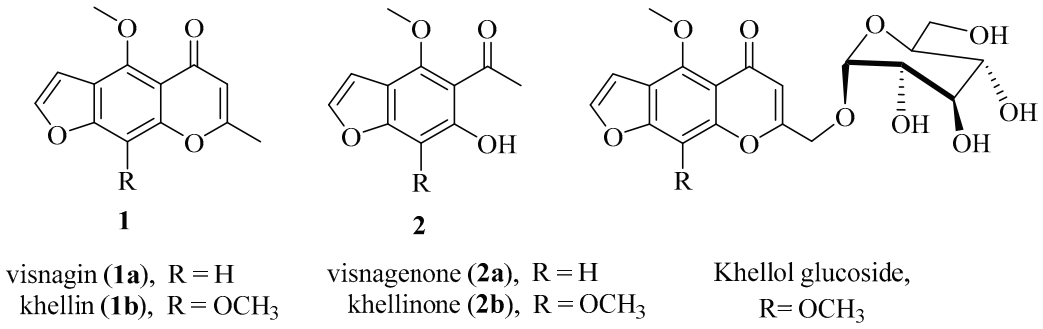

Figure 1. Chemical structure of furochromone derivatives.

An extension of our work on the preparation of novel heterocyclic compounds resultant from the naturally occurring visnagin and khellin [21–23,29], we synthesized and described several derivatives which contained a benzofuran moiety (visnaginone, khellinone) incorporated with thiazole, pyrimidine, pyrazole, and quinazolinone derivatives. The antimicrobial activity of the prepared compounds were evaluated.

2. Results and Discussion

2.1. Synthesis

In the present work, the natural furochromones (visnagin **1a** or khellin **1b**) are highly sensitive to alkali. Hence, aqueous alkaline hydrolysis of **1a** and **1b** using potassium hydroxide with heating and stirring at 40–50 °C for 1–2 h lead to form visnagenone **2a** or khellinone **2b**, respectively [22,23]. Moreover, heating under reflux cyclic alfa, beta-unsaturated ketones (visnagenone **2a** or khellinone **2b**) with 6-aminothiouracil (**3**) in dimethylformamide solution [21,22] with stirring for 4–6 h or 14–16 h under (TLC) afforded new compounds respectively, 6-((1-(6-hydroxy-(4-methoxy or 4,7-dimethoxy)-benzofuran-5-yl)ethylidene)amino)-2-thioxo-2,3-dihydropyrimidin-4(1*H*)-one (**4a**,**b**) and (7-methoxy or 7,11-dimethoxy)-6-methyl-1-thioxo-1,2-dihydro-3*H*-furo[3,2-g]pyrimido[1,6-a] quinazolin-3-one (**5a**,**b**) in good yield obtained. Also, another method, stirring under reflux of **4a** or **4b** in dimethylformamide solution for 8–10 h afforded the same products **5a** and **5b**, respectively. The ^{1}H-NMR spectrum of compound **4a** showed three singlet broad signal at 10.80, 11.19 and 16.11 ppm corresponding to the three protons of the (2NH) and one (OH) groups, which were D_2O exchangeable and ^{1}H-NMR spectrum of compound **5a** showed one singlet broad signal at 11.20 ppm conforming to the one proton of the one (NH) group (D_2O exchangeable) and the mass spectra of **4a**, **4b**, **5a** and **5b** showed molecular ion peaks at *m/z* 331 (M^+, 100%) and 361 (M^+, 100%), 313 (M^+, 100%), 343 (M^+, 100%) respectively (Scheme 1).

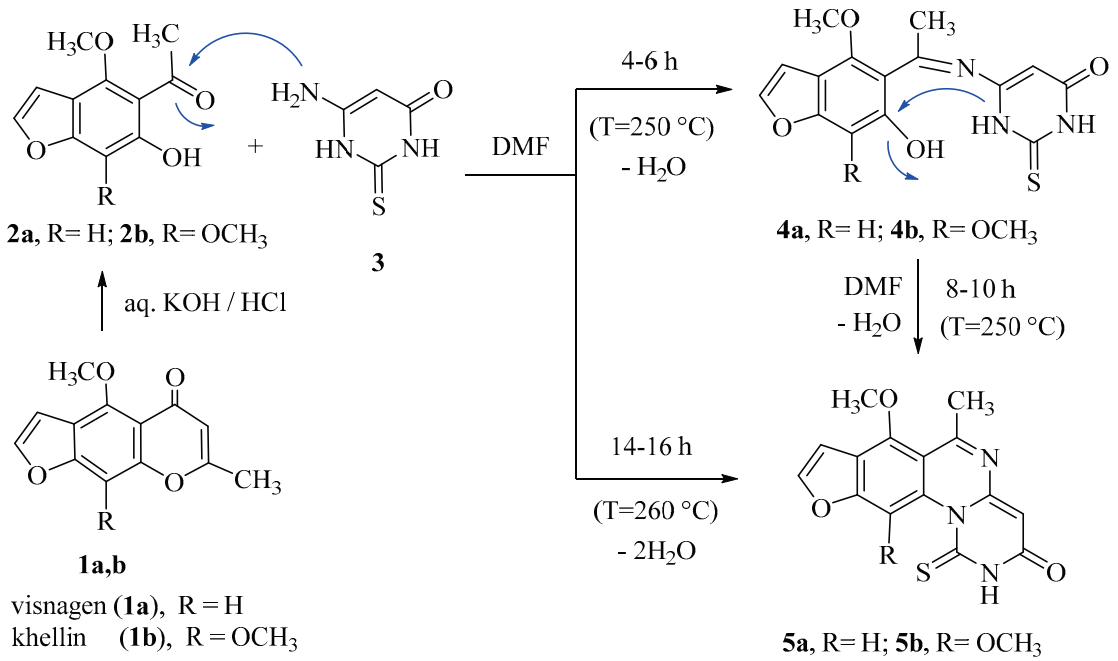

Scheme 1. Synthesis of furopyrimido quinazolinones from visnagenone and khellinone derivatives.

In this research, simple and convenient methods to the syntheses of furopyrimido quinazoline, furothiazolo pyrimido quinazolinone and furothiazolo pyrimido quinazolinone benzylidene derivatives [30]. Thus, refluxing of **5a** or **5b** with chloroacetic acid in glacial acetic acid/acetic anhydride and anhydrous sodium acetate for 3–5 h or 13–15 h with control via (TLC) to give new compounds followed by, 2-(((7-methoxy or 7,11-dimethoxy)-6-methyl-3-oxo-3*H*-furo[3,2-g]pyrimido[1,6-a] quinazolin-1-yl)thio)acetic acid (**6a**,**b**) and (9-methoxy or 9,13-dimethoxy)-8-methyl-2-hydro-5*H*,14a*H*-furo[3,2-g]thiazolo[2′,3′:2,3]pyrimido[1,6-a]quinazoline-3,5-dione (**7a**,**b**) in high yields. Moreover, the boiling of **6a** or **6b** in dimethylformamide solution resulted in the same formation of **7a** and **7b**. The IR spectrum of compounds **6a** and **6b** exposed the presence of broad band absorption at 3340–3350 cm^{-1} indicative of one (OH) group and **6a** = 1745, 1684 cm^{-1} and **6b** = 1748, 1681 cm^{-1} of the two carbonyl groups. The ^{1}H-NMR spectrum of **6a** showed a singlet broad signal at 13.70 ppm corresponding to the one protons of the one (OH) group, which were D_2O exchangeable. Also, ^{1}H-NMR spectrum of **7b** displayed a five singlet signal at δ 2.33, 3.97, 4.24, 5.62 and 7.39 ppm conforming to the thirteen protons of the methyl, two methoxy, (CH_2), (CH, thiazole) and (CH, pyrimidine) groups, respectively. As well as using one-pot synthesis as follows: when a ternary mixture of **5a** or **5b**, chloroacetic acid and a proper aldehyde namely; benzaldehyde, 4-chlorobenzaldehyde or 4-methoxybenzaldehyde respectively, was heated under reflux in a mixture of acetic acid and acetic anhydride in the presence of anhydrous sodium acetate afforded the conforming 2-(substituted-benzylidene)-9,(substituted)-methoxy-8-methyl-2-hydro-5*H*,14a*H*-furo[3,2-g]thiazolo [2′,3′:2,3]pyrimido[1,6-a]quinazoline-3,5-dione (**8a**–**f**) in high yields. In another route, we obtained on the same compounds (**8a**–**f**) via refluxing of **7a** or **7b** with appropriate aromatic aldehyde in dioxane solution containing a catalyst amount of piperidine for 10–12 h. ^{1}H-NMR spectrum of **8a** showed six singlets at 2.30, 3.91, 5.59, 7.32, 7.85 and 8.05 ppm conforming to the 10 protons of the methyl, methoxy, thiazole proton, pyrimidine proton, phenyl proton and (CH) proton groups, respectively and two doublet signals at 6.75, 7.72 ppm of the two protons (J = 2.30 Hz, furan). The structures assignments for compounds were established on their elemental analysis and spectral (IR, ^{1}H, ^{13}C-NMR, and MS) data are shown in the experimental section (Scheme 2).

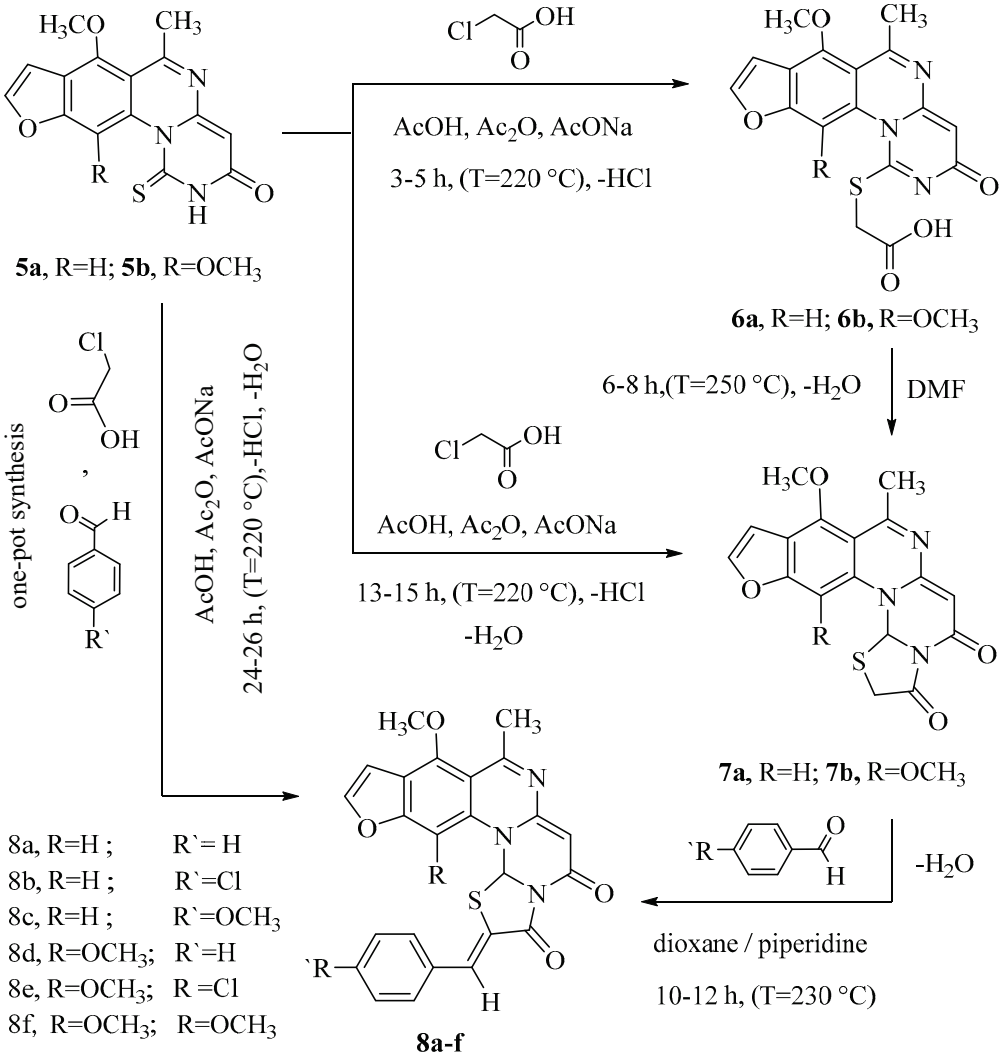

Scheme 2. Synthesis of furothiazolopyrimidoquinazolinone derivatives.

Alkylation of an ethanolic potassium hydroxide solution of **5a** or **5b** with 3-chloro-pentane-2,4-dione (3-chloroacetylacetone) [30], yielded the 3-(((7-methoxy or 7,11-dimethoxy)-6-methyl-3-oxo-3*H*-furo[3,2-g]pyrimido[1,6-a]quinazolin-1-yl)thio)pentane-2,4-dione (**9a**,**b**) in high yield. The IR spectra of **9a** and **9b** showed a strong absorption bands at **9a** = 1725, 1721, 1682 cm^{-1} and **9b** = 1728, 1722, 1684 cm^{-1} characteristic to three carbonyl groups, respectively. The ^{13}C-NMR (DMSO-d_6, ppm) of **9a** showed signals at 68.2, 91.3 and 96.5 for three carbon atoms of (CH), (CH, phenyl) and (CH, pyrimidine) and signals at 168.6, 184.5 and 188.2 three carbon atoms of the three carbonyl groups, and the molecular ion peaks of **9a** and **9b** at *m/z* 411 (95%) and 441 (90%), respectively. On the other hand, compounds **9a** and **9b**, as a typical 1,3-diketone condensation with each of hydrazine hydrate, urea and thiourea to afford the corresponding 1-((3,5-dimethyl-1*H*-pyrazol-4-yl)thio)-(7-methoxy or 7,11-dimethoxy)-6-methyl-3*H*-furo[3,2-g]pyrimido[1,6-a]quinazolin-3-one (**10a**,**b**) and 1-((4,6-dimethyl-2-(oxo or thioxo)-1,2-dihydropyrimidin-5-yl)thio)-(7-methoxy or 7,11-dimethoxy)-6-methyl-3*H*-furo[3,2-g] pyrimido[1,6-a]quinazolin-3-one (**11a**–**d**), respectively. IR spectrum of **10a** and **10b** showed absorption of a broad band at 3380–3360 cm^{-1} corresponding to NH group. Also, the compounds **11a**–**d** exhibited absorption bands at 3390–3370 cm^{-1} for NH group were detected in the IR spectrum. ^{1}H-NMR spectrum of **10a** showed one singlet at 11.50 ppm corresponding to the one proton of NH group and compound **11a** revealed one singlet at 10.60 ppm for one proton of NH group (D_2O exchangeable). All new compounds

were proven by elemental and spectral analysis (IR, ^{1}H, ^{13}C-NMR and MS) which is mentioned in the experimental part (Scheme 3).

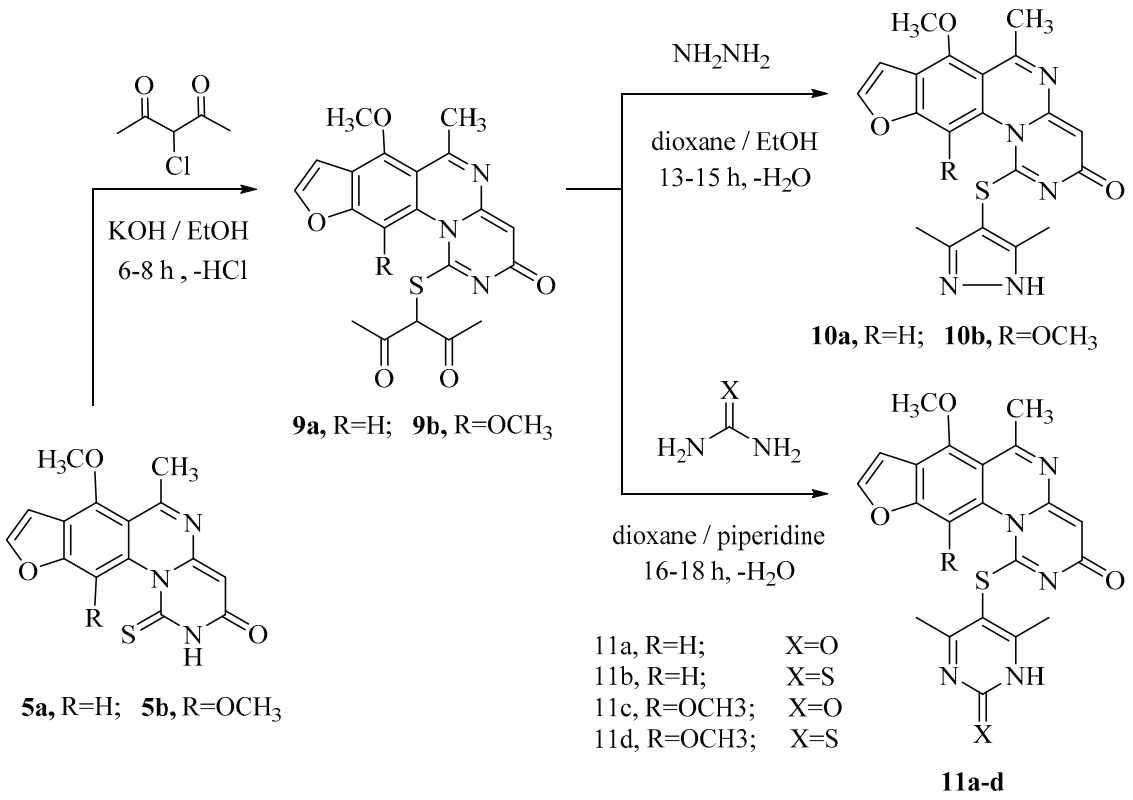

Scheme 3. Synthesis of pyrazole, pyrimidine, -furopyrimido quinazolinone derivatives.

Alkylation of an ethanolic potassium hydroxide solution of **5a** or **5b** with methyl-iodide yielded the (7-methoxy or 7,11-dimethoxy)-6-methyl-1-(methylthio)-3*H*-furo[3,2-g]pyrimido[1,6-a] quinazolin-3-one (**12a**,**b**). Assignment of structures **12a** and **12b** to the reaction products is based on correct elemental analysis and IR, NMR spectroscopy are in agreement with the structure. Thus, ^{1}H-NMR spectrum of **12a** or **12b** showed one singlet signal at 2.80 or 2.88 ppm indicative of three protons to (SCH_3) group and the molecular ion peaks of **12a** or **12b** displayed at *m/z* 327 (M^+, 100%) and 357 (M^+, 100%), respectively. Moreover, oxidation of **12a** or **12b** with hydrogen peroxide in acetic acid yielded the (7-methoxy or 7,11-dimethoxy)-6-methyl-1-(methylsulfonyl)-3*H*-furo[3,2-g] pyrimido[1,6-a]quinazolin-3-one (**13a**,**b**). The IR spectrum of **13a** exposed the presence of two bands at 1162, 1340 cm^{-1} corresponding to (SO_2) group, and ^{1}H-NMR spectrum of **13a** exhibited one singlet at 2.95 agreeing to the three protons of (SO_2CH_3) group. Furthermore, heating under refluxing compounds **12a** or **12b** with secondary aliphatic amines [21,22,30], namely piperazine or morpholine in methanol, produced the (7-methoxy or 7,11-dimethoxy)-6-methyl-1-((piperazin-1-yl) or morpholino)-3*H*-furo[3,2-g]pyrimido[1,6-a]quinazolin-3-one (**14a**–**d**). IR spectrum of **14a** displayed absorption bands at 3390, 1687 cm^{-1} conforming to NH and carbonyl group, respectively. Additionally, the ^{1}H-NMR spectrum of **14c** displayed a singlet broad signal at 10.35 ppm conforming to the one proton of the one (NH) group, which was D_2O exchangeable. The mass spectrum of **13a**, **13b**, **14a**, **14b**, **14c** and **14d** revealed molecular ion peaks at *m/z* 359 (M^+, 84%), 389 (M^+, 80%), 365 (M^+, 83%), 366 (M^+, 78%), 395 (M^+, 76%) and 396 (M^+, 74%), respectively (Scheme 4).

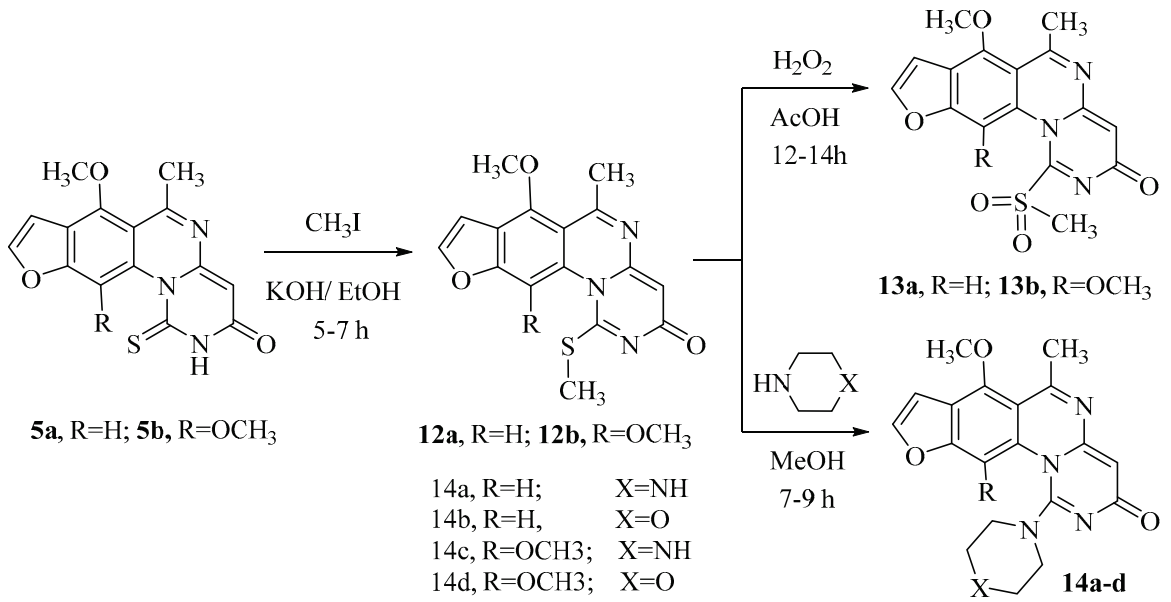

Scheme 4. Synthesis of piperazine, morpholine, -furopyrimido-quinazolinone derivatives.

2.2. Biological Screening

The antimicrobial activity of the compounds was tested in vitro and the results are shown in Tables 1 and 2. Some of these compounds indicated highest antimicrobial activity, comparable to cefotaxime sodium (MIC = 2–5 μmol mL^{-1}). Compounds **8a–f**, **11a–d** and **10a–b** displayed potent antimicrobial activity against Gram-positive bacteria; *Staphylococcus aureus* (ATCC®6538™), *Streptococcus pyogenes* (ATCC®19615™) and Gram-negative bacteria; *Escherichia coli* (ATCC®25922™), *Klebsiella pneumoniae* (ATCC® 10031™). Also, another compounds; **14a–d**, **7a–b** and **9a–b** exhibited moderate antimicrobial activities. The MIC values in μmol mL^{-1} of these compounds were as the following, **8a–f** (1–8), **11 a–d** (6–10), **10a–b** (9–12). Compounds **8a–f** and **11a–d** exposed too higher antifungal activity with MIC in μmol/cm^3 of **8a–f** (2–9) and **11a–d** (7–12) whose results were comparable with the positive control, nystatin (MIC 2-4 μmol mL^{-1}). Some of compounds revealed moderate anti-fungal activity when compared with the nystatin (MIC 2–4 μmol mL^{-1}): **10a–b** (10–14), **14a–d** (12–18), **7a–b** (15–20) and **9a–b** (17–22). The tested fungi were *Aspergillus niger* (ATCC® 16888™), *Alternaria alternate*, *Curvularia lunata* and *Candida albicans* (ATCC®10231™). Thru comparing the observed antimicrobial activities of the furopyrimido quinazolinones, furothiazolo pyrimido quinazolinones obtained in this study to their structures, the (SAR's) were suggested; the presence of the functional groups linked with visnagenone **2a** or khellinone **2b** derivatives, such as thioxo, methyl, hydroxyl, methoxy, amino, chloro, substituted-benzylidene, thiazole, quinazoline, pyrimidine, pyrazole, methylsulfonyl, piperazine and morpholine moieties. Remainder the compounds demonstrated a weak activity compared to the antimicrobial activity of the standard drugs (cefotaxime sodium and nystatin). The thiazolopyrimidine derivatives possessing verified to be effective as antimicrobial agents in previous articles [7,8]. Also, they were active against *Staphylococcus aureus, E. coli,* and *Klebsiella pneumoniae* [7,31] and they were also effective against *Streptococcus pyogenes* and species of fungi, namely, *Aspergillus niger, Candida albicans* [7,32]. In this work and previous reports, most bacteria and fungi types effected susceptible to this class of heterocyclic compounds [33–35]. Moreover, previous results and our findings corroboration the promising antimicrobial activity of furothiazolopyrimidoquinazolinone derivatives which can be developed to higher antimicrobial activities

Table 1. A minimum inhibitory concentration of the compounds against bacteria.

MIC (μmol mL^{-1})				
Compounds	**Microorganisms**			
	Gram-Positive Bacteria		**Gram-Negative Bacteria**	
	Staphylococcus Aureus	***Streptococcus Pyogenes***	***E. coli***	***Klebsiella Pneumoniae***
1a	34	33	31	30
1b	33	32	30	29
2a	31	30	29	28
2b	30	29	28	27
3	37	35	34	33
4a	29	28	27	26
4b	28	27	26	25
5a	27	26	25	24
5b	26	25	24	23
6a	23	22	21	20
6b	22	21	20	19
7a	17	16	15	14
7b	16	15	14	13
8a	8	7	7	5
8b	5	4	3	2
8c	7	6	5	4
8d	7	7	6	4
8e	4	3	2	1
8f	6	5	4	3
9a	19	18	17	16
9b	18	17	16	15
10a	12	11	10	10
10b	11	11	10	9
11a	10	10	9	8
11b	9	8	7	7
11c	10	9	8	7
11d	8	8	7	6
12a	25	24	23	22
12b	24	23	22	21
13a	21	20	19	18
13b	20	19	18	17
14a	14	13	12	11
14b	15	14	14	12
14c	13	12	11	10
14d	14	14	13	12
Cefotaxime sodium	5	4	3	2
Negative control	NI	NI	NI	NI

DMSO was used as the negative control and as the solvent for test compounds and the reference drug. NI–No inhibition.

Table 2. A minimum inhibitory concentration of the compounds against fungi.

MIC (μmol mL^{-1})				
Compounds	**Microorganisms**			
	Aspergillus Niger	***Alternaria Alternata***	***Curvularia Lunata***	***Candida Albicans***
1a	39	38	37	36
1b	38	36	34	33
2a	35	34	33	32
2b	33	32	31	30

Table 2. *Cont.*

Compounds	MIC (μmol mL^{-1})			
	Microorganisms			
	Aspergillus Niger	*Alternaria Alternata*	*Curvularia Lunata*	*Candida Albicans*
3	42	40	39	38
4a	31	30	29	28
4b	30	29	27	26
5a	29	28	26	25
5b	29	27	26	25
6a	26	24	23	22
6b	25	23	22	21
7a	20	18	17	16
7b	19	17	16	15
8a	9	8	8	4
8b	6	5	4	3
8c	8	7	6	5
8d	9	8	7	5
8e	5	4	3	2
8f	7	6	5	4
9a	22	20	19	18
9b	21	19	18	17
10a	14	13	12	11
10b	13	12	11	10
11a	12	11	10	9
11b	10	9	8	8
11c	11	10	9	8
11d	9	9	8	7
12a	28	26	25	24
12b	27	25	24	23
13a	24	22	21	20
13b	23	21	20	19
14a	16	15	14	13
14b	18	16	15	15
14c	15	14	13	12
14d	17	16	15	14
Nystatin	4	3	2	2
Negative control	NI	NI	NI	NI

DMSO was used as the negative control and as the solvent for test compounds and the reference drug. NI–No inhibition.

3. Experimental Section

3.1. General Information

All melting points were taken on an Electrothermal IA 9100 series digital melting point apparatus (Shimadzu, Tokyo, Japan). Elemental analyses were performed on Vario EL (Elementar, Langenselbold, Germany). Microanalytical data were processed in the microanalytical center, Faculty of Science, Cairo University and National Research Centre. The IR spectra (KBr disc) were recorded using a Perkin-Elmer 1650 spectrometer (Waltham, MA, USA). NMR spectra were determined using JEOL 270 MHz and JEOL JMS-AX 500 MHz (JEOL, Tokyo, Japan) spectrometers with Me_4Si as an internal standard. Mass spectra were recorded on an EI Ms-QP 1000 EX instrument (Shimadzu, Japan) at 70 eV. Biological evaluations were done by the antimicrobial unit, Department of Chemistry of Natural and Microbial Products, National Research Centre, Egypt. All starting materials and solvents were purchased from Sigma-Aldrich (Saint Louis, MO, USA).

*3.2. General Procedure for Synthesis of 6-((1-(6-Hydroxy-(4-methoxy or 4,7-dimethoxy)-benzofuran-5-yl) ethylidene)amino)-2-thioxo-2,3-dihydropyrimidin-4(1H)-one (**4a**,**b**)*

A mixture of visnaginone **2a** (2.06 g, 0.01 mol) or khellinone **2b** (2.36 g, 0.01 mol) with 6-amino-2-thioxo-2,3-dihydropyrimidin-4(1*H*)-one **3** (1.43 g, 0.01 mol) in dimethylformamide (40 mL) was refluxed for 4–6 h. The solid formed was filtered off, dried, and crystallized from the proper solvent to give **4a** and **4b**, respectively.

*3.3. Synthesis of 6-((1-(6-Hydroxy-4-methoxybenzofuran-5-yl)ethylidene)amino)-2-thioxo-2,3-dihydro pyrimidin-4(1H)-one (**4a**)*

The compound was obtained from the reaction of visnaginone (**2a**) with 6-amino-thiouracil (**3**) as yellow crystals, crystallized from methanol in 90% yield, m.p. 231 °C. IR (ν, cm^{-1}) KBr: 3370 (brs, 2NH), 3030 (CH-aryl), 2960 (CH-aliph), 1685 (CO, amide), 1630 (C=N). ^{1}H-NMR (DMSO-d_6, ppm) δ 2.38 (s, 3H, CH_3), 3.92 (s, 3H, OCH_3), 6.79 (d, 1H, *J* = 2.35 Hz, furan), 7.80 (d, 1H, *J* = 2.38 Hz, furan), 7.92 (s, 1H, phenyl), 7.94 (s, 1H, pyrimidine), 10.80, 11.19 (br, 2H, 2NH, D_2O exchangeable), 16.11 (br, 1H, OH, D_2O exchangeable); ^{13}C-NMR (DMSO-d_6) δ 21.3 (1C, CH_3), 61.7 (1C, OCH_3), 93.1 (1C, CH, pyrimidine), 98.9 (1C, CH, phenyl), 100.5, 104.5, 108.9, 146.6, 146.9, 154.5, 160.9, 163.2, (8C, Ar-C), 164.1 (1C, C=N-ph), 168.1(1C, C=O), 173.5 (1C, C=S); MS (70 eV, %) *m/z* 331 (M^+, 100%); Anal. Calc. (Found) for $C_{15}H_{13}N_3O_4S$ (331.35): C, 54.37 (54.30); H, 3.95 (3.91); N, 12.68(12.60).

*3.4. Synthesis of 6-((1-(6-Hydroxy-4,7-dimethoxybenzofuran-5-yl)ethylidene)amino)-2-thioxo-2,3-dihydro pyrimidin-4(1H)-one (**4b**)*

The compound was obtained from the reaction of khellinone (**2b**) with 6-amino-thiouracil (**3**) as yellowish crystals, crystallized from dioxane in 84% yield, m.p. 211 °C. IR (ν, cm^{-1}) KBr: 3371(brs, 2NH), 3032 (CH-aryl), 2965 (CH-aliph), 1682 (CO, amide), 1631 (C=N). ^{1}H-NMR (DMSO-d_6, ppm) δ 2.39 (s, 3H, CH_3), 3.94 (s, 6H, $2OCH_3$), 6.80 (d, 1H, *J* = 2.34 Hz, furan), 7.83 (d, 1H, *J* = 2.37 Hz, furan), 7.95 (s, 1H, pyrimidine), 10.81,11.20 (br, 2H, 2NH, D_2O exchangeable), 16.12 (br, 1H, OH, D_2O exchangeable); ^{13}C-NMR (DMSO-d_6) δ 21.4 (1C, CH_3), 61.6 (2C, OCH_3), 93.2 (1C, CH, pyrimidine), 100.5, 104.7, 109.9, 129.3, 146.2, 147.1, 153.8, 158.9, 164.7, (9C, Ar-C), 165.2 (1C, C=N-ph), 167.9 (1C, C=O), 173.8 (1C, C=S); MS (70 eV, %) *m/z* 361 (M^+, 100%); Anal. Calc. (Found) for $C_{16}H_{15}N_3O_5S$ (361.37): C, 53.18 (53.23); H, 4.18 (4.13); N, 11.63 (11.68).

*3.5. General Procedure for Synthesis of (7-Methoxy or 7,11-dimethoxy)-6-methyl-1-thioxo-1,2-dihydro-3H-furo[3,2-g]pyrimido [1,6-a]quinazolin-3-one (**5a**,**b**)*

Method A: A mix of visnaginone **2a** (2.06 g, 0.01 mol) or khellinone **2b** (2.36 g, 0.01 mol) with 6-amino-2-thiouracil (**3**) in DMF (40 mL) was refluxed for 14–16 h. The product precipitated was filtered off and washed with 100 mL water, dried and crystallized from the proper solvent to give **5a** and **5b**, respectively. Method B: A refluxing of **4a** (3.31 g, 0.01 mol) or **4b** (3.61 g, 0.01 mol) in DMF (40 mL) was refluxed for 8–10 h under control (TLC). The final precipitated was filtered off and washed with 50 mL ethanol, dried, and crystallized from the proper solvent to give **5a** and **5b**, respectively.

*3.6. Synthesis of 7-Methoxy-6-methyl-1-thioxo-1,2-dihydro-3H-furo[3,2-g]pyrimido[1,6-a]quinazolin-3-one (**5a**)*

The compound was obtained from the reaction of visnaginone (**2a**) with 6-aminothiouracil (**3**) or compound (**4a**) in dimethylformamide, as yellowish crystals, crystallized from benzene in 85% yield, m.p. 271 °C. IR (ν, cm^{-1}) KBr: 3350 (brs, NH), 3028 (CH-aryl), 2955 (CH-aliph), 1680 (CO, amide), 1635 (C=N). ^{1}H-NMR (DMSO-d_6, ppm) δ 2.32 (s, 3H, CH_3), 3.92 (s, 3H, OCH_3), 6.75 (d, 1H, *J* = 2.33 Hz, furan), 7.33 (s, 1H, pyrimidine), 7.80 (d, 1H, *J* = 2.36 Hz, furan), 8.29 (s, 1H, phenyl), 11.20 (br, 1H, NH, D_2O exchangeable); ^{13}C-NMR (DMSO-d_6) δ 24.5 (1C, CH_3), 61.8 (1C, OCH_3), 79.7 (1C, CH, pyrimidine), 99.1 (1C, CH, phenyl), 104.9, 108.9,116.6, 140.9, 146.6, 148.9, 160.1, 161.2, 164.1 (9C,

Ar-C), 168.2 (1C, C=O), 173.6 (1C, C=S); MS (70 eV, %) *m/z* 313 (M^+, 100%); Anal. Calc. (Found) for $C_{15}H_{11}N_3O_3S$ (313.33): C, 57.50 (57.58); H, 3.54 (3.59); N, 13.41(13.50).

*3.7. Synthesis of 7,11-Dimethoxy-6-methyl-1-thioxo-1,2-dihydro-3H-furo[3,2-g]pyrimido[1,6-a] quinazolin-3-one (**5b**)*

The compound was obtained from the reaction of khellinone (**2b**) with 6-amino-thiouracil (**3**) or compound (**4b**) in dimethylformamide, as yellow crystals, crystallized from toluene in 82% yield, m.p. 251 °C. IR (ν, cm^{-1}) KBr: 3352 (brs, NH), 3029 (CH-aryl), 2957 (CH-aliph), 1681 (CO, amide), 1633 (C=N). ^{1}H-NMR (DMSO-d_6, ppm) δ 2.35 (s, 3H, CH_3), 3.95 (s, 6H, $2OCH_3$), 6.77 (d, 1H, *J* = 2.31 Hz, furan), 7.30 (s, 1H, pyrimidine), 7.82 (d, 1H, *J* = 2.37 Hz, furan), 11.25 (br, 1H, NH, D_2O exchangeable); ^{13}C-NMR (DMSO-d_6) δ 24.6 (1C, CH_3), 61.9 (2C, $2OCH_3$), 80.2 (1C, CH, pyrimidine), 105.1, 109.2, 115.9, 125.8, 137.5, 142.8, 146.5, 149.2, 161.7, 164.8 (10C, Ar-C), 168.4 (1C, C=O), 173.8 (1C, C=S); MS (70 eV, %) *m/z* 343 (M^+, 100%); Anal. Calc. (Found) for $C_{16}H_{13}N_3O_4S$ (343.36): C, 55.97 (55.90); H, 3.82 (3.75); N, 12.24 (12.29).

*3.8. General Procedure for Synthesis of 2-(((7-Methoxy or 7,11-dimethoxy)-6-methyl-3-oxo-3H-furo[3,2-g] pyrimido[1,6-a]quinazolin-1-yl)thio) Acetic Acid (**6a**,**b**)*

A mixture from **5a** (3.13 g, 0.01 mol) or **5b** (3.43 g, 0.01 mol), chloroacetic acid (0.94 g, 0.01 mol) and (0.02 mol) of anhydrous sodium acetate was stirred under reflux in 40 mL of glacial acetic acid and 20 mL of acetic anhydride for 3–5 h. The reaction mixture was cooled and poured into cold water (100 mL). The deposited precipitate was filtered off, and crystallized from appropriate solvent to produce **6a** and **6b**, respectively.

*3.9. Synthesis of 2-((7-Methoxy-6-methyl-3-oxo-3H-furo[3,2-g]pyrimido[1,6-a]quinazolin-1-yl)thio) Acetic Acid (**6a**)*

The compound was obtained from the reaction of (**5a**) with chloroacetic acid, as brownish crystals, crystallized from hexane in 88% yield, m.p. 294 °C. IR (ν, cm^{-1}) KBr: 3340 (brs, OH), 3025 (CH-aryl), 2950 (CH-aliph), 1745 (CO, acid), 1684 (CO, amide), 1631 (C=N). ^{1}H-NMR (DMSO-d_6, ppm) δ 2.30 (s, 3H, CH_3), 3.91 (s, 3H, OCH_3), 4.27 (s, 2H, CH_2), 6.77 (d, 1H, *J* = 2.32 Hz, furan), 7.35 (s, 1H, pyrimidine), 7.78 (d, 1H, *J* = 2.35 Hz, furan), 7.90 (s, 1H, phenyl), 13.70 (br, 1H, OH, D_2O exchangeable); ^{13}C-NMR (DMSO-d_6) δ 23.6 (1C, CH_3), 32.8 (1C, CH_2), 61.7 (1C, OCH_3), 97.2 (1C, CH, phenyl), 100.6 (1C, CH, pyrimidine), 103.4, 105.3, 108.5, 143.7, 146.5, 152.2,158.4, 160.6, 163.9,164.8 (10C, Ar-C), 169.1, 172.8 (2C, 2C=O); MS (70 eV, %) *m/z* 371 (M^+, 100%); Anal. Calc. (Found) for $C_{17}H_{13}N_3O_5S$ (371.37): C, 54.98 (54.91); H, 3.53 (3.58); N, 11.32(11.40).

*3.10. Synthesis of 2-((7,11-Dimethoxy-6-methyl-3-oxo-3H-furo[3,2-g]pyrimido[1,6-a]quinazolin-1-yl)thio) Acetic Acid (**6b**)*

The compound was obtained from the reaction of (**5b**) with chloroacetic acid, as yellowish crystals, crystallized from ethanol in 86% yield, m.p. 283 °C. IR (ν, cm^{-1}) KBr: 3345 (brs, OH), 3027 (CH-aryl), 2952 (CH-aliph), 1748 (CO, acid), 1681 (CO, amide), 1632 (C=N). ^{1}H-NMR (DMSO-d_6, ppm) δ 2.31 (s, 3H, CH_3), 3.95 (s, 6H, $2OCH_3$), 4.25 (s, 2H, CH_2), 6.79 (d, 1H, *J* = 2.35 Hz, furan), 7.38 (s, 1H, pyrimidine), 7.80 (d, 1H, *J* = 2.35 Hz, furan), 13.75 (br, 1H, OH, D_2O exchangeable); ^{13}C-NMR (DMSO-d_6) *δ* 23.4 (1C, CH_3), 32.6 (1C, CH_2), 61.3 (2C, $2OCH_3$), 100.1 (1C, CH, pyrimidine), 101.2, 105.4, 108.8, 124.1, 130.1, 146.2, 146.7, 150.5, 160.1, 164.4, 166.9 (11C, Ar-C), 169.5, 172.9 (2C, 2C=O); MS (70 eV, %) *m/z* 401 (M^+, 100%); Anal. Calc. (Found) for $C_{18}H_{15}N_3O_6S$ (401.39): C, 53.86 (53.80); H, 3.77 (3.71); N, 10.47 (10.42).

*3.11. General Procedure for Synthesis of (9-Methoxy or 9,13-dimethoxy)-8-methyl-2-hydro-5H,14aH-furo[3,2-g]thiazolo[2′,3′:2,3] pyrimido[1,6-a]quinazoline-3,5-dione (**7a**,**b**)*

Method A: A mixture from **5a** (3.13 g, 0.01 mol) or **5b** (3.43 g, 0.01 mol), chloroacetic acid (0.94 g, 0.01 mol) and (0.02 mol) of anhydrous sodium acetate was stirred under reflux in 40 mL of glacial acetic

acid and 20 mL of acetic anhydride on a water bath (60–70 °C) for 13–15 h (TLC). The reaction mixture was allowed to cool to room temperature and poured into water (100 mL). The solid precipitate was filtered off, and crystallized from appropriate solvent to produced **7a** and **7b** in good yields, respectively. Method B: A mixture of **6a** (3.71 g, 0.01 mol) or **6b** (4.01 g, 0.01 mol) in dimethylformamide (35 mL) was refluxed for 6–8 h with (TLC). The final product was filtered off, dried and crystallized from the proper solvent to give **7a** and **7b**, respectively.

*3.12. Synthesis of 9-Methoxy-8-methyl-2-hydro-5H,14aH-furo[3,2-g]thiazolo[2′,3′:2,3]pyrimido[1,6-a] quinazoline-3,5-dione (**7a**)*

The compound was obtained from the reaction of (**5a**) with chloroacetic acid or compound (**6a**) in DMF, as white crystals, crystallized from dioxane in 82% yield, m.p. 338 °C. IR (ν, cm^{-1}) KBr: 3035 (CH-aryl), 2962 (CH-aliph), 1688, 1680 (2CO, amide), 1635 (C=N). ^{1}H-NMR (DMSO-d_6, ppm) δ 2.37 (s, 3H, CH_3), 3.93 (s, 3H, OCH_3), 4.21 (s, 2H, CH_2), 5.57 (s, 1H, CH, thiazole), 6.78 (d, 1H, *J* = 2.34 Hz, furan), 7.38 (s, 1H, pyrimidine), 7.75 (d, 1H, *J* = 2.32 Hz, furan), 7.88 (s, 1H, phenyl); ^{13}C-NMR (DMSO-d_6) δ 23.3 (1C, CH_3), 32.6 (1C, CH_2), 61.8 (1C, OCH_3), 76.1 (1C, CH, thiazole), 94.5 (1C, CH, phenyl), 98.8 (1C, CH, pyrimidine), 101.2, 105.5, 107.9, 142.2, 146.4, 153.5, 159.7, 160.4, 164.5 (9C, Ar-C), 166.4, 170.1 (2C, 2C=O); MS (70 eV, %) *m/z* 355 (M^+, 90%); Anal. Calc. (Found) for $C_{17}H_{13}N_3O_4S$ (355.37): C, 57.46 (57.40); H, 3.69 (3.62); N, 11.82 (11.88).

*3.13. Synthesis of 9,13-Dimethoxy-8-methyl-2-hydro-5H,14aH-furo[3,2-g]thiazolo[2′,3′:2,3]pyrimido[1,6-a] quinazoline-3,5-dione (**7b**)*

The compound was obtained from the reaction of (**5b**) with chloroacetic acid or compound (**6b**) in DMF, as yellowish crystals, crystallized from methanol in 80% yield, m.p. 303 °C. IR (ν, cm^{-1}) KBr: 3038 (CH-aryl), 2966 (CH-aliph), 1685, 1682 (2CO, amide), 1632 (C=N). ^{1}H-NMR (DMSO-d_6, ppm) δ 2.33 (s, 3H, CH_3), 3.97 (s, 6H, $2OCH_3$), 4.24 (s, 2H, CH_2), 5.62 (s, 1H, CH, thiazole), 6.74 (d, 1H, *J* = 2.33 Hz, furan), 7.39 (s, 1H, pyrimidine), 7.77 (d, 1H, *J* = 2.31 Hz, furan); ^{13}C-NMR (DMSO-d_6) δ 23.1 (1C, CH_3), 32.3 (1C, CH_2), 61.7 (2C, $2OCH_3$), 76.4 (1C, CH, thiazole), 97.5 (1C, CH, pyrimidine), 101.4, 105.6, 108.2, 123.6, 127.8, 146.3, 146.8, 152.9, 160.1, 164.7 (10C, Ar-C), 166.2, 170.5 (2C, 2C=O); MS (70 eV, %) *m/z* 385 (M^+, 95%); Anal. Calc. (Found) for $C_{18}H_{15}N_3O_5S$ (385.39): C, 56.10 (56.18); H, 3.92 (3.85); N, 10.90 (10.98).

*3.14. General Procedure for Synthesis of 2-(Substituted-benzylidene)-9,(substituted)-methoxy-8-methyl-2-hydro-5H,14aH-furo[3,2-g] thiazolo[2′,3′:2,3]pyrimido[1,6-a]quinazoline-3,5-dione (**8a–f**)*

Method A: One pot synthesis: A mixture from **5a** (3.13g, 0.01 mol) or **5b** (3.43 g, 0.01 mol), chloroacetic acid (0.94 g, 0.01 mol), the appropriate aromatic aldehyde (10 mmol) and (0.02 mol) of anhydrous sodium acetate was stirred under reflux in 40 mL of glacial acetic acid and 20 mL of acetic anhydride for 24–26 h. The reaction mixture was cooled and poured into ice water. The deposited precipitate was filtered off, and crystallized from appropriate solvent to give (**8a–f**).

Method B: A mixture of compound **7a** (3.55 g, 10 mmol) or **7b** (3.85 g, 10 mmol) and the appropriate aromatic aldehyde (10 mmol) in dioxane (40 mL) containing a catalyst amount of piperidine (0.5 mL) was stirred and heated under reflux for 10–12 h (TLC control). The reaction mixture was cooled, the formed precipitate filtered off, dried and recrystallized from the appropriate solvent to afford (**8a–f**).

*3.15. Synthesis of 2-Benzylidene-9-methoxy-8-methyl-2-hydro-5H,14aH-furo[3,2-g]thiazolo[2′,3′:2,3] pyrimido[1,6-a]quinazoline-3,5-dione (**8a**)*

The compound was obtained from the reaction of (**5a**) and benzaldehyde (1.06 g, 10 mmol) with chloroacetic acid or compound (**7a**) with benzaldehyde, as yellowish crystals, crystallized from dimethylformamide in 75% yield, m.p. > 350 °C. IR (ν, cm^{-1}) KBr: 3050 (CH-aryl), 2945 (CH-aliph), 1685, 1672 (2CO, amide), 1630 (C=N). ^{1}H-NMR (DMSO-d_6, ppm) δ 2.30 (s, 3H, CH_3), 3.91 (s, 3H, OCH_3), 5.59 (s, 1H, CH, thiazole), 6.75 (d, 1H, *J* = 2.31 Hz, furan), 7.32 (s, 1H, pyrimidine), 7.40–7.67(m, 5H,

phenyl), 7.72 (d, 1H, *J* = 2.30 Hz, furan), 7.85 (s, 1H, phenyl), 8.05 (s, 1H, CH); ^{13}C-NMR (DMSO-d_6) δ 23.1 (1C, CH_3), 61.6 (1C, OCH_3), 77.5 (1C, CH, thiazole), 90.8 (1C, CH, phenyl), 92.9 (1C, CH, pyrimidine), 100.7, 104.8, 105.6, (3C, benzofurane), 121.9 (1C, CH), 127.2, 128.1, 128.7, 133.9 (6C, phenyl), 137.5 (1C, thiazole), 140.3, 146.4, 153.8, 160.1, 160.4, 164.2 (6C, pyrimidobenzo furane), 165.6, 168.4 (2C, 2C=O); MS (70 eV, %) *m/z* 443 (M^+, 88%); Anal. Calc. (Found) for $C_{24}H_{17}N_3O_4S$ (443.48): C, 65.00 (65.10); H, 3.86 (3.80); N, 9.48 (9.41).

*3.16. Synthesis of 2-(4-Chlorobenzylidene)-9-methoxy-8-methyl-2-hydro-5H,14aH-furo[3,2-g]thiazolo [2′,3′:2,3]pyrimido[1,6-a]quinazoline-3,5-dione (**8b**)*

The compound was obtained from the reaction of (**5a**) and 4-chlorobenzaldehyde (1.40 g, 10 mmol) with chloroacetic acid or compound (**7a**) with 4-chloro-benzaldehyde, as yellow crystals, crystallized from dioxane in 80% yield, m.p. > 350 °C. IR (ν, cm^{-1}) KBr: 3052 (CH-aryl), 2948 (CH-aliph), 1687, 1674 (2CO, amide), 1631 (C=N). ^{1}H-NMR (DMSO-d_6, ppm) δ 2.31 (s, 3H, CH_3), 3.90 (s, 3H, OCH_3), 5.60 (s, 1H, CH, thiazole), 6.74 (d, 1H, *J* = 2.32 Hz, furan), 7.33 (s, 1H, pyrimidine), 7.45–7.50 (dd, 2H, *J* = 7.60, 7.64 Hz, 4-chlorophenyl), 7.55–7.60 (dd, 2H, *J* = 7.62, 7.66 Hz, 4-chloro phenyl),7.70 (d, 1H, *J* = 2.34 Hz, furan), 7.83 (s, 1H, phenyl), 8.08 (s, 1H, CH); ^{13}C-NMR (DMSO-d_6) δ 23.2 (1C, CH_3), 61.4 (1C, OCH_3), 77.8 (1C, CH, thiazole), 90.2 (1C, CH, phenyl), 92.1 (1C, CH, pyrimidine), 100.3, 104.9, 105.5, (3C, benzofurane), 122.1 (1C, CH), 128.4, 129.2, 132.5, 132.8 (6C, 4-chlorophenyl), 137.9 (1C, thiazole), 140.6, 146.3,153.5, 160.3, 160.7, 164.3 (6C, pyrimidobenzo furane), 165.8, 168.7 (2C, 2C=O); MS (70 eV, %) *m/z* 477 (M^+, 90%); Anal. Calc. (Found) for $C_{24}H_{16}ClN_3O_4S$ (477.92): C, 60.32 (60.39); H, 3.37 (3.44); N, 8.79 (8.85).

*3.17. Synthesis of 9-Methoxy-2-(4-methoxybenzylidene)-8-methyl-2-hydro-5H,14aH-furo[3,2-g]thiazolo [2′,3′:2,3]pyrimido [1,6-a]quinazoline-3,5-dione (**8c**)*

The compound was obtained from the reaction of (**5a**) and 4-methoxy-benzaldehyde (1.36 g, 10 mmol) with chloroacetic acid or compound (**7a**) with 4-methoxybenzaldehyde, as brownish crystals, crystallized from ethanol in 78% yield, m.p. > 350 °C. IR (ν, cm^{-1}) KBr: 3054 (CH-aryl), 2944 (CH-aliph), 1683, 1671 (2CO, amide), 1636 (C=N). ^{1}H-NMR (DMSO-d_6, ppm) δ 2.29 (s, 3H, CH_3), 3.92 (s, 3H, OCH_3), 4.10 (s, 3H, OCH_3), 5.59 (s, 1H, CH, thiazole), 6.71 (d, 1H, *J* = 2.32 Hz, furan), 7.28 (s, 1H, pyrimidine), 7.48–7.53 (dd, 2H, *J* = 7.61, 7.65 Hz, 4-methoxyphenyl), 7.58–7.63 (dd, 2H, *J* = 7.63, 7.67 Hz, 4-methoxyphenyl), 7.69 (d, 1 H, *J* = 2.37 Hz, furan), 7.86 (s, 1 H, phenyl), 8.06 (s, 1H, CH); ^{13}C-NMR (DMSO-d_6) δ 23.4 (1C, CH_3), 58.5 (1C, OCH_3), 61.7 (1C, OCH_3), 77.2 (1C, CH, thiazole), 90.5 (1C, CH, phenyl), 92.4 (1C, CH, pyrimidine), 100.4, 105.1, 105.5, (3C, benzofurane), 122.6 (1C, CH), 123.1, 127.7, 130.1, 155.5 (6C, 4-methoxyphenyl), 137.4 (1C, thiazole), 140.8, 146.2,153.6, 160.1, 160.4, 164.3 (6C, pyrimidobenzofurane), 165.1, 168.6 (2C, 2C=O); MS (70 eV, %) *m/z* 473 (M^+, 87%); Anal. Calc. (Found) for $C_{25}H_{19}N_3O_5S$ (473.50): C, 63.42 (63.49); H, 4.04 (4.12); N, 8.87 (8.95).

*3.18. Synthesis of 2-Benzylidene-9,13-dimethoxy-8-methyl-2-hydro-5H,14aH-furo[3,2-g]thiazolo [2′,3′:2,3]pyrimido[1,6-a]quinazoline-3,5-dione (**8d**)*

The compound was obtained from the reaction of (**5b**) and benzaldehyde (1.06 g, 10 mmol) with chloroacetic acid or compound (**7b**) with benzaldehyde, as yellow crystals, crystallized from acetone in 79% yield, m.p. > 350 °C. IR (ν, cm^{-1}) KBr: 3060 (CH-aryl), 2950 (CH-aliph), 1688, 1678 (2CO, amide), 1638 (C=N). ^{1}H-NMR (DMSO-d_6, ppm) δ 2.33 (s, 3H, CH_3), 3.97 (s, 6H, $2OCH_3$), 5.60 (s, 1H, CH, thiazole), 6.74 (d, 1H, *J*= 2.30 Hz, furan), 7.34 (s, 1H, pyrimidine), 7.45–7.65 (m, 5H, phenyl), 7.74 (d, 1H, *J* = 2.35 Hz, furan), 8.02 (s, 1H, CH); ^{13}C-NMR (DMSO-d_6) δ 23.5 (1C, CH_3), 61.8 (2C, $2OCH_3$), 77.7 (1C, CH, thiazole), 91.7 (1C, CH, pyrimidine), 101.4, 105.3, 108.8, 120.7 (4C, benzo furane), 122.2 (1C, CH), 126.1 (1C, pyrimidine), 127.7, 128.3, 128.8, 134.6 (6C, phenyl), 137.7 (1C, thiazole), 146.2, 146.7, 151.9, 160.6, 164.8 (5C, pyrimidobenzofurane), 165.1, 168.3 (2C, 2C=O); MS (70 eV, %) *m/z* 473 (M^+, 84%); Anal. Calc. (Found) for $C_{25}H_{19}N_3O_5S$ (473.50): C, 63.42 (63.50); H, 4.04 (4.10); N, 8.87 (8.80).

*3.19. Synthesis of 2-(4-Chlorobenzylidene)-9,13-dimethoxy-8-methyl-2-hydro-5H,14aH-furo[3,2-g]thiazolo [2′,3′:2,3]pyrimido[1,6-a]quinazoline-3,5-dione (***8e***)*

The compound was obtained from the reaction of (**5b**) and 4-chlorobenzaldehyde (1.40 g, 10 mmol) with chloroacetic acid or compound (**7b**) with 4-chlorobenzaldehyde, as yellowish crystals, crystallized from methanol in 88% yield, m.p. > 350 °C. IR (ν, cm^{-1}) KBr: 3055 (CH-aryl), 2945 (CH-aliph), 1686, 1674 (2CO, amide), 1634 (C=N). ^{1}H-NMR (DMSO-d_6, ppm) δ 2.30 (s, 3H, CH_3), 3.98 (s, 6H, $2OCH_3$), 5.59 (s, 1H, CH, thiazole), 6.73 (d, 1H, *J* = 2.31 Hz, furan), 7.35 (s, 1H, pyrimidine), 7.47–7.52 (dd, 2H, *J* = 7.68, 7.62 Hz, 4-chlorophenyl), 7.57–7.62 (dd, 2H, *J* = 7.61, 7.65 Hz, 4-chloro phenyl), 7.75 (d, 1H, *J* = 2.36 Hz, furan), 8.04 (s, 1H, CH); ^{13}C-NMR (DMSO-d_6) δ 23.7 (1C, CH_3), 61.9 (2C, $2OCH_3$), 77.6 (1C, CH, thiazole), 91.2 (1C, CH, pyrimidine), 100.5, 105.6, 108.4, 120.8 (4C, benzo furane), 122.4 (1C, CH), 126.3 (1C, pyrimidine), 128.2, 128.8, 131.5, 131.9 (6C, 4-chloro phenyl), 137.5 (1C, thiazole), 146.3, 146.9, 150.8, 160.4, 164.9 (5C, pyrimidobenzofurane), 165.3, 168.1 (2C, 2C=O); MS (70 eV, %) *m/z* 507 (M^+, 98%); Anal. Calc. (Found) for $C_{25}H_{18}ClN_3O_5S$ (507.94): C, 59.12 (59.22); H, 3.57 (3.50); N, 8.27 (8.35).

*3.20. Synthesis of 9,13-Dimethoxy-2-(4-methoxybenzylidene)-8-methyl-2-hydro-5H,14aH-furo[3,2-g]thiazolo [2′,3′:2,3]pyrimido[1,6-a]quinazoline-3,5-dione (***8f***)*

The compound was obtained from the reaction of (**5b**) and 4-methoxy-benzaldehyde (1.36 g, 10 mmol) with chloroacetic acid or compound (**7b**) with 4-methoxybenzaldehyde, as brownish crystals, crystallized from benzene in 73% yield, m.p. > 350 °C. IR (ν, cm^{-1}) KBr: 3052 (CH-aryl), 2944 (CH-aliph), 1685, 1672 (2CO, amide), 1630 (C=N). ^{1}H-NMR (DMSO-d_6, ppm) δ 2.28 (s, 3H, CH_3), 3.95 (s, 6H, $2OCH_3$), 4.12 (s, 3H, OCH_3), 5.55 (s, 1H, CH, thiazole), 6.71 (d, 1H, *J*= 2.32 Hz, furan), 7.37 (s, 1H, pyrimidine), 7.49–7.54 (dd, 2H, *J* = 7.65, 7.61 Hz, 4-methoxyphenyl), 7.58–7.63 (dd, 2H, *J* = 7.62, 7.66 Hz, 4-methoxyphenyl), 7.76 (d, 1H, *J* = 2.35 Hz, furan), 8.06 (s, 1H, CH); ^{13}C-NMR (DMSO-d_6) δ 23.4 (1C, CH_3), 58.2 (1C, OCH_3), 61.8 (2C, $2OCH_3$), 77.3 (1C, CH, thiazole), 91.5 (1C, CH, pyrimidine), 100.2, 105.5, 108.6, 120.5 (4C, benzofurane), 122.7 (1C, CH), 126.1 (1C, pyrimidine), 127.2, 128.4, 129.1, 152.2 (6C, 4-methoxyphenyl), 137.8 (1C, thiazole), 146.1, 146.7, 150.6, 160.5, 164.8 (5C, pyrimidobenzo furane), 165.7, 168.2 (2C, 2C=O); MS (70 eV, %) *m/z* 503 (M^+, 91%); Anal. Calc. (Found) for $C_{26}H_{21}N_3O_6S$ (503.53): C, 62.02 (62.10); H, 4.20 (4.28); N, 8.35 (8.27).

*3.21. General Procedure for Synthesis of 3-(((7-Methoxy or 7,11-dimethoxy)-6-methyl-3-oxo-3H-furo[3,2-g] pyrimido[1,6-a] quinazolin-1-yl)thio)pentane-2,4-dione (***9a**,**b***)*

To a warmed ethanolic potassium hydroxide solution (prepared by dissolving 10 mmol of KOH in 50 mL ethanol) was added each of **5a** (3.13 g, 0.01 mol) or **5b** (3.43 g, 0.01 mol), the heating was continued for 40 min and the mixture was allowed to cool to room temperature, and the proper 3-chloro-pentane-2,4-dione (3-chloroacetylacetone, 1.12 mL, 0.01 mol) was added. The mixture was stirred under reflux for 6–8 h (control TLC), and then cool to room temperature, poured into cold water (100 mL). The solid product precipitated was filtered off, washed with 100 mL water; the product was dried and crystallized from the suitable solvent to afford **9a** and **9b** in good yields, respectively.

*3.22. Synthesis of 3-((7-Methoxy-6-methyl-3-oxo-3H-furo[3,2-g]pyrimido[1,6-a]quinazolin-1-yl)thio)pentane-2,4-dione (***9a***)*

The compound was obtained from the reaction of (***5a***) with 3-chloro-pentane-2,4-dione (3-chloroacetylacetone), as white crystals, crystallized from hexane in 92% yield, m.p. > 350 °C. IR (ν, cm^{-1}) KBr: 3035 (CH-aryl), 2945 (CH-aliph), 1725, 1721 (2CO, acetyl), 1682 (CO, amide), 1638 (C=N). ^{1}H-NMR (DMSO-d_6, ppm) *δ* 2.26 (s, 6H, $2COCH_3$), 2.34 (s, 3H, CH_3), 3.90 (s, 3H, OCH_3), 4.08 (s, 1H, CH), 6.73 (d, 1H, *J* = 2.31 Hz, furan), 7.37 (s, 1H, pyrimidine), 7.62 (s, 1H, phenyl), 7.75 (d, 1H, *J* = 2.33 Hz, furan), ^{13}C-NMR (DMSO-d_6) δ 23.8(1C, CH_3), 26.5 (2C, $2COCH_3$), 61.6 (1C, OCH_3), 68.2 (1C, CH), 91.3 (1C, CH, phenyl), 96.5 (1C, CH, pyrimidine), 100.1, 105.3, 108.5, 142.6, 146.1, 153.5, 157.4, 160.3, 163.8, 165.7 (10C, Ar-C), 168.6, 184.5, 188.2 (3C, 3C=O); MS (70 eV, %) *m/z* 411 (M^+, 95%); Anal. Calc. (Found) for $C_{20}H_{17}N_3O_5S$ (411.43): C, 58.39 (58.32); H, 4.16 (4.10); N, 10.21 (10.16).

*3.23. Synthesis of 3-((7,11-Dimethoxy-6-methyl-3-oxo-3H-furo[3,2-g]pyrimido[1,6-a]quinazolin-1-yl)thio) pentane-2,4-dione (***9b***)*

The compound was obtained from the reaction of (**5b**) with 3-chloro-pentane-2,4-dione (3-chloroacetylacetone), as white crystals, crystallized from dioxane in 90% yield, m.p. 348 °C. IR (ν, cm^{-1}) KBr: 3038 (CH-aryl), 2949 (CH-aliph), 1728, 1722 (2CO, acetyl), 1684 (CO, amide), 1636 (C=N). ^{1}H-NMR (DMSO-d_6, ppm) δ 2.28 (s, 6H, $2COCH_3$), 2.37 (s, 3H, CH_3), 3.98 (s, 6H, $2OCH_3$), 4.15 (s, 1H, CH), 6.72 (d, 1H, *J* = 2.34 Hz, furan), 7.35 (s, 1H, pyrimidine), 7.79 (d, 1H, *J* = 2.37 Hz, furan), ^{13}C-NMR (DMSO-d_6) δ 23.4 (1C, CH_3), 26.1 (2C, $2COCH_3$), 61.9 (2C, $2OCH_3$), 68.5 (1C, CH), 97.1 (1C, CH, pyrimidine), 100.2, 105.7, 108.9, 122.5, 130.2, 146.3, 146.8, 150.7, 159.6, 164.2, 166.4 (11C, Ar-C), 168.8, 185.1, 188.7 (3C, 3C=O); MS (70 eV, %) *m/z* 441 (M^+, 90%); Anal. Calc. (Found) for $C_{21}H_{19}N_3O_6S$ (441.46): C, 57.14 (57.20); H, 4.34 (4.39); N, 9.52 (9.60).

*3.24. General Procedure for Synthesis of 1-((3,5-Dimethyl-1H-pyrazol-4-yl)thio)-(7-methoxy or 7,11-dimethoxy)-6-methyl-3H-furo [3,2-g]pyrimido[1,6-a]quinazolin-3-one (***10a**,**b***)*

A mixture of **9a** (4.11 g, 0.01 mol) or **9b** (4.41 g, 0.01 mol), and hydrazine hydrate (99–100%) in dioxane (30 mL) and ethanol (20 mL) was stirred under reflux for 13–15 h. The reaction mixture was allowed to cool to room temperature, poured into cold water (100 mL). The deposited precipitate was filtered off, dried, and crystallized from the proper solvent to give **10a** and **10b** in good yields, respectively.

*3.25. Synthesis of 1-((3,5-Dimethyl-1H-pyrazol-4-yl)thio)-7-methoxy-6-methyl-3H-furo[3,2-g]pyrimido [1,6-a] quinazolin-3-one (***10a***)*

The compound was obtained from the reaction of (**9a**) with hydrazine hydrate, as yellow crystals, crystallized from dimethylformamide in 95% yield, m.p. > 350 °C. IR (ν, cm^{-1}) KBr: 3375 (brs, NH), 3030 (CH-aryl), 2940 (CH-aliph), 1684 (CO, amide), 1633 (C=N). ^{1}H-NMR (DMSO-d_6, ppm) *δ* 2.28 (s, 3H, CH_3), 2.38 (s, 3H, CH_3), 2.40 (s, 3H, CH_3), 3.92 (s, 3H, OCH_3), 6.75 (d, 1H, *J* = 2.32 Hz, furan), 7.32 (s, 1H, pyrimidine), 7.60 (s, 1H, phenyl), 7.72 (d, 1H, *J* = 2.37 Hz, furan), 11.50 (brs, NH, D_2O exchangeable); ^{13}C-NMR (DMSO-d_6) δ 20.1, 20.3, 23.2 (3C, $3CH_3$), 61.4 (1C, OCH_3), 91.1 (1C, CH, phenyl), 96.3 (1C, CH, pyrimidine), 100.2, 105.1, 107.2, 108.4, 142.3, 144.5, 146.6, 154.1, 158.2, 160.5, 164.4, 166.3 (13C, Ar-C), 168.8 (1C, C=O); MS (70 eV, %) *m/z* 407 (M^+, 100%); Anal. Calc. (Found) for $C_{20}H_{17}N_5O_3S$ (407.45): C, 58.96 (58.88); H, 4.21 (4.15); N, 17.19 (17.10).

*3.26. Synthesis of 1-((3,5-Dimethyl-1H-pyrazol-4-yl)thio)-7,11-dimethoxy-6-methyl-3H-furo[3,2-g]pyrimido [1,6-a]quinazolin-3-one (***10b***)*

The compound was obtained from the reaction of (**9b**) with hydrazine hydrate, as yellowish crystals, crystallized from dioxane in 91% yield, m.p. > 350 °C. IR (ν, cm^{-1}) KBr: 3370 (brs, NH), 3032 (CH-aryl), 2943 (CH-aliph), 1682 (CO, amide), 1635 (C=N). ^{1}H-NMR (DMSO-d_6, ppm) δ 2.30 (s, 3H, CH_3), 2.39 (s, 3H, CH_3), 2.41 (s, 3H, CH_3), 3.98 (s, 6H, $2OCH_3$), 6.77 (d, 1H, *J* = 2.36 Hz, furan), 7.38 (s, 1H, pyrimidine), 7.79 (d, 1H, *J* = 2.34 Hz, furan), 11.55 (brs, NH, D_2O exchangeable); ^{13}C-NMR (DMSO-d_6) δ 20.4, 20.6, 23.5 (3C, $3CH_3$), 61.9 (2C, $2OCH_3$), 96.7 (1C, CH, pyrimidine), 100.3, 105.6, 107.8, 108.5, 122.5, 130.4, 144.8, 146.1, 146.8, 151.4, 160.5, 164.2, 166.6 (14C, Ar-C), 168.9 (1C, C=O); MS (70 eV, %) *m/z* 437 (M^+, 100%); Anal. Calc. (Found) for $C_{21}H_{17}N_5O_4S$ (437.47): C, 57.66 (57.72); H, 4.38 (4.30); N, 16.01 (16.10).

*3.27. General Procedure for Synthesis of 1-((4,6-Dimethyl-2-(oxo or thioxo)-1,2-dihydropyrimidin-5-yl)thio)-(7-methoxy or 7,11-dimethoxy)-6-methyl-3H-furo[3,2-g]pyrimido[1,6-a]quinazolin-3-one (***11a**–**d***)*

A mixture of **9a** (4.11 g, 0.01 mol) or **9b** (4.41 g, 0.01 mol), and urea (0.60 g, 0.01 mol) or thiourea (0. 76 g, 0.01 mol) was stirred under reflux in dioxane (40 mL) in the presence of catalytic amount of piperidine (1 mL) for 16–18 h. The reaction mixture was allowed to cool to room temperature, poured

into water (100 mL), the deposited precipitate was filtered off, washed with ethanol (40 mL), dried and crystallized from proper solvent to afford (**11a**–**d**).

*3.28. Synthesis of 1-((4,6-Dimethyl-2-oxo-1,2-dihydropyrimidin-5-yl)thio)-7-methoxy-6-methyl-3H-furo[3,2-g]pyrimido[1,6-a]quinazolin-3-one (***11a***)*

The compound was obtained from the reaction of (**9a**) with urea, as yellowish crystals, crystallized from dioxane in 86% yield, m.p. > 350 °C. IR (ν, cm^{-1}) KBr: 3380 (brs, NH), 3032 (CH-aryl), 2942 (CH-aliph), 1685, 1680 (2C=O, amide), 1635 (C=N). ^{1}H-NMR (DMSO-d_6, ppm) δ 2.11 (s, 3H, CH_3), 2.28 (s, 3H, CH_3), 2.37 (s, 3H, CH_3), 3.94 (s, 3H, OCH_3), 6.72 (d, 1H, *J* = 2.31 Hz, furan), 7.36 (s, 1H, pyrimidine), 7.63 (s, 1H, phenyl), 7.79 (d, 1H, *J* = 2.38 Hz, furan), 10.60 (brs, NH, D_2O exchangeable); ^{13}C-NMR (DMSO-d_6) δ 20.6, 20.9, 23.5 (3C, $3CH_3$), 61.8 (1C, OCH_3), 85.4 (1C, pyrimidine), 91.5 (1C, CH, phenyl), 97.7 (1C, CH, pyrimidine), 100.4, 105.7, 108.2, 143.1, 146.1, 153.6, 158.5, 160.4, 163.8, 164.7, 165.2, 166.8 (12C, Ar-C), 169.2, 172.5 (2C, 2C=O); MS (70 eV, %) *m/z* 435 (M^+, 92%); Anal. Calc. (Found) for $C_{21}H_{17}N_5O_4S$ (435.46): C, 57.92 (57.85); H, 3.94 (3.99); N, 16.08 (16.15).

*3.29. Synthesis of 1-((4,6-Dimethyl-2-thioxo-1,2-dihydropyrimidin-5-yl)thio)-7-methoxy-6-methyl-3H-furo[3,2-g]pyrimido[1,6-a]quinazolin-3-one (***11b***)*

The compound was obtained from the reaction of (**9a**) with thiourea, as yellow crystals, crystallized from dimethylformamide in 82% yield, m.p. > 350 °C. IR (ν, cm^{-1}) KBr: 3385 (brs, NH), 3035 (CH-aryl), 2944 (CH-aliph), 1681 (C=O, amide), 1632 (C=N). ^{1}H-NMR (DMSO-d_6, ppm) δ 2.10 (s, 3H, CH_3), 2.27 (s, 3H, CH_3), 2.36 (s, 3H, CH_3), 3.91 (s, 3H, OCH_3), 6.70 (d, 1H, *J* = 2.30 Hz, furan), 7.34 (s, 1H, pyrimidine), 7.61 (s, 1H, phenyl), 7.78 (d, 1H, *J* = 2.36 Hz, furan), 12.30 (brs, NH, D_2O exchangeable); ^{13}C-NMR (DMSO-d_6) δ 21.4, 21.8, 23.7 (3C, $3CH_3$), 61.7 (1C, OCH_3), 84.6 (1C, pyrimidine), 91.8 (1C, CH, phenyl), 98.2 (1C, CH, pyrimidine), 100.2, 105.8, 108.1, 143.7, 146.3, 153.8, 158.9, 160.5, 163.9, 164.2, 165.8, 169.6 (12C, Ar-C), 170.1 (1C, C=O), 177.8 (1C, C=S); MS (70 eV, %) *m/z* 451 (M^+, 90%); Anal. Calc. (Found) for $C_{21}H_{17}N_5O_3S_2$ (451.52): C, 55.86 (55.78); H, 3.80 (3.88); N, 15.51 (15.60).

*3.30. Synthesis of 1-((4,6-Dimethyl-2-oxo-1,2-dihydropyrimidin-5-yl)thio)-7,11-dimethoxy-6-methyl-3H-furo[3,2-g]pyrimido[1,6-a]quinazolin-3-one (***11c***)*

The compound was obtained from the reaction of (**9b**) with urea, as yellow crystals, crystallized from methanol in 80% yield, m.p. > 350 °C. IR (ν, cm^{-1}) KBr: 3377 (brs, NH), 3039 (CH-aryl), 2937 (CH-aliph), 1687, 1683 (2C=O, amide), 1638 (C=N). ^{1}H-NMR (DMSO-d_6, ppm) δ 2.09 (s, 3H, CH_3), 2.27 (s, 3H, CH_3), 2.33 (s, 3H, CH_3), 3.99 (s, 6H, $2OCH_3$), 6.75 (d, 1H, *J* = 2.32 Hz, furan), 7.38 (s, 1H, pyrimidine), 7.76 (d, 1H, *J* = 2.37 Hz, furan), 10.74 (brs, NH, D_2O exchangeable); ^{13}C-NMR (DMSO-d_6) δ 20.5, 20.7, 23.7 (3C, $3CH_3$), 61.9 (2C, $2OCH_3$), 87.1(1C, pyrimidine), 98.9 (1C, CH, pyrimidine), 100.2, 105.4, 108.8, 122.3, 130.5, 146.1, 146.9, 152.1, 158.2, 164.1, 164.5, 166.2, 168.5 (13C, Ar-C), 169.8, 171.4 (2C, 2C=O); MS (70 eV, %) *m/z* 465 (M^+, 88%); Anal. Calc. (Found) for $C_{22}H_{19}N_5O_5S$ (465.48): C, 56.77 (56.70); H, 4.11 (4.05); N, 15.05 (15.14).

*3.31. Synthesis of 1-((4, 6-Dimethyl-2-thioxo-1,2-dihydropyrimidin-5-yl)thio)-7,11-dimethoxy-6-methyl-3H-furo[3,2-g]pyrimido[1,6-a]quinazolin-3-one (***11d***)*

The compound was obtained from the reaction of (**9b**) with thiourea, as yellowish crystals, crystallized from dioxane in 80% yield, m.p. > 350 °C. IR (ν, cm^{-1}) KBr: 3388 (brs, NH), 3034 (CH-aryl), 2945 (CH-aliph), 1683 (C=O, amide), 1630 (C=N). ^{1}H-NMR (DMSO-d_6, ppm) δ 2.13 (s, 3H, CH_3), 2.25 (s, 3H, CH_3), 2.32 (s, 3H, CH_3), 4.01 (s, 6H, $2OCH_3$), 6.73 (d, 1H, *J* = 2.34 Hz, furan), 7.36 (s, 1H, pyrimidine),7.80 (d, 1H, *J* = 2.38 Hz, furan), 12.50 (brs, NH, D_2O exchangeable); ^{13}C-NMR (DMSO-d_6) δ 21.5, 21.9, 23.8 (3C, $3CH_3$), 62.01 (2C, $2OCH_3$), 86.1 (1C, pyrimidine), 99.3 (1C, CH, pyrimidine), 100.4, 105.2, 108.7, 122.7, 130.4, 146.3, 146.7, 151.9, 159.1, 164.3, 164.5, 166.9, 168.2 (13C, Ar-C), 169.8(1C, C=O),

178.5 (1C, C=S); MS (70 eV, %) *m/z* 481 (M^+, 86%); Anal. Calc. (Found) for $C_{22}H_{19}N_5O_4S_2$ (481.54): C, 54.87 (54.95); H, 3.98 (3.90); N, 14.54 (14.47).

*3.32. General Procedure for Synthesis of (7-Methoxy or 7,11-dimethoxy)-6-methyl-1-(methylthio)-3H-furo[3,2-g]pyrimido[1,6-a]quinazolin-3-one (***12a**,**b***)*

To a warmed ethanolic KOH solution (prepared by dissolving 10 mmol of KOH in 50 mL ethanol) was added each of **5a** (3.13 g, 0.01 mol) or **5b** (3.43 g, 0.01 mol), the heating was continued for 30 min and the mixture was allowed to cool to room temperature, and methyl iodide (0.62 mL, 0.01 mol) was added. The mixture was stirred under reflux for 5–7 h, then cool to room temperature, poured into cold water (100 mL). The solid product precipitated was filtered off, washed with water; the product was dried and crystallized from the proper solvent to produce **12a** and **12b**, respectively.

*3.33. Synthesis of 7-Methoxy-6-methyl-1-(methylthio)-3H-furo[3,2-g]pyrimido[1,6-a]quinazolin-3-one (***12a***)*

The compound was obtained from the reaction of (**5a**) with methyl iodide, as yellow crystals, crystallized from methanol in 90% yield, m.p. 329 °C. IR (ν, cm^{-1}) KBr: 3035 (CH-aryl), 2962 (CH-aliph), 1685 (CO, amide), 1630 (C=N). ^{1}H-NMR (DMSO-d_6, ppm) δ 2.30 (s, 3H, CH_3), 2.80 (s, 3H, SCH_3), 3.90 (s, 3H, OCH_3), 6.73 (d, 1H, *J* = 2.31 Hz, furan), 7.34 (s, 1H, pyrimidine), 7.64 (s, 1H, phenyl), 7.78 (d, 1H, *J* = 2.35 Hz, furan); ^{13}C-NMR (DMSO-d_6) δ 18.9 (1C, SCH_3), 23.8 (1C, CH_3), 61.4 (1C, OCH_3), 92.7 (1C, CH, phenyl), 98.9 (1C, CH, pyrimidine), 100.3, 105.2, 108.5, 145.2, 146.4, 153.7, 158.3, 160.9, 164.6, 167.8 (10C, Ar-C), 169.1 (1C, C=O); MS (70 eV, %) *m/z* 327 (M^+, 100%); Anal. Calc. (Found) for $C_{16}H_{13}N_3O_3S$ (327.36): C, 58.71 (58.78); H, 4.00 (4.10); N, 12.84 (12.90).

*3.34. Synthesis of 7,11-Dimethoxy-6-methyl-1-(methylthio)-3H-furo[3,2-g]pyrimido[1,6-a]quinazolin-3-one (***12b***)*

The compound was obtained from the reaction of (**5b**) with methyl iodide, as yellowish crystals, crystallized from ethanol in 86% yield, m.p. 311 °C. IR (ν, cm^{-1}) KBr: 3038 (CH-aryl), 2965 (CH-aliph), 1683 (CO, amide), 1633 (C=N). ^{1}H-NMR (DMSO-d_6, ppm) δ 2.35 (s, 3H, CH_3), 2.88 (s, 3H, SCH_3), 3.97 (s, 6H, $2OCH_3$), 6.78 (d, 1H, *J*=2.32 Hz, furan), 7.38 (s, 1H, pyrimidine), 7.80 (d, 1H, *J* = 2.34 Hz, furan); ^{13}C-NMR (DMSO-d_6) δ 19.2 (1C, SCH_3), 23.6 (1C, CH_3), 61.8 (2C, $2OCH_3$), 99.4 (1C, CH, pyrimidine), 100.1, 105.7, 108.2, 122.7, 130.5, 146.1, 146.8, 151.5, 159.7, 164.4, 168.2 (11C, Ar-C), 169.7 (1C, C=O); MS (70 eV, %) *m/z* 357 (M^+, 100%); Anal. Calc. (Found) for $C_{17}H_{15}N_3O_4S$ (357.38): C, 57.13 (57.22); H, 4.23 (4.28); N, 11.76 (11.66).

*3.35. General Procedure for Synthesis of (7-Methoxy or 7,11-dimethoxy)-6-methyl-1-(methylsulfonyl)-3H-furo[3,2-g]pyrimido[1,6-a] quinazolin-3-one (***13a**,**b***)*

A mixture of **12a** (3.27 g, 0.01 mol) or **12b** (3.57 g, 0.01 mol), and excess amount of hydrogen peroxide (5 mL) in acetic acid (40 mL) was heated gently with stirring for 12–14 h with (TLC). The reaction mixture was allowed to cool to 0 °C. The deposited precipitate was filtered off, and crystallized from the proper solvent to afford **13a** and **13b**, respectively.

*3.36. Synthesis of 7-Methoxy-6-methyl-1-(methylsulfonyl)-3H-furo [3,2-g]pyrimido[1,6-a]quinazolin-3-one (***13a***)*

The compound was obtained from the reaction of (**12a**) with hydrogen peroxide, as yellowish crystals, crystallized from benzene in 75% yield, m.p. 241 °C. IR (ν, cm^{-1}) KBr: 3032 (CH-aryl), 2920 (CH-aliph), 1687 (CO, amide), 1632 (C=N), 1162, 1340 (SO_2). ^{1}H-NMR (DMSO-d_6, ppm) δ 2.34 (s, 3H, CH_3), 2.95 (s, 3H, SO_2CH_3), 3.92 (s, 3H, OCH_3), 6.76 (d, 1H, *J* = 2.36 Hz, furan), 7.37 (s, 1H, pyrimidine), 7.61 (s, 1H, phenyl), 7.81 (d, 1H, *J* = 2.32 Hz, furan); ^{13}C-NMR (DMSO-d_6) δ 23.5 (1C, CH_3), 35.6 (1C, SO_2CH_3), 61.3 (1C, OCH_3), 93.5 (1C, CH, phenyl), 99.4 (1C, CH, pyrimidine), 100.2, 105.4, 108.7, 140.3, 145.5, 146.2, 153.9, 160.8, 164.4, 168.1 (10C, Ar-C), 169.5 (1C, C=O); MS (70 eV, %) *m/z* 359 (M^+, 84%); Anal. Calc. (Found) for $C_{16}H_{13}N_3O_5S$ (359.36): C, 53.48 (53.40); H, 3.65 (3.57); N, 11.69 (11.61).

*3.37. Synthesis of 7,11-Dimethoxy-6-methyl-1-(methylsulfonyl)-3H-furo[3,2-g]pyrimido[1,6-a]quinazolin-3-one (***13b***)*

The compound was obtained from the reaction of (**12b**) with hydrogen peroxide, as yellow crystals, crystallized from toluene in 75% yield, m.p. 221 °C. IR (ν, cm^{-1}) KBr: 3029 (CH-aryl), 2918 (CH-aliph), 1684 (CO, amide), 1628 (C=N), 1160, 1342(SO_2). ^{1}H-NMR (DMSO-d_6, ppm) δ 2.29 (s, 3H, CH_3), 2.97 (s, 3H, SO_2CH_3), 4.01 (s, 6H, $2OCH_3$), 6.80 (d, 1H, *J* = 2.30 Hz, furan), 7.31 (s, 1H, pyrimidine), 7.75 (d, 1H, *J* = 2.33 Hz, furan); ^{13}C-NMR (DMSO-d_6) δ 23.3 (1C, CH_3), 35.8 (1C, SO_2CH_3), 61.9 (2C, $2OCH_3$), 99.8 (1C, CH, pyrimidine), 100.4, 105.7, 108.9, 122.4, 130.1, 140.6, 146.3, 146.8, 151.5, 164.7, 168.5(11C, Ar-C), 169.5 (1C, C=O); MS (70 eV, %) *m/z* 389 (M^+, 80%); Anal. Calc. (Found) for $C_{17}H_{15}N_3O_6S$ (389.38): C, 52.44 (52.50); H, 3.88 (3.80); N, 10.79 (10.71).

*3.38. General Procedure for Synthesis of (7-Methoxy or 7,11-dimethoxy)-6-methyl-1-((piperazin-1-yl) or morpholino)-3H-furo[3,2-g]pyrimido[1,6-a]quinazolin-3-one (***14a–d***)*

In a warm solution of **12a** (3.27 g, 0.01 mol) or **12b** (3.57 g, 0.01 mol), in methanol (50 mL) was added the freshly distilled 2nd amine, namely piperazine (0.95 mL, 0.01 mol) or morpholine (0.86 mL, 0.01 mol). The reaction mixture was stirred under reflux for 7–9 h, then allowed to cool to 0 °C for 14 h and the solid obtained was filtered, washed with water (100 mL) dried and recrystallized from appropriate solvent to produce (**14a–d**).

*3.39. Synthesis of 7-Methoxy-6-methyl-1-(piperazin-1-yl)-3H-furo[3,2-g]pyrimido[1,6-a]quinazolin-3-one (***14a***)*

The compound was obtained from the reaction of (**12a**) with piperazine, as pale yellow crystals, crystallized from dioxane in 79% yield, m.p. 202 °C. IR (ν, cm^{-1}) KBr: 3390 (br, NH), 3044 (CH-aryl), 2940 (CH-aliph), 1687 (CO, amide), 1620 (C=N). ^{1}H-NMR (DMSO-d_6, ppm) δ 2.29 (s, 3H, CH_3), 2.82–2.91 (m, 8H, piperazine), 3.92 (s, 3H, OCH_3), 6.78 (d, 1H, *J* = 2.36 Hz, furan), 7.38 (s, 1H, pyrimidine), 7.66 (s, 1H, phenyl), 7.81 (d, 1H, *J* = 2.37 Hz, furan), 10.30 (brs, NH, D_2O exchangeable); ^{13}C-NMR (DMSO-d_6) δ 23.2 (1C, CH_3), 48.3 (2C, $2CH_2$, piperazine), 52.5 (2C, $2CH_2$, piperazine), 61.7 (1C, OCH_3), 91.8 (1C, CH, phenyl), 98.4 (1C, CH, pyrimidine), 100.1, 105.3, 108.2, 144.6, 146.1, 153.8, 154.9, 160.3, 164.4, 168.1(10C, Ar-C), 169.3 (1C, C=O); MS (70 eV, %) *m/z* 365 (M^+, 83%); Anal. Calc. (Found) for $C_{19}H_{19}N_5O_3$ (365.39): C, 62.46 (62.55); H, 5.24 (5.18); N, 19.17 (19.24).

*3.40. Synthesis of 7-Methoxy-6-methyl-1-morpholino-3H-furo[3,2-g]pyrimido[1,6-a]quinazolin-3-one (***14b***)*

The compound was obtained from the reaction of (**12a**) with morpholine, as yellow crystals, crystallized from methanol in 75% yield, m.p. 171 °C. IR (ν, cm^{-1}) KBr: 3040 (CH-aryl), 2936 (CH-aliph), 1685 (CO, amide), 1622 (C=N). ^{1}H-NMR (DMSO-d_6, ppm) δ 2.30 (s, 3H, CH_3), 3.14–3.23 (m, 8H, morpholine), 3.90 (s, 3H, OCH_3), 6.76 (d, 1H, *J* = 2.34 Hz, furan), 7.33 (s, 1H, pyrimidine), 7.64 (s, 1H, phenyl), 7.80 (d, 1H, *J* = 2.35 Hz, furan); ^{13}C-NMR (DMSO-d_6) δ 23.1 (1C, CH_3), 51.5 (2C, $2CH_2$, morpholine), 55.8 (2C, $2CH_2$, morpholine), 61.9 (1C, OCH_3), 91.5 (1C, CH, phenyl), 99.5 (1C, CH, pyrimidine), 100.7, 105.6, 108.4, 144.7, 146.3, 153.9, 155.2, 160.7, 164.8, 168.9 (10C, Ar-C), 169.8 (1C, C=O); MS (70 eV, %) *m/z* 366 (M^+, 78%); Anal. Calc. (Found) for $C_{19}H_{18}N_4O_4$ (366.38): C, 62.29 (62.37); H, 4.95 (4.88); N, 15.29 (15.22).

*3.41. Synthesis of 7,11-Dimethoxy-6-methyl-1-(piperazin-1-yl)-3H-furo[3,2-g]pyrimido[1,6-a]quinazolin-3-one (***14c***)*

The compound was obtained from the reaction of (**12b**) with piperazine, as yellowish crystals, crystallized from ethanol in 74% yield, m.p. 184 °C. IR (ν, cm^{-1}) KBr: 3395 (br, NH), 3048 (CH-aryl), 2944 (CH-aliph), 1689 (CO, amide), 1624 (C=N). ^{1}H-NMR (DMSO-d_6, ppm) δ 2.31 (s, 3H, CH_3), 2.85–2.94 (m, 8H, piperazine), 3.97 (s, 6H, $2OCH_3$), 6.81 (d, 1H, *J* = 2.32 Hz, furan), 7.36 (s, 1H, pyrimidine), 7.84 (d, 1H, *J* = 2.30 Hz, furan), 10.35 (brs, NH, D_2O exchangeable); ^{13}C-NMR (DMSO-d_6) δ 23.5 (1C, CH_3), 48.6 (2C, $2CH_2$, piperazine), 52.8 (2C, $2CH_2$, piperazine), 61.8 (2C, $2OCH_3$), 99.6(1C, CH, pyrimidine),

100.5, 105.7, 108.9, 122.3, 130.2, 146.4, 146.5, 151.8, 154.1, 164.8, 168.5 (10C, Ar-C), 169.7(1C, C=O); MS (70 eV, %) *m/z* 395 (M^+, 76%); Anal. Calc. (Found) for $C_{20}H_{21}N_5O_4$ (395.42): C, 60.75 (60.82); H, 5.35 (5.43); N, 17.71 (17.78).

*3.42. Synthesis of 7,11-Dimethoxy-6-methyl-1-morpholino-3H-furo[3,2-g]pyrimido[1,6-a]quinazolin-3-one (**14d**)*

The compound was obtained from the reaction of (**12b**) with morpholine, as yellowish crystals, crystallized from n-hexane in 72% yield, m.p. 156 °C. IR (ν, cm^{-1}) KBr: 3039 (CH-aryl), 2934 (CH-aliph), 1683 (CO, amide), 1626 (C=N). ^{1}H-NMR (DMSO-d_6, ppm) δ 2.32 (s, 3H, CH_3), 3.16–3.25 (m, 8H, morpholine), 3.97 (s, 6H, $2OCH_3$), 6.79 (d, 1H, *J* = 2.33 Hz, furan), 7.37 (s, 1H, pyrimidine), 7.82 (d, 1H, *J* = 2.37 Hz, furan); ^{13}C-NMR (DMSO-d_6) δ 23.7 (1C, CH_3), 53.8 (2C, $2CH_2$, morpholine), 57.6 (2C, $2CH_2$, morpholine), 61.9 (2C, $2OCH_3$), 99.8 (1C, CH, pyrimidine), 100.4, 105.3, 108.7, 122.6, 130.1, 146.2, 146.8, 151.3, 154.2, 164.5, 168.6 (11C, Ar-C), 169.4 (1C, C=O); MS (70 eV, %) *m/z* 396 (M^+, 74%); Anal. Calc. (Found) for $C_{20}H_{20}N_4O_5$ (396.40): C, 60.60 (60.68); H, 5.09 (5.16); N, 14.13 (14.20).

3.43. Biological Screening

The antimicrobial activity of the newly prepared compounds was tested in vitro against Gram-positive bacteria *Staphylococcus aureus* (ATCC®6538™), *Streptococcus pyogenes* (ATCC®19615™), Gram-negative bacteria *Escherichia coli* (ATCC®25922™), *Klebsiella pneumoniae* (ATCC® 10031™) and the fungi *Aspergillus niger* (ATCC® 16888™), *Alternaria alternate, Curvularia lunata* and *Candida albicans* (ATCC®10231™). The newly prepared compounds were dissolved in dimethyl sulfoxide (DMSO) and tested for their antimicrobial activity by the agar disk diffusion technique. Cefotaxime sodium and nystatin [34,35] were used as the standard drugs for antibacterial and antifungal assays, respectively. A solution of 100 μg mL^{-1} of the tested compound was practical and microplate-wells, 1 cm in diameter, were used. Zones of inhibition were measured with calipers or automated scanners and were paralleled with those of the standards. Cefotaxime sodium (0.15 μmol mL^{-1}) and nystatin (0.037 μmol mL^{-1}) were used as the standard drugs for antibacterial and antifungal activity, respectively. Compound-impregnated disks were placed on an agar plate containing a standard suspension of microorganisms. The plate was incubated for 24 h at 37 °C. For the assessment of the minimum inhibitory concentration (MIC) by the serial plate dilution way [34,35], 5 mg of each tested compound was dissolved in 1 mL of DMSO separately to prepare stock solutions. Serial dilutions were prepared from each stock solution. The plates were incubated at 37 °C for 24 h. MIC is defined as the lowest concentration (μmol mL^{-1}) of the tested compound that results in no visible growth on the plates. DMSO was used as the solvent control to ensure that the solvent had no effect on bacterial growth. The results are shown in Tables 1 and 2.

4. Conclusions

In this work, we synthesized novel heterocyclic compounds with potent antimicrobial activity starting from furochromones (visnagenone **2a** or khellinone **2b**). New derivatives were prepared in good yields such as; furopyrimido quinazolinones, furothiazolo pyrimido quinazolinones, substituted-benzyliden-furothiazolo pyrimido quinazolinones, pyrazolo furopyrimido quinazolin-ones, oxo or thioxo-pyrimidin-furopyrimido quinazolinones and methylthio, methylsulfonyl, piperazino or morpholino-furopyrimido quinazolinones. Some new prepared compounds such as substituted-benzylidene-furothiazolo pyrimido quinazolinones **8a–f** showed higher activity against the tested microorganisms (bacteria and fungi).

Funding: This research received no external funding.

Acknowledgments: The author is extremely grateful to Department of Chemistry of Natural and Microbial Products, National Research Centre for helping us to screen the newly synthesized compounds for antimicrobial activity.

Conflicts of Interest: The author a declare no conflict of interest.

References

1. Trease, G.E.; Evans, W.C. *Pharmacognosy*, 12th ed.; Bailliere Tindall: Eastbourne, UK, 1983; p. 385.
2. Wallis, T.E. *Textbook of Pharmacognosy*, 5th ed.; Whitefriars: London, UK, 1967; p. 244.
3. El-Domiaty, M.M. Improved high-performance liquid chromatographic determination of khellin and visnagin in Ammi visnaga fruits and pharmaceutical formulations. *J. Pharm. Sci.* **1992**, *81*, 475–478. [CrossRef] [PubMed]
4. Bhagavathula, A.S.; Al-Khatib, A.J.M.; Elnour, A.A.; Kalbani, N.M.S.A.; Shehab, A. Ammi visnaga in treatment of urolithiasis and hypertriglyceridemia. *Pharmacogn. Res.* **2015**, *7*, 397–400. [CrossRef]
5. Gammill, R.B.; Day, C.E.; Schurr, P.E. Khellin analogues. 1. General topological requirements for lipid-altering activity in furochromones. *J. Med. Chem.* **1983**, *26*, 1672–1674. [CrossRef] [PubMed]
6. De Leeuw, J.; Assen, Y.; Van Der Beek, N.; Bjerring, P.; Martino Neumann, H. Treatment of vitiligo with khellin liposomes, ultraviolet light and blister roof transplantation. *J. Eur. Acad. Dermatol. Venereol.* **2011**, *25*, 74–81. [CrossRef] [PubMed]
7. Abdou, S.E.; El-Qusy, S.M.; Ghabrial, S.S.; Haggag, M.I. Reactions with visnaginone: Synthesis, cyclisation and microbial evaluation of some visnaginone thiosemicarbazone derivatives. *Mod. App. Sci.* **2011**, *5*. [CrossRef]
8. El-Nakkady, S.S.; Roaiah, H.F.; El-Serwy, W.S.; Soliman, A.M.; El-Moez, S.I.; Abdel-Rahman, A.A. Antitumor and antimicrobial activities of some hetero aromatic benzofurans derived from naturally occurring visnagin. *Acta Pol. Pharm.* **2012**, *69*, 645–655. [PubMed]
9. Kandil, A.; Gobran, W.; Samaan, H.A.; Abu-Shady, H. The spasmolytic potential of a new khellin derivative. *J. Drug Res.* **1977**, *9*, 35.
10. Oguro, K.; Kubota, K.; Kimura, T.; Hashimoto, K. Effects of various coronary vasodilators on myocardial oxygen consumption. *Jpn. J. Pharmacol.* **1973**, *23*, 459–466. [CrossRef] [PubMed]
11. Oguro, K.; Hashimoto, K. Quanttative and comparative studies of pharma-cological features in the coronary, femoral and renal circulations with different coronary vasodilators. *Jpn. J. Pharmacol.* **1974**, *24*, 227–233. [CrossRef] [PubMed]
12. Vedaldi, D.; Caflleri, S.; Dall'Acqua, F.; Andrea, L.; Bovalini, L.; Martelli, P. Khellin, a naturally occurring furochromone, used for the photochemotherapy of skin diseases: Mechanism of action. *Farmaco* **1988**, *4*, 333–346.
13. Trabalzini, L.; Martelli, P.; Bovalini, L.; Dall'Acqua, F.; Sage, E. Photosensitization of DNA of defined sequence by furochromones, Khellin and Visnagen. *J. Photochem. Photobiol. B* **1990**, *7*, 317–336. [CrossRef]
14. Elgazwy Abdel-Sattar, S.H.; Edrees Mastoura, M.; Ismail Nasser, S.M. Molecular modeling study bioactive natural product of khellin analogues as a novel potential pharmacophore of EGFR inhibitors. *J. Enzym. Inhib. Med. Chem.* **2013**, *28*, 1171–1181. [CrossRef] [PubMed]
15. Melzig, L.; Rauhut, C.B.; Knochel, P. 2, 3-Functionalization of furans, benzofurans and thiophenes via magnesiation and sulfoxide-magnesium exchange. *Chem. Commun.* **2009**, 3536–3538. [CrossRef] [PubMed]
16. Mustafa, A. Furochromones. In *Furopyrans and Furopyrones*; John Wiley and Sons: London, UK; New York, NY, USA; Sydney, Australia, 1967; pp. 102–159.
17. Gammill, R.B.; Hyde, B.R. Total synthesis of the lipid-altering and antiatherosclerotic furochromone khellin. The furoic acid route to highly functionalized benzofurans. *J. Org. Chem.* **1983**, *48*, 3863–3865. [CrossRef]
18. Galal, S.A.; Abd EL-All, A.S.; Abdallah, M.M.; EL-Diwani, H.I. Synthesis of potent antitumor and antiviral benzofuran derivatives. *Bioorg. Med. Chem. Lett.* **2009**, *19*, 2420–2428. [CrossRef] [PubMed]
19. Kim, S.; Salim, A.A.; Swanson, S.M.; Kinghorn, A.D. Potential of cyclopenta[b]benzofurans from Aglaia species in cancer chemotherapy. *Anticancer Agents Med. Chem.* **2006**, *6*, 319–345. [CrossRef] [PubMed]
20. Hudson, J.B.; Towers, G.H.N. Phytomedicines as antivirals. *Drugs Future* **1999**, *24*, 295–320. [CrossRef]
21. Abu-Hashem, A.A.; Youssef, M.M. Synthesis of new visnagen and khellin furochromone pyrimidine derivatives and their anti-inflammatory and analgesic activity. *Molecules* **2011**, *16*, 1956–1972. [CrossRef] [PubMed]
22. Abu-Hashem, A.A.; El-Shazly, M. Synthesis of new quinoxaline, pyrimidine, and pyrazole furochromone derivatives as cytotoxic agents. *Monatsh. Chem.* **2017**, *148*, 1853–1863. [CrossRef]

23. Keshk, E.M.; Abu-Hashem, A.A.; Girges, M.M.; Abdel-Rahman, A.H.; Badria, F.A. Synthesis of benzo[1,2-b:5,4-b]difuranyl-triazoles, oxadiazoles, thiazolidione, thiadiazoles, and the use of DNA in evaluation of their biological activity. *Phosphorus Sulufur Silicon Relat. Elem.* **2004**, *179*, 1577–1593. [CrossRef]
24. Kamal, A.; Shankaraiah, N.; Prabhakar, S.; Reddy, C.R.; Markandeya, N.; Reddy, K.L.; Devaiah, V. Solid-phase synthesis of new pyrrolobenzo diazepine-chalcone conjugates: DNA-binding affinity and anticancer activity. *Bioorg. Med. Chem. Lett.* **2008**, *18*, 2434–2439. [CrossRef] [PubMed]
25. Abd Elhafez, O.M.; El Khrisy Eel, D.; Badria, F.; Fathy Ael, D. Synthesis and biological investigation of new thiazolidinone and oxadiazoline coumarin derivatives. *Arch. Pharm. Res.* **2003**, *26*, 686–696. [CrossRef] [PubMed]
26. Wenzel, N.I.; Chavain, N.; Wang, Y.; Friebolin, W.; Maes, L.; Pradines, B.; Lanzer, M.; Yardley, V.; Brun, R.; Herold-Mende, C.; et al. Antimalarial versus cytotoxic properties of dual drugs derived from 4-aminoquinolines and Mannich bases: Interaction with DNA. *J. Med. Chem.* **2010**, *53*, 3214–3226. [CrossRef] [PubMed]
27. Scozzafava, A.; Owa, T.; Mastrolorenzo, A.; Supuran, C.T. Anticancer and antiviral sulfonamides. *Curr. Med. Chem.* **2003**, *10*, 925–953. [CrossRef] [PubMed]
28. Rescifina, A.; Chiacchio, M.A.; Corsaro, A.; De Clercq, E.; Iannazzo, D.; Mastino, A.; Piperno, A.; Romeo, G.; Romeo, R.; Valveri, V. Synthesis and biological activity of isoxazolidinyl polycyclic aromatic hydrocarbons: Potential DNA intercalators. *J. Med. Chem.* **2006**, *49*, 709–715. [CrossRef] [PubMed]
29. Abu-Hashem, A.A.; El-Shazly, M. Synthesis, reactions and biological activities of furochromones: A review. *Eur. J. Med. Chem.* **2015**, *90*, 633–665. [CrossRef] [PubMed]
30. El-Gazzar, A.B.A.; Youssef, A.M.S.; Youssef, M.M.; Abu-Hashem, A.A.; Badria, F.A. Design and synthesis of azolopyrimidoquinolines, pyrimidoquinazolines as anti-oxidant, anti-inflammatory and analgesic activities. *Eur. J. Med. Chem.* **2009**, *44*, 609–624. [CrossRef] [PubMed]
31. Riyadh, S.M.; Farghaly, T.A.; Gomha, S.M. Novel polyazaheterocyclic systems: Synthesis, antitumor, and antimicrobial activities. *Arch. Pharm. Res.* **2010**, *33*, 1721–1728. [CrossRef] [PubMed]
32. Ali, T.E.; Ibrahim, M.A. Synthesis and Antimicrobial Activity of Chromone-linked 2-Pyridone Fused with 1,2,4-Triazoles, 1,2,4-Triazines and 1,2,4-Triazepines Ring Systems. *J. Braz. Chem. Soc.* **2010**, *21*, 1007–1016. [CrossRef]
33. Khalil, A.M.; Berghot, M.A.; Gouda, M.A. Synthesis and antibacterial activity of some new heterocycles incorporating phthalazine. *Eur. J. Med. Chem.* **2009**, *44*, 4448–4454. [CrossRef] [PubMed]
34. Jain, S.R.; Kar, A. The antibacterial activity of some essential oils and their combinations. *Planta Med.* **1971**, *20*, 118–123. [CrossRef] [PubMed]
35. Abu-Hashem, A.A. Synthesis and biological activity of pyrimidines, quinolines, thiazines and pyrazoles bearing a common thieno moiety. *Acta Pol. Pharm. Drug Res.* **2018**, *75*, 59–70.

Sample Availability: Samples of the synthesized compounds are available from the authors.

© 2018 by the author. Licensee MDPI, Basel, Switzerland. This article is an open access article distributed under the terms and conditions of the Creative Commons Attribution (CC BY) license (http://creativecommons.org/licenses/by/4.0/).

molecules

MDPI

Article

New Nitrogen Compounds Coupled to Phenolic Units with Antioxidant and Antifungal Activities: Synthesis and Structure–Activity Relationship

Ana Bettencourt [1], Marián Castro [2], João Silva [3], Francisco Fernandes [1], Olga Coutinho [3], M. João Sousa [3], M. Fernanda Proença [1,*] and Filipe Areias [1,3,4,*]

1 Department of Chemistry, University of Minho, Campus de Gualtar, 4710-057 Braga, Portugal; abete@quimica.uminho.pt (A.B.); francisco.fernandes@upmc.fr (F.F.)
2 Department of Pharmacology, Center for Research in Molecular Medicine and Chronic Diseases (CiMUS), Universidade de Santiago de Compostela, Avenida de Barcelona 22, 15782 Santiago de Compostela, Spain; marian.castro@usc.es
3 Department of Biology, Universidade do Minho, Campus de Gualtar, 4710-057 Braga, Portugal; jp.silva@gmail.com (J.S.); olgapc@bio.uminho.pt (O.C.); mjsousa@bio.uminho.pt (M.J.S.)
4 School of Chemical Science and Engineering, Yachay Tech University, Yachay City of Knowledge, 100650 Urcuqui, Ecuador
* Correspondence: fproenca@quimica.uminho.pt (M.F.P.); fareias@yachaytech.edu.ec (F.A.); Tel: +35-8995293765 (F.A.)

Academic Editor: Josef Jampilek
Received: 9 September 2018; Accepted: 2 October 2018; Published: 3 October 2018

Abstract: A selection of 1-amino-2-arylidenamine-1,2-(dicyano)ethenes **3** was synthesized and cyclized to 2-aryl-4,5-dicyano-1*H*-imidazoles **4** upon reflux in ethyl acetate/acetonitrile, in the presence of manganese dioxide. These compounds were tested for their antioxidant capacity by cyclic voltammetry, 2,2-diphenyl-1-picrylhydrazyl (DPPH) radical and deoxyribose degradation assays. The minimum inhibitory concentration of all compounds was evaluated against two yeast species, *Saccharomyces cerevisiae* and *Candida albicans*. Their toxicity was tested in mammal fibroblasts. Among the synthesised compounds, two presented dual antioxidant/antifungal activity without toxic effects in fibroblasts. The new compounds synthesized in this work are potential biochemical tools and/or therapeutic drugs.

Keywords: Imidazoles; phenolic compounds; antifungal activity; MIC; antioxidant capacity; structure-activity relationship

1. Introduction

The synthesis of novel antioxidants is an important area for the pharmaceutical, cosmetic, and food industries [1,2]. Indeed, antioxidants have matchless properties in the conservation of many market products, and an important function in the prevention of many degenerative pathologies, such as, cancer, cardiovascular diseases, arthritis, arteriosclerosis, and the normal process of aging [3,4].

The antioxidant capacity of a compound is associated with its ability to act as a scavenger of free radicals [5]. The chelation capacity of metal ions is another important property of an efficient antioxidant, because iron and copper ions can initiate the production of hydroxyl radicals by the Fenton reaction [6]. Phenolic compounds, such as quercetin and gallic acid, are typical examples of potent antioxidants [7].

The resistance of pathogenic fungi to actual drugs on the market supports the need for the synthesis of novel antifungal agents [8], presenting selective toxicity to fungi without toxic effects to other organisms [9]. Nevertheless, commercial antifungals do not present this selective toxicity.

Additionally, the actual antifungal agents are highly persistent in the environment, and they present a threat to living beings in general [10]. Nitrogen heterocycles, like fluconazole and miconazole, are examples of systemic antifungals with a wide spectrum of action on fungi [11].

In this study, the imidazole ring, present in many antifungal agents, was coupled with the phenolic unit, which is known to confer antioxidant capacity, to create new nitrogen heterocycles. The compounds synthesized were assayed for their antioxidant and antifungal activities, and the results allowed for an understanding of a relationship between chemical structure and activity (SAR).

2. Results

2.1. Chemistry

The products and reactions reported in this section are summarized in Table 1. The 1,2-(dicyano) ethenes **3a**–**3e**, used as starting materials for the imidazole scaffolds studied in this work, were prepared by the reaction of diaminomaleonitrilo **1** with phenolic aldehydes **2a**–**2e**, in ethanol and using sulphuric acid as catalyst. The products **3a**–**3e** were isolated at 81–97% yield after approximately 10 minutes at room temperature.

The cyclization of the 1,2-(dicyano)ethenes **3a**–**3e** to the corresponding imidazoles **4a**–**4d** was performed under reflux in tetrahydrofuran (THF), using an excess of MnO_2. The products were isolated in 50–70% yield after 8 hr to 5 days. All attempts to prepare compound **4e** from **3e**, with either acid or base catalysis, varying the solvent and using nitrogen atmosphere, resulted in the formation of dark materials, possibly as the result of extensive oxidation.

Table 1. Experimental conditions for the synthesis of target compounds **3** and **4**.

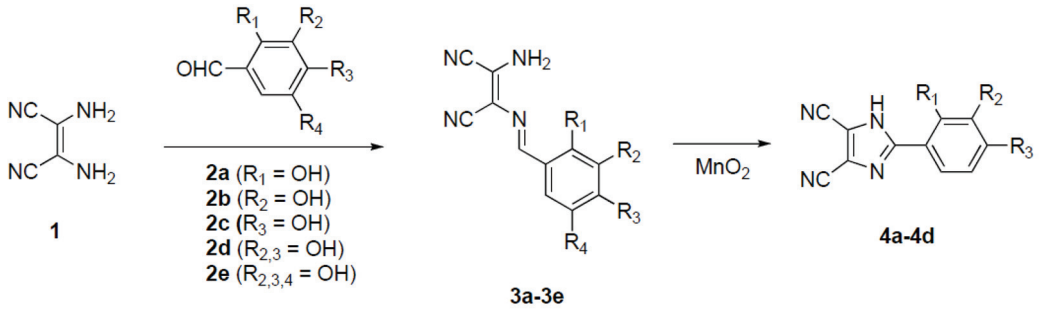

Compound	R^1	R^2	R^3	R^4	Reaction Conditions	Yield (%)
3a	OH	H	H	H	**1** + **2a** (1.0 equiv.), EtOH, H_2SO_4, r.t., 10 min	97
3b	H	OH	H	H	**1** + **2b** (1.0 equiv.), EtOH, H_2SO_4, r.t., 10 min	82
3c	H	H	OH	H	**1** + **2c** (1.0 equiv.), EtOH, H_2SO_4, r.t., 10 min	87
3d	H	OH	OH	H	**1** + **2d** (1.0 equiv.), EtOH, H_2SO_4, r.t., 10 min	81
3e	H	OH	OH	OH	**1** + **2e** (1.0 equiv.), EtOH, H_2SO_4, r.t., 10 min	92
4a	OH	H	H	H	**3a**, ethyl acetate/acetonitrile, MnO_2, reflux, 14 h	50
4b	H	OH	H	H	**3b**, ethyl acetate/acetonitrile, MnO_2, reflux, 5 days	70
4c	H	H	OH	H	**3c**, ethyl acetate/acetonitrile, MnO_2, reflux, 8 days	63
4d	H	OH	OH	H	**3d**, ethyl acetate/acetonitrile, MnO_2, reflux, 24 h	55

r.t. (room temperature).

2.2. Antioxidant Capacity

The antioxidant capacity of 1,2-(dicyano)ethenes **3a**–**3e** and imidazoles **4a**–**4d** was assessed through a step-by-step cascade using three different experimental procedures. Initially, we determined the anodic peak potential (E_p) of all compounds by the cyclic voltammetry technique because this potential represents the ability of compounds to donate their electrons, and it can be used as a parameter of the scavenging activity [12]. Subsequently, we determined and confirmed the scavenging activity by the DPPH$^{\bullet}$ assay for the compounds that presented the lowest potentials of each chemical series (**3e** and **4d**) [13]. Finally, we determined the antioxidant capacity by the deoxyribose degradation

assay for the two previous compounds, because this assay can indicate both the scavenging and the chelating activities of these compounds [14]. The results obtained were compared with the reference antioxidant trolox.

Previous work showed that compounds selected by their electrochemical behavior are likely to act as radical scavengers [12]. In this study, cyclic voltammetry was used to test the anodic peak potential of the synthesized compounds. The anodic peak potential (E_p) and the half peak potential ($E_{p/2}$) were used to measure the easiness of oxidation, and consequently the antioxidant capacity of the compounds. The obtained peak and half peak potentials are presented in Table 2. The oxidation peak potentials of the tested compounds vary from 0.113 V up to 0.896 vs. saturated calomel electrode (SCE), depending on the number of hydroxyl groups in the aromatic ring. Published literature corroborates our current observation, stating that compounds with two or more hydroxyl groups have lower anodic peak potentials and higher antioxidant capacities than monosubstituted phenols [15]. The voltammograms obtained for the oxidation of 1,2-(dicyano)ethenes **3a**–**3c** with the 2-hydroxy, 3-hydroxy, and 4-hydroxy substituents in the aromatic ring presented values for the peak potential that were equal to or higher than 0.476 V. The 1,2-(dicyano)ethenes **3d**–**3e**, with the 3,4-di-hydroxyphenyl and 3,4,5-tri-hydroxyphenyl substituents presented lower peak potentials, varying from 0.113 to 0.248 V. These differences in electrochemical behavior indicate that the number of hydroxyl groups of the phenolic unit is responsible for the easiness of oxidation of the compounds.

Table 2. Data from cyclic voltammetry, DPPH$^{\bullet}$ and deoxyribose degradation assays for the target compounds.

Compound	E_p (mV vs. ECS)	$E_{p/2}$ (mV vs. ECS)	DPPH IC_{50} (μM)	% Inhibition of deoxyribose degradation
3a	688	649	n.d.	n.d.
3b	740	-	n.d.	n.d.
3c	476	361	n.d.	n.d.
3d	248	185	n.d.	n.d.
3e	113	40	3.7 ± 0.7	62.1 ± 2.3
4a	783	758	n.d.	n.d.
4b	896	712	n.d.	n.d.
4c	620	534	n.d.	n.d.
4d	254	166	12.0 ± 1.0	59.0 ± 3.5
Trolox	173	107	9.0 ± 0.2	23.4 ± 2.6

E_p (Anodic peak potential); $E_{p/2}$ (half peak potential); SCE (saturated calomel electrode); DPPH$^{\bullet}$ (2,2-diphenyl-1-picrylhydrazile radical); IC_{50} (50% inhibitory concentration); n.d. (not determined).

The peak potentials of compounds **3d**–**3e** were of the same order of magnitude or even lower than the peak potential of trolox (E_p = 0.173 V), suggesting that these compounds have a high scavenging capacity. Indeed, the peak potentials of the previous compounds (**3d**–**3e**) were compared with the peak potential for trolox, a standard antioxidant, as these values represented the tendency of the compounds to give up their electrons. In the literature, antioxidant/prooxidant activity has been associated with the oxidation potential, and compounds with a low peak potential (lower than 0.450 mV) were identified as antioxidants [12,15].

For each compound series, the scavenging activity of the synthesized molecules with the lowest peak potential (**3e** and **4d**) was assessed by the DPPH radical assay. Compound **3e** (3.7 ± 0.7 μM) presented an IC_{50} value that was lower than trolox (9.0 ± 0.2 μM), establishing that this compound is an efficient radical scavenger.

The imidazole **4d**, substituted with the 3,4-di-hydroxyphenyl moiety, presented a peak potential value of 0.254 V, which was the lowest of this series (Table 2). The IC_{50} value obtained for this imidazole in the DPPH radical assay, 12.0 ± 1.0 μM, showed that there was a slight decrease in the scavenging activity as consequence of cyclization. Despite this decrease in activity, imidazole **4d** could be considered to be a scavenger that is almost as potent as trolox.

To finalize the antioxidant study, the most potent scavengers of each chemical series were assayed on the deoxyribose degradation assay. The compounds were assayed at their IC_{50} concentration, as determined by the $DPPH^{\bullet}$ assay. This experimental approach permitted us to estimate the antioxidant capacity of the synthesized compounds at equipotent scavenging concentrations. The compounds **3e** and **4d** inhibited the deoxyribose degradation by approximately 60%, whereas trolox inhibited deoxyribose degradation only by 23.4 ± 2.6%. The higher antioxidant capacity of the compounds assessed, substituted with 3,4-di-hydroxyphenyl or 3,4,5-tri-hydroxyphenyl moieties, would be a consequence of the combination of their scavenging activity and of their capacity to chelate iron ions. These results agree with the literature reporting that phenolic compounds with 3,4-di-hydroxyphenyl or 3,4,5-tri-hydroxyphenyl moieties, such as quercetin and gallic acid, respectively, have potent scavenging activities and chelating capacities for iron, and both contribute to their high antioxidant activities [16–19]. Our hypothesis was valid because the deoxyribose was oxidized with hydroxyl radicals ($HO^{\bullet}$) produced through the ascorbate–iron pair by the Fenton reaction [14]. These results are important, as many pathological diseases are associated with an increase of free iron concentration, as a consequence of a disruption of iron homeostasis [20]. Additionally, free iron can react with ascorbate that exists at high concentration inside the cells, generating $HO^{\bullet}$ by the Fenton reaction [21]. In summary, compounds **3e** and **4d** present excellent properties as antioxidant agents.

2.3. Antifungal Activity

The antifungal activity of the synthesized compounds was tested on two yeast species by the method of liquid microdilution, and compared with the reference antifungals fluconazole and miconazole. We chose the *Saccharomyces cerevisiae* as the model yeast in this study, because it is not pathogenic at normal conditions, but it can provoke serious infections in persons with a depressed immune system, such as patients with human immunodeficiency virus infection and acquired immune deficiency syndrome (HIV/AIDS) [22]. We also tested the activity of the compounds on *Candida albicans* because it is an opportunistic yeast that is frequently found in systemic infections [23]. Therefore, there is a high interest in the development of new antifungals with activity on these two yeasts.

Minimum inhibitory concentration (MIC) values, defined as the lowest concentration of compound able to cause 80% inhibition of cellular growth, were assessed for all compounds. Miconazole presented MIC values on *Saccharomyces cerevisiae* and *Candida albicans* of 100.0 and 0.78 μM, respectively, while MIC values for fluconazole were 50.0 and 1.56 μM, respectively (Table 3). These MIC values exhibited showed that miconazole is more potent than fluconazole on *Candida albicans*, while fluconazole is more potent than miconazole on *Saccharomyces cerevisiae*. In addition, *Candida albicans* is more sensitive than *Saccharomyces cerevisiae* to these two antifungal agents.

In the assessment of the antifungal activity of 1,2-(dicyano)ethenes **3a**–**3e**, we observed that compound **3e**, with a 3,4,5-tri-hydroxyphenyl moiety, achieved 80% inhibition of the growth of *Saccharomyces cerevisiae* at a concentration of 50 μM (Table 3). Therefore, **3e** showed antifungal activity that was equipotent to fluconazole, and more potent than miconazole. On *Candida albicans*, **3e** presented a MIC of 100 μM, having weaker activity than miconazole and fluconazole. The highest antifungal activity of **3e** compared to the other compounds of this series seemed to be related with the lowest anodic peak potential and the highest antioxidant capacity of this compound. Therefore, we confirmed the presence of a synergistic effect between the phenolic moiety (3,4,5-tri-hydroxyphenyl) and the rest of the molecule common to all 1,2-(dicyano)ethenes. The other compounds of the series did not achieve the MIC on the yeast species considered in our study at the highest concentration evaluated in each case, due to their limited solubility in aqueous solution (Table 3).

Table 3. Values of minimum inhibitory concentration (MIC) on yeast and the viability of fibroblasts at the indicated concentrations of the compounds.

Compound	Antifungal Activity MIC (μM)		Cellular Viability (%)
	Saccharomyces cerevisiae	*Candida albicans*	Fibroblasts
3a	>200.0 *	>200.0 *	n.d.
3b	>200.0 *	>200.0 *	n.d.
3c	>400.0 *	>400.0 *	n.d.
3d	>400.0*	>400.0 *	n.d.
3e	**50.0**	**100.0**	**97.3 ± 1.9**
4a	>400.0 *	>400.0 *	n.d.
4b	>400.0 *	>400.0 *	n.d.
4c	>400.0 *	>400.0 *	n.d.
4d	**400.0**	**600.0**	**94.8 ± 3.5**
Miconazole	**100.0**	**0.78**	n.d.
Fluconazole	**50**	**1.56**	n.d.

n.d. (not determined). * Not achieved at highest concentration tested.

In the evaluation of antifungal activity of imidazoles **4a**–**4d**, we observed that **4d** with the 3,4-di-hydroxyphenyl unit had MIC values of 400 and 600 μM on *Saccharomyces cerevisiae* and *Candida albicans*, respectively, showing weaker activity than fluconazole and miconazole. The highest antifungal activity of **4d** appeared to be also related with its highest antioxidant capacity in this series. There was also an increase of antifungal activity with the cyclization, because the 1,2-(dicyano)ethene **3d**, which is the respective linear precursor of imidazole **4d**, did not present any antifungal activity.

These results agree with our initial hypothesis, because there is a synergistic effect when the phenolic moiety is coupled to the nitrogen heterocycle, which was based on previous published works demonstrating that the antifungal activity increases when a phenolic antioxidant is added to a solution of antifungal agent [24]. Nevertheless, market antifungal agents do not incorporate a phenolic moiety, but they are coupled to aromatic groups substituted with chlorine or fluorine atoms [25]. Therefore, these market antifungal agents have low solubility in water and adverse consequences to the environment [10].

As previously explained, an ideal antifungal must be highly toxic for fungi and not present any toxicity for other living beings [26]. Therefore, we studied the toxicity of **3e** and **4d** on fibroblasts using the lactate dehydrogenase (LDH) release method to obtain toxicological information in mammalian cells [27]. We observed that these two compounds were not toxic for fibroblasts at concentrations that presented antifungal activity, because there was no significant release of LDH to the extracellular media (Table 3). The results showed that **3e** and **4d** presented antifungal activity at concentrations that did not result in toxicity for fibroblasts. In addition, the two compounds have the advantage of being substituted with phenolic units, which form hydrogen bonds with water molecules, and as a result, they have more solubility in the aqueous medium than compounds substituted with chlorine and fluorine atoms as the market antifungal agents.

3. Materials and Methods

3.1. Chemistry

Chemicals and solvents were of analytical grade and they were purchased from market sources and used without purification.

All compounds were fully characterized by spectroscopic data and compared with the data available in the literature. The IR spectra were recorded on a Bomem MB 104 instrument (ABB Bomem Inc., Quebec, Canada) using sodium chloride plates and Nujol mulls. The NMR spectra were recorded on a Varian Unity Plus (^{1}H: 300 MHz and ^{13}C: 75 MHz) or on a Bruker Avance 3400 (^{1}H: 400 MHz and ^{13}C: 100 MHz) (Bruker Corporation, Billerica, MA, USA), and deuterated DMSO was used as

solvent. The chemical shifts were expressed in parts per million (ppm), and the coupling constants, J, were reported in Hertz (Hz). The peak patterns were explained as follows: s, singlet; d, doublet; t, triplet; m, multiplet. The reactions were monitored by thin layer chromatography (TLC) using aluminium plates pre-coated with silica gel 60 F254 (Merck) and mixtures of dichloromethane/ethanol (9/1) and/or chloroform/ethyl acetate/ acetic acid (16/8/1) as an eluent. The melting points were determined on a Stuart SMP3 melting point apparatus.

3.1.1. General Procedure for the Synthesis of the 1-amino-2-arylidenamine-1,2-(dicyano)ethenes (**3a**–**3e**)

One drop of concentrated sulphuric acid (0.01 mL) was added to a suspension of diaminomaleonitrile **1** and benzaldehyde **2** (1 molar equivalent) in ethanol. The reaction was stirred for 10 minutes at room temperature. The yellow solid was filtered, washed with cold diethyl ether, and identified as the title compound **3**.

1-Amino-1,2-dicyano-2-(2′-hydroxybenzylidenamine) ethene (**3a**). 1 (0.65 g, 6.0 mmol), 2-hydroxibenzaldehyde 2a (0.65 mL, 6.08 mmol), ethanol (10 mL). Yellow solid identified as **3a** (1.24 g, 97%). Mp 251–254 °C. IR (NaCl): 3465, 3404, 3343, 3191, 2244, 2207, 1626, 1615, 1608, 1562, 1496, 1279, 1230, 1213, 1157, 1118. ^{1}H-NMR (DMSO-d_6, 300 MHz) δ 6.88 (t, 1H, J = 7.8 Hz, H′$_5$); 6.92 (dd, 1H, J_1 = 8.1 Hz, J_2 = 0.6 Hz, H′$_3$), 7.32 (dt, 1H, J_1 = 7.8 Hz, J_2 = 1.8 Hz, H′$_4$), 8.03 (dd, 1H, J_1 = 7.8 Hz, J_2 = 1.8 Hz, H′$_6$), 8.58 (s, 1H, H$_4$), 7.84 (s, 2H, NH$_2$), 10.42 (s, 1H, OH′). ^{13}C-NMR (DMSO-d_6, 300 MHz) δ 158,2 (C′$_2$), 152.8 (C$_4$), 133.2 (C′$_4$), 128.9 (C′$_6$), 126.1 (C$_1$), 121.2 (C′$_1$), 119.4 (C′$_5$), 116.4 (C′$_3$), 114.6 (CN), 113.4 (CN), 103.4 (C$_2$). Anal. Calcd. for $C_{11}H_8N_4O$: C, 62.3; H, 3.8; N, 26.4. Found: C, 62.3; H, 3.8; N, 26.1.

1-Amino-1,2-dicyano-2-(3 ´-hydroxibenzilidenamine) ethene (**3b**). 1 (0.65 g, 6.0 mmol), 3-hydroxybenzaldehyde 2b (0.73 g, 6.0 mmol), ethanol (8 mL). Yellow solid identified as **3b** (1.04 g, 82%). Mp 231–233 °C. IR (NaCl): 3401, 3379, 3299, 3205, 2244, 2205, 1625, 1611, 1587, 1561, 1491, 1396, 1288, 1225, 1215, 1150. ^{1}H-NMR (DMSO-d_6, 300 MHz) δ 6.90 (ddd, 1H, J_1 = 8.1 Hz, J_2 = 2.4, J_3 = 0.9 Hz, H′$_4$), 7.25 (t, J = 8.1 Hz,1H, H′$_5$), 7.37 (t, 1H, J = 2.1, H′$_2$), 7.43 (d, 1H, J = 8.1 Hz, H′$_6$), 7.88 (s, 2H, NH$_2$), 8.16 (s, 1H, H$_4$), 9.64 (s, 1H, OH′). ^{13}C-NMR (DMSO-d_6, 300 MHz) δ 157.7 (C′$_3$), 155.4 (C$_4$), 136.8 (C′$_1$), 129.7 (C′$_5$), 126.8 (C$_1$), 120.3 (C′$_6$), 118.8 (C′$_4$), 115.3 (C′$_2$), 114.5 (CN), 113.8 (CN), 102.7 (C$_2$). Anal. Calcd. for $C_{11}H_8N_4O$: C, 62.3; H, 3.8; N, 26.4. Found: C, 62.3; H, 3.9; N, 26.3.

1-Amino-1,2-dicyano-2-(4 ´-hydroxybenzilidenamine) ethene (**3c**). 1 (0.65 g, 6.0 mmol), 4-hydroxybenzaldehyde **2c** (0.73 g, 6.0 mmol), ethanol (10 mL). Yellow solid identified as **3c** (1.11 g, 87%). Mp 226–228 °C. IR (NaCl): 3455, 3410, 3322, 3272, 3184, 2231, 2207, 1625, 1610, 1589, 1567, 1512, 1306, 1264, 1235, 1207, 1162, 1112. ^{1}H-NMR (DMSO-d_6, 300 MHz) δ 6.82 (d, 2H, J = 8.7 Hz, H′$_{3+5}$), 7.65(s, 2H, NH$_2$), 7.86 (d, 2H, J = 8.7 Hz, H′$_{2+6}$), 8.14 (s, 1H, H$_4$), 10.21 (s, 1H, OH′). ^{13}C-NMR (DMSO-d_6, 300 MHz) δ 161.0 (C′$_p$), 155.1 (C$_4$), 131.2 (C′$_o$), 126.9 (C′$_1$), 125.5 (C$_1$), 115.7 (C′$_m$), 114.7 (CN), 114.0 (CN), 103.4 (C$_2$). Anal. Calcd. for $C_{11}H_8N_4O.1,1H_2O$: C, 57.0; H, 4.4; N, 24.2. Found: C, 57.2; H, 4.4; N, 24.0.

1-Amine-1,2-dicyano-2-(3 ´,4 ´-dihydroxybenzilidenamine) ethene (**3d**). 1 (0.32 g, 3.0 mmol), 3,4-dihydroxybenzaldehyde 2d (0.41 g, 3.0 mmol), ethanol (1.5 mL). Yellow solid identified as **3d** (0.55 g, 81%). Mp 219–222 °C. IR (NaCl): 3465, 3349, 3297, 3169, 2230, 2201, 1603, 1590, 1565, 1528, 1340, 1299, 1264, 1193, 1167, 1102. ^{1}H-NMR (DMSO-d_6, 300 MHz) δ 6.81 (d, 1H, J = 8.1, H′$_5$), 7.29 (dd, 1H, J_1 = 8.1 Hz, J_2 = 2.0 Hz, H′$_6$), 7.40 (d, 1H, J = 2.0 Hz, H′$_2$), 7.60 (s, 2H, NH$_2$), 8.06 (s, 1H, H$_4$), 9.15 (s, 1H, OH′), 9.80 (s, 1H, OH′). ^{13}C-NMR (DMSO-d_6, 300 MHz) δ 155.6 (C$_4$), 149.7 (C′$_4$), 145.7 (C′$_3$), 127.4 (C′$_1$), 125.3 (C$_1$), 122.8 (C′$_6$), 115.5 (C′$_2$), 115.5 (C′$_5$), 114.8 (CN), 114.0 (CN), 103.6 (C$_2$). Anal. Calcd. for $C_{11}H_8N_4O_2.1,1H_2O$: C, 53,5; H, 4.1; N, 22.7. Found: C, 53.5; H, 4.1; N, 22.7.

1-Amino-1,2-dicyano-2-(3 ´,4 ´,5 ´-trihydroxybenzilidenamine)ethene (**3e**). 1 (0.22 g, 2.0 mmol), 3,4,5-trihydroxybenzaldehyde 2e (0.34 g, 2.0 mmol), ethanol (1 mL). Yellow solid identified as **3e** (0.45 g, 92%). Mp > 300 °C (dec.). IR (NaCl): 3473, 3445, 3359, 3256, 3182, 2242, 2205, 1606, 1591, 1561, 1529, 1401, 1338, 1311, 1231, 1190, 1177, 1136. ^{1}H-NMR (DMSO-d_6, 300 MHz) δ 6.93 (s, 2H, H′$_{2+6}$), 7.56 (s,

2H, NH_2), 7.98 (s, 1H, H_4), 9.09 (s, >2H; OH′). ^{13}C-NMR (DMSO-d_6, 300 MHz) δ 156.1 (C_4), 146.1 (C'_m), 138.0 (C'_p), 126.1 (C'_1), 125.1 (C_1), 114.8 (CN), 114.1 (CN), 108.7 (C'_o), 103.7 (C_2). Anal. Calcd. for $C_{11}H_8N_4O_3$.0,1H_2O: C, 53.7; H, 3.4; N, 22.8. Found: C, 53.7; H, 3.5; N, 22.6.

3.1.2. General Procedure for the Synthesis of the 2-aryl-4,5-dicyano-1H-imidazoles (**4a**–**4d**)

Manganese dioxide was added to a solution of **3** in ethyl acetate/acetonitrile, and the mixture was kept under reflux until TLC indicated the complete consumption of reagent **3**. The manganese dioxide suspension was filtered using fiberglass paper, and the solvent was partially removed under reduced pressure. The yellow solid was filtered, washed with cold dichloromethane, and identified as the title compound **4**.

4,5-Dicyano-2-(2´-hydroxyphenyl)-1H-imidazole (**4a**). 3a (0.30 g, 1.42 mmol), manganese dioxide (6.16 g), ethyl acetate/acetonitrile (50/5 mL) and reflux for 14 hours. The yellow solid was identified as **4a** (0.15 g, 50%). Mp > 300 °C (dec.). IR (NaCl): 3441, 3335, 3240, 2250, 2237, 1675, 1607, 1551, 1521, 1473, 1403, 1351, 1308, 1293, 1264, 1226, 1154, 1111. ^{1}H-NMR (DMSO-d_6, 300 MHz) δ 6.94 (t, 1H, J = 7.8 Hz, H'_5), 7.02 (d, 1H, J = 7.8 Hz, H'_3), 7.34 (dt, 1H, J_1 = 7.8 Hz, J_2 = 1.5 Hz, H'_4), 7.94 (dd, 1H, J_1 = 7.8 Hz, J_2 = 1.5 Hz, H'_6), 10.00–13.00 (s, >1H, NH + OH′). ^{13}C-NMR (DMSO-d_6, 300 MHz) δ 155.4 (C'_2), 149.3 (C_2), 132.1 (C'_4), 128.7 (C'_6), 119.7 (C'_5), 116.5 (C'_3), 113.8 (C'_1), 111.5 (CN), not visible (C_4/C_5). Anal. Calcd. for $C_{11}H_6N_4O$.0,9H_2O: C, 58.3; H, 3.5; N, 24.7. Found: C, 58.6; H, 3.6; N, 24.4.

4,5-Diciano-2-(3´-hidroxifenil)-1H-imidazole (**4b**). 3b (0.30 g, 1.42 mmol), manganese dioxide (6.16 g) ethyl acetate/acetonitrile (50/5 mL) and reflux for five days. The yellow solid was identified as **4b** (0.21 g, 70%). Mp 264–267 °C. IR (NaCl): 3471, 3369, 3223, 2248, 2242, 1664, 1612, 1590, 1567, 1529, 1490, 1409, 1392, 1328, 1287, 1229, 1207, 1107. ^{1}H NMR (DMSO-d_6, 300 MHz) δ 6.91 (ddd, 1H, J_1 = 7.8 Hz, J_2 2.4 Hz, J_3 = 1.2 Hz, H'_4), 7.33 (t, 1H, J = 7.8 Hz, H'_5), 7.35-7.50 (m, 2H, H'_{2+6}), 9.86 (s, 1H, OH′), 12.00–16.00 (s, <1H, NH). ^{13}C-NMR (DMSO-d_6, 300 MHz) δ 157.9 (C'_3), 151.1 (C_2), 130.4 (C'_5), 128.8 (C'_1), 118.0 (C'_4), 117.0 (C'_6), 113.0 (C'_2), 111.4 (CN), not visible (C_4/C_5). Anal. Calcd. for $C_{11}H_6N_4O$.0,6H_2O: C, 59.6; H, 3.3; N, 25.3. Found: C, 59.8; H, 3.5; N, 25.0.

4,5-Dicyano-2-(4´-hydroxyphenyl)-1H-imidazole (**4c**). 3c (0.30 g, 1.42 mmol), manganese dioxide (6.16 g), ethyl acetate/acetonitrile (30/5 mL) and reflux for eight days. The yellow solid was identified as **4c** (0.19 g, 63%). Mp 279–281 °C. IR (NaCl): 3435, 3387, 3148, 2242, 2233, 1648, 1613, 1593, 1492, 1403, 1311, 1281, 1241, 1177, 1123. ^{1}H-NMR (DMSO-d_6, 300 MHz) δ 6.89 (d, 2H, J = 9.0 Hz, H'_{3+5}), 7.80 (d, 2H, J = 9.0 Hz, H'_{2+6}), 10.16 (s, 1H, OH′), 12.00–16.00 (s, <1H, NH). ^{13}C-NMR (DMSO-d_6, 300 MHz) δ 159.9 (C'_p), 151.5 (C_2), 128.2 (C'_o), 118.6 (C'_1), 116.0 (C'_m), 111.6 (CN), not visible (C_4/C_5). Anal. Calcd. for $C_{11}H_6N_4O$.1,9H_2O: C, 54.1; H, 4.0; N, 22.9. Found: C, 54.0; H, 4.2; N, 22.8.

4,5-Dicyano-2-(3´,4´-dihydroxyphenyl)-1H-imidazole (**4d**). 3d (0.25 g, 1.10 mmol), manganese dioxide (2.38 g), ethyl acetate/acetonitrile (50/10 mL) and reflux for 24 hours. The yellow solid was identified as **4d** (0.14 g, 55%). Mp > 300 °C (dec.). IR (NaCl): 3484, 3366, 3183, 2245, 2236, 1656, 1620, 1605, 1543, 1506, 1397, 1323, 1289, 1256, 1227, 1183, 1118. ^{1}H-NMR (DMSO-d_6, 300 MHz) δ 6.84 (d, 1H, J = 8.1 Hz, H'_5), 7.28 (dd, 1H, J_1 = 8.1 Hz, J_2 = 2.1 Hz, H'_6), 7.38 (d, 1H, J = 2.1 Hz, H'_2), 9.38 (s, 1H, OH′), 9.63 (s, 1H, OH′) and the NH signal is not visible on spectrum. ^{13}C-NMR (DMSO-d_6, 300 MHz) δ 151.8 (C_2), 148.3 (C'_4), 145.7 (C'_3), 119.1 (C'_1), 118.3 (C'_6), 116.0 (C'_5), 113.7 (C'_2), 111.7 (CN), not visible (C_4/C_5). Anal. Calcd. for $C_{11}H_6N_4O_2$.1,2H_2O: C, 53.2; H, 3.4; N, 22.6. Found: C, 53.2; H, 3.4; N, 22.5.

3.2. Antioxidant Capacity

3.2.1. Cyclic Voltammetry Technique

Cyclic voltammograms were obtained in a conventional three-electrode cell. The working electrode was a glassy carbon electrode; a saturated calomel electrode (SCE) and a platinum wire were

used as reference electrode and counter electrode, respectively. Cyclic voltammograms were recorded at a scan rate of 50 mV s^{-1} and all solutions were purged with argon before assays.

Solutions of the test compounds (1.0 mM) in a 1:1 (v/v) water/ethanol solution containing 0.14 M KCl and phosphate buffer (1.8 mM KH_2PO_4 and 10.1 mM Na_2HPO_4) were prepared, and the pH of the solutions was adjusted to pH = 7.4.

The experiments were done using Autolab PGSTAT 30 running with GPES (General Purpose Electrochemical System) version 4.6 software PG (Ecochimie, Utrecht, Netherlands).

3.2.2. DPPH Radical Method

The DPPH$^{\bullet}$ scavenging activity of the compounds was measured as already described [13]. A 0.002% ethanolic DPPH solution was used in the assays, and trolox was used as reference antioxidant. The IC_{50} value was determined for the compounds with the lowest oxidation potential from each chemical series.

3.2.3. Deoxyribose Degradation Method

Antioxidant effects of compounds on hydroxyl radicals (HO$^{\bullet}$) were determined as described previously [14]. Reaction mixtures contained deoxyribose, KH_2PO_4–KOH buffer, ascorbic acid, $FeCl_3$, H_2O_2, and synthesized compounds (assessed at IC_{50} concentration obtained in DPPH$^{\bullet}$ assay). After one hour of incubation at 37 °C, the colour appeared by adding 1 mL of thiobarbituric acid and 1 mL of trichloroacetic acid. The reaction mixture was then heated in boiling water for 15 min, and the absorbance of the resulting solutions was measured at 532 nm.

3.3. Determination of Antifungal Activity

MIC values were evaluated by the method of liquid microdilution described in the standard document CLSI M27-3A [28,29]. The antifungal activity of the synthesized compounds was evaluated for the yeasts *Saccharomyces cerevisiae* PYCC 4072 and *Candida albicans* PYCC 3436^{T}. For all tests, a culture of yeasts was prepared in agar tubes with medium YEPD and agar to guaranty purity and an excellent growth. An inoculum was transferred to a culture medium RPMI-1640, with 0.165 M of buffer 4-morpholinepropanesulfonic acid (Merck, Darmstadt, Germany), pH = 7.0. An aliquot of 0.1 mL of this cellular suspension was added to 0.1 mL of solution with the synthesized compound in microplate wells, with the final density of the inoculum being 2.25×10^3 cells/mL. The inoculated microplaques were incubated for 48 hours at temperatures of 30 and 37 °C for *Saccharomyces cerevisiae* and *Candida albicans*, respectively. The MIC values were then measured at 640 nm. Fluconazole and miconazole (Pfizer Inc., New York, NY, USA) were used as the reference controls.

3.4. Analysis of Toxicity in Mammalian Fibroblast

Cellular viability was determined by the lactate dehydrogenase (LDH) method, as already described [27]. The fibroblast cell line L929 (European Collection of Animal Cell Cultures) was used in the tests. Cells were incubated with the compounds and a small volume of medium was collected for the determination of extracellular LDH. The cells were after lysed to obtain the intracellular LDH. The enzyme activity was evaluated at 340 nm. The LDH released to the extracellular medium was described as a percentage of the total LDH activity.

4. Conclusions

Compounds **3e** and **4d** substituted with 3,4-di-hydroxyphenyl or 3,4,5-tri-hydroxyphenyl units presented high antioxidant activities, as determined by cyclic voltammetry, DPPH$^{\bullet}$, and deoxyribose degradation assays. These two compounds also displayed antifungal activity against the yeasts *Saccharomyces cerevisiae* and *Candida albicans* at concentrations not toxic to fibroblasts.

The cyclization of 1,2-(dicyano)ethene **3d** producing imidazole **4d**, increased the antifungal activity. In addition, we observed a synergistic effect between the nitrogen heterocycle and the phenolic unit, combined in the same molecule. In this work, we describe the synthesis of compounds **3e** and **4d** with dual antioxidant/antifungal activity involving two original scaffolds.

Author Contributions: Conceptualization, M.F.P. and F.A.; Funding acquisition, M.F.P.; Investigation, J.S., F.F. and F.A.; Methodology, A.B., M.J.S. and M.F.P.; Supervision, A.B, O.C., M.J.S. and F.A.; Data curation, M.C.; Writing—original draft, A.B., M.C., M.J.S, M.F.P. and F.A.

Funding: This research was funded by the Portuguese Fundação para a Ciência e Tecnologia (PPCDT/QUI/59356). Filipe Areias gratefully acknowledges a post-PhD grant from the Portuguese FCT (SFRH/BPD/26106).

Conflicts of Interest: The authors declare no conflict of interest.

References

1. Finley, J.W.; Kong, A.N.; Hintze, K.J.; Jeffery, E.H.; Ji, L.L.; Lei, X.G. Antioxidants in Foods: State of the Science Important to the Food Industry. *J. Agric. Food Chem.* **2011**, *59*, 6837–6846. [CrossRef] [PubMed]
2. Maia, A.M.; Baby, A.R.; Yasaka, W.J.; Suenaga, E.; Kaneko, T.M.; Velasco, M.V. Validation of HPLC stability-indicating method for Vitamin C in semisolid pharmaceutical/cosmetic preparations with glutathione and sodium metabisulfite, as antioxidants. *Talanta* **2007**, *71*, 639–643. [CrossRef] [PubMed]
3. Losada-Barreiro, S.; Bravo-Díaz, C. Free radicals and polyphenols: The redox chemistry of neurodegenerative diseases. *Eur. J. Med. Chem.* **2017**, *133*, 379–402. [CrossRef] [PubMed]
4. Griffiths, K.; Aggarwal, B.B.; Singh, R.B.; Buttar, H.S.; Wilson, D.; De Meester, F. Food Antioxidants and Their Anti-Inflammatory Properties: A Potential Role in Cardiovascular Diseases and Cancer Prevention. *Diseases* **2016**, *4*, 28. [CrossRef] [PubMed]
5. Alov, P.; Tsakovska, I.; Pajeva, I. Computational Studies of Free Radical-Scavenging Properties of Phenolic Compounds. *Curr. Top. Med. Chem.* **2015**, *15*, 85–104. [CrossRef] [PubMed]
6. Galano, A.; Mazzone, G.; Alvarez-Diduk, R.; Marino, T.; Alvarez-Idaboy, J.R.; Russo, N. Food Antioxidants: Chemical Insights at the Molecular Level. *Annu. Rev. Food Sci. Technol.* **2016**, *7*, 335–352. [CrossRef] [PubMed]
7. Van Acker, S.A.; de Groot, M.J.; van den Berg, D.J.; Tromp, M.N.; Kelder, G.; van der Vijgh, W.J.; Bast, A. A Quantum Chemical Explanation of the Antioxidant Activity of Flavonoids. *Chem. Res. Toxicol.* **1996**, *9*, 1305–1312. [CrossRef] [PubMed]
8. Sanglard, D. Emerging threats in antifungal-resistant fungal pathogens. *Front. Med.* **2016**, *3*, 1–10. [CrossRef] [PubMed]
9. Davey, P.G.; Wilcox, M.; Irving, W.; Thwaites, G. *Antimicrobial Chemotherapy*, 7th ed.; University Press: Oxford, UK, 2015.
10. Peng, X.; Huang, Q.; Zhang, K.; Yu, Y.; Wang, Z.; Wang, C. Distribution, behavior and fate of azole antifungals during mechanical, biological, and chemical treatments in sewage treatment plants in China. *Sci. Total Environ.* **2012**, *426*, 311–317. [CrossRef] [PubMed]
11. Campoy, S.; Adrio, J.L. Antifungals. *Biochem. Pharmacol.* **2017**, *133*, 86–96. [CrossRef] [PubMed]
12. Oroian, M.; Escriche, I. Antioxidants: Characterization, natural sources, extraction and analysis. *Food Res. Int.* **2015**, *74*, 10–36. [CrossRef] [PubMed]
13. Villaño, D.; Fernández-Pachón, M.S.; Moyá, M.L.; Troncoso, A.M.; García-Parrilla, M.C. Radical scavenging ability of polyphenolic compounds towards DPPH free radical. *Talanta* **2007**, *15*, 230–235. [CrossRef] [PubMed]
14. Sadowska-Bartosz, I.; Galiniak, S.; Bartosz, G. Modification of the deoxyribose test to detect strong iron binding. *Acta Biochim. Pol.* **2017**, *64*, 195–198. [CrossRef] [PubMed]
15. Simić, A.; Manojlović, D.; Šegan, D.; Todorović, M. Electrochemical Behavior and Antioxidant and Prooxidant Activity of Natural Phenolics. *Molecules* **2007**, *12*, 2327–2340. [CrossRef] [PubMed]
16. Han, R.M.; Zhang, J.P.; Skibsted, L.H. Reaction Dynamics of Flavonoids and Carotenoids as Antioxidants. *Molecules* **2012**, *17*, 2140–2160. [CrossRef] [PubMed]
17. Vlachodimitropoulou, E.; Sharp, P.A.; Naftalin, R.J. Quercetin–iron chelates are transported via glucose transporters. *Free Radic. Biol. Med.* **2011**, *15*, 934–944. [CrossRef] [PubMed]

18. Marino, T.; Galano, A.; Russo, N. Radical Scavenging Ability of Gallic Acid toward OH and OOH Radicals. Reaction Mechanism and Rate Constants from the Density Functional Theory. *J. Phys. Chem. B* **2014**, *118*, 10380–10389. [CrossRef] [PubMed]
19. Fazary, A.E.; Taha, M.; Ju, Y. Iron Complexation Studies of Gallic Acid. *J. Chem. Eng. Data* **2009**, *54*, 35–42. [CrossRef]
20. Thomas, C.; Mackey, M.M.; Diaz, A.A.; Cox, D.P. Hydroxyl radical is produced via the Fenton reaction in submitochondrial particles under oxidative stress: Implications for diseases associated with iron accumulation. *Redox Rep.* **2009**, *14*, 102–108. [CrossRef] [PubMed]
21. Muhoberac, B.B.; Vidal, R. Abnormal iron homeostasis and neurodegeneration. *Front. Aging Neurosci.* **2013**, *5*, 1–9. [CrossRef] [PubMed]
22. Wadhwa, A.; Kaur, R.; Bhalla, P. *Saccharomyces cerevisiae* as a cause of oral thrush & diarrhoea in an HIV/AIDS patient. *Trop. Gastroenterol.* **2010**, *31*, 227–228. [PubMed]
23. Sardi, J.C.; Scorzoni, L.; Bernardi, T.; Fusco-Almeida, A.M.; Giannini, M.J. Candida species: Current epidemiology, pathogenicity, biofilm formation, natural antifungal products and new therapeutic options. *J. Med. Microbiol.* **2013**, *62*, 10–24. [CrossRef] [PubMed]
24. Silva, C.R.; Neto, J.B.; Campos, R.; Figueiredo, N.S.; Sampaio, L.S.; Magalhães, H.I.; Cavalcanti, B.C.; Gaspar, D.M.; Andrade, G.M.; Lima, I.S.; et al. Synergistic Effect of the Flavonoid Catechin, Quercetin, or Epigallocatechin Gallate with Fluconazole Induces Apoptosis in *Candida tropicalis* Resistant to Fluconazole. *Antimicrob. Agents Chemother.* **2014**, *58*, 1468–1478. [CrossRef] [PubMed]
25. Zirngibl, L. *Antifungal Azoles: A Comprehensive Survey of Their Structures and Properties*; Wiley-VCH: Weinheim, Germany; New York, NY, USA; Chichester, UK; Brisbane, Australia; Singapore; Toronto, ON, Canada, 1998.
26. Mazu, T.K.; Bricker, B.A.; Flores-Rozas, H.; Ablordeppey, S.Y. The Mechanistic Targets of Antifungal Agents: An Overview. *Mini Rev. Med. Chem.* **2016**, *16*, 555–578. [CrossRef] [PubMed]
27. Cummings, B.S.; Wills, L.P.; Schnellmann, R.G. Measurement of Cell Death in Mammalian Cells. *Curr. Protoc. Pharmacol.* **2004**, *12*, 1–24.
28. Wayne, P.A. *CLSI. Reference Method for Broth Dilution Antifungal Susceptibility Testing of Yeasts, Approved Standard*, 3rd ed.; CLSI Document M27-A3; Clinical and Laboratory Standards Institute: Wayne, PA, USA, 2008.
29. Areias, F.M. Novos Compostos Heterocíclicos de Azoto Com Unidades Fenólicas: Síntese E Atividade Biológica. Ph.D. Thesis, Minho University, Braga, Portugal, 2006.

Sample Availability: Samples of the compounds are available from the authors.

© 2018 by the authors. Licensee MDPI, Basel, Switzerland. This article is an open access article distributed under the terms and conditions of the Creative Commons Attribution (CC BY) license (http://creativecommons.org/licenses/by/4.0/).

molecules

MDPI

Article

Dibasic Derivatives of Phenylcarbamic Acid against Mycobacterial Strains: Old Drugs and New Tricks?

Ivan Malík [1,*], Jozef Csöllei [2], Ivan Solovič [3,4], Šárka Pospíšilová [1], Hana Michnová [1], Josef Jampílek [1], Alois Čížek [5], Iva Kapustíková [1], Jana Čurillová [1], Mária Pecháčová [1], Jiřina Stolaříková [6], Daniel Pecher [7,8] and Michal Oravec [9]

1 Department of Pharmaceutical Chemistry, Faculty of Pharmacy, Comenius University in Bratislava, Odbojárov 10, SK-832 32 Bratislava, Slovakia; sharka.pospisilova@gmail.com (Š.P.); michnova.hana@gmail.com (H.M.); josef.jampilek@gmail.com (J.J.); kapustikova@fpharm.uniba.sk (I.K.); curilova2@uniba.sk (J.Č.); mariapech901@gmail.com (M.P.)
2 Department of Chemical Drugs, Faculty of Pharmacy, University of Veterinary and Pharmaceutical Sciences in Brno, Palackého 1946/1, CZ-612 42 Brno, Czech Republic; csolleij@vfu.cz
3 Clinic for Tuberculosis and Lung Diseases, National Institute for Tuberculosis, Lung Diseases and Thoracic Surgery, Vyšné Hágy, SK-059 84 Vysoké Tatry, Slovakia; solovic@hagy.sk or ivan.solovic@ku.sk
4 Department of Public Health, Faculty of Health, Catholic University in Ružomberok, Hrabovská cesta 1A, SK-034 01 Ružomberok, Slovakia
5 Clinic for Department of Infectious Diseases and Microbiology, Faculty of Veterinary Medicine, University of Veterinary and Pharmaceutical Sciences, Palackého 1946/1, CZ-612 42 Brno, Czech Republic; cizeka@vfu.cz
6 Laboratory for Mycobacterial Diagnostics and Tuberculosis, Regional Institute of Public Health, Partyzánské náměstí 7, CZ-702 00 Ostrava, Czech Republic; Jirina.Stolarikova@zu.cz
7 Department of Pharmaceutical Analysis and Nuclear Pharmacy, Faculty of Pharmacy, Comenius University in Bratislava, Odbojárov 10, SK-832 32 Bratislava, Slovakia; pecher1@uniba.sk
8 Toxicological and Antidoping Center, Faculty of Pharmacy, Comenius University in Bratislava, Odbojárov 10, SK-832 32 Bratislava, Slovakia
9 Global Change Research Institute CAS, Belidla 986/4a, CZ-603 00 Brno, Czech Republic; oravec.m@czechglobe.cz
* Correspondence: malikivan001@gmail.com; Tel.: +421-2-501-117-227

Received: 5 September 2018; Accepted: 24 September 2018; Published: 28 September 2018

Abstract: In order to provide a more detailed view on the structure–antimycobacterial activity relationship (*SAR*) of phenylcarbamic acid derivatives containing two centers of protonation, 1-[2-[({[2-/3-(alkoxy)phenyl]amino}carbonyl)oxy]-3-(dipropylammonio)propyl]pyrrolidinium oxalates (**1a–d**)/dichlorides (**1e–h**) as well as 1-[2-[({[2-/3-(alkoxy)phenyl]amino}carbonyl)oxy]-3-(dipropylammonio)propyl]azepanium oxalates (**1i–l**)/dichlorides (**1m–p**; alkoxy = butoxy to heptyloxy) were physicochemically characterized by estimation of their surface tension (γ; Traube's stalagmometric method), electronic features (log ε; UV/Vis spectrophotometry) and lipophilic properties (log k_w; isocratic RP-HPLC) as well. The experimental log k_w dataset was studied together with computational logarithms of partition coefficients (log *P*) generated by various methods based mainly on atomic or combined atomic and fragmental principles. Similarities and differences between the experimental and *in silico* lipophilicity descriptors were analyzed by unscaled principal component analysis (PCA). The *in vitro* activity of compounds **1a–p** was inspected against *Mycobacterium tuberculosis* CNCTC My 331/88 (identical with $H_{37}R_v$ and ATCC 2794, respectively), *M. tuberculosis* $H_{37}R_a$ ATCC 25177, *M. kansasii* CNCTC My 235/80 (identical with ATCC 12478), the *M. kansasii* 6509/96 clinical isolate, *M. kansasii* DSM 44162, *M. avium* CNCTC My 330/80 (identical with ATCC 25291), *M. smegmatis* ATCC 700084 and *M. marinum* CAMP 5644, respectively. *In vitro* susceptibility of the mycobacteria to reference drugs isoniazid, ethambutol, ofloxacin or ciprofloxacin was tested as well. A very unique aspect of the research was that many compounds from the set **1a–p** were highly efficient almost against all tested mycobacteria. The most promising derivatives showed *MIC* values varied from 1.9 μM to 8 μM, which were lower compared to those of used

standards, especially if concerning ability to fight *M. tuberculosis* $H_{37}R_a$ ATCC 25177, *M. kansasii* DSM 44162 or *M. avium* CNCTC My 330/80. Current *in vitro* biological assays and systematic *SAR* studies based on PCA approach as well as fitting procedures, which were supported by relevant statistical descriptors, proved that the compounds **1a**–**p** represented a very promising molecular framework for development of 'non-traditional' but effective antimycobacterial agents.

Keywords: dibasic phenylcarbamates; surface tension; electronic properties; lipophilicity; *Mycobacterium* spp.

1. Introduction

The treatment of commonly encountered species of tuberculous and non-tuberculous mycobacteria responsible for a multiplicity of different types of infections, including pulmonary, respiratory, cutaneous, and systemic infections, by (i) brand new classes of promising compounds preferably acting on novel targets; or (ii) 'non-typical' antimycobacterial drug candidates is still in very dynamic and progressive debate [1–6]. The strategy was successfully used in a case of *in vitro* screening of some β-lactam antibiotics (ceftaroline or ceftazidime) in a combination with an β-lactamase inhibitor avibactam against *Mycobacterium avium* complex [3,4]. Another encouraged example was *in vitro* and *ex vivo* testing of tricyclic thioridazine (Figure 1a), an old neuroleptic phenothiazine. The molecule was used alone or in a combinatorial therapy with anti-tuberculosis drugs (isoniazid, rifampin, linezolid or moxifloxacin) against *M. tuberculosis* regardless of its antibiotic resistance phenotype and was highly active due to its multi mechanisms of action [5,6].

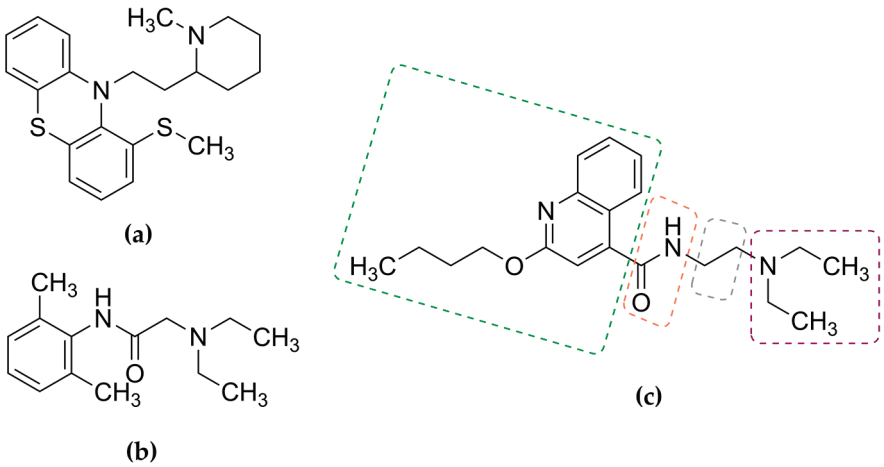

Figure 1. Chemical structure of thioridazine (**a**), a neuroleptic drug containing a phenothiazine scaffold (**a**); as well as effective local anesthetics (**b**) lidocaine (xylocaine); and (**c**) dibucaine (cinchocaine). All these compounds showed notable *in vitro* efficiency against some mycobacterial strains [5–12]. Structural fragments of dibucaine were color-coded as follows: a lipophilic moiety (a dark green framework), polar group (orange), connecting hydrocarbon chain (gray) and salt-forming (basic) group (dark red), respectively.

Antimycobacterial properties of compounds originally designed and tested as local anesthetics (LAs) have been investigated sporadically. Moreover, their application to management of the infections caused by a broad spectrum of species of the *Mycobacterium* genus has not been systematically reviewed. Nevertheless, Schmidt and Rosenkranz [7] as well as Fujii et al. [8] found that lidocaine (xylocaine; Figure 1b), a highly efficient LA drug [9,10], notably inhibited *in vitro* growth of some strains of human

M. tuberculosis, *M. bovis* or *M. kansasii*. Similarly, a quinoline core-containing dibucaine (cinchocaine; Figure 1c) [11], was able to effectively *in vitro* fight rapidly growing *M. phlei* [12].

A common structural feature of given efficient LAs (and promising antimycobacterials) was presence of a lipophilic moiety, polar anilido or amido group, connecting hydrocarbon chain and salt-forming fragment. All considered moieties were color-differentiated for a molecule of dibucaine (cinchocaine; Figure 1c).

Sequencing of *Mycobacterium* spp. genomes proved that these microorganisms produced a variety of enzymes [13–15] able to hydrolyze ester, anilide or amide bonds in a chemical structure of antimycobacterial drug candidates. Isosteric replacement of these polar groups with a carbamate moiety would provide very good proteolytic stability, especially if the modified structural arrangement of novel derivatives would be as follows: Aryl–NH–C(O)O–Alkyl [16]. The carbamate functionality imposes a degree of conformational restriction due to delocalization of non-bonded electrons on nitrogen into a carboxyl moiety. Participation of the carbamate group in hydrogen bonding through carboxyl and backbone N–H [17] should be also taken into account. Considering the importance of the carbamate functionality, its incorporation into a structure of novel antimycobacterial agents was one of key tasks in a process of their design and synthesis [18–20].

Currently evaluated 1-[2-[({[2-/3-(alkoxy)phenyl]amino}carbonyl)oxy]-3-(dipropylammonio)-propyl]pyrrolidinium/azepanium oxalates/dichlorides (**1a**–**p**; alkoxy = butoxy to heptyloxy; Table 1, Scheme 1) were synthesized with intention to find effective LAs with favorable toxicity profiles [21]. The compounds contained two types of an anionic counterpart (**1a**–**d** and **1i**–**l** versus **1e**–**h** and **1m**–**p**; Table 1) in order to achieve convenient aqueous solubility in biological assays [21].

It was found that all tested derivatives showed higher indices defining their relative surface (U_s) as well as infiltration (U_i) local anesthetic efficiency than reference LA drugs cocaine (U_s = 1.0, U_i = 3.6) or procaine (U_s = 0.1, U_i = 1.0) [21]. The most effective dibasic molecule in given types of local anesthesia was 1-[2-[({[3-(pentyloxy)phenyl]amino}carbonyl)oxy]-3-(dipropylammonio)propyl]-pyrrolidinium dichloride (**1f**) with U_s = 130 and U_i = 250 (Table S1 in Supplementary Materials), respectively.

It might be expected that the carbamate moiety was sterically protected due to branching of both connecting hydrocarbon chain and salt-forming group. Rotatable bonds of the 2-/3-alkoxy side chain *R* could also contribute to the steric hindrance (Table 1). It was proved by *ab initio* procedures that an intramolecular hydrogen bond between N–H of the carbamate functionality and oxygen atom of the 2-alkoxy chain was formed [22]. Such structural arrangements of compounds would provide stability against effects of various mycobacterial enzymes and would consider them promising candidates for antimycobacterial agents.

It was observed that surface tension (relative surface activity), electronic and lipophilic properties of carbamate group-containing molecules notably influenced the *in vitro* antimycobacterial efficiency [23–25]. However, the set **1a**–**p** has not been satisfactorily characterized by values of relevant physicochemical descriptors [26] (Table S1).

In a first part of this study, attention was turned on more precise physicochemical characterization of the derivatives **1a**–**p**. The research aimed determination of compounds' ability to decrease surface tension of water (γ), estimation of electronic properties described by logarithms of molar absorption coefficients (log ε) of their methanolic solutions, which were investigated in the UV/Vis region of an electromagnetic spectrum, as well as evaluation of lipophilic features defined by calculated log k_w parameters. These log k_w were based on extrapolation procedures of estimated logarithms of retention factors (log k) to elution with 100% water by reversed-phase high-performance liquid chromatography (RP-HPLC). In addition, relationships between the log k_w dataset and calculated logarithms of partition coefficients (log P) related to the octan-1-ol/water partitioning system were explored in order to provide a critical view on possibilities to predict lipophilic properties of the compounds based on two-dimensional (2D) visualization of their chemical structures.

Next, a very essential objective of the research was *in vitro* screening of the derivatives **1a**–**p** against various strains of tuberculous and non-tuberculous mycobacteria, i.e., *M. tuberculosis* CNCTC

My 331/88, *M. tuberculosis* $H_{37}R_a$ ATCC 25177, *M. kansasii* CNCTC My 235/80, a *M. kansasii* 6509/96 clinical isolate, *M. kansasii* DSM 44162, *M. avium* CNCTC My 330/80, *M. smegmatis* ATCC 700084 and *M. marinum* CAMP 5644, respectively.

A key aim of the study was to find some structural and physicochemical features of the compounds **1a**–**p**, which might appear to be notable for their *in vitro* antimycobacterial efficiency.

2. Results and Discussion

2.1. Synthesis of the Compounds **1a**–**p**

The investigated compounds **1a**–**p** were prepared by multi step pathways using 2-aminophenol (**1′a**) and 3-aminophenol (**1′b**), respectively, as starting molecules (Scheme 1). Very briefly, a reaction of **1′a** or **1′b** with acetanhydride led to *N*-(2-/3-hydroxyphenyl)ethanamide (**2′a** or **2′b**). A solution of **2′a** or **2′b** in anhydrous ethanol (EtOH) was added to sodium ethanoate. After mixing, 1-bromoalkane (alkane = butane to heptane) was added in order to prepare a series of *N*-(2-/3-alk-oxyphenyl)ethanamides (**3′a**–**h**; alkoxy = butoxy to heptyloxy). The molecules **3′a**–**h** were suspended in 18% hydrochloric acid and heated up to reflux. The solutions were cooled, neutralized and crude intermediates were extracted into diethyl ether (DEE). The organic layer was dried, filtered and solutions were removed *in vacuo* giving 2-/3-alkoxyanilines (**4′a**–**h**; alkoxy = butoxy to heptyloxy) [27]. Reulting intermediates **4′a**–**h** were dissolved in anhydrous toluene and added continuously into a saturated solution of phosgene [27]. The mixed solutions were refluxed, toluene was removed *in vacuo* providing desired 1-alkoxy-2-/3-isocyanatobenzenes (**5′a**–**h**).

Into an aqueous solution of *N*-propylpropanamine (**6′**), a (±)-2-(chloromethyl)oxirane reagent was added and solution was allowed to stand at room temperature (r.t.; 48h). The mixture was heated up to 75 °C and treated with 38% sodium hydroxide. The cooled solution was filtered and a crude intermediate was formed. Extraction of the filtrate with DEE, drying and removal of the organic layer provided additional amount of the intermediate [28], which isolation and crystallization from absolute EtOH led to (±)-*N*-(oxiran-2-ylmethyl)-*N*-propylpropanamine (**7′**).

The addition of pyrrolidine or azepane to **7′** in anhydrous propan-2-ol (2-PrOH) provided 1-(dipropylamino)-3-pyrrolidin-1-ylpropan-2-ol (**8′a**) or 1-azepan-1-yl-3-(dipropylamino)-propan-2-ol (**8′b**) [29].

Oily 1-(1-azacycloalkyl)-3-(dipropylamino)propan-2-yl (2-/3-alkoxyphenyl)carbamates (**9′a**–**p**; azacycloalkyl = pyrrolidinyl or azepanyl) were prepared by a reaction of 1-alkoxy-2-/3-isocyanato-benzenes **5′a**–**h** with a dibasic alcohol **8′a** or **8′b** in anhydrous toluene.

Addition of a saturated solution of oxalic acid in anhydrous EtOH or ethereal hydrogen chloride to the bases **9′a**–**p** dissolved in chloroform led to solid colorless 1-[2-[({[2-/3-(alkoxy)phenyl]-amino}carbonyl)oxy]-3-(dipropylammonio)propyl]pyrrolidinium oxalates (**1a**–**d**)/dichlorides (**1e**–**h**) and 1-[2-[({[2-/3-(alkoxy)phenyl]amino}carbonyl)oxy]-3-(dipropylammonio)propyl]azepanium oxalates (**1i**–**l**)/dichlorides (**1m**–**p**; Scheme 1, Table 1) as well. More detailed procedures describing syntheses of particular intermediates and final molecules were provided in Supplementary Materials.

Chemical structure of the compounds **9′a**–**p** and **1a**–**p** was previously verified by their infrared (IR) spectra, which confirmed presence of all key groups. In addition, elemental analyses results (% C, H, N) were within ±0.40% of theoretical values for both bases **9′a**–**p** and salts **1a**–**p** [21]. Melting points (m.p.′s), R_f values (TLC) and acid-base pK_{a1} and pK_{a2} parameters of **1a**–**p** were already published [21,26] and can be found in Table S1.

Current liquid chromatography high resolution mass spectroscopy (HPLC-HR-MS) analyses, which were performed on the LC Agilent Infinity System coupled with the Quadrupole Time-Of-Flight Mass Spectrometer (6520 Accurate Mass Q-TOF LC/MS), confirmed structural identity of the intermediates **9′a**–**p** (Supplementary Materials).

After re-crystallization from a mixture of acetone/ethanol (subgroups **1a**–**d, 1e**–**h** and **1m**–**p**) or acetone (**1i**–**l**), high-resolution mass spectra (HR-MS) of these salts were measured by the Dionex

UltiMate 3000 High-Performance Liquid Chromatograph coupled with the LTQ Orbitrap XL Hybrid Ion Trap-Orbitrap Fourier Transform Mass Spectrometer equipped with a HESI II (heated electrospray ionization) source in a positive (**1a–d**, **1i–l**) or negative (**1e–h**, **1m–p**) mode. The analyses confirmed structural identity of given molecules.

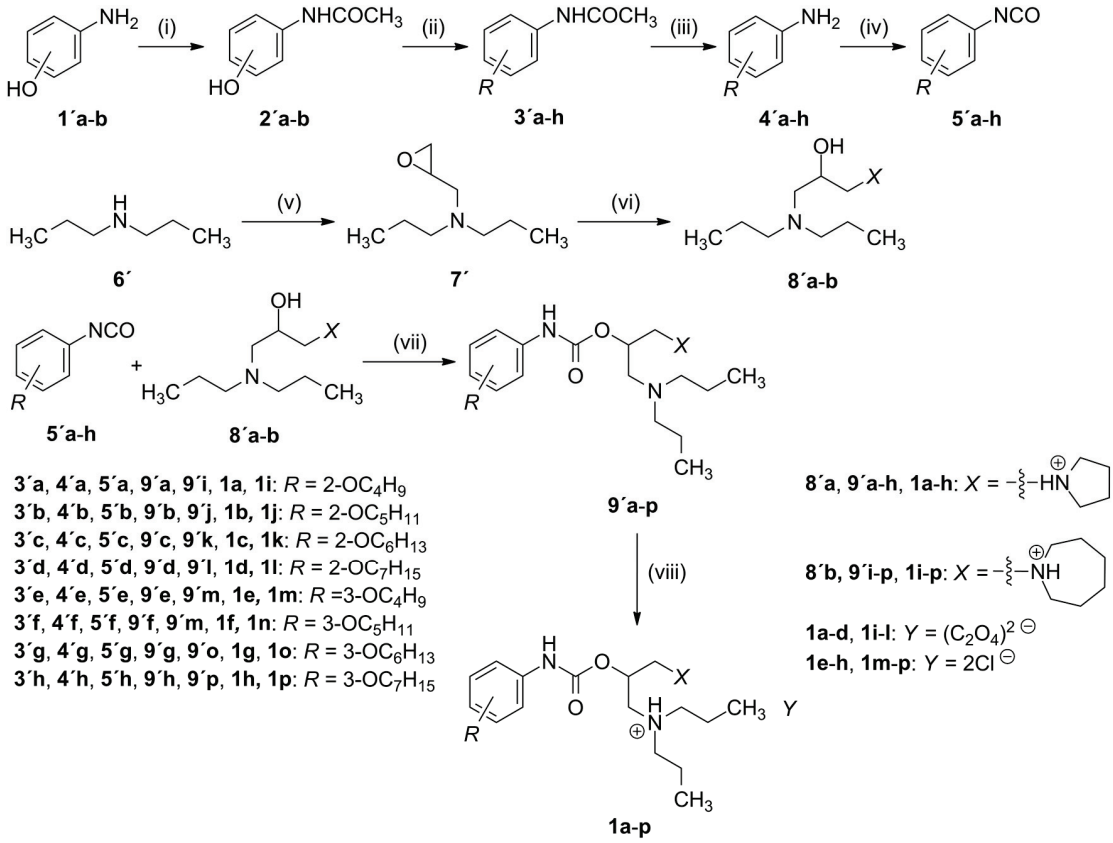

Scheme 1. Synthesis of 1-[2-[({[2-/3-(alkoxy)phenyl]amino}carbonyl)oxy]-3-(dipropylammonio)-propyl]pyrrolidinium/azepanium oxalates/dichlorides (**1a–p**; alkoxy = butoxy to heptyloxy). *Reagents and conditions*: (i) $(CH_3CO)_2O$, reflux (1h); (ii) Na, anhydrous EtOH, 1-bromoalkane (alkane = butane to heptane), r.t. (12h), reflux (3h); (iii) 18% HCl, reflux (2h); (iv) phosgene, anhydrous toluene, reflux (3h); (v) (±)-2-(chloromethyl)oxirane, 35 °C (2h), r.t. (48h), 38% NaOH; (vi) pyrrolidine/azepane, anhydrous 2-PrOH, reflux (6h); (vii) anhydrous toluene, reflux (8h); (viii) saturated solution of (a) oxalic acid in anhydrous EtOH or (b) ethereal hydrogen chloride.

2.2. Determination and Prediction of Some Physicochemical Properties of the Compounds **1a–p**

2.2.1. Surface Tension

Surface tension (relative surface activity; γ) of aqueous solutions of the compounds **1a–p** ($c = 2.0 \times 10^{-3}$ M) was determined by a drop count technique [30,31] using a Traube stalagmometer. All evaluated substances were able to decrease surface tension of water ($\gamma = 0.07259$ N/m) at 21 °C.

Elongation of the 2-/3-alkoxy side chain *R* led to more surface-active derivatives within homological sets **1a–d**, **1e–h**, **1i–l** and **1m–p**. This behavior was also in agreement with conclusions of a research paper [32]. The 2-alkoxy substituted molecules **1a–d** and **1i–l** showed lower ability to reduce surface tension of water than their 3-alkoxy substituted isomers **1e–h** or **1m–p** (Table 1, Figure 2).

Relationships between the number of carbon atoms forming the chain *R* (n_c) and γ values (in N/m units) was inspected using a linear function, polynomial function of 2nd order and sigmoidal fitting, respectively.

Equations related to the most relevant functions and values of common statistical descriptors, namely, number of points (number of cases; *n*), degrees of freedom (*DF*), reduced chi-square (χ^2_{red}), residual sum of squares (*RSS*), correlation coefficient (*R*), adjusted coefficient of determination (*Adj.* R^2), root mean squared error (standard deviation; *RMSE*), norm of residuals (*NR*), Fisher's significance ratio (Fisher's *F*-test; *F*) and probability of obtaining the *F* Ratio (significance of a whole model; *Prob* > *F*), respectively, can be found in Table S2.

Indication of a significance level of the *F* Ratio was as follows: one star symbol (*) for statistically significant, two stars symbol (**) for statistically very significant or three stars symbol (***) for statistically extremely significant level was used. The regression equations and their statistical characteristics were calculated and visualized by the Origin Pro *ver.* 9.0.0 SR2 software (OriginLab Corporation, Northampton, MA, USA).

The relationships between n_c and γ were described most precisely by statistically significant (**1a**–**d**, **1i**–**l** and **1m**–**p**) or very significant (**1e**–**h**) models built on polynomial functions of 2nd order (Figure 2, Equations (S1–S4) in Table S2).

Table 1. Chemical structure of evaluated compounds **1a**–**p**, their surface tension γ (relative surface activity; in N/m units), wavelengths of observed absorption maxima (λ_1, $\lambda_{2\,(Ch\text{-}T)}$, λ_3) and logarithms of molar absorption coefficients (log ε_1, log $\varepsilon_{2\,(Ch\text{-}T)}$, log ε_3) of compounds' methanolic solutions ($c = 8.0 \times 10^{-5}$ M), which were investigated in the UV/Vis region of an electromagnetic spectrum.

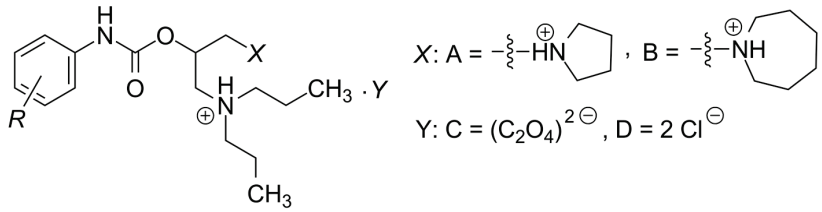

Comp.	*R*	*X*	*Y*	γ (N/m)	λ_1	log ε_1	$\lambda_{2\,(Ch\text{-}T)}$	[1] log $\varepsilon_{2\,(Ch\text{-}T)}$	λ_3	log ε_3
1a	2-OC_4H_9	A	C	0.06464	208	4.51	236	4.19	280	3.63
1b	2-OC_5H_{11}	A	C	0.06366	208	4.39	236	4.05	280	3.51
1c	2-OC_6H_{13}	A	C	0.06222	208	4.58	238	4.52	278	3.49
1d	2-OC_7H_{15}	A	C	0.05985	208	4.43	236	4.08	280	3.55
1e	3-OC_4H_9	A	D	0.06316	210	4.65	238	4.24	279	3.59
1f	3-OC_5H_{11}	A	D	0.06285	210	4.55	237	4.27	279	3.62
1g	3-OC_6H_{13}	A	D	0.06105	210	4.54	237	4.13	279	3.48
1h	3-OC_7H_{15}	A	D	0.05786	210	4.66	237	4.27	279	3.63
1i	2-OC_4H_9	B	C	0.06302	208	4.44	236	4.08	280	3.57
1j	2-OC_5H_{11}	B	C	0.06206	208	4.54	236	4.22	280	3.71
1k	2-OC_6H_{13}	B	C	0.06065	208	4.42	236	4.10	280	3.57
1l	2-OC_7H_{15}	B	C	0.05853	208	4.44	236	4.14	280	3.59
1m	3-OC_4H_9	B	D	0.06298	210	4.52	238	4.09	279	3.44
1n	3-OC_5H_{11}	B	D	0.06154	210	4.56	238	4.18	279	3.52
1o	3-OC_6H_{13}	B	D	0.05925	210	4.52	238	4.01	279	3.37
1p	3-OC_7H_{15}	B	D	0.05692	210	4.65	238	4.20	279	3.56

[1] log $\varepsilon_{2\,(Ch\text{-}T)}$, Logarithms of molar absorption coefficients observed at the charge-transfer absorption maximum $\lambda_{2\,(Ch\text{-}T)}$ = 236–238 nm.

The derivatives containing an azepanium moiety (**1i**–**l**, **1m**–**p**) showed slightly higher ability to decrease surface tension of water than their positional isomers with a pyrrolidinium salt-forming group (**1a**–**d**, **1e**–**h**). The most surface active were 1-[2-[({[3-(heptyloxy)phenyl]amino}carbonyl)-oxy]-3-(dipropylammonio)propyl]azepanium dichloride (**1p**) with γ = 0.05692 N/m and 1-[2-[({[3-(heptyloxy)phenyl]amino}carbonyl)oxy]-3-(dipropylammonio)propyl]pyrrolidinium dichloride (**1h**), which showed γ = 0.05786 N/m (Table 1, Figure 2).

Very similar behaviors to present findings were observed when Čižmárik with co-workers [33,34] analyzed structurally similar compounds **JC-01a**–**l**, effective LAs [33], which contained only one

centrum of basicity (Figure 3). All given molecules showed ability to decrease surface tension of water and 3-alkoxy substituted derivatives **JC-01g–l** (alkoxy = propoxy to octyloxy) were more efficient surfactants than their 2-alkoxy positional isomers **JC-01a–f**. Relationships between n_c (n_c = 3–8) and γ (in N/m units) of these alkoxy positional isomers were described very satisfactorily by polynomial functions of 2nd order [34].

Concerning presently analyzed dichlorides **1m–p**, branching of their connecting chain and presence of a dipropylammonium moiety resulted in the γ values (Table 1), which were slightly lower in comparison to those of **JC-01h–k** [34].

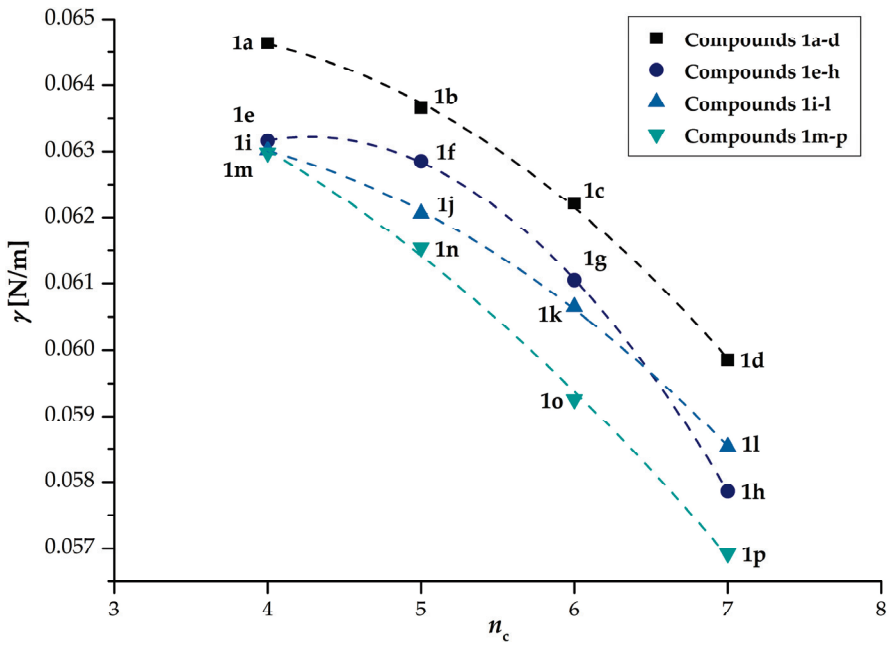

Figure 2. Relationships between number of carbon atoms forming the 2-/3-alkoxy side chain R (n_c; alkoxy = butoxy to heptyloxy) and γ values (in N/m units) of the compounds **1a–p**.

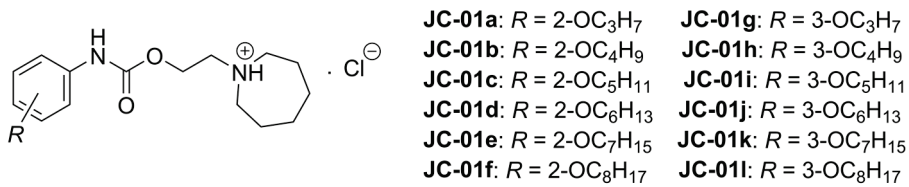

Figure 3. Chemical structure of the compounds **JC-01a–l**, effective local anesthetics [33], which were able to decrease surface tension of water [34].

2.2.2. Electronic Properties

Electronic properties of the molecules **1a–p** (Table 1) were characterized by logarithms of molar absorption coefficients (log ε) of their methanolic solutions (c = 8.0 × 10^{-5} M) investigated in the UV/Vis region of an electromagnetic spectrum.

The solutions showed three absorption maxima in a near ultraviolet (quarz) region of this spectrum between 200 nm and 400 nm [35], namely, λ_1 = 208–210 nm, $\lambda_{2\,(\text{Ch-T})}$ = 236–238 nm and λ_3 = 278–280 nm (Table 1), respectively. Positions of these absorption bands in the spectrum were typical for derivatives of (substituted) phenylcarbamic acid and the bands were assigned as first local excitation (λ_3), charge-transfer ($\lambda_{2\,(\text{Ch-T})}$) and second local excitation (λ_1) absorption maxima, respectively [36]. The λ_1 and $\lambda_{2\,(\text{Ch-T})}$ maxima of 2-alkoxy substituted compounds **1a–d** and **1i–l** were slightly lower compared to those of their 3-alkoxy substituted positional isomers **1e–h** and **1m–p**

(Table 1), respectively. Chemical structures of analyzed derivatives **1a–d** and **1i–l** indicated that steric inability of both carbamoyloxy and alkoxy groups to achieve coplanarity inhibited 'proper' resonance.

The log $\varepsilon_{2\,(\text{Ch-T})}$ parameters of compounds **1a–p**, which were observed at $\lambda_{2\,(\text{Ch-T})}$, varied from 4.01 (**1o**) to 4.52 (**1c**). The methanolic solutions of **1a–h** were characterized by higher log $\varepsilon_{2\,(\text{Ch-T})}$ values than those of **1i–p** and ranged from 4.05 (**1b**) to 4.52 (**1c**; Table 1), excluding the molecules **1j** (4.22) and **1l** (4.14). In addition, there was found nor linear neither quasi-parabolic relationship between number of carbon atoms forming the side chain R (n_c) and log $\varepsilon_{2\,(\text{Ch-T})}$ values (Figure S1 in Supplementary Materials).

In next sections of the paper, which are aimed at relationships between structure and *in vitro* activity, special consideration is devoted to the log $\varepsilon_{2\,(\text{Ch-T})}$ values because they could be the most sensitive to differences in electronic environment of a phenylcarbamoyloxy moiety due to different position and length of a substituent R [36].

2.2.3. Lipohydrophilic Properties

Lipophilicity has been the physicochemical parameter of notable importance in *QSAR* and *SAR* studies as a predominant descriptor encoding information on a network of inter- and intramolecular forces affecting drug transport *via* lipophilic compartments as well as drug's interactions with target effector sites [37,38].

A classical shake-flask method for a partitioning measurement of a compound in the octan-1-ol/buffer (or water) system, thus estimation of its log P_{exp} value, is quite time-consuming, it requires the solute to be pure and with adequate solubility in an aqueous phase. Insolubility often means that highly lipophilic compounds may not be determined accurately [39]. Concerning these issues very seriously, RP-HPLC was rather applied to estimate lipophilic properties of the molecules **1a–p** than the shake-flask alternative.

Octadecyl-functionalized silica gel was currently used as a stationary phase (SPh) and a gradient of two solvents at different volume ratios modified retention properties of the SPh [39,40]. Liquid binary mixtures of methanol (MeOH) with water were employed as mobile phases (MPhs) in the isocratic RP-HPLC. The MeOH modifier was preferred because of similarity of both observed and extrapolated lipophilicity parameters with the ones determined in the octan-1-ol/water partition system, considering also sensitivity to *H*-bond donor properties of investigated compounds [41].

The modifier was applied in different volume concentrations, which varied from 85% to 100% (v/v) with 5% increments. This interval was chosen due to very high lipophilicity of investigated salts. Practically, lower volume concentration of MeOH, i.e., less than 85% (v/v) in used MPhs, caused uncertainty of retention times (t_r) due to notable peaks broadening, especially within subsets **1i–l** and **1m–p**. In addition, their t_r values were considerably prolonged with increase in water content (v/v) of the MPhs so it was no longer possible to determine t_r values in such MPhs. Taking the 85–100% volume concentrations range, the isocratic separation was feasible and reasonable retention of the compounds **1a–p** was observed in all MPhs. The highest t_r parameters were found for the molecules **1k** (t_r = 47.108 min) and **1l** (t_r = 70.012 min) in the MPh containing 85% proportion (v/v) of MeOH (Table 2).

In addition, purity (in percentages) of the compounds **1a–p** was verified by RP-HPLC. Areas of their peaks were measured using the MPh, which contained 90% proportion (v/v) of MeOH. The purity of given salts varied from 96.82% (**1j**) to 99.65% (**1m**; Table S3).

Estimated retention factor (capacity factor; k) values were found in an area from 0.5063 (**1e**) to 2.5096 (**1l**) if pure MeOH was used as the MPh, and from 3.6174 (**1e**) to 30.4159 (**1l**) if the 80:20 MeOH/water (v/v) MPh was applied (Table S3).

Regarding a group of oxalates (Scheme 1), a pyrrolidium moiety-containing derivatives **1a–d** showed lower log k values in all used MPhs than those with an azepanium fragment **1i–l**. Same trends were observed for dichlorides, i.e., the compounds **1e–h** showed lower log k outputs compared to those of a series **1m–p**.

Elongation of the *R* substituent (Table 1) led to increase in t_r as well as log *k* values within all evaluated subgroups **1a–d**, **1e–h**, **1i–l** and **1m–p** (Table 2). Increase in a volume concentration (*v*/*v*) of MeOH caused shortening of both t_r and log *k* for all analyzed compounds **1a–p** (Table 2).

El Tayar et al. [42,43] investigated lipophilic properties of protonated basic compounds, which were therapeutically used as psychoactive agents, and inspected relationships between their log *k* values and volume concentrations (*v*/*v*) of MeOH. They found that these relationships were notably influenced by nature of solutes. The models were preferably built on linear functions and MeOH exerted its own solvophobic effect in the MPhs, which contained more than 80% (*v*/*v*) of given organic modifier if focusing on analyses of neutral and non-ionic compounds.

For partially and completely ionized polar compounds, the relationships appeared to be nearly parabolic but the parts of parabolic curves, which corresponded to MeOH-rich eluents (80% or higher volume concentration (*v*/*v*) of MeOH) were regarded as linear [42,43].

Paschke et al. [44] analyzed a series of highly lipophilic tetrachlorobenzyltoluene isomers by isocratic RP-HPLC and found linear relationships ($R > 0.9995$) between their log *k* values and volume concentrations of MeOH, which varied from 80% to 100% (*v*/*v*).

Table 2. Retention times t_r (RP-HPLC) and lipophilicity indices log *k* (RP-HPLC) of the compounds **1a–p** estimated in the mobile phases with a various volume ratio (*v*/*v*) of a methanol (MeOH) organic modifier and water.

Comp.	Mobile Phase MeOH/Water (*v*/*v*)									
	80:20		85:15		90:10		95:5		Pure MeOH	
	t_r (min)	log *k*	t_r (min)	log *k*	t_r (min)	log *k*	t_r (min)	log *k*	t_r (min)	log *k*
1a	13.883	0.7165	10.694	0.5756	7.830	0.3958	5.766	0.2008	4.224	−0.0403
1b	17.200	0.8254	12.647	0.6656	9.449	0.5064	6.514	0.2841	4.526	0.0203
1c	25.694	1.0206	16.950	0.8162	11.292	0.6053	7.431	0.3683	5.246	0.1287
1d	31.000	1.1092	19.600	0.8882	13.553	0.7022	7.892	0.4052	5.385	0.1573
1e	10.330	0.5584	6.917	0.3183	5.400	0.1478	3.822	−0.1454	3.329	−0.2956
1f	12.400	0.6574	9.200	0.4911	6.280	0.2546	4.022	−0.0941	3.340	−0.2913
1g	17.200	0.8254	11.402	0.6104	7.483	0.3679	5.153	0.1182	3.583	−0.2067
1h	22.003	0.9521	13.701	0.7159	8.532	0.4565	5.788	0.2092	3.556	−0.2153
1i	24.020	0.9881	16.917	0.8153	11.691	0.6240	7.765	0.3954	5.127	0.1205
1j	29.525	1.0863	20.021	0.8981	13.060	0.6828	8.520	0.4509	5.295	0.1449
1k	47.108	1.3023	27.001	1.0424	16.533	0.8038	9.641	0.5221	6.938	0.3303
1l	70.012	1.4831	38.800	1.2152	22.636	0.9619	11.670	0.6271	7.756	0.3996
1m	15.731	0.7805	9.218	0.4922	6.420	0.2695	4.685	0.0424	3.519	−0.2275
1n	22.183	0.9502	12.370	0.6542	8.156	0.4205	4.995	0.0941	3.947	−0.1047
1o	29.174	1.0807	13.651	0.7059	9.634	0.5174	5.095	0.1095	4.127	−0.0618
1p	33.719	1.1484	17.129	0.8215	11.332	0.6072	5.801	0.2051	3.925	−0.1102

On the other hand, observed log *k* data could not be used in terms of a universal scale to express lipophilicity of compounds because the log *k* values were dependent on chromatographic conditions, i.e., they depended on both MPhs and SPhs. Extrapolation of estimated solute retention (log *k*) to elution with 100% water (calculation of log k_w) would definitely be much more precise approach than using of log *k*, because the k_w parameters were independent of any effect of the organic modifier and relied on the SPh alone [45]. It has been recognized that the log k_w descriptor was very efficient for anticipation of *in vitro* antimycobacterial properties of compounds [46–49].

According to the authors' opinions based on systematic scientific literature survey, a current research paper was the first, which aimed the log k_w parameters of 2-/3-alkoxyphenylcarbamic acid derivatives containing two centers of protonation. The log k_w values were extrapolated from intercepts of a relationship between log *k* and volume fraction of the MPh modifier (φ_M) using the Snyder–Soczewiński linear solvent strength model [50–52]. The relationship was justified by $R > 0.9900$, *Adj.* $R^2 > 0.9750$ as well as $F > 180.00$ for calculation of particular log k_w parameters (Table 3).

Table 3. Extrapolated log k_w parameters (RP-HPLC) of analyzed molecules **1a**–**p** and values of statistical descriptors (χ^2_{red}, *RSS*, *R*, *Adj.* R^2, *RMSE*, *NR*, *F* and *Prob* > *F*), which characterized a linear relationship between the log *k* and φ_M values for a particular compound. The φ_M parameter was a volume fraction of MeOH in the isocratic elution RP-HPLC.

Comp.	log k_w	[1] *S*	[2] χ^2_{red}	[3] *RSS*	[4] *R*	[5] *Adj.* R^2	[6] *RMSE*	[7] *NR*	[8] *F*	[9] *Prob* > *F*
1a	3.7688	3.7768	0.0011	0.0034	0.9953	0.9875	0.0335	0.0580	317.64	0.0001 ***
1b	4.0454	3.9834	0.0018	0.0055	0.9931	0.9817	0.0429	0.0744	215.17	0.0007 ***
1c	4.6049	4.4634	0.0002	0.0007	0.9993	0.9982	0.0152	0.0263	2155.37	0.0001 ***
1d	4.9487	4.7736	0.0011	0.0033	0.9971	0.9923	0.0332	0.0574	518.15	0.0002 ***
1e	4.0258	4.3434	0.0013	0.0038	0.9960	0.9894	0.0354	0.0614	375.47	0.0003 ***
1f	4.6722	4.9652	0.0028	0.0084	0.9932	0.9821	0.0530	0.0917	219.79	0.0007 ***
1g	4.9446	5.1128	0.0013	0.0040	0.9969	0.9919	0.0366	0.0634	487.75	0.0002 ***
1h	5.5384	5.6830	0.0042	0.0126	0.9923	0.9795	0.0648	0.1122	192.51	0.0008 ***
1i	4.4679	4.3102	0.0014	0.0042	0.9955	0.9879	0.0376	0.0652	328.27	0.0004 ***
1j	4.8466	4.6600	0.0016	0.0048	0.9956	0.9882	0.0401	0.0695	337.19	0.0004 ***
1k	5.2359	4.9286	0.0005	0.0017	0.9987	0.9964	0.0234	0.0406	1106.57	0.0001 ***
1l	5.8966	5.5102	0.0007	0.0020	0.9988	0.9965	0.0259	0.0449	1127.92	0.0001 ***
1m	4.7099	4.9316	0.0004	0.0013	0.9990	0.9972	0.0205	0.0356	1442.73	0.0001 ***
1n	5.2087	5.3398	0.0011	0.0032	0.9978	0.9941	0.0325	0.0564	673.05	0.0001 ***
1o	5.6569	5.7628	0.0045	0.0134	0.9920	0.9789	0.0668	0.1157	186.23	0.0009 ***
1p	6.1749	6.2672	0.0022	0.0067	0.9966	0.9909	0.0474	0.0820	438.042	0.0001 ***

[1] *S*, Slope; [2] χ^2_{red}, reduced chi-square; [3] *RSS*, residual sum of squares; [4] *R*, correlation coefficient; [5] *Adj.* R^2, adjusted coefficient of determination; [6] *RMSE*, root mean squared error (standard deviation); [7] *NR*, norm of residuals; [8] *F*, Fisher's significance ratio (Fisher's *F*-test); [9] *Prob* > *F*, probability of obtaining the *F* Ratio (significance of a whole model). Indication of a significance level of the *F* Ratio was as follows: *** (three stars), extremely significant.

Goodness of fit for all proposed models generating log k_w, in other words, quantity used to test whether any given data were well described by a suggested function, was adjusted by χ^2_{red} values, which varied from 0.0002 (**1c**) to 0.0045 (**1o**). As can be seen, the linear relationships minimized *RSS* values, as variabilities about regression lines, which ranged from 0.0007 (**1c**) to 0.0134 (**1o**). The linearity was also proved by calculated *RMSE* parameters, as standard deviations of the data about regression lines, which were found in an interval from 0.0152 (**1c**) to 0.0668 (**1o**; Table 3).

The extrapolated log k_w values of compounds **1a**–**p** (Table 3) were in accordance with their elution order and hydrophobicity and varied from 3.7688 (**1a**) to 6.1749 (**1p**). Assuming presence of an identical azacycloalkyl moiety, oxalates (**1a**–**d**, **1i**–**l**) were less lipophilic than corresponding positional isomers synthesized as dichlorides (**1e**–**h**, **1m**–**p**; Table 3). As expected, 1-[2-[({[3-(hept-yloxy)phenyl]amino}carbonyl)oxy]-3-(dipropylammonio)propyl]azepanium oxalate (**1l**) and 1-[2-[({[3-(heptyloxy)phenyl]amino}carbonyl)oxy]-3-(dipropylammonio)propyl]azepanium dichloride (**1p**; Table 1) were found to be the most lipophilic showing log k_w of 5.8966 (**1l**) and 6.1749 (**1p**; Table 3), respectively.

Increase in n_c (Table 1) led to higher log k_w values in all inspected subgroups **1a**–**d**, **1e**–**h**, **1i**–**l** and **1m**–**p**. These relationships were defined by statistically significant (**1e**–**h**, **1i**–**l**), very significant (**1a**–**d**) and extremely significant (**1m**–**p**) linear functions and values of relevant statistical descriptors (Equations (S5)–(S8) in Table S4).

The *S* index (Table 3) in RP-HPLC has been a function of molecular structure parameters. For sets of non-polar homologues, linear relationships between their *S* and number of carbon atoms in a hydrocarbon side chain was found. Increase in size and van der Waals volume of a solute led to increased *S* parameter as well [53].

Results of present analyses agreed with given conclusions. Increase in length of the side chain *R* led to higher *S* within all inspected homological subgroups. The compounds containing an azepanium moiety showed higher *S* parameters, which varied from 4.3102 (**1i**) to 6.2672 (**1p**), than those with a pyrrolidium group, i.e., from 3.7768 (**1a**) to 5.6830 (**1h**; Table 3), if same position and length of *R* was presumed.

The slope *S* values of linear regression functions used to obtain log k_w were connected with specific hydrophobic surface areas of compounds and could serve as indicative measure of uniformity of retention mechanisms. If the uniformity was observed, a convenient model between the slope(s) and intercept(s), i.e., log k_w values, was anticipated [40]. Statistically extremely significant relationship between the log k_w and *S* values of **1a**–**p** was found and described by Equation (1):

$$S = 0.9449\ (\pm 0.0823) \times \log k_w + 0.2755\ (\pm 0.4087) \quad (1)$$

$$n = 16,\ DF = 14,\ \chi^2_{red} = 0.0470,\ RSS = 0.6586,\ R = 0.9508,\ Adj.\ R^2 = 0.8971,$$
$$RMSE = 0.2169,\ NR = 0.8115,\ F = 131.75,\ Prob > F = 0.0001\ ***$$

Based on values of statistical descriptors provided above, the uniformity of a retention mechanism was proven and suitability of chosen MPhs was confirmed for lipophilicity evaluation of the derivatives **1a**–**p**.

Statistical analyses indicated that both position and length of the side chain *R* (Equations (S9) and (S10) in Table S5) were more important factors, which contributed to the uniformity of retention behavior, compared to nature (and physicochemical properties) of a salt-forming fragment (Equations (S11) and (S12) in Table S5) of inspected compounds, despite the fact that all partial models built on linear regression analyses were statistically extremely significant.

To provide better understanding and give a critical review of relationships between the experimental lipophilicity measures and *in silico* prediction of lipophilic properties, the log k_w dataset was studied together with computational logarithms of partition coefficients (log *P*).

Practical estimation of log P_{exp} for some molecules from the set **1a**–**p** by a shake-flask method was not possible due to their insolubility in phosphate buffer systems (p*H* = 7.30). Thus, the lack of enough reliable log P_{exp} values would be a very limiting factor for eventual investigation of the relationships between log P_{exp} and *in silico* log *P*. On the other hand, linear models between log k_w and log P_{exp} were already observed [39], so interchangeability of these descriptors was fully justified.

The log *P* parameters of non-protonated forms of analyzed compounds, i.e., **9′a**–**p** (Scheme 1, Table 4), were calculated for the octan-1-ol/water partitioning system. These values were generated by the ChemBioDraw Ultra 12.0 software package (CambridgeSoft, Cambridge, MA, USA), various Java and non-Java interactive applets as well.

The Ghose and Crippen's log P_{Cr} [54,55], Viswanadhan's log P_V [56], Broto's log P_B [57] and Leo's CLOGP 4.0 [58] atomic and atomic/fragmental-based approaches were chosen to calculate the log *p* values (Table 4) by the ChemBioDraw Ultra 12.0 software, respectively. The Virtual Computer Chemistry Laboratory [59], a freely available web-based tool working in Java environment, was used to calculate log *P* by the Wang's XLOGP 2.0 [60], Cheng's XLOGP 3.0 [61], Moriguchi's MLOGP [62], Sander's (Actelion's) ACLOGP [63], Molinspiration's miLogP 2.2 [64], ALOGP [65] and Tetko's ALOGPs 2.1 [66] method (Tables 4 and 5), respectively. All these methods integrated algorithms combining atomic and fragmental principles, except for ALOGPs 2.1, which considered a molecule in the whole [66].

Finally, the SILICOS-IT hybrid method, which used proprietary fragment- and property-based principles, was also employed to generate log *P* parameters (log $P_{S\text{-}IT}$; Table 5). The method was implemented in the SwissADME applet, a free web tool designed to evaluate pharmacokinetics and drug-likeness of small molecules [67].

A common issue connected with given *in silico* approaches [26] was that they did not allow to correctly predict log *p* values of particular salts **1a**–**p**. This was the reason why current research targeted on the calculations related to non-protonated bases **9′a**–**p**.

The compounds **9′i**–**p** showed higher log *P* than their positional isomers **9′a**–**h**, which contained a different salt-forming moiety. Almost all used predictor tools indicated the molecules **9′a**–**p** highly lipophilic with log *p* > 4.27 (Tables 4 and 5), excluding the MLOGP method. The calculations based on MLOGP indicated moderate or high lipophilicity of these substances, which log *P* were found in a range from 2.75 (**9′a** and **9′e**) to 3.76 (**9′l** and **9′p**; Table 5).

The CLOGP 4.0 predicted the highest lipophilic nature of the bases **9′a**–**p** and their log *P* varied from 6.23 (**9′a** and **9′e**) to 8.94 (**9′l** and **9′p**; Table 4). As might be assumed, all employed atomic and atomic/fragmental methods did not consider a position of the side chain *R* when generating log *P* (Tables 4 and 5). Only the whole-molecule ALOGPs 2.1 approach took into account this aspect, so the 2-alkoxy substituted compounds **9′a**–**d** and **9′i**–**l** were less lipophilic than their 3-alkoxy substituted positional isomers **9′e**–**h** and **9′m**–**p** (Table 5), respectively.

It was found that linear relationships between the extrapolated log k_w values of compounds **1a–p** (Table 3) and particular *in silico* log *P* parameters of non-protonated derivatives **9′a–p**, namely, log P_{Cr}, log P_V, log P_B, CLOGP 4.0, XLOGP 2.0, XLOGP 3.0, MLOGP, ACLOGP, miLogP 2.2, ALOGP, log $P_{S\text{-}IT}$ and ALOGPs 2.1 (Tables 4 and 5), respectively, were statistically extremely significant (*Prob* > *F* = 0.0001) and were defined by *R* > 0.9300, *Adj.* R^2 > 0.8650, *F* > 99.00 and other common statistical descriptors (Equations (S13)–(S24) in Table S6).

Table 4. Values of logarithms of partition coefficients of basic (non-protonated) compounds **9′a–p** predicted for the octan-1-ol/water partitioning system by the Ghose and Crippen′s approach (log P_{Cr}), Viswanadhan′s principle (log P_V), Broto′s algorithm (log P_B) and CLOGP method (CLOGP 4.0), respectively, as well as by both XLOGP approaches (XLOGP 2.0 and XLOGP 3.0).

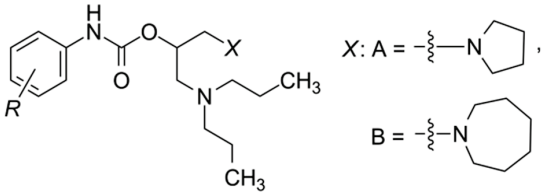

Comp.	*R*	*X*	log P_{Cr}	log P_V	log P_B	CLOGP 4.0	XLOGP 2.0	XLOGP 3.0
9′a	2-OC_4H_9	A	4.59	4.45	4.51	6.23	4.52	5.14
9′b	2-OC_5H_{11}	A	5.00	4.85	4.97	6.76	5.09	5.68
9′c	2-OC_6H_{13}	A	5.42	5.24	5.42	7.29	5.66	6.22
9′d	2-OC_7H_{15}	A	5.84	5.64	5.88	7.82	6.23	6.77
9′e	3-OC_4H_9	A	4.59	4.45	4.51	6.23	4.52	5.14
9′f	3-OC_5H_{11}	A	5.00	4.85	4.97	6.76	5.09	5.68
9′g	3-OC_6H_{13}	A	5.42	5.24	5.42	7.29	5.66	6.22
9′h	3-OC_7H_{15}	A	5.84	5.64	5.88	7.82	6.23	6.77
9′i	2-OC_4H_9	B	5.42	5.24	5.42	7.35	5.24	5.86
9′j	2-OC_5H_{11}	B	5.84	5.64	5.88	7.88	5.81	6.40
9′k	2-OC_6H_{13}	B	6.26	6.04	6.33	8.41	6.38	6.84
9′l	2-OC_7H_{15}	B	6.67	6.43	6.79	8.94	6.95	7.48
9′m	3-OC_4H_9	B	5.42	5.24	5.42	7.35	5.24	5.86
9′n	3-OC_5H_{11}	B	5.84	5.64	5.88	7.88	5.81	6.40
9′o	3-OC_6H_{13}	B	6.26	6.04	6.33	8.41	6.38	6.84
9′p	3-OC_7H_{15}	B	6.67	6.43	6.79	8.94	6.95	7.48

Table 5. Values of logarithms of partition coefficients of basic (non-protonated) compounds **9′a–p** predicted for the octan-1-ol/water partitioning system by the MLOGP, ACLOGP, miLogP 2.2, ALOGP, SILICOS-IT (log $P_{S\text{-}IT}$) and ALOGPs 2.1 method, respectively.

Comp.	MLOGP	ACLOGP	miLogP 2.2	ALOGP	log $P_{S\text{-}IT}$	ALOGPs 2.1
9′a	2.75	5.05	5.30	5.42	4.27	5.18
9′b	2.96	5.52	5.80	5.87	4.68	5.57
9′c	3.16	5.98	6.32	6.33	5.10	5.93
9′d	3.36	6.45	6.81	6.79	5.53	6.25
9′e	2.75	5.05	5.32	5.42	4.27	5.21
9′f	2.96	5.52	5.83	5.87	4.68	5.61
9′g	3.16	5.98	6.33	6.33	5.10	5.95
9′h	3.36	6.45	6.84	6.79	5.53	6.32
9′i	3.16	5.69	6.31	6.33	4.78	5.93
9′j	3.36	6.16	6.81	6.79	5.20	6.23
9′k	3.56	6.62	7.32	7.24	5.62	6.54
9′l	3.76	7.08	7.82	7.70	6.04	6.77
9′m	3.16	5.69	6.33	6.33	4.78	5.97
9′n	3.36	6.16	6.84	6.79	5.20	6.27
9′o	3.56	6.62	7.34	7.24	5.62	6.59
9′p	3.76	7.08	7.85	7.70	6.04	6.83

In an effort to characterize these relationships more precisely, similarities and differences between given descriptors were analyzed by using unscaled principal component analysis (PCA), a powerful multivariate statistical technique, that analyzed a set of values, in which observations were described by several inter-correlated quantitative dependent variables. A set of new orthogonal variables, called principal components (PCs), and pattern of similarity of observations was a result the analysis [68].

Current PCAs were performed by the Origin Pro *ver.* 9.0.0 SR2 software. Number of concerned PCs was determined by visual evaluation of a scree plot, as a relationship between calculated eigenvalues (λ_e) and number of PCs. The λ_e descriptor measured amount of variation retained by each PC [68]. The first two PCs, i.e., Principal Component 1 (PC 1) and Principal Component 2 (PC 2), of the analysis accounted for 99.26% of the total variance in the data. It meant that other PCs might be ignored without losing any substantial information. The PCs did not prove existence of 'real' parameters, they only indicated that existence of these descriptors was mathematically possible within the set of analyzed values.

A relationship between PC 1 and PC 2 resulted in division of examined compounds into characteristic groups. Differences in lipophilic properties of the bases **9′a**–**p** were reflected in their PC 1 values. One group, defined by negative PC 1 values, included derivatives containing a pyrrolidin-1-yl moiety (**9′a**–**c**, **9′e**–**g**) as well as molecules with both azepan-1-yl fragment and butoxy side chain (**9′i**, **9′m**). Conversely, second group, which was characterized by positive PC 1 values, encompassed compounds containing an azepan-1-yl moiety (**9′j**–**l**, **9′n**–**p**) as well as derivatives with both sterically smaller azacycloalkyl ring and heptyloxy substituent (**9′d**, **9′h**). The most negative PC 1 value was generated for the least lipophilic derivative **9′a**, which salt **1a** showed the lowest experimental lipophilicity (log k_w = 3.7688). The most positive PC 1 output was registered for the most lipophilic compound **9′p**, a base of the most lipophilic salt **1p** (log k_w = 6.1749; Figure 4).

It was found that PC 2 took into consideration a type of an azacycloalkyl moiety as well as position and length of *R*. The derivatives **9′a**–**h** showed higher PC 2 than the compounds **9′i**–**p**. Higher PC 2 were assigned to the 3-alkoxy substituted molecules compared to their 2-alkoxy positional isomers, when assuming their identical salt-forming moiety.

Increase in n_c of the side chain *R* led to higher PC 1 as well as PC 2. There were found no compounds (points), which could be regarded as outliers to the remaining ones along PC 1 or PC 2 (Figure 4).

The PCA-based 2D biplot showed both PC scores (PC 1, PC 2) of evaluated compounds (green dots) and loadings of variables indicated as orange straight lines [68]. The lines characterizing log k_w, log $P_{I\text{-}IT}$, XLOGP 2.0, XLOGP 3.0 and ACLOGP variables were located on upper right side of this biplot. The line related to log k_w formed the smallest angles with those of log $P_{I\text{-}IT}$, XLOGP 2.0 or XLOGP 3.0, which meant that these descriptors correlated each other most positively. Conversely, the largest angle was observed between the lines connected with log k_w and CLOGP 4.0, so these variables were unlikely to correlate each other (Figure 4).

The PC 1 was influenced almost equally by loadings of all inspected variables, as indicated particular scores on top axis. The scores varied from 0.27 (log k_w) to 0.28 (log P_{Cr}, log P_V, log P_B, miLogP 2.2 and ALOGP, respectively). The most positive impact on PC 2 showed a loading of the log k_w and log $P_{I\text{-}IT}$ variable, which scored approximately 0.45 and 0.37, respectively, on right axis. Conversely, the strongest inverse relationship was found between PC 2 and loading of the CLOGP 4.0 variable (−0.28; Figure 4).

Following visualization, the *in silico* log $P_{I\text{-}IT}$, XLOGP 2.0 and XLOGP 3.0 descriptors might be used to characterize lipophilic properties of analyzed salts and bases, especially if they contained highly lipophilic side chain *R*. Those molecules were defined by positive values of both PC 1 and PC 2. In addition, very close grouping was observed for **9′l** with **9′p** (Figure 4).

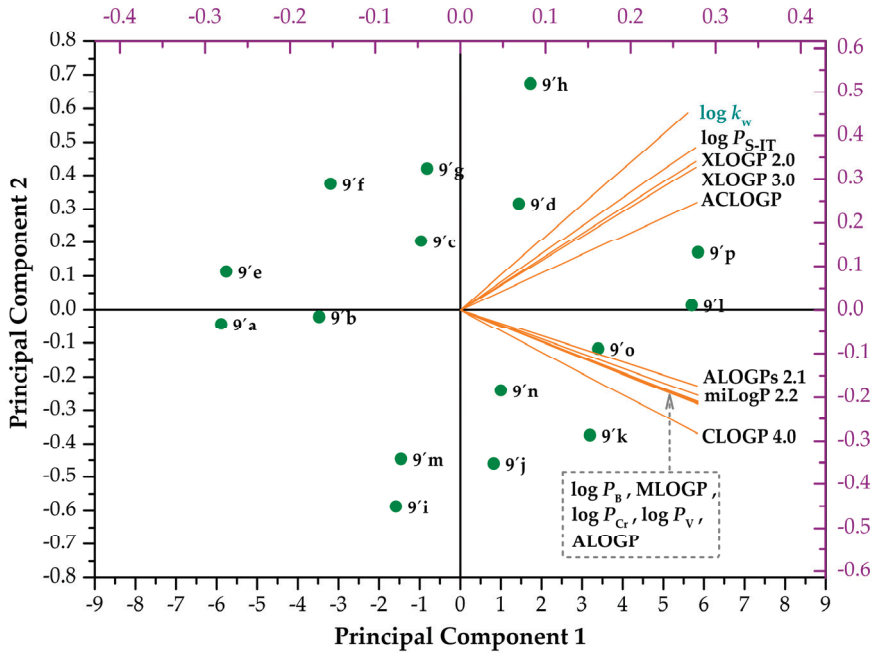

Figure 4. Two-dimensional biplot (mapping) showing both Principal Component 1 and 2 scores of the compounds **9′a–p** and loadings of extrapolated chromatographic (log k_w; **1a–p**) and *in silico* lipophilicity variables, i.e., log $P_{S\text{-}IT}$, XLOGP 2.0, XLOGP 3.0, ACLOGP, ALOGPs 2.1, miLogP 2.2, CLOGP 4.0, log P_{Cr}, log P_V, log P_B, MLOGP and ALOGP, respectively.

Considering observed physicochemical characteristics of the compounds **1a–p**, there was found statistically extremely significant linear relationship between the γ and log k_w values. This dependence was expressed by Equation (2) and values of relevant statistical descriptors as follows:

$$\gamma = -0.0031\ (\pm 0.0003) \times \log k_w + 0.0765\ (\pm 0.0015) \quad (2)$$

$$n = 16,\ DF = 14,\ \chi'^2_{red} = 6.436 \times 10^{-7},\ RSS = 9.010 \times 10^{-6},\ R = 0.9383,\ Adj.\ R^2 = 0.8718,$$
$$RMSE = 8.022 \times 10^{-4},\ NR = 0.0030,\ F = 103.02,\ Prob > F = 0.0001\ ***$$

Linearity of this model was adjusted by relatively very low χ^2_{red}, *RSS* and *RMSE* values. The γ and log k_w parameters of **1i–p** showed the most positive impact to final statistical analysis data (Equation (S28) in Table S7) connected with Equation (2) compared to those of a subset **1a–h** (Equation (S27) in Table S7).

One of the major tasks to consider in drug design is the ability of a compound to cross biological membranes. The blood–brain barrier (*BBB*) is a critical biological structure for maintaining homeostasis of central nervous system and preventing damage to the brain. Compounds primarily designed as neuroactive agents are required to cross the *BBB* to provide their therapeutic effect. Conversely, molecules that target other compartments of a body ideally should not cross this barrier to avoid possible psychotropic side effects. Thus, the task of predicting the *BBB* permeability of new compounds is of great importance [69].

Norinder and Haeberlein [70] suggested some simple rules to preliminary answer a question whether a drug candidate would be able to cross the *BBB*. Very briefly, if a sum of nitrogen and oxygen atoms ($n_N + n_O$) in a molecule was ≤ 5 or if [CLOGP $-$ ($n_N + n_O$)] > 0 then the compound would have a good chance to enter the brain by passive diffusion. The originally employed CLOGP was a lipophilicity descriptor generated *in silico*. In addition, molecular weight (MW) of such compound should be ≤ 450 to facilitate brain permeation [71].

Each of the oxalates **1a–d** and **1i–l** contained ($n_N + n_O$) = 10, each of the chlorides **1e–h** and **1m–p** contained ($n_N + n_O$) = 6 (Table 1), respectively. If presently calculated CLOGP 4.0 parameter would be replaced with log $P_{S\text{-}IT}$ (Table 5), which was closer to a 'real' log k_w lipophilicity descriptor (Figure 4), only basic forms of the most lipophilic compounds **1l** and **1p**, i.e., the substances **9′l** and **9′p**, might be considered to possess very limited brain permeation. On the other hand, calculated MW > 450 for these derivatives [21] indicated that they might not be able to passively cross the *BBB*.

2.3. In Vitro Antimycobacterial Assays

The *in vitro* activity of compounds **1a–p** was inspected against *Mycobacterium tuberculosis* CNCTC My 331/88 (identical with $H_{37}R_v$ and ATCC 2794, respectively; abbreviation used: MT_v $H_{37}R_v$), *M. tuberculosis* $H_{37}R_a$ ATCC 25177 (MT_a $H_{37}R_a$), *M. kansasii* CNCTC My 235/80 (identical with ATCC 12478; *MK* 235/80), a *M. kansasii* 6509/96 clinical isolate (*MK* 6509/96), *M. kansasii* DSM 44162 (*MK* DSM), *M. avium* CNCTC My 330/80 (identical with ATCC 25291; *MA* 330/80), *M. smegmatis* ATCC 700084 (*MS*) and *M. marinum* CAMP 5644 (*MM*), respectively, by the methods described earlier [20,72–75]. *In vitro* susceptibitity of given mycobacteria to reference drugs isoniazid (INH), ethambutol (EMB), ofloxacin (OFLX) or ciprofloxacin (CPX) was tested as well (Tables 6 and 7).

A value of a minimum inhibitory concentration (*MIC*) was the lowest concentration of a tested compound, (i) which inhibited growth of MT_v $H_{37}R_v$, *MK* 235/80, *MK* 6509/96 and *MA* 330/80, respectively; (ii) at which no visible growth of MT_a $H_{37}R_a$, *MS*, *MK* DSM as well as *MM* was observed [20,72–75].

The *in vitro* screening procedures related to particular mycobacterial strains were repeated three times and the *MIC* values, reported in Tables 6 and 7 (in μM units), were average values of these determinations.

A very unique aspect of a present research was that many compounds from the set **1a–p** were *in vitro* efficient against almost all tested mycobacteria. The most promising molecules with observed $MIC \leq 8$ μM were indicated in gray (Tables 6 and 7).

The 3-alkoxy substituted derivatives **1e–h** and **1m–p** were slightly more effective against all screened strains than their 2-alkoxy substituted isomers **1a–d** and **1i–l**, respectively. 1-[2-[({[3-(Heptyloxy)phenyl]amino}carbonyl)oxy]-3-(dipropylammonio)propyl]azepanium dichloride (**1p**) was the most active against almost complete spectrum of tested microorganisms ($MIC \leq 8$ μM), excluding *MA* 330/80 only. Comparable efficiency to **1p** was observed for 1-[2-[({[3-(heptyloxy)phenyl]amino}carbonyl)oxy]-3-(dipropylammonio)propyl]pyrrolidinium dichloride (**1h**), which also showed $MIC \leq 8$ μM against almost all tested mycobacteria, excluding *MA* 330/80 as well as *MS*. In addition, antimycobacterial activity of 1-[2-[({[3-(pentyloxy)phenyl]amino}carbonyl)oxy]-3-(dipropylammonio)propyl]azepanium dichloride (**1n**) and 1-[2-[({[3-(hexyloxy)phenyl]amino}carbonyl)oxy]-3-(dipropylammonio)propyl]azepanium dichloride (**1o**), respectively, was only slightly lower compared to activity of the substances **1p** and **1h** (Tables 6 and 7).

It was found that MT_v $H_{37}R_v$ was not so sensitive to the compounds **1a–p** as to INH (*MIC* = 0.5 μM and 1 μM). The most promising substances **1d**, **1h**, **1l**, **1n** or **1p** showed *MIC* = 4 μM and 8 μM (Table 6), respectively.

Similar trends were observed when evaluating susceptibility of *MK* 235/80. The molecules **1h**, **1n** and **1p** showed *MIC* = 8 μM, however, the OFLX reference drug was more active (*MIC* = 0.5 μM and 1 μM; Table 6). Comparable ability to fight *MK* 6509/96 was found for the derivative **1h**, series **1n–p** (*MIC* = 4 μM and 8 μM) and INH (*MIC* = 2–8 μM; Table 6), respectively.

All 3-alkoxy substituted molecules **1e–h** and **1m–p** were more active against MT_a $H_{37}R_a$ (*MIC* = 3.7–8.1 μM) than INH (*MIC* = 36.5 μM) or CPX (*MIC* = 48.3 μM). The dibasic compounds were also able to fight *MK* DSM more effectively, their *MIC* values ranged from 1.9 μM (**1h**) to 16.2 μM (**1e**), than INH (*MIC* = 29.2 μM; Table 6). Moreover, the derivatives **1g**, **1h** and **1n–p** were almost equally efficient against *MA* 330/80 as EMB (*MIC* = 16 μM; Table 7).

If attention was paid to the 2-alkoxy substituted compounds **1a**–**d** and **1i**–**l**, 1-[2-[({[2-(heptyloxy)phenyl]amino}carbonyl)oxy]-3-(dipropylammonio)propyl]pyrrolidinium dichloride (**1d**) was more active against both MT_a $H_{37}R_a$ (*MIC* = 12.5 μM) and *MK* DSM (*MIC* = 6.2 μM) than INH (Table 6).

Waisser et al. [76] *in vitro* tested two series of structurally similar molecules **JC-01a**–**l** (Figure 3) and **JC-02a**–**l** (Figure 5) against MT_v $H_{37}R_v$, *MK* 235/80, *MK* 6509/96 and *MA* 330/80, respectively. The authors found that the compounds with an azepanium group were antimycobacterially more promising agents than the ones containing a pyrrolidinium heterocycle.

Current *in vitro* assays revealed that both branching of a connecting hydrocarbon chain and presence of 'an additional' dipropylammonium group within a salt-forming part of tested compounds **1a**–**p** were favorable for their antimycobacterial activity and they were more effective than the sets **JC-01a**–**l** and **JC-02a**–**l**.

The INH standard was less effective against *MS* (*MIC* = 117 μM) as well as *MM* (*MIC* = 467 μM) than almost all screened phenylcarbamic acid-based substances, exluding the derivatives **1a**, **1i**, **1k** or **1l** (Table 7). 1-[2-[({[2-(Pentyloxy)phenyl]amino}carbonyl)oxy]-3-(dipropylammonio)propyl]-azepanium oxalate (**1j**) was the most active against *MS* (*MIC* = 6.2 μM), the molecule **1h** fight *MM* most efficiently (*MIC* < 3.7 μM). On the other hand, these strains were sensitive to lower MICs of CPX (*MIC* = 0.4 μM and 0.8 μM; Table 7). It should be also mentioned that both sets **JC-01a**–**l** (Figure 3) and **JC-02a**–**l** (Figure 5) have not been *in vitro* tested against MT_a $H_{37}R_a$, *MK* DSM, *MS* or *MM*.

Table 6. The *in vitro* activity (*MIC* values in μM units) of investigated compounds **1a**–**p** and reference drugs isoniazid (INH), ethambutol (EMB), ofloxacin (OFLX) and ciprofloxacin (CPX) against *M. tuberculosis* CNCTC My 331/88 (*M. tuberculosis* $H_{37}R_v$; MT_v $H_{37}R_v$), *M. tuberculosis* $H_{37}R_a$ ATCC 25177 (MT_a $H_{37}R_a$), *M. kansasii* CNCTC My 235/80 (*MK* 235/80), *M. kansasii* 6509/96 (*MK* 6509/96) and *M. kansasii* DSM 44162 (*MK* DSM), respectively.

Comp.	*MIC* [μM]									
	MT_v $H_{37}R_v$		MT_a $H_{37}R_a$	*MK* 235/80			*MK* 6509/96			*MK* DSM
	[1] 14-d	[2] 21-d	[3] 7-d	7-d	14-d	21-d	7-d	14-d	21-d	7-d
1a	32	32	213	62.5	62.5	62.5	32	62.5	62.5	53
1b	16	32	52	32	32	62.5	32	32	62.5	26.1
1c	16	16	25	32	32	32	16	16	16	12.7
1d	8	8	12.5	16	16	32	8	16	16	6.2
1e	16	32	8.1	32	32	32	16	16	32	16.2
1f	16	16	<3.9	16	16	32	8	16	16	7.9
1g	8	16	<3.8	16	16	16	8	8	16	3.8
1h	4	8	<3.7	8	8	8	4	4	8	1.9
1i	16	32	203	32	62.5	62.5	16	32	32	51
1j	16	32	199	16	32	62.5	16	32	32	50
1k	8	16	195	16	32	62.5	16	32	32	98
1l	4	8	96	16	32	32	16	16	32	382
1m	8	16	15.4	16	16	32	8	16	16	7.7
1n	4	8	7.5	8	8	8	4	8	8	7.5
1o	8	16	7.3	8	16	16	4	8	8	3.6
1p	4	8	7.1	8	8	8	4	8	8	3.6
INH	0.5	1	36.5	>250	>250	>250	2	4	8	29.2
EMB	1	2	–	–	–	–	1	2	2	–
OFLX	1	2	–	0.5	1	1	0.5	0.5	1	–
CPX	–	–	48.3	–	–	–	–	–	–	3.0

[1] 14-d, 14-Day cultivation; [2] 21-d, 21-day cultivation; [3] 7-d, 7-day cultivation. The most promising values of compounds´ *in vitro* antimycobacterial activity (*MIC* ≤ 8 μM) were indicated in gray cells of Table 6.

The chemometric PCA tool was applied to study activity–activity relationships of the compounds **1a**–**p** to explore similarities or differences in their impact on particular mycobacterial strains. The analysis was carried out by the XLSTAT *ver.* 2016.02.28451 software (Addinsoft, New York,

NY, USA), a statistical application for Microsoft Excel *ver.* 2013 (Microsoft Corp., Redmont, WA, USA). Number of PCs was determined using visual evaluation of a scree plot, as a relationship between calculated λ_e and number of PCs. A present selection of PCs was based on a Kaiser–Guttman rule, as the most common stopping rule in PCA [77], which aimed an average value of $\lambda_e > 1.0$. The first two interpreted PCs of the analysis (with $\lambda_e > 1.0$) accounted for 89.59% of the total variance in the data as follows: 77.22% (PC 1) and 12.37% (PC 2), respectively.

Table 7. The *in vitro* activity (*MIC* values in μM units) of investigated compounds **1a**–**p** and reference drugs isoniazid (INH), ethambutol (EMB), ofloxacin (OFLX) and ciprofloxacin (CPX) against *M. avium* CNCTC My 330/80 (*MA* 330/80), *M. smegmatis* ATCC 700084 (*MS*) and *M. marinum* CAMP 5644 (*MM*), respectively.

Comp.	*MIC* [μM]			
	MA 330/80		*MS*	*MM*
	[1] 14-d	[2] 21-d	[3] 3-d	21-d
1a	125	125	213	106
1b	62.5	125	104	52
1c	32	62.5	51	25.5
1d	32	32	24.9	12.5
1e	62.5	62.5	16.2	32.5
1f	32	32	15.8	<3.9
1g	16	16	15.4	<3.8
1h	8	16	15.0	<3.7
1i	62.5	125	203	51
1j	62.5	125	6.2	50
1k	32	62.5	390	98
1l	32	62.5	382	191
1m	16	32	30.7	15.4
1n	16	16	15.0	15.0
1o	16	16	7.3	7.3
1p	16	16	7.1	7.1
INH	> 250	> 250	117	467
EMB	16	16	–	–
OFLX	32	62.5	–	–
CPX	–	–	0.4	0.8

[1] 14-d, 14-Day cultivation; [2] 21-d, 21-day cultivation; [3] 3-d, 3-day cultivation. The most promising values of compounds *in vitro* antimycobacterial activity (*MIC* ≤ 8 μM) were indicated in gray cells of Table 7.

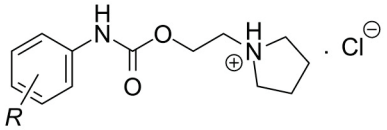

JC-02a: *R* = 2-OC_3H_7 **JC-02g**: *R* = 3-OC_3H_7
JC-02b: *R* = 2-OC_4H_9 **JC-02h**: *R* = 3-OC_4H_9
JC-02c: *R* = 2-OC_5H_{11} **JC-02i**: *R* = 3-OC_5H_{11}
JC-02d: *R* = 2-OC_6H_{13} **JC-02j**: *R* = 3-OC_6H_{13}
JC-02e: *R* = 2-OC_7H_{15} **JC-02k**: *R* = 3-OC_7H_{15}
JC-02f: *R* = 2-OC_8H_{17} **JC-02l**: *R* = 3-OC_8H_{17}

Figure 5. Chemical structure of the derivatives of 2-/3-alkoxyphenylcarbamic acids **JC-02a**–**l** (alkoxy = propoxy to octyloxy), which were *in vitro* screened against MT_v $H_{37}R_v$, *MK* 235/80, *MK* 6509/96 and *MA* 330/80 [76], respectively.

The quality of 2D representation of a variable was visualized by a distance between the projected variable onto a plane and circle of correlation. The loadings of variables were indicated as variously colored vectors, connected with particular mycobacterial strains, and numbered according to their position in the circle of radius 1 in an absolute value (Figure 6). In more detail, the digit 1 was assigned to the vector built on the log (1/*MIC* [M]) values, which were connected with 14-d *in vitro* testing of the compounds **1a**–**p** against MT_v $H_{37}R_v$ (MT_v $H_{37}R_v$, 14-d). Analogously, numbering of other vectors

was as follows: 2 (MT_v $H_{37}R_v$, 21-d), 3 (*MK* 235/80, 7-d), 4 (*MA* 330/80, 14-d), 5 (*MK* 235/80, 21-d), 6 (*MK* 235/80, 14-d), 7 (*MK* 6509/96, 14-d), 8 (*MK* 6509/96, 7-d), 9 (*MA* 330/80, 21-d), 10 (*MK* 6509/96, 21-d), 11 (MT_a $H_{37}R_a$, 7-d), 12 (*MM*, 21-d), 13 (*MK* DSM, 7-d) and 14 (*MS*, 3-d), respectively.

A position of the variable in mapping could be defined by values of square cosines (cos2), which estimated quality of representation. The sum of cos2 for variables on PCs is equal to one. The higher cos2, the more perfect representation of a variable by chosen PCs [68]. The highest sum of cos2 on PC 1 and PC 2 was found for the vector 1 (MT_v $H_{37}R_v$, 14-d). This vector was characterized by cos2 = 0.961 (Table S8) indicating its almost exclusive representation by both PC 1 and PC 2. In addition, its position was the closest to a circle of correlation (Figure 6) compared to positions of the vectors 2–14. The cos2 values on particular PCs related to concerned vectors are listed in Table S8.

The vectors 1–3 were defined by PC 1 > 0.75 and PC 2 > 0.25, the vectors 4–10 were described by PC 1 > 0.75 and PC 2, which could be found in an interval from 0.25 to -0.25. Furthermore, PC 1 > 0.75 together with PC 2 between −0.35 and −0.53 were used to characterize the vectors 11–13. Finally, the vector 14 was described by PC 1 < 0.75 and PC 2 < −0.50 (Figure 6), respectively.

Visual assessment indicated the smallest angles between the vectors 5–10. A relatively sharp angle was also observed between 1 and 2 as well as 12 and 13, respectively. Conversely, there was found 'almost orthogonal' arrangement of the vectors 1 and 14. Regarding this visualization, it could be assumed that the compounds **1a**–**p** showed (i) similar mechanisms of action against *MK* 235/80, *MK* 6509/96 and *MA* 330/80, respectively; (ii) different mechanisms of action against MT_v $H_{37}R_v$ and *MS*.

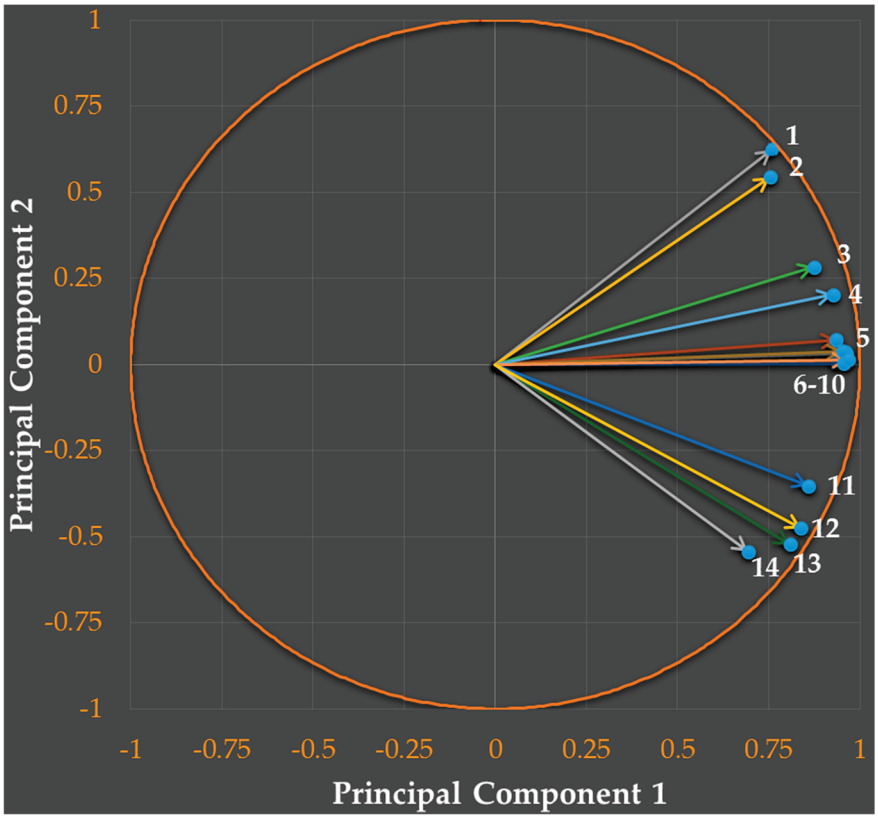

Figure 6. Two-dimensional mapping of the loadings of variables (variously colored vectors) indicating their (i) positions towards a circle of correlation; and (ii) relationships to both Principal Component 1 and 2. Numbering of the vectors was as follows: 1 (the vector built on the log (1/*MIC* [M]) values, which were observed after 14-d *in vitro* cultivation against MT_v $H_{37}R_v$), 2 (MT_v $H_{37}R_v$, 21-d), 3 (*MK* 235/80, 7-d), 4 (*MA* 330/80, 14-d), 5 (*MK* 235/80, 21-d), 6 (*MK* 235/80, 14-d), 7 (*MK* 6509/96, 14-d), 8 (*MK* 6509/96, 7-d), 9 (*MA* 330/80, 21-d), 10 (*MK* 6509/96, 21-d), 11 (MT_a $H_{37}R_a$, 7-d), 12 (*MM*, 21-d), 13 (*MK* DSM, 7-d) and 14 (*MS*, 3-d), respectively.

2.4. Structure–Activity Relationships

As suggested in previous sections of the paper, surface tension (relative surface activity γ; in N/m units), electronic (log $\varepsilon_{2\,(\text{Ch-T})}$) and lipophilic (log k_w) properties of the compounds **1a–p** might notably affect their *in vitro* efficiency (in log (1/*MIC* [M]) units) against tested mycobacterial strains. The PCA approach was applied for preliminary *SAR* studies of these derivatives by the XLSTAT *ver.* 2016.02.28451 software. Number of PCs was determined using visual evaluation of a scree plot, as a relationship between calculated λ_e and number of PCs. The first three PCs of the analysis with $\lambda_e > 1.0$ [77] accounted for 90.01% of the total variance in the data as follows: 69.59% (PC 1), 14.35% (PC 2) and 6.07% (PC 3), respectively.

The 2D visualization of relationships between the vectors describing physicochemical parameters and *in vitro* antimycobacterial activities of the compounds **1a–p** on axes (i) PC 1 and PC 2 (Figure S2), as well as (ii) PC 1 and PC 3 (Figure S3) revealed the closest connection between lipophilicity (log k_w; vector A) and efficiency against MT_v $H_{37}R_v$ (14-d; 1). In addition, there were found notably negatively correlated variables (vectors), which were positioned on opposed quadrants of the loading plots (Figures S2 and S3). These correlations aimed γ (C) versus log k_w (A) or C versus the vectors built on *in vitro* activity against MT_v $H_{37}R_v$ (14-d; 1), MT_v $H_{37}R_v$ (21-d; 2), *MA* 330/80 (14-d; 3) as well as *MK* 235/80 (7-d; 4). It seemed that 'almost orthogonal' arrangement of the vector characterizing log $\varepsilon_{2\,(\text{Ch-T})}$ (B) to those of antimycobacterial activities (5–14; Figure S3) indicated no correlation.

A linear, quasi-parabolic (polynomial function of 2nd order) and sigmoidal function, respectively, was also employed in order to investigate *SAR* in more detailed manner. The research focused on relationships between the independent variables (γ, log $\varepsilon_{2\,(\text{Ch-T})}$, log k_w) and dependent variable(s), i.e., biological values (in log (1/*MIC* [M]) units).

Resulting equations and values of common statistical descriptors, namely, n, DF, χ^2_{red}, RSS, R, $Adj.\ R^2$, $RMSE$, NR, F and $Prob > F$, respectively, were calculated by using the Origin Pro *ver.* 9.0.0 SR2 software. In addition, only statistically significant ($Prob > F$ values varied from 0.0100 to <0.0500; one-star indication), very significant ($Prob > F$ from 0.0010 to <0.0100; two stars indication) or extremely significant ($Prob > F$ from 0.0000 to <0.0010; three stars indication) relationships between the independent and dependent variables were presented in next paragraphs. These models were also characterized by $R \geq 0.9000$, $Adj.\ R^2 \geq 0.7750$ and $F \geq 25.00$, respectively.

Respecting given criteria, the following discussion considered relationships connected with MT_v $H_{37}R_v$, *MK* 235/80, *MK* 6509/96, *MK* DSM, *MA* 330/80 and *MS* as well. Conversely, there were found no statistically significant, very significant neither extremely significant models related to MT_a $H_{37}R_a$ or *MM*. It should be also noted that suggested models meeting those requirements were connected mostly with the subgroups containing a limited number of compounds ($n = 8$). However, it was not possible to perform the specific PCA for such subsets due to this restriction, i.e., number of effective observations was lower ($n = 8$) than number of examined variables ($n = 17$). This was a reason why next sections were focused mainly on linear, quasi-parabolic or sigmoidal fitting procedures and their statistical descriptions.

2.4.1. Models Related to *Mycobacterium tuberculosis* CNCTC My 331/88

Notable linear relationships between the γ or log k_w parameters and log (1/*MIC* [M]) values based on both 14-d and 21-d *in vitro* screenings against MT_v $H_{37}R_v$ were observed for the series **1a–h**. These models were defined by Equations (3)–(6) and found to be statistically very significant or extremely significant. Decrease in γ and increase in log k_w of these derivatives led to their more promising antitubercular profile.

$$MT_v\ H_{37}R_v\ (\text{14-d})/\mathbf{1a\text{-}h}\text{: } \log(1/MIC\ [\text{M}]) = -120.2060\ (\pm 12.9578) \times \gamma + 12.3509\ (\pm 0.8027) \quad (3)$$

$$n = 8,\ DF = 6,\ \chi^2_{red} = 0.0058,\ RSS = 0.0347,\ R = 0.9669,\ Adj.\ R^2 = 0.9240,$$
$$RMSE = 0.0761,\ NR = 0.1863,\ F = 86.06,\ Prob > F = 0.0001\ ^{***}$$

$$MT_v\ H_{37}R_v\ (14\text{-d})/\mathbf{1a\text{-}h}: \log(1/MIC\ [M]) = 0.4301\ (\pm 0.0737) \times \log k_w + 2.9438\ (\pm 0.3393) \quad (4)$$

$$n = 8,\ DF = 6,\ \chi^2_{red} = 0.0133,\ RSS = 0.0798,\ R = 0.9220,\ Adj.\ R^2 = 0.8251,$$
$$RMSE = 0.1153,\ NR = 0.2825,\ F = 34.03,\ Prob > F = 0.0011\ **$$

$$MT_v\ H_{37}R_v\ (21\text{-d})/\mathbf{1a\text{-}h}: \log(1/MIC\ [M]) = -103.4692\ (\pm 18.7975) \times \gamma + 11.1642\ (\pm 1.1644) \quad (5)$$

$$n = 8,\ DF = 6,\ \chi^2_{red} = 0.0122,\ RSS = 0.0730,\ R = 0.9136,\ Adj.\ R^2 = 0.8072,$$
$$RMSE = 0.1103,\ NR = 0.2702,\ F = 30.30,\ Prob > F = 0.0015\ **$$

$$MT_v\ H_{37}R_v\ (21\text{-d})/\mathbf{1a\text{-}h}: \log(1/MIC\ [M]) = 0.3957\ (\pm 0.0633) \times \log k_w + 2.9505\ (\pm 0.2911) \quad (6)$$

$$n = 8,\ DF = 6,\ \chi^2_{red} = 0.0098,\ RSS = 0.0587,\ R = 0.9312,\ Adj.\ R^2 = 0.8449,$$
$$RMSE = 0.0989,\ NR = 0.2424,\ F = 39.13,\ Prob > F = 0.0008\ ***$$

It seemed that ability to decrease surface tension of water was slightly more important than increase in lipophilicity of inspected compounds **1a**–**h** with the intention to improve their antitubercular properties, especially when concerning 14-d *in vitro* biological evaluation.

It would not be reasonable to suggest some biparametric linear models containing γ, log k_w and log (1/*MIC* [M]) parameters with an attempt to provide more satisfactory values of statistical descriptors related to the set **1a**–**h**. The reason not to apply bilinear reggresion analyses would be that statistically extremely significant relationships between γ and log k_w (Equations (S25)–(S28) in Table S7) were already observed.

Current findings were only in partial agreement with a research of Čižmárik et al. [38,78,79], who studied derivatives of 2-/3-alkoxyphenylcarbamic acid (alkoxy = propoxy do decyloxy), which basic part was formed by only one azacycloalkyl moiety (pyrrolidinium or piperidinium). The authors employed a linear, quasi-parabolic and sigmoidal model, respectively, to provide comprehensive *QSAR* investigation. They found that simultaneous increase in lipophilicity and *in vitro* antitubercular activity of these molecules was quite limited [78,79]. In addition, this behavior was also observed when inspecting relationships between the *in silico* log *p* values (CLOGP 4.0) and *in vitro* efficiency of these monobasic compounds against non-tuberculous *MK* 235/80, *MK* 6509/96 and *MA* 330/80, respectively [38].

The antitubercular activities of derivatives **1a**–**p** might theoretically indicate that comparable efficiency of homologues containing a pyrrolidinium group would be observed, if length of their side chain *R* would be beyond a certain border, i.e., if *R* = 2-/3-OC_8H_{17} or 2-/3-OC_9H_{19}.

A cell envelope of MT_v $H_{37}R_v$ is composed of three major segments, namely, a plasma membrane, cell wall core and outermost layer. The cell wall core, which is essential for viability, consists of peptidoglycan (PG) in covalent attachment *via* phosphoryl-*N*-acetylglucosaminosyl-rhamnosyl linkage units with heteropolysaccharide arabinogalactan (AG). The AG is in turn esterified at its non-reducing ends to long-chain (C_{70}–C_{90}) mycolic acids. The latter form the bulk of the inner leaflet of the outer membrane, with the outer layer consisting of a variety of non-covalently attached (glyco)lipids, polysaccharides, lipoglycans, and proteins [80].

Results of present statistical analyses indicated that not only lipophilic nature of the compounds **1a**–**p**, possible interactions of their side chain *R* with some components of the cell wall or ability do decrease surface tension of water in order to 'non-specifically' disrupt the cell envelope could be decisive for their *in vitro* efficiency. In fact, suggested mechanisms of antitubercular action might become more relevant for the subgroup **1a**–**h** compared to **1i**–**p**.

A closer look at the relationships between inspected physichochemical and biological descriptors among particular positional isomers proved that there were calculated more convenient statistical values for the 2-alkoxy substituted compounds **1a**–**d** and **1i**–**l** (Equations (S29)–(S32) in Table S9) compared to those of the 3-alkoxy substituted isomers **1e**–**h** and **1m**–**p**, respectively.

2.4.2. Models Related to the *Mycobacterium kansasii* Species

Statistically significant linear relationships between the log k_w parameters and log (1/*MIC* [M]) values connected with *in vitro* testing of the series **1a**–**h** against *MK* 235/80 were found. The *MIC* values observed after 7-d and 14-d cultivation were the same (Table 6), so both proposed models were defined by Equation (7). More prospective anti-*MK* 235/80 compounds showed higher log k_w values.

$$MK\ 235/80\ (14\text{-d})/\mathbf{1a\text{-}h}\text{: } \log(1/MIC\ [\mathrm{M}]) = 0.4395\ (\pm 0.0650) \times \log k_w + 2.6388\ (\pm 0.2990) \quad (7)$$

$$n = 8,\ DF = 6,\ \chi^2_{red} = 0.0103,\ RSS = 0.0620,\ R = 0.9403,\ Adj.\ R^2 = 0.8648,$$
$$RMSE = 0.1016,\ NR = 0.2489,\ F = 45.76,\ Prob > F = 0.0001\ ***$$

Statistically extremely significant linear models between the log k_w and log (1/*MIC* [M]) values resulting from 7-d and 21-d *in vitro* screening of the subgroup **1a**–**h** against *MK* 6509/96 were also set. The observed dependences were defined by Equations (8) and (9). Higher log k_w values were related to more promising anti-*MK* 6509/96 agents.

$$MK\ 6509/96\ (7\text{-d})/\mathbf{1a\text{-}h}\text{: } \log(1/MIC\ [\mathrm{M}]) = 0.5072\ (\pm 0.0757) \times \log k_w + 2.5914\ (\pm 0.3485) \quad (8)$$

$$n = 8,\ DF = 6,\ \chi^2_{red} = 0.0140,\ RSS = 0.0842,\ R = 0.9392,\ Adj.\ R^2 = 0.8624,$$
$$RMSE = 0.1185,\ NR = 0.2901,\ F = 44.86,\ Prob > F = 0.0001\ ***$$

$$MK\ 6509/96\ (21\text{-d})/\mathbf{1a\text{-}h}\text{: } \log(1/MIC\ [\mathrm{M}]) = 0.5061\ (\pm 0.0737) \times \log k_w + 2.3356\ (\pm 0.3393) \quad (9)$$

$$n = 8,\ DF = 6,\ \chi^2_{red} = 0.0133,\ RSS = 0.0798,\ R = 0.9418,\ Adj.\ R^2 = 0.8682,$$
$$RMSE = 0.1153,\ NR = 0.2825,\ F = 47.12,\ Prob > F = 0.0005\ ***$$

Increase in lipophilicity of the derivatives **1a**–**h** was more important factor to positively influence their efficiency compared to surface properties. However, it could be assumed that constant increase in lipophilicity due to elongation of the side chain *R* would not led to more promising derivatives, as observed for a subgroup **1i**–**p** (Table 6).

Statistically very significant and extremely significant linear relationships between the γ or log k_w and log (1/*MIC* [M]) descriptors were also found when concerning the molecules **1a**–**h** and their 7-d *in vitro* efficiency against *MK* DSM. The models were characterized by Equations (10) and (11), respectively.

Highly lipophilic compounds with ability to decrease surface tension of water more markedly showed higher potential to fight given *mycobacterium*. Conversely, increase in lipophilicity due to increase in number of carbons of the azacycloalkyl fragment (**1i**–**p**) would not be a guaranty of improvement in anti-*MK* DSM activity (Table 6).

$$MK\ \mathrm{DSM}\ (7\text{-d})/\mathbf{1a\text{-}h}\text{: } \log(1/MIC\ [\mathrm{M}]) = -192.0357\ (\pm 33.5781) \times \gamma + 16.8889\ (\pm 2.0800) \quad (10)$$

$$n = 8,\ DF = 6,\ \chi^2_{red} = 0.0388,\ RSS = 0.2330,\ R = 0.9192,\ Adj.\ R^2 = 0.8192,$$
$$RMSE = 0.1971,\ NR = 0.4827,\ F = 32.71,\ Prob > F = 0.0012\ **$$

$$MK\ \mathrm{DSM}\ (7\text{-d})/\mathbf{1a\text{-}h}\text{: } \log(1/MIC\ [\mathrm{M}]) = 0.7579\ (\pm 0.0817) \times \log k_w + 1.5371\ (\pm 0.3758) \quad (11)$$

$$n = 8,\ DF = 6,\ \chi^2_{red} = 0.0163,\ RSS = 0.0979,\ R = 0.9670,\ Adj.\ R^2 = 0.9240,$$
$$RMSE = 0.1277,\ NR = 0.3129,\ F = 86.15,\ Prob > F = 0.0001\ ***$$

2.4.3. Models Related to *Mycobacterium avium* CNCTC My 330/80

Different models were suggested when exploring relationships between γ and log (1/*MIC* [M]) values resulting from 14-d and 21-d *in vitro* screening of the compounds **1a**–**p** against *MA* 330/80. Concerning well-known differences in their salt-forming fragment, a statistically very significant linear model was found for a subgroup **1a**–**h** (14-d) and defined by Equation (12).

$$MA\ 330/80\ (14\text{-d})/\mathbf{1a\text{-}h}\text{: } \log(1/MIC\ [\mathrm{M}]) = -150.5250\ (\pm 29.7405) \times \gamma + 13.7803\ (\pm 1.8423) \quad (12)$$

$$n = 8,\ DF = 6,\ \chi'^2_{\mathrm{red}} = 0.0305,\ RSS = 0.1828,\ R = 0.9001,\ Adj.\ R^2 = 0.7790,$$
$$RMSE = 0.1745,\ NR = 0.4275,\ F = 25.61,\ Prob > F = 0.0032\ **$$

If a main criterion to consider was a position of compounds' side chain *R*, a bilinear model between γ and log (1/*MIC* [M]) was regarded as the most convenient for two subsets **1e**–**h** and **1m**–**p** (Figure 7).

A bilinear model proposed by Kubinyi [81] was generally applicable and presented a smooth synthesis of both linear and non-linear parts of *SAR* as an effort to simulate a complex process in a rather simplistic way.

The compounds with γ varying from 0.05692 N/m (**1p**) to 0.06154 N/m (**1n**) showed a comparable capability to act against *MA* 330/80 (21-d). Further increase in γ, i.e., minor ability to decrease surface tension of water, resulted in sharp decrease in their antimycobacterial efficiency. The observed behavior could indicate a non-specific mechanism of action of these derivatives, which might be based on their ability to disrupt an outermost layer of a cell envelope of *MA* 330/80. The layer, which consists of diverse amphiphilic glycolipids, namely, mycosides C, glycolipids, peptidolipids, and phospholipids, respectively, hinders diffusion of chemotherapeutic agents *via* the wall thus causing multiple drug-resistance by exclusion [82].

Statistically very significant or extremely significant linear relationships between log k_w and log (1/*MIC* [M]) resulting from 14-d and 21-d *in vitro* screening of the compounds **1a**–**h** were also observed. The suggested models were defined by Equations (13) and (14). As expected, higher log k_w values were connected with more effective agents.

$$MA\ 330/80\ (14\text{-d})/\mathbf{1a\text{-}h}\text{: } \log(1/MIC\ [\mathrm{M}]) = 1.6968\ (\pm 0.3122) \times \log k_w + 0.6051\ (\pm 0.0678) \quad (13)$$

$$n = 8,\ DF = 6,\ \chi'^2_{\mathrm{red}} = 0.0113,\ RSS = 0.0675,\ R = 0.9643,\ Adj.\ R^2 = 0.9182,$$
$$RMSE = 0.1061,\ NR = 0.2599,\ F = 79.57,\ Prob > F = 0.0001\ ***$$

$$MA\ 330/80\ (21\text{-d})/\mathbf{1a\text{-}h}\text{: } \log(1/MIC\ [\mathrm{M}]) = 1.8560\ (\pm 0.4695) \times \log k_w + 0.5458\ (\pm 0.1020) \quad (14)$$

$$n = 8,\ DF = 6,\ \chi'^2_{\mathrm{red}} = 0.0255,\ RSS = 0.1528,\ R = 0.9092,\ Adj.\ R^2 = 0.7978,$$
$$RMSE = 0.1596,\ NR = 0.3909,\ F = 28.62,\ Prob > F = 0.0081\ **$$

Statistical characteristics given above might support a hypothesis, which was based on a non-specific mechanism of action of the molecules **1a**–**h** against *MA* 330/80. However, the model related to 21-d *in vitro* biological evaluation (Equation (14)) provided clearly worse values of the statistical descriptors than those connected with 14-d *in vitro* screening (Equation (13)).

If attention was turned to the 3-alkoxy substituted derivatives **1e**–**h** and **1m**–**p**, increase in their log k_w up to approximately 5.1000 (Table 3) meant sharp increase in activity against *MA* 330/80 (21-d). Further increase in lipophilicity beyond this border was not reflected in higher antimycobacterial potential of the compounds **1n**, **1h**, **1o** and **1p** showing log k_w of 5.2087, 5.5384, 5.6569 and 6.1749 (Table 3, Figure 8), respectively.

2.4.4. Models Related to *Mycobacterium smegmatis* ATCC 700084

There was observed a very significant quasi-parabolic relationship between the log $\varepsilon_{2\,(\mathrm{Ch\text{-}T})}$ values and log (1/*MIC* [M]) parameters connected with 3-d *in vitro* evaluation of the pyrrolidium moiety-containing compounds **1c**–**h** against *MS* (Equation (S33) in Table S9). The possibility to exclude the molecules **1a** and **1b** from a current analysis was based on the observation that they showed the lowest efficiency against given *mycobacterium* (Table 7).

It was found that anti-*MS* activity increased with increasing log $\varepsilon_{2\,(\mathrm{Ch\text{-}T})}$, reached a maximum if this independent variable was between 4.24 and 4.27 (**1e**, **1f** and **1h**) and then decreased with

further increase in the log $\varepsilon_{2\,(\text{Ch-T})}$ values (Figure S4, Table 1). This behavior, defined as a cut-off effect, was originally reviewed and rationalized in number of mechanistic ways by Hansch and Clayton a few decades ago [83].

It was also found that lower γ and higher log k_w did not lead to increase in anti-*MS* activity of the compounds **1i**–**p**, as explored by some models, which were not provided because of their statistical insignificance ($Prob > F \geq 0.0500$).

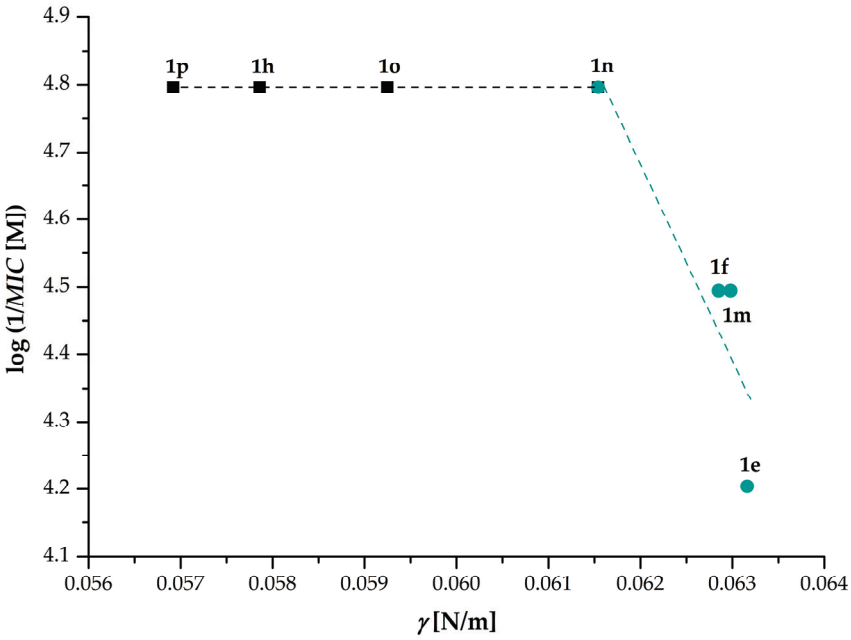

Figure 7. Bilinear relationship between the γ (in N/m units) and log (1/*MIC* [M]) parameters resulting from 21-d *in vitro* screening of the 3-alkoxy substituted compounds **1e**–**h** and **1m**–**p** (alkoxy = butoxy to heptyloxy) against *MA* 330/80.

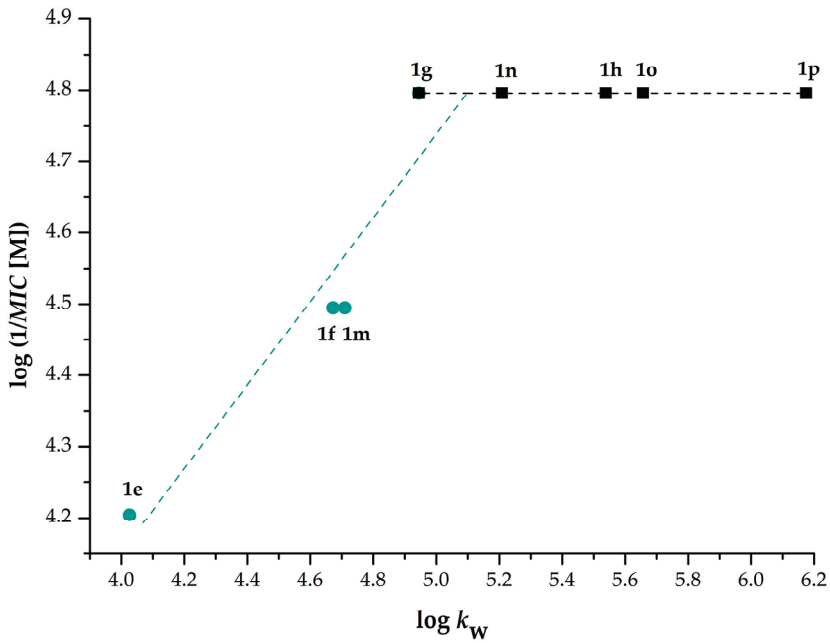

Figure 8. Bilinear relationship between the log k_w and log (1/*MIC* [M]) parameters resulting from 21-d *in vitro* screening of the 3-alkoxy substituted compounds **1e**–**h** and **1m**–**p** (alkoxy = butoxy to heptyloxy) against *MA* 330/80.

3. Materials and Methods

3.1. General Information

Liquid chromatography high resolution mass spectroscopy (HPLC-HR-MS) analyses of the compounds **9′a–p** (Supplementary Materials) were performed on a chromatographic apparatus consisting of the LC Agilent Infinity System (Agilent Technologies, Santa Clara, CA, USA) equipped with a gradient pump (1290 Bin Pump VL), automatic injector (1260 HiPals), and column thermostat (1290 TCC). The LC system was coupled with the Quadrupole Time-Of-Flight mass spectrometer (6520 Accurate Mass Q-TOF LC/MS). Q-TOF was equipped with an electrospray ionization source operated in a positive and negative ionization mode as well.

For data acquisition and processing, a personal computer with the Mass Hunter software *ver*. MassHunter Workstation B 04.00 (Agilent Technologies) was used.

Each of the compounds **9′a–p** was dissolved in 50% (v/v) MeOH to reach a concentration of 1 mg/L. Particular solutions were filtered via 0.22 μm nylon syringe filter and 1.0 μL was used for the HPLC-HR-MS analyses at 35 °C using the RP-C_{18} column Zorbax Extend-C_{18}, 2.1 × 50 mm, 1.7 μm (Agilent Technologies).

The mobile phases consisted of 0.1% aqueous solution of formic acid in demineralized water (mobile phase A) and acetonitrile (mobile phase B). Gradient elution was used with linear gradient from 5% to 95% of acetonitrile *per* 8 min. The flow rate of a mobile phase was set to 400 μL/min.

The MS spectrometer was operated in a positive and negative ionization mode, respectively, keeping particular specifications as follows: drying gas temperature 360 °C, drying gas flow 12 L/min, nebulizing gas pressure 60 psi, ESI source voltage 4000 V, fragmentor voltage 125 V, skimmer voltage 65 V and collision gas N_2, respectively. The m/z ratios of both $[M + H]^+$ and $[M - H]^-$ ions were recorded in an interval from 50 m/z to 1500 m/z. Observed m/z values of the adducts were compared to the theoretical ones. The difference (in ppm units; Supplementary Materials) was calculated according to Equation (15):

$$Difference = [(m/z_{\text{ theoretical}} - m/z_{\text{ obtained}})/m/z_{\text{ theoretical}}] \times 10^6 \quad (15)$$

High-resolution mass spectra of the compounds **1a–p** were measured using the Dionex UltiMate 3000 high-performance liquid chromatograph (Thermo Scientific, West Palm Beach, FL, USA) coupled with the LTQ Orbitrap XL Hybrid Ion Trap-Orbitrap Fourier Transform Mass Spectrometer (Thermo Scientific) equipped with a HESI II (heated electrospray ionization) source operating in a positive (**1a–d**, **1i–l**) or negative (**1e–h**, **1m–p**) mode. The HPLC system was controlled through the Chromeleon Chromatography Data System *ver*. 7.2 (Thermo Scientific). The separation was performed on a C_{18}-Hypersil Gold (3 μm, 50 mm × 2.1 mm) column (Thermo Scientific). A mobile phase consisted of water Purelab Classic (ELGA LabWater, High Wycombe, Bucks, UK) and acetonitrile hypergrade for LC-MS LiChrosolv (Merck KGaA, Darmstadt, Germany) in 80:20 volume ratio (v/v). Total flow rate was 0.3 mL/min, injection volume was 1 μL, and column temperature was set to 30 °C, respectively.

The UV/Vis spectra of methanolic solutions of analyzed compounds **1a–p** ($c = 8.0 \times 10^{-5}$ M) were observed on the 8452A Diode Array spectrophotometer HP-8452A (Hewlett-Packard, Palo Alto, CA, USA) at 21 °C. Methanol for UV-spectroscopy (Merck, Darmstadt, Germany) was used for preparation of these solutions. Results of the UV/Vis analyses were collected and stored digitally using the ChemStation controller software (Agilent Technologies, Waldbronn, Germany). The HP-8452A apparatus measured a complete range of compounds' spectrum from 190 nm to 820 nm.

The HPLC separation module Waters e2695 equipped with a Waters 2996 PDA Detector (Waters Corp., Milford, MA, USA) and chromatographic column Symmetry C_{18} × 5 μm, 4.6 × 250 mm, Part No. W21751W016 (Waters Corp.) were used for estimation of lipophilic properties of the compounds **1a–p** at 21 °C.

The HPLC separation process was monitored by the Empower 3 Chromatography Data Software (Waters Corp.) working on a personal computer HP Compaq (Hewlett-Packard, Palo Alto, CA, USA) equipped with Intel® Core™ i5 processor (Intel Corp., Santa Clara, CA, USA), 2400 CPU, 3.10 GHz, and 4.00 GB of RAM, respectively. The computer operated on the Windows 7 Professional system, a 64-bit version (Microsoft Corp., Redmont, WA, USA).

Isocratic elution was carried out using mobile phases consisting of methanol *p.a.* (MeOH; Honeywell, Paris, France) and purified water in various volume ratios (80:20, 85:15, 90:10, 95:5 (v/v) and pure MeOH, respectively). Distilled water (CentralChem, Bratislava, Slovak Republic) was purified by the Aquinity2 P10 ultra-pure water system for production of ultra-pure water with an integrated 10 L permeate tank (membraPure, Hennigsdorf, Germany).

Total flow of the column was 1.0 mL/min, injection volume was 4 μL and column temperature was set to 40 °C. The detection wavelengths varying from 236 nm to 238 nm were chosen for current experimental procedures.

3.2. Synthesis of Compounds

Presently analyzed 1-[2-[({[2-/3-(alkoxy)phenyl]amino}carbonyl)oxy]-3-(dipropylammonio)-propyl]pyrrolidinium oxalates (**1a**–**d**)/dichlorides (**1e**–**h**) as well as 1-[2-[({[2-/3-(alkoxy)phenyl]-amino}carbonyl)oxy]-3-(dipropylammonio)propyl]azepanium oxalates (**1i**–**l**)/dichlorides (**1m**–**p**; alkoxy = butoxy to heptyloxy) were prepared by multi step pathways (Scheme 1) using 2-aminophenol (**1a**) and 3-aminophenol (**1b**), respectively, as starting compounds [21,27–29].

Procedures for preparation of reaction intermediates **2′a**, **2′b**, **3′a**–**h**, **4′a**–**h**, **5′a**–**h**, **7′**, **8′a**, **8′b**, **9′a**–**p** and final molecules **1a**–**p** were originally published in research papers [21,27–29] and are provided in Supplementary Materials. In addition, HPLC-HR-MS spectral characterizations of the compounds **9′a**–**p** are included as well.

Spectral data (IR), elemental analyses results (% C, H, N), melting point (m.p.) values, R_f parameters (TLC) and acid-base dissociation constants (pK_{a1}, pK_{a2}), respectively, of solid colorless compounds **1a**–**p** can be found in the papers [21,26] and some of given characteristics are also listed in Supplementary Materials.

The molecules **1a**–**p** were re-crystallized from mixture of acetone/ethanol (**1a**–**d, 1e**–**h, 1m**–**p**) or acetone (**1i**–**l**) before being spectrally, physicochemically and biologically investigated. Present HR-MS spectral description of these compounds was given below.

The compound **1a**: HR-MS for $C_{24}H_{42}N_3O_3$ $[M + H]^+$ calculated 420.32207 m/z, found 420.32343 m/z; **1b**: HR-MS for $C_{25}H_{44}N_3O_3$ $[M + H]^+$ calculated 434.33772 m/z, found 434.33920 m/z; **1c**: HR-MS for $C_{25}H_{46}N_3O_3$ $[M + H]^+$ calculated 448.35337 m/z, found 448.35471 m/z. **1d**: HR-MS for $C_{27}H_{47}N_3O_3$ $[M + H]^+$ calculated 462.36902 m/z, found 462.37048 m/z; **1e**: HR-MS for $C_{24}H_{40}N_3O_3$ $[M - H]^-$ calculated 418.30751 m/z, found 418.30746 m/z; **1f**: HR-MS for $C_{25}H_{42}N_3O_3$ $[M - H]^-$ calculated 432.32316 m/z, found 432.32294 m/z; **1g**: HR-MS for $C_{26}H_{44}N_3O_3$ $[M - H]^-$ calculated 446.33881 m/z, found 446.33912 m/z; **1h**: HR-MS for $C_{27}H_{46}N_3O_3$ $[M - H]^-$ calculated 460.35446 m/z, found 460.35458 m/z; **1i**: HR-MS for $C_{26}H_{46}N_3O_3$ $[M + H]^+$ calculated 448.35337 m/z, found 448.35458 m/z; **1j**: HR-MS for $C_{27}H_{48}N_3O_3$ $[M + H]^+$ calculated 462.36902 m/z, found 462.37045 m/z; **1k**: HR-MS for $C_{28}H_{50}N_3O_3$ $[M + H]^+$ calculated 476.38567 m/z, found 476.38608 m/z; **1l**: HR-MS for $C_{29}H_{52}N_3O_3$ $[M + H]^+$ calculated 490.40192 m/z, found 490.40210 m/z; **1m**: HR-MS for $C_{26}H_{44}N_3O_3$ $[M - H]^-$ calculated 446.33881 m/z, found 446.33908 m/z; **1n**: HR-MS for $C_{27}H_{46}N_3O_3$ $[M - H]^-$ calculated 460.35446 m/z, found 460.35474 m/z; **1o**: HR-MS for $C_{28}H_{48}N_3O_3$ $[M - H]^-$ calculated 474.37011 m/z, found 474.36996 m/z; **1p**: HR-MS for $C_{29}H_{50}N_3O_3$ $[M - H]^-$ calculated 488.38576 m/z, found 488.38596 m/z.

3.3. Determination and Prediction of Physicochemical Properties

3.3.1. Estimation of Surface Tension

Surface tension (relative surface activity; γ) of the derivatives **1a**–**p** was determined by a drop count method using a glassy Traube stalagmometer (Kavalier Glass, Prague, Czech Republic). Number of drops of compounds' and reference solutions were counted between upper and lower marks of the stalagmometer [30,31]. Aqueous solutions of the molecules **1a**–**p** were prepared with distilled, deionized water ($c = 2.0 \times 10^{-3}$ M). Distilled deionized water was also used as a reference solution, which showed $\gamma = 0.07259$ N/m. The drops were allowed to form at constant temperature 21 °C. The experimental procedure was described in a paper [31]. Current measurements were done in six replicates and average γ values (in N/m units) were reported (Table 1).

3.3.2. Estimation of Electronic Properties

The log ε values characterizing methanolic solutions of the compounds **1a**–**p** ($c = 8.0 \times 10^{-5}$ M) were observed at λ_1 = 208–210 nm, $\lambda_{2\,(\text{Ch-T})}$ = 236–238 nm and λ_3 = 278–280 nm (Table 1), respectively, in a near ultraviolet (quarz) region of the electromagnetic spectrum between 200 nm and 400 nm [35]. The log ε values for presently observed absorption maxima were calculated following the Lambert-Beer's law, which was discussed in [35], for example, and expressed by Equation (16):

$$A = \varepsilon \times c \times l \tag{16}$$

where the A parameter represented absorbance of a compound's solution, the ε descriptor was a molar absorption coefficient (in L/mol/cm units) and l was path length (in cm units).

3.3.3. Estimation and *In Silico* Investigation of Lipohydrophilic Properties

Lipophilicity of the compounds **1a**–**p** was determined by reversed-phase high-performance liquid chromatography (RP-HPLC). Methanol (MeOH)/water mobile phases with varying volume ratio of the organic modifier and water (80:20, 85:15, 90:10, 95:5 (v/v) and pure MeOH, respectively) were chosen.

A methanolic solution of potassium iodine was used for dead time (t_d) determination. Retention factors (capacity factors; k) were calculated according to Equation (17):

$$k = (t_\text{r} - t_\text{d})/t_\text{d} \tag{17}$$

where t_r was retention time of a solute (in min), the t_d parameter denoted dead time of potassium iodine, an unretained analyte (in min).

The observed retention (t_r) and dead (t_d) times were means of three independent determinations. Average t_d values of potassium iodine in used MPhs were as follows: 2.237 min (MeOH/water ratio (v/v) was 80:20), 2.245 min (85:15), 2.245 min (90:10), 2.228 min (95:5) and 2.210 min (pure MeOH), respectively.

The log k_w values, i.e., the logarithms of extrapolated retention (capacity) factors for 100% water in the isocratic RP-HPLC, were determined from intercepts of linear plots between the log k and ϕ_M (a volume fraction of an organic modifier in the isocratic elution RP-HPLC) according to Equation (18):

$$\log k = \log k_\text{w} - S \times \phi_\text{M} \tag{18}$$

where the S parameter represented the slope of a regression curve, which was related to solvent strength of a pure organic solvent [51,52].

Purity (in percentages) of the compounds **1a**–**p** was also verified by RP-HPLC. Areas of their peaks were measured using the MPh, which contained 90% proportion (v/v) of MeOH. The purity of given salts is provided in Table S3.

The log *p* values of non-protonated bases **9a′–p** (Scheme 1, Table 4) for the octan-1-ol/water partitioning system were calculated by the Ghose and Crippen′s log P_{Cr} [54,55], Viswanadhan′s log P_V [56], Broto's log P_B [57] and Leo's CLOGP 4.0 [58] atomic as well as combined atomic and fragmental methods using the ChemBioDraw Ultra 12.0 software package (CambridgeSoft, Cambridge, MA, USA).

The Virtual Computer Chemistry Laboratory [59], a freely available web-based tool working in Java environment, was taken to generate log *P* by the Wang's XLOGP 2.0 [60], Cheng's XLOGP 3.0 [61], Moriguchi's MLOGP [62], Sander's (Actelion's) ACLOGP [63], Molinspiration's miLogP 2.2 [64], ALOGP [65] and Tetko's ALOGPs 2.1 [66] method (Tables 4 and 5), respectively. All these approaches integrated algorithms based on atomic/fragmental principles, excluding ALOGPs 2.1, which considered a molecule in the whole [66].

The SILICOS-IT hybrid method, which used a proprietary fragment- and property-based principles, was also employed to generate log *P* parameters (log $P_{S\text{-}IT}$; Table 5). The method was implemented in the SwissADME applet, a free web tool designed to evaluate pharmacokinetics and drug-likeness of small molecules [67].

3.4. In Vitro Antimycobacterial Assays

The *in vitro* activity of compounds **1a–p** was inspected against *Mycobacterium tuberculosis* CNCTC My 331/88 (identical with $H_{37}R_v$ and ATCC 2794, respectively; abbreviation used: MT_v $H_{37}R_v$), *M. kansasii* CNCTC My 235/80 (identical with ATCC 12478; *MK* 235/80), the *M. kansasii* 6509/96 clinical isolate (*MK* 6509/96) and *M. avium* CNCTC My 330/80 (identical with ATCC 25291; *MA* 330/80), respectively, in the Laboratory for Mycobacterial Diagnosis and Tuberculosis (Institute of Public Health in Ostrava, Czech Republic). These strains were purchased from the National Reference Laboratory—Czech National Collection of Type Cultures (CNCTC; The National Institute of Public Health, Prague, Czech Republic), excluding *MK* 6509/96, which was clinically isolated because the INH-resistant *M. kansasii* strains have not been found in Czech Republic or Slovak Republic. In the experiments, dilution of the strains was as follows: 10^{-3} M (MT_v $H_{37}R_v$), 10^{-4} M (*MK* 235/80, *MK* 6509/96) and 10^{-5} M (*MA* 330/80), respectively.

The molecules **1a–p** were also *in vitro* screened against an avirulent *M. tuberculosis* $H_{37}R_a$ ATCC 25177 (MT_a $H_{37}R_a$), *M. kansasii* DSM 44162 (*MK* DSM), *M. smegmatis* ATCC 700084 (*MS*) and *M. marinum* CAMP 5644 (*MM*), respectively, in the Department of Infectious Diseases and Microbiology (Faculty of Veterinary Medicine, University of Veterinary and Pharmaceutical Sciences in Brno, Czech Republic).

Standard drugs. Isoniazid (INH), ethambutol (EMB), ofloxacin (OFLX) and ciprofloxacin (CPX) reference drugs were purchased from Sigma-Aldrich (Darmstadt, Germany), respectively, showing purity of analytical grade.

Determination of a minimum inhibitory concentration (MIC) against MT_v $H_{37}R_v$, *MK 235/80, MK 6509/96 and MA 330/80*. Efficiency of the compounds **1a–p** and standard drugs (INH, EMB and OFLX, respectively) against given mycobacteria were determined in lyophilized Šula's semisynthetic medium (Sevac, Prague, Czech Republic) by a dilution-micromethod [20,72,84].

Each tested mycobacterial strain was simultaneously inoculated into Petri plates containing the Šula's medium for sterility control and growth of the inoculum [84]. All screened molecules were added to this medium as solutions in dimethyl sulfoxide (DMSO; Sigma-Aldrich, Irvine, UK). In the *in vitro* assays, following concentrations of the solutions were used: 1000, 500, 250, 125, 62.5, 32, 16, 8, 4, 2, 1, 0.5 and 0.25 μM, respectively. The inoculated plates kept in microtone bags were incubated at 37 °C. Particular reading was carried out macroscopically on a stand with a bottom magnifying mirror using a magnifying glass.

Growth in the plates [20,72] was evaluated after 7, 14 and 21 days (*MK* 235/80, *MK* 6509/96) or after 14 and 21 days (MT_v $H_{37}R_v$, *MA* 330/80).

The value of a minimum inhibitory concentration (*MIC*) was the lowest concentration (on the above concentration scale) of a tested compound, which inhibited growth of the mycobacteria [20,72]. The screening was repeated three times and the *MIC* values (in μM units), reported in Tables 6 and 7, were the same.

Determination of a minimum inhibitory concentration (MIC) against MT_a $H_{37}R_a$. The *mycobacterium* was grown on Middlebrook broth (MB; MiddleBrook Pharmaceuticals, Inc., Westlake, TX, USA), supplemented with Oleic-Albumin-Dextrose-Catalase (OADC) supplement (Difco, Lawrence, KS, USA) and salicylate-derived mycobactin J (2 μg/mL; Allied Monitor Inc., Fayette, MO, USA), an iron-binding siderophore [85,86].

At log phase growth, a culture sample (10 mL) was centrifuged at 15,000 rpm/20 min using a bench top centrifuge MPW-65R (MPW Med Instruments, Warsaw, Poland). Following removal of the supernatant, a pellet was washed in fresh liquid Middlebrook 7H9GC broth (MiddleBrook Pharmaceuticals, Inc.) and re-suspended in a fresh OADC-supplemented MB (10 mL).

Turbidity was adjusted to match the McFarland standard No. 1 [87] containing approximately 3×10^8 Colony Forming Units (CFU) with MB broth. Further 1:20 dilution of the culture was performed in MB broth.

Susceptibility of MT_a $H_{37}R_a$ was investigated in a 96-well plate format. In the experiments, sterile deionized water (300 μL) was added to all outer-perimeter wells of the plates to minimize evaporation of the medium in test wells during incubation. Each evaluated compound (100 μL) was incubated with MT_a $H_{37}R_a$ (100 μL). Dilutions of each compound were prepared in triplicate and final concentrations varied from 1000 μg/mL to 8 μg/mL. All tested molecules were dissolved in DMSO (Sigma-Aldrich, Irvine, UK), and subsequent dilutions were made in supplemented MB broth. The plates were sealed with parafilm and incubated at 37 °C for 7 days.

Following incubation, 10% addition a water-soluble dye, the alamarBlue reagent (AbD Serotec, Kidlington, UK) was mixed into each well. This resaurin-based reagent served as an oxidation-reduction indicator of metabolic function and cellular health in cell viability bioassays [88].

Absorbance readings at 570 nm and 600 nm were taken, initially for background subtraction and after 24h re-incubation. The subtraction is necessary for strongly colored compounds, where the color may interfere with the interpretation of any color change. For non-interfering compounds, a blue color in a well was interpreted as absence of growth and pink color was scored as growth [73,74].

The minimum inhibitory concentration (*MIC*) was defined as the lowest concentration of a compound, at which no visible bacterial growth was observed. In other words, the *MIC* was the lowest concentration that prevented visual color change from blue to pink. The *MIC* value has been routinely and widely used in bacterial assays and it has been a standard detection limit according to the Clinical and Laboratory Standards Institute [73,74]. Clinically used antimycobacterials INH and CPX were applied as reference drugs. The estimated *MIC* values (in μM units) were provided in Table 6.

Determination of a minimum inhibitory concentration (MIC) against MK DSM, MS and MM. A broth dilution micromethod in Middlebrook 7H9 medium (Difco, Lawrence, MO, USA) supplemented with BD BBL Middlebrook OADC Enrichment medium (Becton, Dickinson & Company, Franklin Lakes, NJ, USA) containing 8.5 g NaCl, 50.0 g bovine albumin (fraction V), 20.0 g dextrose, 0.03 g catalase, and 0.6 mL oleic acid [89], respectively, was used to determine the *MIC* values for given strains, as described [75].

Tested phenylcarbamic acid-based molecules **1a**–**p** as well as standard drugs INH and CPX were dissolved in DMSO (Sigma-Aldrich, Irvine, UK) and final concentration of DMSO did not exceed 2.5% of the total solution composition. The final concentrations, varying from 256 μg/mL to 0.125 μg/mL, were obtained by a two-fold serial dilution of a stock solution in a microtiter plate with sterile medium.

Bacterial inocula were prepared by transferring colonies from culture into sterile water. Cell density was adjusted to the 0.5 McFarland units [87] using the cell density meter Densi-La-Meter (LIAP, Riga, Latvia). Final inoculum was made by 1:1000 dilution of the suspension with sterile water. Drug-free controls, sterility controls and controls consisted of medium and DMSO alone were

included. Results were determined visually after static incubation in darkness in aerobic atmosphere for: (i) 3 days at 37 °C in a case of *MS*; (ii) 7 days at 37 °C (*MK* DSM) and (iii) 21 days at 28 °C (*MM*), respectively.

The *MIC* parameter was defined as the lowest concentration of a compound, at which no visible bacterial growth was observed. The *MIC* value has been routinely and widely used in bacterial assays considering it a standard detection limit according to the Clinical and Laboratory Standards Institute [73,74]. Presently observed *MIC* values (in μM units) are provided in Tables 6 and 7.

3.5. Calculations and Statistical Analyses

Regression equations of relevant fitting procedures and their statistical characteristics were calculated and visualized by the Origin Pro *ver.* 9.0.0 SR2 software (OriginLab Corporation, Northampton, MA, USA).

In a current research, those statistical parameters were calculated: number of points (number of cases; *n*), degrees of freedom (*DF*), reduced chi-square ($\chi,^2_{red}$), residual sum of squares (*RSS*), correlation coefficient (*R*), adjusted coefficient of determination (*Adj.* R^2), root mean squared error (standard deviation; *RMSE*), norm of residuals (*NR*), Fisher's significance ratio (Fisher's *F*-test; *F*) and probability of obtaining *F* Ratio (significance of a whole model; *Prob* > *F*), respectively.

The analyses were also focused on indication of a significance level of calculated *F* Ratio as follows: * (one star)—statistically significant; ** (two stars)—statistically very significant; *** (three stars)—statistically extremely significant. Detailed information regarding given statistical descriptors could be found in a research paper [47].

The chemometric principal component analysis (PCA) tool was used to explore relationships between (i) experimental and *in silico* lipophilicity descriptors, (ii) *in vitro* efficiency against all tested mycobacterial strains as well as (iii) physicochemical descriptors and *in vitro* biological activities of the compounds **1a**–**p**. The PCA is a mathematical algorithm that reduces the dimensionality of the data while retaining most of variation in the data set. It accomplishes this reduction by identifying directions, called principal components (PCs), along which the variation in the data is maximal. By using a few components, each sample can be represented by relatively few numbers instead of by values for thousands of variables. Samples can then be plotted, making it possible to visually assess similarities and differences between samples and determine whether samples can be grouped [90].

The PCA was performed by the XLSTAT *ver.* 2016.02.28451 software (Addinsoft, New York, NY, USA), a cloud-based statistical application for statistics and data analyses, which worked as an add-on to the Microsoft Excel *ver.* 2013 software (Microsoft Corp., Redmont, WA, USA).

4. Conclusions

In summary, determination of physicochemical properties and *in vitro* antimymycobacterial screening in connection with *SAR* analyses of 1-[2-[({[2-/3-(alkoxy)phenyl]amino}carbonyl)oxy]-3-(dipropylammonio)propyl]pyrrolidinium oxalates (**1a**–**d**)/dichlorides (**1e**–**h**) and 1-[2-[({[2-/3-(alkoxy)phenyl]amino}carbonyl)oxy]-3-(dipropylammonio)propyl]azepanium oxalates (**1i**–**l**)/di- chlorides (**1m**–**p**; alkoxy = butoxy to heptyloxy) were considered main objectives of the research.

All compounds **1a**–**p** in aqueous solutions ($c = 2.0 \times 10^{-3}$ M) were able to decrease surface tension of water ($\gamma = 0.07259$ N/m) at 21 °C and their γ varied from 0.05692 N/m (**1p**) to 0.06464 N/m (**1a**). Relationships between number of carbon atoms forming their side chain *R* (n_c) and γ values (in N/m units) were described most precisely by statistically significant or very significant models based on polynomial functions of 2nd order within all homological subsets **1a**–**d**, **1e**–**h**, **1i**–**l** and **1m**–**p**.

Electronic properties of the molecules **1a**–**p** were characterized by logarithms of molar absorption coefficients (log ε) of their methanolic solutions ($c = 8.0 \times 10^{-5}$ M) investigated in the UV/Vis region of an electromagnetic spectrum. The solutions showed three absorption maxima in a near ultraviolet (quarz) region of the spectrum between 200 nm and 400 nm. The maxima were found at λ_1 = 208–210 nm (second local excitation band), $\lambda_{2\,(Ch\text{-}T)}$ = 236–238 nm (charge-transfer band) and

λ_3 = 278–280 nm (first local excitation band), respectively. There was observed nor linear neither quasi-parabolic relationship between n_c and log $\varepsilon_{2\,(Ch\text{-}T)}$, as the maximum being the most sensitive to differences in electronic environment of a phenylcarbamoyloxy moiety due to different position and length of a substituent *R*.

The log k_w values, as descriptors characterizing lipophilic properties of **1a**–**p**, were extrapolated from intercepts of statistically extremely significant linear relationships between log *k* parameters and volume fractions of MeOH modifier (ϕ_M) using the Snyder–Soczewiński solvent strength model. These log k_w values were in accordance with an elution order and hydrophobicity of the molecules **1a**–**p** and varied from 3.7688 (**1a**) to 6.1749 (**1p**). Increase in length of their side chain *R* led to higher *S*, as a function of molecular structure parameters, within all homological sets. The compounds containing an azepanium moiety showed higher *S* than those with a pyrrolidium group presuming same position and length of *R*. The calculated *S* parameters varied from 3.7788 (**1a**) to 6.2672 (**1p**). A statistically extremely significant relationship between the log k_w and *S* values was found.

The experimental log k_w dataset was studied together with computational logarithms of partition coefficients (log *P*). The log *P* parameters of non-protonated bases **9′a**–**p** were calculated for the octan-1-ol/water partitioning system using the Ghose and Crippen′s log P_{Cr}, Viswanadhan′s log P_V, Broto's log P_B, Leo's CLOGP 4.0, Wang's XLOGP 2.0, Cheng's XLOGP 3.0, Moriguchi's MLOGP, Sander's (Actelion's) ACLOGP, Molinspiration's miLogP 2.2, ALOGP, SILICOS-IT and Tetko´s ALOGPs 2.1 method as well. Similarities and differences between log k_w and *in silico* descriptors were analyzed by unscaled principal component analysis (PCA). There was confirmed high sensitivity of PCA for detecting of small differerences between analyzed positional isomers, which given *in silico* methods could not perform with satisfactory visibility. The log $P_{I\text{-}IT}$, XLOGP 2.0 and XLOGP 3.0 descriptors might be used to characterize lipophilic properties of investigated salts and bases, especially if they contained highly lipophilic side chain *R*.

The compounds **1a**–**p** were *in vitro* screened against *Mycobacterium tuberculosis* CNCTC My 331/88 (identical with $H_{37}R_v$; abbreviation used: MT_v $H_{37}R_v$), *M. tuberculosis* $H_{37}R_a$ ATCC 25177 (MT_a $H_{37}R_a$), *M. kansasii* CNCTC My 235/80 (*MK* 235/80), the *M. kansasii* 6509/96 clinical isolate (*MK* 6509/96), *M. kansasii* DSM 44162 (*MK* DSM), *M. avium* CNCTC My 330/80 (*MA* 330/80), *M. smegmatis* ATCC 700084 (*MS*) and *M. marinum* CAMP 5644 (*MM*), respectively. *In vitro* susceptibility of given mycobacteria to clinically used reference drugs isoniazid (INH), ethambutol (EMB), ofloxacin (OFLX) or ciprofloxacin (CPX) was tested as well.

A very unique aspect of a present research was that many compounds from the set **1a**–**p** were *in vitro* efficient against almost all tested mycobacterial strains. The compounds **1h** and **1p** were the most active practically against the whole spectrum of tested mycobacteria (*MIC* $\leq$ 8 μM), excluding *MA* 330/80.

All 3-alkoxy substituted molecules **1e**–**h** and **1m**–**p** were more efficient against MT_a $H_{37}R_a$ (*MIC* = 3.7–8.1 μM) than INH or CPX. The dibasic compounds also inhibited growth of *MK* DSM more effectively (*MIC* = 1.9–16.2 μM) compared to INH. Moreover, the derivatives **1g**, **1h** and **1n**–**p** showed approximately equal activity against *MA* 330/80 (*MIC* = 16 μM) as EMB. Regarding MT_v $H_{37}R_v$, however, none of the molecules **1a**–**p** showed similar ability to fight given *mycobacterium* as INH. Comparable activity against *MK* 6509/96 was found for the substances **1h**, **1n**–**p** (*MIC* = 4 μM and 8 μM) and INH. If concerning the 2-alkoxy substituted compounds **1a**–**d** and **1i**–**l**, the derivative **1d** was more promising against MT_a $H_{37}R_a$ (*MIC* = 12.5 μM) and *MK* DSM (*MIC* = 6.2 μM) than INH. The INH standard was also less effective against *MS* or *MM* than practically all tested phenylcarbamic acid-based substances, from which were **1j** (*MIC* = 6.2 μM; anti-*MS*) and **1h** (*MIC* < 3.7 μM; anti-*MM*) the most efficient.

The chemometric PCA approach as well as fitting procedures, supported by relevant equations and adequate statistical analyses, were used to comprehensively investigate *SAR* of the derivatives **1a**–**p**. It seemed that ability to decrease surface tension of water was slightly more important than increase in lipophilicity of a pyrrolidinium moiety-containing compounds **1a**–**h** in order to improve

their efficiency against both MT_v $H_{37}R_v$ and *MA* 330/80. The compounds with γ varying from 0.05692 N/m (**1p**) to 0.06154 N/m (**1n**) showed comparable potential to act against *MA* 330/80 (21-d). Further increase in γ, i.e., minor ability to decrease surface tension of water, resulted in sharp decrease in their antimycobacterial efficiency. If attention was turned to the 3-alkoxy substituted molecules **1e**–**h** and **1m**–**p**, increase in their log k_w up to approximately 5.1000 led to sharp increase in activity against *MA* 330/80 (21-d). Further increase in lipophilicity beyond this border did not result in higher antimycobacterial activity of **1n** (log k_w = 5.2087), **1h** (log k_w = 5.5384), **1o** (log k_w = 5.6569) or **1p** (log k_w = 6.1749).

Increase in lipophilicity of the molecules **1a**–**h** was more important factor, which positively influenced their efficiency against *MK* 235/80, *MK* 6509/96 and *MK* DSM, compared to surface properties. Conversely, incease in lipophilicity over 'a certain value' (log k_w of approximately 5.2000) together with different size and steric properties of a salt-forming group (**1i**–**p**) would not be a guaranty of improvement in antimycobacterial activity.

There was observed a statistically very significant model between log $\varepsilon_{2\ (Ch\text{-}T)}$ and log (1/*MIC* [M]) connected with 3-d *in vitro* evaluation of the compounds **1c**–**h** against *MS*. It was found that activity increased with increasing log $\varepsilon_{2\ (Ch\text{-}T)}$, reached a maximum if the independent variable was between 4.24 and 4.27 (**1e**, **1f** and **1h**) and then decreased with further increase in the log $\varepsilon_{2\ (Ch\text{-}T)}$ values.

Overall, the results of current *in vitro* biological screening and *SAR* investigations of the molecules **1a**–**p** might reveal new horizons in discovery of very effective 'non-traditional' antimycobacterial agents based on a phenylcarbamic acid structural scaffold.

Supplementary Materials: The supplementary materials are available online.

Author Contributions: I.M. suggested the research idea, created the concept and designed the study, investigated electronic and lipophilic properties of the compounds **1a**–**p**, analyzed the data related to *in vitro* antimycobacterial screening, performed *in silico* studies, interpreted results, explored and statistically characterized proposed models, performed PCAs and fitting procedures, interpreted PCAs and *SAR*s, wrote and revised the paper; J.C. designed chemical structures of the compounds **1a**–**p** and synthesized them, estimated their spectral characteristics (IR) and elemental analyses, contributed reagents/materials tools; I.S. suggested the research idea, created the concept and designed the study, interpreted results from *in vitro* biological assays; Š.P., H.M. and J.S. performed *in vitro* antimycobacterial evaluation of the molecules **1a**–**p**, contributed reagents/materials tools; J.J. and A.Č. suggested the research idea, created the concept and designed the study, contributed reagents/materials tools; I.K. estimated purity and lipophilic properties of the compounds**1a**–**p**, analyzed results from isocratic RP-HPLC, contributed reagents/materials tools; J.Č. and M.P. estimated surface tension (relative surface activity) and electronic properties of the compounds **1a**–**p**; D.P. measured and interpreted HPLC-HR-MS spectra of the intermediates **9′a**–**p** (not biologically investigated); M.O. measured and interpreted HR-MS spectra of the compounds **1a**–**p**. The authors have approved a final version of the manuscript.

Acknowledgments: The authors very gratefully acknowledge financial support received especially from the Faculty of Pharmacy, Comenius University in Bratislava (Slovak Republic). The research was also supported by the grant projects of the Comenius University in Bratislava No. UK/241/2018 and UK/229/2018 as well as grant project of the Faculty of Pharmacy, Comenius University in Bratislava No. FaF UK/9/2018. The authors wish to express their gratitude to the Scientific Grant Agency of the Ministry of Education, Science, Research and Sport of the Slovak Republic for providing financial support by a grant project VEGA No. 1/0040/17. The HPLC/HRMS system forms a part of the National Infrastructure CzeCOS ProCES CZ.02.1.01/0.0/0.0/16_013/0001609; Michal Oravec was supported by the National Sustainability Program (NPU I; Grant No. LO1415). The research was also partially supported by Sanofi-Aventis Pharma Slovakia, s.r.o. (Slovak Republic).

Conflicts of Interest: The authors declare no conflict of interest.

Abbreviations

The following abbreviations are used in this manuscript:

2-PrOH	Propan-2-ol
3-d	3-Day cultivation
7-d	7-Day cultivation
14-d	14-Day cultivation
21-d	21-Day cultivation
λ_e	Eigenvalues (principal component analysis)

χ^2_{red}	Reduced chi-square (statistical analysis)
ϕ_M	Volume fraction of a mobile phase modifier (RP-HPLC)
CPX	Ciprofloxacin
Adj. R^2	Adjusted coefficient of determination (statistical analysis)
DEE	Diethyl ether
DF	Degrees of freedom (statistical analysis)
DMSO	Dimethyl sulfoxide
EtOH	Ethanol
EMB	Ethambutol
F	Fisher's *F*-test (Fisher's significance ratio; statistical analysis)
INH	Isoniazid
IR	Infrared
k	Retention (capacity) factor (RP-HPLC)
LA/LAs	Local anesthetic/local anesthetics
log k_w	Lipophilicity index; values extrapolated from intercepts of a linear relationship between the logarithm of retention factor *k* (log *k*) and volume fraction of a mobile phase modifier (ϕ_M; RP-HPLC)
MeOH	Methanol
MA	*Mycobacterium avium*
MIC	Minimum inhibitory concentration (in μM units)
MK	*Mycobacterium kansasii*
MM	*Mycobacterium marinum*
MS	*Mycobacterium smegmatis*
MT	*Mycobacterium tuberculosis*
n_c	Number of carbon atoms forming an 2-/3-alkoxy side chain (*R*)
NR	Norm of residuals (statistical analysis)
OFLX	Ofloxacin
PC	Principal Component (principal component analysis)
PCA/PCAs	Principal component analysis/principal component analyses
Prob > *F*	Probability of obtaining the *F* Ratio (statistical analysis)
RMSE	Root mean squared error (standard deviation; statistical analysis)
RSS	Residual sum of squares (statistical analysis)
S	Slope (RP-HPLC)
SAR/*SARs*	Structure–activity relationship/Structure–activity relationships
t_r	Retention time of a compound (RP-HPLC)

References

1. Squeglia, F.; Romano, M.; Ruggiero, A.; Berisio, R. Molecular players in tuberculosis drug development: Another break in the cell wall. *Curr. Med. Chem.* **2017**, *24*, 3954–3969. [CrossRef] [PubMed]
2. Da Silva, P.B.; Campos, D.L.; Ribeiro, C.M.; da Silva, I.C.; Pavan, F.R. New antimycobacterial agents in the pre-clinical phase or beyond: Recent advances in patent literature (2001–2016). *Expert Opin. Ther. Pat.* **2017**, *27*, 269–282. [CrossRef] [PubMed]
3. Wu, M.L.; Aziz, D.B.; Dartois, V.; Dick, T. NTM Drug discovery: Status, gaps and the way forward. *Drug Discov. Today* **2018**, *23*, 1502–1519. [CrossRef] [PubMed]
4. Deshpande, D.; Srivastava, S.; Chapagain, M.L.; Lee, P.S.; Cirrincione, K.N.; Pasipanodya, J.G.; Gumbo, T. The discovery of ceftazidime/avibactam as an anti-*Mycobacterium avium* agent. *J. Antimicrob. Chemother.* **2017**, *72* (Suppl. 2), i36–i42. [CrossRef] [PubMed]
5. Amaral, L.; Viveiros, M.; Kristiansen, J.E. 'Non-Antibiotics': Alternative therapy for the management of MDRTB and MRSA in economically disadvantaged countries. *Curr. Drug Targets* **2006**, *7*, 887–891. [CrossRef] [PubMed]
6. Amaral, L.; Viveiros, M. Thioridazine: A non-antibiotic drug highly effective, in combination with first line anti-tuberculosis drugs, against any form of antibiotic resistance of *Mycobacterium tuberculosis* due to its multi-mechanisms of action. *Antibiotics* **2017**, *6*, 3. [CrossRef] [PubMed]

7. Schmidt, R.M.; Rosenkranz, H.S. Antimicrobial activity of local anesthetics: Lidocaine and procaine. *J. Infect. Dis.* **1970**, *121*, 597–607. [CrossRef] [PubMed]
8. Fujii, H.; Nakajima, H.; Hirose, T.; Mochizuki, T.; Fukaura, A.; Ota, S.; Sugihara, S.; Tazawa, H.; Takahashi, T. Growth inhibition of mycobacteria by lidocaine in fiberoptic bronchoscopic aspirates. *JJSRE* **1993**, *15*, 108–115. [CrossRef]
9. Goldberg, L. Pharmacological properties of xylocaine. *Sven. Tandl. Tidskr.* **1947**, *40*, 819–830.
10. Gordh, T. Xylocain—A new local analgesic. *Anesthesia* **1949**, *4*, 4–9. [CrossRef]
11. Miescher, K. Studies of local anesthetics. *Helv. Chim. Acta* **1932**, *15*, 163–190. [CrossRef]
12. Agarwal, N.; Kalra, V.K. Studies on the mechanism of action of local anesthetics on proton translocating ATPase from *Mycobacterium phlei*. *Biochim. Biophys. Acta* **1984**, *764*, 316–323. [CrossRef]
13. Nakayama, Y. The electrophoretical analysis of esterase and catalase and its use in taxonomical studies of mycobacteria. *Jpn. J. Microbiol.* **1967**, *11*, 95–101. [CrossRef]
14. Prigozhin, D.M.; Mavrici, D.; Huizar, J.P.; Vansell, H.J.; Alber, T. Structural and biochemical analyses of *Mycobacterium tuberculosis N*-acetylmuramyl-L-alanine amidase R_v3717 point to a role in peptidoglycan fragment recycling. *J. Biol. Chem.* **2013**, *288*, 31549–31555. [CrossRef] [PubMed]
15. Sultana, R.; Vemula, M.H.; Banerjee, S.; Guruprasad, L. The PE16 (R_v1430) of *Mycobacterium tuberculosis* is an esterase belonging to serine hydrolase superfamily of proteins. *PLoS ONE* **2013**, *8*, e55320. [CrossRef] [PubMed]
16. Vacondio, F.; Silva, C.; Mor, M.; Testa, B. Qualitative structure–metabolism relationships in the hydrolysis of carbamates. *Drug Metab. Rev.* **2010**, *42*, 551–589. [CrossRef] [PubMed]
17. Moraczewski, A.L.; Banaszynski, L.A.; From, A.M.; White, C.E.; Smith, B.D. Using hydrogen bonding to control carbamate C−N rotamer equilibria. *J. Org. Chem.* **1998**, *63*, 7258–7262. [CrossRef] [PubMed]
18. Combrink, K.D.; Denton, D.A.; Harran, S.; Ma, Z.; Chapo, K.; Yan, D.; Bonventre, E.; Roche, E.D.; Doyle, T.B.; Robertson, G.T.; et al. New C25 carbamate rifamycin derivatives are resistant to inactivation by ADP-ribosyl transferases. *Bioorg. Med. Chem. Lett.* **2007**, *17*, 522–526. [CrossRef] [PubMed]
19. Velikorodov, A.V.; Urlyapova, N.G.; Daudova, A.D. Synthesis and antimycobacterial activity of carbamate derivatives of 1,2-oxazine. *Pharm. Chem. J.* **2006**, *40*, 380–382. [CrossRef]
20. Férriz, J.M.; Vávrová, K.; Kunc, F.; Imramovský, A.; Stolaříková, J.; Vavříková, E.; Vinšová, J. Salicylanilide carbamates: Antitubercular agents active against multidrug-resistant *Mycobacterium tuberculosis* strains. *Bioorg. Med. Chem.* **2010**, *18*, 1054–1061. [CrossRef] [PubMed]
21. Csöllei, J.; Búčiová, Ľ.; Čižmárik, J.; Kopáčová, L. Studies of local anaesthetics CXII. Preparation and activity of dibasic alkylesters of 2-, and 3-alkoxy-substituted phenylcarbamic acids. *Československ. Farm.* **1993**, *42*, 127–129. (In Slovak)
22. Pavelčík, F.; Remko, M.; Čižmárik, J.; Majer, J. Crystal and molecular structure of heptacain hydrochloride. *Collect. Czechoslov. Chem. Commun.* **1986**, *51*, 264–270. [CrossRef]
23. Waisser, K.; Doležal, R.; Palát, K., Jr.; Čizmárik, J.; Kaustová, J. *QSAR* Study of antimycobacterial activity of quaternary ammonium salts of piperidinylethyl esters of alkoxysubstituted phenylcarbamic acids. *Folia Microbiol.* **2006**, *51*, 21–24. [CrossRef]
24. Blaser, A.; Palmer, B.D.; Sutherland, H.S.; Kmentova, I.; Franzblau, S.G.; Wan, B.; Wang, Y.; Ma, Z.; Thompson, A.M.; Denny, W.A. Structure−activity relationships for amide-, carbamate-, and urea-linked analogues of the tuberculosis drug (6*S*)-2-nitro-6-{[4-(trifluoromethoxy)benzyl]oxy}-6,7-dihydro-5*H*-imidazo[2,1-*b*][1,3]oxazine (PA-824). *J. Med. Chem.* **2012**, *55*, 312–326. [CrossRef] [PubMed]
25. Gonec, T.; Pospisilova, S.; Holanova, L.; Stranik, J.; Cernikova, A.; Pudelkova, V.; Kos, J.; Oravec, M.; Kollar, P.; Cizek, A.; et al. Synthesis and antimicrobial evaluation of 1-[(2-substituted phenyl)carbamoyl]naphthalen-2-yl carbamates. *Molecules* **2016**, *21*, 1189. [CrossRef] [PubMed]
26. Malík, I.; Sedlárová, E.; Csöllei, J.; Andriamainty, F.; Čižmárik, J.; Kečkéšová, S. The physicochemical properties of dibasic alkyl esters of 2- and 3-alkyloxy substituted phenylcarbamic acid. *Acta Fac. Pharm. Univ. Comen.* **2007**, *54*, 136–145.
27. Čižmárik, J.; Borovanský, A.; Švec, P. Study of local anesthetics LII. Piperidinoethyl esters of alkoxyphenylcarbamic acids. *Acta Fac. Pharm.* **1976**, *29*, 53–79.
28. Heywood, D.L.; Phillips, B. The reaction of epichlorohydrin with secondary amines. *J. Am. Chem. Soc.* **1958**, *80*, 1257–1259. [CrossRef]

29. Schleppnik, A.A.; Gutsche, C.D. Synthesis of polysubstituted triptych-boroxazolidines. *J. Org. Chem.* **1962**, *27*, 3684–3686. [CrossRef]
30. Dilmohamud, B.A.; Seeneevassen, J.; Rughooputh, S.D.D.V.; Ramasami, P. Surface tension and related thermodynamic parameters of alcohols using the Traube stalagmometer. *Eur. J. Phys.* **2005**, *26*, 1079–1084. [CrossRef]
31. Vazquez, G.; Alvarez, E.; Navaza, J.M. Surface tension of alcohol water + water from 20 to 50 °C. *J. Chem. Eng. Data* **1995**, *40*, 611–614. [CrossRef]
32. Stopková, L.; Gališinová, J.; Šuchtová, Z.; Čižmárik, J.; Andriamainty, F. Determination of critical micellar concentration of homologous 2-alkoxyphenylcarbamoyloxyethylmorpholinium chlorides. *Molecules* **2018**, *23*, 1064. [CrossRef] [PubMed]
33. Čižmárik, J.; Borovanský, A.; Švec, P. Study of local anesthetics. LVII. Perhydroazepinylethyl esters of alkoxyphenylcarbamic acids. *Česk. Farm.* **1976**, *25*, 118–121. (In Slovak) [PubMed]
34. Blešová, M.; Čižmárik, J.; Bachratá, M.; Bezáková, Ž.; Borovanský, A. Chromatographic parameters, pK_a, and surface activity of a series of hydrochlorides of perhydroazepinylethyl esters of alkoxyphenylcarbamic acids and their relation to anaesthetic activity. *Collect. Czechoslov. Chem. Commun.* **1985**, *50*, 1133–1140. [CrossRef]
35. Yadav, L.D.S. Ultraviolet and Visible Spectroscopy. In *Organic Spectroscopy*; Yadav, L.D.S., Ed.; Springer: Amsterdam, The Netherlands, 2005; pp. 7–51. [CrossRef]
36. Čižmárik, J.; Borovanský, A. Synthesis, u.v. and i.r. spectra of 2-piperidnoethyl esters of alkyloxyphenylcarbamic acids. *Chem. Zvesti* **1975**, *29*, 119–123.
37. Rutkowska, E.; Pajak, K.; Jóźwiak, K. Lipophilicity–methods of determination and its role in medicinal chemistry. *Acta Pol. Pharm.* **2013**, *70*, 3–18. [PubMed]
38. Waisser, K.; Doležal, R.; Čižmárik, J. Graphic demonstration of the structure–antimycobacterial activity relationships in the series of ester phenylcarbamic acid with piperidine or pyrrolidine moiety. *Folia Pharm. Univ. Carol.* **2008**, *37*, 65–76.
39. Van de Waterbeemd, H.; Kansy, M.; Wagner, B.; Fischer, H. Lipophilicity Measurement by Reversed-Phase High Performance Liquid Chromatography (RP-HPLC). In *Lipophilicity in Drug Action and Toxicology. Methods and Principles in Medicinal Chemistry*; Pliška, V., Testa, B., van de Waterbeemd, H., Eds.; VCh Verlag: Weinheim, Germany, 1996; pp. 73–88. ISBN 3-527-29383-3.
40. Valkó, K.; Slégel, P. New chromatographic hydrophobicity index (ϕ_0) based on the slope and the intercept of the log k' versus organic phase concentration plot. *J. Chromatogr. A* **1993**, *631*, 49–61. [CrossRef]
41. Du, Ch.M.; Valko, K.; Bevan, Ch.; Reynolds, D.; Abraham, M.H. Rapid method for estimating octanol–water partition coefficient (log P_{oct}) from isocratic RP-HPLC and a hydrogen bond acidity term (A). *J. Liq. Chrom. Rel. Technol.* **2001**, *24*, 635–649. [CrossRef]
42. El Tayar, N.; van de Waterbeemd, H.; Testa, B. Lipophilicity measurements of protonated basic compounds by reversed-phase high-performance liquid chromatography: I. Relationship between capacity factors and the methanol concentration in methanol–water eluents. *J. Chromatogr. A* **1985**, *320*, 293–304. [CrossRef]
43. El Tayar, N.; van de Waterbeemd, H.; Testa, B. Lipophilicity measurements of protonated basic compounds by reversed-phase high-performance liquid chromatography: II. Procedure for the determination of a lipophilic index measured by reversed-phase high-performance liquid chromatography. *J. Chromatogr. A* **1985**, *320*, 305–312. [CrossRef]
44. Paschke, A.; Manz, M.; Schüürmann, G. Application of different RP-HPLC methods for the determination of the octanol/water partition coefficient of selected tetrachlorobenzyltoluenes. *Chemosphere* **2001**, *45*, 721–728. [CrossRef]
45. Montanari, M.L.C.; Montanari, C.A.; Piló-Veloso, D.; Cass, Q.B. Estimation of the RP-HPLC lipophilicity parameters log k', and log k_w, a comparison with the hydrophobicity index ϕ_0. *J. Liq. Chromatogr. Relat. Technol.* **1997**, *20*, 1703–1715. [CrossRef]
46. Flieger, J.; Tatarczak-Michalewska, M.; Wujec, M.; Pitucha, M.; Świeboda, R. RP-HPLC Analysis and *in vitro* identification of antimycobacterial activity of novel thiosemicarbazides and 1,2,4-triazole derivatives. *J. Pharm. Biomed. Anal.* **2015**, *107*, 501–511. [CrossRef] [PubMed]
47. Goněc, T.; Malík, I.; Csöllei, J.; Jampílek, J.; Stolaříková, J.; Solovič, I.; Mikuš, P.; Keltošová, S.; Kollár, P.; O'Mahony, J.; et al. Synthesis and *in vitro* antimycobacterial activity of novel *N*-arylpiperazines containing an ethane-1,2-diyl connecting chain. *Molecules* **2017**, *22*, 2100. [CrossRef] [PubMed]

48. Carta, A.; Paglietti, G.; Rahbar Nikookar, M.E.; Sanna, P.; Sechi, L.; Zanetti, S. Novel substituted quinoxaline 1,4-dioxides with *in vitro* antimycobacterial and anticandida activity. *Eur. J. Med. Chem.* **2002**, *37*, 355–366. [CrossRef]
49. Moreno, E.; Gabano, E.; Torres, E.; Platts, J.A.; Ravera, M.; Aldana, I.; Monge, A.; Pérez-Silanes, S. Studies on log $P_{o/w}$ of quinoxaline di-*N*-oxides: A comparison of RP-HPLC experimental and predictive approaches. *Molecules* **2011**, *16*, 7893–7908. [CrossRef] [PubMed]
50. Snyder, L.R.; Poppe, H. Mechanism of solute retention in liquid–solid chromatography and the role of the mobile phase in affecting separation: Competition versus 'sorption'. *J. Chromatogr. A* **1980**, *184*, 363–413. [CrossRef]
51. Valkó, K.; Snyder, L.R.; Glajch, J.L. Retention in reversed-phase liquid chromatography as a function of mobile-phase composition. *J. Chromatogr. A* **1993**, *656*, 501–520. [CrossRef]
52. Soczewiński, E. Mechanistic molecular model of liquid–solid chromatography: Retention–eluent composition relationships. *J. Chromatogr. A* **2002**, *965*, 109–116. [CrossRef]
53. Chen, N.; Yhang, Y.; Lu, P. Effects of molecular structure on the *S* index in the retention equation in reversed-phase high-performance liquid chromatography. *J. Chromatogr. A* **1992**, *606*, 35–42. [CrossRef]
54. Ghose, A.K.; Crippen, G.M. Atomic physicochemical parameters for three-dimensional structure-directed quantitative structure–activity relationships. I. Partition coefficients as a measure of hydrophobicity. *J. Comput. Chem.* **1986**, *7*, 565–577. [CrossRef]
55. Ghose, A.K.; Crippen, G.M. Atomic physicochemical parameters for three-dimensional structure-directed quantitative structure–activity relationships. II. Modeling dispersive and hydrophobic interactions. *J. Chem. Inform. Comput. Sci.* **1987**, *27*, 21–35. [CrossRef]
56. Viswanadhan, N.V.; Ghose, K.A.; Reyankar, R.G.; Robins, K.R. Atomic physicochemical parameters for three-dimensional structure-directed quantitative structure–activity relationships 4. Additional parameters for hydrophobic and dispersive interactions and their application for an automated superposition of certain naturally occurring nucleoside antibiotics. *J. Chem. Inform. Comput. Sci.* **1989**, *29*, 163–172. [CrossRef]
57. Broto, P.; Moreau, G.; Vandycke, C. Molecular structures: Perception, autocorrelation descriptor and *SAR* studies. System of atomic contributions for the calculation of the *n*-octanol/water partition coefficients. *Eur. J. Med. Chem.* **1984**, *19*, 71–78.
58. Leo, A. The octanol–water partition coefficient of aromatic solutes: The effect of electronic interactions, alkyl chains, hydrogen bonds, and *ortho*-substitution. *J. Chem. Soc. Perkin Trans. II* **1983**, *20*, 825–838. [CrossRef]
59. Tetko, I.V.; Gasteiger, J.; Todeschini, R.; Mauri, A.; Livingstone, D.; Ertl, P.; Palyulin, V.A.; Radchenko, E.V.; Zefirov, N.S.; Makarenko, A.S.; et al. Virtual computational chemistry laboratory–design and description. *J. Comput. Aided Mol. Des.* **2005**, *19*, 453–463. [CrossRef] [PubMed]
60. Wang, R.; Gao, Y.; Lai, L. Calculating partition coefficient by atom-additive method. *Perspect. Drug Discov. Des.* **2000**, *19*, 47–66. [CrossRef]
61. Cheng, T.; Zhao, Y.; Li, X.; Lin, F.; Xu, Y.; Zhang, X.; Li, Y.; Wang, R.; Lai, L. Computation of octanol–water partition coefficients by guiding an additive model with knowledge. *J. Chem. Inf. Model.* **2007**, *47*, 2140–2148. [CrossRef] [PubMed]
62. Moriguchi, I.; Hirono, S.; Liu, Q.; Nakagome, I.; Matsushita, Y. Simple method of calculating octanol/water partition coefficient. *Chem. Pharm. Bull.* **1992**, *40*, 127–130. [CrossRef]
63. Sander, T.; Freyss, J.; von Korff, M.; Reich, J.R.; Rufener, C. OSIRIS, an entirely in-house developed drug discovery informatics system. *J. Chem. Inf. Model.* **2009**, *49*, 232–246. [CrossRef] [PubMed]
64. Molinspiration Cheminformatics, Slovenský Grob, Slovak Republic. Available online: http://www.molinspiration.com/cgi-bin/properties (accessed on 7 June 2018).
65. Viswanadhan, V.N.; Rami Reddy, M.; Bacquet, R.J.; Erion, M.D. Assessment of methods used for predicting lipophilicity: Application to nucleosides and nucleoside bases. *J. Comput. Chem.* **1993**, *14*, 1019–1026. [CrossRef]
66. Tetko, I.V.; Tanchuk, V.Y. Application of associative neural networks for prediction of lipophilicity in ALOGPS 2.1 program. *J. Chem. Inf. Comput. Sci.* **2002**, *42*, 1136–1145. [CrossRef] [PubMed]
67. Daina, A.; Michielin, O.; Zoete, V. SwissADME: A free web tool to evaluate pharmacokinetics, drug-likeness and medicinal chemistry friendliness of small molecules. *Sci. Rep.* **2017**, *7*, E42717–E42729. [CrossRef] [PubMed]
68. Abdi, H.; Williams, L.J. Principal component analysis. *WIREs Comp. Stat.* **2010**, *2*, 433–459. [CrossRef]

69. Carpenter, T.S.; Kirshner, D.A.; Lau, E.Y.; Wong, S.E.; Nilmeier, J.P.; Lightstone, F.C. A method to predict blood–brain barrier permeability of drug-like compounds using molecular dynamics simulations. *Biophys. J.* **2014**, *107*, 630–641. [CrossRef] [PubMed]
70. Norinder, U.; Haeberlein, M. Computational approaches to the prediction of blood–brain distribution. *Adv. Drug Deliv. Rev.* **2002**, *54*, 291–313. [CrossRef]
71. Van de Waterbeemd, H.; Camenisch, G.; Folkers, G.; Chretien, J.R.; Raevsky, O.A. Estimation of blood–brain barrier crossing of drugs using molecular size and shape, and *H*-bonding descriptors. *J. Drug Targets* **1998**, *6*, 151–165. [CrossRef] [PubMed]
72. Imramovsky, A.; Pesko, M.; Kralova, K.; Vejsova, M.; Stolarikova, J.; Vinsova, J.; Jampilek, J. Investigating spectrum of biological activity of 4- and 5-chloro-2-hydroxy-*N*-[2-(arylamino)-1-alkyl-2-oxoethyl]benzamides. *Molecules* **2011**, *16*, 2414–2430. [CrossRef] [PubMed]
73. Clinical and Laboratory Standards Institute (CLSI). *Methods for Antimicrobial Susceptibility Testing of Anaerobic Bacteria; Approved Standard*, 8th ed.; CLSI Document M11-A8; CLSI: Wayne, NJ, USA, 2012; pp. 10–56.
74. Clinical and Laboratory Standards Institute (CLSI). *Performance Standards for Antimicrobial Susceptibility Testing*, 24th ed.; Informational Supplement M100-S24; CLSI: Wayne, NJ, USA, 2014; pp. 106–211.
75. Brown-Elliott, B.A.; Cohen, S.; Wallace, R.J., Jr. Susceptibility Testing of Mycobacteria. In *Antimicrobial Susceptibility Testing Protocols*; Schwalbe, R., Steele-Moore, L., Goodwin, A.C., Eds.; CRC Press (Taylor and Francis Group): Boca Raton, FL, USA, 2007; pp. 243–274.
76. Waisser, K.; Dražková, K.; Čižmárik, J.; Kaustová, J. Antimycobacterial activity of basic ethylesters of alkoxy-substituted phenylcarbamic acids. *Folia Microbiol.* **2003**, *48*, 45–50. [CrossRef]
77. Jackson, D.A. Stopping rules in principal components analysis: A comparison of heuristical and statistical approaches. *Ecology* **1993**, *74*, 2204–2214. [CrossRef]
78. Čižmárik, J.; Waisser, K.; Doležal, R. *QSAR* Study of antimycobacterial activity of esters of phenylcarbamic acids. *Acta Fac. Pharm. Univ. Comen.* **2008**, *55*, 90–95.
79. Čižmárik, J.; Waisser, K. Review of potential antituberculotics: Esters of substituted phenylcarbamic acids. *Folia Pharm. Univ. Carol.* **2008**, *37*, 91–94.
80. Grzegorzewicz, A.E.; de Sousa-d'Auria, C.; McNeil, M.R.; Huc-Claustre, E.; Jones, V.; Petit, C.; Angala, S.K.; Zemanová, J.; Wang, Q.; Belardinelli, J.M.; et al. Assembling of the *Mycobacterium tuberculosis* cell wall core. *J. Biol. Chem.* **2016**, *291*, 18867–18879. [CrossRef] [PubMed]
81. Kubinyi, H. Quantitative structure–activity relationships. 7. The bilinear model, a new model for nonlinear dependence of biological activity on hydrophobic character. *J. Med. Chem.* **1977**, *20*, 625–629. [CrossRef] [PubMed]
82. David, H.L.; Rastogi, N.; Clavel-Sérès, S.; Clément, F.; Thorel, M.-F. Structure of the cell envelope of *Mycobacterium avium*. *Zent. Bakteriol. Mikrobiol. Hyg. A* **1987**, *264*, 49–66. [CrossRef]
83. Hansch, C.; Clayton, J.M. Lipophilic character and biological activity of drugs II. The parabolic case. *J. Pharm. Sci.* **1973**, *62*, 1–21. [CrossRef] [PubMed]
84. Šula, L. WHO Co-operative studies on a simple culture technique for the isolation of mycobacteria. 1. Preparation, lyophilization and reconstitution of a simple semi-synthetic concentrated liquid medium; culture technique; growth pattern of different mycobacteria. *Bull. World Health Organ.* **1963**, *29*, 589–606. [PubMed]
85. De Voss, J.J.; Rutter, K.; Schroeder, B.G.; Su, H.; Zhu, Y.; Barry, C.E., III. The salicylate-derived mycobactin siderophores of *Mycobacterium tuberculosis* are essential for growth in macrophages. *Proc. Natl. Acad. Sci. USA* **2000**, *97*, 1252–1257. [CrossRef] [PubMed]
86. Schwartz, B.D.; De Voss, J.J. Structure and absolute configuration of mycobactin J. *Tetrahedron Lett.* **2001**, *42*, 3653–3655. [CrossRef]
87. Atlas, R.; Snyder, J. Reagents, Stains, and Media: Bacteriology. In *Manual of Clinical Microbiology (2-Volume Set)*, 11th ed.; Jorgensen, J.H., Pfaller, M.A., Carroll, K.C., Funke, G., Landry, M.L., Richter, S.S., Warnock, D.W., Eds.; ASM Press: Washington, DC, USA, 2015; Volume 1, pp. 316–349. [CrossRef]
88. Franzblau, S.G.; Witzig, R.S.; McLaughlin, J.C.; Torres, P.; Madico, G.; Hernandez, A.; Degnan, M.T.; Cook, M.B.; Quenzer, V.K.; Ferguson, R.M.; et al. Rapid, low-technology *MIC* determination with clinical *Mycobacterium tuberculosis* isolates by using the microplate Alamar Blue assay. *J. Clin. Microbiol.* **1998**, *36*, 362–366. [PubMed]

89. Long, J.E.; DeJesus, M.; Ward, D.; Baker, R.E.; Ioerger, T.; Sassetti, C.M. Identifying Essential Genes in *Mycobacterium Tuberculosis* by Global Phenotypic Profiling. In *Gene Essentiality. Methods and Protocols*; Lu, L.J., Ed.; Humana Press (Springer): New York, NY, USA, 2015; pp. 79–98. [CrossRef]
90. Ringnér, M. What is principal component analysis? *Nat. Biotechnol.* **2008**, *26*, 303–304. [CrossRef] [PubMed]

Sample Availability: Samples of the compounds **1a–p** are available from the authors Ivan Malík and Jozef Csöllei.

© 2018 by the authors. Licensee MDPI, Basel, Switzerland. This article is an open access article distributed under the terms and conditions of the Creative Commons Attribution (CC BY) license (http://creativecommons.org/licenses/by/4.0/).

molecules

MDPI

Article

Synthesis, Bacteriostatic and Anticancer Activity of Novel Phenanthridines Structurally Similar to Benzo[*c*]phenanthridine Alkaloids

Pavel Lasák [1], Kamil Motyka [2], Vladimír Kryštof [3] and Jakub Stýskala [1,*]

1 Department of Organic Chemistry, Faculty of Science, Palacký University, 17. Listopadu 1192/12, CZ-771 46 Olomouc, Czech Republic; pavellasak@seznam.cz
2 Institute of Molecular and Translation Medicine, Faculty of Medicine, Palacký University, Hněvotínská 5, CZ-779 00 Olomouc, Czech Republic; kamil.motyka@gmail.com
3 Laboratory of Growth Regulators, Faculty of Science, Palacký University and Institute of Experimental Botany ASCR, Šlechtitelů 27, CZ-783 71 Olomouc, Czech Republic; vladimir.krystof@upol.cz
* Correspondence: jakub.styskala@upol.cz; Tel.: +42-058-563-4466

Received: 31 July 2018; Accepted: 24 August 2018; Published: 27 August 2018

Abstract: In this study, we report the synthesis, antibacterial and anticancer evaluation of 38 novel phenanthridines that were designed as analogs of the benzo[*c*]phenanthridine alkaloids. The prepared phenanthridines differ from the benzo[*c*]phenanthridines in the absence of a benzene A-ring. All novel compounds were prepared from 6-bromo-2-hydroxy-3-methoxybenzaldehyde in several synthetic steps through reduction of Schiff bases and accomplished by radical cyclization. Twelve derivatives showed high antibacterial activity against *Bacillus subtilis*, *Micrococcus luteus* and/or *Mycobacterium vaccae* at single digit micromolar concentrations. Some compounds also displayed cytotoxicity against the K-562 and MCF-7 cancer cell lines at as low as single digit micromolar concentrations and were more potent than chelerythrine and sanguinarine. The active compounds caused cell-cycle arrest in cancer cells, increased levels of p53 protein and caused apoptosis-specific fragmentation of PARP-1. Biological activity was connected especially with the presence of the *N*-methyl quaternary nitrogen and 7-benzyloxy substitution (compounds **7i**, **7j**, **7k**, and **7l**) of phenanthridine.

Keywords: phenanthridines; benzo[*c*]phenanthridines; radical cyclization; antiproliferative; antibacterial activity

1. Introduction

Benzo[*c*]phenanthridine alkaloids contain a chrysene-skeleton-based heterocyclic core and are classified as isoquinoline alkaloids (Figure 1). They are distributed especially in the plant family *Papaveraceae* and display a broad spectrum of biological activities, including anti-inflammatory, antimicrobial, antifungal and antitumor effects [1–7]. Sanguinarine and chelerythrine are the best-known benzo[*c*]phenanthridine alkaloids, most frequently studied for their antitumor effects [8]. As flat polyaromatic compounds they directly interact with DNA [9]. However, cell cycle arrest and induction of cell death caused by these alkaloids probably occurs not only due to DNA damage alone, but as a combined result of targeting other cellular structures, including topoisomerases, tubulin and antiapoptotic protein Bcl-X_L [10,11]. Importantly, these alkaloids act at concentrations comparable to those of cytostatics used as anticancer drugs.

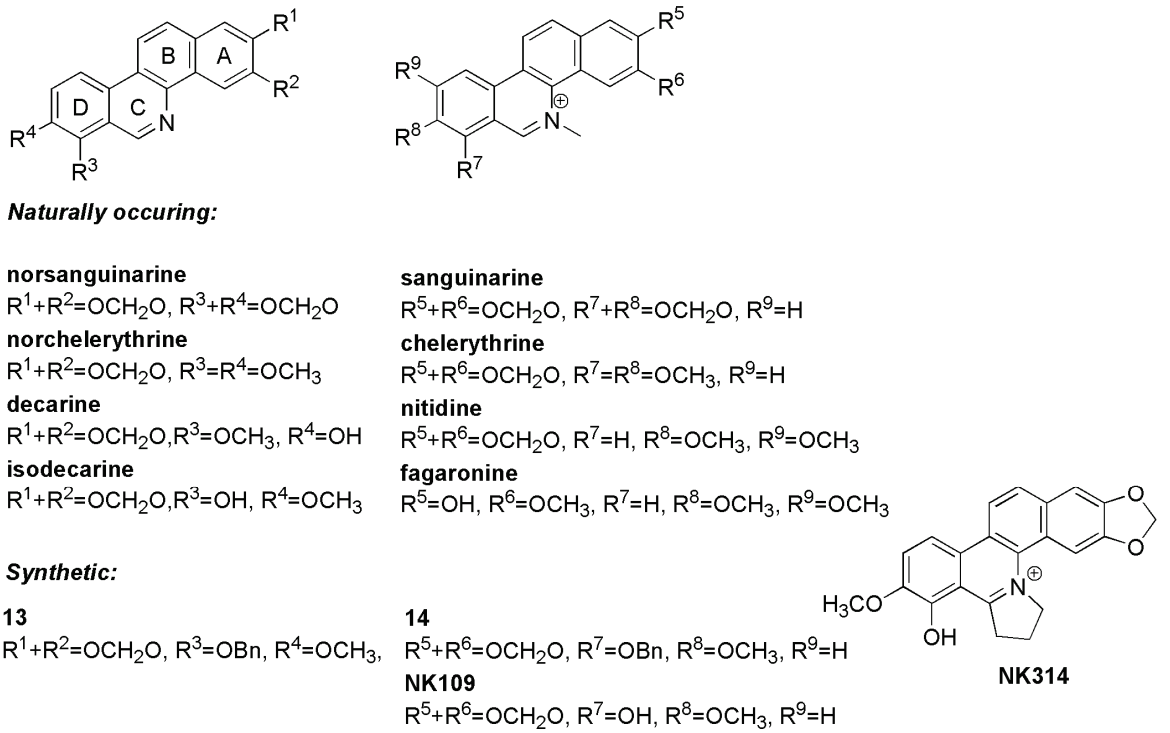

Figure 1. Structures of some benzo[*c*]phenanthridines.

Benzo[*c*]phenanthridine alkaloids have been subjected to chemical modifications with the aim of understanding their structure-activity relationships and to improve their biological functions. Early studies indicated that the activity of benzo[*c*]phenanthridine alkaloids can be linked to the presence of their cationic quaternary nitrogen [12]. The quaternary iminium may undergo nucleophilic addition to biological amines or thiols, modify DNA and proteins and as a consequence induce cell death. In contrast, a recent report suggests that the iminium group is not essential for cytotoxicity in cancer cell lines [13]. Other systematic studies examined the correlation between the type of substituents at positions 2, 3, 7, 8 and 9 of their skeletons and antiproliferative activity [14] and revealed that cationic iminium alkaloids displayed stronger activity than their corresponding uncharged bases. The cytotoxic activity was further increased if these quaternary bases were 7,8-oxygenated [15].

These studies led to identification of NK109, the 7-*O*-demethylated synthetic analogue of chelerythrine, that was shown to have submicromolar dose growth-inhibitory activity against cancer cell lines, i.e., significantly lower than chelerythrine [16–19] (Figure 1). Further modification of NK109, in which ring C was fused to a pyrrolidine cycle, yielded NK314 with even stronger activities in several cancer models [20–22]. The molecular mechanism of action of these compounds has been often attributed to inhibition of topoisomerases, which are also targeted by the related compounds nitidine and fagaronine [23].

To our knowledge, there have not been many attempts to modify the heterocyclic skeleton of benzo[*c*]phenanthridines up until now in order to modify their biological activity. With the exception of benzo[*h*]quinolones, which are structurally related to the benzo[*c*]phenanthridines but lack the D-ring [24], and phenanthridines lacking the A-ring [25], most other reports describe the synthesis of various isomeric and aza-analogous structures such as benzo[*i*]phenanthridines and dibenzo[*c*,*h*]cinnolines [26], benzo[*c*]phenanthrolines [27], pyridophenanthrolines and azapyrimido-phenanthrolines [28] or compounds containing the 3,4-dihydroisoquinolin-2-ium scaffold [29,30].

We therefore decided to prepare novel phenanthridines related to benzo[*c*]phenanthridines lacking the benzene A-ring (Figure 2), because previous work has suggested that phenanthridines may

retain biological activity [25]. The series contains derivatives differing in the presence and position of hydroxy and methoxy groups, 2,3- or 3,4-methylenedioxy bridges and 7-benzyloxy groups, but all compounds contain an 8-methoxy group. Some derivatives have been prepared either as free bases or protonated salts. In some compounds, the heterocyclic nitrogen is available in a quaternary form with methyl substitution. Thus, such variability allowed us to build a preliminary structure-activity relationship for antibacterial and antiproliferative activity, and to compare the phenanthridines with known benzo[*c*]phenanthridines (Figure 1).

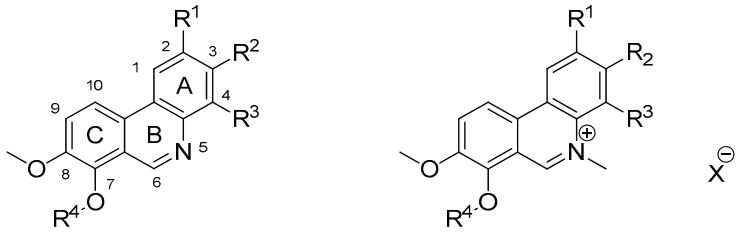

R^1, R^2, R^3 = H, OMe, $R^1 + R^2$ or $R^2 + R^3 = OCH_2O$; R^4 = H, Me, Bn; X = I, Cl, ClO_4, HSO_4, NO_3,

Figure 2. Desired phenanthridines for biological evaluation (for details see Table 1).

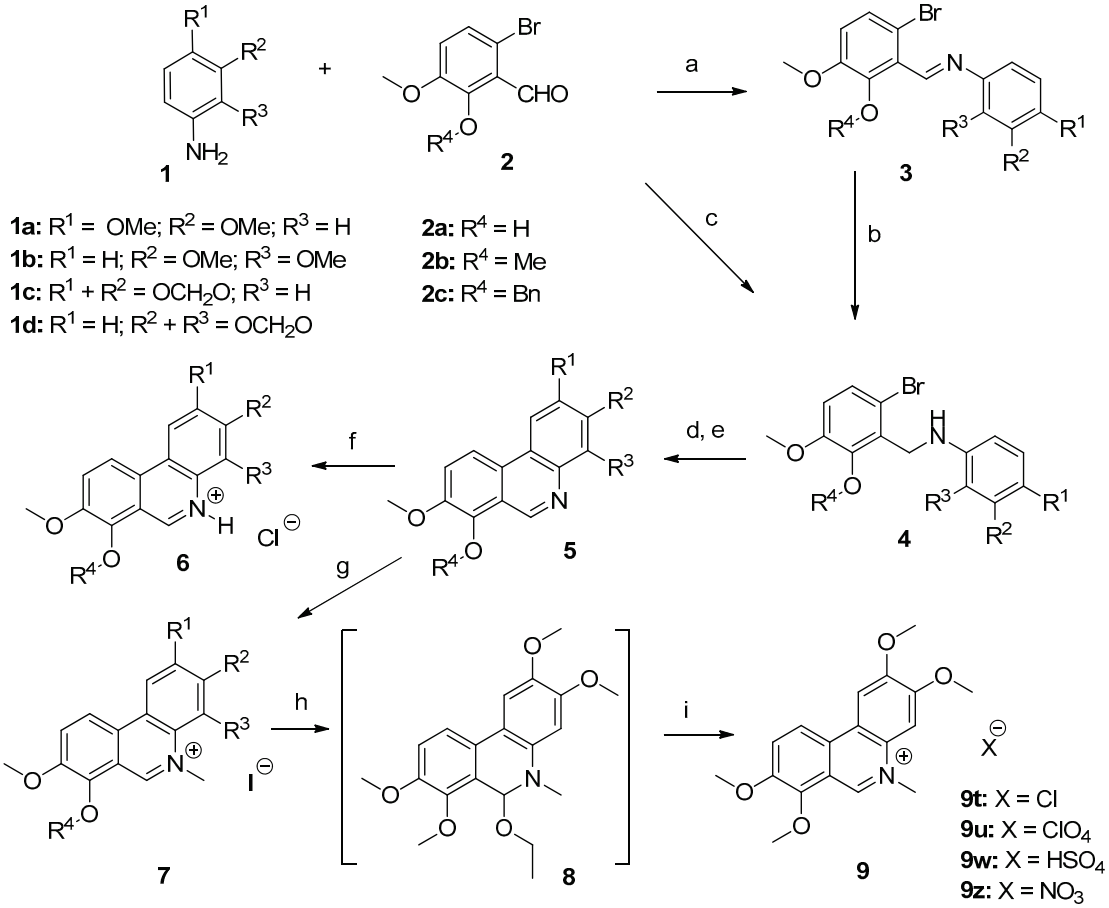

Scheme 1. The synthetic route for the preparation of phenanthridine derivatives. *Reagents and conditions*: (a) EtOH, reflux, 1 h; (b) $NaBH_4$, EtOH, r.t., 2 h; (c) $NaBH(OAc)_3$, toluene, r.t., 1 h; (d) Bu_3SnH, AIBN, toluene, 104–106 °C, 3–6 h; (e) activated MnO_2, r.t., 18 h; (f) HCl, dioxane, r.t.; (g) MeI, ACN, r.t., 7 days; (h) NaOH, EtOH, r.t., 1 h; (i) HX, r.t., 10 min.

Table 1. Numbering of compounds **3**–**7**.

Compound Number						Type of Substitution			
3	**4**	**5**	**6**	**7**		R^1	R^2	R^3	R^4
•	•	•	•		a:	$-OCH_3$	$-OCH_3$	H	H
		•	•		b:	H	$-OCH_3$	$-OCH_3$	H
•	•	•	•	•	c:	$-OCH_2O-$		H	H
•	•	•	•	•	d:	H	$-OCH_2O-$		H
	•	•	•	•	e:	$-OCH_3$	$-OCH_3$	H	CH_3
	•	•	•	•	f:	H	$-OCH_3$	$-OCH_3$	CH_3
	•	•	•	•	g:	$-OCH_2O-$		H	CH_3
	•	•	•	•	h:	H	$-OCH_2O-$		CH_3
	•	•	•	•	i:	$-OCH_3$	$-OCH_3$	H	benzyl
	•	•	•	•	j:	H	$-OCH_3$	$-OCH_3$	benzyl
	•	•	•	•	k:	$-OCH_2O-$		H	benzyl
	•	•	•	•	l:	H	$-OCH_2O-$		benzyl

• Newly prepared compounds (for general structures see Scheme 1).

For the preparation of novel phenanthridine derivatives we adapted methodologies from benzo[*c*]phenanthridine chemistry. Many synthetic approaches to the benzo[*c*]phenanthridine nucleus have been reported, with most routes involving the construction of either the B or C ring in the final or semifinal stage. These synthetic methods are summarized in reviews [31,32]. Our synthesis of desired phenanthridine compounds is based on our previous experience with the synthesis of isodecarine [33] and metabolites of benzo[*c*]phenanthridines [34], where a radical cyclization leading to ring C closure was used to accomplish the construction of the benzo[*c*]phenanthridine heterocyclic system. By this method we prepared phenanthridine derivatives where the B ring is formed.

2. Results and Discussion

2.1. Chemistry

For the preparation of phenanthridines, selected anilines possessing substitution in positions 2,3 (**1b [35]**, **1d [36]**) and 3,4 (**1a**, **1c**) with methylenedioxy or dimethoxy groups were used for the reactions. Commercially available 6-bromo-2-hydroxy-3-methoxybenzaldehyde (**2a**) needed for introduction of the C-ring aromatic core was used as is or after modification of the hydroxyl group to obtain the methoxyaldehyde **2b** [25] or benzyloxyaldehyde **2c** [16].

Reductive amination of aldehydes **2a**–**2c** with selected anilines **1a**–**1d** by $NaBH(OAc)_3$ in toluene proceeded quantitatively and afforded the corresponding novel secondary amines **4**. We have also verified an alternative two-step route leading to the same secondary amines through their isolated Schiff bases **3**. The preparation of Schiff bases **3a**, **3c**, and **3d** possessing unsubstituted hydroxyl groups proceeded smoothly providing products that readily precipitated from the reaction mixture with excellent nearly quantitative yields. Facile reduction of their iminium double bonds by $NaBH_4$ in ethanol led to the corresponding secondary amines **4a**, **4c**, and **4d**. Surprisingly, the condensation leading to the formation of Schiff bases with substituted hydroxyl group (R^4 = benzyl or methyl) under the same reaction conditions was not quantitative (conversions ranged from 50–75%) and subsequent isolation attempts by conventional methods were complicated. Therefore, we tried to influence the reaction equilibrium by increasing the ratio of aniline to aldehyde, prolonging the reaction time, performing the reactions in alternative solvents or by use of a microwave reactor, but unfortunately, without any satisfactory improvement. In summary, reductive amination seems to be a more suitable method for the preparation of these sorts of amines **4**.

To obtain compounds possessing a phenanthridine core, amines **4** needed to be cyclized. For this purpose, several synthetic approaches including palladium-catalyzed cross-coupling cyclization [37–41] or base-promoted homolytic aromatic substitution [42,43] were tested with amines

4a and **4e**, unfortunately, the reactions failed or yields were very low. During these experiments debromination was the main reaction observed. Finally, radical cyclization by Bu_3SnH using AIBN (azobisisobutyronitrile) as a radical initiator in toluene and subsequent aromatization by activated MnO_2 [44] afforded the desired novel phenanthridine derivatives **5** in various yields. During all radical cyclization reactions we observed formation of debrominated starting amines **10** as side products in amounts of 10–20% (Scheme 2). Formation of these reduced compounds is in accordance with earlier results [33]. Further side products were detected when 3,4-disbstituted (R^1 and R^2) amines **4** were subjected to the radical cyclization conditions. Apart from reduced amines **10**, cyclized regioisomers **11** were also observed as minor products. In the case of substituted amines **4**, where R^4 is benzyl or methyl the amount of **11** was around 5%, whereas the ratio of these regioisomers was much higher (up to 30%, based on HPLC analysis) for the unsubstituted hydroxylamines **4a**–**4d** (Scheme 2).

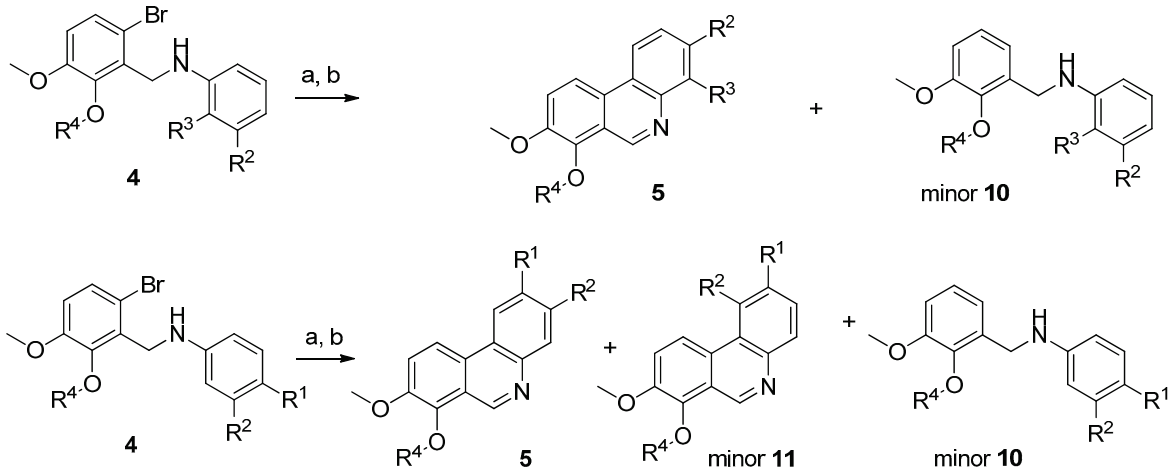

Scheme 2. Side reaction products formed during radical cyclization of **4** to **5**. *Reagents and conditions*: (a) Bu_3SnH, AIBN, toluene, 104–106 °C, 3–6 h; (b) activated MnO_2, r.t., 18 h.

Crystallization was utilized here as a useful method for the separation of most phenanthridines **5** from their reaction by-products. Unfortunately, a problem concerning the isolation of pure compounds was observed with hydroxyphenanthridines **5a**–**5d**. The byproducts formed had similar properties to the targeted molecules, with only silica gel column chromatography providing pure compound **5d**, but again with difficulties. For these reasons the remaining hydroxyphenanthridines **5a**–**5c** were obtained by catalytic hydrogenation of the corresponding benzyl derivatives **5i**–**5k**. This benzyl group deprotection proceeded under atmospheric pressure of hydrogen on 10% Pd/C. Under these conditions reduction of the iminium double bond can occur, so subsequent stirring of the reaction mixture in air or by addition of MnO_2 was necessary for rearomatization. Alternatively, to avoid the need for this re-oxidation step benzyl group removal could also be achieved by acid hydrolysis with HCl followed by treatment with aqueous NH_3 to obtain the free bases (Scheme 3).

Phenanthridine derivatives **5** were converted to their hydrochlorides **6** by addition of HCl into dioxane solutions of the free bases (Scheme 1). Surprisingly these compounds have very low solubility in water, and even in other polar solvents (DMSO, EtOH, DMF) which hindered biological testing.

N-methylation of phenanthridines **5** was carried out with methyl iodide in acetonitrile under mild conditions to give *N*-methylphenanthridinium iodides **7**. These conditions enabled the selective methylation, even of the phenanthridines possessing a free hydroxyl group. Similarly to the hydrochlorides **6**, the prepared quaternary iodides **7** were also surprisingly very poorly soluble in water. To verify the possibility if the anion exchange can influence the solubility of these compounds, selected quaternary iodides were transformed in a NaOH/EtOH solution into their unisolated colorless pseudobases **8**. Different salts (chloride, hydrogensulfate, perchlorate, and nitrate) were obtained by

addition of large excess of corresponding acids to provide the anion modified *N*-methylphenanthridine precipitates. It was found that anion exchange did not improve solubility of these mentioned compounds significantly. For illustration, we demonstrate experimentally the preparation of various salts of compound **9**, which were confirmed by elemental analysis.

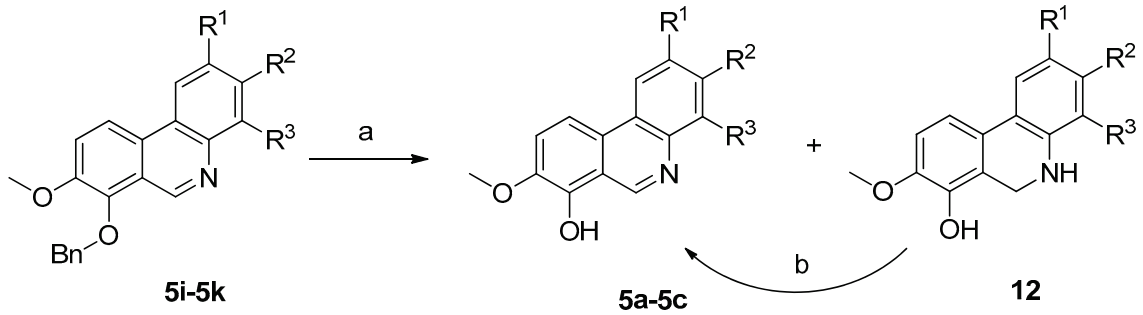

Scheme 3. Convenient route for the preparation of hydroxy phenanthridines **5a**–**5c**. *Reagents and conditions*: (a) H_2/10% Pd(C), atm. pressure, r.t. or HCl/EtOH, reflux 2.5 h, then aq. NH_3; (b) air (O_2) or MnO_2; r.t.

2.2. Biological Assays

2.2.1. Antibacterial Activity

Prepared derivatives were screened for antibacterial activity against representative Gram-positive bacteria (*Bacillus. subtilis,* ATCC 6633; *Micrococcus luteus,* ATCC 10240; *Mycobacterium vaccae*, DSM 43514; *Staphylococcus aureus*, CCM 2524) and Gram-negative bacteria (*Pseudomonas aeruginosa*, CCM 3955; *Escherichia coli*, CCM 3954) using agar diffusion assays [45]. Derivatives with zones of inhibition $\geq$20 mm were subjected to a further assay [46] that determines their minimum inhibitory concentrations (MIC). From the measured data (Table 2) it is possible to make a few general conclusions regarding their structure-activity relationships:

(1) Antibacterial activity was observed only for derivatives containing a phenanthridine skeleton. No tested strain was susceptible to representative intermediates **3** and **4**.
(2) Derivatives with benzyl substituent as R^4 (**5k**, **5l**, **7i**, **7j**, **7k**, and **7l**) showed high antibacterial activity against *B. subtilis*, *M. luteus* and/or *M. vaccae* with MIC in single digit micromolar values.
(3) Compounds with a charged nitrogen bearing methyl group (**7i**, **7j**, **7k** and **7l**) demonstrated high activity as well. To summarize, the most active compounds have a similar structural motif—a phenanthridine skeleton with a charged *N*-methyl nitrogen and a benzyl group as a R^4 substituent.

These points are noteworthy for potential structural exploitation in further antibacterial agent development. To compare the antibacterial activity results for well-known natural (chelerythrine, sanguinarine, isodecarine, norchelerythrine) or synthetic compounds (NK-109, **13**, **14**) with similar structure motifs are presented in Table 2 as well. From the measured results it is evident that some prepared derivatives provided similar or even better activity than these compounds (MIC in micromolar or submicromolar values). All newly reported compounds were less active than a previously developed analogue 14, with 7j performing better than that reference compound only against *M. luteus*. No compound displayed any relevant activity against Gram-negative bacteria. If the structures are compared the importance of the presence of a charged *N*-methyl nitrogen in the molecule is confirmed.

Table 2. Antibacterial activity.

Compound	Diameter of Inhibition Zone in Agar Diffusion Assay (mm) (MIC) (μmol L^{-1})					
	B. subtilis (ATCC 6633)	*M. luteus* (ATCC 10240)	*M. vaccae* (DSM 43514)	*S. aureus* (CCM 2524)	*P. aeruginosa* (CCM 3955)	*E. coli* (CCM 3954)
5a	13	14	15	15	15	12
5b	12	15	20(>200)	19	20(>200)	0
5c	18	17	25(50)	18	16	0
5d	33(50)	22(50)	23(25)	18	15	0
5e	22(>200)	18	23(200)	13	12	12
5f	35(50)	30(100)	31(25)	20(50)	15	13
5g	20(100)	14	16	11	12	0
5h	34(50)	30(100)	22(25)	20(50)	15	0
5i	28(50)	22(50)	18	17	15	0
5j	19	18	17	19	13	12
5k	41(6.25)	33(3.13)	31(12.5)	24(25)	16	11
5l	34(12.5)	30(3.13)	32(12.5)	20(50)	15	0
6e	0	13	19	13	15	14
6f	11	16	12	0	15	15
6g	11	16	12	0	15	15
6h	0	15	14	12	16	11
6i	14	16	13	11	18	0
6j	11	16	12	0	18	10
6k	12	15	14	14	17	0
6l	12	10	10	14	0	0
7c	13	20	10	15	0	0
7d	13	19	21(100)	15	0	0
7e	11	26(50)	11	12	14	13
7f	13	36(25)	21(50)	17	13	12
7g	39(6.25)	48(12.5)	18	15	14	12
7h	26(25)	40(50)	15	14	15	11
7i	25(25)	42(3.13)	40(6.25)	13	10	0
7j	35(12.5)	42(0.78)	40(12.5)	13	12	0
7k	30(12.5)	42(3.13)	30(3.13)	20(50)	0	12
7l	30(25)	37(3.13)	30(3.13)	18	0	0
9t	15	25(50)	21(50)	15	10	10
9u	15	20(25)	25(50)	18	13	10
9w	17	20(50)	21(50)	17	10	12
9z	15	33(25)	21(50)	17	13	10
13	15	12	16	15	0	0
14	25(0.78)	22(6.25)	23(0.78)	24(0.78)	0	15
norchelerythrine	14	11	17	18	0	0
isodecarine	16	11	12	16	0	0
NK-109	32(1.56)	27(12.5)	45(12.5)	25(12.5)	0	15
chelerythrine	30(3.13)	26(50)	32(3.13)	24(6.25)	0	16
sanguinarine	29(3.13)	27(25)	27(6.25)	24(6.25)	0	17
Ciprofloxacin *	20(7.5)	22(0.26)	27(0.26)	20(15.0)	15(3.75)	20(7.5)

* used as a standard.

2.2.2. Anticancer Activity In Vitro

Benzo[*c*]phenanthridine alkaloids are known to display antiproliferative and anticancer activities [8,18]. Due to their structural analogy, the preliminary in vitro anticancer activity of the newly prepared compounds was evaluated on two established cancer cell lines, MCF-7 (breast carcinoma) and K-562 (chronic myelogeneous leukemia). The resulting data are presented in Table 3 and show that several of the new compounds have significant activity in both cell lines, with single digit micromolar EC_{50} values.

Table 3. Anticancer activity in vitro.

Compounds	EC_{50} (μM) *	
	K-562	**MCF-7**
3a	>50	>50
3c	>50	>50
3d	>50	>50
4a	>50	>50
4c	71 ± 2	79 ± 1
4d	>50	>50
4e	40 ± 8	70 ± 5
4f	>25	>25
4g	51 ± 5	75 ± 2
4h	>12	>12
4i	>50	>50
4j	>25	>25
4k	>50	>50
4l	>50	>50
5a	11 ± 1	17 ± 6
5b	40 ± 5	24 ± 4
5c	59 ± 4	17 ± 1
5d	19 ± 6	12 ± 1
5e	29 ± 6	27 ± 6
5f	13 ± 1	10 ± 2
5g	8.7 ± 1.3	7.2 ± 2.9
5h	14 ± 1	10 ± 1
5i	19 ± 8	15 ± 5
5j	36 ± 11	23 ± 5
5k	4.2 ± 1.1	3.2 ± 0.9
5l	>50	>50
6a	8.7 ± 1.2	18 ± 3
6c	60 ± 8	17 ± 4
6d	>50	>50
6e	24 ± 1	34 ± 6
6f	82 ± 7	39 ± 3
6g	15 ± 3	20 ± 2
6h	59 ± 12	45 ± 6
6i	67 ± 18	43 ± 9
6j	14 ± 1	21 ± 2
6k	>50	>50
6l	>50	>50
7c	82 ± 10	57 ± 7
7d	41 ± 4	16 ± 1
7e	>50	38 ±
7f	81 ± 17	69 ± 7
7g	29 ± 13	11 ± 6
7h	>50	>50
7i	6.4 ± 1.1	5.3 ± 1.1
7j	0.8 ± 0.2	2.6 ± 0.3
7k	5.1 ± 0.7	1.8 ± 0.8
7l	8.3 ± 1.4	7.7 ± 0.9
9t	>50	>50
9u	>50	45 ± 4
9w	>50	36 ± 9
9z	>50	>50
13	94 ± 6	48 ± 2
14	0.9 ± 0.2	1.4 ± 0.1
norchelerythrine	>100	>100
isodecarine	>100	>100
NK-109	1.0 ± 0.1	4.6 ± 0.6
chelerythrine	8.6 ± 1.8	5.9 ± 0.5
sanguinarine	2.2 ± 0.2	2.0 ± 0.2
cisplatin	4.7 ± 0.4	11 ± 1

* Values are means of triplicates and indicate concentration that kills 50% of cells during a three-day cultivation.

Derivative **7j** reached submicromolar values in K-562 cells and was even more potent than chelerythrine and sanguinarine. The most active compounds bear 7-benzyloxy substitution and either 2,3-dimethoxy or an isosteric 2,3-methylenedioxy bridge and are either *N*5-methylated (**7j**, **7k**) or contain an unsubstituted *N*5 (**5k**). Compounds without a benzyl moiety or with 3,4-dimethoxy/3,4-methylenedioxy substitution were less potent. Interestingly, removal of the methyl from *N*5 of **7j**, that also uncharged the nitrogen, decreased potency (**5j**). In contrast, presence of the quaternary nitrogen (methylated) significantly reduced the activity of several compounds (compare especially pairs **5f** and **7f**, **5g** and **7g**, **5h** or **7h**). According to previous studies, the activity of benzo[*c*]phenanthridine alkaloids can be explained by the presence of a cationic quaternary nitrogen [12,15]. These conclusions however probably cannot be applied to phenanthridines, because many of these compounds with a quaternary nitrogen have poor activity and one of the most potent compounds (**5k**) does not contain a quaternary nitrogen at all.

With the aim of directly comparing the activity of phenanthridines with the corresponding benzo[*c*]phenanthridines, we prepared also four variously substituted benzo[*c*]phenanthridines—**13 [16,33]**, **14** [33], isodecarine [33] and norchelerythrine (Figure 1). In line with the abovementioned findings for phenanthridines, the presence of the benzyloxy functionality at position 7 correlated with in vitro anticancer activity for compounds **13** and **14**. However, previous studies indicated that the activity of benzo[*c*]phenanthridine alkaloids can be explained by the presence of a cationic quaternary nitrogen atom [12]. We also observed lack of cellular activity with isodecarine and norchelerythrine, which were prepared as demethylated derivatives of the very potent NK-109 and chelerythrine, respectively. Compound **14**, killing both cancer cell lines with EC_{50} values around 1 μM, contains not only a benzyloxy functionality, but also a quaternary nitrogen that could be essential for its activity. We cannot rule out the possibility that this cation is even more important for the activity.

2.2.3. Mechanism of Cellular Activity

Anticancer activity of benzo[*c*]phenanthridine alkaloids relates at least partly to their ability to inhibit topoisomerase I or II. For example, nitidine and fagaronine inhibit the topoisomerase I—mediated DNA relaxation [23].

Their synthetic derivatives NK109 and NK314 exerted their cytotoxic activity through inhibition of topoisomerase II, followed by DNA breaks [19,22]. DNA damage usually results in a cell cycle arrest and eventually leads to apoptosis. We therefore treated MCF-7 cells with several compounds and NK109 as a control. Interestingly, these compounds influenced the cell cycle profile in different manners (Figure 3). The most potent **7k** reduced S and G2/M phases, **7g** reduced S phase and caused slight accumulation in G2/M, whereas the only weakly cytotoxic **6g** resulted in strong G2/M arrest. NK109 used as a control also arrested cells in G2/M. These differences suggest that the compounds may have different molecular targets.

DNA damage induces various responses, including stabilization and activation of tumor suppressor protein p53 [47]. In the following experiments, we analyzed levels and activities of tumor suppressor protein p53, which is typically activated in cells upon topoisomerase inhibition. We performed immunoblotting of proteins extracted from MCF-7 cells treated for 24 h with compounds **6g**, **7k** and **7g**. Levels of p53 and its typical downstream target $p21^{waf1}$ were both increased (Figure 4). In addition, fragmentation of PARP producing a 89 kDa band was observed in cells treated with **7k** and NK109, indicating ongoing apoptosis. This fragmentation was dose-dependent for compound **7k**. In contrast, neither **6g** nor **7g** triggered PARP fragmentation, which is in line with their weaker cytotoxicities.

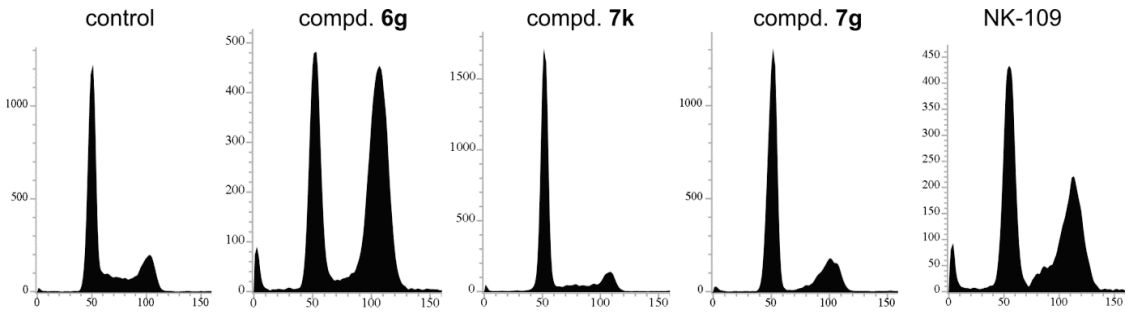

Figure 3. Cell cycle effects of compounds **7k**, **7g**, **6g** and NK-109 in MCF-7 cells treated for 24 h with doses corresponding to 3 × EC_{50} values (60, 5.4, 33 and 13.8 μM, respectively). Cells were harvested and then flow cytometric analysis of DNA stained by propidium iodide (10,000 counts) was performed as described in the Materials and Methods section.

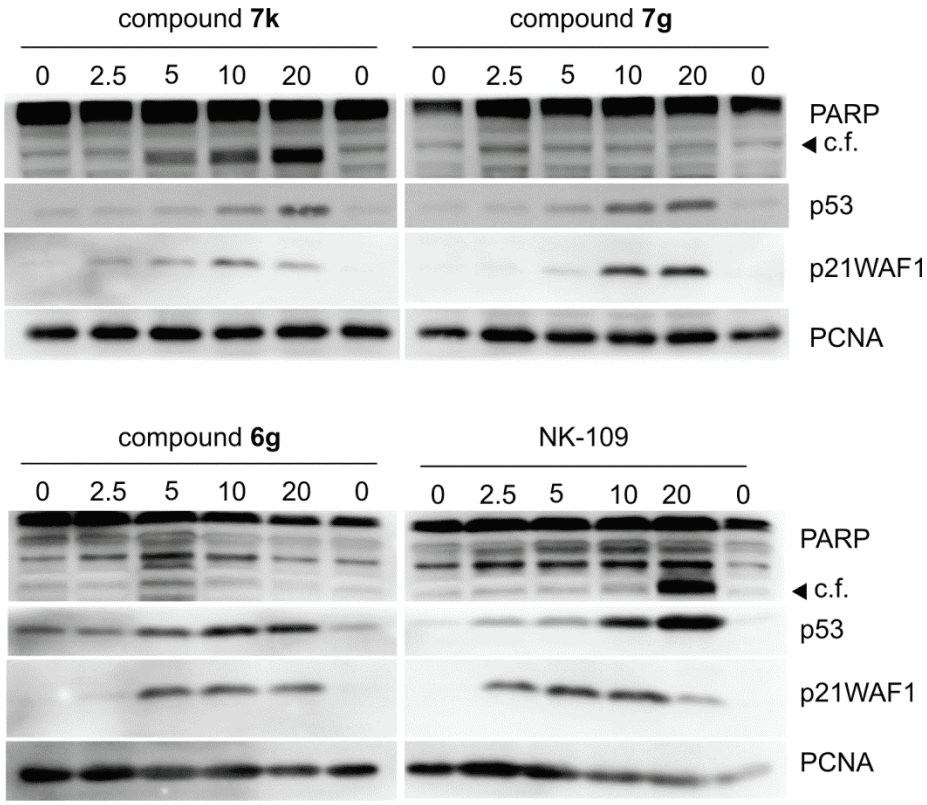

Figure 4. Dose-dependent effect of compounds **7k**, **7g**, **6g** and **NK-109** on p53 and its activity in MCF-7 cells. The cells were treated for 24 h with indicated doses of compounds (given in μM) and then specific proteins were analyzed by immunoblotting as described in the Materials and Methods section. C.f., 89 kDa cleavage fragment of PARP.

3. Materials and Methods

3.1. Chemistry

3.1.1. General Information

All commercially available reagents were used without further purification and purchased from standard chemical suppliers. Reactions were monitored by LC/MS analyses on a UHPLC-MS system (Thermo Scientific, Waltham, MA, USA) consisting of a UHPLC chromatograph equipped with a photodiode array detector and a triple quadrupole mass spectrometer using a C18 column at 30 °C and

flow rate of 800 μL/min. ^{1}H and ^{13}C-NMR spectra were measured on an ECA 400II (^{1}H: 399.78 MHz, ^{13}C: 100.53 MHz) NMR spectrometer (JEOL Resonance, Tokyo, Japan). Samples were dissolved and subsequently measured in DMSO-d_6 or $CDCl_3$. Chemical shifts (δ) are reported in ppm and referenced to the middle of the solvent signal (DMSO-d_6: 2.50 ppm, 39.51 ppm; $CDCl_3$: 7.27 ppm, 77.00 ppm. Data are reported as follows: chemical shift (multiplicity [singlet (s), doublet (d), doublet of doublet (dd), triplet (t), quartet (q), multiplet (m), broad resonance (br)], coupling constants [Hz], integration). All the NMR spectra were acquired at ambient temperature. All recorded ^{1}H and ^{13}C-NMR spectra are available as Supplementary material. High resolution mass spectra (HRMS) measurements were performed on an Orbitrap mass analyzer (Thermo Scientific, Waltham, MA, USA) equipped with Heated Electrospray Ionization (HESI). The spectrometer was tuned to obtain a maximum response for *m/z* 70–700. Elemental analyses were performed on an EA 1108 Elemental Analyser (Fisons Instruments, Thermo Scientific, Waltham, MA, USA). Thin layer chromatography (TLC) were performed on pre-coated silica gel 60 F254 plates (Merck, Prague, Czech Republic) and visualized by exposure to UV light (254 or 366 nm). Melting points were measured on a Boetius stage apparatus (WEB Analytik, Dresden, Germany) and are uncorrected.

3.1.2. Synthesis of Compounds **3–9**

3-Bromo-2-{[(3,4-dimethoxyphenyl)imino]methyl}-6-methoxyphenol (**3a**). To a solution of aniline **1a** (410 mg; 2.67 mmol) in anhydrous EtOH (15 mL) was added benzaldehyde **2a** (600 mg; 2.60 mmol). The reaction mixture was stirred at reflux for 1 h and then slowly cooled to 0–5 °C. Resultant precipitate was filtered off, washed with ice-cold EtOH (2 mL) and dried. Compound **3a** (921 mg, 97%) was obtained as an orange microcrystalline solid. Mp. = 157–159 °C; ^{1}H-NMR (400 MHz, $CDCl_3$) δ = 15.27 (s, 1H), 9.05 (s, 1H), 7.02 (d, *J* = 8.8 Hz, 1H), 6.98–6.89 (m, 3H), 6.78 (d, *J* = 8.8 Hz, 1H), 3.94 (s, 3H), 3.92 (s, 3H), 3.90 (s, 3H); ^{13}C-NMR (101 MHz, $CDCl_3$) δ = 160.4, 154.6, 149.6, 148.8, 148.7, 140.0, 121.8, 116.4, 115.7, 114.7, 113.1, 111.4, 105.1, 56.2, 56.1, 56.0; HRMS (HESI, *m/z*): $[M + H]^+$ calcd. for $C_{16}H_{17}BrNO_4$, 366.0341; found 366.0335.

2-[(1,3-Benzodioxole-5-ylimino)methyl]-3-bromo-6-methoxyphenol (**3c**). Schiff base **3c** was obtained in a similar manner to compound **3a** using benzaldehyde **2a** (750 mg; 3.25 mmol), aniline **1c** (445 mg; 3.25 mmol) and anhydrous EtOH (20 mL). Compound **3c** (1.09 g; 92%) was obtained as a dark red microcrystalline solid. Mp. = 176–178 °C; ^{1}H-NMR (400 MHz, $CDCl_3$) δ = 15.07 (br. s, 1H), 9.02 (s, 1H), 7.03 (d, *J* = 8.7 Hz, 1H), 6.92–6.89 (m, 1H), 6.88–6.85 (m 2H), 6.78 (d, *J* = 8.7 Hz, 1H), 6.03 (s, 2H), 3.91 (s, 3H); ^{13}C-NMR (101 MHz, $CDCl_3$) δ = 160.6, 154.4, 148.8, 148.7, 147.4, 141.4, 122.0, 116.5, 116.0, 115.9, 114.9, 108.7, 101.8, 101.5, 56.3; HRMS (HESI, *m/z*): $[M + H]^+$ calcd. for $C_{15}H_{13}BrNO_4$, 350.0028; found 350.0023.

2-[(1,3-Benzodioxole-4-ylimino)methyl]-3-bromo-6-methoxyphenol (**3d**). Schiff base **3d** was obtained in a similar manner to compound **3a** using benzaldehyde **2a** (572 mg; 2.48 mmol), aniline **1d** (350 mg; 2.55 mmol) and anhydrous EtOH (15 mL). Compound **3d** (737 mg; 85%) was obtained as a pale orange microcrystalline solid. Mp. = 195–196 °C; ^{1}H-NMR (400 MHz, $CDCl_3$) δ = 15.18 (s, 1H), 9.40 (s, 1H), 7.05 (d, *J* = 8.6 Hz, 1H), 6.96–6.88 (m, 2H), 6.82–6.77 (m, 2H), 6.09 (s, 2H), 3.92 (s, 3H); ^{13}C-NMR (101 MHz, $CDCl_3$) δ = 164.3, 154.7, 148.9, 148.7, 140.3, 129.3, 122.2, 121.9, 116.7, 116.3, 116.0, 115.0, 107.7, 101.7, 56.2; HRMS (HESI, *m/z*): $[M + H]^+$ calcd. for $C_{15}H_{13}BrNO_4$, 350.0028; found 350.0022.

3-Bromo-2-{[(3,4-dimethoxyphenyl)amino]methyl}-6-methoxyphenol (**4a**). To a suspension of the Schiff base **3a** (921 mg, 2.51 mmol) in anhydrous EtOH (25 mL) was added $NaBH_4$ (95 mg; 2.51 mmol). After 2 h of stirring at room temperature the reaction mixture was neutralized by adding an aqueous solution of 10% AcOH (1 mL). The suspension dissolved into solution, which was concentrated under reduced pressure. The residue was extracted with a mixture of EtOAc (20 mL) and water (20 mL). The aqueous phase was washed with EtOAc (20 mL). The combined EtOAc phases were dried over

Na_2SO_4, filtered and concentrated under reduced pressure to provide a yellow crude oil (737 mg, 80%). TLC R_f = 0.3 (hexane/EtOAc 10:3 *v*/*v*); ^{1}H-NMR (400 MHz, $CDCl_3$) δ = 7.05 (d, *J* = 9.3 Hz, 1H), 6.74 (d, *J* = 8.3 Hz, 1H), 6.66 (d, *J* = 8.3 Hz, 1H), 6.47 (d, *J* = 2.1 Hz, 1H), 6.37 (dd, *J* = 2.1, 8.3, Hz, 1H), 5.89 (brs, 2H), 4.53 (s, 2H), 3.85 (s, 3H), 3.83 (s, 3H), 3.80 (s, 3H); ^{13}C-NMR (101 MHz, $CDCl_3$) δ = 149.7, 146.6, 146.2, 142.7, 141.7, 123.4, 123.2, 115.1, 112.7, 111.2, 106.1, 100.5, 56.5, 56.1, 55.7, 45.8; HRMS (HESI, *m*/*z*): $[M + H]^+$ calcd. for $C_{16}H_{19}BrNO_4$, 368.0492; found 368.0498.

2-[(1,3-Benzodioxole-5-ylamino)methyl]-3-bromo-6-methoxyphenol (**4c**). The secondary amine **4c** was obtained in a similar manner as compound **4a** using Schiff base **3c** (1.0 g; 2.9 mmol), $NaBH_4$ (109 mg; 2.9 mmol) and anhydrous EtOH (25 mL). The resulting crude product was a pale yellow oil (1.0 g, 99%). A sample for analysis was prepared by crystallization from toluene (100 mg/3 mL) and standing this solution at −20 °C. Mp. = 95–98 °C as a colorless crystalline compound; TLC R_f = 0.3 (hexane/EtOAc 10:3 *v*/*v*); ^{1}H-NMR (400 MHz, DMSO-d_6) δ = 9.34 (s, 1H), 7.02 (d, *J* = 8.7 Hz, 1H), 6.86 (d, *J* = 8.7 Hz, 1H), 6.64 (d, *J* = 8.2 Hz, 1H), 6.42 (d, *J* = 1.8 Hz, 1H), 6.12 (dd, *J* = 8.3, 2.3 Hz, 1H), 5.82 (s, 2H), 5.21 (t, *J* = 5.2 Hz, 1H), 4.19 (d, *J* = 5.2 Hz, 2H), 3.79 (s, 3H); ^{13}C-NMR (101 MHz, DMSO-d_6) δ = 147.6, 147.1, 146.2, 144.6, 138.1, 124.7, 122.2, 115.6, 112.2, 108.3, 103.4, 99.9, 95.4, 56.0, 42.9; HRMS (HESI, *m*/*z*): $[M + H]^+$ calcd. for $C_{15}H_{15}BrNO_4$, 352.0179; found 352.0182.

2-[(1,3-Benzodioxole-4-ylamino)methyl]-3-bromo-6-methoxyphenol (**4d**). The secondary amine **4d** was obtained in a similar manner as compound **4a** using Schiff base **3d** (500 mg; 1.43 mmol), $NaBH_4$ (54 mg; 1.43 mmol) and anhydrous EtOH (13 mL). The resulting crude product was a pale yellow oil (500 mg, 99%). A sample for analysis was prepared by crystallization from toluene (100 mg/3 mL) and standing this solution at −20 °C. Mp. = 89–90 °C as a colorless crystalline compound; TLC R_f = 0.3 (hexane/EtOAc 10:3 *v*/*v*); ^{1}H-NMR (400 MHz, $CDCl_3$) δ = 7.07 (d, *J* = 8.7 Hz, 1H), 6.75 (t, *J* = 8.0 Hz, 1H), 6.68 (d, *J* = 8.7 Hz, 1H), 6.60 (d, *J* = 8.2 Hz, 1H), 6.36 (d, *J* = 7.8 Hz, 1H), 5.90 (s, 2H), 4.59 (s, 2H), 3.87 (s, 3H); ^{13}C-NMR (101 MHz, $CDCl_3$) δ = 147.2, 146.2, 145.6, 134.6, 132.2, 123.9, 123.3, 122.2, 115.7, 111.1, 107.8, 100.6, 99.8, 56.1, 43.7; HRMS (HESI, *m*/*z*): $[M + H]^+$ calcd. for $C_{15}H_{15}BrNO_4$, 352.0179; found 352.0183.

N-(6-Bromo-2,3-dimethoxybenzyl)-3,4-dimethoxyaniline (**4e**). To a solution of bromobenzaldehyde **2b** (1.0 g; 4.08 mmol) and aniline **1a** (644 mg; 4.20 mmol) in anhydrous toluene (50 mL) was added $NaBH(OAc)_3$ (2.6 g; 12.2 mmol). The resulting suspension was stirred at room temperature for 1 h, and then washed with water (2 × 35 mL) and brine (1 × 40 mL). The aqueous phase was extracted with toluene (1 × 40 mL). The combined organic extracts were dried over Na_2SO_4, filtered and concentrated under reduced pressure. To induce crystallization of the product, MeOH (8 mL) was added to the residue. The resulting solid was filtered off, washed with cold MeOH (1 mL) and dried. Compound **4e** was obtained as a slightly pink crystalline solid (1.19 g; 76%). Mp. = 79–80 °C; TLC R_f = 0.2 (hexane/EtOAc 10:3 *v*/*v*); ^{1}H-NMR (400 MHz, $CDCl_3$) δ = 7.26 (d, *J* = 8.8 Hz, 1H), 6.79–6.72 (m, 2H), 6.43 (d, *J* = 2.6 Hz, 1H), 6.33 (dd, *J* = 8.5, 2.6 Hz, 1H), 4.42 (s, 2H), 4.02 (br. s, 1H), 3.87 (s, 3H), 3.86 (s, 3H), 3.85 (s, 3H), 3.80 (s, 3H); ^{13}C-NMR (101 MHz, $CDCl_3$) δ = 152.3, 149.8, 148.7, 142.7, 141.7, 132.6, 128.0, 115.2, 113.0, 112.9, 104.6, 99.5, 61.5, 56.6, 55.9, 55.7, 43.9; HRMS (HESI, *m*/*z*): $[M + H]^+$ calcd. for $C_{17}H_{21}BrNO_4$, 382.0654; found 382.0648.

N-(6-Bromo-2,3-dimethoxybenzyl)-2,3-dimethoxyaniline (**4f**). The secondary amine **4f** was prepared in a similar manner as the amine **4e** using bromobenzaldehyde **2b** (400 mg; 1.63 mmol), aniline **1b** (258 mg; 1.68 mmol) and $NaBH(OAc)_3$ (1.04 g; 4.9 mmol) in anhydrous toluene (20 mL). The residue was crystallized from EtOH/water to provide compound **4f** (212 mg; 34%) as a colorless microcrystalline solid. Mp. = 52–53 °C; TLC R_f = 0.5 (hexane/EtOAc 10:3 *v*/*v*); ^{1}H-NMR (400 MHz, DMSO-d_6) δ = 7.34 (d, *J* = 8.8 Hz, 1H), 6.98 (d, *J* = 8.8 Hz, 1H), 6.85 (t, *J* = 8.2 Hz, 1H), 6.52 (dd, *J* = 8.2, 1.2 Hz, 1H), 6.33 (dd, *J* = 8.2, 1.2 Hz, 1H), 4.85 (t, *J* = 6.2 Hz, 1H), 4.33 (d, *J* = 6.2 Hz, 2H), 3.80 (s, 3H), 3.77 (s, 3H), 3.72 (s, 3H), 3.60 (s, 3H); ^{13}C-NMR (101 MHz, DMSO-d_6) δ = 152.1, 148.4, 141.6, 135.0, 131.9, 127.9, 124.2,

119.5, 114.4, 113.8, 104.7, 101.6, 61.2, 59.5, 55.9, 55.5, 42.2; HRMS (HESI *m/z*): $[M + H]^+$ calcd. for $C_{17}H_{21}BrNO_4$, 382.0654; found 382.0648.

N-(6-Bromo-2,3-dimethoxybenzyl)-1,3-benzodioxole-5-amine (**4g**). The secondary amine **4g** was prepared in a similar manner as the amine **4e** using bromobenzaldehyde **2b** (400 mg; 1.63 mmol), aniline **1c** (231 mg; 1.68 mmol) and $NaBH(OAc)_3$ (1.04 g; 4.9 mmol) in anhydrous toluene (20 mL). The residue was crystallized from EtOH/water to provide compound **4g** (275 mg; 46%) as a pale yellow microcrystalline solid. Mp. = 74–75 °C; TLC R_f = 0.4 (hexane/EtOAc 10:3 *v/v*); ^{1}H-NMR (400 MHz, DMSO-d_6) δ = 7.34 (d, *J* = 8.8 Hz, 1H), 7.00 (d, *J* = 8.8 Hz, 1H), 6.65 (d, *J* = 8.3 Hz, 1H), 6.41 (d, *J* = 2.3 Hz, 1H), 6.12 (dd, *J* = 8.3, 2.3 Hz, 1H), 5.82 (s, 2H), 5.26 (t, *J* = 5.3 Hz, 1H), 4.16 (d, *J* = 5.2 Hz, 2H), 3.81 (s, 3H), 3.75 (s, 3H); ^{13}C-NMR (101 MHz, DMSO-d_6) δ = 152.1, 148.5, 147.7, 144.6, 138.1, 132.0, 127.7, 115.0, 113.7, 108.4, 103.2, 99.9, 95.2, 61.1, 55.9, 43.0; HRMS (HESI *m/z*): $[M + H]^+$ calcd. for $C_{16}H_{17}BrNO_4$, 366.0341; found 366.0337.

N-(6-Bromo-2,3-dimethoxybenzyl)-1,3-benzodioxole-4-amine (**4h**). The secondary amine **4h** was prepared in a similar manner as the amine **4e** using bromobenzaldehyde **2b** (253 mg; 1.03 mmol), aniline **1d** (142 mg; 1.04 mmol) and $NaBH(OAc)_3$ (660 mg; 3.1 mmol) in anhydrous toluene (12 mL). The residue was crystallized from MeOH to provide compound **4h** (302 mg; 80%) as a colorless microcrystalline solid. Mp. = 90–92 °C; TLC R_f = 0.3 (hexane/EtOAc 10:3 *v/v*); ^{1}H-NMR (400 MHz, DMSO-d_6) δ = 7.33 (d, *J* = 8.7 Hz, 1H), 6.98 (d, *J* = 9.2 Hz, 1H), 6.65 (t, *J* = 7.8 Hz, 1H), 6.46 (d, *J* = 8.2 Hz, 1H), 6.27 (dd, *J* = 7.8, 0.9 Hz, 1H), 5.90 (s, 2H), 4.82 (t, *J* = 6.0 Hz, 1H), 4.40 (d, *J* = 6.0 Hz, 2H), 3.80 (s, 3H), 3.77 (s, 3H); ^{13}C-NMR (101 MHz, DMSO-d_6) δ = 152.1, 148.4, 147.0, 133.2, 132.7, 131.8, 127.7, 122.1, 114.6, 113.7, 107.2. 100.0, 98.3, 61.0, 55.9, 42.6; HRMS (HESI *m/z*): $[M + H]^+$ calcd. for $C_{16}H_{17}BrNO_4$, 366.0341; found 366.0337.

N-[2-(Benzyloxy)-6-bromo-3-methoxybenzyl]-3,4-dimethoxyaniline (**4i**). The secondary amine **4i** was prepared in a similar manner as amine **4e** using bromobenzaldehyde **2c** (1.0 g; 3.11 mmol), aniline **1a** (491 mg; 3.21 mmol) and $NaBH(OAc)_3$ (1.98 g; 9.4 mmol) in anhydrous toluene (50 mL). The residue was crystallized from MeOH to provide compound **4i** (1.16 g; 81%) as a light pink microcrystalline solid. Mp.= 79–81 °C; TLC R_f = 0.3 (hexane/EtOAc 10:3 *v/v*); ^{1}H-NMR (400 MHz, DMSO-d_6) δ = 7.43–7.29 (m, 6H), 7.03 (d, *J* = 8.8 Hz, 1H), 6.69 (d, *J* = 8.8 Hz, 1H), 6.39 (d, *J* = 8.6 Hz, 1H), 6.15 (dd, *J* = 8.6, 2.6 Hz, 1H), 5.10 (t, *J* = 5.6 Hz, 1H), 4.99 (s, 2H), 4.17 (d, *J* = 5.4 Hz, 2H), 3.86 (s, 3H), 3.61 (s, 6H); ^{13}C-NMR (101 MHz, DMSO-d_6) δ = 152.2, 149.8, 147.1, 143.7, 140.3, 137.1, 132.4, 128.4, 128.3, 128.1, 127.9, 115.0, 114.4, 113.6, 103.0, 98.7, 75.1, 56.6, 56.0, 55.1, 42.9; HRMS (HESI *m/z*): $[M + H]^+$ calcd. for $C_{23}H_{25}BrNO_4$, 458.0967; found 458.0961.

N-[2-(Benzyloxy)-6-bromo-3-methoxybenzyl]-2,3-dimethoxyaniline (**4j**). The secondary amine **4j** was prepared in a similar manner as the amine **4e** using bromobenzaldehyde **2c** (900 mg; 2.80 mmol), aniline **1b** (442 mg; 2.89 mmol) and $NaBH(OAc)_3$ (1.78 g; 8.4 mmol) in anhydrous toluene (45 mL). The residue was crystallized from EtOH to provide compound **4j** (758 mg; 75%) as a pale yellow microcrystalline solid. Mp. = 86–87 °C; TLC R_f = 0.5 (hexane/EtOAc 10/3 *v/v*); ^{1}H-NMR (400 MHz, DMSO-d_6) δ = 7.46–7.30 (m, 6H), 7.02 (d, *J* = 8.8 Hz, 1H), 6.81 (t, *J* = 8.2 Hz, 1H), 6.46 (d, *J* = 8.0 Hz, 1H), 6.32 (d, *J* = 8.3 Hz, 1H), 5.01 (s, 2H), 4.85 (t, *J* = 6.2 Hz, 1H), 4.27 (d, *J* = 4.9 Hz, 2H), 3.85 (s, 3H), 3.71 (s, 3H), 3.55 (s, 3H); ^{13}C-NMR (101 MHz, DMSO-d_6) δ = 152.2, 152.1, 147.0, 141.5, 137.1, 135.1, 132.2, 128.3, 128.2, 128.1, 128.0, 124.1, 114.4, 113.7, 104.6, 101.6, 74.9, 59.4, 56.0, 55.5, 42.4; HRMS (HESI *m/z*): $[M + H]^+$ calcd. for $C_{23}H_{25}BrNO_4$, 458.0967; found 458.0961.

N-[2-(Benzyloxy)-6-bromo-3-methoxybenzyl]-1,3-benzodioxole-5-amine (**4k**). The secondary amine **4k** was prepared in a similar manner as the amine **4e** using bromobenzaldehyde **2c** (600 mg; 1.87 mmol), aniline **1c** (263 mg; 1.93 mmol) and $NaBH(OAc)_3$ (1.19 g; 5.6 mmol) in anhydrous toluene (33 mL). The residue was crystallized from MeOH/acetone/water mixture to provide compound **4k** (791 mg;

96%) as a pale brown microcrystalline solid. Mp. = 77–80 °C; TLC R_f = 0.5 (hexane/EtOAc 10:3 *v*/*v*); ^{1}H-NMR (400 MHz, DMSO-d_6) δ = 7.41–7.27 (m, 6H), 7.04 (d, *J* = 9.1 Hz, 1H), 6.64 (d, *J* = 8.3 Hz, 1H), 6.38 (d, *J* = 2.3 Hz, 1H), 6.08 (dd, *J* = 8.3, 2.3 Hz, 1H), 5.82 (s, 2H), 5.23 (t, *J* = 5.2 Hz, 1H), 4.98 (s, 2H), 4.12 (d, *J* = 5.4 Hz, 2H), 3.86 (s, 3H); ^{13}C-NMR (101 MHz, DMSO-d_6) δ = 152.2, 147.7, 147.2, 144.6, 138.1, 137.1, 132.2, 128.3, 128.3, 128.1, 127.9, 115.1, 113.7, 108.4, 103.2, 99.9, 95.3, 75.0, 56.1, 43.2; HRMS (HESI *m*/*z*): [M + H]$^+$ calcd. for $C_{22}H_{21}BrNO_4$, 442.0654; found 442.0648.

N-[2-(Benzyloxy)-6-bromo-3-methoxybenzyl]-1,3-benzodioxole-4-amine (**4l**). The secondary amine **4l** was prepared in a similar manner as the amine **4e** using bromobenzaldehyde **2c** (1.0 g; 3.11 mmol), aniline **1d** (439 mg; 3.20 mmol) and $NaBH(OAc)_3$ (1.98 g; 9.3 mmol) in anhydrous toluene (45 mL). The residue was crystallized from EtOH to provide compound **4l** (1.24 g; 90%) as a white microcrystalline solid. Mp. = 94–96 °C; TLC R_f = 0.4 (toluene); ^{1}H-NMR (400 MHz, DMSO-d_6) δ = 7.41–7.31 (m, 6H), 7.03 (d, *J* = 9.6 Hz, 1H), 6.62 (t, *J* = 8.3 Hz, 1H), 6.41 (d, *J* = 7.6 Hz, 1H), 6.26 (d, *J* = 7.6 Hz, 1H), 5.86 (s, 2H), 5.01 (s, 2H), 4.75 (t, *J* = 6.0 Hz, 1H), 4.33 (d, *J* = 6.0 Hz, 2H), 3.85 (s, 3H); ^{13}C-NMR (101 MHz, DMSO-d_6) δ = 152.2, 147.1, 147.0, 137.1, 133.2, 132.7, 132.1, 128.3 (2×), 128.1, 127.9, 122.1, 114.7, 113.8, 107.3, 100.0, 98.4, 74.9, 56.1, 42.7; HRMS (HESI *m*/*z*): [M + H]$^+$ calcd. for $C_{22}H_{21}BrNO_4$, 442.0654; found 442.0652.

2,3,8-Trimethoxyphenanthridin-7-ol (**5a**). To a suspension of benzylated phenanthridine **5i** (52 mg; 0.14 mmol) in MeOH (8 mL) was added 10% Pd/C (5 mg) and the mixture was vigorously stirred under atmospheric pressure of hydrogen for 4 h. It was then filtered and concentrated under reduced pressure to afford compound **5a** (28 mg; 71%) as an orange microcrystalline solid. Mp. = 212–215 °C; TLC R_f = 0.2 ($CHCl_3$/MeOH 40/2 *v*/*v*); ^{1}H-NMR (400 MHz, DMSO-d_6) δ = 9.88 (br. s., 1H), 9.40 (s, 1H), 8.18 (d, *J* = 9.1 Hz, 1H), 7.98 (s, 1H), 7.64 (d, *J* = 8.8 Hz, 1H), 7.47 (s, 1H), 4.00 (s, 3H), 3.95 (s, 3H), 3.93 (s, 3H); ^{13}C-NMR (101 MHz, DMSO-d_6) δ = 149.9, 149.3, 145.5, 143.7, 142.7, 138.7, 126.4, 118.0, 117.7, 116.4, 112.8, 109.7, 102.7, 56.9, 55.9, 55.5; HRMS (HESI *m*/*z*): [M + H]$^+$ calcd. for $C_{16}H_{16}NO_4$ 286.1079; found 286.1074.

3,4,8-Trimethoxyphenanthridin-7-ol (**5b**). Compound **5b** was prepared in a similar manner as the base **5a** using benzylated phenanthridine **5j** (20 mg; 0.09 mmol), 10% Pd/C (2 mg) and MeOH (4 mL). After stirring for 4 h under atmospheric pressure of hydrogen, the reaction mixture was filtered. The filtrate contained both fully aromatized debenzylated product **5b** and partially reduced debenzylated form **12b** as a side product. Therefore, the mixture was vigorously stirred in air until only fully aromatized product was present (ca. 2 h). The solution was allowed to stand overnight at −20 °C and the resulting precipitate was filtered off to afford **5b** (10 mg; 66%) as an orange crystalline solid. Mp.= 199–202 °C; TLC R_f = 0.2 ($CHCl_3$/MeOH 40/2 *v*/*v*); ^{1}H-NMR (400 MHz, DMSO-d_6) δ = 9.88 (s, 1H), 9.51 (d, *J* = 0.5 Hz, 1H), 8.35 (d, *J* = 9.3 Hz, 1H), 8.11 (d, *J* = 9.1 Hz, 1H), 7.63 (d, *J* = 9.1 Hz, 1H), 7.48 (d, *J* = 9.3 Hz, 1H), 3.96 (s, 3H), 3.95 (s, 6H); ^{13}C-NMR (101 MHz, DMSO-d_6) δ = 151.0, 147.9, 144.2, 144.0, 143.1, 138.0, 126.6, 118.6, 118.2, 117.7, 115.8, 114.3, 112.5, 61.2, 56.7, 56.4; HRMS (HESI *m*/*z*): [M + H]$^+$ calcd. for $C_{16}H_{16}NO_4$ 286.1079; found 286.1074.

3-Methoxy-[1,3]*dioxolo[4,5-b]phenanthridin-4-ol* (**5c**). Compound **5k** (100 mg; 0.28 mmol) was added to ethanol (4 mL) containing aqueous 35% HCl (3 mL). This reaction mixture was heated in a sealed vial at 100 °C for 2.5 h. After removal of volatiles, the residue was diluted with water (5 mL) and alkalized with aqueous NH_3 solution to pH = 8–9. The precipitated solid was filtered off, washed with water and dried to provide compound **5c** (57 mg; 76%) as an orange crystalline solid. A sample for analysis was prepared by crystallization from larger amount of THF. Mp. = 260–270 °C (decomp.); R_f = 0.2 ($CHCl_3$/MeOH 40/2 *v*/*v*); ^{1}H-NMR (400 MHz, DMSO-d_6) δ = 9.85 (s, 1H), 9.39 (s, 1H), 8.14 (s, 1H), 8.11 (d, *J* = 8.7 Hz, 1H), 7.63 (d, *J* = 9.0 Hz, 1H), 7.43 (s, 1H), 6.21 (s, 2H), 3.96 (s, 3H); ^{13}C-NMR (101 MHz, DMSO-d_6) δ = 148.2, 147.84, 145.6, 143.8, 142.5, 140.04, 126.9, 119.5, 118.2, 116.56, 113.0, 106.9, 101.8, 100.0, 56.8; HRMS (HESI *m*/*z*): [M + H]$^+$ calcd. for $C_{15}H_{12}NO_4$, 270.0766; found 270.0760.

7-Methoxy-[1,3]*dioxolo[4,5-c]phenanthridin-6-ol* (**5d**). To a stirred solution of the secondary amine **4d** (300 mg; 0.85 mmol) and Bu_3SnH (460 μL; 1.70 mmol) in anhydrous toluene (15 mL) at 70 °C was added AIBN (210 mg, 1.28 mmol) and temperature was raised and maintained at 104–108 °C for a period of 3 h. Due to no further conversion of starting material (**4d**), another portion of Bu_3SnH (160 μL; 0.60 mmol) and AIBN (50 mg, 0.30 mmol) were added to the reaction mixture and heating continued for a further 3 h. The reaction mixture was then cooled to room temperature, activated MnO_2 [44] (222 mg, 2.56 mmol) was added and stirring continued overnight. The suspension was filtered and the filtrate concentrated under reduced pressure. Addition of cyclohexane (30 mL) to the residue resulted in the exclusion of a red precipitate, which was filtered off and further purified by silica gel gradient column chromatography (hexane/EtOAc 5/1–5/3 *v*/*v*) to afford compound **5d** (30 mg; 13%) as an orange microcrystalline solid. Mp. = 246–248 °C; R_f = 0.2 ($CHCl_3$/MeOH 40/2 *v*/*v*); ^{1}H-NMR (400 MHz, DMSO-d_6) δ = 9.99 (s, 1H), 9.44 (s, 1H), 8.16 (d, *J* = 8.8 Hz, 1H), 8.08 (d, *J* = 8.8 Hz, 1H), 7.63 (d, *J* = 8.8 Hz, 1H), 7.35 (d, *J* = 8.8 Hz, 1H), 6.25 (s, 2H), 3.95 (s, 3H); ^{13}C-NMR (101 MHz, DMSO-d_6) δ = 148.6, 146.1, 144.5, 143.3, 142.3, 129.3, 126.5, 119.5, 118.4, 115.8, 115.7, 112.7, 109.4, 102.0, 56.7; HRMS (HESI *m*/*z*): $[M + H]^+$ calcd. for $C_{15}H_{12}NO_4$, 270.0766; found 270.0761.

2,3,7,8-Tetramethoxyphenanthridin (**5e**). To a stirred solution of the secondary amine **4e** (600 mg, 1.57 mmol) and Bu_3SnH (845 μL; 3.14 mmol) in anhydrous toluene (30 mL) at 70 °C was added AIBN (387 mg, 2.36 mmol) and temperature of the reaction mixture was raised and maintained at 104–108 °C for a period of 3 h. The reaction was carried out under an inert atmosphere of argon. After 3 h the reaction mixture was slowly cooled to room temperature and activated MnO_2 (409 mg; 4.71 mmol) was added. The resulting mixture was stirred overnight, then filtered and concentrated under reduced pressure. Addition of cyclohexane (8 mL) to the residue resulted in the exclusion of a brown precipitate. The suspension was left to stand overnight at 5 °C, and the next day it was filtered, washed with cyclohexane (2 mL) and recrystallized from $CHCl_3$/hexane. Compound **5e** (185 mg, 39%) was obtained as a beige crystalline solid. Mp. = 154–158 °C ($CHCl_3$/hexane); R_f = 0.2 ($CHCl_3$/MeOH 40/1 *v*/*v*); ^{1}H-NMR (400 MHz, DMSO-d_6) δ = 9.35 (s, 1H), 8.51 (d, *J* = 8.8 Hz, 1H), 8.03 (s, 1H), 7.74 (d, *J* = 9.1 Hz, 1H), 7.51 (s, 1H), 4.02 (s, 3H), 4.00 (s, 6H), 3.93 (s, 3H); ^{13}C-NMR (101 MHz, DMSO-d_6) δ = 150.1, 149.6, 148.9, 145.0, 144.1, 139.0, 126.4, 120.2, 118.9, 118.5, 117.6, 109.8, 102.6, 61.4, 56.6, 56.0, 55.6; HRMS (HESI *m*/*z*): $[M + H]^+$ calcd. for $C_{17}H_{18}NO_4$, 300.1236; found 300.1230.

3,4,7,8-Tetramethoxyphenanthridine (**5f**). Phenanthridine **5f** was prepared in a similar manner as the compound **5e** using amine **4f** (467 mg; 1.22 mmol), Bu_3SnH (660 μL; 2.44 mmol), AIBN (301 mg, 1.83 mmol) and MnO_2 (318 mg; 3.66 mmol) in anhydrous toluene (23 mL). The recrystallization from $CHCl_3$/hexane afforded compound **5f** (150 mg; 41%) as a beige crystalline solid. Mp. = 142–144 °C; TLC R_f = 0.2 ($CHCl_3$/MeOH 40/1 *v*/*v*); ^{1}H-NMR (400 MHz, DMSO-d_6) δ = 9.47 (s, 1H), 8.46 (d, *J* = 9.1 Hz, 1H), 8.42 (d, *J* = 9.1 Hz, 1H), 7.75 (d, *J* = 9.1 Hz, 1H), 7.52 (d, *J* = 9.1 Hz, 1H), 4.01 (s, 3H), 3.99 (s, 3H), 3.96 (s, 6H); ^{13}C-NMR (101 MHz, DMSO-d_6) δ = 151.2, 149.3, 147.5, 144.5, 144.0, 138.0, 126.7, 119.7, 119.3, 118.4, 118.2, 117.8, 114.6, 61.5, 61.3, 56.5, 56.4; HRMS (HESI *m*/*z*): $[M + H]^+$ calcd. for $C_{17}H_{18}NO_4$, 300.1236; found 300.1230.

3,4-Dimethoxy-[1,3]*dioxolo[4,5-b]phenanthridine* (**5g**). Phenanthridine **5g** was prepared in a similar manner as compound **5e** using secondary amine **4g** (265 mg; 0.72 mmol), Bu_3SnH (390 μL; 1.45 mmol), AIBN (178 mg, 1.09 mmol), MnO_2 (189 mg; 2.17 mmol) in anhydrous toluene (13 mL). Compound **5g** (55 mg, 27%) was obtained as a beige microcrystalline solid. Mp. = 172–174 °C; TLC R_f = 0.2 ($CHCl_3$/MeOH 40/1 *v*/*v*); ^{1}H-NMR (400 MHz, DMSO-d_6) δ = 9.33 (d, *J* = 0.5 Hz, 1H), 8.44 (d, *J* = 9.0 Hz, 1H), 8.20 (s, 1H), 7.73 (d, *J* = 9.3 Hz, 1H), 7.46 (s, 1H), 6.23 (s, 2H), 3.99 (s, 3H), 3.98 (s, 3H); ^{13}C-NMR (101 MHz, DMSO-d_6) δ = 149.0, 148.4, 148.1, 145.2, 143.9, 140.2, 126.9, 119.5, 119.5, 119.1, 118.7, 107.0, 102.0, 100.0, 61.4, 56.6; HRMS (HESI *m*/*z*): $[M + H]^+$ calcd. for $C_{16}H_{14}NO_4$, 284.0923; found 284.0917.

6,7-Dimethoxy-[1,3]*dioxolo[4,5-c]phenanthridine* (**5h**). Phenanthridine **5h** was prepared in a similar manner as the product **5e** using amine **4h** (478 mg; 1.31 mmol), Bu_3SnH (700 μL; 2.61 mmol), AIBN (322 mg; 1.96 mmol) and MnO_2 (340 mg; 3.92 mmol) in anhydrous toluene (23 mL). The recrystallization from $CHCl_3$/hexane afforded compound **5h** (135 mg; 37%) as a brown crystalline solid. Mp. = 163–166 °C; TLC R_f = 0.2 ($CHCl_3$/MeOH 40/1 *v*/*v*); ^{1}H-NMR (400 MHz, DMSO-d_6) δ = 9.40 (s, 1H), 8.42 (d, *J* = 9.1 Hz, 1H), 8.23 (d, *J* = 8.8 Hz, 1H), 7.75 (d, *J* = 9.0 Hz, 1H), 7.39 (d, *J* = 8.6 Hz, 1H), 6.27 (s, 2H), 4.00 (s, 3H), 3.99 (s, 3H); ^{13}C-NMR (101 MHz, DMSO-d_6) δ = 149.5, 148.1, 146.2, 144.7, 142.3, 129.1, 126.4, 122.3, 119.8, 119.5, 118.3, 115.7, 109.7, 102.1, 61.5, 56.5; HRMS (HESI *m*/*z*): $[M + H]^+$ calcd. for $C_{16}H_{14}NO_4$, 284.0923; found 284.0917.

7-(Benzyloxy)-2,3,8-trimethoxyphenanthridine (**5i**). Phenanthridine **5i** was prepared in a similar manner as phenanthridine **5e** using secondary amine **4i** (1.27 g, 2.78 mmol), Bu_3SnH (1.5 mL; 5.55 mmol), AIBN (684 mg; 4.16 mmol) and MnO_2 (724 mg, 8.33 mmol) in anhydrous toluene (50 mL). The recrystallization from $CHCl_3$/hexane afforded compound **5i** (240 mg; 23%) as a beige crystalline solid. Mp. = 155–156 °C; TLC R_f = 0.2 ($CHCl_3$/MeOH 40/1 *v*/*v*); ^{1}H-NMR (400 MHz, DMSO-d_6) δ = 9.25 (s, 1H), 8.51 (d, *J* = 9.1 Hz, 1H), 8.01 (s, 1H), 7.76 (d, *J* = 9.1 Hz, 1H), 7.53–7.49 (m, 2H), 7.46 (s, 1H), 7.41–7.30 (m, 3H), 5.25 (s, 2H), 4.04 (s, 3H), 4.01 (s, 3H), 3.92 (s, 3H); ^{13}C-NMR (101 MHz, DMSO-d_6) δ = 150.0, 149.5, 149.0, 145.2, 142.6, 138.9, 137.1, 128.6, 128.4, 128.2, 126.3, 120.5, 118.7, 118.5, 117.5, 109.8, 102.6, 75.0, 56.7, 56.0, 55.5; HRMS (HESI *m*/*z*): $[M + H]^+$ calcd. for $C_{23}H_{22}NO_4$, 376.1549; found 376.1543.

7-(Benzyloxy)-3,4,8-trimethoxyphenanthridine (**5j**). Phenanthridine **5j** was prepared in a similar manner as phenanthridine **5e** using secondary amine **4j** (950 mg, 2.07 mmol), Bu_3SnH (1115 μL; 4.15 mmol), AIBN (511 mg, 3.11 mmol) and MnO_2 (541 mg, 6.22 mmol) in anhydrous toluene (37 mL). The recrystallization from $CHCl_3$/hexane afforded compound **5j** (233 mg; 30%) as a slightly gray microcrystalline solid. Mp. = 153–155 °C; TLC R_f = 0.3 ($CHCl_3$/MeOH 40/1 *v*/*v*); ^{1}H-NMR (400 MHz, DMSO-d_6) δ = 9.38 (s, 1H), 8.45 (d, *J* = 8.8 Hz, 1H), 8.40 (d, *J* = 9.1 Hz, 1H), 7.77 (d, *J* = 9.1 Hz, 1H), 7.55–7.48 (m, 3H), 7.42–7.30 (m, 3H), 5.26 (s, 2H), 4.04 (s, 3H), 3.96 (s, 3H), 3.93 (s, 3H); ^{13}C-NMR (101 MHz, DMSO-d_6) δ = 151.2, 149.4, 147.6, 143.9, 143.0, 137.9, 137.0, 128.7, 128.4, 128.2, 126.6, 120.1, 119.1, 118.3, 118.2, 117.8, 114.5, 75.1, 61.3, 56.6, 56.4; HRMS (HESI *m*/*z*): $[M + H]^+$ calcd. for $C_{23}H_{22}NO_4$, 376.1549; found 376.1543.

4-(Benzyloxy)-3-methoxy-[1,3]*dioxolo[4,5-b]phenanthridine* (**5k**). Phenanthridine **5k** was prepared in a similar manner as phenanthridine **5e** using secondary amine **4k** (730 mg; 1.65 mmol), Bu_3SnH (890 μL; 3.30 mmol), AIBN (407 mg, 2.48 mmol) and MnO_2 (430 mg; 4.95 mmol) in anhydrous toluene (29 mL). The recrystallization from $CHCl_3$/hexane afforded compound **5k** (280 mg; 47%) as a brown crystalline solid. Mp.= 129–131 °C; TLC R_f = 0.3 ($CHCl_3$/MeOH 40/1 *v*/*v*); ^{1}H-NMR (400 MHz, DMSO-d_6) δ = 9.25 (s, 1H), 8.43 (d, *J* = 9.1 Hz, 1H), 8.18 (s, 1H), 7.76 (d, *J* = 9.1 Hz, 1H), 7.53–7.49 (m, 2H), 7.43–7.31 (m, 4H), 6.21 (s, 2H), 5.24 (s, 2H), 4.03 (s, 3H); ^{13}C-NMR (101 MHz, DMSO-d_6) δ = 149.1, 148.4, 148.0, 145.4, 142.4, 140.0, 137.0, 128.6, 128.4, 128.2, 126.7, 120.6, 119.3, 118.9, 118.6, 106.9, 101.9, 99.9, 75.0, 56.6; HRMS (HESI *m*/*z*): $[M + H]^+$ calcd. for $C_{22}H_{18}NO_4$, 360.1236; found 360.1230.

6-(Benzyloxy)-7-methoxy-[1,3]*dioxolo[4,5-c]phenanthridine* (**5l**). Phenanthridine **5l** was prepared in a similar manner as phenanthridine **5e** using secondary amine **4l** (1.1 g; 2.48 mmol), Bu_3SnH (1.34 mL; 4.95 mmol), AIBN (610 mg, 3.72 mmol) and MnO_2 (645 mg; 7.42 mmol) in anhydrous toluene (40 mL). The recrystallization from $CHCl_3$/hexane afforded compound **5l** (555 mg; 62%) as a beige crystalline solid. Mp.= 163–164 °C; TLC R_f = 0.3 ($CHCl_3$/MeOH 40/1 *v*/*v*); ^{1}H-NMR (400 MHz, DMSO-d_6) δ = 9.27 (s, 1H), 8.42 (d, *J* = 9.1 Hz, 1H), 8.21 (d, *J* = 8.7 Hz, 1H), 7.78 (d, *J* = 9.1 Hz, 1H), 7.50 (d, *J* = 6.9 Hz, 2H), 7.41 – 7.30 (m, 4H), 6.25 (s, 2H), 5.26 (s, 2H), 4.04 (s, 3H); ^{13}C-NMR (101 MHz, DMSO-d_6) δ = 149.62, 148.32, 146.25, 143.13, 142.34, 136.87, 129.06, 128.77, 128.40, 128.28, 126.38, 120.24, 119.31, 119.10, 118.41, 115.68, 109.71, 102.07, 75.07, 56.56; HRMS (HESI *m*/*z*): $[M + H]^+$ calcd. for $C_{22}H_{18}NO_4$, 360.1236; found 360.1230.

3.1.3. General Procedure for the Preparation of Phenanthridine Hydrochlorides **6a–6l**

The above prepared phenanthridine derivatives **5** (ca. 20 mg) were dissolved in dioxane (2–3 mL). To the resulting solution a 4 M HCl in dioxane solution (1.5 mL) was added resulting in formation of a yellow-orange precipitate. To the suspension was added ether (4 mL). The precipitate was filtered off, washed with ether (2 mL) and dried under vacuum over KOH. The yields of hydrochlorides **6** were within 80–95%. All compounds were proved by elemental analysis; the recorded values were within +/−0.4%.

7-Hydroxy-2,3,8-trimethoxyphenanthridin-5-ium chloride (**6a**). Elemental analysis, calcd. for $C_{16}H_{16}ClNO_4$ (321.8), C, 59.73; H, 5.01; N, 4.35; found C, 59.83; H, 5.11; N, 4.08.

7-Hydroxy-3,4,8-trimethoxyphenanthridin-5-ium chloride (**6b**). Elemental analysis, calcd. for $C_{16}H_{16}ClNO_4$ (321.8), C, 59.73; H, 5.01; N, 4.35; found C, 59.74; H, 4.90; N, 4.18.

4-Hydroxy-3-methoxy-[1,3]*dioxolo[4,5-b]phenanthridin-6-ium chloride* (**6c**). Elemental analysis, calcd. for $C_{15}H_{12}ClNO_4$ (305.7), C, 58.93; H, 3.96; N, 4.58; found C, 58.73; H, 3.77; N, 4.88.

6-Hydroxy-7-methoxy-[1,3]*dioxolo[4,5-c]phenanthridin-4-ium chloride* (**6d**). Elemental analysis, calcd. for $C_{15}H_{12}ClNO_4$ (305.7), C, 58.93; H, 3.96; N, 4.58; found C, 58.65; H, 3.98; N, 4.73.

2,3,7,8-Tetramethoxyphenanthridin-5-ium chloride (**6e**). Elemental analysis, calcd. for $C_{17}H_{18}ClNO_4$ (335.8), C, 60.81; H, 5.40; N, 4.17; found C, 61.15; H, 5.63; N, 4.26.

3,4,7,8-Tetramethoxyphenanthridin-5-ium chloride (**6f**). Elemental analysis, calcd. for $C_{17}H_{18}ClNO_4$ (335.8), C, 60.81; H, 5.40; N, 4.17; found C, 61.01; H, 5.31; N, 4.02.

3,4-Dimethoxy-[1,3]*dioxolo[4,5-b]phenanthridin-6-ium chloride* (**6g**). Elemental analysis, calcd. for $C_{16}H_{14}ClNO_4$ (319.7), C, 60.10; H, 4.41; N, 4.38; found C, 60.01; H, 4.71; N, 4.22.

6,7-Dimethoxy-[1,3]*dioxolo[4,5-c]phenanthridin-4-ium chloride* (**6h**). Elemental analysis, calcd. for $C_{16}H_{14}ClNO_4$ (319.7), C, 60.10; H, 4.41; N, 4.38; found C, 60.24; H, 4.69; N, 4.48.

7-(Benzyloxy)-2,3,8-trimethoxyphenanthridin-5-ium chloride (**6i**). Elemental analysis, calcd. for $C_{23}H_{22}ClNO_4$ (411.9), C, 67.07; H, 5.38; N, 3.40; found C, 67.17; H, 5.31; N, 3.46.

7-(Benzyloxy)-3,4,8-trimethoxyphenanthridin-5-ium chloride (**6j**). Elemental analysis, calcd. for $C_{23}H_{22}ClNO_4$ (411.9), C, 67.07; H, 5.38; N, 3.40; found C, 67.22; H, 5.46; N, 3.20.

4-(Benzyloxy)-3-methoxy-[1,3]*dioxolo[4,5-b]phenanthridin-6-ium chloride* (**6k**). Elemental analysis, calcd. for $C_{22}H_{18}ClNO_4$ (395.8), C, 66.75; H, 4.58; N, 3.54; found C, 66.66; H, 4.75; N, 3.44.

6-(Benzyloxy)-7-methoxy-[1,3]*dioxolo[4,5-c]phenanthridin-4-ium chloride* (**6l**). Elemental analysis, calcd. for $C_{22}H_{18}ClNO_4$ (395.8), C, 66.75; H, 4.58; N, 3.54; found C, 66.58; H, 4.80; N, 3.32.

4-Hydroxy-3-methoxy-6-methyl-[1,3]*dioxolo[4,5-b]phenanthridin-6-ium iodide* (**7c**). The free base **5c** (20 mg; 0.08 mmol) was dissolved in ACN (10 mL) and MeI (19 μL; 0.3 mmol) was added. The reaction mixture was allowed to stand at r.t. in the dark place without stirring. After 7 days, the precipitated crystalline solid was filtered and washed with cold ACN (1 mL) to obtain poorly soluble substance **7c** (18 mg; 61%) as a dark orange crystalline solid. Mp. = 250–255 °C; ^{1}H-NMR (400 MHz, DMSO-d_6) δ = 11.35 (br. s, 1H), 9.95 (s, 1H), 8.50 (s, 1H), 8.35 (d, *J* = 9.0 Hz, 1H), 8.05 (d, *J* = 9.1 Hz, 1H), 7.97 (s, 1H), 6.41 (s, 2H), 4.56 (s, 3H), 4.05 (s, 3H); ^{13}C-NMR (101 MHz, DMSO-d_6) δ = 150.7, 150.1, 147.42, 145.7, 145.2,

130.22, 127.6, 124.0, 122.7, 114.6, 113.5, 103.71, 101.4, 98.6, 57.0, 46.1; HRMS (HESI *m/z*): $[M - I]^+$ calcd. for $C_{16}H_{14}NO_4$, 284.0923; found 284.0917; elemental analysis, calcd. for $C_{16}H_{14}INO_4$ (411.2), C, 46.74; H, 3.43; N, 3.41; found C, 46.70; H, 3.66; N, 3.35.

6-Hydroxy-7-methoxy-4-methyl-[1,3]*dioxolo[4,5-c]phenanthridin-4-ium iodide* (**7d**). The quaternary salt **7d** was prepared in a similar manner as compound **7c** using base **5d** (10 mg; 0.04 mmol), MeI (9 μL; 0.15 mmol) and ACN (3 mL). Compound **7d** (9 mg; 61%) was obtained as a dark orange crystalline solid. Mp. = 236–239 °C; ^{1}H-NMR (400 MHz, DMSO-d_6) δ = 11.52 (br. s, 1H), 9.90 (s, 1H), 8.49 (d, *J* = 8.6 Hz, 1H), 8.26 (d, *J* = 8.8 Hz, 1H), 8.00 (d, *J* = 8.8 Hz, 1H), 7.69 (dd, *J* = 1.0, 8.8 Hz, 1H), 6.38 (s, 2H), 4.65 (s, 3H), 4.04 (s, 3H); ^{13}C-NMR (101 MHz, DMSO-d_6) δ = 152.0, 148.8, 147.4, 145.7, 138.1, 126.9, 124.2, 120.9, 120.0, 118.4, 113.7, 113.0, 112.4, 103.1, 56.8, 48.2; HRMS (HESI *m/z*): $[M - I]^+$ calcd. for $C_{16}H_{14}NO_4$, 284.0923; found 284.0917; elemental analysis, calcd. for $C_{16}H_{14}INO_4$ (411.2), C, 46.74; H, 3.43; N, 3.41; found C, 46.88; H, 3.54; N, 3.32.

2,3,7,8-Tetramethoxy-5-methylphenanthridinium iodide (**7e**). The quaternary salt **7e** was prepared in a similar manner as compound **7d** using base **5e** (280 mg, 0.94 mmol), MeI (230 μL; 3.74 mmol) and ACN (14 mL). Compound **7e** (372 mg; 90%) was obtained as a dark orange needle-like crystalline solid. Mp. = 263–266 °C; ^{1}H-NMR (400 MHz, DMSO-d_6) δ = 9.96 (s, 1H), 8.84 (d, *J* = 9.3 Hz, 1H), 8.33 (s, 1H), 8.20 (d, *J* = 9.3 Hz, 1H), 7.73 (s, 1H), 4.70 (s, 3H), 4.13 (s, 6H), 4.10 (s, 6H); ^{13}C-NMR (101 MHz, DMSO-d_6) δ = 152.0, 151.5, 149.9, 146.9, 145.6, 129.1, 127.7, 125.3, 120.8, 119.2, 118.7, 103.9, 100.7, 62.1, 57.0, 56.8, 56.6, 46.0; HRMS (HESI *m/z*): $[M - I]^+$ calcd. for $C_{18}H_{20}NO_4$, 314.1392; found 314.1387; elemental analysis, calcd. for $C_{18}H_{20}INO_4$ (441.3), C, 48.99; H, 4.57 N, 3.17; found C, 48.92; H, 4.15; N, 3.12.

3,4,7,8-Tetramethoxy-5-methylphenanthridinium iodide (**7f**). The quaternary salt **7f** was prepared in a similar manner as compound **7d** using base **5f** (60 mg, 0.20 mmol), MeI (50 μL, 0.80 mmol) and ACN (5 mL). Compound **7f** (42 mg; 47%) was obtained as an orange crystalline solid. Mp. = 186–188 °C; ^{1}H-NMR (400 MHz, DMSO-d_6) δ = 9.95 (s, 1H), 8.81 (d, *J* = 9.3 Hz, 1H), 8.70 (d, *J* = 9.3 Hz, 1H), 8.19 (d, *J* = 9.3 Hz, 1H), 7.89 (d, *J* = 9.3 Hz, 1H), 4.81 (s, 3H), 4.13 (s, 3H), 4.09 (s, 3H), 4.08 (s, 3H), 3.99 (s, 3H); ^{13}C-NMR (101 MHz, DMSO-d_6) δ = 154.4, 153.6, 150.0, 146.4, 140.1, 128.3, 128.1, 126.2, 120.5, 120.2, 118.5, 118.0, 116.9, 62.2, 61.8, 56.9, 51.1, 39.5; HRMS (HESI *m/z*): $[M - I]^+$ calcd. for $C_{18}H_{20}NO_4$, 314.1392; found 314.1387.

3,4-Dimethoxy-6-methyl-[1,3]*dioxolo[4,5-b]phenanthridin-6-ium iodide* (**7g**). The quaternary salt **7g** was prepared in a similar manner as substance **7d** using base **5g** (30 mg, 0.11 mmol), MeI (25 μL; 0.42 mmol) and ACN (6 mL). Compound **7g** (40 mg; 89%) was obtained as a bright yellow crystalline solid. Mp. > 300 °C; ^{1}H-NMR (400 MHz, DMSO-d_6) δ = 9.96 (s, 1H), 8.71 (d, *J* = 9.3 Hz, 1H), 8.58 (s, 1H), 8.19 (d, *J* = 9.3 Hz, 1H), 8.04 (s, 1H), 6.44 (s, 2H), 4.62 (s, 3H), 4.11 (s, 3H), 4.08 (s, 3H); ^{13}C-NMR (101 MHz, DMSO-d_6) δ = 151.1, 150.4, 150.0, 147.2, 145.5, 130.6, 128.1, 125.5, 122.8, 119.1, 118.7, 103.9, 101.2, 98.5, 62.1, 57.0, 46.4; HRMS (HESI *m/z*): $[M - I]^+$ calcd. for $C_{17}H_{16}NO_4$, 298.1079; found 298.1074.

6,7-Dimethoxy-4-methyl-[1,3]*dioxolo[4,5-c]phenanthridin-4-ium iodide* (**7h**). The quaternary salt **7h** was prepared in a similar manner as the substance **7d** using free base **5h** (90 mg; 0.32 mmol), MeI (80 μL; 1.27 mmol) and ACN (5 mL). Compound **7h** (26 mg; 19%) was obtained as a blood-red crystalline solid. Mp. = 223–224 °C; ^{1}H-NMR (400 MHz, DMSO-d_6) δ = 9.95 (s, 1H), 8.64 (d, *J* = 9.1 Hz, 1H), 8.59 (d, *J* = 8.8 Hz, 1H), 8.16 (d, *J* = 9.3 Hz, 1H), 7.76 (d, *J* = 8.8 Hz, 1H), 6.42 (s, 2H), 4.71 (s, 3 H), 4.11 (s, 3H), 4.07 (s, 3H); ^{13}C-NMR (101 MHz, DMSO-d_6) δ = 152.1, 150.2, 149.1, 146.7, 138.2, 127.6, 126.0, 120.9, 120.2, 118.7, 118.6, 118.0, 112.8, 103.3, 62.2, 56.9, 48.7; HRMS (HESI *m/z*): $[M - I]^+$ calcd. for $C_{17}H_{16}NO_4$, 298.1079; found 298.1074.

7-(Benzyloxy)-2,3,8-trimethoxy-5-methylphenanthridinium iodide (**7i**). The quaternary salt **7i** was prepared in a similar manner as compound **7d** using free base **5i** (91 mg; 0.24 mmol), MeI (60 μL; 0.97 mmol) and ACN (9 mL). Compound **7i** (77 mg; 61%) was obtained as a bright yellow crystalline solid. Mp. = 207–210 °C; ^{1}H-NMR (400 MHz, DMSO-d_6) δ = 9.79 (s, 1H), 8.83 (d, *J* = 9.3 Hz, 1H), 8.30 (s, 1H), 8.20 (d, *J* = 9.1 Hz, 1H), 7.70 (s, 1H), 7.58 (d, *J* = 7.5 Hz, 2H), 7.43–7.30 (m, 3H), 5.40 (s, 2H), 4.68 (s, 3H), 4.12 (s, 6H), 4.09 (s, 3H); ^{13}C-NMR (101 MHz, DMSO-d_6) δ = 152.0, 151.5, 150.2, 146.7, 143.9, 136.3, 128.9, 128.9, 128.4, 128.3, 127.5, 125.0, 120.7, 119.4, 119.1, 103.9, 100.7, 75.4, 57.0, 56.7, 56.6, 46.2; HRMS (HESI *m*/*z*): $[M - I]^+$ calcd. for $C_{24}H_{24}NO_4$, 390.1705; found 390.1700.

7-(Benzyloxy)-3,4,8-trimethoxy-5-methylphenanthridinium iodide (**7j**). The quaternary salt **7j** was prepared in a similar manner as compound **7d** using free base **5j** (150 mg; 0.40 mmol), MeI (100 μL; 1.6 mmol) and ACN (7 mL). Compound **7j** (123 mg; 60%) was obtained as a light orange microcrystalline solid. Mp. = 169–173 °C; ^{1}H-NMR (400 MHz, DMSO-d_6) δ = 9.79 (s, 1H), 8.80 (d, *J* = 9.3 Hz, 1H), 8.70 (d, *J* = 9.1 Hz, 1H), 8.20 (d, *J* = 9.1 Hz, 1H), 7.89 (d, *J* = 9.3 Hz, 1H), 7.59 (d, *J* = 7.0 Hz, 2 H), 7.48–7.26 (m, 3H), 5.41 (s, 2H), 4.79 (s, 3H), 4.10 (s, 3H), 4.08 (s, 3H), 3.98 (s, 3H); ^{13}C-NMR (101 MHz, DMSO-d_6) δ = 154.4, 153.5, 150.3, 144.6, 140.1, 136.3, 128.9, 128.4, 128.3, 128.2, 127.9, 126.0, 120.4, 120.2, 118.8, 118.5, 117.0, 75.6, 61.8, 57.0, 56.9, 51.3; HRMS (HESI *m*/*z*): $[M - I]^+$ calcd. for $C_{24}H_{24}NO_4$, 390.1705; found 390.1700.

4-(Benzyloxy)-3-methoxy-6-methyl-[1,3]*dioxolo[4,5-b]phenanthridin-6-ium iodide* (**7k**). The quaternary salt **7k** was prepared in a similar manner as compound **7d** using free base **5k** (91 mg, 0.25 mmol), MeI (60 μL, 1.0 mmol) and ACN (8 mL). The reaction was conducted at 50 °C for 36 h. Compound **7k** (77 mg; 61%) was obtained as a pale yellow crystalline solid. Mp. = 198–201 °C; ^{1}H-NMR (400 MHz, DMSO-d_6) δ = 9.81 (s, 1H), 8.69 (d, *J* = 9.1 Hz, 1H), 8.55 (s, 1H), 8.19 (d, *J* = 9.3 Hz, 1H), 8.01 (s, 1H), 7.61–7.56 (m, 2H), 7.42–7.31 (m, 3H), 6.44 (s, 2H), 5.38 (s, 2H), 4.60 (s, 3H), 4.10 (s, 3H); ^{13}C-NMR (101 MHz, DMSO-d_6) δ = 151.1, 150.4, 150.2, 147.0, 143.7, 136.3, 130.5, 128.9, 128.4, 128.3, 128.0, 125.3, 122.8, 119.2, 119.2, 103.9, 101.3, 98.5, 75.4, 56.9, 46.7; HRMS (HESI *m*/*z*): $[M - I]^+$ calcd. for $C_{23}H_{20}NO_4$, 374.1392; found 374.1387.

6-(Benzyloxy)-7-methoxy-4-methyl-[1,3]*dioxolo[4,5-c]phenanthridin-4-ium iodide* (**7l**). The quaternary salt **7l** was prepared in a similar manner as compound **7d** with using free base **5l** (36 mg, 0.1 mmol), MeI (24 μL, 0.4 mmol) and ACN (4 mL). The reaction was conducted at 50 °C for 36 h. Compound **7l** (28 mg; 55%) was obtained as a light orange solid. Mp. = 169–172 °C; ^{1}H-NMR (400 MHz, DMSO-d_6) δ = 9.80 (s, 1H), 8.64 (d, *J* = 9.2 Hz, 1H), 8.58 (d, *J* = 8.7 Hz, 1H), 8.17 (d, *J* = 9.2 Hz, 1H), 7.75 (d, *J* = 8.7 Hz, 1H), 7.64–7.52 (m, 2H), 7.44–7.28 (m, 3H), 6.40 (s, 2H), 5.39 (s, 2H), 4.69 (s, 3H), 4.08 (s, 3H); ^{13}C-NMR (101 MHz, DMSO-d_6) δ = 152.0, 150.2, 149.2, 145.0, 138.2, 136.2, 128.9, 128.5, 128.4, 127.6, 125.8, 120.8, 120.2, 119.0, 118.6, 118.5, 112.9, 103.3, 75.6, 56.9, 48.9; HRMS (HESI *m*/*z*): $[M - I]^+$ calcd. for $C_{23}H_{20}NO_4$, 374.1392; found 374.1387.

3.1.4. Preparation of 2,3,7,8-tetramethoxy-5-methylphenanthridinium Salts **9t**–**9z**

To a suspension of quaternary iodide **7e** (54 mg; 0.11 mmol) in EtOH (18 mL) was added 1.25 N aqueous NaOH (180 μL; 0.22 mmol). After 1 h of stirring the resulting colorless solution was diluted with water (2 mL) and concentrated under reduced pressure to remove EtOH resulting in precipitation of a white crystalline solid (pseudobase **8**), which was not isolated. To the suspension of pseudobase was added 20% aqueous solution of corresponding acid (10 mL) and the mixture was stirred for 10 min, and then cooled to 0 °C. The resulting yellow precipitate was filtered, washed with ice water (2 mL) and dried at 110 °C.

2,3,7,8-Tetramethoxy-5-methylphenanthridinium chloride (**9t**): Yield 35 mg (82%) as a yellow microcrystalline compound. Mp. = 220–222 °C; ^{1}H-NMR (400 MHz, DMSO-d_6) δ = 9.96 (s, 1H),

8.83 (d, *J* = 9.2 Hz, 1H), 8.29 (s, 1H), 8.17 (d, *J* = 9.3 Hz, 1H), 7.72 (s, 1H), 4.71 (s, 3H), 4.12 (s, 3H), 4.11 (s, 3H), 4.10 (s, 3H), 4.09 (s, 3H); ^{13}C-NMR (101 MHz, DMSO-d_6) δ = 152.0, 151.5, 149.9, 146.8, 145.6, 129.1, 127.6, 125.2, 120.8, 119.18, 118.68, 103.9, 100.7, 62.1, 57.1, 56.7, 56.6, 46.0; elemental analysis, calcd. for $C_{18}H_{20}ClNO_4$ (349.8), C, 61.80; H, 5.76; N, 4.00; found C, 61.83; H, 5.69; N, 4.03.

2,3,7,8-Tetramethoxy-5-methylphenanthridinium perchlorate (**9u**): Yield 40 mg (80%) as a light orange microcrystalline compound. Mp. = above 300 °C; ^{1}H-NMR (400 MHz, DMSO-d_6) δ = 9.93 (s, 1H), 8.80 (d, *J* = 9.2 Hz, 1H), 8.28 (s, 1H), 8.17 (d, *J* = 9.3 Hz, 1H), 7.70 (s, 1H), 4.69 (s, 3H), 4.12 (s, 3H), 4.12 (s, 3H), 4.09 (s, 6H); ^{13}C-NMR (101 MHz, DMSO-d_6) δ = 152.0, 151.5, 149.9, 146.8, 145.6, 129.1, 127.6, 125.2, 120.8, 119.18, 118.68, 103.9, 100.7, 62.1, 57.1, 56.7, 56.6, 46.0; elemental analysis, calcd. for $C_{18}H_{20}ClNO_8$ (413.8), C, 52.24; H, 4.87; N, 3.38; found C, 52.12; H, 4.68; N, 3.35.

2,3,7,8-Tetramethoxy-5-methylphenanthridinium hydrogensulfate (**9w**): Yield 38 mg (75%) as a yellow microcrystalline compound. Mp. = 272–280 °C; ^{1}H-NMR (400 MHz, DMSO-d_6) δ = 9.94 (s, 1H), 8.82 (d, *J* = 9.2 Hz, 1H), 8.30 (s, 1H), 8.18 (d, *J* = 9.3 Hz, 1H), 7.72 (s, 1H), 4.70 (s, 3H), 4.12 (s, 3H), 4.12 (s, 3H), 4.10 (s, 3H), 4.09 (s, 3H); ^{13}C-NMR (101 MHz, DMSO-d_6) δ = 152.0, 151.5, 149.9, 146.8, 145.6, 129.1, 127.6, 125.2, 120.8, 119.18, 118.68, 103.9, 100.7, 62.1, 57.1, 56.7, 56.6, 46.0; elemental analysis, calcd. for $C_{18}H_{21}NO_8S$ (411.4), C, 52.55; H, 5.14; N, 3.40; found C, 52.40; H, 5.24; N, 3.43.

2,3,7,8-Tetramethoxy-5-methylphenanthridinium nitrate (**9z**): Yield 37 mg (80%) as a light orange microcrystalline compound. Mp. = 266–269 °C; ^{1}H-NMR (400 MHz, DMSO-d_6) δ = 9.95 (s, 1H), 8.83 (d, *J* = 9.2 Hz, 1H), 8.32 (s, 1H), 8.19 (d, *J* = 9.3 Hz, 1H), 7.72 (s, 1H), 4.70 (s, 3H), 4.12 (s, 6H), 4.10 (s, 6H); ^{13}C-NMR (101 MHz, DMSO-d_6) δ = 152.0, 151.5, 149.9, 146.8, 145.6, 129.1, 127.6, 125.2, 120.8, 119.18, 118.68, 103.9, 100.7, 62.1, 57.1, 56.7, 56.6, 46.0; elemental analysis, calcd. for $C_{18}H_{20}N_2O_7$ (376.1), C, 57.44; H, 5.36; N, 7.44; found C, 57.36; H, 5.45; N, 7.48.

3.2. Antibacterial Activity Testing

3.2.1. Agar Diffusion Test

Overnight cultures of test organisms were grown in LB broth for 18–24 h and standard suspensions of 1.5 × 10^8 CFU/mL were prepared in a sterile saline solution (0.9% NaCl) according to a $BaSO_4$ 0.5 McFarland Standard. The standardized suspension (0.1 mL) was added to 34 mL of sterile, melted and tempered (47–50 °C) Mueller-Hinton No. 2 agar. After gentle mixing, the inoculated melted agar was poured into a sterile Petri dish (145 mm × 20 mm, Greiner Bio-One, Kremsmünster, Austria) and allowed to solidify next to the flame with lids slightly ajar. Wells of 9 mm diameter were cut from the Petri dish agar and filled with 50 μL of the test sample solution. Solutions were made at 20 mM in DMSO and diluted in MeOH to 2 mM. The Petri dish was incubated at 37 °C for 18–24 h and the inhibition zone diameters were measured (mm) with an electronic caliper after 24–48 h.

3.2.2. MIC Determination

Antibacterial activity of the compounds was determined by measuring their minimum inhibitory concentrations (MIC) using the broth microdilution method. Each well of a 96-well microtiter plate was filled with 50 μL of sterile iron deficient MH2 broth. Each test compound was dissolved in DMSO making a 10 mM solution, then diluted with sterile MH2 broth to 800 μM. Exactly 50 μL of the compound solution was added to the first well of the microtiter plate and 2-fold serial dilutions were made down each row of the plate. A pre culture of bacteria was grown in Luria-Bertani broth overnight at 37 °C. This was diluted to McFarland standard 0.5 (1.5 × 10^8 CFU) with saline. 100 μL of the bacterial suspension was further diluted with 14.9 mL of MHII broth. Exactly 50 μL of bacterial (in broth) inoculum (1 × 10^6 CFU/mL) was then added to each well giving a total volume of 100 μL/well and 5 × 10^5 CFU/mL and a compound concentration gradient of 200–0.1 μM. The plate was incubated at

37 °C. After 18 h, each well was examined visually for bacterial growth. The MIC was recorded as the lowest compound concentration required to inhibit bacterial growth as judged by turbidity relative to a row of wells diluted with a the solvent DMSO as a growth control. Ciprofloxacin was included in a control row at a concentration gradient of 5 μg/mL–0.0025 μg/L.

3.3. Anticancer Activity In Vitro

The in vitro anticancer activity was determined using MCF-7 (breast adenocarcinoma) and K-562 (chronic myelogeneous leukemia) cell lines as described earlier [48]. Briefly, cells were treated in triplicate with three different doses of each compound for 72 h. After treatments, Calcein AM solution was added, and fluoresence from live cells was measured at 485 nm/538 nm (excitation/emission) using a Fluoroskan Ascent microplate reader (Thermo Scientific, Waltham, MA, USA). The EC_{50} value, that is, the drug concentration reducing number of live cells to 50%, was calculated from the dose response curves that resulted from the assays. The cells were maintained in DMEM medium supplemented with 10% fetal bovine serum, penicillin (100 U/mL), and streptomycin (100 μg/mL) and cultivated at 37 °C in 5% CO_2.

3.3.1. Cell Cycle Analysis

Cell cycle analysis was performed as described earlier [48]. Briefly, subconfluent cells were treated with different concentrations of test compound for 24 h. The cultures were pulse-labeled with 10 μM 5-bromo-2′-deoxyuridine (BrdU) for 30 min at 37 °C prior to harvesting. The cells were then washed in PBS, fixed with 70% ethanol, and denatured in 2 M HCl. Following neutralization, the cells were stained with anti-BrdU fluorescein-labeled antibodies, washed, stained with propidium iodide, and analyzed by flow cytometry using a 488 nm laser (FACSVerse, Becton Dickinson, Franklin Lakes, NJ, USA).

3.3.2. Immunoblotting

Immunoblotting was performed as described earlier [48]. Briefly, cellular lysates were prepared by harvesting cells in Laemmli sample buffer. Proteins were separated on SDS-polyacrylamide gels and electroblotted onto nitrocellulose membranes. After blocking, the membranes were incubated with specific primary antibodies overnight, washed and then incubated with peroxidase-conjugated secondary antibodies. Finally, peroxidase activity was detected with ECL+ reagents (AP Biotech, Prague, Czech Republic) using a LAS-4000 CCD camera (AP Biotech, Prague, Czech Republic). Specific antibodies against PARP were purchased from Santa Cruz Biotechnology (Dallas, TX, USA) peroxidase-labeled secondary antibodies was from Sigma Aldrich (Prague, Czech Republic, peroxidase-labeled secondary antibodies) or were generously gifted by Dr. B. Vojtěšek (p53, p21WAF1, PCNA).

4. Conclusions

In this work we extended a previously developed method for the preparation of novel phenanthridine derivatives, which were derived from benzo[*c*]phenanthridines by deletion of the A-ring. Derivatives were prepared with substituents on the formed skeleton that mimic biologically active benzo[*c*]phenanthridines. The main principle for the preparation of the aforementioned compounds was based on the radical cyclization of reduced Schiff bases prepared by the condensation of appropriate aromatic aldehydes and amines. The prepared compounds were tested for antibacterial and anticancer cytotoxic effects and compared with several compounds containing a benzo[*c*]phenanthridine skeleton (e.g., chelerythrine, sanguinarine, isodecarine, norchelerythrine, NK-109). Several derivatives displayed antibacterial activity against *Bacillus subtilis*, *Micrococcus luteus* and/or *Mycobacterium vaccae* and cytotoxicity against K-562 and MCF-7 cancer cell lines at micromolar concentrations; these compounds typically contained a *N*-methylated quaternary nitrogen and

7-benzyloxy substitution. The mechanism of action of the novel phenanthridines however remains still unclear.

Supplementary Materials: The copies of ^{1}H- and ^{13}C-NMR spectra are available online.

Author Contributions: P.L. synthesized all compounds; K.M. evaluated the antimicrobial activity and analyzed the data; V.K. evaluated the anticancer activity and analyzed the data, J.S. conceived and designed the experiments and wrote the paper.

Funding: This research was funded by the Czech-National Program for Sustainability grant number LO1304, Palacky University grant numbers IGA_PrF_2018_029, IGA_LF_2018_032 and IGA_PrF_2018_006, and OP PIK grant number CZ.01.1.02/0.0/0.0/15_019/0004431.

Acknowledgments: Authors thank H. Rezková, E. Řezníčková and P. Pospíšilová for technical assistance.

Conflicts of Interest: The authors declare no conflict of interest.

References

1. Dvořák, Z.; Kubán, V.; Klejdus, B.; Vičar, J.; Ulrichová, J.; Hlaváč, J.; Šimánek, V. Quaternary benzo[*c*]phenanthridines sanguinarine and chelerythrine: A review of investigations from chemical and biological studies. *Heterocycles* **2006**, *68*, 2403. [CrossRef]
2. Ahsan, H.; Reagan-Shaw, S.; Breur, J.; Ahmad, N. Sanguinarine induces apoptosis of human pancreatic carcinoma AsPC-1 and BxPC-3 cells via modulations in Bcl-2 family proteins. *Cancer Lett.* **2007**, *249*, 198–208. [CrossRef] [PubMed]
3. Jang, B.-C.; Park, J.-G.; Song, D.-K.; Baek, W.-K.; Yoo, S.K.; Jung, K.-H.; Park, G.-Y.; Lee, T.-Y.; Suh, S.-I. Sanguinarine induces apoptosis in A549 human lung cancer cells primarily via cellular glutathione depletion. *Toxicol. Vitro* **2009**, *23*, 281–287. [CrossRef] [PubMed]
4. Miao, F.; Yang, X.-J.; Zhou, L.; Hu, H.-J.; Zheng, F.; Ding, X.-D.; Sun, D.-M.; Zhou, C.-D.; Sun, W. Structural modification of sanguinarine and chelerythrine and their antibacterial activity. *Nat. Prod. Res.* **2011**, *25*, 863–875. [CrossRef] [PubMed]
5. Ishikawa, T. Benzo[*c*]phenanthridine bases and their antituberculosis activity. *Med. Res. Rev.* **2001**, *21*, 61–72. [CrossRef]
6. Šimánek, V. Benzophenanthridine alkaloids. In *The Alkaloids*; Brossi, A., Ed.; Academic Press: New York, NY, USA, 1985; Volume 26, pp. 185–240.
7. Galadari, S.; Rahman, A.; Pallichankandy, S.; Thayyullathil, F. Molecular targets and anticancer potential of sanguinarine—A benzophenanthridine alkaloid. *Phytomedicine* **2017**, *34*, 143–153. [CrossRef] [PubMed]
8. Slaninová, I.; Pěnčíková, K.; Urbanová, J.; Slanina, J.; Táborská, E. Antitumour activities of sanguinarine and related alkaloids. *Phytochem. Rev.* **2014**, *13*, 51–68. [CrossRef]
9. Maiti, M.; Nandi, R.; Chaudhuri, K. Sanguinarine: A monofunctional intercalating alkaloid. *FEBS Lett.* **1982**, *142*, 280–284. [CrossRef]
10. Wang, X.; Tanaka, M.; Krstin, S.; Peixoto, H.; Wink, M. The interference of selected cytotoxic alkaloids with the cytoskeleton: An insight into their modes of action. *Molecules* **2016**, *21*, 906. [CrossRef] [PubMed]
11. Chan, S.-L.; Lee, M.C.; Tan, K.O.; Yang, L.-K.; Lee, A.S.Y.; Flotow, H.; Fu, N.Y.; Butler, M.S.; Soejarto, D.D.; Buss, A.D.; et al. Identification of chelerythrine as an inhibitor of BclXL function. *J. Biol. Chem.* **2003**, *278*, 20453–20456. [CrossRef] [PubMed]
12. Caolo, M.A.; Stermitz, F.R. Benzophenanthridinium salt equilibria. *Heterocycles* **1979**, *12*, 11. [CrossRef]
13. Romo-Pérez, A.; Miranda, L.D.; Chávez-Blanco, A.D.; Dueñas-González, A.; del Rayo Camacho-Corona, M.; Acosta-Huerta, A.; García, A. Mild C(sp3)–H functionalization of dihydrosanguinarine and dihydrochelerythrine for development of highly cytotoxic derivatives. *Eur. J. Med. Chem.* **2017**, *138*, 1–12. [CrossRef] [PubMed]
14. Zee-Cheng, R.K.Y.; Yan, S.-J.; Cheng, C.C. Antileukemic activity of ungeremine and related compounds. Preparation of analogs of ungeremine by a practical photochemical reaction. *J. Med. Chem.* **1978**, *21*, 199–203. [CrossRef] [PubMed]
15. Hatae, N.; Fujita, E.; Shigenobu, S.; Shimoyama, S.; Ishihara, Y.; Kurata, Y.; Choshi, T.; Nishiyama, T.; Okada, C.; Hibino, S. Antiproliferative activity of O4-benzo[*c*]phenanthridine alkaloids against HCT-116 and HL-60 tumor cells. *Bioorg. Med. Chem. Lett.* **2015**, *25*, 2749–2752. [CrossRef] [PubMed]

16. Nakanishi, T.; Suzuki, M.; Mashiba, A.; Ishikawa, K.; Yokotsuka, T. Synthesis of NK109, an anticancer benzo[*c*]phenanthridine alkaloid. *J. Org. Chem.* **1998**, *63*, 4235–4239. [CrossRef]
17. Kanzawa, F.; Nishio, K.; Ishida, T.; Fukuda, M.; Kurokawa, H.; Fukumoto, H.; Nomoto, Y.; Fukuoka, K.; Bojanowski, K.; Saijo, N. Anti-tumour activities of a new benzo[*c*]phenanthridine agent, 2,3-(methylenedioxy)-5-methyl-7-hydroxy-8-methoxybenzo[c]phenanthridinium hydrogensulphate dihydrate (NK109), against several drug-resistant human tumour cell lines. *Br. J. Cancer* **1997**, *76*, 571–581. [CrossRef] [PubMed]
18. Nakanishi, T.; Masuda, A.; Suwa, M.; Akiyama, Y.; Hoshino-Abe, N.; Suzuki, M. Synthesis of derivatives of NK109, 7-OH Benzo[*c*]phenanthridine alkaloid, and evaluation of their cytotoxicities and reduction-resistant properties. *Bioorg. Med. Chem. Lett.* **2000**, *10*, 2321–2323. [CrossRef]
19. Fukuda, M.; Inomata, M.; Nishio, K.; Fukuoka, K.; Kanzawa, F.; Arioka, H.; Ishida, T.; Fukumoto, H.; Kurokawa, H.; Oka, M.; et al. A Topoisomerase II inhibitor, NK109, induces DNA single- and double-strand breaks and apoptosis. *Jpn. J. Cancer Res.* **1996**, *87*, 1086–1091. [CrossRef] [PubMed]
20. Hisatomi, T.; Sueoka-Aragane, N.; Sato, A.; Tomimasu, R.; Ide, M.; Kurimasa, A.; Okamoto, K.; Kimura, S.; Sueoka, E. NK314 potentiates antitumor activity with adult T-cell leukemia-lymphoma cells by inhibition of dual targets on topoisomerase II and DNA-dependent protein kinase. *Blood* **2011**, *117*, 3575–3584. [CrossRef] [PubMed]
21. Toyoda, E.; Kagaya, S.; Cowell, I.G.; Kurosawa, A.; Kamoshita, K.; Nishikawa, K.; Iiizumi, S.; Koyama, H.; Austin, C.A.; Adachi, N. NK314, a topoisomerase II inhibitor that specifically targets the α isoform. *J. Biol. Chem.* **2008**, *283*, 23711–23720. [CrossRef] [PubMed]
22. Guo, L.; Liu, X.; Nishikawa, K.; Plunkett, W. Inhibition of topoisomerase II and G2 cell cycle arrest by NK314, a novel benzo[*c*]phenanthridine currently in clinical trials. *Mol. Cancer Ther.* **2007**, *6*, 1501–1508. [CrossRef] [PubMed]
23. Wang, L.K.; Johnson, R.K.; Hecht, S.M. Inhibition of topoisomerase I function by nitidine and fagaronine. *Chem. Res. Toxicol.* **1993**, *6*, 813–818. [CrossRef] [PubMed]
24. Janin, Y.L.; Bisagni, E.; Carrez, D. Synthesis of some benzo[*h*]quinoline derivatives. *J. Heterocycl. Chem.* **1993**, *30*, 1129–1131. [CrossRef]
25. Bernardo, P.H.; Wan, K.-F.; Sivaraman, T.; Xu, J.; Moore, F.K.; Hung, A.W.; Mok, H.Y.K.; Yu, V.C.; Chai, C.L.L. Structure−activity relationship studies of phenanthridine-based Bcl-X L inhibitors. *J. Med. Chem.* **2008**, *51*, 6699–6710. [CrossRef] [PubMed]
26. Yu, Y.; Singh, S.K.; Liu, A.; Li, T.-K.; Liu, L.F.; LaVoie, E.J. Substituted dibenzo[*c,h*]cinnolines: Topoisomerase I-targeting anticancer agents. *Bioorg. Med. Chem.* **2003**, *11*, 1475–1491. [CrossRef]
27. Yapi, A.-D.; Desbois, N.; Chezal, J.-M.; Chavignon, O.; Teulade, J.-C.; Valentin, A.; Blache, Y. Design and preparation of aza-analogues of benzo[*c*]phenanthridine framework with cytotoxic and antiplasmodial activities. *Eur. J. Med. Chem.* **2010**, *45*, 2854–2859. [CrossRef] [PubMed]
28. Steinhauer, T.N.; Girreser, U.; Meier, C.; Cushman, M.; Clement, B. One-step synthetic access to isosteric and potent anticancer nitrogen heterocycles with the benzo[*c*]phenanthridine scaffold. *Chem. A Eur. J.* **2016**, *22*, 8301–8308. [CrossRef] [PubMed]
29. Hou, Z.; Yang, R.; Zhang, C.; Zhu, L.-F.; Miao, F.; Yang, X.-J.; Zhou, L. 2-(Substituted phenyl)-3,4-dihydroisoquinolin-2-iums as novel antifungal lead compounds: Biological evaluation and structure-activity relationships. *Molecules* **2013**, *18*, 10413–10424. [CrossRef] [PubMed]
30. Yang, X.; Yao, Y.; Qin, Y.; Hou, Z.; Yang, R.; Miao, F.; Zhou, L. Synthesis and in vitro antifungal activities of new 2-aryl-6,7-methylenedioxy-3,4-dihydroisoquinolin-2-ium bromides. *Chem. Pharm. Bull.* **2013**, *61*, 731–739. [CrossRef] [PubMed]
31. Ishikawa, T.; Ishii, H. Recent advances on antitumor-active benzo[*c*]phenanthridine alkaloids. *Heterocycles* **1999**, *50*, 627. [CrossRef]
32. Mackay, S.P.; Meth-Cohn, O.; Waigh, R.D. Synthesis of quaternary benzo[*c*]phenanthridine alkaloids and their analogues. *Adv. Heterocycl. Chem.* **1996**, *67*, 345–389. [CrossRef]
33. Stýskala, J.; Cankař, P.; Soural, M.; Hradil, P.; Vičar, J.; Šimánek, V.; Hlaváč, J. Synthesis of isodecarine. *Heterocycles* **2007**, *73*, 769. [CrossRef]
34. Stýskala, J.; Hlaváč, J.; Cankař, P. Synthesis of oxidative dihydroxy metabolites of benzo[*c*]phenanthridines. *Tetrahedron* **2013**, *69*, 4670–4678. [CrossRef]

35. Larghi, E.L.; Obrist, B.V.; Kaufman, T.S. A formal total synthesis of the marine alkaloid aaptamine. *Tetrahedron* **2008**, *64*, 5236–5245. [CrossRef]
36. Meisels, A.; Sondheimer, F. The constituents of casimiroa edulis llave et lex. III. 1 The structure of casimiroin 2. *J. Am. Chem. Soc.* **1957**, *79*, 6328–6333. [CrossRef]
37. Majumdar, K.; Taher, A.; Debnath, P. palladium-catalyzed intramolecular biaryl coupling: A highly efficient avenue for benzannulated pyranoquinolines and julolidine derivatives. *Synthesis* **2009**, *2009*, 793–800. [CrossRef]
38. Harayama, T.; Aktyama, T.; Kawano, K. A convenient synthesis of benzo[*c*]phenanthridine alkaloid, chelerythrine, by the palladium-assisted internal biaryl coupling reaction. *Chem. Pharm. Bull.* **1996**, *44*, 1634–1636. [CrossRef]
39. Campeau, L.-C.; Parisien, M.; Leblanc, M.; Fagnou, K. Biaryl synthesis via direct arylation: Establishment of an efficient catalyst for intramolecular processes. *J. Am. Chem. Soc.* **2004**, *126*, 9186–9187. [CrossRef] [PubMed]
40. Harayama, T.; Akiyama, T.; Akamatsu, H.; Kawano, K.; Abe, H.; Takeuchi, Y. Total synthesis of benzo[*c*]phenanthridine alkaloids, chelerythrine and 12-methoxydihydrochelerythrine, by a palladium-assisted internal biaryl coupling reaction. *Synthesis* **2001**, *2001*, 0444–0450. [CrossRef]
41. Ackermann, L. Carboxylate-assisted transition-metal-catalyzed C−H bond functionalizations: Mechanism and scope. *Chem. Rev.* **2011**, *111*, 1315–1345. [CrossRef] [PubMed]
42. De, S.; Mishra, S.; Kakde, B.N.; Dey, D.; Bisai, A. Expeditious approach to pyrrolophenanthridones, phenanthridines, and benzo[*c*]phenanthridines via organocatalytic direct biaryl-coupling promoted by potassium tert -butoxide. *J. Org. Chem.* **2013**, *78*, 7823–7844. [CrossRef] [PubMed]
43. Dewanji, A.; Murarka, S.; Curran, D.P.; Studer, A. Phenyl hydrazine as initiator for direct arene C–H arylation via base promoted homolytic aromatic substitution. *Org. Lett.* **2013**, *15*, 6102–6105. [CrossRef] [PubMed]
44. Carpino, L.A. Simple preparation of active manganese dioxide from activated carbon. *J. Org. Chem.* **1970**, *35*, 3971–3972. [CrossRef]
45. Murray, P.R.; Baron, E.J.; Pfaller, M.A.; Tenover, F.C.; Yolken, R.H. *Manual of Clinical Microbiology*, 7th ed.; American Society for Microbiology: Washington, DC, USA, 1999.
46. *Methods for Dilution Antimicrobial Susceptibility Tests for Bacteria that Grow Aerobically*, 8th ed.; Approved Standard Document M07-A7; Clinical and Laboratory Standards Institute (CLSI): Villanova, PA, USA, 2009.
47. Williams, A.B.; Schumacher, B. p53 in the DNA-damage-repair process. *Cold Spring Harb. Perspect. Med.* **2016**, *6*, a026070. [CrossRef] [PubMed]
48. Zatloukal, M.; Jorda, R.; Gucký, T.; Řezníčková, E.; Voller, J.; Pospíšil, T.; Malínková, V.; Adamcová, H.; Kryštof, V.; Strnad, M. Synthesis and in vitro biological evaluation of 2,6,9-trisubstituted purines targeting multiple cyclin-dependent kinases. *Eur. J. Med. Chem.* **2013**, *61*, 61–72. [CrossRef] [PubMed]

Sample Availability: Samples of the compounds are not available.

© 2018 by the authors. Licensee MDPI, Basel, Switzerland. This article is an open access article distributed under the terms and conditions of the Creative Commons Attribution (CC BY) license (http://creativecommons.org/licenses/by/4.0/).

molecules

MDPI

Article

Synthesis of 2,6-Diamino-Substituted Purine Derivatives and Evaluation of Cell Cycle Arrest in Breast and Colorectal Cancer Cells

Bartolomeo Bosco [1], Andrea Defant [2], Andrea Messina [1], Tania Incitti [1], Denise Sighel [1,2], Angela Bozza [1], Yari Ciribilli [1], Alberto Inga [1], Simona Casarosa [1,*] and Ines Mancini [2,*]

1 Centre for Integrative Biology (CIBIO), University of Trento, Via Sommarive 9, 38123 Trento, Italy; bartolomeo.bosco@unitn.it (B.B.); andrea.messina@unitn.it (A.M.); tania.incitti@gmail.com (T.I.); denise.sighel@unitn.it (D.S.); angela.bozza@aulss8.veneto.it (A.B.); yari.ciribilli@unitn.it (Y.C.); alberto.inga@unitn.it (A.I.)

2 Laboratory of Bioorganic Chemistry, Department of Physics, University of Trento, Via Sommarive 14, 38123 Trento, Italy; andrea.defant@yahoo.it

* Correspondence: simona.casarosa@unitn.it (S.C.); ines.mancini@unitn.it (I.M.); Tel.: +39-461-281-548 (I.M.)

Received: 16 July 2018; Accepted: 8 August 2018; Published: 10 August 2018

Abstract: Reversine is a potent antitumor 2,6-diamino-substituted purine acting as an Aurora kinases inhibitor and interfering with cancer cell cycle progression. In this study we describe three reversine-related molecules, designed by docking calculation, that present structural modifications in the diamino units at positions 2 and 6. We investigated the conformations of the most stable prototropic tautomers of one of these molecules, the *N*6-cyclohexyl-*N*6-methyl-*N*2-phenyl-7*H*-purine-2,6-diamine (**3**), by Density Functional Theory (DFT) calculation in the gas phase, water and chloroform, the last solvent considered to give insights into the detection of broad signals in NMR analysis. In all cases the H*N*(9) tautomer resulted more stable than the H*N*(7) form, but the most stable conformations changed in different solvents. Molecules **1**–**3** were evaluated on MCF-7 breast and HCT116 colorectal cancer cell lines showing that, while being less cytotoxic than reversine, they still caused cell cycle arrest in G2/M phase and polyploidy. Unlike reversine, which produced a pronounced cell cycle arrest in G2/M phase in all the cell lines used, similar concentrations of **1**–**3** were effective only in cells where p53 was deleted or down-regulated. Therefore, our findings support a potential selective role of these structurally simplified, reversine-related molecules in p53-defective cancer cells.

Keywords: reversine; microwave-assisted synthesis; molecular docking; cell cycle arrest; endoreduplication; p53

1. Introduction

Pluripotent cells play a relevant role in regenerative medicine, due to their capability of differentiating into many cell types. Pluripotency can be achieved in vitro, by over-expressing specific genes or by chemical induction, using a combination of synthetic molecules [1]. Among them the 2,6-diamino-substituted purine reversine (*N*6-cyclohexyl-*N*2-(4-morpholinophenyl)-7*H*-purine-2,6-diamine), firstly synthesized by Schultz and coworkers [2], is a promising molecule. In fact, it induces de-differentiation of C2C12 murine myoblasts and allows their subsequent differentiation in adipocytes, osteoblasts [3], neural progenitor-like cells [4] and cardiomyocytes [5], under specific conditions. Besides showing dedifferentiation properties, reversine is a kinase inhibitor able to interfere with the growth of several solid tumors, by specifically inhibiting the G2/M checkpoint and cytokinesis. Reversine is an inhibitor of Aurora kinases, Cyclin Dependent Kinases

(CDK) and Monopolar Spindle 1 (Mps1), proteins which have a crucial role in mitotic regulation. Aurora-A kinase is a Ser/Thr kinase that affects centrosomes maturation, mitotic entry, centrosome separation, spindle formation and cytokinesis [6]. Aurora-B kinase can modulate various tasks during mitosis, including chromosome migration to the spindle equator, chromosome segregation and cytokinesis [7]. Mps1 is involved in the regulation of spindle checkpoint in part by acting at the level of CDK1-cyclinB complex [8], therefore contributing to the proper attachment of chromosomes to the spindle microtubules before chromosome separation. Interestingly, this protein has emerged as a potential target for cancer therapy and reversine is known to inhibit Mps1 more efficiently than Aurora-B kinase, based on experimental and computational approaches [9]. As inhibitor of Aurora-A and Aurora-B kinases and Mps1, reversine causes an incorrect mitotic spindle assembly and chromosome separation, cell cycle arrest in G2/M phase, endoreduplication and eventually cell death due to a phenomenon called "mitotic catastrophe" observed in many cancer cell lines [10–16]. Moreover, reversine treatment of human follicular thyroid cancer cells leads to the activation of autophagy due to its capability to down-regulate mTOR [17]. Very recently, reversine has been reported to significantly inhibit the growth of urothelial carcinoma cell lines through activation of AMP activated protein kinase pathway, leading to cell death [18].

The transcription factor p53 is described as the guardian of the genome because it is implicated in several important cell functions, such as DNA repair, cell cycle regulation and apoptosis, preventing tumor formation. In normal conditions the p53 signaling pathway is in standby mode, but in response to cellular stresses p53 is activated and through its sequence-specific DNA binding activity it mediates the transcription of a large number of target genes. p53 is the most commonly mutated gene in many types of human cancers, losing in this way its tumor suppressor properties. Loss of heterozygosity (LOH) is also a frequent event resulting in complete lack of wild type p53 expression in cancer cells. In breast cancer numerous p53 coding mutations were identified, even if the frequency of p53 mutation in this cancer varies among subtypes and overall is approximately at 20% [19]. p53 has been observed to play an important role in modulation of reversine effect. It has been demonstrated that silencing of p53, and the consequent loss of transcriptional activation of its target p21, whose checkpoint function can prevent endoreduplication, renders fibroblasts more sensitive to reversine [10].

A structure activity relationship (SAR) study on a series of reversine-like molecules showing different substitutions on both C-6 purine and C-2 piperazine moieties was carried out with the aim to optimize biological activity, selectivity and oral bioavailability [20]. We report here three 2,6-diamino substituted purine derivatives, selected by docking calculation focused on Aurora-B kinase and Mps1 inhibition, which present the insertion of a new *N*-heterocycle unit in the C-2 substitution and a *N*-methyl group in C-6 unit, enhancing the structural diversity of reversine analogues. In particular, we focused on DFT calculations applied to the first structural investigation of the prototropic tautomers of one of these molecules. The effect of molecules **1**–**3** has been also compared to reversine on breast and colorectal cancer cell lines. We observed that they promoted aberrant mitosis and endoreduplication leading to cell death, possibly via mitotic catastrophe. Moreover, the compounds had a stronger effect when p53 function was ablated.

2. Results and Discussion

2.1. Selection and Synthesis of Compounds **1**–**3**

The design of the molecules **1**–**3** (Figure 1) was performed via structure selection based on docking calculations, considering both energy values and interactions of the complexes between the molecules and the two known target proteins of reversine, Aurora-B kinase and Mps1. The results by Autodock Vina indicated that compound **1**, which preserves the reversine skeleton, and the structurally simplified molecules **2** and **3** gave complexes with very similar energy values to those of reversine (Table S1).

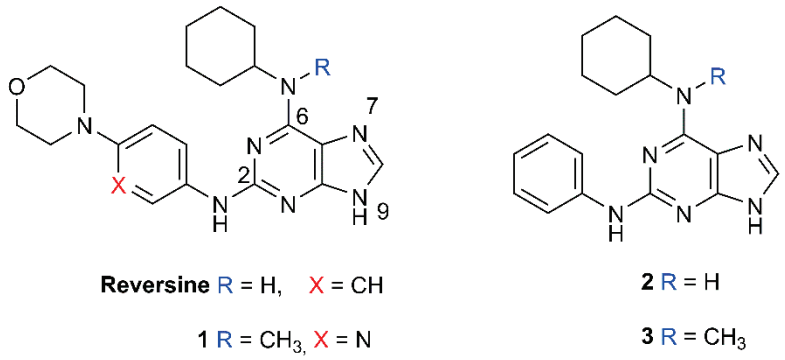

Figure 1. Molecular structures of reversine and synthetic compounds **1**–**3**.

Products **2** [21] and **3** were obtained by reacting aniline with **4** and **5**, respectively, the latter were derived by nucleophilic substitution of cyclohexylamine or methylcyclohexylamine with 2,6-dichloropurine (Scheme 1). The production of **5** proceeded with higher yields and in a cleaner way compared to **4**. In fact the methyl-*N*6 substituent as in **5** prevented the formation of the by-product, resulting by the substitution of a second unit of 2,6-dichloropurine at the *N*6 position, as observed in the synthesis of product **4**. The synthesis of **1** was challenging due to the poor nucleophilicity of the aryl amine **6**. Different reaction conditions were compared (Buchwald-Hartwing amination, butanol in the presence of trimethylsilyl chloride or triethylamine; *N*-methyl-2-pyrrolidone (NMP), 150 °C, *p*-toluenesulfonic acid monohydrate in DMSO, trifluoroacetic acid (TFA) in EtOH) under conventional heating or microwave (MW) irradiation, as well as different leaving groups (chlorine as in **5** or a fluorine analogue obtained by 6-chloro-2-fluoro-9*H*-purine). The MW irradiation of **5** and **6** in ethanol in the presence of TFA proved to be the best procedure, although still giving a poor yield in line with data for reactions using similar nucleophiles [21].

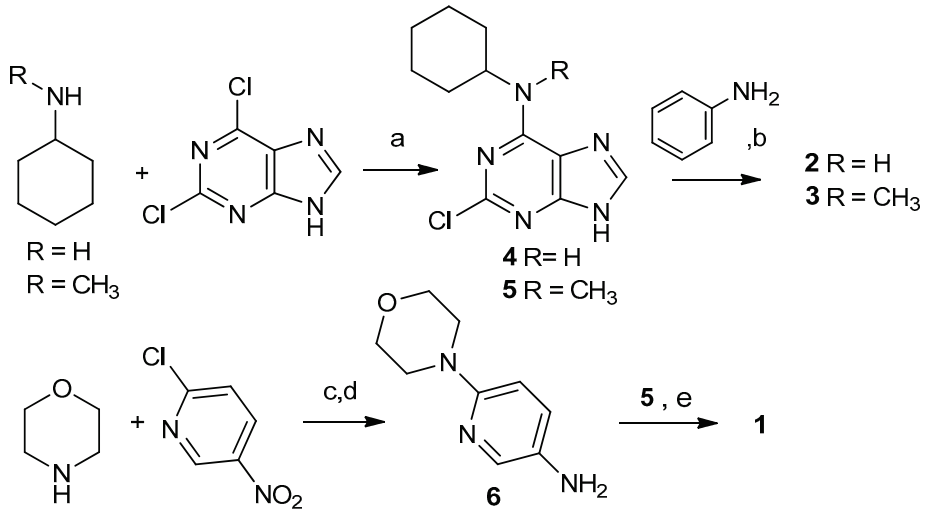

Scheme 1. Synthesis of molecules **1**–**3**. *Reagents and conditions*: (**a**) ethanol, TEA, reflux 75 °C, 14 h; (**b**) *N*-methyl-2-pyrrolidone, reflux 150 °C, 14 h; (**c**) DCM, TEA, 12 h; (**d**) H_2, Pd/C, 2 h; (**e**) ethanol, TFA, Microwave 120 °C, 2.30 h.

The obtained products were characterized by spectrometric measurements including ESI-MS/MS and high resolution experiments by EI-MS technique, and by extensive NMR analysis (see Materials and Methods and Supplementary Material). Prior to their biological evaluation, compound **1** was purified by preparative RP-18 HPLC and the purity of **2** and **3** was evaluated using silica gel HPLC (Materials and Methods).

2.2. Study on the Tautomeric Forms of Product **3**

Both ^{1}H- and ^{13}C-NMR spectra of products **1** and **3** recorded in $CDCl_3$ solution at room temperature showed very broad H_3C-*N* and HC-*N* signals (Figures S1 and S3), a behavior also observed for the precursor **5**. The broad nature of these signals would normally suggest the presence of tautomers and/or restricted conformations. This is in line with the report of coexisting tautomers of purine bases, with the prototropic H*N*(7) and H*N*(9) as the preferred species, where the intramolecular proton-transfer is accompanied by migration of π electrons. In general their relative populations could be affected by structural factors such as aromaticity, intramolecular interactions, substituent effects able to modify the electronic distribution within the molecule, repulsions of lone electron pairs and also by external influences such as solvent and temperature [22].

In order to gather information on the effective structures of the molecule and to provide details on the interactions involved with biological targets, we decided to further investigate the tautomeric forms of **3**. Thanls to MarvinSketch software analysis the two most probable tautomers were predicted to be the prototropic H*N*(7) and H*N*(9) forms. Firstly, a series of conformations for each tautomer were evaluated by Density Functional Theory (DFT) calculation [22] at a B3LYP/6-31G(d,p) level of theory in the gas-phase, obtaining the corresponding energy values and indications on the energy-minimized structures for the two prototropic forms. In both cases the most stable conformers displayed an *anti*-position of the phenyl-*N*(2) and cyclohexyl-*N*(6) groups (Table 1, entries 1 and 8), with the H*N*(9) structure as the favored one (E = −1027.75607832 a.u.). On the contrary, the structure associated to the highest energy value is the *syn*-H*N*(7) tautomer (Table 1, entry 7). These predictions are in agreement with H*N*(9) tautomer being more favored than H*N*(7), as reported for neutral purine in the gas phase and in non-polar solvents [23], due to the possibility of a stabilizing intramolecular interaction between the hydrogen at *N*(9) position and the lone electron pair on the *N*(1) atom. Besides, the energy minimized structure reported in entry 1 displayed a length of 1.36139 Å for the C(6)-*N* bond, a value which is really intermediate between 1.47357 Å calculated for a single C-N distance and 1.26715 Å for a double C=N distance, indicating a restricted rotation around this bond.

Afterwards, the conformations of the two tautomers were also evaluated in chloroform since it is the solvent used in NMR analysis. The most stable structure (Table 1, entry 1; E = −1027.76438045 a.u.) presented the same conformation as obtained from calculation in the gas phase. Moreover, all the conformations considered for the H*N*(9) tautomer were much more stable than the corresponding ones for the H*N*(7) isomer. Notably, the latter result is in line with both the detections of a single tautomer by NMR spectra and with the very similar energy values for the *anti*- and *syn*-H*N*(9) tautomer obtained by rotation around the *N*-C(6) bond (entries 1 and 3, respectively). These data support their coexistence in solution, responsible for the very broad signals attributable to *N*-CH_3 group (δ_H 3.39 and δ_C 30.1 ppm), to the cyclohexylmethine carbon (δ_C 54.8 ppm) and to C(6) (δ_C 152.3 ppm).

The evaluation of the predominant structure of a ligand molecule present in solution is important in theoretical drug design. It is known that a more biologically relevant water-phase environment can significantly change the relative stability of various tautomers if compared with the gas phase condition [23]. DFT calculations were thus performed in water for the H*N*(9) and H*N*(7) forms of **3** by using the Polarized Continuum Model (PCM). The data reported in Table 1 suggest a similar behavior for the analyzed species both in gas phase and in chloroform solution: the H*N*(9) tautomer resulted more stable than the H*N*(7), with the most stable conformation showing a *syn*-position of the phenyl-*N*(2) and cyclohexyl-*N*(6) groups (E = −1027.76745565 a.u.), very close in energy to the one displaying the *anti*-position (Table 1, entries 3 and 4, respectively).

Table 1. Minimized structures and energy values of four conformations for each prototropic tautomer H*N*(9) and H*N*(7) of compound **3** (entries 1–4 and 5–8, respectively) evaluated by DFT at level B3LYP/6-31G(d,p) in the gas phase, in chloroform and in water. Numbering positions follow the indication in Figure 1.

Entry	Minimized Structure	Condition	ΔE (kJ/mol)
1	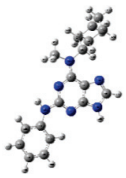	gas phase	–
		$CHCl_3$	–
		water	17.58954
2	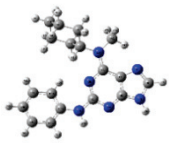	gas phase	6.33039
		$CHCl_3$	6.24671
		water	4.35136
3	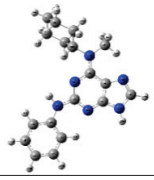	gas phase	1.56063
		$CHCl_3$	1.86188
		water	–
4	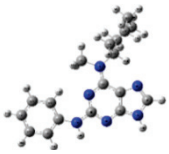	gas phase	3.46017
		$CHCl_3$	3.11708
		water	1.058552
5	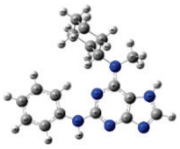	gas phase	4.92875
		$CHCl_3$	21.17926
		water	18.43052
6	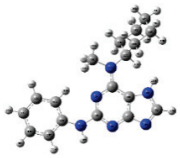	gas phase	6.7195
		$CHCl_3$	29.88213
		water	21.50576
7	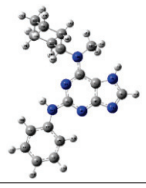	gas phase	35.5933
		$CHCl_3$	22.57268
		water	13.31767
8	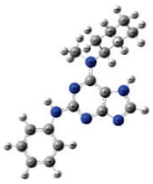	gas phase	2.87441
		$CHCl_3$	26.39267
		water	17.58954

To gain insight into the probable structural behavior of these molecules involved in interactions with the targets, docking calculations were carried out on both the prototropic forms (Table S1). The results obtained for **3** were in line with the higher stability of H*N*(9) than H*N*(7) tautomer derived by DFT calculations. In both the Aurora-B kinase and Monopolar spindle 1 complexes, H*N*(9) tautomer emerged as the most stable, combining the evaluation of energy data and both H-bonds and hydrophobic interactions with the enzymes. The same trend was observed for molecule **1**. In the case of **2** slightly lower energy values were obtained for H*N*(9) tautomer, but more interactions were associated to H*N*(7) isomer.

2.3. Biological Evaluation

We evaluated the growth inhibition effect of the synthetic products in comparison to reversine on two cancer cell lines: the MCF-7 breast cancer (MCF-7 Vector) line and the HCT116 colorectal cancer line. In parallel, we tested whether the effect of reversine and/or molecules **1**–**3** was influenced by the presence of p53 by analyzing their effects both on MCF-7shp53 cell line, stably transfected with a short harpin RNA against p53, and the HCT116p53$^{-/-}$ cells, in which p53 was eliminated by homologous recombination [24,25]. As already demonstrated both cell lines, showed severely reduced or completely abolished levels of full length p53 (Figure S4) [26]. We evaluated the growth inhibition effects by MTT (3-[4,5-dimethylthiazol-2-yl]-2,5 diphenyl tetrazolium bromide) assay after 24 h of treatment, using DMSO (0.1%) as negative control and reversine as positive control (Figure S5). All the compounds **1**–**3** suppressed the growth of MCF-7 and HCT116 cells in a dose-dependent manner. It was evident that their cytotoxicity was similar in the different cancer cell lines, even though HCT116 cells showed a higher resistance to the treatments than MCF-7 cells. Based on MTT results, we calculated the EC_{50} values of reversine and molecules **1**–**3** in MCF-7 and HCT116 cell lines (Table 2). The data demonstrate that these molecules were less toxic than reversine and that EC_{50} indexes were similar for p53 wild-type and p53 compromised cells.

Table 2. Cytotoxicity values (EC_{50}, μM) of reversine and molecules **1**–**3** tested on MCF-7 breast cancer (Vector and p53 downregulated) and HCT116 colorectal cancer (p53$^{+/+}$ and p53$^{-/-}$) cell lines.

Compound	MCF-7 Vector	MCF-7 shp53	HCT116 p53$^{+/+}$	HCT116 p53$^{-/-}$
Reversine	9.5	11.0	16.7	7.5
1	99.5	111.2	117.2	157.9
2	35.3	39.7	40.4	38.1
3	35.7	36.5	73.2	67.6

We next investigated the impact of the products **1**–**3** on cell cycle by flow cytometry. The compounds were able to elicit cell cycle arrest in G2/M phase in a dose-dependent manner, particularly when p53 was compromised. Specifically, after 24 h of treatment, compound **1** and **2** at 5 μM concentration and compound **3** at 10 μM concentration caused a significant cell cycle arrest in MCF-7shp53, but not in MCF-7 vector. The data obtained were statistically significant, as shown by the merge of three experiments (Figure 2A,B). Similar results were obtained in HCT116 cells, even though these cells showed a stronger cycle arrest than MCF-7. Specifically, the fraction of HCT116 cells arrested in the G2/M phase upon treatment with the same dosages used on breast cancer cells (5 μM of **2** and 10 μM of **3**), was 95.22% and 39.63% respectively (Figures S6 and S7). Furthermore, at these concentrations a new peak corresponding to polyploid cells appeared, probably originating from endo-reduplication, an effect caused by the inhibition of mitotic spindle Aurora-A and Aurora-B kinases, and Mps1 [12,14]. The data obtained in triplicates were statistically significant, as shown in Figure 2C,D. The comparison between the effects of analogues **2** and **3** allows us to speculate on the role of the methyl group in C6 position, which represents the only structural difference between the two compounds. Based on the obtained data, the presence of a methyl group in the structure of **3**

decreased the efficacy of the molecule. This suggests that the C6-methyl group is responsible for a different and possibly weaker interaction between Aurora kinases and the compound.

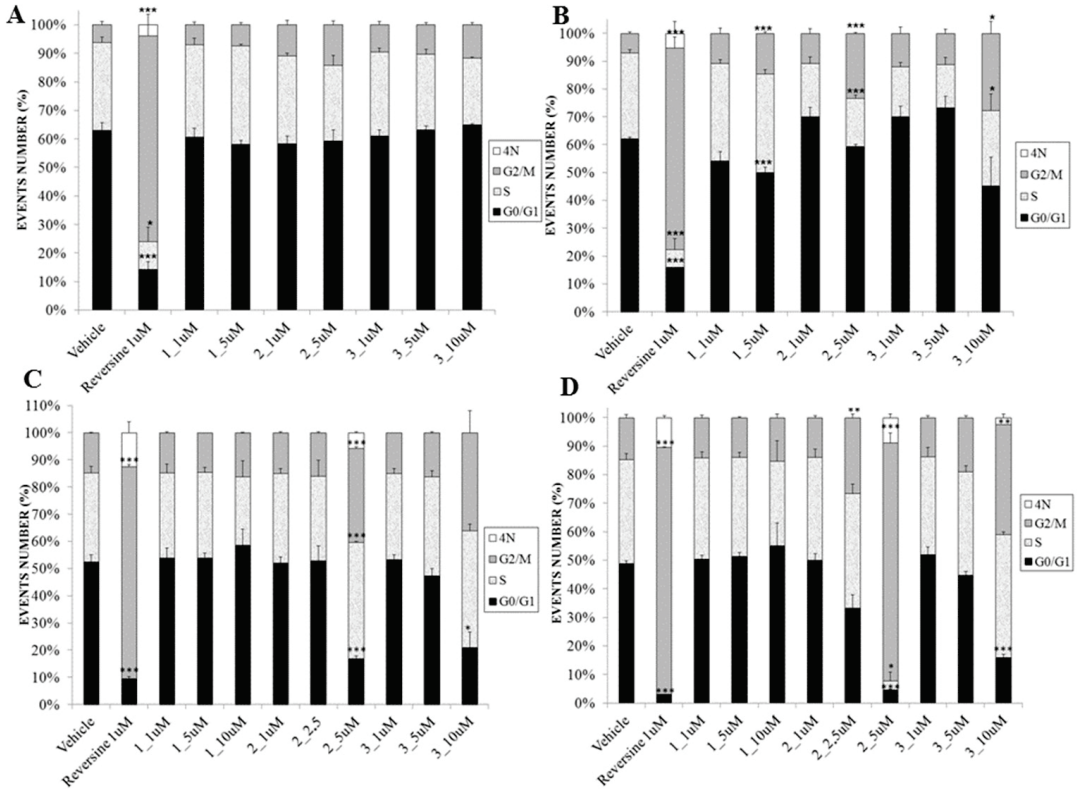

Figure 2. Cell cycle analysis after treatments with compounds **1**–**3** at different concentrations on: (**A**) MCF-7 Vector; (**B**) MCF-7shp53; (**C**) HCT116p53$^{+/+}$ and (**D**) HCT116p53$^{-/-}$. The results are expressed as mean ± SEM of three independent experiments (* p-value < 0.05; ** p-value < 0.01; *** p-value < 0.005).

A plasma membrane staining was then performed to analyze the effect of the molecules at a morphological level. MCF-7 and HCT116 cell lines were stained and analyzed by fluorescence microscopy upon one and four days of treatment with reversine and **1**–**3** (0.1% DMSO was used as control). Treated MCF-7 cells were larger in size and their number was lower with respect to the control. Furthermore, as shown by 4′,6-diamidino-2-phenylindole (DAPI) staining, many cells presented several nuclei, fused together (Figure S8). This is probably due to the inability to form two separate nuclei during M phase of the cell cycle. Cells could then bypass the G2/M checkpoint by avoiding cell division, therefore generating two fused nuclei inside the same cell. This loop then continues until the cells undergo apoptosis [27,28]. In accordance with data obtained by flow cytometry, this effect was higher in MCF-7shp53 with respect to MCF-7 control cells. Specifically, compound **2** at a 5 μM concentration caused a stronger effect when p53 was down-regulated, while compound **3** at a 10 μM concentration caused cell cycle arrest and endoreduplication only in MCF-7shp53 cells. This result provides an additional confirmation of cell cycle arrest in G2/M phase, probably caused by incorrect mitotic spindle formation and chromosome segregation. Accordingly, similar effects were obtained in HCT116 cells. Specifically, 2.5 μM of **2** and 5 μM of **3** caused cell cycle arrest and endoreduplication in HCT116p53$^{-/-}$ cells but not in HCT116p53$^{+/+}$ cells, with morphological changes more visible at day 4 with respect to day1 (Figure 3).

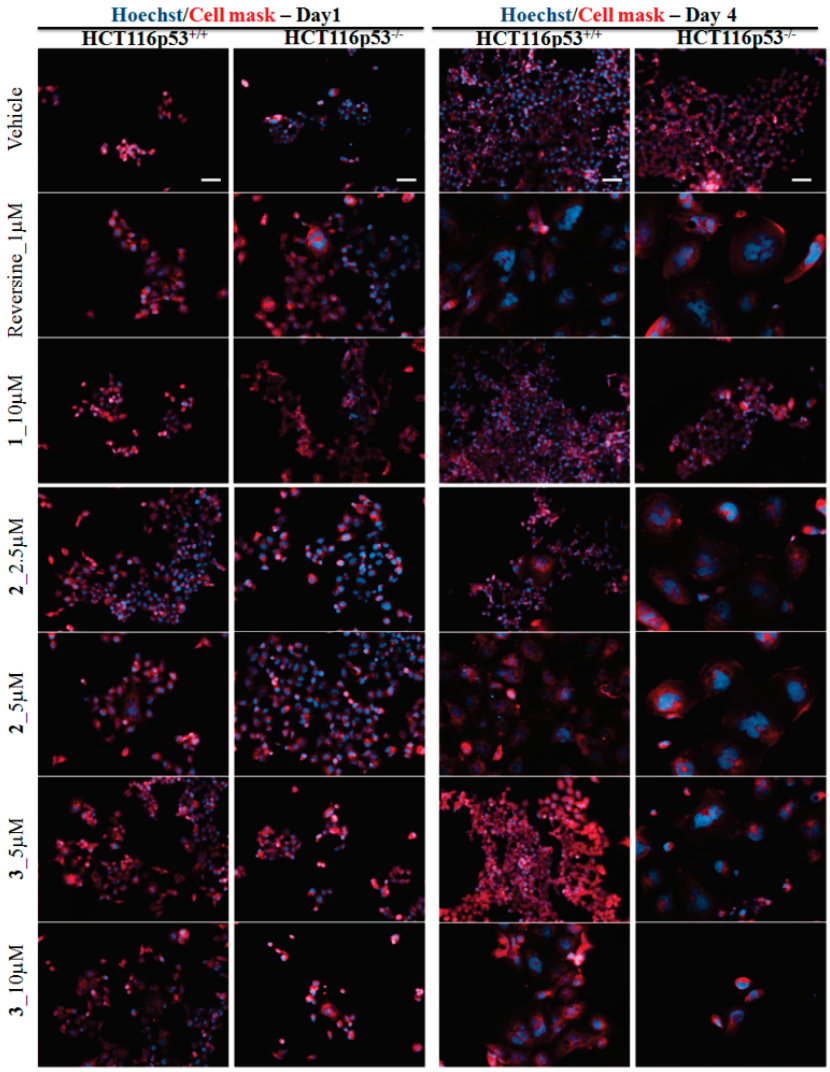

Figure 3. Nuclei and cell membrane staining on HCT116p53$^{+/+}$ and HCT116p53$^{-/-}$ after compounds **1**–**3** treatments at day 1 and day 4 (Scale bar = 50 μm).

The tested molecules are able to stabilize p53 in MCF-7 vector cells at the same concentrations that cause cell cycle aberrations in MCF7shp53. HCT116p53$^{+/+}$ showed upregulation of p53 after treatment with 1 μM reversine as well as with the products **1**–**3** at 1 μM dose, a concentration lower than the lowest effective dose observed in the previous experiments (Figure 4). Our data support the idea that p53 plays a regulatory role in mitotic spindle formation and control of chromosome segregation. p53 is stabilized in response to cellular damage, it accumulates, triggers a reversible G2 arrest and can activate the transcription of genes able to restore microtubules function. Breast cancer 1 (BRCA1) and DNA repair complex proteins could be implicated in this process [27]. Consistent with this view, in wild-type cells p53 could orchestrate damage repair to the mitotic spindle caused by reversine and **1**–**3** so that cell cycle is not strongly affected. Interestingly, p53-null cells treated with a molecule that causes a low genotoxic stress undergo endoreduplication and then die from apoptosis [28].

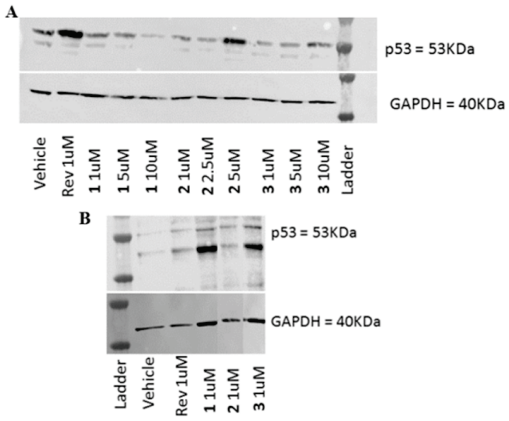

Figure 4. Western blot analysis to determine p53 expression after one day of treatment with different concentration of reversine and compounds **1**–**3** on A MCF-7 Vector and B HCT116p53$^{+/+}$.

The 3D structures of the H*N*(7) and H*N*(9) tautomers of **1**–**3**, obtained by docking calculation with both kinases have been analyzed in detail. In the complexes with both kinases, for **1** and **3**, it was evident that Me-*N*-C6 group is located inside the active center with no steric hindrance and is not involved in any interactions. In particular, regarding the complexes of Aurora B (2VGO) with the H*N*(9) tautomers, a good overlapping of the structures of reversine and of **1**–**3** becomes particularly evident, but the *N*-cyclohexyl unit takes on the same disposition for reversine and **2**, differently from **1** and **3** (Figure S9). Moreover, a different disposition is evident for the H*N*(7) tautomers of **2** and **3** in the complexes, as evident in Figure S10. Notably, in the docking calculation of **2** with both Aurora-B kinase and Monopolar Spindle 1 (Table S1), the energy differences between H*N*(9) and H*N*(7) tautomers resulted lower than the corresponding values obtained for **1** and **3**. This suggest a favored condition for the H*N*(7) isomer in **2** due to the absence of the *N*-methyl C(6) group. Moreover, the rotation around the *N*-C(6) bond may increase the conformations of this isomer, differently from the restricted rotation in **3** and **1**. These computational data support the higher kinase inhibition by molecule **2** than **3** and **1**.

3. Materials and Methods

3.1. Chemistry

3.1.1. General

Reversine and all reagents were purchased from Sigma Aldrich (St. Louis, MO, USA) and used without further purification. The reaction yields were calculated for the products after chromatographic purification. Thin layer chromatography (TLC): Merck silica gel F_{254} or reversed phase Merck RP-18 F_{254} (Merck, Darmstadt, Germany), with visualization with UV light. Flash chromatography (FC): Merck Si 15–25 μm; preparative thin layer chromatography (PLC): 20 × 20 cm Merck Kieselgel 60 F_{254} 0.5 mm plates. MW-assisted reactions were carried out using a mono-mode CEM Discover SP reactor (CEM, Matthews, NC, USA) in a sealed vessel (200 W max). NMR spectra were recorded on an Avance 400 spectrometer (Bruker, Billerica, MA, USA) using a 5 mm BBI probe ^{1}H at 400 MHz and ^{13}C at 100 MHz in $CDCl_3$ (relative to δ_H 7.25 and δ_C 77.00 ppm), or in $(CD_3)_2SO$ (relative to δ_H 2.50 and δ_C 39.50 ppm), δ values in ppm, *J* values in Hz; assignments are supported by heteronuclear single quantum correlation (HSQC) and heteronuclear multiple bond correlation (HMBC) experiments. Electrospray ionization (ESI)-MS mass spectra were recorded using a Bruker Esquire-LC spectrometer by direct infusion of a methanol solution (source temperature 300 °C, drying gas N_2, 4 L/min, scan range *m*/*z* 100–1000). Electron ionization (EI) mass spectra (*m*/*z*; rel%) and high resolution (HR)-EI data were recorded with a Kratos-MS80 mass spectrometer (SIS, Ringoes, NJ, USA), heating at 213 °C for **2**, at 276 °C for **1** and at 417 °C for **3**.

3.1.2. Typical Reaction Procedure for Precursors **4** and **5**

To a solution of 2,6-dichloropurine (260 mg, 1.38 mmol, 1.0 equiv) in EtOH (2 mL) cyclohexylamine or methylcyclohexylamine (1.52 mmol, 1.1 equiv) and Et_3N (1.52 mmol, 1.1 equiv) were added. The reaction mixture was irradiated at 90 °C for 1.5 h in a microwave reactor. The obtained white precipitate was filtered and chromatographically purified under the indicated conditions.

2-Chloro-N-cyclohexyl-9H-purin-6-amine (**4**). TLC (CH_2Cl_2:MeOH = 94:6 *v*/*v*): R_f = 0.55. Purification by silica gel PLC (CH_2Cl_2:MeOH = 94:6 *v*/*v*) Yield: 65%. ^{1}H-NMR (DMSO-d_6) δ 13.05 (br s, 2H, NH_2), 8.08 (s, 1H), 7.95 (brs, 1H, NH), 4.60 (br s), 3.96 (br s cyclohexyl CH), 1.89, 1.73 and 1.26 (series of m, 10H, cyclohexyl). ^{13}C-NMR (DMSO-d_6) δ 154.2, 152.9, 150.5, 139.2(N=CH), 117.8, 48.8 (cyclohexyl CH), 32.1 (2C), 25.1 (2C), 24.8. Significant HMBC correlation: 1.26 ppm with 48.8 ppm. ESI(−)-MS: *m*/*z* 250/252 in ca. 3:1 ratio, $[M - H]^-$.

2-Chloro-N-cyclohexyl-N-methyl-9H-purin-6-amine (**5**). TLC (hexane: EtOAc = 4:6 *v*/*v*): R_f = 0.62. Purification by silica gel FC (hexane:EtOAc, from 7:3 to 4:6 *v*/*v*). Yield: 80%. ^{1}H-NMR ($CDCl_3$) δ 13.30 (br s, 1H, *N*H), 7.84 (s, 1H, H=CN), 4.88(br s, 1H, cyclohexyl CH), 3.18 (br s, 3H, *N*CH_3), 1.86, 1.73, 1.17 (series of m, 10H, cyclohexyl). ^{13}C-NMR (DMSO-d_6, detectable signals) δ 154.5, 152.9, 138.7(HC=N), 118.3 (br), 25.7(2C), 25.4. ESI(−)-MS: *m*/*z* 264/266 in 3:1 ratio, $[M - H]^-$.

3.1.3. Synthesis of 6-Morpholinopyridin-3-amine (**6**)

A mixture of 2-chloro-5-nitropyridine (303 mg, 1.91 mmol, 1.0 equiv), morpholine (0.5 mL, 5.74 mmol, 3.0 equiv) and Et_3N (483 mg, 0.67 mL, 2.5 equiv) in CH_2Cl_2 (4 mL) was stirred at room temperature overnight. The reaction mixture was diluted with water (10 mL) and extracted with CH_2Cl_2 (30 mL × 3). The combined organic layers were washed with water (30 mL × 6) and brine (1 × 30 mL), dried over anhydrous Na_2SO_4 and concentrated in vacuo to give a yellow solid. 70 mg of the yellow solid (0.335 mmol, 1.0 eq) were diluted in EtOH (5 mL) and a spatula tip of catalyst Pd/C was added. The obtained mixture was hydrogenated for 2 h, using a Hypem XP hydrogen generator (h2planet, Milan, Italy), Pressure was set at 1.5 bar. The crude mixture was filtered on Celite, and the filtrate was evaporated to obtain a red solid. Yield: 93% over two steps. TLC (hexane:ethyl acetate = 4:6 *v*/*v* + Et_3N): R_f = 0.15. ^{1}H-NMR ($CDCl_3$) δ 7.79 (d, *J* = 2.7 Hz, 1H), 7.01 (dd, *J* = 8.8, 2.7 Hz, 1H), 6.73 (brs, 2H, NH_2), 6.56 (d, *J* = 8.8 Hz, 1H), 3.82 (m, 4H), 3.33 (m, 4H). ^{13}C-NMR ($CDCl_3$) δ 154.02, 135.09, 134.58, 126.42, 108.41, 66.80 (2C), 47.08 (2C). ESI(−)MS: *m*/*z* 178 $[M - H]^-$.

3.1.4. Synthesis of *N*6-Cyclohexyl-*N*6-methyl-*N*2-(6-morpholinopyridin-3-yl)-7*H*-purine-2,6-diamine (**1**)

A mixture of **5** (22.5 mg, 0.085 mmol, 1 equiv), **6** (60 mg, 0,34 mmol, 4 equiv) and trifluoroacetic acid (0.1 equiv.), in ethanol (2 mL), was microwave irradiated at 120 °C, for 2.5 h. The reaction mixture was concentrated in vacuo and the residue was submitted to preparative HPLC (RP-18 LiChroSphere 7 μm, acetonitrile/water 1:1 + 0.1% TFA, flow 5 mL/min, detection at 268 nm, 3.1 min) obtaining **1** trifluoracetate salt as a white powder (10.7 mg, yield 25%). ^{1}H-NMR ($CDCl_3$) δ 12.40 (br s, 1H), 7.94 (brd, *J* = 7.8 Hz, 1H), 7.83 (s, 1H), 7.79 (brs, 1H), 7.03 (brd, *J* = 8.1 Hz, 1H), 6.57 (brd, *J* = 8.1 Hz, 1H), 3.82 (m, 4H), 3.35 (m, 4H), 3.20 (brs, NCH_3), 2.16–1.28 (series of m, 10H). ^{13}C-NMR ($CDCl_3$) detectable signals by HSQC correlation δ 7.83 with δ 135.7 (C-8) and by HMBC correlations: δ 53.6, 151.9, 118.4, 133.6, 127.0, 108.6, 66.2, 46.6. ESI(+)-MS: *m*/*z* 409 $[M + H]^+$; MS/MS (409): *m*/*z* 327. The solid, dissolved in methanol, was treated with Et_3N, the mixture evaporated in vacuo and the residue eluted through RP-18 LiChrolut with water/methanol, gradient elution to obtain free **1**. ESI(−)MS: *m*/*z* 407 $[M - H]^-$; MS/MS(407): *m*/*z* 325. EI-MS: *m*/*z* 408 (M^+, 5), 368 (4), 326 (1), 229 (2), 179 (23). HRMS(EI) calcd. for $C_{21}H_{28}N_8O$, 408.23861, found 408.23683.

3.1.5. Typical Reaction Procedure for Products **2** and **3**

Compound **4** or **5** (0.188 mmol, 1.0 equiv.) was dissolved in *N*-methyl-2-pyrrolidone and aniline (0.56 mmol, 3.0 equiv.) was added. The reaction mixture was heated at 150 °C for 14 h, then ice-water (15 mL) was added and the mixture was extracted with EtOAc (20 mL × 2). The combined organic layers were washed with ice-water mixture (15 mL × 5) and brine (20 mL), dried over anhydrous $MgSO_4$, and concentrated under reduced pressure to give a brown syrup. The crude residue was purified by silica gel FC eluting with hexane/EtOAc (from 7:3 to 4:6 *v*/*v*). The purity of **2** and **3** was verified by analytical HPLC injection (Si60 LiChroSphere 15–25 μm, 254 nm) with hexane/2-propanol 9:1.

*N*6-Cyclohexyl-*N*2-phenyl-7*H*-purine-2,6-diamine (**2**). TLC (EtOAc): R_f = 0.42. Yield: 70%. ^{1}H-NMR ($CDCl_3$) δ 13.0 (br. s., 1H, NH), 7.51 (brd., *J* = 7.8 Hz, 2H), 7.31 (brt, *J* = 7.8 Hz, 2H), 7.05 (brt, *J* = 7.8 Hz, 1H), 7.03 (s. 1H, purine), 6.57 (s, 1H, NH, exchangeable by CD_3OD addition), 5.59 and 4.01 (1:1 two brs, 1H, NH), 2.05 (m, 1H), 1.74 (m, 2H), 1.64 (m, 2H), 1.33 (m, 6H), in agreement with reported data [21]. ^{13}C-NMR ($CDCl_3$) δ 156.6, 154.4, 150.3 (v br), 139.9, 135.9, 129.2 (2C), 123.0, 121.2 (2C), 114.7 (br), 49.3 (v br), 33.3 (2C), 25.6, 24.9 (2C). ESI(+)-MS: *m*/*z* 309 $[M + H]^+$; MS/MS (309): *m*/*z* 227. EI-MS: *m*/*z* 308 (M^+, 100), 225 (67). HRMS(EI) calcd. for $C_{17}H_{20}N_6$, 308.17494, found 308.17510.

*N*6-Cyclohexyl-*N*6-methyl-*N*2-phenyl-7*H*-purine-2,6-diamine (**3**). TLC (EtOAc): R_f = 0.54. Yield: 74%. ^{1}H-NMR ($CDCl_3$) δ 12.61 (brs., 1H, NH), 7.54 (brd, *J* = 7.8 Hz, 2H), 7.31 (brt, *J* = 7.8 Hz, 2H), 7.04 (brt, *J* = 7.8 Hz, 1H), 6.92 (s., 1H, NH, exchangeable), 6.77 (s, 1H, purine), 5.17 (br s, 1H, NH), 3.39 (br s, 3H, NCH_3), 1.90–1.12 (series of m, 10H). ^{13}C-NMR ($CDCl_3$) δ 154.8, 155.6, 152.3 (br), 140.2, 134.6, 129.1 (2C), 122.6, 120.6 (2C), 114.7 (br), 54.8 (very br), 30.1 (br, CH_3), 25.7 and 25.8 (5C). ESI(+)-MS: *m*/*z* 323 $[M + H]^+$; MS/MS (323): *m*/*z* 241 EI-MS: *m*/*z* 322 (M^+, 95), 307 (50), 265 (56), 240 (72). HRMS(EI) calcd. for $C_{18}H_{22}N_6$, 322.19059, found 322.19071.

3.2. Computational Analysis

DFT calculation was performed for the tautomers of **3** in the gas phase, in chloroform and in water by using Polarized Continuum Model (PCM). Calculations were carried out on a PC running at 3.4 GHz on an Intel i7 2600 quad core processor with 8 GB RAM and 1 TB hard disk with Windows 7 Home Premium 64-bit SP1 as an operating system. Ligands were build using PC Model version 6.0 (Serena Software, Bloomington, IN, USA). A Gaussian 03W revision E.01 program [29] with graphical interface GaussView 4.0. was used in the geometry optimization at a density functional theory (DFT) level of theory and invoking gradient with 6-31G(d,p) basis set for all the atoms. The gradient-corrected DFT with the three-parameter hybrid functional (B3) [30] for the exchange part and the Lee–Yang–Parr (LYP) correlation function [31] were utilized. The optimized structural parameters were employed in the vibrational energy calculations at the DFT levels to characterize all stationary points as minima. No imaginary wave number modes were obtained for each optimized structure, proving that a local minimum on the potential energy surface was actually found. The minimized molecules were saved in pdb extension.

AutoDock Tools (ADT) package version 1.5.6rc3 was employed to generate the docking input files and to analyze docking results, whereas Autodock Vina 1.1.2 [32] was taken for docking calculation. The structures of Aurora-B (PDB ID: 2VGO) and Mps1 (PDB ID: 3HF9) kinases were determined by X-ray crystallography with a resolution of 1.7 Å and 2.6 Å respectively [12,33]. The structures were modified as follows: the ligand and all the crystallization water molecules were removed saving the file in pdb extension. All the hydrogen atoms were added by AutoDock Tools (ADT) and Gasteiger–Marsili charges were calculated saving the resulting file in pdbqt extension. Rotatable bonds were defined for each minimized ligand molecule. For the docking calculation a grid box of 16 × 16 × 16 Å in *x*, *y*, *z* directions was created, spacing of 1.00 Å and centered at $x = 10.52$, $y = -0.323$, $z = 3.0766$ for 2VGO and a grid box of 14 × 14 × 14 Å in *x*, *y*, *z* directions was created, spacing of 1.00 Å and centered

at x = 0.572, y = 17.486, z = 51.185 for 3H9F. Vina parameters were set as follows: exhaustiveness of the local search =100 and number of conformations to calculate =10. Results are expressed as energy associated to each ligand-enzyme complex in terms of Gibbs free energy values (Table S1). The visual ligand-enzyme interactions were displayed using LigPlot [34].

3.3. Biological Evaluation

3.3.1. General

The purity of the tested compounds is >99% as established by HPLC analysis. The compounds were dissolved in DMSO. All treatments were conducted 24 h after cell seeding in culture medium.

3.3.2. Cell Culture

p53 wild-type (MCF-7 Vector) and silenced version of MCF-7 (MCF-7 shp53) were received from Reuven Agami [17]. HCT116 $p53^{+/+}$ and the derivative $p53^{-/-}$ cell lines were obtained from Bert Vogelstein [19]. All cell lines were cultured in RPMI pH 7.4 (Thermo Fisher Scientific, Waltham, MA, USA) supplemented with 10% Fetal Bovine Serum (Mill Creek, Rochester, MN, USA), 1X L-Glutamine and Pen/Strep (Lonza, Basel, Switzerland) at 37 °C with 5% CO_2 in a humidified atmosphere. For MCF-7, 0.5 μg/mL Puromycin (Sigma Aldrich) was added to the culture medium to maintain selection of the vectors.

3.3.3. Cell Viability Assay (MTT Assay)

For the MTT assay, 5×10^3 cells/100 μL were plated into 96-well tissue culture plates. The day after, cells were treated with medium containing 0.1% DMSO alone or medium containing several concentrations of reversine or analogues (0.01 μM, 0.1 μM, 0.5 μM, 1 μM, 5 μM, 10 μM, 50 μM, 100 μM and 300 μM). After 24 h incubation, cell viability was determined by tetrazolium dye 3-(4,5-dimethylthiazol-2yl)-2,5-diphenyl-2H-tetrazolium bromide (MTT) (5 mg/mL in phosphate buffer saline (PBS); Sigma Aldrich) which was added to fresh medium (final concentration: 0.5 mg/mL). The yellow redox indicator MTT is reduced to a dark blue final product, MTT-formazan, by the mitochondrial dehydrogenases of living cells. Following 1 h-incubation at 37 °C, the medium was discarded and cells were lysed by adding 100 μL DMSO. Finally absorbance was examined at 590 nm wavelength using an Infinite M200 microplate reader (TECAN, Mannedorf, Switzerland). Each experiment has been run in triplicate and results are the merge of three experiments.

3.3.4. Cell Cycle Assay

Cell cycle analysis was performed on at least 30,000 events for each sample with FACSCantoTM A using BD Diva Software 6.1.3 (BD Bioscience, San Jose, CA, USA) and the DNA profile was analyzed by ModFit LT 4.1 (Verity Software House, Topsham, ME, USA). Cells were treated with 0.1% DMSO, 1 μM Reversine or different concentrations of each **1**–**3** (1 μM, 2.5 μM, 5 μM and 10 μM) for 24 h, detached with trypsin-EDTA, collected by centrifugation and washed three times with PBS. Cells were stained with propidium iodide using BD CycletestTM Plus DNA Kit (BD Bioscience) and then analyzed by flow cytometry. Results obtained are the merge of three experiments.

3.3.5. Membrane and Nuclei Staining

After treatments, cultured cells were washed twice with PBS and fixed with 4% formaldehyde/PBS for 20 min at room temperature. After three washes in PBS, cells were stained with Hoechst (Thermo Fisher Scientific, Waltham, MA, USA; 1:10,000) and Cell Mask (Thermo Fisher Scientific, Waltham, MA, USA; 1:10,000) and then visualized with a Zeiss Axio Observer Z1 instrument (Carl Zaiss, Oberkochen, Germany) using Zeiss AxioVision v.4.8.1.

3.3.6. Western Blot

Cells were cultured in 10 cm^2/well and treated with 1 μM reversine or different concentrations of analogues (1 μM, 2.5 μM, 5 μM and 10 μM) for 24 and 96 h. 0.1% DMSO was used as negative control. Cells were detached with trypsin-EDTA, collected by centrifugation and washed with PBS. Samples were then lysed in 150 μL RIPA buffer (Sigma Aldrich) and the proteins were quantified by BCA assay (Thermo Scientific). 15 μg of extracted proteins were loaded on NuPAGETM 4–12% Bis-Tris acrylamide Gel (Thermo Fisher Scientific) and then transferred onto a nitrocellulose membrane using a Tris-Glycine buffer. Blocking was performed overnight with 5% not-fat dry milk, 0.1% TWEENTM and PBS1X. Immunodetection was obtained using the following primary antibodies: p53 (DO1, 1:4000; Santa Cruz Biotechnologies, Dallas, TX, USA) and GAPDH (1:10,000; Santa Cruz Biotechnologies). The secondary antibody used was horse alpha-mouse Human Recombinant Peroxidase (1:10,000; Vector Laboratories, Burlingame, CA, USA). Finally, western blots were analyzed by ECL and detected with ChemiDocTM XRS+ (Bio-Rad, Hercules, CA, USA) using ImageLab software (Bio-Rad).

3.3.7. Statistical Analysis

Data are presented as mean ± SEM of three independent experiments. GraphPad Prism 6 software (GraphPad software, La Jolla, CA, USA) was used and ANOVA test was performed for comparisons. Statistical significance was defined as a p value less than 0.05 in all tests.

4. Conclusions

Based on the known antitumor effects of reversine, we have selected three structurally related molecules, designed as kinase inhibitors, by a docking calculation approach. They are 2,6-diamino substituted purines, two of them characterized by a simpler structure than reversine and easily accessible by synthesis. A first in vitro evaluation showed that molecules **1**–**3** were less cytotoxic than reversine in breast cancer MCF-7 and colorectal HCT116 cancer cell lines. They caused a significant arrest in G2/M phase in a cell-type dependent mode, as HCT116 cells were more responsive than MCF-7. Moreover, in both cancer cell lines, the molecules showed an interesting increased efficacy when p53 was down-regulated. These results have been confirmed by membrane and nuclei staining. In conclusion, these biological experiments suggest that the presence of a *N*-methyl group in position C6 has a decisive role in affecting the activity of the tested molecules. It is clearly evident comparing the structures of **2** and **3**, where the methyl absence in **2** increases its biological effect requiring a lower concentration to cause the mitotic spindle catastrophe in the cell lines tested. A similar behavior was observed also for reversine and its most structurally similar molecule **1**. Based on the findings in this work and on their easily accessible molecular structures, compounds **2** and **3** are worthy of further biological investigations.

Supplementary Materials: The following material is available online at http://www.mdpi.com/1420-3049/23/ /1996/s1: computational details; Table S1: Data from docking calculation by Autodock Vina of reversine and the H*N*(7) and H*N*(9) tautomers of each molecule **1**–**3** with Aurora-B Kinase and Monopolar Spindle 1; Figures S1–S3: NMR spectra ($CDCl_3$) of compounds **1**–**3**; Figure S4: Western Blot to control the presence or absence of p53 in MCF7 and HCT cell lines. Cells were treated with and without doxorubicin; Figure S5: Data for reversine and **1**–**3** which suppressed the growth of human cancer cells; Figure S6: Representative images from analysis of MCF-7 vector and MCF-7shp53 cell cycle after the treatment with different doses of **1**–**3**; Figure S7: Representative images from analysis of HCT116 wt and HCT116 $p53^{-/-}$ cell cycle after the treatment with different doses of **1**–**3**; Figure S8: Nuclei and cell membrane staining on MCF-7 Vector and MCF-7shp53 after **1**–**3** treatments at day 1 and day 4 (Scale bar = 50 μm); Figure S9: Superimposed structures of H*N*(9) tautomers of reversine (green) and molecules 1(red), 2 (magenta) and 3 (blue) in the complexes with Aurora-B kinase (2VGO), as obtained by docking calculation; Figure S10: Superimposed structures of H*N*(7) tautomers of molecules 2 (magenta) and 3 (blue) in the complexes with Aurora-B kinase (2VGO), as obtained by docking calculation.

Author Contributions: B.B., I.M., A.D. and D.S. performed the design, synthesis and structural characterization; A.D. carried out the computational analysis; B.B., S.C., A.M. and T.I. designed the biological experiments; B.B., T.I. and A.B. performed the biological experiments; Y.C. and A.I. contributed to reagents/cell lines; B.B., I.M. and S.C. wrote the paper.

Funding: This research received no external funding.

Acknowledgments: We would like to thank Isabella Pesce and all the Cell Analysis and Separation Core Facility for supervision in the flow cytometry analysis. Thanks to Adriano Sterni and Mario Rossi, Department of Physics for technical support. We are grateful to all members of Neural Development and Regeneration and Molecular Neuropathology laboratories for their support and helpful discussions.

Conflicts of Interest: The authors declare no conflict of interest.

References

1. Anastasia, L.; Pelissero, G.; Venerando, B.; Tettamanti, G. Cell reprogramming: Expectations and challenges for chemistry in stem cell biology and regenerative medicine. *Cell Death Differ.* **2010**, *17*, 1230–1237. [CrossRef] [PubMed]
2. Chen, S.; Zang, Q.; Wu, X.; Schultz, P.G.; Ding, S. Dedifferentiation of lineage committed cells by a small molecule. *J. Am. Chem. Soc.* **2004**, *126*, 410–411. [CrossRef] [PubMed]
3. Anastasia, L.; Sampaolesi, M.; Papini, N.; Oleari, D.; Lamorte, G.; Tringali, C.; Monti, E.; Galli, D.; Tettamanti, G.; Cossu, G.; et al. Reversine-treated fibroblasts acquire myogenic competence in vitro and in regenerating skeletal muscle. *Cell Death Differ.* **2006**, *13*, 2042–2051. [CrossRef] [PubMed]
4. Lee, E.K.; Bae, G.U.; You, J.S.; Lee, J.C.; Jeon, Y.J.; Park, J.W.; Park, J.H.; Ahn, S.H.; Kim, Y.K.; Choi, W.S.; et al. Reversine increases the plasticity of lineage-committed cells toward neuroectodermal lineage. *J. Biol. Chem.* **2009**, *284*, 2891–2901. [CrossRef] [PubMed]
5. Pikir, B.S.; Susilowati, H.; Hendrianto, E.; Abdulrantam, F. Reversine increase the plasticity of bone marrow-derived mesenchymal stem cell for generation of cardiomyocyte in vitro. *Acta Med. Indones.* **2012**, *44*, 23–27. [PubMed]
6. Marumoto, T.; Zhang, D.; Saya, H. Aurora-A—A guardian of poles. *Nat. Rev. Cancer* **2005**, *5*, 42–50. [CrossRef] [PubMed]
7. Hauf, S.; Cole, R.; LaTerra, S.; Zimmer, C.; Schnapp, G.; Walter, R.; Heckel, A.; van Meel, J.; Rieder, C.L.; Peters, J.M. The small molecule Hesperadin reveals a role for Aurora B in correcting kinetochore–microtubule attachment and in maintaining the spindle assembly checkpoint. *J. Cell Biol.* **2003**, *161*, 281–294. [CrossRef] [PubMed]
8. London, N.; Biggins, S. Signalling dynamics in the spindle checkpoint response. *Nat. Rev. Mol. Cell Biol.* **2014**, *15*, 736–748. [CrossRef] [PubMed]
9. Hiruma, Y.; Koch, A.; Dharadhar, S.; Joosten, R.P.; Perrakis, A. Structural basis of reversine selectivity in inhibiting Mps1 more potently than Aurora B kinase. *Proteins Struct. Funct. Bioinf.* **2016**, *84*, 1761–1766. [CrossRef] [PubMed]
10. Piccoli, M.; Palazzolo, G.; Conforti, E.; La-morte, G.; Papini, N.; Creo, P.; Fania, C.; Scaringi, R.; Bergante, S.; Tringali, C.; et al. The synthetic purine reversine selectively induces cell death of cancer cells. *J. Cell. Biochem.* **2012**, *113*, 3207–3217. [CrossRef] [PubMed]
11. Jemaà, M.; Galluzzi, L.; Kepp, O.; Boilève, A.; Lissa, D.; Senovilla, L.; Harper, F.; Pierron, G.; Berardinelli, F.; Antoccia, A.; et al. Preferential killing of p53-deficient cancer cells by reversine. *Cell Cycle* **2012**, *11*, 2149–2158. [CrossRef] [PubMed]
12. D'Alise, A.M.; Amabile, G.; Iovino, M.; Di Giorgio, F.P.; Bartiromo, M.; Sessa, F.; Villa, F.; Musacchio, A.; Cortese, R. Reversine, a novel Aurora kinases inhibitor, inhibits colony formation of human acute myeloid leukemia cells. *Mol. Cancer Ther.* **2008**, *7*, 1140–1149. [CrossRef] [PubMed]
13. Hsieh, T.C.; Traganos, F.; Darzynkiewicz, Z.; Wu, J.M. The 2,6-disubstituted purine reversine induces growth arrest and polyploidy in human cancer cells. *Int. J. Oncol.* **2007**, *31*, 1293–1300. [CrossRef] [PubMed]
14. Santaguida, S.; Tighe, A.; D'Alise, A.M.; Taylor, S.S.; Musacchio, A. Dissecting the role of MPS1 in chromosome biorientation and the spindle checkpoint through the small molecule inhibitor reversine. *J. Cell Biol.* **2010**, *190*, 73–87. [CrossRef] [PubMed]
15. Kuo, C.H.; Lu, Y.C.; Tseng, Y.S.; Shi, C.S.; Chen, S.H.; Chen, P.T.; Wu, F.L.; Chang, Y.P.; Lee, Y.R. Reversine induces cell cycle arrest, polyploidy, and apoptosis in human breast cancer cells. *Breast Cancer* **2012**, *21*, 358–369. [CrossRef] [PubMed]

16. Hua, S.C.; Chang, T.C.; Chen, H.R.; Lu, C.H.; Liu, Y.W.; Chen, S.H.; Yu, H.I.; Chang, Y.P.; Lee, Y.R. Reversine, a 2,6-disubstituted purine, as an anti-cancer agent in differentiated and undifferentiated thyroid cancer cells. *Pharm. Res.* **2012**, *29*, 1990–2005. [CrossRef] [PubMed]
17. Lu, C.H.; Liu, Y.W.; Hua, S.C.; Yu, H.I.; Chang, Y.P.; Lee, Y.R. Autophagy induction of reversine on human follicular thyroid cancer cells. *Biomed. Pharmacother.* **2012**, *66*, 642–647. [CrossRef] [PubMed]
18. Fang, C.Y.; Chen, J.S.; Chang, S.K.; Shen, C.H. Reversine induces autophagic cell death through the AMP-activated protein kinase pathway in urothelial carcinoma cells. *Anti-Cancer Drugs* **2018**, *29*, 29–39. [CrossRef] [PubMed]
19. Gasco, M.; Shami, S.; Cook, T. The p53 pathway in breast cancer. *Breast Cancer Res.* **2002**, *4*, 70–76. [CrossRef] [PubMed]
20. Kumar, D.V.; Hoarau, C.; Bursavich, M.; Slattum, P.; Gerrish, D.; Yager, K.; Saunders, M.; Shenderovich, B.L.; Roth, R.; McKinnon, A.; et al. Lead optimization of purine based orally bioavailable Mps1 (TTK) inhibitors. *Bioorg. Med. Chem. Lett.* **2012**, *22*, 4377–4385. [CrossRef] [PubMed]
21. Perreira, M.; Jiang, J.K.; Klutz, A.M.; Gao, Z.G.; Shainberg, A.; Lu, C.; Craig, J.T.; Jacobson, K.A. Reversine and its 2-substituted adenine derivatives as potent and selective adenosine receptor antagonists. *J. Med. Chem.* **2005**, *48*, 4910–4918. [CrossRef] [PubMed]
22. Raczynska, E.D.; Kaminska, B. Prototropy and p-electron delocalization for purine and its radical ions–DFT studies. *J. Phys. Org. Chem.* **2010**, *23*, 828–835. [CrossRef]
23. Raczyńska, E.D.; Kamińska, B. Variations of the tautomeric preferences and π-electron delocalization for the neutral and redox forms of purine when proceeding from the gas phase (DFT) to water (PCM). *J. Mol. Model.* **2013**, *19*, 3947–3960. [CrossRef] [PubMed]
24. Brummelkamp, T.R.; Bernards, R.; Agami, R. A system for stable expression of short interfering RNAS in mammalian cells. *Science* **2002**, *296*, 550–553. [CrossRef] [PubMed]
25. Sur, S.; Pagliarini, R.; Bunz, F.; Rago, C.; Diaz, L.A.; Kinzler, K.W.; Vogelstein, B.; Papadopoulos, N. A Panel of isogenic human cancer cells suggests a therapeutic approach for cancers with inactivated p53. *Proc. Natl. Acad. Sci. USA* **2009**, *106*, 3964–3969. [CrossRef] [PubMed]
26. Zaccara, S.; Tebaldi, T.; Pederiva, C.; Ciribilli, Y.; Bisio, A.; Inga, A. p53-Directed translational control can shape and expand the universe of p53 target genes. *Cell Death Differ.* **2014**, *21*, 1522–1534. [CrossRef] [PubMed]
27. Sato, K.; Ohta, T.; Venkitaraman, A.R. A mitotic role for the DNA damage responsive CHK2 kinase. *Nat. Cell Biol.* **2010**, *12*, 424–425. [CrossRef] [PubMed]
28. Lukin, D.J.; Carvajal, L.A.; Liu, W.; Silverman, L.R.; Manfredi, J.J. p53 Promotes cell survival due to the reversibility of its cell cycle checkpoints. *Mol. Cancer Res.* **2015**, *13*, 16–28. [CrossRef] [PubMed]
29. Frisch, M.J.; Trucks, G.W.; Schlegel, H.B.; Scuseria, G.E.; Robb, M.A.; Cheeseman, J.R.; Montgomery, J.A.; Vreven, T., Jr.; Kudin, K.N.; Burant, J.C.; et al. *Gaussian*; Revision E.01; Gaussian, Inc.: Wallingford, CT, USA, 2004.
30. Becke, A.D. Density-functional thermochemistry. III. The role of exact exchange. *J. Chem. Phys.* **1993**, *98*, 5648–5652. [CrossRef]
31. Lee, C.; Yang, W.; Parr, R.G. Development of the Colle-Salvetti correlation-energy formula into a functional of the electron density. *Phys. Rev. B* **1988**, *37*, 785–789. [CrossRef]
32. Trott, O.; Olson, A.J. AutoDock Vina: Improving the speed and accuracy of docking with a new scoring function, efficient optimization, and multithreading. *J. Comp. Chem.* **2010**, *31*, 455–461. [CrossRef] [PubMed]
33. Filippakopoulos, P.; Soundararajan, M.; Keates, T.; Elkins, J.M.; King, O.; Fedorov, O.; Picaud, S.S.; Pike, A.C.W.; Yue, W.; Chaikuad, A.; et al. Small-molecule kinase inhibitors provide insight into Mps1 cell cycle function. *Nat. Chem. Biol.* **2010**, *6*, 359–368. [CrossRef]
34. Laskowski, R.A.; Swindells, M.B. LigPlot+: Multiple ligand–protein interaction diagrams for drug discovery. *J. Chem. Inf. Model.* **2011**, *51*, 2778–2786. [CrossRef] [PubMed]

Sample Availability: Samples of the compounds **1**, **2** and **3** are available from the authors.

© 2018 by the authors. Licensee MDPI, Basel, Switzerland. This article is an open access article distributed under the terms and conditions of the Creative Commons Attribution (CC BY) license (http://creativecommons.org/licenses/by/4.0/).

MDPI AG
Grosspeteranlage 5
4052 Basel
Switzerland
Tel.: +41 61 683 77 34

Molecules Editorial Office
E-mail: molecules@mdpi.com
www.mdpi.com/journal/molecules

Disclaimer/Publisher's Note: The title and front matter of this reprint are at the discretion of the Guest Editor. The publisher is not responsible for their content or any associated concerns. The statements, opinions and data contained in all individual articles are solely those of the individual Editor and contributors and not of MDPI. MDPI disclaims responsibility for any injury to people or property resulting from any ideas, methods, instructions or products referred to in the content.

Academic Open
Access Publishing

mdpi.com

ISBN 978-3-7258-8316-5